Partitioning of Radar Signals in Stationary and Ground Moving Targets by use of Low-Rank and Compressed Sensing Methods

DISSERTATION
to obtain the degree of
Doctor of Engineering

submitted by
Dipl.-Ing. Reinhard Panhuber

submitted to the School of Science and Technology
of the University of Siegen
Siegen 2022

Supervisor and first appraiser
Prof. Dr.-Ing. Joachim Ender
University of Siegen

Second appraiser
Prof. Dr.-Ing. habil. Michael Schmitt
Universität der Bundeswehr München

Date of the oral examination
28. November 2022

Declaration

I hereby declare that except where specific reference is made to the work of others, the contents of this dissertation are original and have not been submitted in whole or in part for consideration for any other degree or qualification in this, or any other university. This dissertation is my own work and contains nothing which is the outcome of work done in collaboration with others, except as specified in the text and Acknowledgments.

Wachtberg, 7.12.2022

Reinhard Panhuber

Humor ist das Salz des Lebens und wer gut gesalzen ist,
bleibt lange frisch.

— Karel Čapek

Dedicated to Theresa, Toni, Henry, and all who will follow.

Die lohnendsten Forschungen sind diejenigen,
welche, indem sie den Denker erfreu'n,
zugleich der Menschheit nützen

— Christian Doppler

Acknowledgments

This research would not be possible without the support I have received during the last couple of years. A sincere thank you goes to my supervisors in Siegen university:

Prof. Ender, for his guidance, availability and readiness for questions. His contribution to my research and to the radar community is invaluable.

Prof. Loffeld, for his sharp comments and assistance within the university. Unfortunately, it was not granted to him to witness the completion of this work.

I would like to say a sincere thank you to Prof. Dr.-Ing. habil. Michael Schmitt from the Bundeswehr University Munich who stepped in as a appraiser for Prof. Loffeld and made it possible for me to complete this thesis.

I would also like to thank my co-workers and managers in Fraunhofer FHR:

My team leader, Dr. Ludger Prünte. Our discussions and his original point of view, were always important. His efforts to provide the needed working environment for my thesis are highly appreciated.
My colleagues, especially Oliver Biallawons and Rudolf Hoffmann, for always being there with good advice, comments, and friendly help.
My heads of department, Dr. Brenner and Dr. Bürger for always encouraging my scientific endeavors, and supporting the PhD process within the department.
A special thank you goes to Christoph Reising for his extraordinary effort to make this work understandable for the rest of mankind.

I deeply thank my family: My parents, for their unwavering willingness to help, and for being a pillar of stability and trust in my life.

My wife, for her immense support during this research and for her endurance in keeping me free of obligations by taking care of the kids. Otherwise, i would never have been able to complete this work. Unknowingly, she is the true hero behind this PhD.

Abstract

The aim of this thesis is to develop an approach which evades the most fundamental short coming of space-time adaptive processing (STAP): its need for training data. STAP is the state-of-the-art approach for conducting ground moving target indication (GMTI). Among other things, an extensive amount of research was conducted in the recent decades to reduce its computational complexity or the required amount of training data. However, non has been done to avoid it completely. In doing so and using measurement data from the current cell under test (CUT) alone, most short comings can be avoided as there are: clutter residuals from not sufficiently suppressed clutter contributions and target masking or self-nulling. This is advantageous in case of heterogeneous busy environments e. g. urban areas. This work presents the first approach to do so for which compressive sensing (CS) and affine rank minimization (ARM) techniques are used. By exploiting the correlated nature of GMTI clutter signals a low rank matrix can be formed from the measurement matrix corresponding to the CUT. This is done by focusing the clutter ridge in the angle-Doppler domain a. k. a. radar scene. Moving targets sparsely present in the radar scene are invariant with respect to the focus operation i. e. they remain sparse. The focused radar scene therefore renders to be the sum of a low rank and a sparse matrix which can be separated by use of an compressed robust principal component analysis (CRPCA) approach. The aim after separation is the low rank matrix to contain all clutter contributions and the sparse matrix to hold all moving targets. As a prerequisite for this to work, however, the so called rank sparsity incoherence condition must be met. Among other things this means that the low rank matrix must not contain spiky entries. This is not fulfilled as the clutter ridge by its very nature is spiky. To mitigate this issue a model based projection filter is applied onto the measurement data as a preconditioning step. The required parameters of the model projection filter are estimated during the clutter focused operation. Depending on the quality of the estimated parameters, all clutter energy is suppressed in the preconditioning step resulting the low rank matrix to be empty. In case the preconditioning step is not able to suppress all clutter contributions, the clutter residuals are usually of non spiky nature allowing to apply the aforementioned CRPCA separation. In summary, this is a three step approach for which an auto-clutter focus (ACF) algorithm, a model based projection filter, and an CRPCA based separation model are presented in this work. With them it is possible to separate strictly static from moving targets. As such effects like internal clutter motion are not covered and are subject to future research. The approach is evaluated thoroughly by use of a simulation model. As mentioned before this work is based on CS and ARM techniques. Most standard methods from the literature, however, do not consider the practical needs of radar signal processing e. g. they suffer from restrictions to real numbers, slow convergence rate, low reconstruction performance, or knowledge of unknown parameters like the precise number of sparse entries or the exact rank of a low rank matrix. Therefore, various CS and ARM algorithms are combined and extended in this work to comprise a set of

high performative CS, ARM, and CRPCA algorithms which do not suffer the aforementioned restrictions. In summary, the work presented here represents a completely new approach to solving the GMTI problem. Nevertheless, as GMTI renders to be a complex task further research is needed with regard to a practical application.

Zusammenfassung

Das Ziel dieser Arbeit ist es, einen Ansatz zu entwickeln, der die grundlegendste Schwachstelle von space-time adaptive processing (STAP) vermeidet: die Notwendigkeit von Trainingsdaten. STAP ist der modernste Ansatz zur Detektion von sich relativ zur Erdoberfläche bewegenden Zielen, besser bekannt als ground moving target indication (GMTI). In den letzten Jahrzehnten wurde unter anderem viel geforscht, um die Komplexität der Berechnungen oder die erforderliche Menge an Trainingsdaten für STAP zu verringern. Es wurde jedoch nichts unternommen, um sie vollständig zu vermeiden. Auf diese Weise und bei Verwendung von Messdaten der cell under test (CUT) alleine, ist es jedoch möglich die größten Nachteile von STAP zu vermeiden. Diese wären: Clutter-Residuale von nicht ausreichend unterdrückten Clutter-Beiträgen und Zielmaskierung. Dies ist vor allem in heterogenen und stark frequentierten Umgebungen, z. B. in städtischen Gebieten, von Vorteil. In dieser Arbeit wird ein erster Ansatz vorgestellt, bei dem compressive sensing (CS) und affine rank minimization (ARM) Techniken zum Einsatz kommen. Durch Ausnutzung der starken Korrelation von GMTI Clutter-Signalen, wird aus der Messmatrix einer CUT eine Matrix niedrigen Ranges geformt. Dies erfolgt durch Fokussierung der sogenannten Clutter-Ridge in der Winkel-Doppler-Domäne bzw. Radarszene. Bewegtziele, die in der Radarszene nur spärlich vorhanden sind, sind gegenüber der Fokussierungsoperation unveränderlich, d. h. sie bleiben spärlich. Die fokussierte Radarszene kann daher als Summe einer dünn besetzen Matrix und einer Matrix niedrigen Ranges formuliert werden, welche mittels eines compressed robust principal component analysis (CRPCA) Ansatzes separiert werden können. Nach der Separation sollen alle Cluttersignalanteile in der Matrix niedrigen Ranges und alle Bewegtziele in der dünn besetzen Matrix enthalten sein. Eine Voraussetzung dafür ist jedoch die sogenannte Rank-Sparsity-Inkohärenzbedingung. Unter anderem bedeutet dies, dass die Matrix niedrigen Ranges ansatzweise homogen in ihrer Amplitude verteilt sein muss. Diese Voraussetzung ist jedoch nicht gegeben, da die Clutter-Ridge als solche große Amplituden im Vergleich zu ihren Nebenzipfel aufweist. Um dieses Problem zu entschärfen, wird ein modellbasiertes Projektionsfilter als Vorstufe auf die Messdaten angewendet. Die dafür benötigten Parameter werden während des Fokussierungsprozesses geschätzt. Je nach Qualität der geschätzten Parameter wird die gesamte Clutterenergie bereits im Vorkonditionierungsschritt unterdrückt, was dazu führt, dass die niederrangige Matrix nahezu leer ist. Falls die Vorkonditionierung nicht in der Lage ist, alle Clutter-Beiträge zu unterdrücken, sind die Clutter-Reste in der Regel jedoch nicht mehr heterogen verteilt, so dass die oben beschriebene Separation mittels CRPCA angewendet werden kann. In Summe handelt es sich um einen dreistufigen Ansatz, für den in dieser Arbeit ein auto-clutter focus (ACF)-Algorithmus, ein modellbasierter Projektionsfilter und ein CRPCA-basiertes Trennmodell vorgestellt werden. Damit ist es möglich, rein statische von bewegten Zielen zu trennen. Andere Effekte wie z. B. Clutte-reigenbewegungen werden jedoch nicht erfasst und sind Gegenstand künftiger Forschung. Der Ansatz wird mit Hilfe eines Simulationsmodells gründlich evaluiert. Wie bereits erwähnt, basiert

diese Arbeit auf CS- und ARM-Techniken. Die meisten Standardmethoden aus der Literatur berücksichtigen jedoch nicht die praktischen Bedürfnisse der Radarsignalverarbeitung, z. B. leiden sie unter der Beschränkung auf reelle Zahlen, einer langsamen Konvergenzrate, einer geringen Rekonstruktionsleistung oder der Kenntnis unbekannter Parameter, wie der genauen Anzahl der Einträge in der dünn besetzten Matrix oder des exakten Rangs der niederrangigen Matrix. Daher werden in dieser Arbeit verschiedene CS- und ARM-Algorithmen kombiniert und erweitert, um eine Reihe leistungsfähiger CS-, ARM- und CRPCA-Algorithmen zu schaffen, die nicht unter den oben genannten Einschränkungen leiden. Die hier vorgestellte Arbeit stellt einen völlig neuen Ansatz zur Lösung des GMTI-Problems dar. Da sich GMTI jedoch als komplexe Aufgabe erweist, sind weitere Forschungen im Hinblick auf eine praktische Anwendung erforderlich.

Contents

1. Introduction

The flooding in the western part of Germany in the year 2021 were devastating. Heavy local rain showers with extreme intensity of $150\,\mathrm{l/m^2}$ per minute caused small streams to swell into raging floods. Thousands of houses were flooded and entire streets were washed away. The highway A1 near Erftstadt was washed out and became impassable. The telecommunications network collapsed, leaving many localities cut off from the outside world. Organizing and coordinating emergency services in such a situation renders to be a challenging task. In order to get such situations under control, an up-to-date situation report is required. Among the many possibilities to obtain such, ground moving target indication (GMTI) is a convenient approach to help acquiring situational awareness.

The aim of GMTI is to detect targets moving relative to the earth surface and to estimate their positions, velocities, and moving directions. Like many other developments in the field of radar technology, GMTI was first used for military purpose. It allows to build up situational awareness of a region i. e. it answers questions such as: Are there moving entities? Where? How fast? How many? When did it start? From where did they come and where are they going? This type of information is not only of interest for military purposes but also for civilian traffic applications e. g. monitoring of shipping routes or building up situational awareness in case of natural disasters like flooding or earth quakes. Which directions are survivors heading, which roads are still usable or where are aid convoys progressing? Among the many possibilities to acquire it, GMTI has its own particular advantages. Compared to alternative sensors like cameras, infra-red sensors, light detection and ranging (LIDAR), ground personnel with global positioning system (GPS) and communication equipment etc., radar is not affected by rain or fog and is able to cover wide areas providing real time updates. Since it is self illuminating it also works at night and can be quickly deployed anywhere. However, there is no free lunch. These benefits are accompanied with high technical effort as for GMTI a fully coherent multichannel air- or spaceborne radar front end along with a high performance processing back end is required. The resulting high costs explain the initially purely military driven application and development of GMTI. The technological progress and the involved miniaturization and cost reduction, however, also allows for civil applications and developments. Especially recent advancements in 5G communication equipment benefit radar development. Full digital front ends become a mass product allowing for an increased number of available channels in GMTI systems. What used to be the question of how to run GMTI with as few channels as possible will soon be the question of what to better with so many channels that will be available. Technically, GMTI includes the case of a stationary radar, yet commonly, GMTI is conducted from moving platforms like airplanes, drones, or satellites. The principal challenge of GMTI therefore is to find targets which are moving relative to the earth surface, where in turn the earth surface itself is also moving relative to the air- or spaceborne radar system. The undesired radar echoes of the earth surface, also called clutter, as well as the moving targets

render to be of non stationary nature with respect to the radar system. The key question now is, how to suppress the undesired moving signal part from the desired one? The signal processing state-of-the-art approach used to do so undoubtedly is space-time adaptive processing (STAP). Initially developed in 1968 it still is a very active research topic. In its very essence, STAP forms an optimal filter to suppress all clutter contributions from the received signal by use of training data. Every signal component contained within the training data will be filtered out. In order for the STAP approach to work, there are the following requirements to the training data:

- sufficient data is available
- same clutter signal structure or statistic as the cell under test (CUT)
- no moving target within training data.

Violating the first two prerequisites results in non sufficiently suppressed clutter signals called clutter residuals. A violation of the latter requirement results in target masking or target self nulling as the STAP filter gets trained to also suppress moving target signal components. In case all requirements can be fulfilled, STAP is an optimal approach to use. It does not need any information about the measurement process e.g. any information about the antenna configuration, pulse repetition frequency (PRF), antenna beam width, radar velocity and orientation etc. Everything is learned from the training data at hand. The big question now is where to get it? There is no other alternative than to take it from surrounding range gates of the CUT and to hope it will meet all aforementioned requirements. The success of this approach certainly depends on the deployment area. In regions of homogeneous landscape e.g. big fields, grasslands, steppes, deserts, sea etc. enough training data certainly will be available. However, when it comes to heterogeneous regions e.g. if land-sea junctions, mountains, big buildings, or wanes are present it is likely that the first two stated requirements cannot be fulfilled. The research efforts conducted in the recent decades try to mitigate the results of violated requirements. The primary objective was to reduce the amount of required training data. The main reason this was done, however, was not to robustify STAP regarding heterogeneous clutter environments. Rather, the mathematically optimal form of STAP requires a large number of training data. A direct consequence is a very high computational burden. Since processing power was historically rather limited, much effort was done to develop sub optimal STAP approaches with the aim to reduce it. As a result a plethora of algorithms emerged ranging from training data independent methods like most notably Post-Doppler-STAP to data dependent methods e.g. sub space methods. The interested reader may refer to [1] for a good overview. Some more sophisticated approaches incorporate knowledge of the measurement process. An interesting approach is the space-time autoregressive (STAR) algorithm which models the measurement process as an auto-regressive one. This can be done since clutter measurements are of correlated nature. By super imposing a multidimensional finite impulse response (FIR) filter structure on the sample process the number of required training data can be reduced dramatically. Another example is Kronecker-STAP which exploits the fact that the clutter covariance matrix is of low rank nature and can be formulated by use of a Kronecker product. This again reduces the required number of training samples. Nevertheless, a common necessity among all approaches is the need for training data. As such, the consequences when violating the accompanying requirements are still present. A common

procedure when conducting research is to apply every newly emerging signal processing framework onto old problems and to look if any improvement is achievable. In this very manner the approaches presented in this work were developed. The signal processing framework at hand is compressive sensing (CS) and affine rank minimization (ARM) developed in 2004. From a linear algebra point of view, CS and ARM allow to find unique solutions to under determined linear equation systems given they are either of sparse or low rank nature. Another point of view is that CS and ARM try to directly find the inverse image corresponding to a linear mapping rather than using a pseudo-inverse mapping. CS and ARM are formulated as optimization problems, where in case of CS the number of non zero entries within the solution a. k. a. sparsity and in case of ARM the rank of the solution is minimized. The traditionally used minimum least-square solution renders to be the Moore-Penrose pseudo-inverse. CS and ARM techniques are applied with great successes in many fields e.g. image processing, hyperspectral imaging, control engineering, radar signal processing, etc. The interested reader may refer to [1] for a collective overview. Beside CS and ARM, another extremely popular signal processing framework must of course be mentioned, namely neural networks and their variants. Researchers everywhere try to solve every problem what so ever by use of neural networks. Their charm consists of the fact that there is no need to have any understanding of the problem to be solved. The neural network approach solves the problem on its own, nearly no expertize is needed from the creator. The only thing left to do is to select the architecture of the network e.g. how many layers, convolutional layers, fully connected layers, which type of activation function etc. Quiet frankly, even this procedure renders to be of trial and error nature as up to now no real knowledge of how these networks internally work is available. The only but most striking requirement is to posses enough training data which covers every possible manifestation occurring in the deployed environment. At its core, a neural network is be a multidimensional non linear function. In case a rectified linear unit (ReLU) function is used as activation function, it is a piecewise linear function. The shape of this function is formed by fitting it to the training data and its corresponding desired output values a.k.a training. Neural networks are highly flexible and able to adapt to many input- output relations. They are celebrating unbelievable successes in areas where sufficient training data is available. In case of image, audio, and video processing overwhelmingly big data sets are available. Other areas are well controllable e.g. in the field of control engineering, machine monitoring, or medical diagnosis. Unfortunately, large data sets are not available in the field of GMTI, nor is the environment well controlled. A pure GMTI-neural network (NN) approach therefore seems questionable. An interesting approach, however, is deep unfolding. The idea behind this approach is that it is possible to unroll an iterative algorithm with a fixed number of iterations, e.g. one that solves a CS or ARM problem, into layers similar to a NN. The individual layers are connected by a number of trainable parameters. In case of gradient descent algorithms, those parameters might be regularization coefficients or step sizes. These can now be trained by the NN approach to be optimal in every former iteration step or now layer rather than be constant and hand trimmed or set by pessimistic boundaries given by e.g. Lipschitz constants. The deep unfolding approach combines the benefits of both worlds, the modeling of the measurement process as well as trainable reconstruction algorithms. This seems to be a promising research direction for future GMTI approaches. Needless to say, being able to start with deep unfolding some adequate measurement process

model needs to be found. In this work, an attempt is made to evade STAPs fundamental problem: the need for training data. The key idea in this work is to exploit the correlated nature of the clutter signal to form a low rank matrix. This is done by focusing the so called clutter ridge in the angle-Doppler domain, also called radar scene within this work, for which an auto-clutter focus (ACF) algorithm was developed. Sparse moving targets in the radar scene are invariant with respect to the focus operations i.e. they stay sparse. The focused scene can therefore be modeled as the sum of a sparse and a low rank matrix, where the sparse matrix holds all moving targets and the low rank matrix all clutter contributions. This sum may now be separated by use of an compressed robust principal component analysis (CRPCA) approach. Unfortunately, this is not possible directly. For a successful separation to work, the so called rank sparsity incoherence condition must be fulfilled. Among other things this means that the low rank matrix must not contain spiky entries. The clutter ridge, however, is by its very nature extremely spiky. Therefore, an intermediate preconditioning step is introduced. Using a model based projection filter a major part of the clutter energy is filtered out before the separation is performed. In the best case, all clutter energy is reduced in the preconditioning step. If clutter residuals occur, those remain to be of non spiky nature and as such may be separated by use of the CRPCA approach. The approaches will be evaluated extensively by use of numerical simulations. The aforementioned approaches build upon CS, ARM, and CRPCA algorithms. However, common algorithms from the literature are not do not consider the practical needs of radar signal processing e. g. they suffer from restrictions to real numbers, slow convergence rate, low reconstruction performance, or knowledge of unknown parameters like the precise number of sparse entries or the exact rank of a low-rank matrix.

The major contributions of this work to radar signal processing therefore are:

- combine and extend CS and ARM algorithms to comprise a set of high performative CS, ARM, and CRPCA algorithms
- development of an ACF algorithm, a model based projection filter, and an CRPCA based separation approach to separate static from moving targets.

A more detailed list of the developed contributions can be found in the conclusions.

The approaches developed in this work are illustrated and evaluated by means of a simulation model assuming a uniform linear array (ULA) and a flat earth scenario. Further corresponding simulation parameters are listed in Tab 1.0.1. They corresponds to a common airborne GMTI system.

This work is organized as follows: in the following Chapter 2, the radar signal model and rigorous justifications for the usually assumed simplifications applied in the GMTI case are derived. Furthermore, STAP is introduced in brevity. Chapter 3 to 5 presents brief introductions of the CS, ARM, and robust principal component analysis (RPCA) approaches. Chapter 6 presents the improved CS, ARM, and RPCA algorithms. Chapter 7 presents the application of CS and ARM algorithms onto GMTI. Finally, Chapter 8 concludes this work with a summary, conclusion, and an outlook.

Parameter	Symbol	Value
# transmit (TX) Channels	N_{tx}	1
# receive (RX) Channels	N_{rx}	32
# Pulses	N_{p}	64
Wave Form	-	LFM chirp
Center Frequency	f_{c}	10 GHz
Bandwidth	b_{r}	15 MHz
PRF	f_{p}	3 kHz
Element Antenna Pattern	$G_{\mathrm{tx}}\left(\vec{u}\right)$, $G_{\mathrm{rx}}\left(\vec{u}\right)$	cos-Pattern
Element antenna beam width (ABW)	ABW	10°
Maximum Target Velocity	$v_{\mathrm{t,max}}$	55 m/s
Maximum Platform Velocity	$v_{\mathrm{p,max}}$	130 m/s
Platform Height	h_{p}	10 km
Minimum Slant Range	r_{min}	10 km
Maximum Slant Range	r_{max}	100 km

Table 1.0.1.: Air-borne GMTI scenario parameters.

2. Fundamentals of Ground Moving Target Indication

All subsequent signal models of e. g. clutter or target signals are modeled as a superposition of general point targets. The specification from a point to a target or clutter signal is usually done by imposing additional parameters e. g. some random reflectivity coefficient etc. Hence, it is convenient to first introduce a general radar point target signal model which is done in Section 2.1. The specification to clutter signals is presented in Section 2.2, which shows some valuable insights into the nature of clutter signals. These come in handy when a dictionary for clutter signals is set up in Chapter 7. With known signal models for targets and clutter, the space-time adaptive processing (STAP) approach and the need for a 2D processing in space and time is presented in Section 2.3. Finally, Section 2.3.5 elaborates on the limitations on STAP which motivates the new approaches presented in this work.

2.1. Radar System Description

In this section the radar signal models used for ground moving target indication (GMTI) processing are derived briefly. These models are valid only for given assumptions which usually hold for the GMTI case e. g. that targets do not move considerably during the measurement process[1]. In order to be able to tell if a signal model for a given assumption is valid, a general non-relativistic description for a radar signal corresponding to an arbitrarily moving target is introduced at first. Thereafter, common approximations considerably simplifying the general signal description are presented which eventually yield the signal models applied in the GMTI case. It is assumed that the reader is familiar with common radar processing steps e. g. a matched filter (MF), ambiguity functions etc. as these are used throughout this work. In case more details of these steps are desired, the interested reader may refer to excellent text books e. g. [2].

The general radar transmit and receive scheme is shown in Fig. 2.1.1, for which all signals are defined as complex signals as this allows for short mathematical manipulations. The intended transmit (TX) signal s_{tx} is of arbitrary choice but taken to be symmetrically centered at zero Hz. It undergoes a sequence of common filter and amplification steps denoted by the base band transfer function $H_{\mathrm{b,tx}}$, followed by an up conversion into the pass band or radio frequency (RF) band, respectively. The conversion process is not discussed in detail here. The interested reader may look into quadrature modulation or any other sophisticated conversion scheme [3]. Instead, the up conversion is modeled by ideal mixers i. e. no side bands else than the desired pass band emerge. Therefore, the signal is subject to a simple frequency shift of ω_{c} and phase offset ϕ_{up}.

[1] This means the targets appear quasi-static during one pulse and do not move considerably during one coherent processing interval (CPI). This is commonly known as stop-and-go approximation.

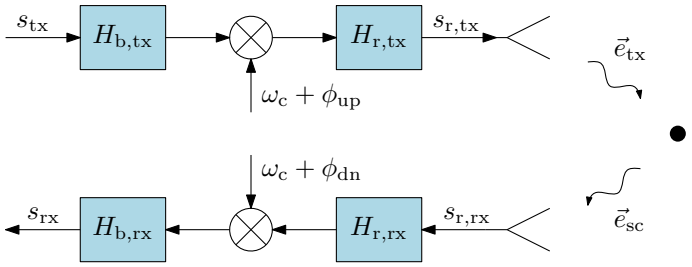

Figure 2.1.1.: General radar transmit and receive scheme.

Further common filter and amplification steps in the pass band are represented by the transfer function $H_{\mathrm{r,tx}}$. At this point, if desired, physically real signals are obtained from the analytic band pass signal $s_{\mathrm{r,tx}}$ by taking its real part. The electromagnetic (EM) wave $\vec{e}_{\mathrm{tx}}$ transmitted by the TX antenna and the scattered wave $\vec{e}_{\mathrm{sc}}$ received by the receive (RX) antenna are described in more detail in Section 2.1.1. In a similar manner to the transmit scheme, the received signal $s_{\mathrm{r,rx}}$ is amplified and filtered described by the transfer functions $H_{\mathrm{r,rx}}$ and $H_{\mathrm{b,rx}}$ and down converted by an ideal mixer, for which a different phase offset ϕ_{dn} is possible. The final received signal usable for signal processing is denoted as s_{rx}. Interestingly, it cannot be expected to be centered around zero Hz due to possible target motion induced Doppler shifts.

Unlike what is presented in many text books, the received signal s_{rx} cannot generally be described as a time-delayed echo of the intended transmitted signal s_{tx}. Next to the obvious influence of the TX and RX paths, also the target parameters have a major influence on the received signal form. In the following section, the general non-relativistic radar process for an arbitrarily moving point target is presented. In Section 2.1.3, common approximations and their validity are discussed. Finally, Section 2.1.4 discusses the space-time signal model required for GMTI applications.

2.1.1. The General Non-Relativistic Radar Process

The general radar setup for one TX and RX antenna pair is depicted in Fig. 2.1.2, where x, y, and z denote the coordinate axes in the antenna reference frame. In principle, an EM wave emitted from a TX antenna located at position $\vec{q}$ gets scattered from a point target located at position $\vec{r}$ and received by an RX antenna located at position $\vec{p}$. The location of the point target is commonly described in the spherical coordinates $\begin{bmatrix} r & \varphi & \vartheta \end{bmatrix}^{\mathrm{T}}$ with respect to the antenna frame, where $r = \|\vec{r}\|$ denotes the range, $\varphi \in [-\pi, \pi)$ the azimuthal, and $\vartheta \in [0, \pi]$ the polar angle. The velocity vectors $\vec{v}_{\mathrm{p}}$ and $\vec{v}_{\mathrm{t}}$ indicate the platform and target velocity, however, relative to the earth surface fixed reference frame. In the antenna frame the resulting velocity vector is therefore $\vec{v}_{\mathrm{t}} - \vec{v}_{\mathrm{p}}$. Furthermore, θ and ψ denote the angles between the line of sight (LOS) vector $\vec{u}$ and the antenna x and y axis. The LOS vector can be expressed in the antenna coordinates as

$$\vec{u} = \frac{\vec{r}}{r} = \begin{bmatrix} \sin(\vartheta)\cos(\varphi) \\ \sin(\vartheta)\sin(\varphi) \\ \cos(\vartheta) \end{bmatrix}$$

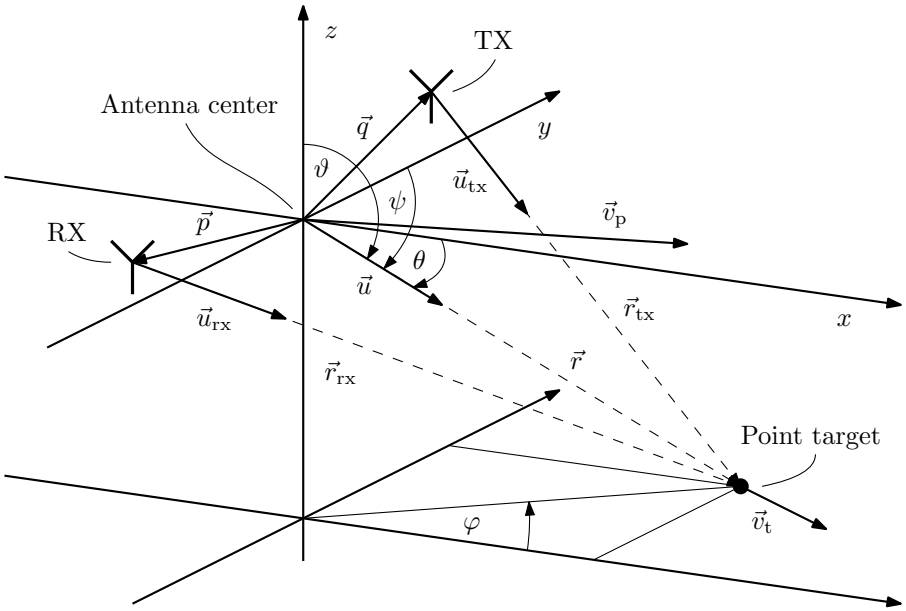

Figure 2.1.2.: General radar geometry in the antenna reference frame.

or likewise as

$$\vec{u} = \begin{bmatrix} \cos(\theta) \\ \cos(\psi) \\ \cos(\vartheta) \end{bmatrix} = \begin{bmatrix} u \\ v \\ w \end{bmatrix}.$$

For the assumed flat earth GMTI case, θ a. k. a. cone angle and its directional cosine u are of special interest which will be explained in more detail in Section 2.2. Furthermore,

$$\vec{r}_{\mathrm{tx}} = \vec{r} - \vec{q}$$
$$\vec{r}_{\mathrm{rx}} = \vec{r} - \vec{p}$$

denote the target location with respect to the TX and RX antenna positions and

$$\vec{u}_{\mathrm{tx}} = \frac{\vec{r}_{\mathrm{tx}}}{r_{\mathrm{tx}}}$$
$$\vec{u}_{\mathrm{rx}} = \frac{\vec{r}_{\mathrm{rx}}}{r_{\mathrm{rx}}}$$

the corresponding LOS vectors with $r_{\mathrm{tx}} = \|\vec{r}_{\mathrm{tx}}\|$ and $r_{\mathrm{rx}} = \|\vec{r}_{\mathrm{rx}}\|$.

In the following, a general description of the emerging radar signal is derived. For this, the radar is assumed to be stationary while the target is moving. To begin with, it is necessary to recognize that the transmit and receive process need to be considered separately. During the transmit process, the point target experiences a phase modulated version of the transmitted radar signal induced by the point targets motion. This is known as the Doppler effect for a stationary source and a moving receiver which is the point target in this case. During the receive process, the point target appears as a moving source radiating a wave whose phase was determined by the first Doppler effect. The radiated wave is again subject to a motion induced phase modulation. This is known as the Doppler effect corresponding to a moving source and a stationary receiver.

Hence, the Doppler effect occurs twice, once for transmit and once for the receive process. This physical fact is ignored by most radar signal derivations which only consider one time delayed signal.

The determination of an arbitrary radar signal is done conveniently by decomposing it into its harmonic components and synthesize them at the points of interest. Unfortunately, due to motion induced phase variation i. e. a time dependent Doppler effect, no closed form solution for the finally received signal can be given as will be seen later. Nevertheless, well known results can be derived from them for common assumptions made e. g. stop and go conditions etc. which will be presented later. To the contrary of other derivations directly arriving at these simplified results, statements can be made when these are permissible.

The time sequence of the transmit and receive process is illustrated in Fig. 2.1.3. Let t'', t', and t denote the corresponding times at which the EM wave was transmitted by the TX antenna, scattered at the point target, and finally received by the RX antenna.

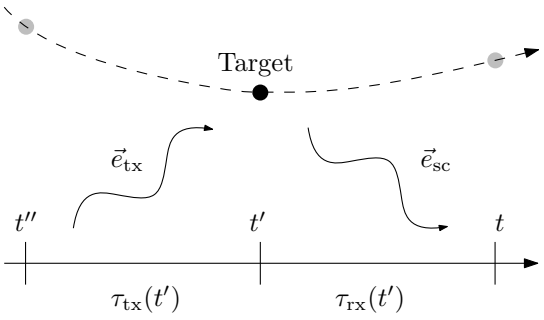

Figure 2.1.3.: General time sequence of the scatter process.

Furthermore, let

$$\tau_{\mathrm{tx}}\left(t'\right) = t' - t'' = \frac{r_{\mathrm{tx}}\left(t'\right)}{c_0} \tag{2.1.1}$$

be the transmit delay,

$$\tau_{\mathrm{rx}}\left(t'\right) = t - t' = \frac{r_{\mathrm{rx}}\left(t'\right)}{c_0} \tag{2.1.2}$$

the receive delay, and

$$\tau\left(t'\right) = \tau_{\mathrm{rx}}\left(t'\right) + \tau_{\mathrm{tx}}\left(t'\right) \tag{2.1.3}$$

be the total round trip delay time (RTDT) [4]. Note, that these inherently depend on the distances to the point target at t', the scatter point in time. Next, let the transmit signal be a burst of consecutive pulses defined as

$$s_{\mathrm{tx}}\left(t''\right) = \sum_{n_{\mathrm{p}}=0}^{N_{\mathrm{p}}-1} s_{\mathrm{tx},n_{\mathrm{p}}}\left(t'' - n_{\mathrm{p}} t_{\mathrm{p}}\right), \tag{2.1.4}$$

where N_{p} denotes the number of pulses emitted within a CPI, t_{p} the pulse repetition interval (PRI), and

$$s_{\mathrm{tx},n_{\mathrm{p}}}\left(x\right) = \mathrm{rect}\left(x/T_{\mathrm{p}}\right) a_{\mathrm{tx},n_{\mathrm{p}}}\left(x\right) \mathrm{e}^{\mathrm{j}\phi_{\mathrm{tx},n_{\mathrm{p}}}(x)} \tag{2.1.5}$$

the n_{p}-th pulse wave form with T_{p} denoting the pulse length, $a_{\mathrm{tx},n_{\mathrm{p}}}\left(x\right)$ an amplitude and

$\phi_{\mathrm{tx},n_\mathrm{p}}(x)$ a corresponding phase modulation. Furthermore, $s_{\mathrm{tx},n_\mathrm{p}}(x)$ is taken to be a band limited base band signal of bandwidth b_r. The derivation of the received radar signal is considerably easier if the signals are treated by use of their harmonics. Assuming the radar system is linear with respect to $s_\mathrm{tx}(t'')$, this can be achieved by use of the inverse Fourier transform (IFT) as

$$s_\mathrm{tx}(t'') = \frac{1}{2\pi} \int_{-\pi b_\mathrm{r}}^{\pi b_\mathrm{r}} S_\mathrm{tx}(\omega_\mathrm{b})\, \mathrm{e}^{\mathrm{j}\omega_\mathrm{b} t''} \mathrm{d}\omega_\mathrm{b},$$

where $\omega_\mathrm{b} = 2\pi f_\mathrm{b}$ is the angular base band frequency and $S_\mathrm{tx}(\omega_\mathrm{b})$ is the Fourier transform (FT) of (2.1.4). Hence, the radar signal can be calculated by a superposition of its complex harmonic signal components

$$s_\mathrm{b,tx}(t'', \omega_\mathrm{b}) = S_\mathrm{tx}(\omega_\mathrm{b})\, \mathrm{e}^{\mathrm{j}\omega_\mathrm{b} t''}. \tag{2.1.6}$$

Following the typical transmit processing scheme as depicted in Fig. 2.1.1, $s_\mathrm{b,tx}(t'', \omega_\mathrm{b})$ is subject to a sequence of filtering, amplification, and mixing stages before being emitted via the TX antenna[2]. This process can be summarized as

$$s_\mathrm{r,tx}\left(t'', \omega_\mathrm{b}\right) = C_\mathrm{up}(\omega_\mathrm{b})\, s_\mathrm{b,tx}\left(t'', \omega_\mathrm{b}\right) \mathrm{e}^{\mathrm{j}(\omega_\mathrm{c} t'' + \phi_\mathrm{up})}, \tag{2.1.7}$$

where

$$C_\mathrm{up}(\omega_\mathrm{b}) = H_\mathrm{b,tx}(\omega_\mathrm{b})\, H_\mathrm{r,tx}(\omega_\mathrm{b} + \omega_\mathrm{c})$$

denotes an up conversion coefficient[3] reflecting any magnitude and phase modification corresponding to the harmonic component ω_b. The latter term in (2.1.7) is a frequency shift from the base band up into the RF range with ω_c being the center angular frequency and ϕ_up a corresponding phase offset which typically depends on the local oscillator (LO) phase offset. The up conversion process is assumed to be ideal i. e. all emerging side bands else than the desired RF band are filtered out [3]. Substituting (2.1.6) into (2.1.7) yields another form of the RF signal

$$s_\mathrm{r,tx}\left(t'', \omega_\mathrm{r}\right) = a_\mathrm{r,tx}(\omega_\mathrm{r})\, \mathrm{e}^{\mathrm{j}(\omega_\mathrm{r} t'' + \phi_\mathrm{up})}, \tag{2.1.8}$$

where

$$a_\mathrm{r,tx}(\omega_\mathrm{r}) = C_\mathrm{up}(\omega_\mathrm{r} - \omega_\mathrm{c})\, S_\mathrm{tx}(\omega_\mathrm{r} - \omega_\mathrm{c})$$

and

$$\omega_\mathrm{r} = \omega_\mathrm{b} + \omega_\mathrm{c} \tag{2.1.9}$$

is the angular radar signal frequency. As defined before, this signal is radiated via the TX antenna with respect to t''. Among other evanescent components it emits a transverse electromagnetic

[2] Note that a complex signal cannot be transmitted via a physical antenna. The formulation as complex analytic band pass signal, however, allows for a convenient short notation. The physically emitted real signal is $\mathrm{Re}\{s_\mathrm{tx}(t, \omega_\mathrm{b})\}$.

[3] The up conversion coefficient $C_\mathrm{up}(\omega_\mathrm{b})$ cannot be interpreted as a classical transfer function since the frequency shift renders the transmit chain as a linear time variant system. Transfer functions, however, can only be defined on linear time invariant systems, hence no impulse response function can be identified with $C_\mathrm{up}(\omega_\mathrm{b})$. Nevertheless, it is still possible to identify a harmonic sinusoidal in the base band to its corresponding harmonic in the RF band via $C_\mathrm{up}(\omega_\mathrm{b}) = H_\mathrm{b,tx}(\omega_\mathrm{b})\, H_\mathrm{r,tx}(\omega_\mathrm{b} + \omega_\mathrm{c})$ and an additional frequency shift.

(TEM) spherical wave

$$\vec{e}_{\mathrm{tx}}\left(\vec{x},t'',\omega_{\mathrm{r}}\right)=a_{\mathrm{w}}\left(\vec{x},\omega_{\mathrm{r}}\right)\vec{i}_{\mathrm{tx}}\mathrm{e}^{\mathrm{j}(\omega_{\mathrm{r}}t''-k_{\mathrm{r}}\|\vec{x}\|)+\mathrm{j}\phi_{\mathrm{up}}}, \tag{2.1.10}$$

where the unit vector $\vec{i}_{\mathrm{tx}}$ denotes an arbitrary polarization direction in the spherical coordinates φ and ϑ, $k_{\mathrm{r}}=\omega_{\mathrm{r}}/c_0$ the wave number, and

$$a_{\mathrm{w}}\left(\vec{x},\omega_{\mathrm{r}}\right)=\frac{a_{\mathrm{r,tx}}\left(\omega_{\mathrm{r}}\right)g_{\mathrm{tx}}\left(\vec{u}_x,\omega_{\mathrm{r}}\right)}{\|\vec{x}\|}$$

a complex wave amplitude. Within $a_{\mathrm{w}}\left(\vec{x},\omega_{\mathrm{r}}\right)$, $\vec{x}$ denotes any point in space with respect to the phase center of the TX antenna and $g_{\mathrm{tx}}\left(\vec{u}_x,\omega_{\mathrm{r}}\right)\in\mathbb{C}$ an antenna gain coefficient representing the effect of the antenna on the harmonic component with respect to the radar frequency and the pointing direction given by the LOS vector $\vec{u}_x=\vec{x}/\|\vec{x}\|$. From the definition of the antenna gain, $g_{\mathrm{tx}}\left(\vec{u}_x,\omega_{\mathrm{r}}\right)$ can be implicitly identified as

$$G_{\mathrm{tx}}\left(\vec{u}_x,\omega_{\mathrm{r}}\right)=\frac{4\pi}{2\eta_{\mathrm{w}}}\left|g_{\mathrm{tx}}\left(\vec{u}_x,\omega_{\mathrm{r}}\right)\right|^2, \tag{2.1.11}$$

where $\eta_{\mathrm{w}}=\sqrt{\mu_0/\varepsilon_0}\simeq 120\pi\,\Omega$ is the free space impedance. A derivation of (2.1.11) can be found in the Appendix A.2.1. Notice the factor $2\eta_{\mathrm{w}}$, which accounts for the translation from a (voltage) signal into an EM wave quantity. Notice further, that $g_{\mathrm{tx}}\left(\vec{u}_x,\omega_{\mathrm{r}}\right)$ already accounts for mutual coupling effects e. g. the coupling between the TX and RX antenna, the influence of the antenna mounting gear, the (earth) ground, or the impact of a radome.[4] For a distance of $\|\vec{x}\|>d_{\mathrm{F}}$, where d_{F} is the Fraunhofer distance, the TEM wave $\vec{e}_{\mathrm{tx}}\left(\vec{x},t,\omega_{\mathrm{r}}\right)$ is the governing component of the generated waves. For electrically large antennas common for radar applications i. e. $D>2.5\lambda_{\mathrm{r}}$, with D denoting the largest aperture size of the antenna and $\lambda_{\mathrm{r}}=2\pi c_0/\omega_{\mathrm{r}}$ the radar wave length, the Fraunhofer distance is defined as $d_{\mathrm{F}}=2D^2/\lambda_{\mathrm{r}}$ [5]. In case of $\|\vec{x}\|\leq d_{\mathrm{F}}$, near field effects occur which can not be described sufficiently via (2.1.10). Within this work only far fields are considered. The transmitted wave form can be synthesized by

$$\vec{e}_{\mathrm{tx}}\left(\vec{x},t''\right)=\frac{\vec{i}_{\mathrm{tx}}}{2\pi}\int_{\omega_{\mathrm{c}}-\pi b_{\mathrm{r}}}^{\omega_{\mathrm{c}}+\pi b_{\mathrm{r}}}a_{\mathrm{w}}\left(\vec{x},\omega_{\mathrm{r}}\right)\mathrm{e}^{\mathrm{j}(\omega_{\mathrm{r}}t''-k_{\mathrm{r}}\|\vec{x}\|)+\mathrm{j}\phi_{\mathrm{up}}}\mathrm{d}\omega_{\mathrm{r}} \tag{2.1.12}$$

$$=\frac{\vec{i}_{\mathrm{tx}}}{2\pi}\mathrm{e}^{\mathrm{j}\phi_{\mathrm{up}}}\int_{\omega_{\mathrm{c}}-\pi b_{\mathrm{r}}}^{\omega_{\mathrm{c}}+\pi b_{\mathrm{r}}}a_{\mathrm{w}}\left(\vec{x},\omega_{\mathrm{r}}\right)\mathrm{e}^{-\mathrm{j}\omega_{\mathrm{r}}\frac{\|\vec{x}\|}{c_0}}\mathrm{e}^{\mathrm{j}\omega_{\mathrm{r}}t''}\mathrm{d}\omega_{\mathrm{r}} \tag{2.1.13}$$

$$=\frac{\vec{i}_{\mathrm{tx}}}{\|\vec{x}\|}s'_{\mathrm{tx}}\left(t''-\frac{\|\vec{x}\|}{c_0}\right)\mathrm{e}^{\mathrm{j}\omega_{\mathrm{c}}\left(t''-\frac{\|\vec{x}\|}{c_0}\right)+\mathrm{j}\phi_{\mathrm{up}}}, \tag{2.1.14}$$

where $s'_{\mathrm{tx}}\left(t''\right)$ is a modified version of $s_{\mathrm{tx}}\left(t''\right)$ due to the TX path and antenna transfer coefficients $C_{\mathrm{up}}\left(\omega_{\mathrm{b}}\right)$ and $g_{\mathrm{tx}}\left(\vec{u}_x,\omega_{\mathrm{r}}\right)$. Notice, that (2.1.14) is only valid in case $\vec{x}$ denotes a time independent location[5]. Unfortunately, this condition is not given in case of an arbitrary moving target.

With respect to t', the TEM wave $\vec{e}_{\mathrm{tx}}\left(\vec{x},t'\right)$ arrives at the point targets position given by $\vec{r}_{\mathrm{tx}}\left(t'\right)$

[4] This accounts for more effects than the commonly assumed uncoupled antenna gain. As a consequence G_{tx} in (2.1.11) must also include coupling effects.

[5] Otherwise there is no Fourier pair available allowing for a closed form time signal.

relative to the TX antenna reference frame. For a single harmonic frequency the field at the target is

$$\vec{e}_{\mathrm{tx}}\left(\vec{r}_{\mathrm{tx}}\left(t'\right),t',\omega_{\mathrm{r}}\right)=a_{\mathrm{w}}\left(\vec{r}_{\mathrm{tx}}\left(t'\right),\omega_{\mathrm{r}}\right)\vec{i}_{\mathrm{tx}}\mathrm{e}^{\mathrm{j}(\omega_{\mathrm{r}}t'-k_{\mathrm{r}}r_{\mathrm{tx}}(t'))+\mathrm{j}\phi_{\mathrm{up}}}. \tag{2.1.15}$$

Since the location $\vec{r}_{\mathrm{tx}}\left(t'\right)$ is time dependent, (2.1.14) can not be exploited directly. Furthermore, a motion induced phase modulation gives rise to the aforementioned Doppler effect. For the harmonic component ω_{r}, the emerging angular frequency at the point targets position at time t' can be calculated by

$$\begin{aligned}\omega_{\mathrm{sc}}\left(t'\right)&=\frac{\partial}{\partial t'}\arg\left(\vec{e}_{\mathrm{tx}}\left(\vec{r}_{\mathrm{tx}}\left(t'\right),t',\omega_{\mathrm{r}}\right)\right)\\&=\frac{\partial}{\partial t'}\left(\omega_{\mathrm{r}}t'-k_{\mathrm{r}}r_{\mathrm{tx}}\left(t'\right)+\phi_{\mathrm{up}}\right)\\&=\omega_{\mathrm{r}}-k_{\mathrm{r}}\left\langle\vec{u}_{\mathrm{tx}}\left(t'\right),\vec{v}_{\mathrm{t}}\left(t'\right)-\vec{v}_{\mathrm{p}}\right\rangle\\&=\omega_{\mathrm{r}}-k_{\mathrm{r}}v_{\mathrm{rtx}}\left(t'\right)\\&=\omega_{\mathrm{r}}\left(1-\frac{v_{\mathrm{rtx}}\left(t'\right)}{c_0}\right)\\&=\alpha_{\mathrm{tx}}(t')\omega_{\mathrm{r}},\end{aligned} \tag{2.1.16}$$

where $\vec{v}_{\mathrm{t}}\left(t'\right)-\vec{v}_{\mathrm{p}}$ denotes the targets velocity vector with respect to the antenna reference frame and $v_{\mathrm{rtx}}\left(t'\right)$ the radial velocity component with respect to $\vec{u}_{\mathrm{tx}}\left(t'\right)$. For sake of readability, the dependencies ω_{sc} on t' is omitted in the further text. Note, that (2.1.16) renders to be the Doppler frequency for a stationary source (here the TX antenna) and moving receiver (the point target) with the scaling factor

$$\alpha_{\mathrm{tx}}(t')=\left(1-v_{\mathrm{rtx}}(t')/c_0\right). \tag{2.1.17}$$

This modulated harmonic component gets scattered by the point target. The corresponding spherical wave is a new wave oscillating with ω_{sc}. It can be described in a similar manner to (2.1.10) as

$$\vec{e}_{\mathrm{sc}}\left(\vec{x}_{\mathrm{sc}},t,\omega_{\mathrm{sc}}\right)=a_{\mathrm{sc}}\left(\vec{x}_{\mathrm{sc}},\omega_{\mathrm{sc}}\right)\vec{i}_{\mathrm{sc}}\mathrm{e}^{\mathrm{j}(\omega_{\mathrm{sc}}t-k_{\mathrm{sc}}\|\vec{x}_{\mathrm{sc}}\|)+\mathrm{j}\phi_{\mathrm{up}}+\mathrm{j}\phi_{\mathrm{tx}}}, \tag{2.1.18}$$

where the origin of $\vec{x}_{\mathrm{sc}}$ is at the point targets position at scatter time t', $k_{\mathrm{sc}}=\omega_{\mathrm{sc}}/c_0$ is the corresponding wave number and ϕ_{up} remains constant. In addition, a constant phase term ϕ_{tx} is introduced which which is necessary to adjust the phase position of the wave according to the physical boundary conditions. At the point targets position i. e. $\|\vec{x}_{\mathrm{sc}}\|=0$ at scatter time $t=\tau_{\mathrm{tx}}\left(t'\right)$, the total phase of (2.1.18) must be ϕ_{up} as this was the phase of the wave at transmission time. Thus, the constant phase offset results to

$$\phi_{\mathrm{tx}}=-\omega_{\mathrm{sc}}\tau_{\mathrm{tx}}\left(t'\right). \tag{2.1.19}$$

Furthermore,

$$a_{\mathrm{sc}}\left(\vec{x}_{\mathrm{sc}},\omega_{\mathrm{sc}}\right)=\frac{a_{\mathrm{w}}\left(\vec{r}_{\mathrm{tx}},\omega_{\mathrm{sc}}/\alpha_{\mathrm{tx}}\right)\alpha_{\mathrm{r}}\left(\vec{u}_{\mathrm{tx}},\vec{u}_{x_{\mathrm{sc}}},\omega_{\mathrm{sc}},\vec{i}_{\mathrm{tx}}\right)}{\|\vec{x}_{\mathrm{sc}}\|}$$

denotes the complex wave amplitude with $\alpha_{\mathrm{r}}\in\mathbb{C}$ being a reflection coefficient depending on the incident direction $\vec{u}_{\mathrm{tx}}$ at scatter time t', the scatter direction $\vec{u}_{x_{\mathrm{sc}}}=\vec{x}_{\mathrm{sc}}/\|\vec{x}_{\mathrm{sc}}\|$, the observed

angular frequency ω_{sc} and the polarization direction of the incident wave $\vec{i}_{\mathrm{tx}}$. It can be identified implicitly from the radar equation as

$$\sigma_{\mathrm{r}} = \left|\alpha_{\mathrm{r}}\left(\vec{u}_{\mathrm{tx}}, \vec{u}_{x_{\mathrm{sc}}}, \omega_{\mathrm{sc}}, \vec{i}_{\mathrm{tx}}\right)\right|^2, \tag{2.1.20}$$

where σ_{r} denotes the targets radar cross section (RCS) [2]. Finally,

$$\vec{i}_{\mathrm{sc}} = \boldsymbol{R}_{\mathrm{sc}}\left(\vec{u}_{\mathrm{tx}}, \vec{u}_{x_{\mathrm{sc}}}, \omega_{\mathrm{sc}}, \vec{i}_{\mathrm{tx}}\right) \cdot \vec{i}_{\mathrm{tx}}$$

is the polarization direction of the reflected wave with $\boldsymbol{R}_{\mathrm{sc}} \in \mathbb{R}^{3\times3}$ denoting a rotation matrix describing the reflective behavior of the point target.

With respect to t, the scattered wave $\vec{e}_{\mathrm{sc}}\left(\vec{x}_{\mathrm{sc}}, t, \omega_{\mathrm{sc}}\right)$ is observed by the RX antenna located at position $-\vec{r}_{\mathrm{rx}}(t')$ relative to the point targets reference frame at t' i. e. at the scattered waves origin. The time dependent motion again causes a phase modulation giving rise to the aforementioned second Doppler effect. The observed angular Doppler frequency at the RX antennas position at time t is

$$\begin{aligned}
\omega_{\mathrm{r,rx}}\left(t'\right) &= \frac{\partial}{\partial t}\arg\left(\vec{e}_{\mathrm{sc}}\left(-\vec{r}_{\mathrm{rx}}(t'), t, \omega_{\mathrm{sc}}\right)\right) \\
&= \frac{\partial}{\partial t}\left(\omega_{\mathrm{sc}}(t')t - k_{\mathrm{sc}}r_{\mathrm{rx}}(t') + \phi_{\mathrm{up}} + \phi_{\mathrm{tx}}\right) \\
&= \frac{\partial}{\partial t}\omega_{\mathrm{sc}}(t')\left(t - \frac{r_{\mathrm{rx}}(t')}{c_0}\right) \\
&= \frac{\partial}{\partial t}\omega_{\mathrm{sc}}(t')\left(t - \tau_{\mathrm{rx}}\left(t'\right)\right) \\
&= \frac{\partial}{\partial t}\omega_{\mathrm{sc}}(t')t' \\
&= \frac{\partial\omega_{\mathrm{sc}}(t')}{\partial t}t' + \omega_{\mathrm{sc}}(t')\frac{\partial t'}{\partial t} \\
&= \omega_{\mathrm{r}}\frac{\partial\alpha_{\mathrm{tx}}(t')}{\partial t}t' + \omega_{\mathrm{sc}}(t')\frac{\partial t'}{\partial t} \\
&= -\frac{\omega_{\mathrm{r}}}{c_0}a_{\mathrm{rtx}}(t')\frac{\partial t'}{\partial t}t' + \omega_{\mathrm{sc}}(t')\frac{\partial t'}{\partial t} \\
&= \omega_{\mathrm{sc}}(t')\frac{\partial t'}{\partial t}\left(1 - \frac{a_{\mathrm{rtx}}(t')}{\alpha_{\mathrm{tx}}(t')c_0}t'\right) \\
&= \alpha_{\mathrm{rx}}(t')\omega_{\mathrm{sc}}(t')\left(1 - \frac{a_{\mathrm{rtx}}(t')}{\alpha_{\mathrm{tx}}(t')c_0}t'\right),
\end{aligned}$$

where $a_{\mathrm{rtx}}(t')$ denotes the radial acceleration with respect to $\vec{u}_{\mathrm{tx}}$,

$$\begin{aligned}
\frac{\partial t'}{\partial t} = \alpha_{\mathrm{rx}}(t') &= \left(\frac{\partial t}{\partial t'}\right)^{-1} = \left(\frac{\partial\left(t' + \tau_{\mathrm{rx}}\left(t'\right)\right)}{\partial t'}\right)^{-1} \\
&= \left(1 + \frac{1}{c_0}\frac{\partial r_{\mathrm{rx}}(t')}{\partial t'}\right)^{-1} \\
&= \frac{1}{1 + \frac{v_{\mathrm{rrx}}(t')}{c_0}}
\end{aligned}$$

by using (2.1.2)[6] and $v_{\mathrm{rrx}}(t')$ is the radial velocity component with respect to $\vec{u}_{\mathrm{rx}}$ at t'. Due to better readability, the dependence of $\omega_{\mathrm{r,rx}}$ on t' is dropped in the following notation. For the remainder of this work we assume gracefully, that the radial acceleration is negligible i. e.

$$\frac{a_{\mathrm{rtx}}(t')}{\alpha_{\mathrm{tx}}(t')c_0}t' \ll 1.$$

In this case, the observed angular Doppler frequency at the RX antennas position becomes

$$\omega_{\mathrm{r,rx}}\left(t'\right) = \alpha_{\mathrm{rx}}(t')\omega_{\mathrm{sc}}(t') \tag{2.1.21}$$

$$= \alpha_{\mathrm{trx}}(t')\omega_{\mathrm{r}}. \tag{2.1.22}$$

Note, that (2.1.21) renders to be the Doppler modulation for the case of a moving source (here the point target) and a stationary receiver (the RX antenna) with a scaling factor of

$$\alpha_{\mathrm{rx}}(t') = \frac{1}{1+\frac{v_{\mathrm{rrx}}(t')}{c_0}}. \tag{2.1.23}$$

The combined Doppler modulation shows a factor of

$$\alpha_{\mathrm{trx}}(t') = \alpha_{\mathrm{tx}}(t')\alpha_{\mathrm{rx}}(t') = \frac{1-\frac{v_{\mathrm{rtx}}(t')}{c_0}}{1+\frac{v_{\mathrm{rrx}}(t')}{c_0}} = \frac{c_0 - v_{\mathrm{rtx}}\left(t'\right)}{c_0 + v_{\mathrm{rrx}}\left(t'\right)}. \tag{2.1.24}$$

The wave observed by the RX antenna can be formulated in a similar manner as the wave scattered by the point target. Doing so yields

$$\vec{e}_{\mathrm{rx}}\left(0,t,\omega_{\mathrm{r,rx}}\right) = a_{\mathrm{sc}}\left(\vec{x}_{\mathrm{sc}},\omega_{\mathrm{r,rx}}/\alpha_{\mathrm{rx}}\right)\vec{i}_{\mathrm{sc}}\mathrm{e}^{\mathrm{j}\omega_{\mathrm{r,rx}}t+\mathrm{j}\phi_{\mathrm{up}}+\mathrm{j}\phi_{\mathrm{tx}}+\mathrm{j}\phi_{\mathrm{rx}}}, \tag{2.1.25}$$

where the constant phase term ϕ_{rx} is introduced to adjust the phase position of the wave according to the physical boundary conditions. At the receive time $t = \tau\left(t'\right)$, the total phase of (2.1.25) must be ϕ_{up} as this was the phase of the wave at transmission time (any phase offset due to the scatter process is covered by a_{sc}). Thus, the constant phase offset results to

$$\phi_{\mathrm{rx}} = -\omega_{\mathrm{sc}}\left(\alpha_{\mathrm{rx}}(t')\tau_{\mathrm{rx}}\left(t'\right) + \left(\alpha_{\mathrm{rx}}(t')-1\right)\tau_{\mathrm{tx}}\left(t'\right)\right).$$

The signal received by the antenna is

$$s_{\mathrm{r,rx}}\left(t,\omega_{\mathrm{r,rx}}\right) = a_{\mathrm{r,rx}}\left(\omega_{\mathrm{r,rx}}\right)\mathrm{e}^{\mathrm{j}\omega_{\mathrm{r,rx}}t+\mathrm{j}\phi_{\mathrm{up}}+\mathrm{j}\phi_{\mathrm{tx}}+\mathrm{j}\phi_{\mathrm{rx}}} \tag{2.1.26}$$

where

$$a_{\mathrm{r,rx}}\left(\omega_{\mathrm{r,rx}}\right) = a_{\mathrm{sc}}\left(-\vec{r}_{\mathrm{rx}},\omega_{\mathrm{r,rx}}/\alpha_{\mathrm{rx}}\right)g_{\mathrm{rx}}\left(\vec{u}_{\mathrm{rx}},\omega_{\mathrm{r,rx}},\vec{i}_{\mathrm{sc}}\right)$$

is a complex amplitude with $g_{\mathrm{rx}} \in \mathbb{C}$ being an RX antenna gain coefficient representing the effect of the antenna on the received signal with respect to frequency, direction, and polarization of the impinging wave. Note, that the RX antenna observers the angular frequency $\omega_{\mathrm{r,rx}} =$

[6] The form $\frac{\partial t'}{\partial t} = \left(\frac{\partial t}{\partial t'}\right)^{-1}$ is valid as long as $\frac{\partial t}{\partial t'} \neq 0$.

$\alpha_{\mathrm{rx}}\omega_{\mathrm{sc}}$, hence, any frequency dependency corresponds to $\omega_{\mathrm{r,rx}}$. The complex amplitude g_{rx} can be identified implicitly as

$$G_{\mathrm{rx}}\left(\vec{u}_x, \omega_{\mathrm{r,rx}}, \vec{i}_{\mathrm{sc}}\right) = \frac{(4\pi)^2 \, 2\eta_{\mathrm{w}}}{\lambda_{\mathrm{r,rx}}^2} \left| g_{\mathrm{rx}}\left(\vec{u}_x, \omega_{\mathrm{r,rx}}, \vec{i}_{\mathrm{sc}}\right)\right|^2, \tag{2.1.27}$$

where the additional factor of $4\pi/\lambda_{\mathrm{r,rx}}^2$ accounts for the antenna cross section. A derivation of (2.1.27) can be found in the Appendix A.2.1. Notice the factor $2\eta_{\mathrm{w}}$, which accounts for the translation from an EM wave into a (voltage) signal quantity. Also, g_{rx} readily accounts for coupling effects just as g_{tx}. The received signal (2.1.26) is subject to a sequence of filtering, amplification, and mixing stages before being sampled by a digitizer. This process can be summarized as

$$s_{\mathrm{b,rx}}\left(t, \omega_{\mathrm{r,rx}}\right) = s_{\mathrm{r,rx}}\left(t, \omega_{\mathrm{r,rx}}\right) C_{\mathrm{dn}}\left(\omega_{\mathrm{r,rx}}\right) \mathrm{e}^{-\mathrm{j}(\omega_{\mathrm{c}} t + \phi_{\mathrm{dn}})}, \tag{2.1.28}$$

where

$$C_{\mathrm{dn}}\left(\omega_{\mathrm{r,rx}}\right) = H_{\mathrm{b,rx}}\left(\omega_{\mathrm{r,rx}} - \omega_{\mathrm{c}}\right) H_{\mathrm{r,rx}}\left(\omega_{\mathrm{r,rx}}\right)$$

denotes a down conversion coefficient reflecting any magnitude and phase modification corresponding to the instantaneous angular frequency of the harmonic component $\omega_{\mathrm{r,rx}}$. The observed frequency in the base band shall be denoted as

$$\omega_{\mathrm{b,rx}} = \omega_{\mathrm{r,rx}} - \omega_{\mathrm{c}} \tag{2.1.29}$$

$$= \alpha_{\mathrm{trx}}\omega_{\mathrm{b}} + (\alpha_{\mathrm{trx}} - 1)\omega_{\mathrm{c}}, \tag{2.1.30}$$

where (2.1.9) and (2.1.22) was used. The final received and down converted signal can thus be given as

$$s_{\mathrm{b,rx}}\left(t, \omega_{\mathrm{b,rx}}\right) = a_{\mathrm{b,rx}}\left(\omega_{\mathrm{b,rx}}\right) \mathrm{e}^{\mathrm{j}\omega_{\mathrm{b,rx}} t + \mathrm{j}\phi_{\mathrm{up}} + \mathrm{j}\phi_{\mathrm{tx}} + \mathrm{j}\phi_{\mathrm{rx}} + \mathrm{j}\phi_{\mathrm{c}}}, \tag{2.1.31}$$

where

$$\phi_{\mathrm{c}} = \phi_{\mathrm{up}} - \phi_{\mathrm{dn}} \tag{2.1.32}$$

is a constant phase offset caused by the LO signal and

$$a_{\mathrm{b,rx}}\left(\omega_{\mathrm{b,rx}}\right) = a_{\mathrm{r,rx}}\left(\vec{u}_{\mathrm{rx}}, \omega_{\mathrm{b,rx}} + \omega_{\mathrm{c}}, \vec{i}_{\mathrm{sc}}\right) C_{\mathrm{dn}}\left(\omega_{\mathrm{b,rx}} + \omega_{\mathrm{c}}\right).$$

The final received signal again is the superposition of all received harmonic components. Due to the Doppler modulations, the transmitted frequency band $[-\pi b_{\mathrm{r}}, \pi b_{\mathrm{r}}]$ gets modified to

$$\omega_{\mathrm{b,rx,min}}(t') = (\alpha_{\mathrm{trx}}(t') - 1)\omega_{\mathrm{c}} - \pi b_{\mathrm{r}}\alpha_{\mathrm{trx}}(t')$$
$$\omega_{\mathrm{b,rx,max}}(t') = (\alpha_{\mathrm{trx}}(t') - 1)\omega_{\mathrm{c}} + \pi b_{\mathrm{r}}\alpha_{\mathrm{trx}}(t'),$$

where (2.1.30) was used. Therefore, the superposition is of the form

$$s_{\mathrm{rx}}\left(t\right) = \frac{1}{2\pi} \int_{\omega_{\mathrm{b,rx,min}}}^{\omega_{\mathrm{b,rx,max}}} s_{\mathrm{b,rx}}\left(t, \omega_{\mathrm{b,rx}}\right) \mathrm{d}\omega_{\mathrm{b,rx}} = a_{\mathrm{rx}}\left(t\right) \mathrm{e}^{\mathrm{j}\phi_{\mathrm{rx}}(t)}, \tag{2.1.33}$$

where $a_{\mathrm{rx}}(t) \in \mathbb{R}$ denotes the received amplitude and $\mathrm{e}^{\mathrm{j}\phi_{\mathrm{rx}}(t)}$ the received phase history. Like in the TX case, due to the time dependent delay $\tau_{\mathrm{rx}}(t')$, there is no closed form solution available to (2.1.33).

Summarizing the above derivation, the received signal $s_{\mathrm{rx}}(t)$ may completely differ from the original transmitted signal $s_{\mathrm{tx}}(t)$ due to the in general time dependent motion induced phase modulations. Even worse, no closed form solution can be given for the received signal form. Recall, that the frequency modulation factors α_{tx} and α_{rx}, as well as the amplitudes a_{sc} and $a_{\mathrm{r,rx}}$ directly depend on t' and thus are time dependent quantities. This means for every fixed point in time t, the integral (2.1.33) needs to be evaluated individually. Since the integral form is rather non informative, additional assumptions regarding the point target are introduced which allow for a dramatic simplification of the general scheme presented here. This is the topic of the following sections. Before that, however, the subject of relativistic Doppler should be elaborated in more detail.

2.1.2. On the Relativistic Doppler Effect

In this Section a few words on the relativistic Doppler effect shall be mentioned. For a single transmit frequency ω_{r}, the received frequency according to the derivation in the latter chapter is

$$\begin{aligned}\omega_{\mathrm{r,rx}} &= \alpha_{\mathrm{trx}}\omega_{\mathrm{r}} \\ &= \omega_{\mathrm{r}}\frac{c_0 - v_{\mathrm{rtx}}}{c_0 + v_{\mathrm{rrx}}},\end{aligned} \tag{2.1.34}$$

where (2.1.22) was used. Quiet interestingly and although no relativistic considerations were made, (2.1.34) already turns out to be the exact form of the relativistic Doppler shift for constant radial velocities. The reason therefore is, that emerging time dilatation effects corresponding to the transmit and receive process cancel each other out. More specifically, the relativistic time dilation needs to be considered by use of the Lorentz factor two times. In the TX case, where the target is moving, the clock at the point target is time dilated with respect to the clock resting at the radar i. e. is slower. The point target will therefore observe the same phase history in a shorter period of time and hence measure the increased Doppler frequency [6]

$$\omega_{\mathrm{sc}}^{\mathrm{tgt}} = \omega_{\mathrm{sc}}\gamma_{\mathrm{tx}},$$

where $\omega_{\mathrm{sc}}^{\mathrm{tgt}}$ denotes ω_{sc} measured in the targets reference frame and

$$\gamma_{\mathrm{tx}} = \frac{1}{\sqrt{1 - \frac{v_{\mathrm{rtx}}^2}{c_0^2}}} \tag{2.1.35}$$

is the corresponding Lorentz factor. In the contrary RX case, the point target emits a wave with angular frequency $\omega_{\mathrm{sc}}^{\mathrm{tgt}}$ which in the reference frame of the stationary radar is observed as

$$\begin{aligned}\omega_{\mathrm{r,rx,rel}} &= \frac{\omega_{\mathrm{sc}}^{\mathrm{tgt}}}{1+\frac{v_{\mathrm{rrx}}}{c_0}}\frac{1}{\gamma_{\mathrm{rx}}} \\ &= \omega_{\mathrm{r}}\frac{c_0 - v_{\mathrm{rtx}}}{c_0 + v_{\mathrm{rrx}}}\frac{\gamma_{\mathrm{tx}}}{\gamma_{\mathrm{rx}}},\end{aligned} \tag{2.1.36}$$

where

$$\gamma_{\mathrm{rx}} = \frac{1}{\sqrt{1-\frac{v_{\mathrm{rrx}}^2}{c_0^2}}}$$

is the Lorentz factor in the RX case. In the constant radial velocity scenario, the radial velocities are such that $v_{\mathrm{rtx}} = \pm v_{\mathrm{rrx}}$ (see Section 2.1.3), hence the Lorentz factors cancel each other and $\omega_{\mathrm{r,rx,rel}} = \omega_{\mathrm{r,rx}}$.

For the sake of completeness, it shall be mentioned, that in the literature the relativistic Doppler effect is derived in a different way, namely by using two times the stationary source model [6]. At first the radar acts likewise as a stationary source for the TX case but in the RX case, the scattering point target is taken to be a stationary source with the radar moving. The result is called non-relativistic Doppler frequency, which results to

$$\begin{aligned}\omega'_{\mathrm{r,rx}} &= \omega_{\mathrm{r}}\left(1-\frac{v_{\mathrm{rtx}}}{c_0}\right)\left(1-\frac{v_{\mathrm{rrx}}}{c_0}\right) \\ &= \omega_{\mathrm{r}}\left(1-\frac{v_{\mathrm{rtx}}+v_{\mathrm{rrx}}}{c_0}+\frac{v_{\mathrm{rtx}}v_{\mathrm{rrx}}}{c_0^2}\right).\end{aligned} \tag{2.1.37}$$

To account for relativist time dilation, (2.1.37) must be extended by the Lorentz factor two times yielding [6]

$$\omega_{\mathrm{r,rx,rel}} = \omega'_{\mathrm{r,rx}}\gamma_{\mathrm{tx}}\gamma_{\mathrm{rx}}, \tag{2.1.38}$$

which after short manipulation yields the same form as in (2.1.36). However, the derivation given in (2.1.38) disregards the effect of relativistic aberration i. e. the directions from and to the target in the radar resting frame do not coincide with the directions in the target resting frame i. e. $u_{\mathrm{tx}} \neq -u_{\mathrm{tx}}^{\mathrm{tgt}}$ and $u_{\mathrm{rx}} \neq -u_{\mathrm{rx}}^{\mathrm{tgt}}$. These effects considerably complicate the derivation but finally cancel each other yielding (2.1.38) to be the final result. Nevertheless, the derivation appears patchy. In case the TX and RX antenna are identical, (2.1.36) reduces to the famous equation

$$\omega_{\mathrm{r,rx,rel}} = \omega_{\mathrm{r}}\frac{c_0 - v_{\mathrm{r}}}{c_0 + v_{\mathrm{r}}} = \omega_{\mathrm{r}}\left(1-\frac{2v_{\mathrm{r}}}{c_0+v_{\mathrm{r}}}\right).$$

2.1.3. Common Approximations

Several approximations allow for a closed form radar signal model. Those are presented in the following.

Calibration and Reflectivity

As discussed in Section 2.1.1, the received signal $s_{\mathrm{rx}}(t)$ depends on many individual parameters cluttering the signal model. However, assuming the radar system to be calibrated and the target to behave somewhat nicely, the signal model becomes easier to handle. Calibration addresses two aspects:

- The radar TX and RX paths including the antennas shall be independent with respect to ω_{r} in the desired bands. In this case, the transit and receive wave forms $s_{\mathrm{tx}}(t)$ and $s_{\mathrm{rx}}(t)$ remain unchanged by the radar channels.

- Mutual electromagnetic coupling phenomena shall be corrected for as there is the mutual influence of all antennas to each other, the antenna mounting gear, the earth ground, or a radome. Commonly, these phenomena are frequency dependent and as such the correction for mutual coupling can be combined with correcting for the dependence of ω_{r} of the TX and RX paths at the same time. If the calibration is conducted successfully, the radar appears transparent regarding the transmitted and received EM waves $\vec{e}_{\mathrm{tx}}$ and $\vec{e}_{\mathrm{sc}}$ i. e. the waves can be sampled in space and time without changing their shape due to the presence of the radar.

A convenient description of the mutual coupling and as such for a practical calibration can be done for the final signal model presented in Section 2.1.4 only. However, in order to ease the following approximations, it is assumed that the radar system is already calibrated. This is valid since the radar measurement process and the calibration procedure are linear operations and as such can be interchanged. Hence, the radar can be assumed to be transparent to the EM waves. The theoretical calibration procedure, which establishes a baseline of what a practical calibration can achieve, is discussed in the following. Assume a non moving point target for which no Doppler modulation occurs. In this case the transmission factor for the TX path for a single angular frequency ω_{r} and fixed transmit LOS vectors $\vec{u}_{\mathrm{tx}}$ is

$$c_{\mathrm{p,tx}}(\omega_{\mathrm{r}}, \vec{u}_{\mathrm{tx}}) = \frac{C_{\mathrm{up}}(\omega_{\mathrm{r}})\, g_{\mathrm{tx}}(\vec{u}_{\mathrm{tx}}, \omega_{\mathrm{r}})}{r_{\mathrm{tx}}}. \tag{2.1.39}$$

The distance r_{tx} is not frequency dependent and thus not subject to the calibration procedure. The transmit path coefficient $C_{\mathrm{up}}(\omega_{\mathrm{r}})$ comprises all amplification steps before transmission. Therefore, it is reasonable to identify $C_{\mathrm{up}}(\omega_{\mathrm{r}})$ after calibration with $\sqrt{P_{\mathrm{tx}}}$, where P_{tx} is the final transmit signal power. For this to make sense and to be able to introduce meaningful absolute coefficients describing the radar signal after calibration, the energy of a transmitted pulse $s_{\mathrm{tx},n_{\mathrm{p}}}(t)$ is usually normed without loss of generality to

$$\int_{-T_{\mathrm{p}}/2}^{T_{\mathrm{p}}/2} \left| s_{\mathrm{tx},n_{\mathrm{p}}}(t) \right|^2 \mathrm{d}t = 1. \tag{2.1.40}$$

In a similar manner, the active antenna coefficients $g_{\mathrm{tx}}(\vec{u}_{\mathrm{tx}}, \omega_{\mathrm{r}})$ after calibration can be substituted for a fixed LOS vector $\vec{u}_{\mathrm{tx}}$ by a real gain coefficient $\bar{g}_{\mathrm{tx}}(\vec{u}_{\mathrm{tx}}) \in \mathbb{R}$. Likewise, the transmission factor

for the RX path is

$$c_{\mathrm{p,rx}}\left(\omega_{\mathrm{r}},\vec{u}_{\mathrm{tx}},\vec{u}_{\mathrm{rx}},\vec{i}_{\mathrm{tx}}\right)=\frac{\alpha_{\mathrm{r}}\left(\vec{u}_{\mathrm{tx}},\vec{u}_{\mathrm{rx}},\omega_{\mathrm{r}},\vec{i}_{\mathrm{tx}}\right)}{r_{\mathrm{rx}}}g_{\mathrm{rx}}\left(\vec{u}_{\mathrm{rx}},\omega_{\mathrm{r}},\boldsymbol{R}_{\mathrm{sc}}\cdot\vec{i}_{\mathrm{tx}}\right)C_{\mathrm{dn}}\left(\omega_{\mathrm{r}}\right). \tag{2.1.41}$$

The targets reflectivity coefficient $\alpha_{\mathrm{r}}\left(\vec{u}_{\mathrm{tx}},\vec{u}_{\mathrm{rx}},\omega_{\mathrm{r}},\vec{i}_{\mathrm{tx}}\right)$ and polarization rotation $\boldsymbol{R}_{\mathrm{sc}}\left(\vec{u}_{\mathrm{tx}},\vec{u}_{\mathrm{rx}},\omega_{\mathrm{r}},\vec{i}_{\mathrm{tx}}\right)$ dependencies are usually not calibrated for. Most often, they are unknown and thus are modeled as random variables (RVs), e. g. in case of GMTI land clutter α_{r} may be $\alpha_{\mathrm{r}}\sim\mathcal{CN}\left(0,\sigma_{\mathrm{r}}\right)$ [1]. If information about α_{r} and $\boldsymbol{R}_{\mathrm{sc}}$ is known, this can be exploited e. g. by use of matched illumination [7]. Regarding the calibration process, it is commonly assumed that α_{r} and $\boldsymbol{R}_{\mathrm{sc}}$ are independent with respect to ω_{r}, thus do not change the wave form. Any discrepancies regarding this assumption are accounted to the RV model. The active antenna coefficients $g_{\mathrm{rx}}\left(\vec{u}_{\mathrm{rx}},\omega_{\mathrm{r}},\boldsymbol{R}_{\mathrm{sc}}\left(\cdot\right)\cdot\vec{i}_{\mathrm{tx}}\right)$ after calibration can again be substituted by a real gain coefficients $\bar{g}_{\mathrm{rx}}(\vec{u}_{\mathrm{rx}})\in\mathbb{R}$, where the dependence on the polarization direction $\vec{i}_{\mathrm{sc}}=\boldsymbol{R}_{\mathrm{sc}}\left(\cdot\right)\cdot\vec{i}_{\mathrm{tx}}$ is pulled into the RV α_{r} too. This of course assumes, that all RX antennas are polarized in the same direction (which is usually the case). Finally, the receive path coefficient $C_{\mathrm{dn}}\left(\omega_{\mathrm{r}}\right)$ comprises all amplification steps required to achieve some reasonable noise figure [4]. It is therefore reasonable, to identify $C_{\mathrm{dn}}\left(\omega_{\mathrm{r}}\right)$ after calibration with some mean gain coefficient $g_{\mathrm{dn}}\in\mathbb{R}$. Combining the aforementioned identities, the calibration factor

$$c_{\mathrm{cal}}\left(\omega_{\mathrm{r}}\right)=\frac{\sqrt{P_{\mathrm{tx}}}g_{\mathrm{dn}}\bar{g}_{\mathrm{tx}}(\vec{u}_{\mathrm{tx}})\bar{g}_{\mathrm{rx}}(\vec{u}_{\mathrm{rx}})}{C_{\mathrm{up}}\left(\omega_{\mathrm{r}}\right)C_{\mathrm{dn}}\left(\omega_{\mathrm{r}}\right)g_{\mathrm{tx}}\left(\vec{u}_{\mathrm{tx}},\omega_{\mathrm{r}}\right)g_{\mathrm{rx}}\left(\vec{u}_{\mathrm{rx}},\omega_{\mathrm{r}},\boldsymbol{R}_{\mathrm{sc}}\left(\cdot\right)\cdot\vec{i}_{\mathrm{tx}}\right)} \tag{2.1.42}$$

can be defined for a single TX/RX pair. Applying this calibration factor onto the path factors $c_{\mathrm{p,tx}}$ and $c_{\mathrm{p,rx}}$ yields due to the normalization (2.1.40) a calibrated received amplitude

$$\begin{aligned}x_{\mathrm{cal}}\left(P_{\mathrm{tx}},\alpha_{\mathrm{r}},r_{\mathrm{tx}},r_{\mathrm{rx}},\vec{u}_{\mathrm{tx}},\vec{u}_{\mathrm{rx}}\right)&=c_{\mathrm{p,tx}}\left(\omega_{\mathrm{r}},\vec{u}_{\mathrm{tx}}\right)c_{\mathrm{p,rx}}\left(\omega_{\mathrm{r}},\vec{u}_{\mathrm{tx}},\vec{u}_{\mathrm{rx}},\vec{i}_{\mathrm{tx}}\right)c_{\mathrm{cal}}\left(\omega_{\mathrm{r}}\right)\\&=\frac{\alpha_{\mathrm{r}}\sqrt{P_{\mathrm{tx}}}g_{\mathrm{dn}}\bar{g}_{\mathrm{tx}}(\vec{u}_{\mathrm{tx}})\bar{g}_{\mathrm{rx}}(\vec{u}_{\mathrm{rx}})}{r_{\mathrm{tx}}r_{\mathrm{rx}}}.\end{aligned} \tag{2.1.43}$$

This means applying $c_{\mathrm{cal}}\left(\omega_{\mathrm{r}}\right)$ onto the transmit signal harmonics $s_{\mathrm{b,tx}}(t,\omega_{\mathrm{b}})$ defined in (2.1.6), the received signal becomes

$$s_{\mathrm{rx}}\left(t\right)=x_{\mathrm{cal}}s_{\mathrm{tx}}(t-\tau)\mathrm{e}^{-\mathrm{j}\omega_{\mathrm{c}}\tau+\mathrm{j}\phi_{\mathrm{c}}}$$

in case of a non moving point target. The calibrated receive amplitude x_{cal} determines, in conjunction with the noise figure of the RX path and the Friis formula, the final signal to noise ratio (SNR) [4]. In case the target is moving, Doppler modulation occurs causing an extension of the frequency range. If (2.1.42) accounts for this extended frequency range, (2.1.43) holds too.

As mentioned before, the radar signal process described in Section 2.1.1 is linear and as such the calibration factor (2.1.42) can be drawn into the transmit signal whose signal form as a result gets modulated by the motion of the target only and never more by the transfer functions of the TX and RX paths and antennas. This comes in handy in the approximations described in the following. From this point forward, the radar system is assumed to be calibrated.

Target Induced Phase Modulation

A moving target observes a modulated transmit wave form induced by its own motion. Because of this motion, unfortunately, it is not possible to obtain a closed form solution for the scattered and received fields. Nevertheless, the period of time during which the point target is able to modify the transmit wave form is restricted by the illumination time, which in turn is inherently restricted by the pulse duration T_p. If the targets motion during the illumination time is somewhat limited, the wave forms can be considered unaltered. This allows for a dramatically simplification of the received radar signal description. In this section, two measures regarding the modulation impact are presented which allow to decide whether the impact is negligible or not.

For the following derivations the radar system is assumed to be calibrated. As discussed in Section 2.1.3, some partial TX path calibration factor can be defined as

$$c_{\mathrm{cal,tx}}\left(\omega_\mathrm{r}\right) = \frac{\sqrt{P_\mathrm{tx}}\bar{g}_\mathrm{tx}\left(\vec{u}_\mathrm{tx}\right)}{C_\mathrm{up}\left(\omega_\mathrm{r}\right) g_\mathrm{tx}\left(\vec{u}_\mathrm{tx},\omega_\mathrm{r}\right)}$$

which corrects for any impact of the radars TX path onto the signal form i. e. cancels any frequency dependency. The calibrated field at the point targets position $\vec{r}_\mathrm{tx}\left(t'\right)$ at scatter time t' can be given by use of (2.1.12) as

$$\begin{aligned}
\vec{e}_\mathrm{tx,cal}\left(\vec{r}_\mathrm{tx}\left(t'\right),t'\right) &= \frac{1}{2\pi}\int\limits_{\omega_\mathrm{c}-\pi b_\mathrm{r}}^{\omega_\mathrm{c}+\pi b_\mathrm{r}} c_\mathrm{cal,tx}\left(\omega_\mathrm{r}\right)\vec{e}_\mathrm{tx}\left(\vec{r}_\mathrm{tx}\left(t'\right),t',\omega_\mathrm{r}\right)\mathrm{d}\omega_\mathrm{r} \\
&= \frac{\vec{i}_\mathrm{tx}x_\mathrm{tx,cal}}{2\pi}\int\limits_{\omega_\mathrm{c}-\pi b_\mathrm{r}}^{\omega_\mathrm{c}+\pi b_\mathrm{r}} S_\mathrm{tx}\left(\omega_\mathrm{r}-\omega_\mathrm{c}\right)\mathrm{e}^{-\mathrm{j}\omega_\mathrm{r}\tau_\mathrm{tx}(t')}\mathrm{e}^{\mathrm{j}\omega_\mathrm{r}t'}\mathrm{e}^{\mathrm{j}\phi_\mathrm{up}}\mathrm{d}\omega_\mathrm{r} \\
&= \frac{\vec{i}_\mathrm{tx}x_\mathrm{tx,cal}}{2\pi}\mathrm{e}^{\mathrm{j}\omega_\mathrm{c}(t'-\tau_\mathrm{tx}(t'))+\mathrm{j}\phi_\mathrm{up}}\int\limits_{-\pi b_\mathrm{r}}^{\pi b_\mathrm{r}} S_\mathrm{tx}\left(\omega_\mathrm{b}\right)\mathrm{e}^{-\mathrm{j}\omega_\mathrm{b}\tau_\mathrm{tx}(t')}\mathrm{e}^{\mathrm{j}\omega_\mathrm{b}t'}\mathrm{d}\omega_\mathrm{b} \\
&= \frac{\vec{i}_\mathrm{tx}x_\mathrm{tx,cal}}{2\pi}\mathrm{e}^{\mathrm{j}\omega_\mathrm{c}(t'-\tau_\mathrm{tx}(t'))+\mathrm{j}\phi_\mathrm{up}}\mathcal{F}^{-1}\left\{s_\mathrm{tx}\left(\omega_\mathrm{b}\right)\mathrm{e}^{-\mathrm{j}\omega_\mathrm{b}\tau_\mathrm{tx}(t')}\right\}, \qquad (2.1.44)
\end{aligned}$$

where

$$x_\mathrm{tx,cal} = \frac{\sqrt{P_\mathrm{tx}}\bar{g}_\mathrm{tx}\left(\vec{u}_\mathrm{tx}\right)}{r_\mathrm{tx}\left(t'\right)}$$

is some calibrated amplitude and $\mathcal{F}^{-1}\left\{\cdot\right\}$ denotes the inverse Fourier transform. Now, as mentioned in Section 2.1.1, there does not exist a Fourier pair to obtain a closed form solution to 2.1.44 due to the time dependent delay term $\exp\left(-\mathrm{j}\omega_\mathrm{b}\tau_\mathrm{tx}\left(t'\right)\right)$. Nevertheless, if the modulation is limited such that the shape of the RF wave form is somewhat preserved, i. e. the point target does not move considerably during the time the pulse hits the target, $\tau_\mathrm{tx}\left(t'\right)$ can be assumed constant. This comes in very handy as subsequent signal models can be derived in closed form. As such, if the variation of $\tau_\mathrm{tx}\left(t'\right)$ in (2.1.44) is limited during the illumination time i. e.

$$\triangle\tau_\mathrm{tx}\left(t'\right)\omega_\mathrm{b} = \frac{\omega_\mathrm{b}}{c_0}\left|r_\mathrm{tx}\left(t_\mathrm{il}\right) - r_\mathrm{tx}\left(t'\right)\right| < \pi\gamma_\mathrm{tol} \qquad (2.1.45)$$

with γ_tol being e. g. $1/10$, the effective delay can be assumed constant with respect to t'. Within

(2.1.45), t_{il} denotes any point in time in the period of illumination. In general, however, just like for t', the illumination period cannot be given in closed form. A worst case approximation can be given by assuming a maximum radial velocity $v_{\mathrm{rtx,max}}$ which is constant during the illumination period. In this case, the illumination period in the source time frame $T_{\mathrm{il}}^{\mathrm{src}}$, i. e. in the radar time frame, can be calculated as

$$\begin{aligned} T_{\mathrm{p}} c_0 + v_{\mathrm{rtx,max}} T_{\mathrm{il,tx}}^{\mathrm{src}} &= c_0 T_{\mathrm{il,tx}}^{\mathrm{src}} \\ \rightarrow T_{\mathrm{il,tx}}^{\mathrm{src}} &= \frac{T_{\mathrm{p}}}{1 - \frac{v_{\mathrm{rtx,max}}}{c_0}}. \end{aligned}$$

Due to time dilation, the clock at the moving point target is slower. Hence, the illumination period experienced by the point target $T_{\mathrm{il}}^{\mathrm{tgt}}$ is reduced by the Lorentz factor γ_{tx} defined in (2.1.35) to

$$\begin{aligned} T_{\mathrm{il,tx}}^{\mathrm{tgt}} &= \frac{T_{\mathrm{il,tx}}^{\mathrm{src}}}{\gamma_{\mathrm{tx}}} \\ &= T_{\mathrm{p}} \sqrt{\frac{c_0 + v_{\mathrm{rtx,max}}}{c_0 - v_{\mathrm{rtx,max}}}}. \end{aligned} \tag{2.1.46}$$

The worst case distance occurring in (2.1.45) thus becomes[7]

$$\left| r_{\mathrm{tx}}\left(t_{\mathrm{il}}\right) - r_{\mathrm{tx}}\left(t'\right) \right| = \frac{T_{\mathrm{il,tx}}^{\mathrm{tgt}} v_{\mathrm{rtx,max}}}{2}. \tag{2.1.47}$$

Therefor, by combining (2.1.45), (2.1.46), and (2.1.47) we can deduce that as long as the pulse duration is smaller than

$$T_{\mathrm{p}} \leq \frac{\gamma_{\mathrm{tol}} \lambda_{\mathrm{b}}}{v_{\mathrm{rtx,max}}} \sqrt{\frac{c_0 - v_{\mathrm{rtx,max}}}{c_0 + v_{\mathrm{rtx,max}}}}, \tag{2.1.48}$$

the delay term $\exp\left(-\mathrm{j}\omega_{\mathrm{b}} \tau_{\mathrm{tx}}\left(t'\right)\right)$ in (2.1.44) can be approximated to be constant. In this case the calibrated field at the point targets position (2.1.44) has the closed form solution

$$\vec{e}'_{\mathrm{tx,cal}}\left(\vec{r}_{\mathrm{tx}}\left(t'\right), t'\right) = \vec{i}_{\mathrm{tx}} \frac{\sqrt{P_{\mathrm{tx}}} \bar{g}_{\mathrm{tx}}\left(\vec{u}_{\mathrm{tx}}\right)}{r_{\mathrm{tx}}\left(t'\right)} s_{\mathrm{tx}}\left(t' - \tau_{\mathrm{tx}}\left(t'\right)\right) \mathrm{e}^{\mathrm{j}\omega_{\mathrm{c}}\left(t' - \tau_{\mathrm{tx}}(t')\right) + \mathrm{j}\phi_{\mathrm{up}}}. \tag{2.1.49}$$

A second more reasonable error measure as (2.1.48) may be a correlation loss (CL) between the time dependent form $\vec{e}_{\mathrm{tx,cal}}$ and the assumed time independent solution $\vec{e}'_{\mathrm{tx,cal}}$. Assuming the point target moves at $v_{\mathrm{rtx,max}}$ during T_{il}, the CL is

$$\mathrm{CL}_{\mathrm{tx}} = R_{s_{\mathrm{tx}} s_{\mathrm{tx}}}\left(\frac{T_{\mathrm{il,tx}}^{\mathrm{tgt}} v_{\mathrm{rtx,max}}}{2 c_0}\right), \tag{2.1.50}$$

where $R_{s_{\mathrm{tx}} s_{\mathrm{tx}}}\left(x\right)$ denotes the auto correlation of s_{tx}. In case of a linear frequency modulation (LFM) chirp wave form, the CL is

$$\mathrm{CL}_{\mathrm{tx,chirp}} = \Lambda\left(\frac{v_{\mathrm{rtx,max}}}{2 c_0}\right) \mathrm{sinc}\left(\frac{b_{\mathrm{r}} T_{\mathrm{il,tx}}^{\mathrm{tgt}} v_{\mathrm{rtx,max}}}{2 c_0} \Lambda\left(\frac{v_{\mathrm{rtx,max}}}{2 c_0}\right)\right) \tag{2.1.51}$$

[7] Recall that t' denotes the center of the pulse.

with $\Lambda(x)$ denoting the triangular function. A derivation of (2.1.50) and (2.1.51) can be found in the Appendix A.2.2. Recall now from Section 2.1.1, that the scattered wave is reflected with a modulated frequency, which now can be given for the whole transmit signal uniformly as

$$\begin{aligned}\omega'_{\mathrm{sc}} &= \frac{\partial \arg\left\{\vec{e}'_{\mathrm{tx,cal}}\left(\vec{r}_{\mathrm{tx}}\left(t'\right),t'\right)\right\}}{\partial t'} = \frac{\partial \omega_{\mathrm{c}}\left(t'-\tau_{\mathrm{tx}}\left(t'\right)\right)}{\partial t'} = \omega_{\mathrm{c}}\left(1-\frac{v_{\mathrm{rtx}}\left(t'\right)}{c_0}\right) \\ &= \alpha_{\mathrm{tx}}(t')\omega_{\mathrm{c}}. \end{aligned} \tag{2.1.52}$$

In the following, the receive process is elaborated. Recall now from Section 2.1.1, that the scattered wave oscillates with ω'_{sc}. Recognize further, that the signal shape experienced by the point target is unaltered, thus the calibrated scattered wave can be formulated as

$$\vec{e}'_{\mathrm{sc,cal}}\left(\vec{x}_{\mathrm{sc}},t',\omega'_{\mathrm{sc}}\right) = \vec{i}_{\mathrm{sc}}\frac{\sqrt{P_{\mathrm{tx}}}\bar{g}_{\mathrm{tx}}\left(\vec{u}_{\mathrm{tx}}\right)\alpha_{\mathrm{r}}}{r_{\mathrm{tx}}\left(t'\right)\left\|\vec{x}_{\mathrm{sc}}\right\|}s_{\mathrm{tx}}\left(t'-\tau_{\mathrm{tx}}\left(t'\right)\right)\mathrm{e}^{\mathrm{j}(\omega'_{\mathrm{sc}}t'-k'_{\mathrm{sc}}\|\vec{x}_{\mathrm{sc}}\|)+\mathrm{j}\phi_{\mathrm{up}}+\mathrm{j}\phi'_{\mathrm{tx}}},$$

where the reflection coefficient α_{r} was assumed to be frequency independent and

$$\phi'_{\mathrm{tx}} = -\omega'_{\mathrm{sc}}\tau_{\mathrm{tx}}\left(t'\right)$$

in similar manner to (2.1.19). The receive process works the same way as the transmit process. If condition (2.1.46) and (2.1.50) are likewise fulfilled as

$$T_{\mathrm{p}} \leq \frac{\gamma_{\mathrm{tol}}\lambda_{\mathrm{b}}}{v_{\mathrm{rrx,max}}}\sqrt{\frac{c_0-v_{\mathrm{rrx,max}}}{c_0+v_{\mathrm{rrx,max}}}}$$

and

$$\mathrm{CL}_{\mathrm{rx}} = R_{s_{\mathrm{tx}}s_{\mathrm{tx}}}\left(\frac{T^{\mathrm{tgt}}_{\mathrm{il,rx}}v_{\mathrm{rrx,max}}}{2c_0}\right),$$

the signal received by the RX antenna is

$$s'_{\mathrm{r,rx,cal}}\left(t\right) = \frac{\sqrt{P_{\mathrm{tx}}}\bar{g}_{\mathrm{tx}}\left(\vec{u}_{\mathrm{tx}}\right)\alpha_{\mathrm{r}}\bar{g}_{\mathrm{rx}}}{r_{\mathrm{tx}}\left(t'\right)r_{\mathrm{rx}}\left(t'\right)}s_{\mathrm{tx}}\left(t-\tau\left(t'\right)\right)\mathrm{e}^{\mathrm{j}\omega'_{\mathrm{r,rx}}t+\mathrm{j}\phi_{\mathrm{up}}+\mathrm{j}\phi'_{\mathrm{tx}}+\mathrm{j}\phi'_{\mathrm{rx}}}.$$

The corresponding observed angular frequency can be found in similar manner to (2.1.52) as

$$\begin{aligned}\omega'_{\mathrm{r,rx}} &= \alpha_{\mathrm{rx}}(t')\omega'_{\mathrm{sc}} && (2.1.53)\\ &= \alpha_{\mathrm{trx}}(t')\omega_{\mathrm{c}}. && (2.1.54)\end{aligned}$$

and

$$\phi'_{\mathrm{rx}} = -\omega'_{\mathrm{sc}}\left(\alpha_{\mathrm{rx}}(t')\tau_{\mathrm{rx}}\left(t'\right)+\left(\alpha_{\mathrm{rx}}(t')-1\right)\tau_{\mathrm{tx}}\left(t'\right)\right).$$

The final down converted signal thus becomes

$$s'_{\mathrm{b,rx,cal}}\left(t\right) = x_{\mathrm{cal}}s_{\mathrm{tx}}\left(t-\tau\left(t'\right)\right)\mathrm{e}^{\mathrm{j}\omega_{\mathrm{D}}t+\mathrm{j}\phi_{\mathrm{c}}+\mathrm{j}\phi'_{\mathrm{tx}}+\mathrm{j}\phi'_{\mathrm{rx}}}, \tag{2.1.55}$$

where

$$\begin{aligned}\omega_{\mathrm{D}} &= \omega'_{\mathrm{r,rx}} - \omega_{\mathrm{c}} \\ &= \omega_{\mathrm{c}} \left(\alpha_{\mathrm{trx}}(t') - 1\right) \\ &= \omega_{\mathrm{c}} \left(\frac{c_0 - v_{\mathrm{rtx}}\left(t'\right)}{c_0 + v_{\mathrm{rrx}}\left(t'\right)} - 1\right) \\ &= -\omega_{\mathrm{c}} \frac{v_{\mathrm{rtx}}\left(t'\right) + v_{\mathrm{rrx}}\left(t'\right)}{c_0 + v_{\mathrm{rrx}}\left(t'\right)}\end{aligned} \tag{2.1.56}$$

is the residual offset to the center frequency and is commonly referred to as Doppler frequency. In case $v_{\mathrm{rrx}}\left(t'\right) \ll c_0$, (2.1.56) becomes

$$\omega_{\mathrm{D}} \simeq -\omega_{\mathrm{c}} \frac{v_{\mathrm{rtx}}\left(t'\right) + v_{\mathrm{rrx}}\left(t'\right)}{c_0} \tag{2.1.57}$$

and in the monostatic case

$$\omega_{\mathrm{D}} \simeq -\omega_{\mathrm{c}} \frac{2v_{\mathrm{r}}\left(t'\right)}{c_0}. \tag{2.1.58}$$

Round Trip Delay Time for Constant Radial Velocities

The special case of a target moving with constant speed in a radial direction with respect to the TX and RX antennas allows for a closed form of the RTDT $\tau\left(t'\right)$. Hence, the special case of constant radial velocity yields valuable insights into the radar signal for which it is elaborated here.

We assume a point target to moves with constant speed and $\vec{r}_{\mathrm{tx}}\left(t\right)$ and $\vec{r}_{\mathrm{rx}}\left(t\right)$ to be collinear such that the radial velocities are constant too.[8] In this case, $v_{\mathrm{rtx}} = \langle \vec{u}_{\mathrm{tx}}, \vec{v}_{\mathrm{t}} - \vec{v}_{\mathrm{p}} \rangle = \pm v_{\mathrm{rt}}$ as well as $v_{\mathrm{rrx}} = \langle \vec{u}_{\mathrm{rx}}, \vec{v}_{\mathrm{t}} - \vec{v}_{\mathrm{p}} \rangle = \pm v_{\mathrm{rt}}$ depending on the location of the point target. If $\vec{p} = \vec{q}$ then $v_{\mathrm{rtx}} = v_{\mathrm{rrx}} = \langle \vec{u}, \vec{v}_{\mathrm{t}} - \vec{v}_{\mathrm{p}} \rangle = \pm v_{\mathrm{rt}}$ with $+v_{\mathrm{rt}}$ in case the point targets moves away from the radar. Note, that v_{rt} is related to the antenna reference frame and $\vec{v}_{\mathrm{t}}$ and $\vec{v}_{\mathrm{p}}$ to the earth surface fixed reference frame. For such constant radial velocities, the RTDT $\tau\left(t'\right) = \tau_{\mathrm{tx}}\left(t'\right) + \tau_{\mathrm{rx}}\left(t'\right)$ can be given explicitly. Using

$$r_{\mathrm{rx}}\left(t\right) = r_{\mathrm{rx},0} + v_{\mathrm{rrx}} t, \tag{2.1.59}$$

$\tau_{\mathrm{rx}}\left(t'\right)$ can be determined from (2.1.2) as

$$\tau_{\mathrm{rx}}\left(t'\right) = \frac{1}{1 + \frac{v_{\mathrm{rrx}}}{c_0}} \frac{r_{\mathrm{rx}}\left(t\right)}{c_0}. \tag{2.1.60}$$

Using the same model (2.1.59) for the $r_{\mathrm{tx}}\left(t\right)$, $\tau_{\mathrm{tx}}\left(t'\right)$ can be determined from (2.1.1) as

$$\tau_{\mathrm{tx}}\left(t'\right) = \frac{r_{\mathrm{tx}}\left(t\right) - \tau_{\mathrm{rx}}\left(t'\right) v_{\mathrm{rtx}}}{c_0}. \tag{2.1.61}$$

Combining (2.1.60) and (2.1.61) yields after short manipulation

$$\tau\left(t'\right) = \frac{c_0 - v_{\mathrm{rtx}}}{c_0 + v_{\mathrm{rrx}}} \frac{r_{\mathrm{rx}}\left(t\right)}{c_0} + \frac{r_{\mathrm{tx}}\left(t\right)}{c_0}. \tag{2.1.62}$$

[8] This means either the TX and RX antennas are co-located and the target moves in a radial direction or the point target moves along the line defined by $\vec{p}$ and $\vec{q}$, where $\vec{p}$ and $\vec{q}$ define the positions of the antennas.

In case the TX and RX antennas are the same, (2.1.62) reduces to

$$\tau\left(t'\right) = \frac{1}{1+\frac{v_{\mathrm{rt}}}{c_0}}\frac{2r\left(t\right)}{c_0}.$$

Stop-and-Go Approximation

The range and the RTDT are inherently coupled which can be seen from (2.1.3), (2.1.2), and (2.1.1) as

$$\begin{aligned}\tau\left(t'\right) &= \tau_{\mathrm{tx}}\left(t'\right) + \tau_{\mathrm{rx}}\left(t'\right)\\ &= \frac{r_{\mathrm{tx}}\left(t-\tau_{\mathrm{rx}}\left(t'\right)\right) + r_{\mathrm{rx}}\left(t-\tau_{\mathrm{rx}}\left(t'\right)\right)}{c_0}.\end{aligned}$$

As a consequence, it is not possible to give an explicit formulation for $\tau\left(t'\right)$ without additional knowledge of $\vec{r}_{\mathrm{tx}}\left(t'\right)$ and $\vec{r}_{\mathrm{rx}}\left(t'\right)$ (as it was the case for constant radial velocities). The exact value for $\tau\left(t'\right)$ can be found by use of numerical approaches for simulation setups where $\vec{r}_{\mathrm{tx}}\left(t\right)$ and $\vec{r}_{\mathrm{rx}}\left(t\right)$ are given. For a measurement model, however, an explicit expression for $\tau\left(t'\right)$ is required for which a motion model for $\vec{r}_{\mathrm{tx}}\left(t\right)$ and $\vec{r}_{\mathrm{rx}}\left(t\right)$ needs to be assumed. The most common assumption is, that the target does not move significantly during the travel time. In this case, the phase variation given by (2.1.44) is negligible, i. e.

$$\omega_{\mathrm{b}}\triangle\tau\left(t'\right) = \frac{\omega_{\mathrm{b}}}{c_0}\left|r_{\mathrm{tx}}\left(t'\right) - r_{\mathrm{tx}}\left(t\right) + r_{\mathrm{rx}}\left(t'\right) - r_{\mathrm{rx}}\left(t\right)\right| = k_{\mathrm{b}}\triangle r_{\mathrm{walk}} < \gamma_{\mathrm{tol}} \tag{2.1.63}$$

with $\triangle r_{\mathrm{walk}}$ denoting the range walk. Hence, the RTDT can be simplified to

$$\tau\left(t'\right) \simeq \tau\left(t\right) = \frac{r_{\mathrm{tx}}\left(t\right) + r_{\mathrm{rx}}\left(t\right)}{c_0}. \tag{2.1.64}$$

In case of highly maneuvering targets or long pulses e. g. in case of continuous wave (CW) radars, the stop and go approximation may not valid any more. In this case, more sophisticated motion models are assumed for $\vec{r}_{\mathrm{tx}}\left(t'\right)$ and $\vec{r}_{\mathrm{rx}}\left(t'\right)$, e. g., [8, 9]!

A reasonable alternative compared to the general criterion (2.1.63) is to demand the range walk to be less than the range resolution

$$\triangle r_{\mathrm{walk}} < \gamma_{\mathrm{tol}}\delta r. \tag{2.1.65}$$

The range walk depends on the application scenario. For the case of airborne radar, an estimation of $\triangle r_{\mathrm{walk}}$ for non moving targets can be found in Appendix A.2.3. In addition to determine the range walk for one pulse, it may also be calculated for a whole CPI i. e. $t_{\mathrm{cpi}} = N_{\mathrm{p}}t_{\mathrm{p}}$ to verify the stop-and-go approximation to be valid in any case.

Plane Wave Approximation

This approximation is also known as far field condition for antenna arrays. The length difference between a target to the antenna origin $\|\vec{r}\| = r$ and target to an antenna located at $\vec{x}$ is [4]

$$\triangle l = \|\vec{r} - \vec{x}\| - \|\vec{r}\| . \tag{2.1.66}$$

The length difference in case of a plane wave approximation is

$$\triangle l_{\mathrm{pw}} = - \langle \vec{u}, \vec{x} \rangle . \tag{2.1.67}$$

The error between (2.1.66) and (2.1.67) is negligible if it is only a fraction of the wave length

$$\epsilon = |\triangle l - \triangle l_{\mathrm{pw}}| \leq \gamma_{\mathrm{far}} \lambda_{\mathrm{r}}. \tag{2.1.68}$$

The worst case yielding an upper bound for (2.1.68) is

$$\triangle l_{\mathrm{pw}} = \langle \vec{u}, \vec{x} \rangle = 0 \Rightarrow \triangle l = \sqrt{r^2 + x^2} - r \leq \gamma_{\mathrm{far}} \lambda_{\mathrm{r}}. \tag{2.1.69}$$

In case (2.1.68) holds, then for a given TX and RX antenna pair the corresponding RTDT given by (2.1.3) can be approximated by

$$\begin{aligned} \tau\left(t'\right) &= \frac{r_{\mathrm{tx}}\left(t'\right) + r_{\mathrm{rx}}\left(t'\right)}{c_0} \\ &\simeq \frac{r\left(t'\right) - \langle \vec{u}, \vec{q} \rangle + r\left(t'\right) - \langle \vec{u}, \vec{p} \rangle}{c_0} \\ &= \frac{2r\left(t'\right) - \langle \vec{u}, \vec{p} + \vec{q} \rangle}{c_0}. \end{aligned} \tag{2.1.70}$$

Narrow- and Broadband Beamforming

For GMTI processing, beamforming is of particular importance. Usually a delay and sum beamforming (DSB) approach is applied which depends on the relative bandwidth $b_{\mathrm{r}}/f_{\mathrm{c}}$ of the transmitted signal. In case the relative bandwidth is small, the relative delay term in the complex envelope factor $s_{\mathrm{tx}}\left(t - \tau_{n_{\mathrm{tx}} n_{\mathrm{rx}}}\left(t'\right)\right)$ from (2.1.55) for distinct $\tau_{n_{\mathrm{tx}} n_{\mathrm{rx}}}\left(t'\right)$ is insignificant. This means, that for different TX and RX antenna combinations $s_{\mathrm{tx}}\left(t - \tau_{n_{\mathrm{tx}} n_{\mathrm{rx}}}\left(t'\right)\right)$ does not change significantly, where $n_{\mathrm{tx}} \in [0, N_{\mathrm{tx}})$ denotes the index of the TX and $n_{\mathrm{rx}} \in [0, N_{\mathrm{rx}})$ the index of the RX antenna. In this case, a narrow band beamforming can be done by considering the phase of the exponential term

$$\phi_{n_{\mathrm{tx}} n_{\mathrm{rx}}} = \omega_{\mathrm{c}} \tau_{n_{\mathrm{tx}} n_{\mathrm{rx}}}\left(t'\right) \tag{2.1.71}$$

in (2.1.55) only. Assuming the far field approximation holds, the relative phase difference with respect to the center frequency is

$$\triangle \phi_{n_{\mathrm{tx}} n_{\mathrm{rx}}} \simeq -k_{\mathrm{c}} \left\langle \vec{u}, \vec{p}_{n_{\mathrm{rx}}} + \vec{q}_{n_{\mathrm{tx}}} \right\rangle . \tag{2.1.72}$$

If the relative bandwidth is high, the relative delay term in the complex envelop factor $s_{\mathrm{tx}}\left(t-\tau_{n_{\mathrm{tx}}n_{\mathrm{rx}}}\left(t'\right)\right)$ from (2.1.55) matter and true time shifts need to be used. If this would not be done, the formed beam squints with respect to ω_{r}. Let $\vec{u}_0$ be the desired steering direction and $\vec{u}$ the direction of the impinging wave. The narrow band phase correction for $\vec{u}_0$ is given by (2.1.72). For an impinging wave with different k_*, the narrow band phase delay leads to a focused beam at a different direction, namely [10]

$$-k_{\mathrm{c}}\left\langle\vec{u}_0,\vec{p}_{n_{\mathrm{rx}}}+\vec{q}_{n_{\mathrm{tx}}}\right\rangle=\triangle\phi_{n_{\mathrm{tx}}n_{\mathrm{rx}}}=-k_*\left\langle\vec{u},\vec{p}_{n_{\mathrm{rx}}}+\vec{q}_{n_{\mathrm{tx}}}\right\rangle \tag{2.1.73}$$

or

$$u=\frac{k_{\mathrm{c}}}{k_*}u_0=\frac{f_{\mathrm{c}}}{f_*}u_0$$

where u and u_0 are the directional cosines regarding the inner products in (2.1.73). The total squint for f_* being $f_+=f_{\mathrm{c}}+\frac{b_{\mathrm{r}}}{2}$ and $f_-=f_{\mathrm{c}}-\frac{b_{\mathrm{r}}}{2}$ is

$$\left|u_+-u_-\right|=u_0\frac{b_{\mathrm{r}}/f_{\mathrm{c}}}{\left(1+b_{\mathrm{r}}/f_{\mathrm{c}}/2\right)\left(1-b_{\mathrm{r}}/f_{\mathrm{c}}/2\right)}.$$

Letting $f_*=f_{\mathrm{r}}=f_{\mathrm{c}}+\triangle f$ the squint becomes

$$\frac{\triangle f}{f_{\mathrm{r}}}=-\frac{\triangle u}{u_0}, \tag{2.1.74}$$

where $\triangle u=u-u_0$. If $\triangle u$ is restricted to be below the array resolution $\triangle u=\lambda_{\mathrm{r}}/L$ with L denoting the largest array size and setting $\triangle f=b_{\mathrm{r}}/2$ then (2.1.74) can be converted to

$$L\leq 4\delta r. \tag{2.1.75}$$

Hence, if the biggest aperture size is smaller than $4\delta r$, with $\delta r=c_0/2/b_{\mathrm{r}}$ denoting the range resolution, the squint due to narrow band beamforming is less than the array resolution. In the limit of (2.1.75), the worst case $u_0=1$ was considered.

Range Doppler Coupling and Correlation Loss for LFM Chirp

The range Doppler coupling and correlation loss as such are not approximations, rather effects on the range estimation and the achievable SNR caused by a Doppler offset. These effects are considered here to check if they are of concern since they are usually neglected in the signal model.

In case the received signal can be modeled as a time shifted TX signal as derived in Section 2.1.3, the matched filtered pulse compression is conducted by a convolution of the received signal with the filter response $h_{n_{\mathrm{p}}}\left(t\right)=s^*_{\mathrm{tx},n_{\mathrm{p}}}\left(-t\right)$. The implication of such a pulse compression for a Doppler modulated received signal is measured by means of an ambiguity function (AF) defined as the magnitude of the pulse compression result [2]

$$\mathrm{A}_{n_{\mathrm{p}}}\left(t,f_{\mathrm{D}}\right)=\int_{-\infty}^{\infty}s_{\mathrm{tx},n_{\mathrm{p}}}\left(s\right)s^*_{\mathrm{tx},n_{\mathrm{p}}}\left(s-t\right)\mathrm{e}^{\mathrm{j}2\pi f_{\mathrm{D}}s}\mathrm{d}s.$$

Since the signal energy is normed to unity by (2.1.40), the ambiguity function at the origin is

$$\mathrm{A}_{n_\mathrm{p}}(0,0) = 1.$$

In case of an LFM chirp signal

$$s_{\mathrm{tx},n_\mathrm{p}}(t) = \frac{\mathrm{rect}\left(t/T_\mathrm{p}\right)}{\sqrt{T_\mathrm{p}}} \mathrm{e}^{\mathrm{j}\pi b_\mathrm{r} t^2/T_\mathrm{p}} \tag{2.1.76}$$

the pulse compression result is

$$\mathrm{A}_{n_\mathrm{p}}(t, f_\mathrm{D}) = \Lambda\left(t/T_\mathrm{p}\right) \mathrm{sinc}\left(\left(t b_\mathrm{r} + f_\mathrm{D} T_\mathrm{p}\right) \Lambda\left(t/T_\mathrm{p}\right)\right) \mathrm{e}^{-\mathrm{j}\pi b_\mathrm{r} t^2/T_\mathrm{p}} \tag{2.1.77}$$

with $\Lambda(x)$ denoting the triangular function [2]. The AF reveals a shift in time. The peak of the AF (2.1.77) occurs at

$$\triangle t_\mathrm{dc} = -\frac{f_\mathrm{D} T_\mathrm{p}}{b_\mathrm{r}},$$

and acts as a time offset to (2.1.3) as

$$\tau\left(t'\right) = \tau_\mathrm{rx}\left(t'\right) + \tau_\mathrm{tx}\left(t'\right) + \triangle t_\mathrm{dc}. \tag{2.1.78}$$

In the monostatic case this results in a range shift of

$$\triangle r_\mathrm{dc} = \frac{c_0 \triangle t_\mathrm{dc}}{2} = \frac{v_\mathrm{r} T_\mathrm{p} f_\mathrm{c}}{b_\mathrm{r}}. \tag{2.1.79}$$

In addition to the time shift, the AF provides information about a Doppler induced correlation loss reducing the achievable SNR. This loss, however, is usually neglected as

$$\mathrm{A}_{n_\mathrm{p}}(0, f_\mathrm{D,max}) \simeq 1 \tag{2.1.80}$$

with

$$f_\mathrm{D,max} \simeq -\frac{2 v_\mathrm{r,tot}}{c_0} f_\mathrm{c},$$

where $v_\mathrm{r,tot}$ defined in (A.2.21) is the maximum occurring radial velocity in the GMTI case. Also, time delays due to different spatial locations of the TX and RX antennas are neglected. As such, a common approximation is

$$\mathrm{A}_{n_\mathrm{p}}(\triangle\tau_\mathrm{max}, 0) \simeq 1 \tag{2.1.81}$$

with

$$\triangle\tau_\mathrm{max} = \frac{\triangle r_\mathrm{max}}{c_0} = \frac{\max \|\vec{p} - \vec{q}\|}{c_0},$$

where next to the magnitude also the phase offset due to the exponential term in (2.1.77) is neglected. In case of a LFM chirp the total phase offset is

$$\triangle\phi = \omega_\mathrm{r,max} \frac{\triangle r_\mathrm{max}}{c_0} - \frac{\pi b_\mathrm{r}}{T_\mathrm{p}} \left(\frac{\triangle r_\mathrm{max}}{c_0}\right)^2, \tag{2.1.82}$$

where the first term is a phase shift due to the different spatial location (2.1.77) and the latter term the impact of the MF (2.1.77). The latter term in (2.1.82) matters if

$$2f_{\mathrm{r,max}}c_0 < \gamma_{\mathrm{tol}} \triangle r_{\max} \frac{b_{\mathrm{r}}}{T_{\mathrm{p}}} \tag{2.1.83}$$

with e. g. $\gamma_{\mathrm{tol}} = 1/10$. This, however, becomes significant for ultra short pulse and ultra wide-band radar systems only.

Finally it shall be mentioned, that it is assumed that the AF decays rapidly such that consecutive pulses do not influence each other, hence

$$\mathrm{A}_{n_{\mathrm{p}}}\left(nt_{\mathrm{p}}, f_{\mathrm{D}}\right) = 0 \tag{2.1.84}$$

for $n \in \mathbb{N} \setminus \{0\}$. The pulse compression result for a burst of consecutive pulses as given by (2.1.4)

$$s_{\mathrm{tx}}\left(t\right) = \sum_{n_{\mathrm{p}}=0}^{N_{\mathrm{p}}-1} s_{\mathrm{tx},n_{\mathrm{p}}}\left(t - n_{\mathrm{p}}t_{\mathrm{p}}\right)$$

therefore results to

$$\begin{aligned} \mathrm{A}\left(t, f_{\mathrm{D}}\right) &= \int_{-\infty}^{\infty} s_{\mathrm{tx}}\left(s\right) s_{\mathrm{tx}}^{*}\left(s - t\right) \mathrm{e}^{\mathrm{j}2\pi f_{\mathrm{D}} s} \mathrm{d}s \\ &\simeq \sum_{n_{\mathrm{p}}=0}^{N_{\mathrm{p}}-1} \mathrm{A}_{n_{\mathrm{p}}}\left(t - n_{\mathrm{p}}t_{\mathrm{p}}, f_{\mathrm{D}}\right). \end{aligned} \tag{2.1.85}$$

2.1.4. Space-Time Radar Signals

In this section a space-time signal model required for GMTI processing is discussed. This model will be stated for a multi-channel radar. The reasoning why multiple channels are necessary for GMTI is given in Section 2.3.

As shown in Table 2.1.1, the classical airborne GMTI scenario depicted in Tab. 1.0.1 allows for all approximations given in Section 2.1.3. Since the target induced phase modulation can be

Approximation	Criteria	Result
Target Ind. Phase Modulation	(2.1.51)	$\mathrm{CL}_{\mathrm{chirp}} < -100\,\mathrm{dB}$
Stop-and-Go Approximation	(2.1.65),(A.2.20)	$\triangle r_{\mathrm{walk}} = 3.85 \times 10^{-3}\,\mathrm{m} \ll \delta r = 10\,\mathrm{m}$
Plane Wave Approximation	(2.1.69)	$\triangle l = \lambda_{\mathrm{r}} \times 10^{-4}\,\mathrm{m} \ll \lambda_{\mathrm{r}}/10$
Narrow Band Approximation	(2.1.75)	$L = \lambda_{\mathrm{r,min}} N_{\mathrm{rx}}/2 = 0.96\,\mathrm{m} \ll 4\delta r = 40\,\mathrm{m}$
Range-Doppler Coupling	(2.1.79)	$\triangle r_{\mathrm{dc}} \simeq 3.75\,\mathrm{m} < \delta r = 10\,\mathrm{m}$
MF Doppler CL	(2.1.80)	$\mathrm{A}\left(0, f_{\mathrm{D,max}}\right) \simeq -1\,\mathrm{dB}$
MF Time Delay CL	(2.1.81)	$\mathrm{A}\left(\triangle\tau_{\max}, 0\right) \simeq -0.05\,\mathrm{dB}$
MF Phase Offset	(2.1.83)	$2f_{\mathrm{r,max}}c_0 = 10^{18}\,\mathrm{m/s^2} \gg 4.5 \times 10^{9}\,\mathrm{m/s^2}$

Table 2.1.1.: Validity of airborne GMTI approximations.

neglected, the received signal corresponding to a single point target is given by (2.1.55) as

$$s'_{\mathrm{b,rx,cal}}\left(t\right) = x_{\mathrm{cal}} s_{\mathrm{tx}}\left(t - \tau\left(t'\right)\right) \mathrm{e}^{\mathrm{j}\omega_{\mathrm{D}} t + \mathrm{j}\phi_{\mathrm{c}} + \mathrm{j}\phi'_{\mathrm{tx}} + \mathrm{j}\phi'_{\mathrm{rx}}} \tag{2.1.86}$$

with

$$\begin{aligned}
\omega_{\mathrm{D}} &= -\omega_{\mathrm{c}} \frac{v_{\mathrm{rtx}}\left(t'\right) + v_{\mathrm{rrx}}\left(t'\right)}{c_0 + v_{\mathrm{rrx}}\left(t'\right)} \\
\phi'_{\mathrm{tx}} &= -\omega'_{\mathrm{sc}} \tau_{\mathrm{tx}}\left(t'\right) \\
\phi'_{\mathrm{rx}} &= -\omega'_{\mathrm{sc}} \left(\alpha_{\mathrm{rx}}(t') \tau_{\mathrm{rx}}\left(t'\right) + \left(\alpha_{\mathrm{rx}}(t') - 1\right) \tau_{\mathrm{tx}}\left(t'\right)\right),
\end{aligned}$$

where calibrated signals are assumed. Due to the co-located setting, the occurring radial velocities can be assumed equal, hence $v_{\mathrm{rtx}}\left(t'\right) = v_{\mathrm{rrx}}\left(t'\right)$. Furthermore, the considered velocities are very small compared to c_0. Therefore, the corresponding angular Doppler frequency and phase terms are well approximated by

$$\begin{aligned}
\omega_{\mathrm{D}} &\simeq -\omega_{\mathrm{c}} \frac{2 v_{\mathrm{rt}}\left(t'\right)}{c_0} \\
\phi'_{\mathrm{tx}} &\simeq -\omega_{\mathrm{c}} \tau_{\mathrm{tx}}\left(t'\right) \\
\phi'_{\mathrm{rx}} &\simeq -\omega_{\mathrm{c}} \tau_{\mathrm{rx}}\left(t'\right).
\end{aligned}$$

Next, due to the fulfilled stop and go approximation and since the range Doppler coupling effect of the matched filter can be neglected, the delay terms can be taken according to (2.1.64) as

$$\tau\left(t'\right) \simeq \tau\left(t\right) = \tau_{\mathrm{tx}}\left(t\right) + \tau_{\mathrm{rx}}\left(t\right) = \frac{r_{\mathrm{tx}}\left(t\right) + r_{\mathrm{rx}}\left(t\right)}{c_0}. \tag{2.1.87}$$

The valid plane wave approximation allows according to (2.1.70) for

$$\tau\left(t'\right) \simeq \frac{2r\left(t'\right) - \langle \vec{u}, \vec{p} + \vec{q} \rangle}{c_0}, \tag{2.1.88}$$

where $\vec{q}$ denotes the location of the TX, $\vec{p}$ the location of the RX antenna, and $\vec{u}$ the line of sight vector pointing from the antenna to the target. Using (2.1.87) and (2.1.88), the sum of the phase terms can be further simplified to

$$\begin{aligned}
\phi'_{\mathrm{tx}} + \phi'_{\mathrm{rx}} &\simeq -\frac{\omega_{\mathrm{c}}}{c_0} \left(2r\left(t\right) - \langle \vec{u}, \vec{p} + \vec{q} \rangle\right) \\
&= -2k_{\mathrm{c}} r\left(t\right) + k_{\mathrm{c}} \langle \vec{u}, \vec{p} + \vec{q} \rangle,
\end{aligned}$$

where $k_{\mathrm{c}} = \omega_{\mathrm{c}}/c_0 = 2\pi/\lambda_{\mathrm{c}}$ is the wave number corresponding to the center frequency. Substituting this into the received signal (2.1.86) yields

$$s'_{\mathrm{b,rx,cal}}\left(t\right) = x_{\mathrm{cal}} s_{\mathrm{tx}}\left(t - \tau\left(t\right)\right) \mathrm{e}^{-\mathrm{j}2k_{\mathrm{c}} r(t) + \mathrm{j}\omega_{\mathrm{D}} t + \mathrm{j}k_{\mathrm{c}} \langle \vec{u}, \vec{p} + \vec{q} \rangle + \mathrm{j}\phi_{\mathrm{c}}}.$$

Furthermore, since the Doppler and time delay correlation losses can be neglected, the matched

filter output can be written as

$$y\left(t\right)=x_{\mathrm{cal}}\mathrm{A}\left(t-2r\left(t\right)/c_0,0\right)\mathrm{e}^{-\mathrm{j}2k_{\mathrm{c}}r(t)+\mathrm{j}\omega_{\mathrm{D}}t+\mathrm{j}k_{\mathrm{r}}\langle\vec{u},\vec{p}+\vec{q}\rangle+\mathrm{j}\phi_{\mathrm{c}}}, \tag{2.1.89}$$

since $\mathrm{A}\left(t-2r\left(t\right)/c_0+\triangle\tau_{\max},f_{\mathrm{D}}\right)\simeq\mathrm{A}\left(t-2r\left(t\right)/c_0,0\right)$ holds. Finally, space-time adaptive processing (STAP) is a pulse by pulse processing scheme using multiple antennas. Thus, by use of (2.1.85), the matched filtered signal can be rewritten to

$$y_{n_{\mathrm{tx}}n_{\mathrm{rx}}}\left(t\right)=\sum_{n_{\mathrm{p}}=0}^{N_{\mathrm{p}}-1}x_{\mathrm{cal}}\mathrm{A}_{n_{\mathrm{p}}}\left(t-n_{\mathrm{p}}t_{\mathrm{p}}-2r\left(t\right)/c_0,0\right)\mathrm{e}^{-\mathrm{j}k_{\mathrm{c}}2r(t)+\mathrm{j}\omega_{\mathrm{D}}t+\mathrm{j}k_{\mathrm{c}}\left\langle\vec{u},\vec{p}_{n_{\mathrm{rx}}}+\vec{q}_{n_{\mathrm{tx}}}\right\rangle+\mathrm{j}\phi_{\mathrm{c}}}, \tag{2.1.90}$$

where n_{p} denotes the pulse number, t_{p} the PRI, $\vec{q}_{n_{\mathrm{tx}}}$ the location of the $n_{\mathrm{tx}}-\mathrm{th}$ TX antenna, and $\vec{p}_{n_{\mathrm{rx}}}$ the location of the $n_{\mathrm{rx}}-\mathrm{th}$ RX antenna. Considering the received signal of the n_{r}-th range gate and the n_{p}-th pulse only by selecting

$$t=t_{n_{\mathrm{r}}n_{\mathrm{p}}}=\tau_{n_{\mathrm{r}}}+n_{\mathrm{p}}t_{\mathrm{p}} \tag{2.1.91}$$

with $\tau_{n_{\mathrm{r}}}=2n_{\mathrm{r}}\delta r/c_0$, the measurement model becomes[9]

$$y_{n_{\mathrm{r}}n_{\mathrm{tx}}n_{\mathrm{rx}}n_{\mathrm{p}}}=x_{\mathrm{cal}}\mathrm{e}^{-\mathrm{j}k_{\mathrm{c}}2r+\mathrm{j}\omega_{\mathrm{D}}(\tau_{n_{\mathrm{r}}}+n_{\mathrm{p}}t_{\mathrm{p}})+\mathrm{j}k_{\mathrm{c}}\left\langle\vec{u},\vec{p}_{n_{\mathrm{rx}}}+\vec{q}_{n_{\mathrm{tx}}}\right\rangle+\mathrm{j}\phi_{\mathrm{c}}}, \tag{2.1.92}$$

where $\mathrm{A}_{n_{\mathrm{p}}}\left(nt_{\mathrm{p}},f_{\mathrm{D}}\right)=0$ from (2.1.84) and the stop-and-go approximation $r\left(t_{n_{\mathrm{r}}n_{\mathrm{p}}}\right)\simeq r$ was used. Finally, (2.1.92) can be simplified further by noting that the received complex amplitude x_{cal} is a function depending on the point targets reflectivity coefficient α_{r}. In the GMTI case, α_{r} therefore induces a random phase, potentially changing from pulse to pulse. This renders the remaining phase terms depending on r, ω_{D}, and ϕ_{c} in (2.1.92) unusable and hence the measurement model can be simplified to

$$y_{n_{\mathrm{r}}n_{\mathrm{tx}}n_{\mathrm{rx}}n_{\mathrm{p}}}\left(r,\vec{u},\omega_{\mathrm{D}}\right)=x\left(r\right)\mathrm{e}^{\mathrm{j}\omega_{\mathrm{D}}n_{\mathrm{p}}t_{\mathrm{p}}+\mathrm{j}k_{\mathrm{c}}\left\langle\vec{u},\vec{p}_{n_{\mathrm{rx}}}+\vec{q}_{n_{\mathrm{tx}}}\right\rangle} \tag{2.1.93}$$

with

$$x\left(r\right)=x_{\mathrm{cal}}\left(r,\alpha_{\mathrm{r}}\right)\mathrm{e}^{-\mathrm{j}2k_{\mathrm{c}}r+\mathrm{j}\omega_{\mathrm{D}}\tau_{n_{\mathrm{r}}}+\mathrm{j}\phi_{\mathrm{c}}} \tag{2.1.94}$$

denoting a random complex amplitude. The model given by (2.1.93) renders to be the general measurement model used in the GMTI case. As noted explicitly in (2.1.93), the signal model reveals information about the range r, the LOS direction $\vec{u}$, and the targets Doppler frequency ω_{D} which are to be estimated from $y_{n_{\mathrm{r}}n_{\mathrm{tx}}n_{\mathrm{rx}}n_{\mathrm{p}}}$. All this information is required for STAP processing.

In the following, the general measurement model (2.1.93) is further reduced to follow the simulation setting defined in Tab. 1.0.1. Hence, considering only target range n_{r}, one transmit antenna located at $\vec{q}=\vec{0}$, and the RX antenna to be a uniform linear array (ULA) arranged along

[9] Neglecting straddle losses and range ambiguities.

the antenna x axis as

$$\vec{p}_{n_{\mathrm{rx}}} = \begin{bmatrix} n_{\mathrm{rx}} d \\ 0 \\ 0 \end{bmatrix},$$

the measurement model (2.1.93) becomes

$$y_{n_{\mathrm{rx}} n_{\mathrm{p}}}(u, \omega_{\mathrm{D}}) = x \mathrm{e}^{\mathrm{j}\omega_{\mathrm{D}} n_{\mathrm{p}} t_{\mathrm{p}} + \mathrm{j} k_{\mathrm{c}} u d n_{\mathrm{rx}}}. \tag{2.1.95}$$

The corresponding ULA antenna configuration is sketched in Fig. 2.1.4. By introducing the com-

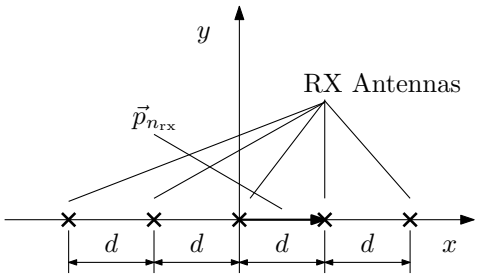

Figure 2.1.4.: ULA RX antenna used for simulations.

mon normalizations

$$\omega_{\mathrm{D}} n_{\mathrm{p}} t_{\mathrm{p}} = \frac{2\pi f_{\mathrm{D}} n_{\mathrm{p}}}{f_{\mathrm{p}}} = 2\pi \bar{f}_{\mathrm{D}} n_{\mathrm{p}}$$

and

$$k_{\mathrm{c}} u d n_{\mathrm{rx}} = \frac{2\pi}{\lambda_{\mathrm{c}}} u d n_{\mathrm{rx}} = 2\pi \bar{d} u n_{\mathrm{rx}} = 2\pi \bar{u} n_{\mathrm{rx}},$$

where $f_{\mathrm{p}} = 1/t_{\mathrm{p}}$ denotes the pulse repetition frequency (PRF),

$$\bar{f}_{\mathrm{D}} = \frac{f_{\mathrm{D}}}{f_{\mathrm{p}}} \tag{2.1.96}$$

the normalized Doppler frequency,

$$\bar{u} = u\bar{d} \tag{2.1.97}$$

the normalized directional cosine, and

$$\bar{d} = \frac{d}{\lambda_{\mathrm{c}}} \tag{2.1.98}$$

the normalized distance between consecutive RX antennas, the signal can be formulated as

$$y_{n_{\mathrm{rx}} n_{\mathrm{p}}}\left(\bar{u}, \bar{f}_{\mathrm{D}}\right) = x g_{n_{\mathrm{rx}} n_{\mathrm{p}}}\left(\bar{u}, \bar{f}_{\mathrm{D}}\right), \tag{2.1.99}$$

where

$$g_{n_{\mathrm{rx}} n_{\mathrm{p}}}\left(\bar{u}, \bar{f}_{\mathrm{D}}\right) = \mathrm{e}^{\mathrm{j}2\pi \bar{f}_{\mathrm{D}} n_{\mathrm{p}} + \mathrm{j}2\pi \bar{u} n_{\mathrm{rx}}} \tag{2.1.100}$$

is the deterministic space-time signal model [1]. A common representation of the measurements

(2.1.99) is to arrange the spatial and temporal samples into a matrix as

$$\boldsymbol{Y}\left(\bar{u},\bar{f}_{\mathrm{D}}\right)=x\begin{bmatrix}1 & \mathrm{e}^{\mathrm{j}2\pi\bar{f}_{\mathrm{D}}} & \dots & \mathrm{e}^{\mathrm{j}2\pi\bar{f}_{\mathrm{D}}(N_{\mathrm{p}}-1)}\\ \mathrm{e}^{\mathrm{j}2\pi\bar{u}} & \mathrm{e}^{\mathrm{j}2\pi\bar{f}_{\mathrm{D}}+\mathrm{j}2\pi\bar{u}} & & \vdots\\ \vdots & & \ddots & \vdots\\ \mathrm{e}^{\mathrm{j}2\pi\bar{u}(N_{\mathrm{rx}}-1)} & \dots & \dots & \mathrm{e}^{\mathrm{j}2\pi\bar{f}_{\mathrm{D}}(N_{\mathrm{p}}-1)+\mathrm{j}2\pi\bar{u}(N_{\mathrm{rx}}-1)}\end{bmatrix}\in\mathbb{C}^{N_{\mathrm{rx}}\times N_{\mathrm{p}}},\tag{2.1.101}$$

$$=x\boldsymbol{G}\left(\bar{u},\bar{f}_{\mathrm{D}}\right)\tag{2.1.102}$$

$$=x\boldsymbol{a}\left(\bar{u}\right)\boldsymbol{b}^{\mathrm{T}}\left(\bar{f}_{\mathrm{D}}\right),\tag{2.1.103}$$

where

$$\boldsymbol{a}\left(\bar{u}\right)=\left[\mathrm{e}^{\mathrm{j}2\pi n_{\mathrm{rx}}\bar{u}}\right]_{n_{\mathrm{rx}}=0}^{N_{\mathrm{rx}}-1}=\begin{bmatrix}1 & \mathrm{e}^{\mathrm{j}2\pi\bar{u}} & \dots & \mathrm{e}^{\mathrm{j}2\pi(N_{\mathrm{rx}}-1)\bar{u}}\end{bmatrix}^{\mathrm{T}}\in\mathbb{C}^{N_{\mathrm{rx}}}\tag{2.1.104}$$

denotes the space vector a. k. a. angular steering vector or array manifold and

$$\boldsymbol{b}\left(\bar{f}_{\mathrm{D}}\right)=\left[\mathrm{e}^{\mathrm{j}2\pi n_{\mathrm{p}}\bar{f}_{\mathrm{D}}}\right]_{n_{\mathrm{p}}=0}^{N_{\mathrm{p}}-1}\in\mathbb{C}^{N_{\mathrm{p}}}\tag{2.1.105}$$

the time vector a. k. a. temporal steering vector. Another common representation of the measurements (2.1.99) is yielded by vectorizing (2.1.101) into

$$\boldsymbol{y}\left(\bar{u},\bar{f}_{\mathrm{D}}\right)=x\boldsymbol{g}\left(\bar{u},\bar{f}_{\mathrm{D}}\right)\in\mathbb{C}^{N_{\mathrm{rx}}N_{\mathrm{p}}},\tag{2.1.106}$$

where

$$\boldsymbol{g}\left(\bar{u},\bar{f}_{\mathrm{D}}\right)=\boldsymbol{b}\left(\bar{f}_{\mathrm{D}}\right)\otimes\boldsymbol{a}\left(\bar{u}\right)\tag{2.1.107}$$

denotes the so called space time vector and $\otimes$ the Kronecker product. The measurement model forms (2.1.99), (2.1.101), and (2.1.106) come in handy in case of theoretical studies as done in Section 2.2. However, it is necessary to discretize the angular Doppler scene domain too in order to allow for a reconstruction of it. Doing so yields

$$y_{n_{\mathrm{rx}}n_{\mathrm{p}};n_{\mathrm{u}}n_{\mathrm{D}}}=x\mathrm{e}^{\mathrm{j}2\pi n_{\mathrm{p}}n_{\mathrm{D}}/N_{\mathrm{D}}+\mathrm{j}2\pi n_{\mathrm{rx}}n_{\mathrm{u}}/N_{\mathrm{u}}},\tag{2.1.108}$$

where $\bar{u}$ and $\bar{f}_{\mathrm{D}}$ span the intervals

$$\bar{u}=2\bar{d}\frac{n_{\mathrm{u}}}{N_{\mathrm{u}}}\in\left[-\bar{d},\bar{d}\right)\tag{2.1.109}$$

$$\bar{f}_{\mathrm{D}}=\frac{n_{\mathrm{D}}}{N_{\mathrm{D}}}\in\left[-1/2,1/2\right),\tag{2.1.110}$$

with the bin indices ranges

$$n_{\mathrm{u}}\in\Omega_{N_{\mathrm{u}}}=\{-N_{\mathrm{u}}/2,-N_{\mathrm{u}}/2+1,\dots,N_{\mathrm{u}}/2-1\}\tag{2.1.111}$$

$$n_{\mathrm{D}}\in\Omega_{N_{\mathrm{D}}}=\{-N_{\mathrm{D}}/2,-N_{\mathrm{D}}/2+1,\dots,N_{\mathrm{D}}/2-1\}\tag{2.1.112}$$

or in case of $d=\lambda_{\mathrm{c}}/2$, $\bar{u}\in[-1/2,1/2)$. Note that $N_{\mathrm{u}}\in2\mathbb{Z}$ and $N_{\mathrm{D}}\in2\mathbb{Z}$ need to be even numbers

if $\bar{u}$ and $\bar{f}_{\mathrm{D}}$ span the whole interval. For the case of multiple present targets the discretized measurement model becomes

$$y_{n_{\mathrm{rx}}n_{\mathrm{p}}} = \sum_{n_{\mathrm{D}}} \sum_{n_{\mathrm{u}}} x_{n_{\mathrm{u}}n_{\mathrm{D}}} \mathrm{e}^{\mathrm{j}2\pi n_{\mathrm{p}} n_{\mathrm{D}}/N_{\mathrm{D}} + \mathrm{j}2\pi n_{\mathrm{rx}} n_{\mathrm{u}}/N_{\mathrm{u}}} \tag{2.1.113}$$

which renders to be a 2D-inverse discrete Fourier transform (IDFT) form mapping from the normalized angle Doppler scene domain $x_{n_{\mathrm{u}}n_{\mathrm{D}}}$ to the channel-pulse measurement domain $y_{n_{\mathrm{rx}}n_{\mathrm{p}}}$. As done in (2.1.101), the scalar measurement model (2.1.113) can also be formulated as a measurement matrix

$$\boldsymbol{Y} = \boldsymbol{A}\boldsymbol{X}\boldsymbol{B}^{\mathrm{T}}, \tag{2.1.114}$$

where $\boldsymbol{X} \in \mathbb{C}^{N_{\mathrm{u}} \times N_{\mathrm{D}}}$ denotes the radar scene a. k. a. reflectivity or scatter map in the angular-Doppler domain,

$$\boldsymbol{A} = \left[\boldsymbol{a}\left(n_{\mathrm{u}}/N_{\mathrm{u}}\right)\right]_{n_{\mathrm{u}} \in \Omega_{N_{\mathrm{u}}}} \in \mathbb{C}^{N_{\mathrm{rx}} \times N_{\mathrm{u}}} \tag{2.1.115}$$

the spatial steering matrix formed by the spatial steering vectors (2.1.104) steered to all angular directions defined by the index set $\Omega_{N_{\mathrm{u}}}$, and

$$\boldsymbol{B} = \left[\boldsymbol{b}\left(n_{\mathrm{D}}/N_{\mathrm{D}}\right)\right]_{n_{\mathrm{D}} \in \Omega_{N_{\mathrm{D}}}} \in \mathbb{C}^{N_{\mathrm{p}} \times N_{\mathrm{D}}} \tag{2.1.116}$$

the corresponding temporal steering matrices formed by the temporal steering vectors (2.1.105) steered to all Doppler directions defined by the index set $\Omega_{N_{\mathrm{D}}}$. Obviously, $\boldsymbol{A}$ and $\boldsymbol{B}$ are IDFT matrices in case of a ULA antenna. Hence, (2.1.114) can be efficiently implemented by use of fast Fourier transforms (FFTs). The unknown target parameters x, $\bar{u}$, and $\bar{f}_{\mathrm{D}}$ are thus encoded within the matrix $\boldsymbol{X}$ by the indices n_{u} and n_{D} within $\boldsymbol{X}$, which correspond to the targets LOS direction and Doppler, and the amplitude at the corresponding indices. The primary goal therefore is, to estimate $\boldsymbol{X}$ from the measurements $\boldsymbol{Y}$. The common space-time vector form, however, is the vectorized form analog to (2.1.106) as

$$\boldsymbol{y} = \mathrm{vec}\left(\boldsymbol{A}\boldsymbol{X}\boldsymbol{B}^{\mathrm{T}}\right) \tag{2.1.117}$$

$$= \left(\boldsymbol{B} \otimes \boldsymbol{A}\right)\boldsymbol{x}, \tag{2.1.118}$$

where $\boldsymbol{x} = \mathrm{vec}\left(\boldsymbol{X}\right) = \begin{bmatrix}\boldsymbol{x}_1^{\mathrm{T}} & \boldsymbol{x}_2^{\mathrm{T}} & \cdots & \boldsymbol{x}_{N_{\mathrm{D}}}^{\mathrm{T}}\end{bmatrix}^{\mathrm{T}}$ denotes the vectorized matrix $\boldsymbol{X} = \begin{bmatrix}\boldsymbol{x}_1 & \boldsymbol{x}_2 & \cdots & \boldsymbol{x}_{N_{\mathrm{D}}}\end{bmatrix}$ formed by stacking all columns on top of each other.

Commonly, (2.1.117) is expressed by use of a general measurement operator a. k. a. sensing operator $\mathcal{A} : \mathbb{C}^{N_1 \times N_2} \to \mathbb{C}^M$ as

$$\boldsymbol{y} = \mathcal{A}\left(\boldsymbol{X}\right), \tag{2.1.119}$$

where $N_1 \times N_2$ can be identified with the scene size $N_{\mathrm{u}} \times N_{\mathrm{D}}$ and the number of measurement samples as $M = N_{\mathrm{rx}}N_{\mathrm{p}}$. In case of missing samples i. e. some pulses or antennas are not present during a CPI,[10] compressive sensing (CS) and affine rank minimization (ARM) can be used to

[10] In this case certain rows in $\boldsymbol{A}$ and/or $\boldsymbol{B}$ are missing.

obtain a solution for (2.1.119), given that the sensing operator $\mathcal{A}$ fulfills certain conditions e. g. the restricted isometry property (RIP) condition. Further details on CS and ARM are discussed in Section 3 and 4.

Finally, the calibration procedure of the derived signal model shall be mentioned here. As discussed at the beginning of this chapter, the signal model was derived assuming the radar to be calibrated. In this case, the radar appears transparent to the EM wave such that it can sample the wave in space and time without any influence on the waves shape due to the presence of the radar. This is clearly not the case in practice. The coupled and non-calibrated measurements are often modeled by use of a mutual coupling matrix $\boldsymbol{C}_{\mathrm{mc}} \in \mathbb{C}^{N_{\mathrm{rx}}N_{\mathrm{p}} \times N_{\mathrm{rx}}N_{\mathrm{p}}}$ as

$$\boldsymbol{y}_{\mathrm{raw}} = x\boldsymbol{C}_{\mathrm{mc}}\boldsymbol{g}\left(\bar{u}, \bar{f}_{\mathrm{D}}\right),$$

where the signal model given in (2.1.106) was used. Obtaining $\boldsymbol{C}_{\mathrm{mc}}$ might be a complicated matter and is beyond the scope of this work. Depending on the types of the used antennas and their arrangement in the array, $\boldsymbol{C}_{\mathrm{mc}}$ might also depend on $\bar{u}$, a fact which most often is clearly not desired. The interested reader may refer to specialized papers e. g. [11, 12, 13, 14, 15, 16]. Once $\boldsymbol{C}_{\mathrm{mc}}$ is known, calibrated measurements are obtained by

$$\boldsymbol{y} = \boldsymbol{C}_{\mathrm{mc}}^{-1}\boldsymbol{y}_{\mathrm{raw}}$$

yielding the signal model given in (2.1.106).

In this section, a simplified space-time point target signal model suitable for the GMTI case was derived. The model follows the approximations verified in Tab. 2.1.1. In the following section, the general point target signal (2.1.99) is specified to clutter signals present in the airborne radar case.

2.2. Airborne Radar Signals

In this section some useful signal models emerging for airborne radar are discussed. In the ground moving target indication (GMTI) application, two major signal types emerge: target and clutter signals. Targets are referred to as moving and clutter as non-moving scatterers relative to the earth surface. Depending on the application scenario, also jamming signals may be considered, however, this is not covered in this work. In general, only radar signals for one particular range gate are considered from this point forward. Also the approximations verified in Section 2.1.4 are used i. e. target and clutter patches can be considered quasi-static during a coherent processing interval (CPI).

The clutter signal can be modeled as a superposition of non-moving scatterers distributed over the visible area $\vec{u} \in [-1, 1)$. Especially for non-moving scatterers, the line of sight (LOS) vector $\vec{u}$ and the emerging Doppler frequencies f_{Dc} are coupled. It is

$$f_{\mathrm{Dc}}\left(\vec{u}\right) = -\frac{2v_{\mathrm{r}}\left(\vec{u}\right)}{\lambda_{\mathrm{c}}}, \tag{2.2.1}$$

where the observed radial velocity is

$$v_{\mathrm{r}}\left(\vec{u}\right) = \langle \vec{u}, -\vec{v}_{\mathrm{p}} \rangle \tag{2.2.2}$$

with $\vec{v}_{\mathrm{p}}$ denoting the platform velocity vector with respect to the earth surface. The term $-\vec{v}_{\mathrm{p}}$ can be identified as the clutter velocity vector with respect to the platform reference frame. This is sketched in Fig. 2.2.1 for a single non-moving scatterer a. k. a. clutter patch. The size of the patch is restricted by the range resolution δr and the minimal occurring angular resolution $\triangle u_{\mathrm{c}}$. In case $-\vec{v}_{\mathrm{p}}$ and the antenna x axis coincide, the radial velocity can be written as

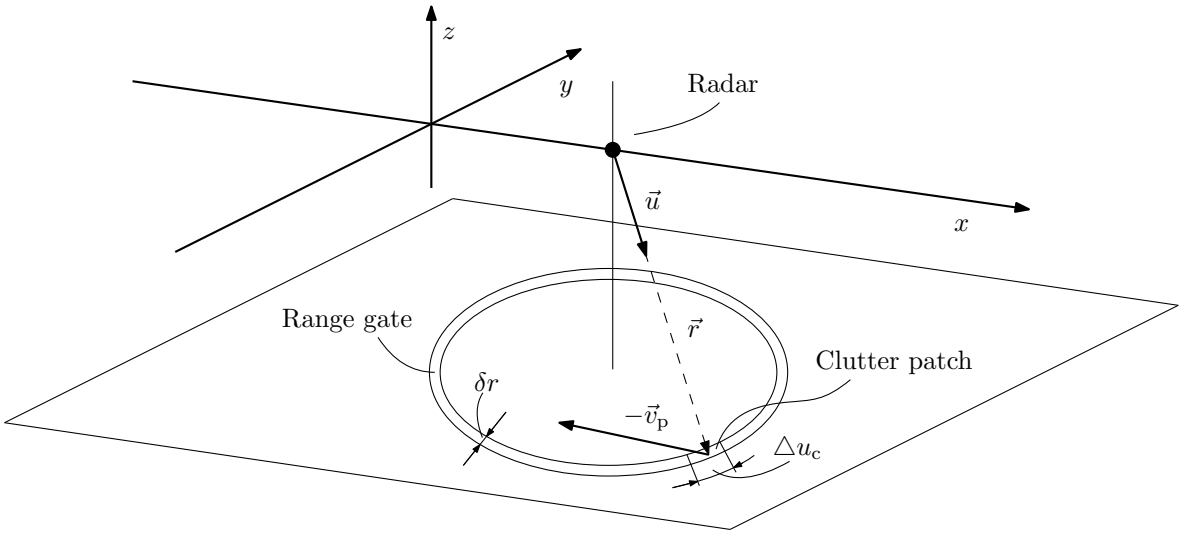

Figure 2.2.1.: Coupling of emerging Doppler frequency and LOS vector $\vec{u}$ for static clutter under flat earth condition.

$$v_{\mathrm{r}}\left(\vec{u}\right) = \left\langle \begin{bmatrix} u \\ v \\ w \end{bmatrix}, - \begin{bmatrix} v_{\mathrm{p}} \\ 0 \\ 0 \end{bmatrix} \right\rangle = -uv_{\mathrm{p}}$$

which directly couples the Doppler frequency and the directional cosine u as

$$f_{\mathrm{Dc}}\left(u\right) = \frac{2uv_{\mathrm{p}}}{\lambda_{\mathrm{c}}}. \tag{2.2.3}$$

The normalized clutter Doppler frequency

$$\bar{f}_{\mathrm{Dc}}\left(u\right) = \frac{f_{\mathrm{Dc}}\left(u\right)}{f_{\mathrm{p}}},$$

with f_{p} denoting the pulse repetition frequency (PRF), can also be expressed in terms of the normalized directional cosine $\bar{u} = u\bar{d}$ defined in (2.1.97) as

$$\bar{f}_{\mathrm{Dc}}\left(\bar{u};\beta\right) = \beta\bar{u}, \tag{2.2.4}$$

where

$$\beta = \frac{2v_{\mathrm{p}}}{df_{\mathrm{p}}} \tag{2.2.5}$$

is the slope of the so called clutter ridge. The term clutter ridge comes from the appearance of the clutter in the angular Doppler domain, which is depicted in Fig. 2.2.2 for $\beta = 1$. As can be seen, the clutter populates only a small portion in the angle-Doppler domain, which is one of the key facts why multiple channels are required for GMTI. In case $\vec{v}_{\mathrm{p}}$ and the antenna x axis do not

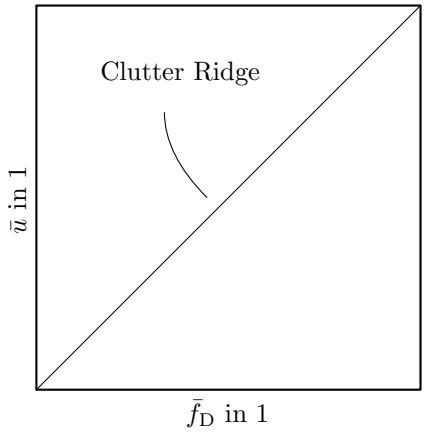

Figure 2.2.2.: Clutter ridge in the angle-Doppler domain for $\beta = 1$.

coincide, the radial velocity (2.2.2) becomes

$$\begin{aligned} v_{\mathrm{r}}(\vec{u}) &= \left\langle \begin{bmatrix} u \\ v \\ w \end{bmatrix}, -v_{\mathrm{p}} \begin{bmatrix} \cos(\varphi_{\mathrm{m}})\sin(\vartheta_{\mathrm{m}}) \\ \sin(\varphi_{\mathrm{m}})\sin(\vartheta_{\mathrm{m}}) \\ \cos(\vartheta_{\mathrm{m}}) \end{bmatrix} \right\rangle \\ &= -v_{\mathrm{p}}\left(\sin(\vartheta)\sin(\vartheta_{\mathrm{m}})\cos(\varphi - \varphi_{\mathrm{m}}) + \cos(\vartheta)\cos(\vartheta_{\mathrm{m}})\right), \end{aligned}$$

where the so-called misalignment angles φ_{m} and ϑ_{m} are the spherical angles pointing along the platform velocity vector $\vec{v}_{\mathrm{p}}$ in the platform frame[11]. It is usually assumed that the vertical velocity component can be neglected with $\vartheta_{\mathrm{m}} \simeq \pi/2$[12], hence

$$\begin{aligned} v_{\mathrm{r}}(u) &\simeq -v_{\mathrm{p}}\sin(\vartheta)\cos(\varphi - \varphi_{\mathrm{m}}) \\ &= -v_{\mathrm{p}}\left(u\cos(\varphi_{\mathrm{m}}) \pm \sin(\varphi_{\mathrm{m}})\sqrt{\sin^2(\vartheta) - u^2}\right). \end{aligned} \tag{2.2.6}$$

By combining (2.1.96), (2.1.97), (2.1.98), (2.2.1), (2.2.5), and (2.2.6), the normalized Doppler frequency in this case becomes

$$\bar{f}_{\mathrm{Dc}}(\bar{u}; \beta, \varphi_{\mathrm{m}}) = \beta\left(\bar{u}\cos(\varphi_{\mathrm{m}}) \pm \sin(\varphi_{\mathrm{m}})\sqrt{\bar{d}^2\sin^2(\vartheta) - \bar{u}^2}\right). \tag{2.2.7}$$

[11] Note $\vec{v}_{\mathrm{p}}$ not $-\vec{v}_{\mathrm{p}}$ as the negative sign is already counted for!

[12] This assumption is not necessarily true in case of airborne GMTI due to air turbulence. In this work, however, this effect is neglected and an extension to incorporate the vertical misalignment is left as a future work.

The clutter signal of a single clutter patch can thus be modeled as

$$\boldsymbol{y}_{\mathrm{c}}\left(\bar{u};\beta,\varphi_{\mathrm{m}}\right)=x_{\mathrm{c}}\left(\bar{u}\right)\boldsymbol{g}_{\mathrm{c}}\left(\bar{u};\beta,\varphi_{\mathrm{m}}\right) \tag{2.2.8}$$

with $x_{\mathrm{c}}\left(\bar{u}\right)$ denoting a clutter patch amplitude and

$$\boldsymbol{g}_{\mathrm{c}}\left(\bar{u};\beta,\varphi_{\mathrm{m}}\right)=\boldsymbol{g}\left(\bar{u},\bar{f}_{\mathrm{Dc}}\left(\bar{u};\beta,\varphi_{\mathrm{m}}\right)\right) \tag{2.2.9}$$

a corresponding space-time signal vector with $\boldsymbol{g}$ defined by (2.1.107). The total clutter signal is obtained by the superposition of all clutter patches as

$$\boldsymbol{y}_{\mathrm{c}}(\beta,\varphi_{\mathrm{m}})=\int_{-\bar{d}}^{\bar{d}}\boldsymbol{y}_{\mathrm{c}}\left(\bar{u};\beta,\varphi_{\mathrm{m}}\right)\mathrm{d}\bar{u}. \tag{2.2.10}$$

The integral form (2.2.10) may also be approximately expressed by use of a matrix as

$$\boldsymbol{y}_{\mathrm{c}}(\beta,\varphi_{\mathrm{m}})=\boldsymbol{G}_{\mathrm{c}}\left(\beta,\varphi_{\mathrm{m}}\right)\boldsymbol{x}_{\mathrm{c}}, \tag{2.2.11}$$

where

$$\boldsymbol{x}_{\mathrm{c}}=\left[x_{\mathrm{c}}\left(\bar{u}_{n_{\mathrm{c}}}\right)\right]_{n_{\mathrm{c}}=-N_{\mathrm{c}}/2}^{N_{\mathrm{c}}/2-1}\in\mathbb{C}^{N_{\mathrm{c}}}$$

is a vector holding the amplitudes of N_{c} individual clutter patches,

$$\boldsymbol{G}_{\mathrm{c}}\left(\beta,\varphi_{\mathrm{m}}\right)=\left[\boldsymbol{g}_{\mathrm{c}}\left(\bar{u}_{n_{\mathrm{c}}};\beta,\varphi_{\mathrm{m}}\right)\right]_{n_{\mathrm{c}}=-N_{\mathrm{c}}/2}^{N_{\mathrm{c}}/2-1}\in\mathbb{C}^{N_{\mathrm{rx}}N_{\mathrm{p}}\times N_{\mathrm{c}}} \tag{2.2.12}$$

is a matrix of space-time clutter vectors steered to all clutter patches located at

$$\bar{u}_{n_{\mathrm{c}}}=\frac{2\bar{d}}{N_{\mathrm{c}}}n_{\mathrm{c}}$$

with

$$N_{\mathrm{c}}=2\left\lceil\frac{N}{\triangle u_{\mathrm{c}}}\right\rceil$$

denoting the number of clutter patches with $N\in\mathbb{N}^{+}$,

$$\triangle u_{\mathrm{c}}=\min\left(\mathrm{ABW},\delta u,\triangle u_{\mathrm{D}}\right)$$

the minimal occurring clutter patch resolution in u,

$$\delta u=\frac{1}{N_{\mathrm{rx}}\bar{d}}$$

the array resolution in u, and

$$\triangle u_{\mathrm{D}}=\triangle f_{\mathrm{D}}\frac{\lambda_{\mathrm{c}}}{2v_{\mathrm{p}}}=\frac{\lambda_{\mathrm{c}}f_{\mathrm{p}}}{2v_{\mathrm{p}}N_{\mathrm{p}}}$$

the Doppler resolution in u, where (2.2.3) was used as an approximation. Due to the random

nature of the reflectivity coefficient $x_{\mathrm{c}}(\bar{u})$ it is not possible to obtain a closed form clutter signal. However, its signal structure is known from space-time adaptive processing (STAP) to consist of numerous clutter contributions which are measured in a somewhat redundant or correlated nature. The radar system obtains such correlated measurements due to its multiple channels. The extreme case in which redundant samples are taken is known as displaced phase center antenna (DPCA) condition [4]. In this case, pulses are emitted at exactly the point in time when a subsequent channel arrives at the position of the preceding channel. This is sketched in Fig. 2.2.3. From a mathematical point of view, these redundant samples can be seen directly from the mea-

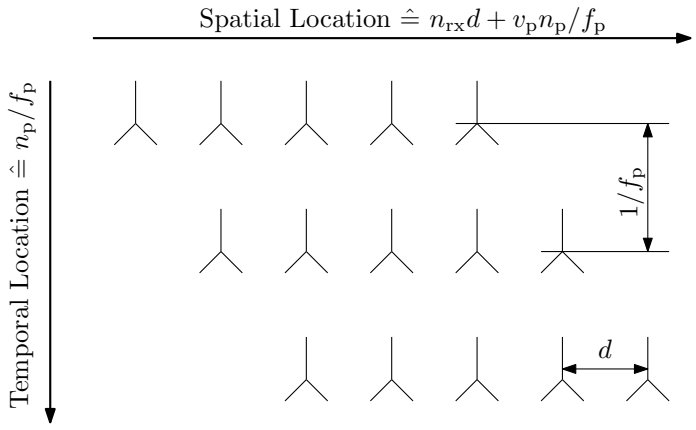

Figure 2.2.3.: Sampling process in space and time with fulfilled DPCA condition.

surements of a single clutter patch in case of no velocity misalignment

$$g_{\mathrm{c},n_{\mathrm{rx}}n_{\mathrm{p}}}(\bar{u};\beta) = \mathrm{e}^{\mathrm{j}2\pi\bar{u}(n_{\mathrm{rx}}+\beta n_{\mathrm{p}})}, \tag{2.2.13}$$

where (2.2.4) was used. In case $\beta \in \mathbb{N}^{+}$[13], one can find

$$\rho_{\mathrm{B}} = N_{\mathrm{rx}} + \beta(N_{\mathrm{p}} - 1) \tag{2.2.14}$$

non redundant samples of the $N_{\mathrm{rx}}N_{\mathrm{p}}$ possible samples for (2.2.13). This is known as Brennan's rule [17] and gives a hint on the possible rank of the emerging clutter covariance matrix

$$\begin{aligned}\boldsymbol{R}_{\mathrm{c}}(\beta,\varphi_{\mathrm{m}}) &= \mathrm{E}\left\{\boldsymbol{y}_{\mathrm{c}}(\beta,\varphi_{\mathrm{m}})\boldsymbol{y}_{\mathrm{c}}^{\mathrm{H}}(\beta,\varphi_{\mathrm{m}})\right\} \\ &= \iint_{-\bar{d}}^{\bar{d}} \mathrm{E}\left\{x_{\mathrm{c}}(\bar{u})\, x_{\mathrm{c}}^{*}(\bar{u}')\right\} \boldsymbol{g}_{\mathrm{c}}(\bar{u};\beta,\varphi_{\mathrm{m}})\, \boldsymbol{g}_{\mathrm{c}}^{\mathrm{H}}(\bar{u}';\beta,\varphi_{\mathrm{m}})\, \mathrm{d}\bar{u}\mathrm{d}\bar{u}'\end{aligned} \tag{2.2.15}$$

as only non redundant samples contribute to the clutter rank. It is known, that Brennan's Rule gives a good hint on the effective clutter rank also in case of non-perfectly redundant samples i. e. for non-DPCA conditions. In this case, the samples are still correlated to each other which results in a decay of the corresponding singular values. A common assumption is that the clutter patch reflection coefficients α_{r} are uncorrelated as

$$\mathrm{E}\left\{\alpha_{\mathrm{r}}(\bar{u})\,\alpha_{\mathrm{r}}^{*}(\bar{u}')\right\} = \sigma_{\mathrm{r}}\delta(\bar{u}-\bar{u}'),$$

[13] Which corresponds to the DPCA condition.

where (2.1.20) was used. The required correlation of the clutter amplitude therefore is

$$\begin{aligned}\mathrm{E}\left\{x_\mathrm{c}\left(\bar{u}\right)x_\mathrm{c}^*\left(\bar{u}'\right)\right\} &= \mathrm{E}\left\{x_\mathrm{cal}\left(\bar{u}\right)x_\mathrm{cal}^*\left(\bar{u}'\right)\right\}\\ &= \frac{P_\mathrm{tx}g_\mathrm{dn}^2}{r^4}\bar{g}_\mathrm{tx}(\bar{u})\bar{g}_\mathrm{rx}(\bar{u})\bar{g}_\mathrm{tx}^*(\bar{u}')\bar{g}_\mathrm{rx}^*(\bar{u}')\,\mathrm{E}\left\{\alpha_\mathrm{r}(\bar{u})\alpha_\mathrm{r}^*(\bar{u}')\right\}\\ &= \frac{P_\mathrm{tx}g_\mathrm{dn}^2}{r^4}\bar{g}_\mathrm{tx}(\bar{u})\bar{g}_\mathrm{rx}(\bar{u})\bar{g}_\mathrm{tx}^*(\bar{u}')\bar{g}_\mathrm{rx}^*(\bar{u}')\sigma_\mathrm{r}\delta\left(\bar{u}-\bar{u}'\right)\\ &= P_\mathrm{c}\left(\bar{u},\bar{u}'\right)\delta\left(\bar{u}-\bar{u}'\right)\end{aligned} \tag{2.2.16}$$

where (2.1.94), (2.1.43) was used and

$$P_\mathrm{c}\left(\bar{u},\bar{u}'\right) = \frac{P_\mathrm{tx}g_\mathrm{dn}^2\sigma_\mathrm{r}}{r^4}\bar{g}_\mathrm{tx}(\bar{u})\bar{g}_\mathrm{rx}(\bar{u})\bar{g}_\mathrm{tx}^*(\bar{u}')\bar{g}_\mathrm{rx}^*(\bar{u}')$$

denotes the clutter patch power. In case of $\bar{u}=\bar{u}'$, the clutter patch power is

$$P_\mathrm{c}\left(\bar{u}\right) = \frac{P_\mathrm{tx}g_\mathrm{dn}^2\bar{G}_\mathrm{tx}(\bar{u})\bar{G}_\mathrm{rx}(\bar{u})\sigma_\mathrm{r}}{(4\pi)^3r^4},$$

where $\bar{G}_\mathrm{tx}$ and $\bar{G}_\mathrm{rx}$ denote the calibrated, i. e. frequency independent, antenna gains for which (2.1.11) and (2.1.27) was used. As such the covariance matrix becomes

$$\boldsymbol{R}_\mathrm{c}\left(\beta,\varphi_\mathrm{m}\right) = \int_{-\bar{d}}^{\bar{d}} P_\mathrm{c}\left(\bar{u}\right)\boldsymbol{g}_\mathrm{c}\left(\bar{u};\beta,\varphi_\mathrm{m}\right)\boldsymbol{g}_\mathrm{c}^\mathrm{H}\left(\bar{u};\beta,\varphi_\mathrm{m}\right)\mathrm{d}\bar{u}. \tag{2.2.17}$$

The internal structure of the covariance matrix can be determined in more detail by noting the identity

$$\boldsymbol{g}\boldsymbol{g}^\mathrm{H} = \left(\boldsymbol{b}\boldsymbol{b}^\mathrm{H}\right)\otimes\left(\boldsymbol{a}\boldsymbol{a}^\mathrm{H}\right)$$

from which it can be seen that the covariance matrix $\boldsymbol{R}_\mathrm{c}$ is a block matrix formed from N_p^2 spatial covariance matrices of size $N_\mathrm{rx}\times N_\mathrm{rx}$. By looking at the individual covariance values

$$R_\mathrm{c}\left(n_\mathrm{rx},n_\mathrm{p},n_\mathrm{rx}',n_\mathrm{p}';\beta,\varphi_\mathrm{m}\right) = \int_{-\bar{d}}^{\bar{d}} P_\mathrm{c}\left(\bar{u}\right)\mathrm{e}^{\mathrm{j}2\pi\bar{u}(n_\mathrm{rx}-n_\mathrm{rx}')+\mathrm{j}2\pi\bar{f}_\mathrm{Dc}(\bar{u};\beta,\varphi_\mathrm{m})\left(n_\mathrm{p}-n_\mathrm{p}'\right)}\mathrm{d}\bar{u}, \tag{2.2.18}$$

it can be seen that the entries depend only on the channel and pulse differences $n_\mathrm{rx}-n_\mathrm{rx}'$ and $n_\mathrm{p}-n_\mathrm{p}'$. As a consequence, the clutter matrix $\boldsymbol{R}_\mathrm{c}\left(\beta,\varphi_\mathrm{m}\right)$ is of Toeplitz-block-Toeplitz form consisting of $2N_\mathrm{p}-1$ block matrices and every block matrix is formed from $2N_\mathrm{rx}-1$ entries [17].

The covariance matrices not only offer a possibility to form a classical clutter filter as done in STAP and shown in Section 2.3, it also provides a possibility to obtain a basis for the clutter signals. The clutter signal $\boldsymbol{y}_\mathrm{c}(\beta,\varphi_\mathrm{m})$ resides in a signal space spanned by all clutter signal vectors given by the space-time clutter signal matrix $\boldsymbol{G}_\mathrm{c}\left(\beta,\varphi_\mathrm{m}\right)$ from (2.2.12). A basis of the clutter signal space is given by the left singular vectors $\boldsymbol{U}$ of $\boldsymbol{G}_\mathrm{c}\left(\beta,\varphi_\mathrm{m}\right)$, where

$$\boldsymbol{U}\boldsymbol{\Sigma}\boldsymbol{V}^\mathrm{H} = \boldsymbol{G}_\mathrm{c}\left(\beta,\varphi_\mathrm{m}\right)$$

denotes the singular value decomposition (SVD) of $\boldsymbol{G}_{\mathrm{c}}(\beta, \varphi_{\mathrm{m}})$ with $\boldsymbol{\Sigma}$ denoting a diagonal matrix holding the corresponding singular values and $\boldsymbol{V}$ the right singular vectors[14]. Using basic linear algebra, the basis of the clutter signal space $\boldsymbol{U}$ may also be found from the Eigendecomposition of

$$\boldsymbol{G}_{\mathrm{c}}\boldsymbol{G}_{\mathrm{c}}^{\mathrm{H}} = \boldsymbol{U}\boldsymbol{\Sigma}\boldsymbol{\Sigma}^{\mathrm{H}}\boldsymbol{U}^{\mathrm{H}}, \tag{2.2.19}$$

where the property $\boldsymbol{V}^{\mathrm{H}}\boldsymbol{V} = \boldsymbol{I}$ was used. Now note, that the covariance matrix may also be expressed compactly in matrix form as

$$\boldsymbol{R}_{\mathrm{c}}(\beta, \varphi_{\mathrm{m}}) = \boldsymbol{G}_{\mathrm{c}}(\beta, \varphi_{\mathrm{m}})\,\mathrm{E}\left\{\boldsymbol{x}_{\mathrm{c}}\boldsymbol{x}_{\mathrm{c}}^{\mathrm{H}}\right\}\boldsymbol{G}_{\mathrm{c}}^{\mathrm{H}}(\beta, \varphi_{\mathrm{m}}) \tag{2.2.20}$$

using (2.2.11) and (2.2.15). Using the common assumption, that the clutter amplitudes are uncorrelated, the covariance matrix becomes

$$\boldsymbol{R}_{\mathrm{c}}(\beta, \varphi_{\mathrm{m}}) = P_{\mathrm{c}}\boldsymbol{G}_{\mathrm{c}}(\beta, \varphi_{\mathrm{m}})\,\boldsymbol{G}_{\mathrm{c}}^{\mathrm{H}}(\beta, \varphi_{\mathrm{m}}), \tag{2.2.21}$$

where $\mathrm{E}\left\{\boldsymbol{x}_{\mathrm{c}}\boldsymbol{x}_{\mathrm{c}}^{\mathrm{H}}\right\} = P_{\mathrm{c}}\boldsymbol{I}$ was used. Comparing (2.2.21) and (2.2.19) reveals that the covariance matrix $\boldsymbol{R}_{\mathrm{c}}$ spans the space of the clutter signal vectors $\boldsymbol{U}$. Hence, the clutter subspace can be determined from the Eigendecomposition of $\boldsymbol{R}_{\mathrm{c}}(\beta, \varphi_{\mathrm{m}})$. This subspace can be used to form an orthogonal projection filter, allowing for an improved clutter suppression. Assuming the clutter patch power to be constant i. e. $P_{\mathrm{c}}(\bar{u}) = P_{\mathrm{c}}$, the covariance matrix (2.2.18) has a closed form solution in case of no velocity misalignment i. e. $\varphi_{\mathrm{m}} = 0$ as

$$R_{\mathrm{c}}(\tilde{n}_{\mathrm{rx}}, \tilde{n}_{\mathrm{p}}; \beta) = 2\bar{d}P_{\mathrm{c}}\,\mathrm{sinc}\left(2\bar{d}\left(\tilde{n}_{\mathrm{rx}} + \beta\tilde{n}_{\mathrm{p}}\right)\right), \tag{2.2.22}$$

where $\mathrm{sinc}(x) = \sin(\pi x)/(\pi x)$ denotes the normalized sinc function and $\tilde{n}_{\mathrm{rx}} = n_{\mathrm{rx}} - n'_{\mathrm{rx}}$ and $\tilde{n}_{\mathrm{p}} = n_{\mathrm{p}} - n'_{\mathrm{p}}$ the channel and pulse differences.[15] In other cases like for present velocity misalignment $\varphi_{\mathrm{m}} \neq 0$[16] or if an antenna pattern was to be considered (which currently is contained within

[14] As known from basic linear algebra, $\boldsymbol{U}$ is a basis of the column space and $\boldsymbol{V}$ a basis of the row space of $\boldsymbol{G}_{\mathrm{c}}$.

[15] Some authors state (2.2.22) by use of the zeroth order Bessel function $2\bar{d}P_{\mathrm{c}}J_0\left(2\pi\bar{d}\left(\tilde{n}_{\mathrm{rx}} + \beta\tilde{n}_{\mathrm{p}}\right)\right)$ which coincides with the $\mathrm{sinc}(\cdot)$ form since $J_0(z) = \sin(z)/z$ [18].

[16] The covariance matrix (2.2.18) can be reformulated into

$$R_{\mathrm{c}}(c, d; \beta, \varphi_{\mathrm{m}}) = P_{\mathrm{c}}\int_{-\bar{d}}^{\bar{d}} \mathrm{e}^{\mathrm{j}2\pi\bar{u}c}\mathrm{e}^{d\sqrt{\rho^2 - P^2}}\,\mathrm{d}\bar{u},$$

with $P_{\mathrm{c}}(\bar{u}) = P_{\mathrm{c}}$, $c = \tilde{n}_{\mathrm{rx}} + \beta\cos(\varphi_{\mathrm{m}})\,\tilde{n}_{\mathrm{p}}$, $d = \beta\sin(\varphi_{\mathrm{m}})\,\tilde{n}_{\mathrm{p}}$, $\rho = \mathrm{j}2\pi\bar{d}\sin(\varphi)$, and $P = \mathrm{j}2\pi\bar{u}$. For this form a closely related Fourier integral is known as

$$\int_{-\infty}^{\infty} \mathrm{e}^{\mathrm{j}2\pi\bar{u}c}\mathrm{e}^{d\sqrt{\rho^2 - P^2}}\,\mathrm{d}\bar{u} = \frac{-d\rho K_1\left(\rho\sqrt{c^2 + d^2}\right)}{\pi\sqrt{c^2 + d^2}}$$

with the constraint $d < 0$ and K_1 denoting the modified Bessel function of first order and second kind [19]. Unfortunately, the integral limits do not match and a reformulation by use of a $\mathrm{rect}\left(\bar{u}/2\bar{d}\right)$ results in the convolution

$$R_{\mathrm{c}}(\tilde{n}_{\mathrm{rx}}, \tilde{n}_{\mathrm{p}}; \beta, \varphi_{\mathrm{m}}) = \frac{-d\rho K_1\left(\rho\sqrt{\tilde{n}_{\mathrm{rx}}^2 + d^2}\right)}{\pi\sqrt{\tilde{n}_{\mathrm{rx}}^2 + d^2}} * R_{\mathrm{c}}(\tilde{n}_{\mathrm{rx}}, \tilde{n}_{\mathrm{p}}; \beta)$$

with $R_{\mathrm{c}}(\tilde{n}_{\mathrm{rx}}, \tilde{n}_{\mathrm{p}}; \beta)$ from (2.2.22). This convolution cannot be evaluated in an efficient manner since the real part of K_1 does not decay rapidly for small mismatch angles φ_{m}.

$P_{\mathrm{c}}(\bar{u})$), a closed form solution of (2.2.18) is not known. In these cases, the covariance matrix $\boldsymbol{R}_{\mathrm{c}}(\beta, \varphi_{\mathrm{m}})$ needs to be evaluated numerically.[17] While the assumption of the clutter power to be constant is rather non-realistic, the subspace filter obtained from it works surprisingly well also for realistic clutter power distributions as shown in Section 7.3.2.

As an important phenomena, internal clutter motion (ICM) has to be mentioned as well. In the case of ICM, the clutter reflectivity changes from pulse to pulse rendering the clutter amplitude $x_{\mathrm{c}}(\bar{u})$ to become an $N_{\mathrm{p}} \times 1$ vector [17]

$$\boldsymbol{x}_{\mathrm{cp}}(\bar{u}) = \left[x_{\mathrm{c},n_{\mathrm{p}}}(\bar{u})\right]_{n_{\mathrm{p}}=0}^{N_{\mathrm{p}}-1}$$

to the contrary of being constant as assumed before. The clutter signal of a single clutter patch changes from (2.2.8) to

$$\boldsymbol{y}_{\mathrm{c}}(\bar{u}; \beta, \varphi_{\mathrm{m}}) = \left(\boldsymbol{x}_{\mathrm{cp}}(\bar{u}) \odot \boldsymbol{b}\left(\bar{f}_{\mathrm{Dc}}(\bar{u}; \beta, \varphi_{\mathrm{m}})\right)\right) \otimes \boldsymbol{a}(\bar{u})$$

and the covariance matrix from (2.2.17) to

$$\boldsymbol{R}_{\mathrm{c}}(\beta, \varphi_{\mathrm{m}}) = \int_{-\bar{d}}^{\bar{d}} \left(\boldsymbol{P}_{\mathrm{c}}(\bar{u}) \odot \boldsymbol{b}\left(\bar{f}_{\mathrm{Dc}}(\bar{u}; \beta, \varphi_{\mathrm{m}})\right)\right) \otimes \boldsymbol{a}(\bar{u})\, \mathrm{d}\bar{u},$$

where

$$\boldsymbol{P}_{\mathrm{c}}(\bar{u}) = \mathrm{E}\left\{\boldsymbol{x}_{\mathrm{cp}}(\bar{u})\, \boldsymbol{x}_{\mathrm{cp}}^{\mathrm{H}}(\bar{u})\right\} \in \mathbb{C}^{N_{\mathrm{p}} \times N_{\mathrm{p}}}$$

is again a Toeplitz matrix. The clutter amplitude $x_{\mathrm{c}}(\bar{u})$ is commonly modeled as a wide-sense stationary (WSS) random processes e. g. the Billingsley model [1].

A single target signal can be modeled by use of (2.1.99) as

$$y_{\mathrm{t},n_{\mathrm{rx}}n_{\mathrm{p}}}\left(x_{\mathrm{t}}, \bar{u}_{\mathrm{t}}, \bar{f}_{\mathrm{Dt}}\right) = x_{\mathrm{t}} \mathrm{e}^{\mathrm{j}2\pi \bar{f}_{\mathrm{Dt}} n_{\mathrm{p}} + \mathrm{j}2\pi \bar{u}_{\mathrm{t}} n_{\mathrm{rx}}} \tag{2.2.23}$$

or in vector form

$$\boldsymbol{y}_{\mathrm{t}}\left(x_{\mathrm{t}}, \bar{u}_{\mathrm{t}}, \bar{f}_{\mathrm{Dt}}\right) = x_{\mathrm{t}} \boldsymbol{g}\left(\bar{u}, \bar{f}_{\mathrm{Dt}}\right). \tag{2.2.24}$$

The random nature of the target amplitude x_{t} can be modeled by well known Swerling models [2]. However, in this work targets are considered as non-fluctuating. The Doppler frequency corresponding to the target is

$$f_{\mathrm{Dt}} = -\frac{2v_{\mathrm{rt}}}{\lambda_{\mathrm{c}}}, \tag{2.2.25}$$

where the radial velocity observed by the radar is [4]

$$v_{\mathrm{rt}} = \langle \vec{u}_{\mathrm{t}}, \vec{v}_{\mathrm{t}} - \vec{v}_{\mathrm{p}} \rangle$$

with $\vec{v}_{\mathrm{t}}$ denoting the target velocity vector with respect to the earth surface. The observed radial

[17] Due to the Toeplitz-block-Toeplitz form only $(2N_{\mathrm{p}} - 1)(2N_{\mathrm{rx}} - 1)$ instead of $N_{\mathrm{p}}^2 N_{\mathrm{rx}}^2$ numerical integrals must be solved. Since only big singular values are of interest, the integration error is allowed to be as big as 10^{-4} for the total and 10^{-2} for the relative error according to tests in Matlab. Special care should be taken to ensure that the central blocks for $\tilde{n}_{\mathrm{p}} = 0$ are hermitian.

velocity can be decomposed into two components

$$v_{\mathrm{rt}} = v_{\mathrm{tu}} + v_{\mathrm{r}}\left(\vec{u}_{\mathrm{t}}\right)$$

with

$$v_{\mathrm{tu}} = \langle \vec{u}_{\mathrm{t}}, \vec{v}_{\mathrm{t}} \rangle$$

and $v_{\mathrm{r}}\left(\vec{u}_{\mathrm{t}}\right)$ defined as in (2.2.2). Hence, the observed Doppler frequency (2.2.25) can be decomposed into

$$f_{\mathrm{Dt}} = f_{\mathrm{Dc}}\left(\vec{u}_{\mathrm{t}}\right) - \frac{2v_{\mathrm{tu}}}{\lambda_{\mathrm{c}}}$$

with the target independent component $f_{\mathrm{Dc}}\left(\vec{u}_{\mathrm{t}}\right)$ defined as in (2.2.1). Consequently, any moving target posses a Doppler offset to stationary clutter reflections. Therefore, moving targets are separated from clutter signals in the angle-Doppler domain as shown in Fig. 2.2.4. In summary,

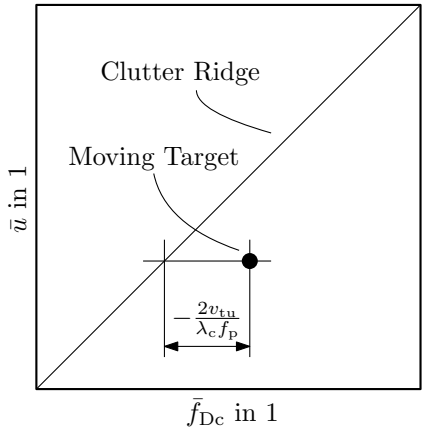

Figure 2.2.4.: Clutter ridge in angle-Doppler domain for $\beta = 1$ with one moving target present.

the signal observed by the radar is

$$\boldsymbol{y} = \sum_{n_{\mathrm{t}}=0}^{N_{\mathrm{t}}-1} \boldsymbol{y}_{\mathrm{t}}\left(x_{n_{\mathrm{t}}}, \bar{u}_{n_{\mathrm{t}}}, \bar{f}_{\mathrm{D},n_{\mathrm{t}}}\right) + \boldsymbol{y}_{\mathrm{c}}(\beta,\varphi_{\mathrm{m}}) + \boldsymbol{n}, \tag{2.2.26}$$

where N_{t} denotes the number of moving targets and $\boldsymbol{n} \sim \mathcal{CN}\left(0, P_{\mathrm{n}}\right)$. An alternative form is obtained by discretizing the radar scene similar to (2.1.119) as

$$\boldsymbol{y} = \mathcal{A}\left(\boldsymbol{X}_{\mathrm{t}}\right) + \boldsymbol{y}_{\mathrm{c}}(\beta,\varphi_{\mathrm{m}}) + \boldsymbol{n}. \tag{2.2.27}$$

In this form, targets are forced to be located at a grid position of the scene matrix $\boldsymbol{X}_{\mathrm{t}}$ which in reality is never fulfilled. Hence, straddle loss will occur when trying to reconstruct $\boldsymbol{X}_{\mathrm{t}}$ from an inverse processing of the sensing operator $\mathcal{A}$. In general, the separation from the moving targets within $\boldsymbol{X}_{\mathrm{t}}$ from the clutter $\boldsymbol{y}_{\mathrm{c}}(\beta,\varphi_{\mathrm{m}})$ is subject to STAP which is discussed in brevity in the next section.

2.3. Space-Time Adaptive Processing

In this section, a short introduction to space-time adaptive processing (STAP) and its prerequisites are given. Next to the inevitable basics and some justification why multiple channels are mandatory for the purpose of ground moving target indication (GMTI), the idea of an orthogonal projection onto the complementary clutter subspace is given in brevity as this idea is used in Chapter 7. Finally, a short summary on STAP detectors is given as these are of major interest for GMTI applications.

2.3.1. The Need for a Multichannel System

On a regular basis, it is questioned if it is really mandatory to use a multichannel radar system for GMTI. This questioning stems mainly from cost considerations as evidently a multichannel radar is more expansive. Unfortunately, the use of a multichannel system is unavoidable. In this section, common ideas how GMTI could be realized with a single channel only and reasons why they are either not possible at all or not suitable are discussed in brevity.

Basically, GMTI is a change detected procedure. The very first, yet naive, idea to detect a change is to conduct two or more measurements and compared them against each other. Consistent signal components indicate static background or clutter and differences in the measurements indicate changes or moving targets. In case of a stationary radar, such measurements can be conducted by use of a single channel only. However, as soon as the channel changes its position, as is the case for a moving platform, the received measurements are quickly not comparable any more. The reason therefore is, that the coherent sum of all reflections cause a rapid decorrelation. From (2.1.95) and (2.2.10), a single static clutter measurement for a single channel is calculated as

$$y_{\mathrm{c}}(l) = \int_{-1}^{1} x_{\mathrm{c}}\left(u\right) \mathrm{e}^{\mathrm{j}k_{\mathrm{c}}ul} \mathrm{d}u,$$

where l denotes the location of the single antenna and the integral denotes the coherent sum of all reflections for a single range gate. The correlation with a displaced channel is

$$r_{y_{\mathrm{c}}y_{\mathrm{c}}}(l, l+\triangle l) = \mathrm{E}\left\{y_{\mathrm{c}}(l) y_{\mathrm{c}}^{*}(l+\triangle l)\right\} = \iint_{-1}^{1} \mathrm{E}\left\{x_{\mathrm{c}}\left(u\right) x_{\mathrm{c}}^{*}\left(u'\right)\right\} \mathrm{e}^{\mathrm{j}k_{\mathrm{c}}(ul-u'l-u'\triangle l)} \mathrm{d}u' \mathrm{d}u.$$

Assuming the clutter amplitudes are uncorrelated as $\mathrm{E}\left\{x_{\mathrm{c}}\left(u\right) x_{\mathrm{c}}^{*}\left(u'\right)\right\} = P_{\mathrm{c}}(u,u')\delta\left(u-u'\right)$ as given by (2.2.16), the correlation becomes

$$r_{y_{\mathrm{c}}y_{\mathrm{c}}}(\triangle l) = \int_{-1}^{1} P_{\mathrm{c}}(u) \mathrm{e}^{-\mathrm{j}k_{\mathrm{c}}u\triangle l} \mathrm{d}u.$$

Neglecting the antenna pattern i. e. $P_{\mathrm{c}}(u) = P_{\mathrm{c}}$, the correlation has the close form solution

$$r_{y_{\mathrm{c}}y_{\mathrm{c}}}(\triangle l) = 2P_{\mathrm{c}} \operatorname{sinc}\left(\frac{2\triangle l}{\lambda_{\mathrm{c}}}\right).$$

A similar derivation for the three dimensional case can be found in [4]. For $\triangle l = \lambda_c/2$, the correlation between the two measurements becomes $r_{y_c y_c}(\lambda_c/2) = 0$, hence, the correlation decays rapidly[18]. The influence of the antenna pattern tapers the main lobe of the sinc-function to become broader, however, this effect is quite limited and the measurements still decorrelate rapidly. In order to acquire a second correlated measurement, already a second channel is required, which conducts a measurement at the very same position a former measurement was taken. This technique is known as displaced phase center antenna (DPCA) and is, due to its poor performance compared to STAP, nowadays only of educational interest [1]. The DPCA scheme is depicted in Fig. 2.2.3.

A second more robust approach would be to conduct Doppler processing. The key idea is, that any moving target causes a Doppler frequency $\neq 0\,\mathrm{Hz}$ and thus can be distinguished from static background reflections. Again this works well for a stationary radar, however, only very limited in the GMTI case. The reason therefore is that, contrary to the stationary case, the earth also moves relative to the radar. The motion of a target of interest, however, is a motion relative the earths motion or, in other words, a motion on top of the earths motion. It is therefore difficult to distinguish between Doppler frequencies caused by the earths motion and Doppler frequencies caused by the moving target. From (2.2.2) it can be seen, that the moving earth causes observable radial velocities in the range of $v_r \in [-v_p, v_p]$, where v_p denotes the platform velocity. The emerging clutter-Doppler spectrum is sketched in Fig. 2.3.1. Doppler frequencies of

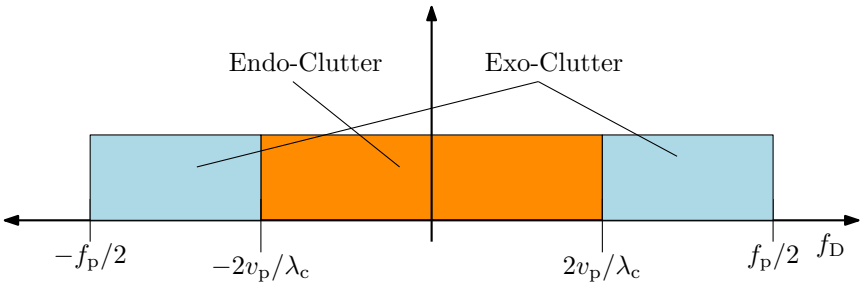

Figure 2.3.1.: Emerging temporal spectrum in the GMTI case.

targets moving slower than v_p will submerge in the Doppler band stemming from the earth. This case is commonly known as endo-clutter and results to be the common case in GMTI applications [4]. The detection of endo-clutter targets is subject to STAP algorithms. The complementary case, where the target moves faster than v_p, is known as exo-clutter case. In this, simple Doppler filtering would be sufficient to detect the moving target. Within the realm of GMTI, however, exo-clutter is of limited practical importance. Quiet the contrary, usually the pulse repetition frequency (PRF) is chosen quiet low in order to avoid range ambiguities. This in turn causes Doppler aliasing, which at first excludes the exo-clutter case and second prohibits pure Doppler processing at all.

A third idea to detect moving targets by use of a single channel only would be to apply a synthetic aperture radar (SAR)-like technique [4]. Using SAR, a spatially resolved radar image of the earth can be calculated. Changes can be detected by comparing two such SAR images created from two independent flyovers. In principle, this approach works, but only with a very high effort to make the two SAR images comparable. In addition to the technically very complex

[18] For $f_c = 10\,\mathrm{GHz}$, $\lambda_c/2 \simeq 15\,\mathrm{mm}$.

co-registration of SAR images, the long acquisition time required is a major disadvantage of this approach. It causes a smearing of moving targets and a low update rate, which makes tracking of targets impossible. Furthermore, the exact positions of moving targets cannot be determined without any additional knowledge[19]. Finally, the process of "comparing" SAR images is also a demanding process to automatize. This falls into the area of image processing for which machine learning algorithms must be trained accordingly. Altogether, this comprises a demanding processing scheme which is currently not suitable for a real-time application.

The solution to distinguish targets moving relative to the earth surface from reflections of the earth itself is to use the information from which directions the reflections arrive. As discussed in the former chapter, the angular direction u and the clutter Doppler frequency f_{Dc} are directly related. This means that the clutter signals occupy only a small portion of the angular Doppler domain. Moving targets, furthermore, are separated from clutter signals in the angle Doppler domain due to the motion induced Doppler offset. The reason for multiple channels therefor is the need for an additional measurement dimension which allows for a separation of clutter from moving targets as depicted in Fig. 2.2.4.

2.3.2. Fundamentals of STAP

The main purpose of STAP is to separate the moving targets from stationary clutter i. e. to suppress $\boldsymbol{y}_{\mathrm{c}}(\beta,\varphi_{\mathrm{m}})$ in (2.2.26). Within the classical STAP approach, (2.2.26) is treated as a purely random variable (RV) signal model with one point target and no clutter parameters given. Hence (2.2.26) becomes

$$\boldsymbol{y} = \boldsymbol{y}_{\mathrm{t}}\left(\bar{u}_{\mathrm{t}}, \bar{f}_{\mathrm{Dt}}\right) + \boldsymbol{y}_{\mathrm{c}} + \boldsymbol{n}$$

with the target signal, clutter, and noise assumed to be uncorrelated. The main goal within STAP is to maximize the signal to interference and noise ratio (SINR) for a given steering direction $\bar{u}_{\mathrm{t}}$ and $\bar{f}_{\mathrm{Dt}}$ defined as

$$\mathrm{SINR}\left(\bar{u}_{\mathrm{t}}, \bar{f}_{\mathrm{Dt}}\right) = \frac{\mathrm{E}\left\{\left|\boldsymbol{w}^{\mathrm{H}}\boldsymbol{y}_{\mathrm{t}}\left(\bar{u}_{\mathrm{t}}, \bar{f}_{\mathrm{Dt}}\right)\right|^2\right\}}{\mathrm{E}\left\{\left|\boldsymbol{w}^{\mathrm{H}}\left(\boldsymbol{y}_{\mathrm{c}} + \boldsymbol{n}\right)\right|^2\right\}} = \frac{P_{\mathrm{t}}\left|\boldsymbol{w}^{\mathrm{H}}\boldsymbol{g}\left(\bar{u}_{\mathrm{t}}, \bar{f}_{\mathrm{Dt}}\right)\right|^2}{\boldsymbol{w}^{\mathrm{H}}\boldsymbol{R}_{\mathrm{cn}}\boldsymbol{w}}, \tag{2.3.1}$$

where $\boldsymbol{w} \in \mathbb{C}^{N_{\mathrm{rx}}N_{\mathrm{P}}}$ is a linear filter vector to be chosen, $P_{\mathrm{t}} = E\left\{|x_{\mathrm{t}}|^2\right\}$ is the received target power, and

$$\boldsymbol{R}_{\mathrm{cn}} = \boldsymbol{R}_{\mathrm{c}} + \boldsymbol{R}_{\mathrm{n}} \tag{2.3.2}$$

is the clutter plus noise covariance matrix with the noise covariance matrix $\boldsymbol{R}_{\mathrm{n}} = P_{\mathrm{n}}\boldsymbol{I}$. Maximization of (2.3.1) yields the so called matched filter (MF) vector

$$\boldsymbol{w}_{\mathrm{mf}}\left(\bar{u}_{\mathrm{t}}, \bar{f}_{\mathrm{Dt}}\right) = \alpha_{\mathrm{mf}}\boldsymbol{R}_{\mathrm{cn}}^{-1}\boldsymbol{g}\left(\bar{u}_{\mathrm{t}}, \bar{f}_{\mathrm{Dt}}\right), \tag{2.3.3}$$

[19] The position of a point target within a SAR image corresponds to its observed Doppler frequency. A target moving relative to the earth surface has an additional Doppler offset and its position is thus shifted accordingly. The correct location can only be determined if the targets velocity would be known. To the contrary, if the true position of a target is known, the corresponding velocity can be determined. This would be possible for cars which usually drive on roads only.

where $\alpha_{\mathrm{mf}} \in \mathbb{R}$ is an arbitrary factor not changing the achievable SINR which is

$$\mathrm{SINR}_{\mathrm{opt}}\left(\bar{u}_{\mathrm{t}}, \bar{f}_{\mathrm{Dt}}\right) = P_{\mathrm{t}} \boldsymbol{g}^{\mathrm{H}}\left(\bar{u}_{\mathrm{t}}, \bar{f}_{\mathrm{Dt}}\right) \boldsymbol{R}_{\mathrm{cn}}^{-1} \boldsymbol{g}\left(\bar{u}_{\mathrm{t}}, \bar{f}_{\mathrm{Dt}}\right).$$

Commonly, the performance of a STAP filter is measured by the SINR loss[20] defined as

$$\mathrm{SINR}_{\mathrm{loss}}\left(\bar{u}_{\mathrm{t}}, \bar{f}_{\mathrm{Dt}}\right) = \frac{\mathrm{SINR}\left(\bar{u}_{\mathrm{t}}, \bar{f}_{\mathrm{Dt}}\right)}{\mathrm{SNR}} = \frac{\left|\boldsymbol{w}^{\mathrm{H}} \boldsymbol{g}\left(\bar{u}_{\mathrm{t}}, \bar{f}_{\mathrm{Dt}}\right)\right|^2}{\boldsymbol{w}^{\mathrm{H}} \boldsymbol{R}_{\mathrm{cn}} \boldsymbol{w}} \frac{P_{\mathrm{n}}}{\left\|\boldsymbol{g}\left(\bar{u}_{\mathrm{t}}, \bar{f}_{\mathrm{Dt}}\right)\right\|_2^2}$$

which for $\boldsymbol{w}_{\mathrm{mf}}\left(\bar{u}_{\mathrm{t}}, \bar{f}_{\mathrm{Dt}}\right)$ is

$$\mathrm{SINR}_{\mathrm{loss,opt}}\left(\bar{u}_{\mathrm{t}}, \bar{f}_{\mathrm{Dt}}\right) = \frac{P_{\mathrm{n}}}{\left\|\boldsymbol{g}\left(\bar{u}_{\mathrm{t}}, \bar{f}_{\mathrm{Dt}}\right)\right\|_2^2} \boldsymbol{g}^{\mathrm{H}}\left(\bar{u}_{\mathrm{t}}, \bar{f}_{\mathrm{Dt}}\right) \boldsymbol{R}_{\mathrm{cn}}^{-1} \boldsymbol{g}\left(\bar{u}_{\mathrm{t}}, \bar{f}_{\mathrm{Dt}}\right). \tag{2.3.4}$$

Usually, the SINR loss is evaluated for $\bar{u}_{\mathrm{t}} = 0$ and $\bar{f}_{\mathrm{Dt}} \in [-1/2, 1/2)$. Figure 2.3.2 illustrates a SINR loss curve for simulation settings listed in Tab. 1.0.1 and $\mathrm{CNR} = 60\,\mathrm{dB}$. Such a graph allows to determine an important figure of merrit of STAP algorithms, namely the minimum detectable Doppler value, which is usually defined as $\bar{f}_{\mathrm{MDD}} = \arg\min_{\bar{f}_{\mathrm{Dt}}} \mathrm{SINR}_{\mathrm{loss}}\left(0, \bar{f}_{\mathrm{Dt}}\right) \geq -3\,\mathrm{dB}$. This value allows to determine the minimum detectable velocity of a moving target. One popular

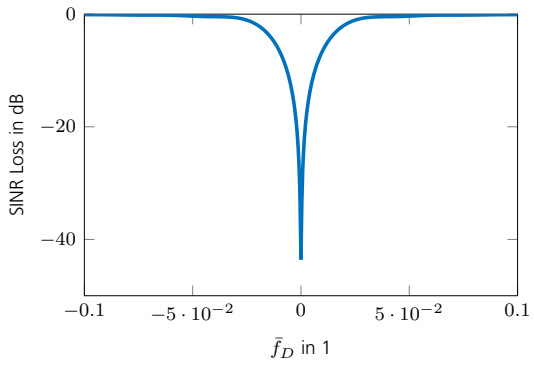

Figure 2.3.2.: SINR loss for $\bar{u} = 0$ and settings listed in Tab. 1.0.1 with $\mathrm{CNR} = 60\,\mathrm{dB}$.

choice to maximize the SINR is to minimize the clutter and noise contributions $\boldsymbol{y}_{\mathrm{c}} + \boldsymbol{n}$ while leaving the desired space-time steering vector under test undistorted

$$\min_{\boldsymbol{w}_{\mathrm{mv}}} \mathrm{E}\left\{\left|\boldsymbol{w}_{\mathrm{mv}}^{\mathrm{H}}\left(\boldsymbol{y}_{\mathrm{c}} + \boldsymbol{n}\right)\right|^2\right\} \text{ s.t. } \boldsymbol{w}_{\mathrm{mv}}^{\mathrm{H}} \boldsymbol{g}\left(\bar{u}_{\mathrm{t}}, \bar{f}_{\mathrm{Dt}}\right) = 1. \tag{2.3.5}$$

This is known as the minimum variance distortionless response (MVDR) principle or Capon beamformer with the well known result

$$\boldsymbol{w}_{\mathrm{mv}} = \frac{\boldsymbol{R}_{\mathrm{cn}}^{-1} \boldsymbol{g}\left(\bar{u}_{\mathrm{t}}, \bar{f}_{\mathrm{Dt}}\right)}{\boldsymbol{g}^{\mathrm{H}}\left(\bar{u}_{\mathrm{t}}, \bar{f}_{\mathrm{Dt}}\right) \boldsymbol{R}_{\mathrm{cn}}^{-1} \boldsymbol{g}\left(\bar{u}_{\mathrm{t}}, \bar{f}_{\mathrm{Dt}}\right)}. \tag{2.3.6}$$

It differs from the MF vector by the particular choice of the denominator through which the MVDR filter achieves some kind of super-resolution compared to a simple Fourier estimator i. e.

[20] Although termed loss it is indeed defined as a gain. Unfortunately, this unfortunate name is used throughout the STAP community.

the filter notch becomes very small [1].

A common necessity to obtain the filter coefficients is the need for the clutter covariance matrix $\boldsymbol{R}_{\mathrm{cn}}$ which is unknown in practice. The most basic approach to determine $\boldsymbol{R}_{\mathrm{cn}}$ is by estimating it as

$$\widehat{\boldsymbol{R}} = \frac{1}{N_{\mathrm{tr}}} \sum_{n_{\mathrm{tr}}=1}^{N_{\mathrm{tr}}} \boldsymbol{y}_{n_{\mathrm{tr}}} \boldsymbol{y}_{n_{\mathrm{tr}}}^{\mathrm{H}}, \tag{2.3.7}$$

where $\widehat{\boldsymbol{R}}$ is the sample covariance matrix (SCM) with N_{tr} being the number of training range gates and $\boldsymbol{y}_{n_{\mathrm{tr}}}$ a training range gate for a particular cell under test (CUT). The common assumption is that no targets are contained withing the training data, which is one of its biggest drawbacks. As a rule of thumb, the number of training gates has to be at least twice as big as the clutter rank. In this case, the SINR loss compared to the optimal achievable performance (2.3.1) is within $3\,\mathrm{dB}$ [17]. In practice, this yields an intractable number of required training gates as well as computational burden. As a consequence, a plethora of sub-optimal approaches were developed to reduce the required number of training gates e. g. diagonal loading (DL)

$$\widehat{\boldsymbol{R}}_{\mathrm{dl}} = \frac{1}{N_{\mathrm{tr}}} \sum_{n_{\mathrm{tr}}=1}^{N_{\mathrm{tr}}} \boldsymbol{y}_{n_{\mathrm{tr}}} \boldsymbol{y}_{n_{\mathrm{tr}}}^{\mathrm{H}} + \mathrm{diag}\left(\epsilon\right),$$

where $\mathrm{diag}\left(\epsilon\right) \in \mathbb{R}^{N_{\mathrm{rx}}N_{\mathrm{p}} \times N_{\mathrm{rx}}N_{\mathrm{p}}}$ is a diagonal matrix with constant entry ϵ which stabilizes the noise singular values of $\widehat{\boldsymbol{R}}$ that require many training samples to estimate. Also, sub-optimal approaches were developed to avoid the required inversion of the big covariance matrix e. g. Pre- and Post-Doppler approaches or other rank reducing transformations. For further information, especially an interesting explanation on how the optimal filter suppresses clutter using an Eigen-decomposition of (2.3.3), the interested reader may refer to common text books e. g. [1]. A further very interesting approach introduces an auto-regressive model for the clutter signal $\boldsymbol{y}_{\mathrm{c}}$ known as space-time autoregressive (STAR), which dramatically reduces the number of required training gates [20, 21].

2.3.3. On the Complementary Clutter Subspace

It was shown in [20] that matched subspace filters offer a higher performance in terms of SINR loss compared to classical filters using the SCM or other sub optimal approaches. We loose a few words on this idea here since it will be used in Chapter 7. As explained in Section 2.2, the clutter signals forming the covariance matrix $\boldsymbol{R}_{\mathrm{c}}$ are of correlated nature. In the continuous case time, it can be shown that the clutter plus noise signal resides in a one dimensional subspace allowing for a perfect separation [22]. This appealing property, however, does not translate into the discrete regime. In the special case of DPCA, the clutter occupies a distinct subspace of a size given by Brennan's rule (2.2.14). Hence, $\mathrm{rank}(\boldsymbol{R}_{\mathrm{c}}) < N_{\mathrm{rx}}N_{\mathrm{p}}$ rendering $\boldsymbol{R}_{\mathrm{c}}$ to be a true low rank matrix. In the more general case, the DPCA condition does not apply, however, the clutter signals still remain strongly correlated. As shown in [1], this results in $\boldsymbol{R}_{\mathrm{c}}$ to be of full rank but its eigenvalues decay more or less rapidly depending on the antenna configuration, internal clutter motion (ICM), system calibration, etc. Nevertheless, an effective clutter rank can be defined as

the number of eigenvalues greater than the noise eigenvalues. Let

$$\boldsymbol{R}_{\mathrm{cn}} = \boldsymbol{U}_{\mathrm{cn}} \boldsymbol{\Lambda}_{\mathrm{cn}} \boldsymbol{U}_{\mathrm{cn}}^{\mathrm{H}}$$

be the eigendecomposition of the clutter plus noise covariance matrix with $\boldsymbol{U}_{\mathrm{cn}}$ being a matrix of eigenvectors and $\boldsymbol{\Lambda}_{\mathrm{cn}}$ a diagonal matrix holding the eigenvalues sorted in descending order. Then, since $\boldsymbol{R}_{\mathrm{cn}} = \boldsymbol{R}_{\mathrm{c}} + \boldsymbol{R}_{\mathrm{n}}$ are hermitian and thus normal matrices, they can be diagonalized by any unitary matrix, hence it follows

$$\boldsymbol{\Lambda}_{\mathrm{cn}} = \boldsymbol{U}_{\mathrm{cn}}^{\mathrm{H}} \boldsymbol{R}_{\mathrm{cn}} \boldsymbol{U}_{\mathrm{cn}} = P_{\mathrm{c}} \boldsymbol{\Lambda}_{\mathrm{c}} + P_{\mathrm{n}} \boldsymbol{I} \tag{2.3.8}$$

and thus

$$\lambda_{\mathrm{cn},i} = P_{\mathrm{c}} \lambda_{\mathrm{c},i} + P_{\mathrm{n}}$$

for $i = [1, 2, \ldots, N_{\mathrm{rx}} N_{\mathrm{p}}]$. It shall be noted that $\boldsymbol{\Lambda}_{\mathrm{c}}$ denotes the eigenvalues with respect to the clutter signal space (2.2.12). As shown in [1], eigenvalues below the noise floor do not contribute to clutter suppression, hence the effective clutter rank is

$$\rho_{\mathrm{eff}} = \sum_{i=1}^{N_{\mathrm{rx}} N_{\mathrm{p}}} \mathbb{I}\left(P_{\mathrm{c}} \lambda_{\mathrm{c},i} > P_{\mathrm{n}}\right), \tag{2.3.9}$$

where $\mathbb{I}(\cdot)$ denotes the indicator function. Now, instead of using the estimated inverse clutter plus noise covariance matrix $\widehat{\boldsymbol{R}}_{\mathrm{cn}}^{-1}$ to suppress the clutter, one may also use an orthogonal projection onto the complementary effective clutter subspace to get rid of the clutter contributions. The projection onto the complementary subspace is given by

$$\mathcal{P}_{\mathrm{c}}^{\perp} = \boldsymbol{I} - \boldsymbol{U}_{\mathrm{eff}} \boldsymbol{U}_{\mathrm{eff}}^{\mathrm{H}}, \tag{2.3.10}$$

where

$$\boldsymbol{U}_{\mathrm{eff}} = [\boldsymbol{u}_{\mathrm{cn},i}]_{i=1}^{\rho_{\mathrm{eff}}} \in \mathbb{C}^{N_{\mathrm{rx}} N_{\mathrm{p}} \times \rho_{\mathrm{eff}}}$$

spans the effective clutter space. The matched subspace filter vector therefore becomes

$$\boldsymbol{w}_{\mathrm{ms}}\left(\bar{u}_{\mathrm{t}}, \bar{f}_{\mathrm{Dt}}\right) = \alpha_{\mathrm{ms}} \mathcal{P}_{\mathrm{c}}^{\perp} \boldsymbol{g}\left(\bar{u}_{\mathrm{t}}, \bar{f}_{\mathrm{Dt}}\right)$$

and its SINR loss

$$\mathrm{SINR}_{\mathrm{loss,ms}}\left(\bar{u}_{\mathrm{t}}, \bar{f}_{\mathrm{Dt}}\right) = \alpha_{\mathrm{ms}} \frac{\boldsymbol{g}^{\mathrm{H}}\left(\bar{u}_{\mathrm{t}}, \bar{f}_{\mathrm{Dt}}\right) \mathcal{P}_{\mathrm{c}}^{\perp} \boldsymbol{g}\left(\bar{u}_{\mathrm{t}}, \bar{f}_{\mathrm{Dt}}\right)}{\left\| \boldsymbol{g}\left(\bar{u}_{\mathrm{t}}, \bar{f}_{\mathrm{Dt}}\right) \right\|_2^2}, \tag{2.3.11}$$

where (2.2.20) was used.[21] Here, $\alpha_{\mathrm{ms}} \in [1/2, 1]$ determines the lower and upper bounds of (2.3.11), where the worst case lower bound is achieved if all complementary effective clutter eigenvalues would be as strong as the noise i. e. $P_{\mathrm{c}} \lambda_{\mathrm{c},i} = P_{\mathrm{n}}$ for $i > \rho_{\mathrm{eff}}$. The benefit of the

[21] Since $\mathcal{P}_{\mathrm{c}}^{\perp} = \boldsymbol{I} - \boldsymbol{U}_{\mathrm{eff}} \boldsymbol{U}_{\mathrm{eff}}^{\mathrm{H}} = \boldsymbol{U}_{\mathrm{reff}} \boldsymbol{U}_{\mathrm{reff}}^{\mathrm{H}}$ with $\boldsymbol{U}_{\mathrm{reff}} = [\boldsymbol{u}_{\mathrm{cn},i}]_{i=\rho_{\mathrm{eff}}+1}^{N_{\mathrm{rx}} N_{\mathrm{p}}} \in \mathbb{C}^{N_{\mathrm{rx}} N_{\mathrm{p}} \times \rho_{\mathrm{reff}}}$ with $\rho_{\mathrm{reff}} = N_{\mathrm{rx}} N_{\mathrm{p}} - \rho_{\mathrm{eff}}$, the SINR loss is

$$\mathrm{SINR}_{\mathrm{loss}} = \frac{\left|\boldsymbol{g}^{\mathrm{H}} \mathcal{P}_{\mathrm{c}}^{\perp} \boldsymbol{g}\right|^2 P_{\mathrm{n}}}{\boldsymbol{g}^{\mathrm{H}} \mathcal{P}_{\mathrm{c}}^{\perp} (P_{\mathrm{c}} \boldsymbol{G}_{\mathrm{c}} \boldsymbol{G}_{\mathrm{c}}^{\mathrm{H}} + P_{\mathrm{n}} \boldsymbol{I}) \mathcal{P}_{\mathrm{c}}^{\perp} \boldsymbol{g} \left\|\boldsymbol{g}\right\|_2^2} = \frac{\left|\boldsymbol{g}^{\mathrm{H}} \mathcal{P}_{\mathrm{c}}^{\perp} \boldsymbol{g}\right|^2 P_{\mathrm{n}}}{\boldsymbol{g}^{\mathrm{H}} \boldsymbol{U}_{\mathrm{reff}} \boldsymbol{\Lambda}_{\mathrm{cn,reff}} \boldsymbol{U}_{\mathrm{reff}}^{\mathrm{H}} \boldsymbol{g} \left\|\boldsymbol{g}\right\|_2^2}$$

matched subspace (MS) filter is that the noise eigenvalues, which usually require a lot of training gates to be estimated well, are not required. However, a practical problem arises when it comes to determine the rank of the clutter covariance matrix ρ which is unknown in general. To the contrary as suggested in (2.3.8), the noise eigenvalues of the SCM are not constant. Since the noise values within $\boldsymbol{n}$ stem from a limited number of RVs, the eigenvalues of $\widehat{\boldsymbol{R}}_{\mathrm{n}}$ are also subject to a distribution, which is known as complex Wishart distribution [23]. Therefore, the simple approach conducted in (2.3.9) is not feasible. In addition, for a wrongly chosen subspace size the performance of MS approach may suffer dramatically [1]. In Chapter 7 an idea to circumvent this problem is discussed.

2.3.4. STAP Detectors

For GMTI applications, STAP is set up as a detection problem. The detection is performed by conducting a Neyman-Pearson test for which a plethora of possible detectors emerged over time. Some of the most commonly used detectors are listed in Tab. 2.3.1, where the following assumptions are taken to be given or not

CFAR — In the constant false alarm rate (CFAR) case, the training and the test data may be of different scale i. e. if $\boldsymbol{R}_{\mathrm{cn}}$ denotes the covariance matrix of the CUT, the covariance matrix corresponding to the training data is assumed to be $\sigma^2\boldsymbol{R}_{\mathrm{cn}}$ with unknown $\sigma^2 \in \mathbb{R}$. Hence, CFAR detectors are capable of handling heterogeneous clutter scenarios.[22]

Adaptive — In case of adaptivity, the covariance matrix $\boldsymbol{R}_{\mathrm{cn}}$ is unknown and needs to be estimated in some manner. For the case of non-adaptivity, $\boldsymbol{R}_{\mathrm{cn}}$ is assumed to be known.

Within the test statistics in Tab. 2.3.1, the acronyms mean the following: matched filter (MF), adaptive matched filter (AMF), Kelly's generalized likelihood ratio test (GLRT), normalized matched filter (NMF), and adaptive coherence estimator (ACE). A common precondition of the test statistics is the absence of a target within the training data, as well as the CUT shares the same covariance matrix structure. The somewhat simpler AMF detector is a simplification of Kelly's GLRT detector which uses the CUT data in its decision statistic [24]. For a large amount of training data, the CUT term in the denominator tends to zero and thus coincides with the AMF detector. Hence, the AMF is computational less expensive, however, suffers from poorer performance in case of

with $\boldsymbol{\Lambda}_{\mathrm{reff}} = \mathrm{diag}\left(\left[\lambda_{\mathrm{c},i}\right]_{i=\rho_{\mathrm{eff}}+1}^{N_{\mathrm{rx}}N_{\mathrm{p}}}\right) \in \mathbb{R}^{\rho_{\mathrm{reff}}\times\rho_{\mathrm{reff}}}$. To see this, note

$$\begin{aligned}\mathcal{P}_{\mathrm{c}}^{\perp}\boldsymbol{G}_{\mathrm{c}}\boldsymbol{G}_{\mathrm{c}}^{\mathrm{H}}\mathcal{P}_{\mathrm{c}}^{\perp} &= \boldsymbol{U}_{\mathrm{reff}}\boldsymbol{U}_{\mathrm{reff}}^{\mathrm{H}}\boldsymbol{U}_{\mathrm{c}}\boldsymbol{\Sigma}_{\mathrm{c}}\boldsymbol{V}_{\mathrm{c}}^{\mathrm{H}}\boldsymbol{V}_{\mathrm{c}}\boldsymbol{\Sigma}_{\mathrm{c}}\boldsymbol{U}_{\mathrm{c}}\boldsymbol{U}_{\mathrm{reff}}\boldsymbol{U}_{\mathrm{reff}}^{\mathrm{H}}\\ &= \boldsymbol{U}_{\mathrm{reff}}\begin{bmatrix}\boldsymbol{0} & \boldsymbol{I}_{\rho_{\mathrm{reff}}\times\rho_{\mathrm{reff}}}\end{bmatrix}\boldsymbol{\Lambda}_{\mathrm{c}}\begin{bmatrix}\boldsymbol{0}\\ \boldsymbol{I}_{\rho_{\mathrm{reff}}\times\rho_{\mathrm{reff}}}\end{bmatrix}\boldsymbol{U}_{\mathrm{reff}}^{\mathrm{H}}\\ &= \boldsymbol{U}_{\mathrm{reff}}\boldsymbol{\Lambda}_{\mathrm{c,reff}}\boldsymbol{U}_{\mathrm{reff}}^{\mathrm{H}}\end{aligned}$$

and

$$\boldsymbol{\Lambda}_{\mathrm{cn,reff}} = \boldsymbol{\Lambda}_{\mathrm{c,reff}} + P_{\mathrm{n}}\boldsymbol{I}.$$

In the worst case, this case becomes $\boldsymbol{\Lambda}_{\mathrm{cn,reff}} = 2P_{\mathrm{n}}\boldsymbol{I}$ which yields the lower bound of (2.3.11).

[22] Some authors define CFAR also to be given when the test statistic is independent of scaling of $\boldsymbol{R}_{\mathrm{cn}}$ alone. While this is true, it is less strict as in our definition.

Name	Detector	CFAR	Adaptive	Disturbance
MF	$\frac{\left\|\boldsymbol{g}^{\mathrm{H}}\boldsymbol{R}^{-1}\boldsymbol{y}\right\|^2}{\boldsymbol{g}^{\mathrm{H}}\boldsymbol{R}^{-1}\boldsymbol{g}} \gtrless \eta_{\mathrm{mf}}$	×	×	Gaussian
AMF	$\frac{\left\|\boldsymbol{g}^{\mathrm{H}}\widehat{\boldsymbol{R}}^{-1}\boldsymbol{y}\right\|^2}{\boldsymbol{g}^{\mathrm{H}}\widehat{\boldsymbol{R}}^{-1}\boldsymbol{g}} \gtrless \eta_{\mathrm{amf}}$	×	✓	Gaussian
Kelly's GLRT	$\frac{\left\|\boldsymbol{g}^{\mathrm{H}}\widehat{\boldsymbol{R}}^{-1}\boldsymbol{y}\right\|^2}{\boldsymbol{g}^{\mathrm{H}}\widehat{\boldsymbol{R}}^{-1}\boldsymbol{g}\left(1+\frac{1}{N_{\mathrm{tr}}}\boldsymbol{y}^{\mathrm{H}}\widehat{\boldsymbol{R}}^{-1}\boldsymbol{y}\right)} \gtrless \eta_{\mathrm{K}}$	×	✓	Gaussian
NMF	$\frac{\left\|\boldsymbol{g}^{\mathrm{H}}\boldsymbol{R}^{-1}\boldsymbol{y}\right\|^2}{(\boldsymbol{g}^{\mathrm{H}}\boldsymbol{R}^{-1}\boldsymbol{g})(\boldsymbol{y}^{\mathrm{H}}\boldsymbol{R}^{-1}\boldsymbol{y})} \gtrless \eta_{\mathrm{nmf}}$	✓	×	compound-Gaussian
ACE	$\frac{\left\|\boldsymbol{g}^{\mathrm{H}}\widehat{\boldsymbol{R}}^{-1}\boldsymbol{y}\right\|^2}{\left(\boldsymbol{g}^{\mathrm{H}}\widehat{\boldsymbol{R}}^{-1}\boldsymbol{g}\right)\left(\boldsymbol{y}^{\mathrm{H}}\widehat{\boldsymbol{R}}^{-1}\boldsymbol{y}\right)} \gtrless \eta_{\mathrm{ace}}$	✓	✓	compound-Gaussian

Table 2.3.1.: Collection of STAP detectors with η denoting the thresholds.

low amount of training data[23] [25]. The NMF and ACE detectors are designed to work also in the compound-Gaussian case i. e. a multiplicative combination of independent random processes. This allows for the modeling of spiky clutter contributions, for which $\boldsymbol{y}_{\mathrm{c}}$ is modeled as a spherically invariant random vector (SIRV)[24] [27]. In addition to the classical estimators given in Tab. 2.3.1, also subspace detectors were developed [29, 30]. Good performance was also shown to be achieved if $\widehat{\boldsymbol{R}}^{-1}$ is replaced with the projection onto the complementary clutter subspace $\mathcal{P}_{\mathrm{c}}^{\perp}$ from (2.3.10) [21]. Such an approach was tested within this work and is presented in more detail in Section 7.3.2.

2.3.5. Prerequisites and Limitations

As shown in the preceding sections, STAP requires an accurate estimate of the SCM $\widehat{\boldsymbol{R}}_{\mathrm{cn}}$ from which it forms a filter to suppress the clutter. As it is unknown in practice, it has to be estimated in some form. In order to do so the following prerequisites are assumed to hold

- Sufficient, independently sampled training data is available
- All training data shares the same clutter structure as the CUT, i. e. $\boldsymbol{R}_{n_{\mathrm{tr}}} = \mathrm{E}\left\{\boldsymbol{y}_{n_{\mathrm{tr}}}\boldsymbol{y}_{n_{\mathrm{tr}}}^{\mathrm{H}}\right\} = \sigma_{n_{\mathrm{tr}}}^2\boldsymbol{R}_{\mathrm{cn}}$
- No training data contains any moving target signals contributions

Violation of any of the above listed prerequisites results in degraded performance. If the required amount of training data is not available, the expected SINR loss compared to the optimal achievable is

$$\frac{\mathrm{SINR}_{\mathrm{loss,exp}}}{\mathrm{SINR}_{\mathrm{loss,opt}}} = \frac{N_{\mathrm{tr}} - N_{\mathrm{rx}}N_{\mathrm{p}} + 2}{N_{\mathrm{tr}} + 1} \text{ for } N_{\mathrm{tr}} \geq N_{\mathrm{rx}}N_{\mathrm{p}}$$

[23] The AMF detector is obtained in many ways, e. g. by conducting a GLRT test assuming covariance matrix $\boldsymbol{R}_{\mathrm{cn}}$ is known and afterwards replacing it with the SCM [25]. Another derivation is to conduct a Wald test on the detection problem [26].

[24] It shall be noted, that the ACE detector is sensitive with respect to the clutter texture statistics and thus not very applicable in practice. This can be circumvented by normalizing the training data as $\bar{\boldsymbol{y}}_{n_{\mathrm{tr}}} = \boldsymbol{y}_{n_{\mathrm{tr}}}/\sqrt{\left\|\boldsymbol{y}_{n_{\mathrm{tr}}}\right\|^2/N_{\mathrm{tr}}}$ prior to calculating the SCM. This, however, diminishes the detection performance [27]. Furthermore, the ACE detector is very sensitive with respect to mismatched target steering vectors [28].

which is known as Reed, Mallot, and Brennan (RMB) rule [1]. The second condition is violated in heterogeneous clutter environment, e. g. land-sea transitions, forest borders, regions of different ICM characteristics etc. The last condition is violated in target-rich environments as in cities or any kind of much traveled roads [31]. In this case, the training data likely contains moving target signals which as a consequence results in target masking. To mitigate the effects of non-homogeneous clutter and target masking, a large amount of STAP algorithms were designed which either reduce the number of training samples in the hope that the available training data is distributed as the CUT e. g. [20, 21], or a preceding selection of the training data is conducted based on some statistical assumptions e. g. [32, 33, 34]. Further attempts try to use apriori knowledge, e. g. a terrain map or even pre-computed covariance matrices, known as knowledge-aided STAP (KA STAP). In recent years, low-rank approximation models received great attention. Among those, an intermediate approach between the classical STAP and affine rank minimization (ARM) regimes is Kronecker-STAP, which attempts to find a low rank matrix which approximates the SCM as [35]

$$\begin{aligned}\widehat{\boldsymbol{A}}, \widehat{\boldsymbol{B}} &= \underset{\operatorname{rank}(\boldsymbol{A})\leq\rho_a, \operatorname{rank}(\boldsymbol{B})\leq\rho_b}{\arg\min} \left\| \widehat{\boldsymbol{R}} - \boldsymbol{B}\otimes\boldsymbol{A} \right\|_{\mathrm{F}}^2 \\ \widehat{\boldsymbol{R}}_{\mathrm{new}} &= \widehat{\boldsymbol{B}}\otimes\widehat{\boldsymbol{A}}.\end{aligned}$$

STAP filtering is conducted by use of $\widehat{\boldsymbol{R}}_{\mathrm{new}}$, which is supposed to be free of moving target components due to the superimposed structure. Nevertheless, also this approach relies on suitable training data and in addition on the validity of the Kronecker-form.

To the contrary, this work attempts to follow a completely different approach, not using training data at all but rather to exploit the correlated nature of stationary clutter directly. By doing so, all of the aforementioned prerequisites are circumvented, which would allow for a successful moving target detection also for heterogeneous clutter or busy areas. Within this work, a uniform linear array (ULA) antenna and furthermore a flat earth scenario is assumed. The approach builds upon compressed robust principal component analysis (CRPCA) which separates low rank from sparse matrices. It is a combination of compressive sensing (CS) and ARM approaches which are described in the following chapter.

3. Fundamentals of Compressive Sensing

In this chapter the compressive sensing (CS) approach is discussed in brevity. The interested reader keen to know more on the basics of CS and its application to radar is referred to [36, 37]. Next to the theoretical basics, two algorithms most commonly used to solve CS problems are shown, namely fast iterative shrinkage-thresholding algorithm (FISTA) and normalized iterative hard thresholding (NIHT). These algorithms illustrate two so-called *denoising schemes* and serve as a reference to the advanced algorithms presented in Chapter 6.

3.1. The Compressive Sensing Approach

The primary objective is to recover an unknown sparse vector $\widetilde{\boldsymbol{s}} \in \mathbb{C}^n$, where the number of sparse entries $\kappa \ll n$, from a limited number of noisy observations of the form

$$\boldsymbol{y} = \boldsymbol{A}\widetilde{\boldsymbol{s}} + \boldsymbol{n}, \tag{3.1.1}$$

where $\boldsymbol{A} \in \mathbb{C}^{M \times n}$ $(M < n)$ is a known affine transformation[1], $\boldsymbol{y} \in \mathbb{C}^M$ is a measurement vector, and $\boldsymbol{n} \in \mathbb{C}^M$ is additive noise with independent identically distributed (i. i. d.) coefficients of zero mean and variance P_{n}. To find a solution to this under-determined linear system, we seek the closest sparse solution which is consistent with the measurements via

$$\min_{\boldsymbol{s}} \|\boldsymbol{s}\|_0 \ \text{subject to}\ h(\boldsymbol{s}) \leq \epsilon^2, \tag{3.1.2}$$

where

$$h(\boldsymbol{s}) = \|\boldsymbol{A}\boldsymbol{s} - \boldsymbol{y}\|_2^2 \tag{3.1.3}$$

is the data fidelity term with $\|\cdot\|_x$ denoting the ℓ_x norm and $\epsilon^2 \geq \|\boldsymbol{n}\|_2^2$ is some constant error energy. In order to find a solution using (3.1.2) the restricted isometry property (RIP) condition

$$(1 - \delta_K(\boldsymbol{A}))\|\boldsymbol{s}\|_2^2 \leq \|\boldsymbol{A}\boldsymbol{s}\|_2^2 \leq (1 + \delta_K(\boldsymbol{A}))\|\boldsymbol{s}\|_2^2 \tag{3.1.4}$$

must be fulfilled [36][2]. Basically (3.1.4) means that the measurement operator $\boldsymbol{A}$ must keep different sparse vectors with at most K entries distinguishable. Low values of $\delta_K(\boldsymbol{A})$ allow for a

[1] For the compressive sensing (CS) algorithms, the problem is usually stated by use of a sensing matrix rather than a sensing operator as defined in (2.1.119). Hence, the sensing operator and the radar scene in $\boldsymbol{y} = \mathcal{A}(\boldsymbol{X})$ are vectorized to $\boldsymbol{y} = \boldsymbol{A}\boldsymbol{x}$. This is possible since within the regime of sparse entries the matrix structure of $\boldsymbol{X}$ is not of importance. By doing so, multidimensional notations are not required and the problem gets easier to handle by use of common linear algebra operations.

[2] To the contrary of the null space property, the RIP condition allows to formulate reconstruction guarantees in the noisy case. It can be shown, that the existence of any reconstruction algorithm (potentially impractical) that can stably recover from noisy measurements requires that $\boldsymbol{A}$ satisfy the lower bound of (3.1.4) with some constant c, where c would depend on the particular reconstruction algorithm [36].

high reconstruction performance. Another interpretation of the RIP condition is, that the measurement matrix $\boldsymbol{A}$ acts like a unitary operator on K-sparse vectors, i. e. only causes a rotation on K-sparse vectors and preserves angles between them, thus keeping K-sparse vectors distinguishable. Random matrices and randomly chosen rows of discrete Fourier transform (DFT) matrices possess this requirement with high probability. Unfortunately program (3.1.2) is NP-hard to solve. From this point forward different approaches to solve (3.1.2) are evaluated. The first and most basic is fast iterative shrinkage-thresholding algorithm (FISTA) presented in section 3.2, which is a soft thresholding (ST) approach. A hard thresholding (HT) counterpart is normalized iterative hard thresholding (NIHT) presented in section 3.3. A most sophisticated approach to solve (3.1.2) the turbo shrinkage-thresholding (TST) algorithm together with its refinement complex successive concave sparsity approximation (CSCSA) which are presented in Chapter 6.

For all the following algorithms presented, the signal to noise ratio (SNR) is defined as

$$\mathrm{SNR} = \frac{\|\boldsymbol{A}\widetilde{\boldsymbol{s}}\|_2^2}{MP_\mathrm{n}} \tag{3.1.5}$$

and the recovery success is measured as squared reconstruction error (SRE)

$$\mathrm{SRE} = \frac{\|\widetilde{\boldsymbol{s}} - \widehat{\boldsymbol{s}}\|_2^2}{\|\widetilde{\boldsymbol{s}}\|_2^2}, \tag{3.1.6}$$

where $\widehat{\boldsymbol{s}}$ is the reconstruction result. For the phase transition plots [38], the SRE was averaged over $N_\mathrm{mc} = 100$ Monte Carlo runs as $\frac{1}{N_\mathrm{mc}} \sum_{i=1}^{N_\mathrm{mc}} \mathrm{SRE}_i$, where SRE_i denotes the SRE of the i^th reconstruction. All algorithms are aborted either after a maximum number of iterations I, or if the residual error defined as

$$\begin{aligned}
\epsilon_\mathrm{rel}^2 &= \frac{\|\boldsymbol{y} - \boldsymbol{A}\widehat{\boldsymbol{s}}\|_2^2}{\|\boldsymbol{y}\|_2^2} && (3.1.7)\\
&\simeq \frac{\|\boldsymbol{y} - \boldsymbol{A}\widetilde{\boldsymbol{s}}\|_2^2}{\|\boldsymbol{y}\|_2^2} = \frac{\|\boldsymbol{n}\|_2^2}{\|\boldsymbol{A}\widetilde{\boldsymbol{s}} + \boldsymbol{n}\|_2^2} && (3.1.8)\\
&\geq \frac{\|\boldsymbol{n}\|_2^2}{\left(\|\boldsymbol{A}\widetilde{\boldsymbol{s}}\|_2 + \|\boldsymbol{n}\|_2\right)^2} = \frac{1}{\left(\|\boldsymbol{A}\widetilde{\boldsymbol{s}}\|_2 \,/\, \|\boldsymbol{n}\|_2 + 1\right)^2} && (3.1.9)\\
&\simeq \frac{\|\boldsymbol{n}\|_2^2}{\|\boldsymbol{A}\widetilde{\boldsymbol{s}}\|_2^2}, && (3.1.10)
\end{aligned}$$

drops below a certain threshold. In (3.1.8) it is assumed that $\widehat{\boldsymbol{s}}$ is close to the true solution $\widetilde{\boldsymbol{s}}$, (3.1.9) used the Cauchy-Schwarz inequality $\|\boldsymbol{u} + \boldsymbol{v}\|_2^2 \leq (\|\boldsymbol{u}\|_2 + \|\boldsymbol{v}\|_2)^2$, and in (3.1.10) it was assumed that $\|\boldsymbol{A}\widetilde{\boldsymbol{s}}\|_2 \,/\, \|\boldsymbol{n}\|_2 \gg 1$. The expectation value of the residual error therefore approximately is

$$\mathrm{E}\left\{\epsilon_\mathrm{rel}^2\right\} \simeq \mathrm{E}\left\{\frac{\|\boldsymbol{n}\|_2^2}{\|\boldsymbol{A}\widetilde{\boldsymbol{s}}\|_2^2}\right\} = \frac{MP_\mathrm{n}}{\|\boldsymbol{A}\widetilde{\boldsymbol{s}}\|_2^2} = \frac{1}{\mathrm{SNR}}.$$

As a last stop criterion the relative improvement from iteration to iteration is used which is defined as

$$d_i = \frac{\|\boldsymbol{s}_i - \boldsymbol{s}_{i-1}\|_2^2}{\|\boldsymbol{s}_{i-1}\|_2^2}. \tag{3.1.11}$$

Parameter	Definition	Value
Dimension	n	625
SNR	(3.1.5)	$40\,\mathrm{dB}$
# iterations max.	I	300

Table 3.1.1.: Simulation parameter for generation of phase transition diagrams.

The success rate is evaluated by use of phase transition plots, where for a given type of sensing operator $\boldsymbol{A}$ (random or DFT) a number of sparse vectors $\widetilde{\boldsymbol{s}}$ are to be reconstructed for different measurement ratios $M/n \in (0,1]$ and sparsity ratios $\kappa/M \in (0,1]$ [38]. In general, the higher the measurement rate M/n is, the easier it is to find a solution to (3.1.2). In case $M/n \geq 1$, the reconstruction problem can be solved in any case[3]. Likewise, the higher the sparsity ratio κ/M is, the more difficult the reconstruction problem becomes. In case $\kappa/M \geq 1$, the reconstruction problem can not be solved at all. Hence, the phase transition plot renders to be a collection of reconstruction problems of varying difficulty. Various reconstruction algorithms now compete on how many problems of varying difficulty they can successfully reconstruct. Usually, a sharp transition of reconstructable from non-reconstructable problems arise for a given algorithm, hence the name phase transition diagram. For a single reconstruction problem, the sparse vector $\widetilde{\boldsymbol{s}}$ is set up by first determining κ and M from the given measurement and sparsity ratios. Then κ support indices are drawn from an i. i. d. $\mathcal{U}(1,n)$ distribution. The entries at the determined indices are drawn from an i. i. d. complex Gaussian distribution. Next, the sensing operators $\boldsymbol{A}$ of size $M \times n$ are set up, where for random sensing operators $\boldsymbol{A} \sim \mathcal{CN}(0,1)$ or for DFT operators $\boldsymbol{A}$ is set up from M randomly selected rows of an $n \times n$ DFT matrix. Finally, the elements of the noise vector $\boldsymbol{n}$ are drawn from an i. i. d. standard complex Gaussian distribution and scaled to the given SNR according to (3.1.5). For every combination of measurement and sparsity ratio 100 Monte Carlo runs were conducted and averaged to generate the phase transition plot. The simulation parameters to generate the phase transition plots in Fig. 3.2.1, Fig. 3.3.1, and Fig. 3.3.2 are listed in Tab. 3.1.1.

Finally it shall be noted, that random sensing matrices are of limited interest in radar engineering and serve here merely as a comparison benchmark since many algorithms in the literature are stated for random sensing matrices alone. For the application of CS algorithms within space-time adaptive processing (STAP), their performance with respect to DFT sensing operators are of interest.

3.2. Fast Iterative Shrinkage Thresholding

The fast iterative shrinkage-thresholding algorithm (FISTA) algorithm tries to find a solution to (3.1.2) by applying the basis pursuit denoise (BPDN) approach which relaxes (3.1.2) to

$$\min_{\boldsymbol{s}} \|\boldsymbol{s}\|_1 \ \text{subject to}\ h(\boldsymbol{s}) \leq \epsilon^2. \tag{3.2.1}$$

[3]For instance by classical least square approaches.

The regularized form of (3.2.1) is

$$\widehat{\boldsymbol{s}} = \arg\min_{\boldsymbol{s}} \lambda \|\boldsymbol{s}\|_1 + h(\boldsymbol{s}), \tag{3.2.2}$$

where $\lambda > 0$ is some regularization parameter. It is of convex nature and can be solved by the iterative thresholding (IT) approach by iteratively updating

$$\boldsymbol{s}_i = \mathcal{S}_{\mathrm{s},\mu\lambda}\left(\boldsymbol{s}_{i-1} - \mu\nabla_{\boldsymbol{s}} h(\boldsymbol{s}_{i-1})\right). \tag{3.2.3}$$

Here, μ is some step size, i the iteration index,

$$\nabla_{\boldsymbol{s}} h(\boldsymbol{s}_{i-1}) = \boldsymbol{A}^{\mathrm{H}}(\boldsymbol{y} - \boldsymbol{A}\boldsymbol{s}_{i-1})$$

denotes the gradient with respect to $\boldsymbol{s}$ at $\boldsymbol{s} = \boldsymbol{s}_{i-1}$, and

$$\left[\mathcal{S}_{\mathrm{s},a}(\boldsymbol{x})\right]_i = (|x_i| - a)_+ \exp(\mathrm{j}\arg(x_i)) \tag{3.2.4}$$

is the nonlinear soft thresholding operator with $(\cdot)_+ = \max(0, \cdot)$. A derivation of the gradient can be found in Appendix A.7.1. The step size is chosen as

$$\mu = \frac{1}{M_{\mathrm{L}}},$$

where M_{L} is the smallest Lipschitz constant of $\nabla_{\boldsymbol{s}} h(\boldsymbol{s})$ [39]. For the parameter λ no optimal value is known, however, the following heuristic formula may be used [40]

$$\lambda = 2c_r\sqrt{P_{\mathrm{n}}}\Phi^{-1}\left(1 - \frac{\alpha_r}{2n}\right), \tag{3.2.5}$$

where $c_r > 1$ is some constant, Φ is the cumulative density function (CDF) of $\mathcal{N}(0,1)$, and $\alpha_r \in [0,1]$ is some parameter. With such a choice, a least absolute shrinkage and selection operator (LASSO) estimator achieves a so-called near-oracle performance with probability at least $1 - \alpha_r$. It is well known, that IT techniques have a low computational complexity, however, they suffer from low convergence rates on the order of $\mathcal{O}(1/i)$ where i denotes the iteration index. To accelerate the IT approach, (3.2.3) is expanded to

$$\begin{aligned}
\boldsymbol{s}_i &= \mathcal{S}_{\mu\lambda}\left(\boldsymbol{s}'_i - \mu\nabla_{\boldsymbol{s}} h\left(\boldsymbol{s}'_i\right)\right) \\
t_{i+1} &= \frac{1 + \sqrt{1 + 4t_i^2}}{2} \\
\boldsymbol{s}'_{i+1} &= \boldsymbol{s}_i + \frac{(t_i - 1)}{t_{i+1}}(\boldsymbol{s}_i - \boldsymbol{s}_{i-1}),
\end{aligned}$$

which is known as FISTA technique. It barely increases the computational complexity but boosts the convergence rate up to $\mathcal{O}(1/i^2)$ [41]. Putting all the above steps together, the final FISTA algorithm is listed in Algorithm 3.1. The threshold selections given in Algorithm 3.1 were evaluated numerically and prove to work well in every case. In the following some simulation results are shown for which λ was chosen according to (3.2.5) with $c_r = 1.05$ and $\alpha = 0.5$. The result

Algorithm 3.1 The FISTA algorithm.

Input: $\boldsymbol{A}$, $\boldsymbol{y}$, μ,λ, I

Initialization:

$\epsilon \leftarrow \min\left(10^{-4}, 5 \cdot 10^{-3}\lambda\right)$

$i \leftarrow 0$, $d \leftarrow \infty$, $t_1 \leftarrow 1$, $\boldsymbol{s}_0 \leftarrow \boldsymbol{0}$, $\boldsymbol{s}'_1 \leftarrow \boldsymbol{0}$

Body:

while $d > \epsilon$ **and** $i < I$ **do**

$i \leftarrow i + 1$

$\boldsymbol{s}_i \leftarrow \mathcal{S}_{\mu\lambda}\left(\boldsymbol{s}'_i - \mu\nabla_{\boldsymbol{s}} h\left(\boldsymbol{s}'_i\right)\right)$

$t_{i+1} \leftarrow (1 + \sqrt{1 + 4t_i^2})/2$

$\boldsymbol{s}'_{i+1} \leftarrow \boldsymbol{s}_i + (t_i - 1)\left(\boldsymbol{s}_i - \boldsymbol{s}_{i-1}\right)/t_{i+1}$

$d \leftarrow \|\boldsymbol{s}_i - \boldsymbol{s}_{i-1}\|_2 \,/\, \|\boldsymbol{s}_{i-1}\|_2$

end while

Output: $\widehat{\boldsymbol{s}} \leftarrow \boldsymbol{s}_i$

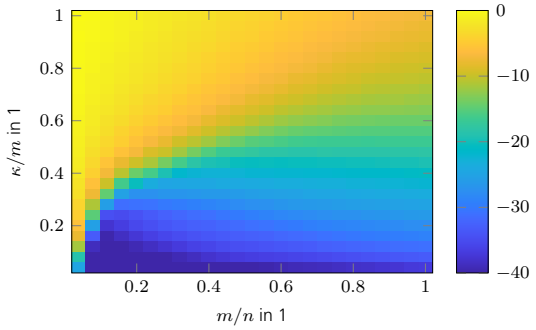

(a) Mean SRE in dB for random sensing operators $\boldsymbol{A} \sim \mathcal{CN}(0, 1)$.

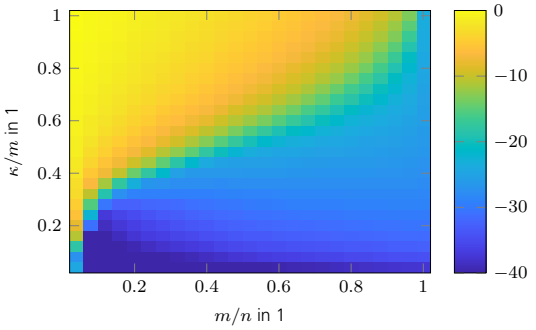

(b) Mean SRE in dB for random DFT sensing operators.

Figure 3.2.1.: Phase transition of FISTA in SRE in dB for simulation parameters listed in Tab. 3.1.1.

for random and discrete Fourier transform (DFT) sensing operators are shown in Fig. 3.2.1a and 3.2.1b. The advantage of FISTA over normalized iterative hard thresholding (NIHT) is its lack of parameters which have to be known somehow or may be even unknown. Its drawback is its slower convergence rate and poor reconstruction performance.

3.3. Normalized Iterative Hard Thresholding

The normalized iterative hard thresholding (NIHT) algorithm tries to find a solution to (3.1.2) by solving the equivalent optimization problem

$$\widehat{\boldsymbol{s}} = \arg\min_{\boldsymbol{s}} h\left(\boldsymbol{s}\right) \text{ subject to } \|\boldsymbol{s}\|_0 \leq K, \tag{3.3.1}$$

where K is a chosen constant. Program (3.3.1) is solved by iteratively updating

$$\boldsymbol{s}_{i+1} = \mathcal{H}_{\mathrm{s},K}\left(\boldsymbol{s}_i - \mu_i \nabla_{\boldsymbol{s}} h\left(\boldsymbol{s}_i\right)\right),$$

where μ_i is some step size and

$$[\mathcal{H}_{\mathrm{s},K}(\boldsymbol{x})]_i = \begin{cases} x_i, & \text{if } |x_i| \geq \boldsymbol{x}^{[K]} \\ 0, & \text{else} \end{cases} \tag{3.3.2}$$

is the nonlinear hard thresholding operator with $\boldsymbol{x}^{[K]}$ being the K^{th} biggest entry in magnitude in vector $\boldsymbol{x}$. As such, $\mathcal{H}_{\mathrm{s},K}(\boldsymbol{x})$ sets all but the K largest elements in magnitude of $\boldsymbol{x}$ to zero. The step size μ_i is updated in every iteration and needs to be verified such that it truly minimizes (3.3.1) [42]. Putting all the above steps together, the final NIHT algorithm is listed in Algorithm 3.2. The threshold selections given in Algorithm 3.2 were evaluated numerically and prove to work well in every case. The simulation results for random sensing and the discrete Fourier transform

Algorithm 3.2 The NIHT algorithm.

Input: $\boldsymbol{A}$, $\boldsymbol{y}$, K, I
Initialization:
1: $\epsilon \leftarrow \min\left(10^{-4}, 5 \cdot 10^{-3}\lambda\right)$
2: $i \leftarrow 0$, $d \leftarrow \infty$, $\boldsymbol{s}_0 \leftarrow \boldsymbol{0}$
Body:
1: **while** $d > \epsilon$ **and** $i < I$ **do**
2: $\mu_i \leftarrow$(13) and (14) in [42]
3: $\boldsymbol{s}_{i+1} \leftarrow \mathcal{H}_{\mathrm{s},K}(\boldsymbol{s}_i - \mu_i \nabla_{\boldsymbol{s}} h(\boldsymbol{s}_i))$
4: $d \leftarrow \|\boldsymbol{s}_{i+1} - \boldsymbol{s}_i\|_2 / \|\boldsymbol{s}_i\|_2$
5: $i \leftarrow i + 1$
6: **end while**
Output: $\widehat{\boldsymbol{s}} \leftarrow \boldsymbol{s}_i$

(DFT) operators are shown in Fig. 3.3.1 and Fig. 3.3.2, where the parameter K was once set to the true number of sparse entries κ of $\widetilde{\boldsymbol{s}}$ and once to twice the number 2κ. As can be seen, the reconstruction success depends heavily on K.

Clearly, neither fast iterative shrinkage-thresholding algorithm (FISTA) nor NIHT are optimal choices for practical problems. Therefore, improved versions are presented in Section 6.1 and 6.2 which show superior reconstruction performance and do not require parameters unknown in practice.

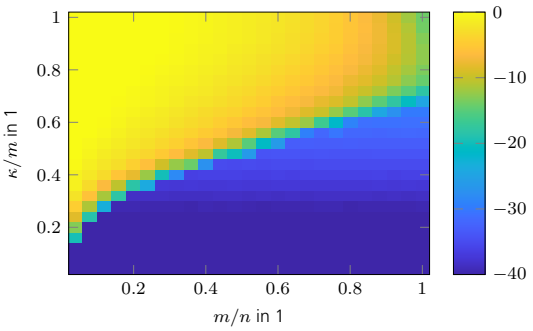

(a) Mean SRE in dB for $K = \kappa$.

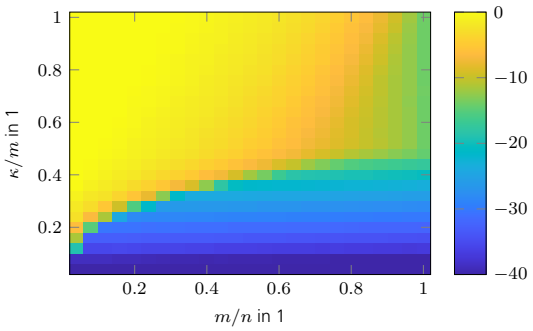

(b) Mean SRE in dB for $K = 2\kappa$.

Figure 3.3.1.: Phase transition of NIHT algorithm for random sensing operators $\boldsymbol{A} \sim \mathcal{CN}(0, 1)$ and simulation parameters listed in Tab. 3.1.1.

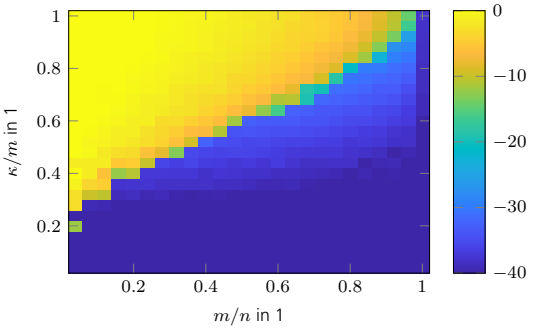

(a) Mean SRE in dB for $K = \kappa$.

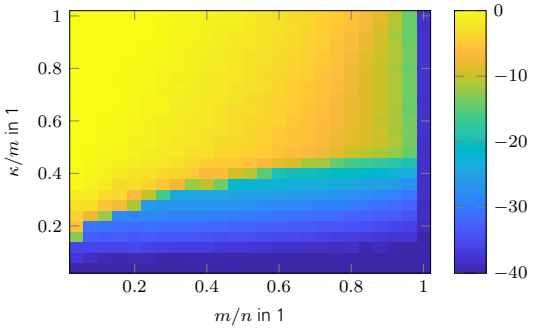

(b) Mean SRE in dB for $K = 2\kappa$.

Figure 3.3.2.: Phase transitions of NIHT algorithm for random DFT sensing operators and simulation parameters listed in Tab. 3.1.1.

4. Fundamentals of Affine Rank Minimization

In this chapter the affine rank minimization (ARM) approach is discussed in brevity. Next to the theoretical basics, two algorithms most commonly used to solve ARM problems are shown, namely singular value thresholding (SVT) and singular value projection (SVP). These algorithms illustrate two so-called *denoising schemes* and serve as a reference to the advanced algorithms presented in Chapter 6.

4.1. The Affine Rank Minimization Approach

The primary objective is to recover an unknown low-rank matrix $\widetilde{\boldsymbol{L}} \in \mathbb{C}^{N_1 \times N_2}$, where $\operatorname{rank}(\widetilde{\boldsymbol{L}}) = \rho \ll n_{\min} = \min(N_1, N_2)$, from a limited number of noisy observations of the form

$$\boldsymbol{y} = \mathcal{A}(\widetilde{\boldsymbol{L}}) + \boldsymbol{n}, \tag{4.1.1}$$

where $\mathcal{A} \in \mathbb{C}^{M \times N_1 \times N_2}$ ($M < N_1 N_2 = n$) is a known affine transformation, $\boldsymbol{y} \in \mathbb{C}^M$ is a measurement vector, and $\boldsymbol{n} \in \mathbb{C}^M$ is additive noise with i. i. .d coefficients of zero mean and variance P_{n}. To find a solution to this under-determined linear system, we seek the closest low-rank solution which is consistent with the measurements via

$$\min_{\boldsymbol{L}} \operatorname{rank}(\boldsymbol{L}) \ \text{subject to}\ h(\boldsymbol{L}) \leq \epsilon^2, \tag{4.1.2}$$

where

$$h(\boldsymbol{L}) = \|\mathcal{A}(\boldsymbol{L}) - \boldsymbol{y}\|_2^2 \tag{4.1.3}$$

is the residual term, and $\epsilon^2 \geq \|\boldsymbol{n}\|_2^2$ some constant noise energy. In order to find a solution using (4.1.2) the restricted rank isometry property (RRIP) condition

$$(1 - \delta_R(\mathcal{A}))\, \|\boldsymbol{L}\|_{\mathrm{F}}^2 \leq \|\mathcal{A}(\boldsymbol{L})\|_{\mathrm{F}}^2 \leq (1 + \delta_R(\mathcal{A}))\, \|\boldsymbol{L}\|_{\mathrm{F}}^2 \tag{4.1.4}$$

for all $\boldsymbol{L}$ with $\operatorname{rank}(\boldsymbol{L}) \leq R$ need to be fulfilled. Basically (4.1.4) means that the measurement operator $\mathcal{A}(\cdot)$ must keep different matrices of rank $\rho \leq R$ distinguishable. Low values of $\delta_R(\mathcal{A})$ allow for a high reconstruction performance. Random matrices and randomly chosen rows of discrete Fourier transform (DFT) matrices possess this requirement. Unfortunately problem (4.1.2), which is known as stable affine rank minimization (ARM) problem, is NP-hard to solve [43].

From this point forward different approaches to find approximate solutions to (4.1.2) are evaluated. The first and most basic is singular value thresholding (SVT) presented in Section 4.2, which is a soft thresholding (ST) approach. A hard thresholding (HT) counterpart is singular value projection (SVP) presented in Section 4.3. A most sophisticated approach to solve (4.1.2) the turbo

singular value thresholding (TSVT) algorithm together with its refinement complex smoothed rank approximation (CSRA) which are presented in Chapter 6. All aforementioned algorithms require an singular value decomposition (SVD) in every iteration step which is a computational bottle neck in case of large low rank matrices are to be reconstructed. Therefore, alternatives were evaluated which avoid this expensive computation. One algorithm doing so is an iterative procedure called the bi-factored gradient descent (BFGD) algorithm [43]. However, for the BFGD algorithm no practical step size determination was available. Hence, an optimal step size determination was developed, which was published at the EUSIPCO 2020 conference in Amsterdam [44] and can be found in the Appendix A.6. The BFGD may serve as a final refinement algorithm and as such is not evaluated in more detail in this work.

For all the following ARM algorithms presented, the signal to noise ratio (SNR) is defined likewise to compressive sensing (CS) as

$$\mathrm{SNR} = \frac{\left\|\mathcal{A}(\widetilde{\boldsymbol{L}})\right\|_2^2}{MP_\mathrm{n}} \tag{4.1.5}$$

and the recovery success is measured as squared reconstruction error (SRE)

$$\mathrm{SRE} = \frac{\left\|\widetilde{\boldsymbol{L}} - \widehat{\boldsymbol{L}}\right\|_\mathrm{F}^2}{\left\|\widetilde{\boldsymbol{L}}\right\|_\mathrm{F}^2}, \tag{4.1.6}$$

where $\widehat{\boldsymbol{L}}$ is the reconstruction result. For the phase transition plots [38], the SRE was averaged like in the CS case over $N_\mathrm{mc} = 100$ Monte Carlo runs. All algorithms are aborted either after a maximum number of iterations i_max, or if the residual error defined as

$$\epsilon_\mathrm{rel}^2 = \frac{\left\|\boldsymbol{y} - \mathcal{A}(\widehat{\boldsymbol{L}})\right\|_2^2}{\|\boldsymbol{y}\|_2^2} \tag{4.1.7}$$

$$\simeq \frac{\left\|\boldsymbol{y} - \mathcal{A}(\widetilde{\boldsymbol{L}})\right\|_2^2}{\|\boldsymbol{y}\|_2^2} = \frac{\|\boldsymbol{n}\|_2^2}{\left\|\mathcal{A}(\widetilde{\boldsymbol{L}}) + \boldsymbol{n}\right\|_2^2} \tag{4.1.8}$$

$$\geq \frac{\|\boldsymbol{n}\|_2^2}{\left(\left\|\mathcal{A}(\widetilde{\boldsymbol{L}})\right\|_2 + \|\boldsymbol{n}\|_2\right)^2} = \frac{1}{\left(\left\|\mathcal{A}(\widetilde{\boldsymbol{L}})\right\|_2 / \|\boldsymbol{n}\|_2 + 1\right)^2} \tag{4.1.9}$$

$$\simeq \frac{\|\boldsymbol{n}\|_2^2}{\left\|\mathcal{A}(\widetilde{\boldsymbol{L}})\right\|_2^2}, \tag{4.1.10}$$

drops below a certain threshold. In (4.1.8) it is assumed that $\widehat{\boldsymbol{L}}$ is close the true solution $\widetilde{\boldsymbol{L}}$, (4.1.9) used the Cauchy-Schwarz inequality $\|\boldsymbol{u}+\boldsymbol{v}\|_2^2 \leq (\|\boldsymbol{u}\|_2 + \|\boldsymbol{v}\|_2)^2$, and in (4.1.9) it was assumed that the $\left\|\mathcal{A}(\widetilde{\boldsymbol{L}})\right\|_2 / \|\boldsymbol{n}\|_2 \gg 1$. The expectation value of the residual error therefore approximately is

$$\mathrm{E}\left\{\epsilon_\mathrm{rel}^2\right\} \simeq \mathrm{E}\left\{\frac{\|\boldsymbol{n}\|_2^2}{\left\|\mathcal{A}(\widetilde{\boldsymbol{L}})\right\|_2^2}\right\} = \frac{MP_\mathrm{n}}{\left\|\mathcal{A}(\widetilde{\boldsymbol{L}})\right\|_2^2} = \frac{1}{\mathrm{SNR}}.$$

Parameter	Definition	Value
Dimension	$N_1 \times N_2$	24×80
SNR	(3.1.5)	$40\,\mathrm{dB}$
# iterations max.	I	300

Table 4.1.1.: Simulation parameter for generation of phase transition diagrams.

As a last stop criterion the relative improvement from iteration to iteration is used which is defined as

$$d_i = \frac{\|\boldsymbol{L}_i - \boldsymbol{L}_{i-1}\|_{\mathrm{F}}^2}{\|\boldsymbol{L}_{i-1}\|_{\mathrm{F}}^2}. \tag{4.1.11}$$

The success rate is again evaluated by use of phase transition plots, where for a given type of sensing operator $\mathcal{A}$ (random or DFT) a number of low-rank matrices $\widetilde{\boldsymbol{L}}$ are to be reconstructed for different measurement ratios ${}^{M}/_{n} \in (0, 1]$ and degree of freedom ratios ${}^{d_\rho}/_{M} \in (0, 1]$, where $d_\rho = \rho\,(N_1 + N_2 - \rho)$ denotes the number of degrees of freedom in a rank-ρ matrix. The low-rank matrices $\widetilde{\boldsymbol{L}}$ are set up by first determining ρ and M from the given ratios. Here it shall be mentioned, that since the rank ρ has to be a whole number, it is not possible to clearly find a suitable integer ρ for every possible d_ρ. Instead, ρ is determined by the closest integer to give the desired d_ρ. Obviously, this only approximates the desired d_ρ, where the approximation becomes better for larger dimensions $N_1 \times N_2$. This however results in very high computation time. With this approach, the resulting ρ may also result to zero, especially for small d_ρ. In this case, no simulations were conducted, which are indicated by blank white entries in the following phase transition plots. For the construction of a true low-rank matrix $\widetilde{\boldsymbol{L}}$, two matrices $\boldsymbol{X}_r \in \mathbb{C}^{N_1 \times \rho}$ and $\boldsymbol{X}_l \in \mathbb{C}^{N_2 \times \rho}$ are set up, whose entries are drawn from an i. i. d. complex Gaussian distribution. In a next step $\boldsymbol{X}_r$ and $\boldsymbol{X}_l$ are orthonormalized. In addition a diagonal matrix determining the singular values of the final low-rank matrix $\boldsymbol{\Sigma}_{\boldsymbol{L}}$ is created. Finally, the low-rank matrix is constructed as $\widetilde{\boldsymbol{L}} = \boldsymbol{X}_r \boldsymbol{\Sigma}_{\boldsymbol{L}} \boldsymbol{X}_l^{\mathrm{H}}$. Next, the sensing operators $\mathcal{A}$ are set up, where for random sensing operators $\mathcal{A} \sim \mathcal{CN}\,(0, 1)$ or for DFT operators $\mathcal{A}$ is set up from M randomly selected rows of an $N_1 N_2 \times N_1 N_2$ DFT matrix following the identity $\boldsymbol{y} = \mathcal{A}\,(\boldsymbol{L}) = \boldsymbol{A}\,\mathrm{vec}\,(\boldsymbol{L})$. Finally, the elements of the noise vector $\boldsymbol{n}$ are drawn from an i. i. d. standard complex Gaussian distribution and scaled the given SNR according to (3.1.5). For every combination of measurement and rank ratio 100 Monte Carlo runs were conducted and averaged to generate the phase transition plot. The simulation parameters to generate the phase transition plots are listed in Tab. 4.1.1.

4.2. Singular Value Thresholding

The singular value thresholding (SVT) algorithm tries to find a solution to (4.1.2) by applying the nuclear norm minimization (NNM) approach which relaxes (4.1.2) to

$$\min_{\boldsymbol{L}} \|\boldsymbol{L}\|_* \ \text{subject to}\ h\,(\boldsymbol{L}) \leq \epsilon^2, \tag{4.2.1}$$

where the nuclear norm $\|\boldsymbol{L}\|_*$, defined as the sum of the singular values of $\boldsymbol{L}$, renders to be the tightest convex envelop to $\operatorname{rank}(\boldsymbol{L})$. The regularized form of 4.2.1 is

$$\widehat{\boldsymbol{L}} = \arg\min_{\boldsymbol{L}} \lambda \|\boldsymbol{L}\|_* + h(\boldsymbol{L}), \tag{4.2.2}$$

where $\lambda > 0$ is some regularization parameter. It is of convex nature and can be solved by the SVT algorithm by iteratively updating

$$\boldsymbol{L}_{i+1} = \mathcal{S}_{\mathrm{l},\mu\lambda}(\boldsymbol{L}_i - \mu\nabla_{\boldsymbol{L}} h(\boldsymbol{L}_i))$$

where μ is some step size, i the iteration index, and

$$\mathcal{S}_{\mathrm{l},a}(\boldsymbol{X}) = \sum_{i=1}^{n_{\min}} (\sigma_i - a)_+ \boldsymbol{u}_i \boldsymbol{v}_i^{\mathrm{H}}, \tag{4.2.3}$$

the so called singular value soft thresholding (ST) denoiser. Furthermore, $\boldsymbol{X} = \boldsymbol{U}\operatorname{diag}(\boldsymbol{\sigma})\boldsymbol{V}^{\mathrm{H}}$ is the singular value decomposition (SVD) of $\boldsymbol{X}$ with $\boldsymbol{u}_i$ and $\boldsymbol{v}_i$ denoting the i^{th} column vector of $\boldsymbol{U}$ and $\boldsymbol{V}$, and $\boldsymbol{\sigma} = \begin{bmatrix}\sigma_1 & \cdots & \sigma_{n_{\min}}\end{bmatrix}^{\mathrm{T}}$ is a vector holding the singular values of $\boldsymbol{X}$ in decreasing order. The step size is chosen as

$$\mu = \frac{n}{M\|\mathcal{A}\|_2^2},$$

where $\|\mathcal{A}\|_2$ is the spectral norm of the sensing operator [45]. For the parameter λ an ideal value does not exist. We use a value derived from (3.2.5) as

$$\lambda = 2c_{\mathrm{r}}\Phi^{-1}\left(1 - \frac{\alpha_{\mathrm{r}}}{2n}\right)\sqrt{P_{\mathrm{n}}\max(N_1, N_2)}, \tag{4.2.4}$$

where $c_r > 1$ is some constant, Φ is the cumulative density function (CDF) of $\mathcal{N}(0,1)$, and $\alpha_r \in [0,1]$ is some parameter. With such a choice, a least absolute shrinkage and selection operator (LASSO) estimator achieves a so-called near-oracle performance[1] with probability at least $1 - \alpha_r$. Given the similarities between the LASSO estimator and the NNM approach we may use this heuristic for a sophisticated choice of λ. To adapt this formula to our needs, we adjusts $\sqrt{P_{\mathrm{n}}}$ to $\sqrt{P_{\mathrm{n}}\max(N_1, N_2)}$ to reflect the noise level present in the singular values in $\widetilde{\boldsymbol{L}}$ [47]. Putting all the above steps together, the final SVT algorithm is listed in Algorithm 4.1. The threshold selections given in Algorithm 4.1 were evaluated numerically and prove to work well in every case. For the conducted simulations the parameter λ was chosen as $c_r = 1.05$ and $\alpha = 0.5$. The result for random and discrete Fourier transform (DFT) sensing operators are shown in Fig. 4.2.1a and 4.2.1b. The odd reconstruction success for low values of M/n result from the very coarse approximation of d_ρ/M since in this case the rank ρ, which has to be an integer number, can not be chosen to be close to the desired degree of freedom ratio. This is a simulation setup effect, which can only be mitigated by increasing the problem size $N_1 \times N_2$ as explained in the beginning of this chapter. The advantage of SVT over singular value projection (SVP) is that a successful reconstruction is possible for a wide range of the regularization parameter λ where

[1] In compressive sensing (CS), oracle performance denotes the performance as one would get if an oracle that foreknows the true support of the true sparse vector $\boldsymbol{x}$ was used to reconstruct the sparse signal [46].

Algorithm 4.1 The SVT algorithm.

Input: $\mathcal{A}$, $\boldsymbol{y}$, λ, I

Initialization:

$\epsilon \leftarrow \min\left(10^{-4}, 5 \cdot 10^{-3}\lambda\right)$

$\mu \leftarrow n/(M \left\|\mathcal{A}\right\|_2^2)$

$i \leftarrow 0$, $d \leftarrow \infty$, $\boldsymbol{L}_0 \leftarrow \boldsymbol{0}$

Body:

while $d > \epsilon$ **and** $i < I$ **do**

$\boldsymbol{L}_{i+1} \leftarrow \mathcal{S}_{\mathrm{l},\mu\lambda}\left(\boldsymbol{L}_i - \mu\nabla_{\boldsymbol{L}} h\left(\boldsymbol{L}_i\right)\right)$

$d \leftarrow \left\|\boldsymbol{L}_{i+1} - \boldsymbol{L}_i\right\|_{\mathrm{F}} / \left\|\boldsymbol{L}_i\right\|_{\mathrm{F}}$

$i \leftarrow i + 1$

end while

Output: $\widehat{\boldsymbol{L}} \leftarrow \boldsymbol{L}_i$

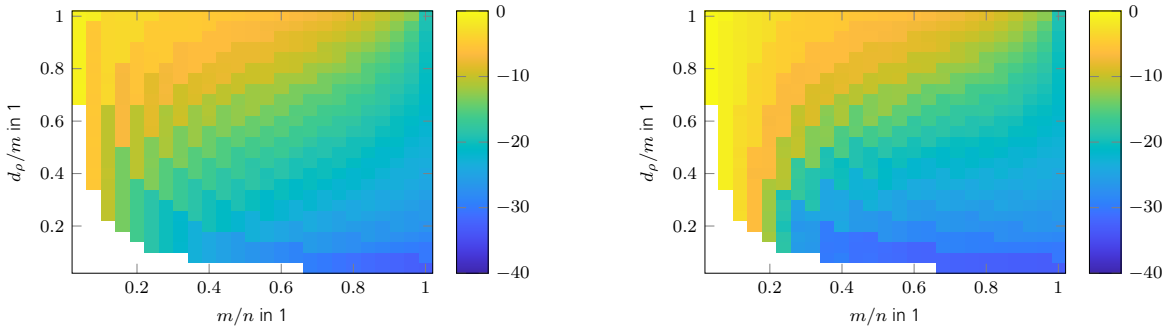

(a) Mean SRE in dB for random sensing operators $\mathcal{A} \sim \mathcal{CN}\left(0, 1\right)$.

(b) Mean SRE in dB for random DFT sensing operators.

Figure 4.2.1.: Phase transition of SVT in SRE in dB for simulation parameters listed in Tab. 4.1.1.

(4.2.4) is a good choice. To the contrary, the parameters of SVP need to be known well, however, are unknown in practice. Its drawback is its slow convergence rate and poor reconstruction performance.

4.3. Singular Value Projection

The singular value projection (SVP) algorithm tries to find a solution to (4.1.2) by solving the equivalent optimization problem

$$\widehat{\boldsymbol{L}} = \arg\min_{\boldsymbol{L}} h\left(\boldsymbol{L}\right) \text{ subject to } \operatorname{rank}\left(\boldsymbol{L}\right) \leq R, \tag{4.3.1}$$

where R is a chosen constant [48]. Program (4.3.1) is solved by iteratively updating

$$\boldsymbol{L}_{i+1} = \mathcal{H}_{\mathrm{l},R}\left(\boldsymbol{L}_i - \mu_i \nabla_{\boldsymbol{L}} h\left(\boldsymbol{L}_i\right)\right),$$

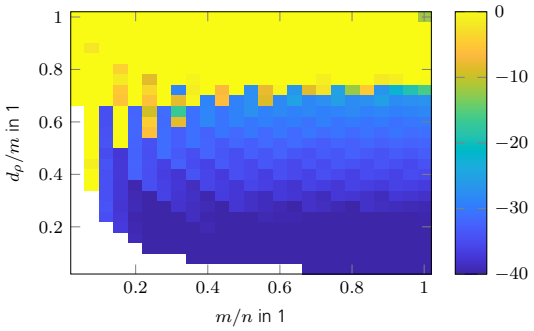

(a) Average squared reconstruction error (SRE) in dB for $R = \rho$.

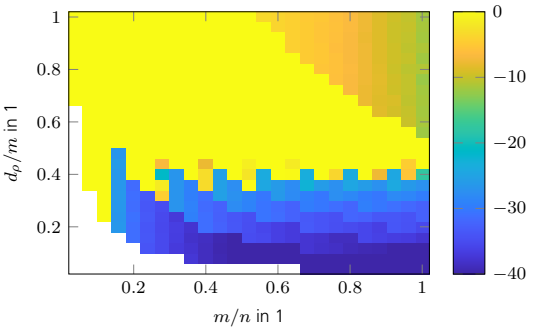

(b) Average SRE in dB for $R = 2\rho$.

Figure 4.3.1.: Phase transition of SVP algorithm for random sensing operators $\mathcal{A} \sim \mathcal{CN}(0, 1)$ and simulation parameters listed in Tab. 4.1.1.

where μ_i is some step size which can be updated in every iteration for faster convergence and better stability, and

$$\mathcal{H}_{\mathrm{l},R}(\boldsymbol{X}) = \sum_{i=1}^{R} \sigma_i \boldsymbol{u}_i \boldsymbol{v}_i^{\mathrm{H}} \tag{4.3.2}$$

is the nonlinear hard thresholding operator which sets all but the R largest singular values of $\boldsymbol{X}$ to zero. Further details can be found in [48, 49]. Putting all the above steps together, the final singular value thresholding (SVT) algorithm is listed in Algorithm 4.2. The threshold selections given in Algorithm 4.2 were evaluated numerically and prove to work well in every case. Phase

Algorithm 4.2 The SVP algorithm.

Input: $\mathcal{A}$, $\boldsymbol{y}$, R, I

Initialization:

$\epsilon \leftarrow \min\left(10^{-4}, 5 \cdot 10^{-3}\lambda\right)$

$i \leftarrow 0$, $d \leftarrow \infty$, $\boldsymbol{L}_0 \leftarrow \boldsymbol{0}$

Body:

while $d > \epsilon$ **and** $i < I$ **do**

$\mu_i \leftarrow$(17) in [49]

$\boldsymbol{L}_{i+1} \leftarrow \mathcal{H}_{\mathrm{l},R}\left(\boldsymbol{L}_i - \mu_i \nabla_{\boldsymbol{L}} h\left(\boldsymbol{L}_i\right)\right)$

$d \leftarrow \left\|\boldsymbol{L}_{i+1} - \boldsymbol{L}_i\right\|_{\mathrm{F}} / \left\|\boldsymbol{L}_i\right\|_{\mathrm{F}}$

$i \leftarrow i + 1$

end while

Output: $\widehat{\boldsymbol{L}} \leftarrow \boldsymbol{L}_i$

transition plots for random and discrete Fourier transform (DFT) sensing operators are shown in Fig. 4.3.1 and Fig. 4.3.2, where the parameter R was once set to the true rank of ρ of $\widetilde{\boldsymbol{L}}$ and once to twice the number 2ρ. As can be seen, the reconstruction success depends heavily on R, which is usually unknown in practice. Nevertheless, in case R is known, the SVP shows a higher reconstruction performance and convergence speed than the SVT algorithm.

Clearly, neither SVT nor SVP are optimal choices for practical problems. Therefore, improved versions are presented in Section 6.6 and 6.4 which show superior reconstruction performance and do not require parameters unknown in practice.

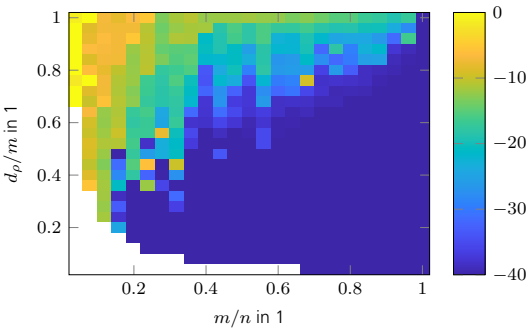

(a) Average SRE in dB for $R = \rho$.

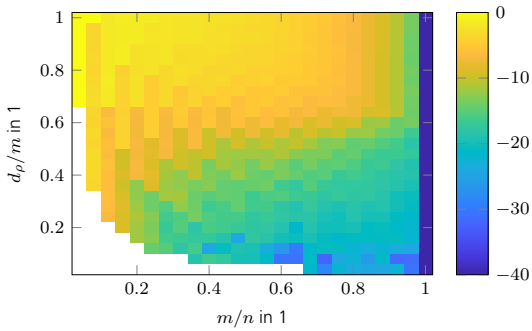

(b) Average SRE in dB for $R = 2\rho$.

Figure 4.3.2.: Phase transitions of SVP algorithm for random DFT sensing operators and simulation parameters listed in Tab. 4.1.1.

5. Fundamentals of Compressive Robust Principal Component Analysis

In this chapter the compressed robust principal component analysis (CRPCA) approach is discussed in brevity, however, no algorithms from the literature will be given. Those are usually a combination from pure compressive sensing (CS) and affine rank minimization (ARM) algorithms which would not serve our purpose here. The interested reader may refer to textbooks e. g. [50]. We therefore omit those and instead refer to the algorithm developed in this work termed turbo compressed robust principal component analysis (TCRPCA) presented in Section 6.6.

5.1. The Compressive Robust Principal Component Approach

The primary objective is to recover an unknown sparse matrix $\widetilde{\boldsymbol{S}} \in \mathbb{C}^{N_1 \times N_2}$ and low-rank matrix $\widetilde{\boldsymbol{L}} \in \mathbb{C}^{N_1 \times N_2}$, where $\left\|\widetilde{\boldsymbol{S}}\right\|_0 = \kappa \ll n = N_1 N_2$ and $\operatorname{rank}\left(\widetilde{\boldsymbol{L}}\right) = r \ll n_{\min} = \min\left(N_1, N_2\right)$, from a limited number of noisy observations of the form

$$\boldsymbol{y} = \mathcal{A}\left(\widetilde{\boldsymbol{S}} + \widetilde{\boldsymbol{L}}\right) + \boldsymbol{n}, \tag{5.1.1}$$

where $\mathcal{A} \in \mathbb{C}^{M \times N_1 \times N_2}$ $(M < n)$ is a known affine transformation, $\boldsymbol{y} \in \mathbb{C}^M$ is a measurement vector, and $\boldsymbol{n} \in \mathbb{C}^M$ is additive noise with i. i. .d coefficients of zero mean and variance P_{n}[1]. To find a solution to this under-determined linear system, we seek the closest sparse and low-rank solution which is consistent with the measurements via

$$\min_{\boldsymbol{S},\boldsymbol{L}} \lambda \left\|\boldsymbol{S}\right\|_0 + \operatorname{rank}\left(\boldsymbol{L}\right) \text{ subject to } h(\boldsymbol{S},\boldsymbol{L}) \leq \epsilon^2, \tag{5.1.2}$$

where

$$h(\boldsymbol{S},\boldsymbol{L}) = \left\|\mathcal{A}\left(\boldsymbol{S}+\boldsymbol{L}\right) - \boldsymbol{y}\right\|_2^2 \tag{5.1.3}$$

and $\epsilon^2 \geq \left\|\boldsymbol{n}\right\|_2^2$ is some constant error energy.

Like for compressive sensing (CS) and affine rank minimization (ARM) problems, the restricted isometry property (RIP) condition (3.1.4) and the restricted rank isometry property (RRIP) condition (4.1.4) need to be fulfilled to allow for successful reconstruction of (5.1.2). In the same way as for CS and ARM, the reconstruction problem (5.1.2) is of NP-hard nature and is thus commonly relaxed to

$$\min_{\boldsymbol{S},\boldsymbol{L}} \lambda \left\|\boldsymbol{S}\right\|_1 + \left\|\boldsymbol{L}\right\|_* \text{ subject to } h(\boldsymbol{S},\boldsymbol{L}) \leq \epsilon^2.$$

[1] The uncompressed case $\boldsymbol{y} = \widetilde{\boldsymbol{S}} + \widetilde{\boldsymbol{L}} + \boldsymbol{n}$ is commonly referred to as robust principal component analysis (RPCA)

However, additional requirements to guarantee a unique solution to (5.1.2) are necessary. Intuitively speaking, it is possible that $\widetilde{\boldsymbol{S}}$ is not only sparse but simultaneously low rank too. Imagine a matrix which consists of very few sparse entries or all sparse entries are clustered into one row or column, then this matrix is a low rank matrix as well. The same holds for $\widetilde{\boldsymbol{L}}$. This is known as the identifiability issue and is elaborated in more detail in the following section.

5.2. On the Rank-Sparsity Incoherence Condition

In this section, fundamental statements regarding the aforementioned identifiability issue in order to be able to distinguish between sparse and low rank matrices are recapitulated from [51]. The derivations contained in this paper provide bounds and conditions for a successful separation in the noiseless non compressed counterpart to (5.1.1) termed principal component pursuit (PCP)

$$(\widehat{\boldsymbol{S}}, \widehat{\boldsymbol{L}}) = \underset{\boldsymbol{S},\boldsymbol{L}}{\arg\min}\, \lambda \left\|\boldsymbol{S}\right\|_1 + \left\|\boldsymbol{L}\right\|_* \text{ subject to } \boldsymbol{S} + \boldsymbol{L} = \boldsymbol{C}. \tag{5.2.1}$$

While (5.2.1) refers to a noiseless signal model, the following remarks deliver helpful guidelines for a successful reconstruction also in the noisy case and thus provide valuable insight into the applicability of compressed robust principal component analysis (CRPCA) to the ground moving target indication (GMTI) problem. As such, recapitulating from [51], let

$$\mathcal{P}(\rho) = \left\{\boldsymbol{M} \in \mathbb{R}^{N_1 \times N_2} | \operatorname{rank}(\boldsymbol{M}) \leq \rho\right\}$$

denote the set of all rank restricted and

$$\mathcal{S}(\kappa) = \left\{\boldsymbol{M} \in \mathbb{R}^{N_1 \times N_2} | \left\|\boldsymbol{M}\right\|_0 \leq \kappa\right\}$$

the set of all sparse matrices. The tangent space $T(\boldsymbol{M})$ with respect to $\mathcal{P}(\operatorname{rank}(\boldsymbol{M}))$ at $\boldsymbol{M}$ is the span of all matrices with either the same row or column space as $\boldsymbol{M}$, hence is

$$T(\boldsymbol{M}) = \left\{\boldsymbol{U}\boldsymbol{X}^{\mathrm{T}} + \boldsymbol{Y}\boldsymbol{V}^{\mathrm{T}} | \boldsymbol{X} \in \mathbb{R}^{N_2 \times \rho}, \boldsymbol{Y} \in \mathbb{R}^{N_1 \times \rho}\right\},$$

where $\boldsymbol{M} = \boldsymbol{U}\boldsymbol{\Sigma}\boldsymbol{V}^{\mathrm{T}}$ denotes the singular value decomposition (SVD) of $\boldsymbol{M}$ with $\boldsymbol{U} \in \mathbb{R}^{N_1 \times \rho}$ and $\boldsymbol{V} \in \mathbb{R}^{N_2 \times \rho}$. Likewise, for any matrix $\boldsymbol{M}$ the tangent space with respect to $\mathcal{S}(\left\|\boldsymbol{M}\right\|_0)$ at $\boldsymbol{M}$ is

$$\Omega(\boldsymbol{M}) = \left\{\boldsymbol{N} \in \mathbb{R}^{N_1 \times N_2} | \operatorname{supp}(\boldsymbol{N}) \subseteq \operatorname{supp}(\boldsymbol{M})\right\}.$$

Since both $T(\boldsymbol{M})$ and $\Omega(\boldsymbol{M})$ are subspaces in $\mathbb{R}^{N_1 \times N_2}$, we can compare vectors in this space. Then it can be shown, that a necessary and sufficient condition for unique identifiability of $(\widetilde{\boldsymbol{S}}, \widetilde{\boldsymbol{L}})$ with respect to the tangent spaces $T(\widetilde{\boldsymbol{L}})$ and $\Omega(\widetilde{\boldsymbol{S}})$ is that they have a trivial intersection

$$T(\widetilde{\boldsymbol{L}}) \cap \Omega(\widetilde{\boldsymbol{S}}) = \{\boldsymbol{0}\}.$$

The tangent space transversality is equivalent to a "linearized" identifiability condition around $(\widetilde{\boldsymbol{S}}, \widetilde{\boldsymbol{L}})$ and is a sufficient condition for local identifiability around $(\widetilde{\boldsymbol{S}}, \widetilde{\boldsymbol{L}})$ but does not imply global

identifiability. The following proposition provides a simple condition for the tangent spaces to intersect transversally

Proposition 5.1. (Proposition 1 from [51]) *Given two matrices $\widetilde{\boldsymbol{S}}$ and $\widetilde{\boldsymbol{L}}$, we have that*

$$\nu(\widetilde{\boldsymbol{S}})\xi(\widetilde{\boldsymbol{L}}) < 1 \Rightarrow \Omega(\widetilde{\boldsymbol{S}}) \cap T(\widetilde{\boldsymbol{L}}) = \{\mathbf{0}\},$$

where

$$\nu(\boldsymbol{M}) \coloneqq \max_{\boldsymbol{N} \in \Omega(\boldsymbol{M}), \|\boldsymbol{N}\|_\infty \leq 1} \|\boldsymbol{N}\|_2 \tag{5.2.2}$$

$$\xi(\boldsymbol{M}) \coloneqq \max_{\boldsymbol{N} \in T(\boldsymbol{M}), \|\boldsymbol{N}\|_2 \leq 1} \|\boldsymbol{N}\|_\infty \tag{5.2.3}$$

The quantity $\nu(\boldsymbol{M})$ is small for a matrix whose spectrum of any element of the tangent space $\Omega(\boldsymbol{M})$ is diffuse, i. e. the singular values of those matrices are not too large. Likewise, the quantity $\xi(\boldsymbol{M})$ being small implies that elements of the tangent space $T(\boldsymbol{M})$ are diffuse or not too sparse. An important consequence of proposition 5.1 is the rank-sparsity principle given in the following theorem.

Theorem 5.1. (Theorem 1 from [51]) *For any matrix $\boldsymbol{M} \neq \mathbf{0}$, it is that*

$$\nu(\boldsymbol{M})\xi(\boldsymbol{M}) \geq 1$$

for $\nu(\boldsymbol{M})$ defined in (5.2.2) and $\xi(\boldsymbol{M})$ defined in (5.2.3).

This states that a matrix can not be at the same time sparse and posses a diffuse row and column space. The next theorem provides sufficient conditions for a successful separation by use of the PCP i. e. in the noiseless case using convex relaxation.

Theorem 5.2. (Theorem 2 from [51]) *Given $\boldsymbol{C} = \widetilde{\boldsymbol{S}} + \widetilde{\boldsymbol{L}}$ with*

$$\nu(\widetilde{\boldsymbol{S}})\xi(\widetilde{\boldsymbol{L}}) < \frac{1}{6},$$

the unique optimum of the PCP program (5.2.1) is $(\widetilde{\boldsymbol{S}}, \widetilde{\boldsymbol{L}})$ provided

$$\lambda \in \left(\frac{\xi(\widetilde{\boldsymbol{L}})}{1 - 4\nu(\widetilde{\boldsymbol{S}})\xi(\widetilde{\boldsymbol{L}})}, \frac{1 - 3\nu(\widetilde{\boldsymbol{S}})\xi(\widetilde{\boldsymbol{L}})}{\nu(\widetilde{\boldsymbol{S}})} \right).$$

This states that if the tangent spaces are sufficiently transverse then the PCP can successfully recover $(\widetilde{\boldsymbol{S}}, \widetilde{\boldsymbol{L}})$ without any knowledge of the tangent spaces. It shall be noted that the presented theorems give conditions for a diffuse sparse plus low rank separation i. e. a separation into a diffuse sparsity pattern (no row or column contains too many zeros) and a diffuse row and column space (row and column spaces are not aligned to any standard coordinate axis and hence do not contain sparse vectors). In fact, a general separation into sparse and low rank matrices is not unique since one can trade entries from sparse into the low rank part arbitrarily. However, a diffuse separation is unique provided the conditions stated above are fulfilled. The next propositions introduces practical bounds for the measures $\nu(\boldsymbol{M})$ and $\xi(\boldsymbol{M})$.

Proposition 5.2. (Proposition 3 from [51]) *Let $\boldsymbol{S} \in \mathbb{R}^{N_1 \times N_2}$ be any matrix with at least $\kappa_{\mathrm{s,min}}(\boldsymbol{S})$ and at most $\kappa_{\mathrm{s}}(\boldsymbol{S})$ entries per row and column, then with $\nu(\boldsymbol{S})$ as defined in (5.2.2) it holds that*

$$\kappa_{\mathrm{s,min}}(\boldsymbol{S}) \leq \nu(\boldsymbol{S}) \leq \kappa_{\mathrm{s}}(\boldsymbol{S}).$$

This proposition states that the measure $\nu(\boldsymbol{S})$ can be controlled by controlling the sparsity ratio $\kappa_{\mathrm{s}}(\boldsymbol{S})$ which not only limits $\|\boldsymbol{S}\|_0$ but also the support i. e. a clustering of sparse entries is not permissible. An equivalent proposition for the low rank case exists for which the incoherency measure

$$\mathrm{inc}(\boldsymbol{L}) = \max\left(\mathrm{inc}_{\mathrm{col}}(\boldsymbol{L}), \mathrm{inc}_{\mathrm{row}}(\boldsymbol{L})\right) \tag{5.2.4}$$

with

$$\begin{aligned}\mathrm{inc}_{\mathrm{col}}(\boldsymbol{L}) &= \max_i \|\mathcal{P}_{\boldsymbol{U}}\boldsymbol{e}_i\|_2 = \max_i \left\|\boldsymbol{U}^{\mathrm{H}}\boldsymbol{e}_i\right\|_2 \\ \mathrm{inc}_{\mathrm{row}}(\boldsymbol{L}) &= \max_i \|\mathcal{P}_{\boldsymbol{V}}\boldsymbol{e}_i\|_2 = \max_i \left\|\boldsymbol{V}^{\mathrm{H}}\boldsymbol{e}_i\right\|_2\end{aligned}$$

is used, where $\boldsymbol{L} = \boldsymbol{U}\boldsymbol{\Sigma}\boldsymbol{V}^{\mathrm{H}}$ is the SVD of $\boldsymbol{L}$, $\mathcal{P}_{\boldsymbol{U}} = \boldsymbol{U}\boldsymbol{U}^{\mathrm{H}}$ is a projection matrix onto the column space, and $\mathcal{P}_{\boldsymbol{V}} = \boldsymbol{V}\boldsymbol{V}^{\mathrm{H}}$ a projection matrix onto the row space of $\boldsymbol{L}$. It measures the incoherence or how well the subspace of $\boldsymbol{L}$ is aligned with the standard basis, where $\mathrm{inc}_{\mathrm{col}}(\boldsymbol{L})$ measures the incoherence with respect to the column space and likewise $\mathrm{inc}_{\mathrm{row}}(\boldsymbol{L})$ the incoherence regarding the row space of $\boldsymbol{L}$. These measures are bounded by

$$\begin{aligned}\sqrt{\frac{\rho}{N_1}} &\leq \mathrm{inc}_{\mathrm{col}}(\boldsymbol{L}) \leq 1 \\ \sqrt{\frac{\rho}{N_2}} &\leq \mathrm{inc}_{\mathrm{row}}(\boldsymbol{L}) \leq 1.\end{aligned}$$

The following proposition establishes a bound on the measure $\xi(\boldsymbol{M})$.

Proposition 5.3. (Proposition 4 from [51]) *Let $\boldsymbol{L} \in \mathbb{R}^{N_1 \times N_2}$ be any matrix, then with $\mathrm{inc}(\boldsymbol{L})$ defined as in (5.2.4) and $\xi(\boldsymbol{L})$ defined as in (5.2.3) it holds that*

$$\mathrm{inc}(\boldsymbol{L}) \leq \xi(\boldsymbol{L}) \leq 2\,\mathrm{inc}(\boldsymbol{L}).$$

This proposition states that the measure $\xi(\boldsymbol{L})$ can be controlled by handling the incoherence of $\boldsymbol{L}$ with respect to the standard basis. This can be done elegantly by use of a quiet common alternative incoherence measure called μ-incoherence

$$\begin{aligned}\mu(\boldsymbol{U}) &\coloneqq \frac{N_1}{\rho}\,\mathrm{inc}_{\mathrm{col}}(\boldsymbol{L})^2 \\ \mu(\boldsymbol{V}) &\coloneqq \frac{N_2}{\rho}\,\mathrm{inc}_{\mathrm{row}}(\boldsymbol{L})^2\end{aligned}$$

with the bounds

$$\begin{aligned}1 \leq \mu(\boldsymbol{U}) &\leq \frac{N_1}{\rho} \\ 1 \leq \mu(\boldsymbol{V}) &\leq \frac{N_2}{\rho},\end{aligned} \tag{5.2.5}$$

where again the bigger measure is used

$$\mu \coloneqq \max(\mu\left(\boldsymbol{U}\right), \mu\left(\boldsymbol{V}\right)). \tag{5.2.6}$$

By use of the Cauchy-Schwarz inequality it follows from (5.2.5) that the maximum entry in magnitude of the dyadic $\boldsymbol{U}\boldsymbol{V}^{\mathrm{H}}$ for a given upper μ-incoherence is [52]

$$\left\|\boldsymbol{U}\boldsymbol{V}^{\mathrm{H}}\right\|_{\infty} \leq \frac{\mu\rho}{\sqrt{N_1 N_2}}. \tag{5.2.7}$$

The incoherence conditions (5.2.5), (5.2.6), and (5.2.7) assert that for small μ the singular vectors are incoherent with the standard basis i. e. are reasonably spread out or in other words not sparse. In addition they ensure that the singular vectors are not too spiky. A final theorem reformulates Theorem 5.2 in terms of incoherence and sparsity measures.

Theorem 5.3. (Corollary 3 from [51]) *Let $\boldsymbol{M} = \widetilde{\boldsymbol{S}} + \widetilde{\boldsymbol{L}}$ with $\kappa_{\mathrm{s}}(\widetilde{\boldsymbol{S}})$ being the maximum number of nonzero entries per row and column and $\mathrm{inc}(\widetilde{\boldsymbol{L}})$ being the maximum incoherence of the row and column space of $\widetilde{\boldsymbol{L}}$ as defined in (5.2.4). Then it holds that if*

$$\kappa_{\mathrm{s}}(\widetilde{\boldsymbol{S}})\,\mathrm{inc}(\widetilde{\boldsymbol{L}}) < \frac{1}{12},$$

the solution of the PCP program (5.2.1) is $(\widetilde{\boldsymbol{S}}, \widetilde{\boldsymbol{L}})$ provided

$$\lambda \in \left(\frac{2\,\mathrm{inc}(\widetilde{\boldsymbol{L}})}{1 - 8\kappa_{\mathrm{s}}(\widetilde{\boldsymbol{S}})\,\mathrm{inc}(\widetilde{\boldsymbol{L}})}, \frac{1 - 6\nu(\kappa_{\mathrm{s}}(\widetilde{\boldsymbol{S}}))\,\mathrm{inc}(\widetilde{\boldsymbol{L}})}{\kappa_{\mathrm{s}}(\widetilde{\boldsymbol{S}})}\right).$$

The derivations so far follow [51], however, [52] gives alternative bounds e. g. the PCP succeeds in any case given

$$\lambda = \frac{1}{\sqrt{\max\left(N_1, N_2\right)}}.$$

Also bounds allowing for a higher reconstruction success compared to those given in Theorem 5.3 are presented, where the major difference is the assumption that the support of $\widetilde{\boldsymbol{S}}$ is uniformly random distributed. While the concrete reconstruction success bounds do not handle the noisy case (and most often depend on the concrete reconstruction algorithm applied), theorem 5.3 states that a control of the sparsity ratio $\kappa_{\mathrm{s}}(\widetilde{\boldsymbol{S}})$ and the incoherence $\mathrm{inc}(\widetilde{\boldsymbol{L}})$ help in finding a unique diffuse decomposition. As such, the following operators are introduced which handle identification issues by restricting $\boldsymbol{S}$ and $\boldsymbol{L}$ to be of identifiable form. The sparsity ratio thresholding operator $\mathcal{Q}_{\kappa_{\mathrm{s}}} : \mathbb{C}^{N_1 \times N_2} \to \mathbb{C}^{N_1 \times N_2}$, which prevents clustering of sparse entries, is defined element-wise as

$$\left[\mathcal{Q}_{\kappa_{\mathrm{s}}}\left(\boldsymbol{S}\right)\right]_{ij} = \begin{cases} s_{ij}, & \text{if } |s_{ij}| \geq \boldsymbol{S}_{i:}^{[\lfloor \kappa_{\mathrm{s}} N_2 \rfloor]} \text{ and } |s_{ij}| \geq \boldsymbol{S}_{:j}^{[\lfloor \kappa_{\mathrm{s}} N_1 \rfloor]} \\ 0, & \text{else} \end{cases}, \tag{5.2.8}$$

where $\kappa_{\mathrm{s}} \in (0, 1)$, s_{ij} denotes the (i, j)-th entry of $\boldsymbol{S}$, $\boldsymbol{S}_{i:}$ the i-th row, $\boldsymbol{S}_{:j}$ the j-th column of $\boldsymbol{S}$ in Matlab notation, and $\boldsymbol{x}^{[a]}$ the a-th biggest entry in magnitude in $\boldsymbol{x}$. The infinity norm thresholding operator $\mathcal{P}_{\varphi} : \mathbb{C}^{N_1 \times N_2} \to \mathbb{C}^{N_1 \times N_2}$, which prevents spikiness in the low rank reconstruction, is

defined element-wise as

$$\left[\mathcal{P}_{\varphi}\left(\boldsymbol{L}\right)\right]_{ij} = \begin{cases} \varphi \exp\left(\mathrm{j}\arg\left(l_{ij}\right)\right), & \text{if } |l_{ij}| \geq \varphi \\ l_{ij}, & \text{else} \end{cases}. \tag{5.2.9}$$

The required parameter φ can be determined from (5.2.7) by

$$\varphi = \frac{\mu\rho c_{\varphi}\left\|\widetilde{\boldsymbol{L}}\right\|_2}{\sqrt{N_1 N_2}}, \tag{5.2.10}$$

where c_{φ} is a parameter set manually usually < 1 [53]. Unfortunately, most parameters in (5.2.10) are unknown since it requires knowledge of the true low rank matrix $\widetilde{\boldsymbol{L}}$. As a rough estimate we may use $\left\|\widetilde{\boldsymbol{L}}\right\|_2 \approx \left\|\mathcal{A}^{\mathrm{H}}\left(\boldsymbol{y}\right)\right\|_2$, $\mu = 1$, and $\rho \approx \min\left(N_1, N_2\right)/2$. Certainly, this estimate is not justified to be anywhere close to an optimal value but it was found from simulations that it is sufficient to apply (5.2.9) for a limited number of iterations e. g. the first 10 iterations. This is enough to bias the intermediate solution $\boldsymbol{L}_i$ to not contain spiky entries.

To the contrary of the pure compressive sensing (CS) and affine rank minimization (ARM) counterparts, no CRPCA algorithms from the literature are presented here since those usually are a simple composition of CS and ARM algorithms. As such, only the algorithm developed in this work termed turbo compressed robust principal component analysis (TCRPCA) is presented which can be found in Section 6.6.

6. Boosting Performance of CS, ARM, and CRPCA Algorithms

Within this chapter, a complete set of algorithms to solve compressive sensing (CS), affine rank minimization (ARM), and compressed robust principal component analysis (CRPCA) problems is presented. These algorithms were designed such that no parameters, unknown in practice, are required and for unavoidable parameters equations are given to determine those. The only parameter required to know is the noise power P_{n}. Furthermore, these algorithms offer very high convergence rate next to low computational complexity due to the use of closed solutions of subsequent optimization problems. The algorithms offer state-of-the-art reconstruction performance, as will be shown by use of phase transition plots. Finally, the algorithms are designed to be capable of complex numbers and are evaluated not only for random sensing operators but also for discrete Fourier transform (DFT) operators, rendering them suitable for radar applications. They are called

- Turbo shrinkage-thresholding (TST)
- Complex successive concave sparsity approximation (CSCSA)
- Turbo singular value thresholding (TSVT)
- Complex smoothed rank approximation (CSRA)
- Turbo compressed robust principal component analysis (TCRPCA)

where TST and CSCSA solve CS problems, TSVT and CSRA solve ARM problems and TCRPCA allows for solving the combined CS and ARM problem.

6.1. Turbo Shrinkage-Thresholding

The turbo shrinkage-thresholding (TST) algorithm is inspired by the turbo algorithms presented in [54, 55, 56], which describe general reconstruction algorithms for compressive sensing (CS) and affine rank minimization (ARM) problems applying the message passing principle. This principle allows for a drastic improvement in convergence speed for right-orthogonally invariant linear (ROIL) sensing operators to which random and discrete Fourier transform (DFT) sensing operators belong[1]. To the best of our knowledge, [54, 55, 56] presented their algorithms for generic and in particular hard thresholding (HT) operators but do not elaborate on soft thresholding (ST)

[1] Consider a linear operator $\mathcal{A}$ with matrix form $\boldsymbol{A}$, the singular value decomposition (SVD) of $\boldsymbol{A}$ is $\boldsymbol{A} = \boldsymbol{U}_A \boldsymbol{\Sigma}_A \boldsymbol{V}_A^{\mathrm{H}}$. If $\boldsymbol{V}_A$ is a Haar distributed random matrix independent of $\boldsymbol{\Sigma}_A$, we say that $\mathcal{A}$ is a right-orthogonally invariant linear (ROIL) operator [57].

operators which are of major interest in our work. The contribution of this work is to fill in required formulas for the complex case, add a final purification step to achieve a pure sparse solution and elaborate on the ST denoiser hence the name TST algorithm.

Like fast iterative shrinkage-thresholding algorithm (FISTA), the TST algorithm tries to find a solution to (3.1.2) by solving the relaxed regularized convex optimization problem

$$\widehat{\boldsymbol{s}} = \arg\min_{\boldsymbol{s}} \lambda \|\boldsymbol{s}\|_1 + h(\boldsymbol{s}), \tag{6.1.1}$$

which is solved by TST by the iterative procedure

$$\begin{aligned} \boldsymbol{r}_i &= \boldsymbol{s}_{i-1} - \mu \nabla_{\boldsymbol{s}} h(\boldsymbol{s}_{i-1}) \\ \boldsymbol{z}_i &= \mathcal{S}_{s,\mu\lambda}(\boldsymbol{r}_i) \\ \boldsymbol{s}_i &= c_i(\boldsymbol{z}_i - \alpha_i \boldsymbol{r}_i), \end{aligned}$$

where μ is some step size, i is the iteration index, and $\mathcal{S}_{\mathrm{s},a}$ is the soft thresholding operator given by (3.2.4). The required parameters $\{\mu, \alpha_i, c_i\}$ are chosen according to the turbo principle such that

$$(\boldsymbol{r}_i - \widetilde{\boldsymbol{s}})^{\mathrm{H}} (\boldsymbol{s}_{i-1} - \widetilde{\boldsymbol{s}}) = 0, \tag{6.1.2}$$

$$(\boldsymbol{r}_i - \widetilde{\boldsymbol{s}})^{\mathrm{H}} (\boldsymbol{s}_i - \widetilde{\boldsymbol{s}}) = 0, \tag{6.1.3}$$

and further that for a given $\boldsymbol{s}_{i-1}$, $\|\boldsymbol{s}_i - \widetilde{\boldsymbol{s}}\|_2^2$ is minimized under (6.1.2) and (6.1.3) [57]. In the above, (6.1.2) ensures that the input and output error of the gradient update step are uncorrelated. Equally, (6.1.3) ensures a decorrelation of the input and output error of the denoising step. This strategy allows for an improved convergence rate compared to classical gradient approaches. In order to fulfill (6.1.2) and (6.1.3), the true solution $\widetilde{\boldsymbol{s}}$ is required to determine exact values for $\{\mu, \alpha_i, c_i\}$. Since $\widetilde{\boldsymbol{s}}$ is unknown, approximate formulations for $\{\mu, \alpha_i, c_i\}$ were derived in [57] for the real valued case. In the general complex case these parameters are

$$\mu = \frac{n}{M \|\boldsymbol{A}\|_2^2} \tag{6.1.4}$$

$$\alpha_i = \begin{cases} \frac{1}{n}\mathrm{div}(\mathcal{S}_{s,\mu\lambda}(\boldsymbol{r}_i)) & \text{if } \boldsymbol{s} \in \mathbb{R}^n \\ \frac{1}{2n}\mathrm{div}(\mathcal{S}_{s,\mu\lambda}(\boldsymbol{r}_i)) & \text{if } \boldsymbol{s} \in \mathbb{C}^n \end{cases} \tag{6.1.5}$$

$$c_i = \frac{(\boldsymbol{z}_i - \alpha_i \boldsymbol{r}_i)^{\mathrm{H}} \boldsymbol{r}_i}{\|\boldsymbol{z}_i - \alpha_i \boldsymbol{r}_i\|_2^2}, \tag{6.1.6}$$

where $\mathrm{div}(\cdot)$ is the divergence operator. Luckily, the divergence can be derived in closed form as

$$\mathrm{div}(\mathcal{S}_{\boldsymbol{S},a}(\boldsymbol{r})) = \sum_{i=1}^{n} \left(2 - \frac{a}{|r_i|}\right) \mathbb{I}(|r_i| > a), \tag{6.1.7}$$

where $\mathbb{I}(\cdot)$ denotes the indicator function. A derivation of (6.1.7) can be found in the Appendix A.3. The next question of course is how to choose λ and thus which shrinkage a should be applied. Too much shrinkage results in a large bias while too little results in a slow conver-

gence rate. As such, an optimal constant λ does not exists, rather λ would need to be adjusted in every iteration. Unfortunately, to the best of the authors knowledge, a closed form solution to determine such an optimal λ is not known to exists. A reasonable choice for the parameter λ is a scaled version of the formula of [40]

$$\lambda = \frac{1}{4} c_r \sqrt{P_{\mathrm{n}}} \Phi^{-1} \left(1 - \frac{\alpha_r}{2n}\right), \tag{6.1.8}$$

which was found from simulations to perform well. The parameter $c_r > 1$ in (6.1.8) is some constant, Φ is the cumulative density function (CDF) of $\mathcal{N}(0,1)$, and $\alpha_r \in [0,1]$ is some parameter. For further details have a look into [41]. The resulting inevitable bias of a constant λ is circumvented by a final purification step, which is conducted using the HT operator $\mathcal{H}_{\mathrm{s},K}(\boldsymbol{x})$ given by (3.3.2). This purification step is an adjustment introduced in TST and not present in the algorithms presented in [54, 55, 56]. It is motivated by the aforementioned bias of the soft thresholding operator $\mathcal{S}_{\boldsymbol{S},\mu\lambda}(\cdot)$ for constant selected λ. As an estimate for K, we conveniently use $\|\boldsymbol{z}_i\|_0$. This final purification step allows for a clean sparse solution. For further details, e. g. proof of convergence, the interested reader may refer to the proofs given in [54, 55, 56] which also hold for the TST version presented here.

Putting all the above steps together, the final TST algorithm is listed in Algorithm 6.1. The threshold selections given in Algorithm 6.1 were evaluated numerically and prove to work well in every case.

Algorithm 6.1 The TST algorithm.

Input: $\boldsymbol{A}$, $\boldsymbol{y}$, λ, I

Initialization:

$\epsilon \leftarrow \min\left(10^{-4}, 5 \cdot 10^{-3}\lambda\right)$

$i \leftarrow 0$, $d \leftarrow \infty$, $\boldsymbol{s}_0 \leftarrow \boldsymbol{0}$, $\mu \leftarrow n/(M\|\boldsymbol{A}\|_2^2)$

Body:

while $d > \epsilon$ **and** $i < I$ **do**

$i \leftarrow i + 1$

$\boldsymbol{r}_i \leftarrow \boldsymbol{s}_{i-1} - \mu \nabla_{\boldsymbol{s}} h(\boldsymbol{s}_{i-1})$

$\boldsymbol{z}_i \leftarrow \mathcal{S}_{s,\mu\lambda}(\boldsymbol{r}_i)$

$\alpha_i \leftarrow \begin{cases} \frac{1}{n}\mathrm{div}\left(\mathcal{S}_{s,\mu\lambda}(\boldsymbol{r}_i)\right) & \text{if } \boldsymbol{s} \in \mathbb{R}^n \\ \frac{1}{2n}\mathrm{div}\left(\mathcal{S}_{s,\mu\lambda}(\boldsymbol{r}_i)\right) & \text{if } \boldsymbol{s} \in \mathbb{C}^n \end{cases}$

$c_i \leftarrow (\boldsymbol{z}_i - \alpha_i \boldsymbol{r}_i)^{\mathrm{H}} \boldsymbol{r}_i / \|\boldsymbol{z}_i - \alpha_i \boldsymbol{r}_i\|_2^2$

$\boldsymbol{s}_i \leftarrow c_i (\boldsymbol{z}_i - \alpha_i \boldsymbol{r}_i)$

$d \leftarrow \|\boldsymbol{s}_i - \boldsymbol{s}_{i-1}\|_2 / \|\boldsymbol{s}_{i-1}\|_2$

end while

$K \leftarrow \|\boldsymbol{z}_i\|_0$

Output: $\widehat{\boldsymbol{s}} \leftarrow \mathcal{H}_{\mathrm{s},K}(\boldsymbol{r}_i)$

In the following, simulation results are shown to illustrate the performance of TST. Phase transition diagrams for random and DFT sensing operators are shown in Fig. 6.1.1. The illustrated reconstruction performance is close but not as high as for e. g. spectral projected gradient for ℓ_1 (SPGL1) shown in Fig. 6.1.2 but higher as for FISTA shown in Fig. 3.2.1a. Compared to FISTA and normalized iterative hard thresholding (NIHT), TST shows an overall better performance. The advantage of TST over FISTA is evident in Fig. 6.1.3 as TST shows a higher convergence rate and

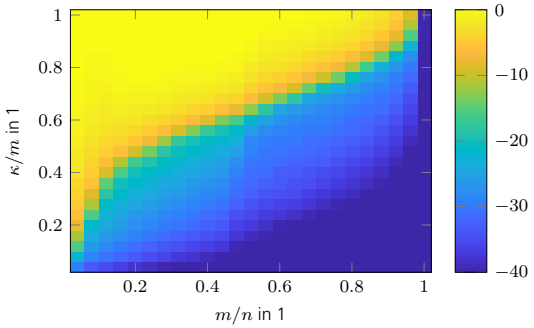

(a) Result of TST for random sensing operator $\boldsymbol{A} \sim \mathcal{CN}(0,1)$.

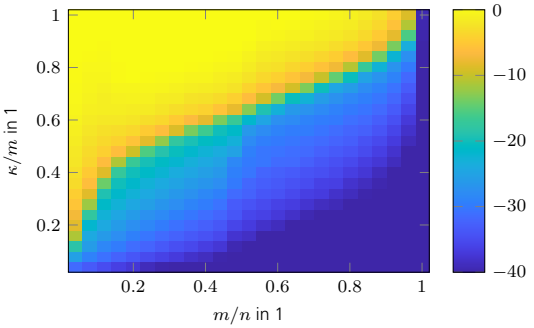

(b) Result of TST for random row DFT sensing operator.

Figure 6.1.1.: Phase transition of TST algorithm in SRE in dB.

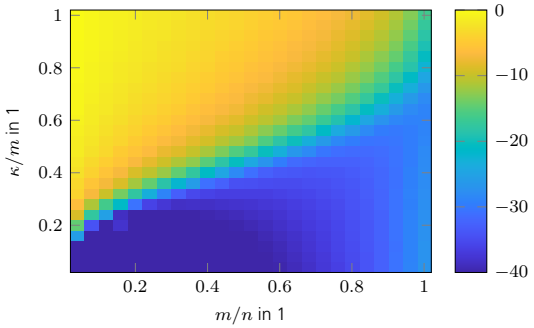

(a) Result of SPGL1 for random sensing operator $\boldsymbol{A} \sim \mathcal{CN}(0,1)$.

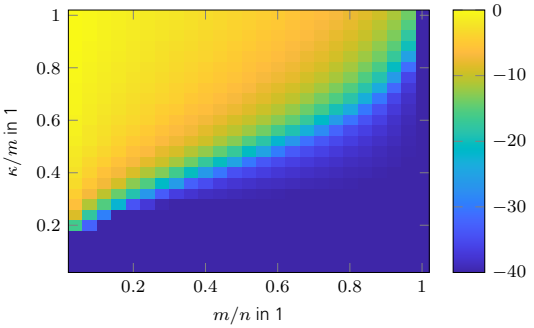

(b) Result of SPGL1 for random row DFT sensing operator.

Figure 6.1.2.: Phase transition of SPGL1 algorithm in SRE in dB.

also achieves a lower reconstruction error. A throughout comparison of TST with remaining CS algorithms in terms of convergence speed was not conducted. Nevertheless, TST is very easy to implement (to the contrary of SPGL1), shows a state-of-the-art convergence rate, has low computational complexity as there are closed form solutions available for all required parameters, and finally it does not require any unknown parameters in general. Hence, it is well suited for practical applications.

6.2. Complex Successive Concave Sparsity Approximation

Despite the convexity of the basis pursuit denoise (BPDN) approach presented in Chapter 3, there is a large gap between the sufficient conditions for the robust recovery of sparse vectors using

$$\min_{\boldsymbol{s}} \|\boldsymbol{s}\|_0 \ \text{subject to}\ h(\boldsymbol{s}) \leq \epsilon^2$$

compared to

$$\min_{\boldsymbol{s}} \|\boldsymbol{s}\|_1 \ \text{subject to}\ h(\boldsymbol{s}) \leq \epsilon^2.$$

In order to narrow this gap, while making the recovery tractable, we may approximate the ℓ_0 norm by a smooth function. The complex successive concave sparsity approximation (CSCSA) al-

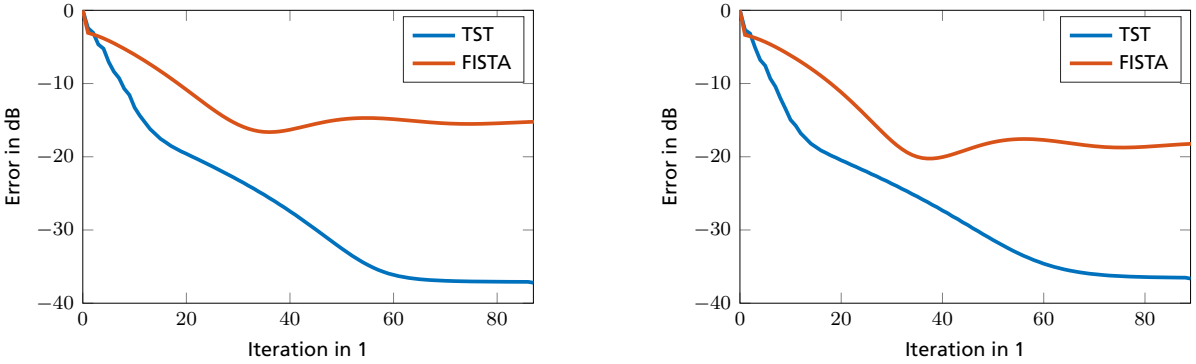

(a) Random sensing operators $\boldsymbol{A} \sim \mathcal{CN}(0, 1)$.

(b) DFT sensing operators with random rows.

Figure 6.1.3.: Comparison of convergence speed of TST and FISTA.

gorithm does so by enforcing a stricter sparsity measure compared to the ℓ_1 norm. The CSCSA is our extension, applicable to complex valued problems, of the successive concave sparsity approximation (SCSA) algorithm from [58], which only works for real valued problems. In this section the idea of CSCSA is presented in brevity, a throughout derivation and more simulation results can be found in the Appendix A.4.

The idea is to substitute the ℓ_0 norm of $\boldsymbol{s} = \begin{bmatrix} s_1 & \cdots & s_n \end{bmatrix}^{\mathrm{T}}$ by a more tractable approximation. In general, the ℓ_0 norm is defined as the number of non zero elements in $\boldsymbol{s}$. Let

$$\delta(x) = \begin{cases} 1 & \text{if } x = 0 \\ 0 & \text{else} \end{cases} \tag{6.2.1}$$

be the Kronecker delta function, then we can define the ℓ_0 norm of $\boldsymbol{s}$ as

$$\|\boldsymbol{s}\|_0 = \sum_{i=1}^{n} \left[1 - \delta\left(|s_i|\right)\right], \tag{6.2.2}$$

where $|s_i|$ denotes the magnitude of s_i. To make (6.2.2) smooth we may approximate it by

$$1 - \delta(|s|) \approx f_\gamma\left(|s|\right) = 1 - \exp\left(-\frac{|s|}{\gamma}\right), \tag{6.2.3}$$

where γ determines how accurately the Kronecker function is approximated. An illustration of this approximation and other common approximations to the ℓ_0 norm are shown in Fig. 6.2.1. As shown in [58], the series $\{f_\gamma\left(|s|\right)\}$ converges point wise to $1 - \delta\left(|s|\right)$ as

$$\lim_{\gamma \to 0^+} f_\gamma\left(|s|\right) = \begin{cases} 0 & \text{if } |s| = 0 \\ 1 & \text{else.} \end{cases}$$

Thus we can define

$$\|\boldsymbol{s}\|_0 \approx \sum_{i=1}^{n} f_\gamma\left(|s_i|\right) = F_\gamma\left(|\boldsymbol{s}|\right), \tag{6.2.4}$$

where $|\boldsymbol{s}|$ denotes a vector which holds the magnitudes of the elements of $\boldsymbol{s}$. The optimization

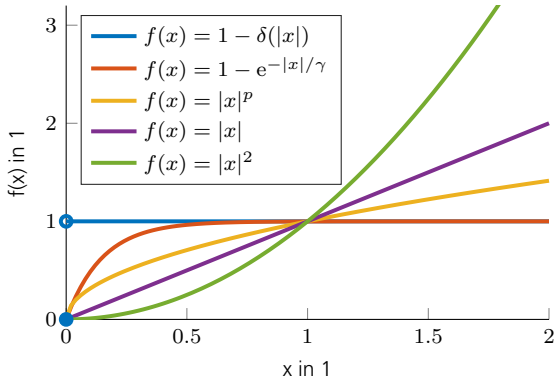

Figure 6.2.1.: Common approximations to the ℓ_0 norm.

problem (3.1.2) may now be relaxed to

$$\min_{\boldsymbol{s}} F_\gamma\left(|\boldsymbol{s}|\right) \text{ subject to } h\left(\boldsymbol{s}\right) \leq \epsilon^2, \tag{6.2.5}$$

where the residual term $h\left(\boldsymbol{s}\right)$ was defined in (3.1.3) and $\epsilon^2 \geq \|\boldsymbol{n}\|_2^2$ is some constant noise energy. The constrained optimization problem (6.2.5), for a fixed γ, can be converted to an unconstrained optimization problem by use of regularization as

$$\widehat{\boldsymbol{s}} = \arg\min_{\boldsymbol{s}} \lambda_\gamma F_\gamma\left(|\boldsymbol{s}|\right) + h\left(\boldsymbol{s}\right). \tag{6.2.6}$$

At this point it shall be noted, that the program (6.2.6) is not convex any more, rather it is a sum of a concave and a convex function. As such (6.2.6) does not posses a unique minimum and it is possible to get stuck in local minima. To circumvent this problem, the graduated non-convexity (GNC) approach is used. The idea of GNC is to start the program (6.2.6) with a solution $\widehat{\boldsymbol{s}}_0$ which is somewhat close to the true solution $\widetilde{\boldsymbol{s}}$ obtained from a convex algorithm e. g. fast iterative shrinkage-thresholding algorithm (FISTA) or turbo shrinkage-thresholding (TST). Then, (6.2.6) is minimized for a γ large enough such that the solution $\widehat{\boldsymbol{s}}$ is closer to $\widetilde{\boldsymbol{s}}$ yet not get stuck in a wrong local minima. Subsequently, γ is reduced by a constant factor $\gamma \leftarrow c\gamma$ to further approximate the ℓ_0 norm and (6.2.6) is minimized using the solution from the previous iteration. The procedure is conducted until a stop criteria is met. The optimization problem can be solved by use of the iterative thresholding (IT) approach by iteratively conducting

$$\boldsymbol{s}_{i+1} = \mathcal{T}^{(\gamma)}_{\mu\lambda_\gamma}\left(\boldsymbol{s}_i - \mu\nabla_{\boldsymbol{s}} h\left(\boldsymbol{s}_i\right)\right), \tag{6.2.7}$$

where μ is some step size and $\mathcal{T}^{(\gamma)}_{\mu\lambda_\gamma}$ is again a thresholding operator given in the Appendix by (A.4.40). It shall be noted that $\mathcal{T}^{(\gamma)}_{\mu\lambda_\gamma}$ is a closed form solution of a subsequent minimization problem emerging from the IT approach. This closed form is possible only through the special choice of the ℓ_0 norm approximation (6.2.3). For different choices, the subsequent minimization problem would require an additional minimization loop increasing the computational complexity. The regularization parameters is set to $\lambda_\gamma = \gamma\lambda$, where for λ (3.2.5) is used. More details regarding the CSCSA algorithm and how γ shall be chosen are given in the Appendix A.4. The CSCSA algorithm was published in the paper *Complex Successive Concave Sparsity Approximation* at the

IRS2020 conference [59].

It is well known, that IT techniques have a low computational complexity, however, they suffer from low convergence rates on the order of $\mathcal{O}\left(1/i\right)$. To accelerate (6.2.7), a FISTA like technique is used which does not increase the computational complexity but boosts the convergence rate up to $\mathcal{O}\left(1/i^2\right)$ [41]. Putting all the above steps together, the final CSCSA algorithm is listed in Algorithm 6.2. It consists of two loops, an inner and an outer one. In the outer loop γ is decreased gradually according to the GNC technique. The inner loop solves (6.2.6) by using a FISTA like technique. The loops are aborted after a maximum number of iterations J and P or if the solutions change, measured by the relative distance between consecutive solutions, drops below certain thresholds ϵ_{o} and ϵ_{i}. The threshold selections given in Algorithm 6.2 are taken from [58] and prove to work well in every case. Simulation results of a CSCSA update onto FISTA,

Algorithm 6.2 The CSCSA algorithm.

Input: $\boldsymbol{A}$, $\boldsymbol{y}$, λ, I, J

Initialization:

$c \leftarrow (0, 0.5)$, $\mu \leftarrow 0.99/\left\|\boldsymbol{A}\right\|_2^2$
$\epsilon_{\mathrm{o}} \leftarrow \min\left(10^{-4}, 5 \cdot 10^{-3}\lambda\right)$
$\epsilon_{\mathrm{i}} \leftarrow \min\left(10^{-3}, 5 \cdot 10^{-3}\lambda\right)$
$\widehat{\boldsymbol{s}} \leftarrow \mathrm{TST}\left(\boldsymbol{A}, \boldsymbol{y}, \lambda, \epsilon_{\mathrm{i}}, J\right)$
$\gamma \leftarrow \max\left(|\widehat{\boldsymbol{s}}|\right)$

Body:

$i \leftarrow 0$, $d_{\mathrm{o}} \leftarrow \infty$
while $d_{\mathrm{o}} > \epsilon_{\mathrm{o}}$ **and** $i < I$ **do**
  $i \leftarrow i + 1$, $j \leftarrow 0$, $d_{\mathrm{i}} \leftarrow \infty$
  $t_1 \leftarrow 1$, $\boldsymbol{z}_1 \leftarrow \widehat{\boldsymbol{s}}$, $\boldsymbol{s}_0 \leftarrow \widehat{\boldsymbol{s}}$
  while $d_{\mathrm{i}} > \epsilon_{\mathrm{i}}$ **and** $j < J$ **do**
    $j \leftarrow j + 1$
    $\boldsymbol{s}_j \leftarrow \mathcal{T}_{\mu\lambda_\gamma}^{(\gamma)}\left(\boldsymbol{z}_j - \mu\boldsymbol{A}^{\mathrm{H}}\left(\boldsymbol{A}\boldsymbol{z}_j - \boldsymbol{y}\right)\right)$
    $t_{j+1} \leftarrow \left(1 + \sqrt{1 + 4t_j^2}\right)/2$
    $\boldsymbol{z}_{j+1} \leftarrow \boldsymbol{s}_j + \left(t_j - 1\right)\left(\boldsymbol{s}_j - \boldsymbol{s}_{j-1}\right)/t_{j+1}$
    $d_{\mathrm{i}} \leftarrow \left\|\boldsymbol{s}_j - \boldsymbol{s}_{j-1}\right\|_2 / \left\|\boldsymbol{s}_{j-1}\right\|_2$
  end while
  $d_{\mathrm{o}} \leftarrow \left\|\boldsymbol{s}_j - \widehat{\boldsymbol{s}}\right\|_2 / \left\|\widehat{\boldsymbol{s}}\right\|_2$
  $\widehat{\boldsymbol{s}} \leftarrow \boldsymbol{s}_j$
  $\gamma \leftarrow c\gamma$
end while

Output: $\widehat{\boldsymbol{s}}$

spectral projected gradient for ℓ_1 (SPGL1), and TST for random and discrete Fourier transform (DFT) sensing operators are shown in Fig. 6.2.2, Fig. 6.2.3, and Fig. 6.2.4. As can be seen CSCSA significantly improves upon the results of the aforementioned algorithms. Also, CSCSA does not depend on any unknown additional parameters and shows very low computational complexity due to available closed form solutions of subsequent minimization problems. In case κ is assumed wrong, the reconstruction performance of normalized iterative hard thresholding (NIHT) drops significantly as given in the comparison plot in Fig. 6.2.5. The curves in Fig. 6.2.5 indicate the $50\,\%$ success rate with respect to the Monte Carlo runs. Success is defined twofold

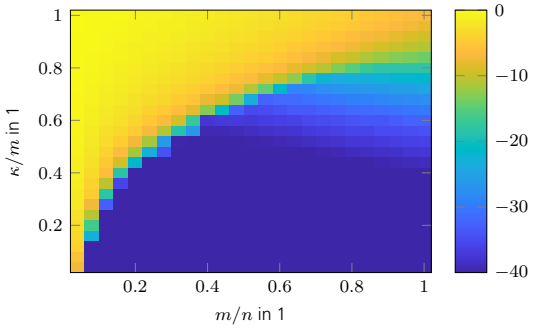

(a) Result for random sensing operator $\boldsymbol{A} \sim \mathcal{CN}(0,1)$.

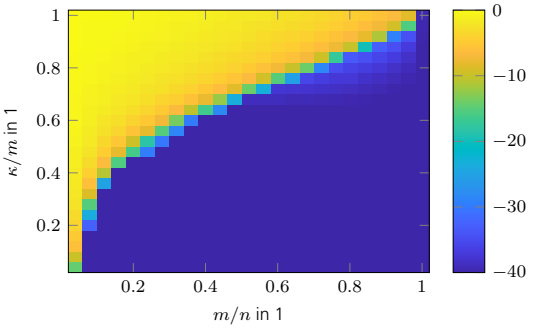

(b) Result for random row DFT sensing operator.

Figure 6.2.2.: Phase transition of FISTA + CSCSA in SRE in dB.

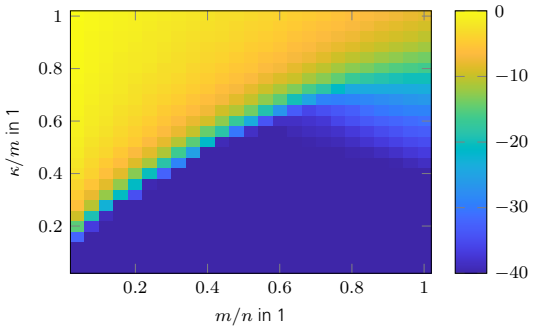

(a) Result for random sensing operator $\boldsymbol{A} \sim \mathcal{CN}(0,1)$.

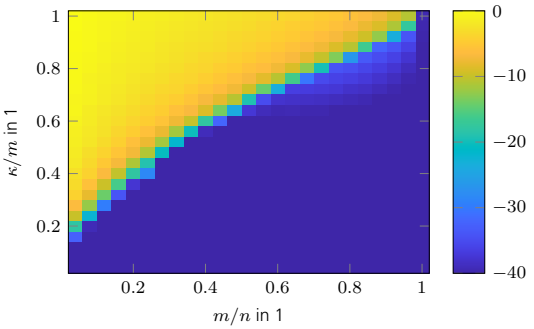

(b) Result for random row DFT sensing operator.

Figure 6.2.3.: Phase transition of SPGL1 + CSCSA in SRE in dB.

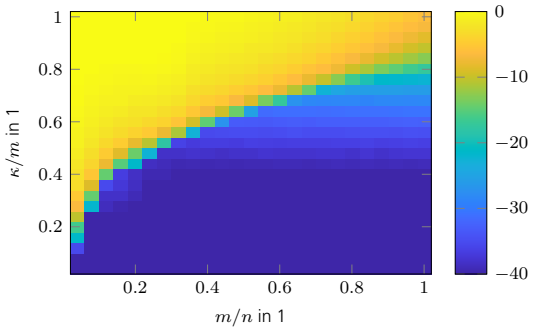

(a) Result for random sensing operator $\boldsymbol{A} \sim \mathcal{CN}(0,1)$.

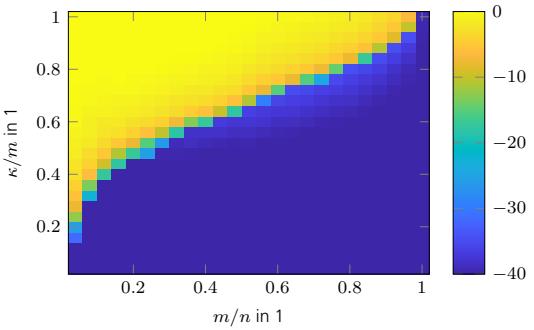

(b) Result for random row DFT sensing operator.

Figure 6.2.4.: Phase transition of TST + CSCSA in SRE in dB.

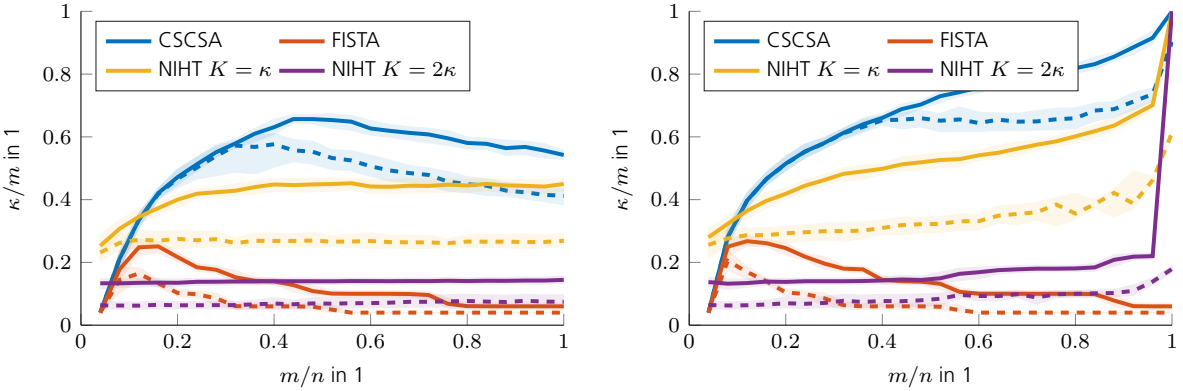

(a) $\boldsymbol{A} \sim \mathcal{CN}(0, 1)$ (b) Random row DFT sensing operator.

Figure 6.2.5.: Comparison of phase transitions.

as either $\mathrm{SRE} \leq -\mathrm{SNR}$ for a strict success definition and $\mathrm{SRE} \leq -(\mathrm{SNR} - 5\,\mathrm{dB})$ for a more lax or less strict success definition. In addition the $25\,\%$ and $75\,\%$ success rate confidence intervals are indicated as shaded areas. As can be seen, the CSCSA refinement improves the reconstruction performance significantly.

6.3. Turbo Singular Value Thresholding

The turbo singular value thresholding (TSVT) algorithm was inspired by turbo affine rank minimization (TARM) presented in [57] which solves for affine rank minimization (ARM) problems applying the turbo principle. This principle is a special form of the more general message passing principle. Within TARM a hard thresholding (HT) operator is applied. Hence, TARM was reworked to use a soft thresholding (ST) operator. After finalizing TSVT it came to our attention, that a similar approach was formerly published in [55] called singular value thresholding-turbo-compressive sensing (SVT-Turbo-CS) conducting the same reconstruction as TSVT. The contributions of this work beyond SVT-Turbo-CS is the expansion into the complex case, adding a final purification step to yield a clear low rank solution and we give a formula how to select the regularization parameter λ.

Problem (4.1.2) is converted to a regularized relaxed convex optimization problem

$$\widehat{\boldsymbol{L}} = \arg\min_{\boldsymbol{L}} \lambda \left\|\boldsymbol{L}\right\|_* + h\left(\boldsymbol{L}\right), \tag{6.3.1}$$

where $\left\|\boldsymbol{L}\right\|_*$ is the nuclear norm of $\boldsymbol{L}$ and $\lambda > 0$ is some regularization parameter and $h\left(\boldsymbol{L}\right)$ denotes the data fidelity term given by (4.1.3). Program (6.3.1) is classically solved by singular value thresholding (SVT) but TSVT does it by iteratively updating

$$\begin{aligned} \boldsymbol{R}_i &= \boldsymbol{L}_{i-1} - \mu \nabla_{\boldsymbol{L}} h\left(\boldsymbol{L}_{i-1}\right) \\ \boldsymbol{Z}_i &= \mathcal{S}_{\mathrm{l},\mu\lambda}\left(\boldsymbol{R}_i\right) \\ \boldsymbol{L}_i &= c_i\left(\boldsymbol{Z}_i - \alpha_i \boldsymbol{R}_i\right) \end{aligned} \tag{6.3.2}$$

where μ is some step size, i is the iteration index, $\mathcal{S}_{\mathrm{l},a}(\boldsymbol{X})$ is the ST operator given by (4.2.3), and α_i and c_i are required parameters explained later. The classical question now is, of course, how to choose λ and thus which shrinkage a should be applied. Too much shrinkage results in a large bias while too little results in a slow convergence rate. As such, an optimal constant λ does not exists, rather λ would need to be adjusted in every iteration. Unfortunately, to the best of the authors knowledge, a closed form solution to determine such an optimal λ is known to exists only for the signal model $\boldsymbol{X} = \widetilde{\boldsymbol{L}} + \boldsymbol{E}$ with the entries of $\boldsymbol{E}$ being i. i. d. normally distributed [60]. However, this does not apply here since the gradient update step as input to $\mathcal{S}_{\boldsymbol{L},a}(\cdot)$ is not of such form. We therefore follow another approach and set the regularization parameter λ as given in (4.2.4) to

$$\lambda = 2c_{\mathrm{r}}\Phi^{-1}\left(1 - \frac{\alpha_{\mathrm{r}}}{2n}\right)\sqrt{P_{\mathrm{n}}\max(N_1, N_2)}, \tag{6.3.3}$$

where $c_{\mathrm{r}} > 1$ is some constant, Φ is the cumulative density function (CDF) of $\mathcal{N}(0,1)$, and $\alpha_r \in [0,1]$ is some parameter. The resulting inevitable bias of a constant λ is circumvented by a final purification step, which is described later. The required parameters $\{\mu, \alpha_i, c_i\}$ are chosen according to the turbo principle such that

$$\left\langle \boldsymbol{R}_i - \widetilde{\boldsymbol{L}}, \boldsymbol{L}_{i-1} - \widetilde{\boldsymbol{L}} \right\rangle_{\mathrm{F}} = 0 \tag{6.3.4}$$

$$\left\langle \boldsymbol{R}_i - \widetilde{\boldsymbol{L}}, \boldsymbol{L}_{i} - \widetilde{\boldsymbol{L}} \right\rangle_{\mathrm{F}} = 0, \tag{6.3.5}$$

where $\langle \boldsymbol{X}, \boldsymbol{Y} \rangle_{\mathrm{F}}$ denotes the Frobenius product, and further that for a given $\boldsymbol{L}_{i-1}$, $\left\|\boldsymbol{L}_i - \widetilde{\boldsymbol{L}}\right\|_{\mathrm{F}}^2$ is minimized under (6.3.4) and (6.3.5) [57]. In the above, (6.3.4) ensures that the input and output error of the gradient update step are uncorrelated. Equally, (6.3.5) ensures a decorrelation of the input and output error of the denoising step. This strategy allows for an improved convergence rate compared to classical gradient approaches. In order to fulfill (6.3.4) and (6.3.5), the true solution $\widetilde{\boldsymbol{L}}$ is required to determine exact values for $\{\mu, \alpha_i, c_i\}$. Since $\widetilde{\boldsymbol{L}}$ is unknown, approximate formulations for $\{\mu, \alpha_i, c_i\}$ were derived in [57] for the real valued case. In the general case these parameters are

$$\mu = \frac{n}{M\left\|\mathcal{A}\right\|_2^2} \tag{6.3.6}$$

$$\alpha_i = \begin{cases} \frac{1}{n}\mathrm{div}\left(\mathcal{S}_{l,\mu\lambda}(\boldsymbol{R}_i)\right) & \text{if } \boldsymbol{X} \in \mathbb{R}^{N_1 \times N_2} \\ \frac{1}{2n}\mathrm{div}\left(\mathcal{S}_{l,\mu\lambda}(\boldsymbol{R}_i)\right) & \text{if } \boldsymbol{X} \in \mathbb{C}^{N_1 \times N_2} \end{cases} \tag{6.3.7}$$

$$c_i = \frac{\langle \boldsymbol{Z}_i - \alpha_i \boldsymbol{R}_i, \boldsymbol{R}_i \rangle_{\mathrm{F}}}{\left\|\boldsymbol{Z}_i - \alpha_i \boldsymbol{R}_i\right\|_{\mathrm{F}}^2}. \tag{6.3.8}$$

For the required divergence operator in (6.3.7), which is to be interpreted in the weak sense i. e. it can fail to exist on negligible sets, a closed form solution exists [60]

$$\mathrm{div}\left(\mathcal{S}_{l,a}(\boldsymbol{X})\right) = \sum_{j=1}^{n_{\min}} \left[\mathbb{I}(\sigma_j > a) + A_j\right] + 2B \tag{6.3.9}$$

for $\boldsymbol{X} \in \mathbb{R}^{N_1 \times N_2}$ or

$$\operatorname{div}\left(\mathcal{S}_{l,a}\left(\boldsymbol{X}\right)\right) = \sum_{j=1}^{n_{\min}} \left[\mathbb{I}\left(\sigma_j > a\right) + A_j\right] + 4B \tag{6.3.10}$$

for $\boldsymbol{X} \in \mathbb{C}^{N_1 \times N_2}$, when $\boldsymbol{X}$ is simple i. e. $\boldsymbol{X}$ has no repeated singular values and 0 otherwise. In (6.3.9) and (6.3.10), $\mathbb{I}\left(\cdot\right)$ denotes the indicator function and

$$A_j = \begin{cases} |N_1 - N_2| \left(1 - \frac{a}{\sigma_i}\right)_+ & \text{if } \boldsymbol{X} \in \mathbb{R}^{N_1 \times N_2} \\ (2|N_1 - N_2| + 1) \left(1 - \frac{a}{\sigma_i}\right)_+ & \text{if } \boldsymbol{X} \in \mathbb{C}^{N_1 \times N_2} \end{cases}$$

$$B = \sum_{i \neq j, i, j = 1}^{n_{\min}} \frac{\sigma_i \left(\sigma_i - a\right)_+}{\sigma_i^2 - \sigma_j^2}.$$

For more details on the derivation of $\{\mu, \alpha_i, c_i\}$, the reader is referred to [57]. The main loop stops if an upper limit I is reached or if the relative change of the intermediate solutions is below a predefined threshold ϵ.

As a last step, a purification step is conducted using a HT operator $\mathcal{H}_{\mathrm{l},R}\left(\boldsymbol{X}\right)$ as defined in (4.3.2). This purification step is an adjustment of TSVT to TARM, where in TARM the final output is $\boldsymbol{Z}_i$ and not $\boldsymbol{L}_i$. The purification step is motivated by the aforementioned bias of the soft thresholding operator $\mathcal{S}_{l,\mu\lambda}\left(\cdot\right)$ for constant non optimally selected λ. As an estimate for R, we conveniently use $\operatorname{rank}\left(\boldsymbol{Z}_i\right)$. This final purification step allows for a clean low-rank solution with, as shown in the simulation results, a slight improvement of the reconstruction performance. For proofs of convergence, unique solutions etc. of TARM and thus TSVT the interested reader may have a look into [57]. Putting all the above steps together, the final TSVT algorithm is listed in Algorithm 6.3. The threshold selections given in Algorithm 6.3 were evaluated numerically and prove to work well in every case.

Algorithm 6.3 The TSVT algorithm.

Input: $\mathcal{A}$, $\boldsymbol{y}$, λ, I

Initialization:

$\epsilon \leftarrow \min\left(10^{-4}, 5 \cdot 10^{-3}\lambda\right)$

$i \leftarrow 0$, $d \leftarrow \infty$, $\boldsymbol{L}_0 \leftarrow \boldsymbol{0}$, $\mu \leftarrow n/(M \left\|\mathcal{A}\right\|_2^2)$

Body:

while $d > \epsilon$ **and** $i < I$ **do**

$i \leftarrow i + 1$

$\boldsymbol{R}_i \leftarrow \boldsymbol{L}_{i-1} - \mu \nabla_{\boldsymbol{L}} h\left(\boldsymbol{L}_{i-1}\right)$

$\boldsymbol{Z}_i \leftarrow \mathcal{S}_{\mathrm{l},\mu\lambda}\left(\boldsymbol{R}_i\right)$

$\alpha_i \leftarrow \begin{cases} \frac{1}{n}\operatorname{div}\left(\mathcal{S}_{l,\mu\lambda}\left(\boldsymbol{R}_i\right)\right) & \text{if } \boldsymbol{X} \in \mathbb{R}^{N_1 \times N_2} \\ \frac{1}{2n}\operatorname{div}\left(\mathcal{S}_{l,\mu\lambda}\left(\boldsymbol{R}_i\right)\right) & \text{if } \boldsymbol{X} \in \mathbb{C}^{N_1 \times N_2} \end{cases}$

$c_i \leftarrow \left\langle \boldsymbol{Z}_i - \alpha_i \boldsymbol{R}_i, \boldsymbol{R}_i \right\rangle_{\mathrm{F}} / \left\|\boldsymbol{Z}_i - \alpha_i \boldsymbol{R}_i\right\|_{\mathrm{F}}^2$

$\boldsymbol{L}_i \leftarrow c_i \left(\boldsymbol{Z}_i - \alpha_i \boldsymbol{R}_i\right)$

$d \leftarrow \left\|\boldsymbol{L}_i - \boldsymbol{L}_{i-1}\right\|_{\mathrm{F}} / \left\|\boldsymbol{L}_{i-1}\right\|_{\mathrm{F}}$

end while

$R \leftarrow \operatorname{rank}\left(\boldsymbol{Z}_i\right)$

Output: $\widehat{\boldsymbol{L}} \leftarrow \mathcal{H}_{\mathrm{l},R}\left(\boldsymbol{R}_i\right)$

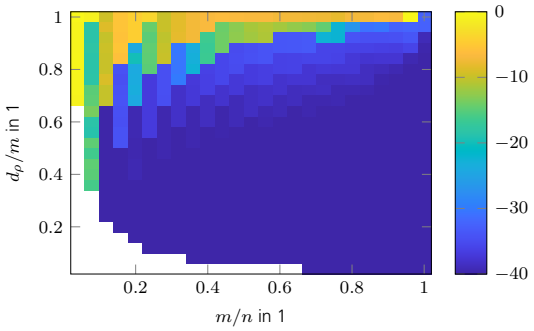

(a) Result for random sensing operator $\mathcal{A} \sim \mathcal{CN}(0,1)$.

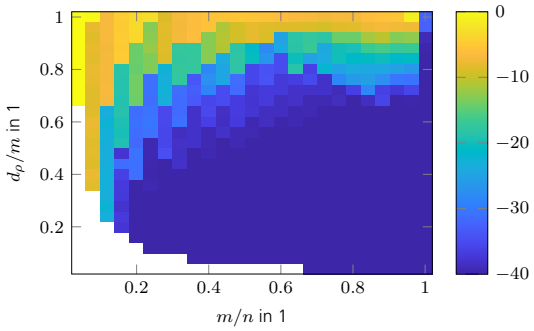

(b) Result for random row DFT sensing operator.

Figure 6.3.1.: Phase transition of TSVT algorithm of squared reconstruction error (SRE) in dB.

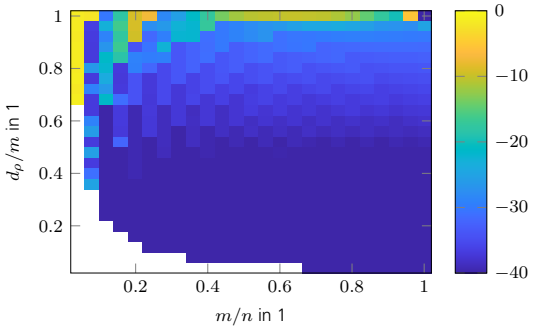

(a) Result of TARM for random sensing operator $\mathcal{A} \sim \mathcal{CN}(0,1)$ in case true rank was given.

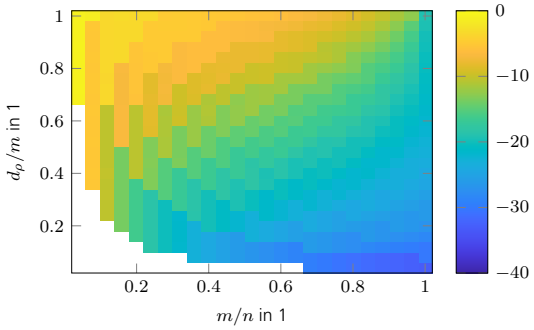

(b) Result of SVT for random sensing operator $\mathcal{A} \sim \mathcal{CN}(0,1)$.

Figure 6.3.2.: Phase transition in SRE in dB.

In the following, simulation results are shown to illustrate the performance of TSVT. Phase transition diagrams for random and discrete Fourier transform (DFT) sensing operators are shown in Fig. 6.3.1. As a comparison the phase transition diagrams of TARM and SVT are shown in Fig. 6.3.2 for random sensing operators. The results of SVT in Fig. 6.3.2b are shown to illustrate the performance gain achieved by TSVT and TARM. As can be seen in Fig. 6.3.2a, the results for TARM are very good, however, only if the true rank of $\widetilde{\boldsymbol{L}}$ is known. In case this parameter is assumed wrong, the reconstruction performance drops significantly as given in the comparison plot in Fig. 6.3.3. The curves in Fig. 6.3.3 indicate the $50\,\%$ success rate with respect to the Monte Carlo runs. Success is defined twofold as either $\mathrm{SRE} \leq -\mathrm{SNR}$ for a strict success definition and $\mathrm{SRE} \leq -(\mathrm{SNR} - 5\,\mathrm{dB})$ for a more lax or less strict success definition. In addition the $25\,\%$ and $75\,\%$ success rate confidence intervals are indicated as shaded areas. For a reconstruction problem with settings $M/n = \rho/M = 0.5$ we plot the per iteration errors in Fig. 6.3.4, where solid lines refer to the intermediate SRE $\|\boldsymbol{L}_i - \widetilde{\boldsymbol{L}}\|_\mathrm{F}^2 / \|\widetilde{\boldsymbol{L}}\|_\mathrm{F}^2$ and dashed lines to the squared residual error $\|\mathcal{A}(\boldsymbol{L}_i) - \boldsymbol{y}\|_2^2 / \|\boldsymbol{y}\|_2^2$. The dotted line reflects $\|\boldsymbol{Z}_i - \widetilde{\boldsymbol{L}}\|_\mathrm{F}^2 / \|\widetilde{\boldsymbol{L}}\|_\mathrm{F}^2$ and as such illustrates the impact of the aforementioned bias of $\mathcal{S}_{\mu\lambda}(\cdot)$. In this simulations we equipped TARM with the true rank of the unknown matrix $\widetilde{\boldsymbol{L}}$ and as can be seen it converges most rapid. SVT converges slowest as its convergence speed $\mathcal{O}(1/i)$ dictates. The TSVT algorithm closely follows TARM despite its non awareness of the rank of $\widetilde{\boldsymbol{L}}$. Interestingly, the final purification step at iteration 20 additionally

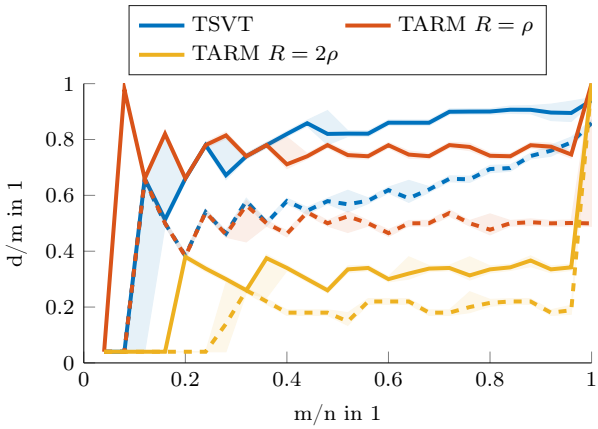

Figure 6.3.3.: Result of TARM for random sensing operator $\mathcal{A} \sim \mathcal{CN}(0, 1)$ in case true rank was known.

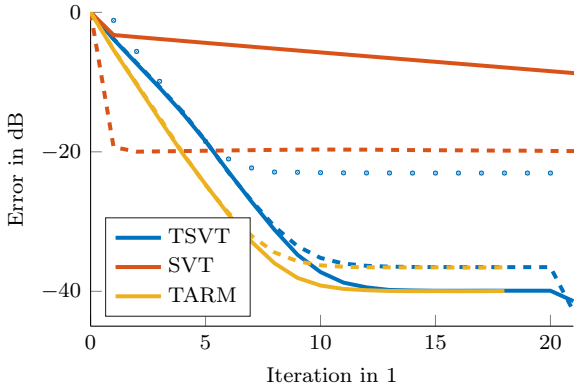

Figure 6.3.4.: Convergence comparison of algorithms.

improves upon the results of TARM. In summary, TSVT is very easy to implement, shows a state-of-the-art convergence rate, has low computational complexity as there are closed form solutions available for all required parameters, and finally it does not require any unknown parameters, e. g. as the true rank ρ of $\widetilde{\boldsymbol{L}}$, in general. Hence, it is well suited for practical applications.

6.4. Complex Smoothed Rank Approximation

Although the performance of turbo singular value thresholding (TSVT) is already good, we can improve upon them in a similar manner as complex successive concave sparsity approximation (CSCSA) does for turbo shrinkage-thresholding (TST) results. The complex smoothed rank approximation (CSRA) algorithm does so by enforcing a stricter rank measure compared to the nuclear norm used in (6.3.1). The CSRA algorithm is our extension based on the smoothed rank function (SRF) algorithm [61] and the smoothed rank approximation (SRA) approach in [62]. CSRA is applicable to complex valued problems and to the contrary of [62] has a closed form solution to a subsequent optimization problem, hence, reduced computational complexity. We give here an idea of how the algorithm works while a thorough derivation of the algorithm can be found in the Appendix A.5.

To enforce a stricter rank measure, a different replacement for the rank function is proposed.

The rank of $\boldsymbol{L} = \boldsymbol{U}\boldsymbol{\Sigma}\boldsymbol{V}^{\mathrm{H}}$, where $\boldsymbol{\Sigma} = \operatorname{diag}(\boldsymbol{\sigma})$, is defined as the number of non zero elements in $\boldsymbol{\sigma}$, where the vector $\boldsymbol{\sigma} = \begin{bmatrix}\sigma_1 & \cdots & \sigma_{n_{\min}}\end{bmatrix}^{\mathrm{T}}$ holds the singular values of $\boldsymbol{L}$. We thus can define the rank of $\boldsymbol{L}$ as

$$\operatorname{rank}(\boldsymbol{L}) = \sum_{i=1}^{n_{\min}} \left[1 - \delta\left(\sigma_i(\boldsymbol{L})\right)\right], \tag{6.4.1}$$

where $\sigma_i(\boldsymbol{L})$ is the i^{th} largest singular value of $\boldsymbol{L}$ and $\delta(x)$ is the Kronecker delta function. To make (A.5.4) smooth we may apply the same idea as used for CSCSA

$$f_\gamma(x) = 1 - \delta(x) \approx 1 - \exp\left(-\frac{|x|}{\gamma}\right).$$

As can be seen, γ determines how close the rank function is approximated. Thus we can define

$$\operatorname{rank}(\boldsymbol{L}) \approx \sum_{i=1}^{n_{\min}} f_\gamma\left(\sigma_i(\boldsymbol{L})\right) = F'_\gamma\left(\boldsymbol{\sigma}(\boldsymbol{L})\right) = F_\gamma(\boldsymbol{L}), \tag{6.4.2}$$

where $\boldsymbol{\sigma}(\boldsymbol{X})$ yields the singular values of $\boldsymbol{X}$ arranged as a vector. The optimization problem (4.1.2) may now be relaxed to

$$\min_{\boldsymbol{L}} F_\gamma(\boldsymbol{L}) \text{ subject to } h(\boldsymbol{L}) \leq \epsilon^2, \tag{6.4.3}$$

where $h(\boldsymbol{L})$ is the data fidelity term given by (4.1.3). The constrained optimization problem (A.5.6) can be converted to an unconstrained one by use of regularization, which yields

$$\min_{\boldsymbol{L}} \lambda F_\gamma(\boldsymbol{L}) + h(\boldsymbol{L}), \tag{6.4.4}$$

where λ again is some regularization parameter. In this approach, $F_\gamma(\boldsymbol{L})$ is not concave nor convex (since $f_\gamma(x)$ is defined also for negative numbers) and not smooth i. e. not differentiable at the origin. Nevertheless, the iterative thresholding (IT) method can be utilized to conduct the desired minimization by iteratively solving

$$\begin{aligned} \boldsymbol{L}_{0i} &= \boldsymbol{L}_i - \mu \nabla_{\boldsymbol{L}} h(\boldsymbol{L}_i) \\ \boldsymbol{L}_{i+1} &= \boldsymbol{U}_{0i} \operatorname{diag}\left(\mathcal{T}_{\mu\lambda}^{(\gamma)}(\boldsymbol{\sigma}_{0i})\right) \boldsymbol{V}_{0i}^{\mathrm{H}} \end{aligned} \tag{6.4.5}$$

where $\boldsymbol{L}_{0i} = \boldsymbol{U}_{0i} \operatorname{diag}(\boldsymbol{\sigma}_{0i}) \boldsymbol{V}_{0i}^{\mathrm{H}}$ is the singular value decomposition (SVD) of the gradient update step $\boldsymbol{L}_{0i}$ and $\mathcal{T}_{\mu\lambda}^{(\gamma)}$ is again a thresholding operator which is given in the Appendix by (A.5.24). To the contrary of [62], we do not need a differenct of convex (D.C.) optimization strategy to solve (A.5.7), rather we have the closed form solution $\mathcal{T}_{\mu\lambda_\gamma}^{(\gamma)}(\cdot)$ to do so. Hence our solution shows lower computational complexity. It shall be noted that, similar to CSCSA, (A.5.7) is not convex any more. In order to avoid getting stuck in local minima the graduated non-convexity (GNC) approach is applied. At first an initial solution $\boldsymbol{L}_0$ is obtained from a convex optimization algorithm like TSVT and γ is chosen big enough such that (6.4.5) does not get stuck in a local minima. After convergence, γ is subsequently reduced until a stopping criteria is met. Details on how to choose γ are given in the Appendix A.5.

It is well known, that IT techniques have a low computational complexity, however, they suffer

from low convergence rates on the order of $\mathcal{O}(1/i)$. To accelerate the proposed approach, a fast iterative shrinkage-thresholding algorithm (FISTA) like technique is used which does not increase computational complexity but boosts the convergence rate up to $\mathcal{O}(1/i^2)$ [41]. Putting all the above steps together, the final CSRA algorithm is listed in Algorithm 6.4. The algorithm consists of two loops, an inner and an outer one. In the outer loop γ is decreased gradually according to the GNC technique. The inner loop solves (6.4.5) by using a FISTA like technique. The loops are aborted after a maximum number of iterations J and P or if the solutions change, measured by the relative distance between consecutive solutions, drops below certain thresholds ϵ_{o} and ϵ_{i}. The threshold selections given in Algorithm 6.4 were found numerically just like done in [58] and prove to work well in every case. A more detailed explanation of the CSRA algorithm is given in

Algorithm 6.4 The CSRA algorithm.

Input: $\mathcal{A}$, $\boldsymbol{y}$, λ, J, P

Initialization:

$c \leftarrow (0, 0.5)$, $\mu \leftarrow 0.99/\left\|\mathcal{A}\right\|_2^2$
$\epsilon_{\mathrm{o}} \leftarrow \min\left(10^{-4}, 5 \cdot 10^{-3}\lambda\right)$
$\epsilon_{\mathrm{i}} \leftarrow \min\left(10^{-3}, 5 \cdot 10^{-3}\lambda\right)$
$\widehat{\boldsymbol{L}} \leftarrow \mathrm{TSVT}\left(\mathcal{A}, \boldsymbol{y}, \lambda, \epsilon_{\mathrm{i}}, J\right)$
$\gamma \leftarrow \left\|\widehat{\boldsymbol{L}}\right\|_2$

Body:

$p \leftarrow 0$, $d_{\mathrm{o}} \leftarrow \infty$
while $d_{\mathrm{o}} > \epsilon_{\mathrm{o}}$ **and** $p < P$ **do**
  $p \leftarrow p + 1$, $j \leftarrow 0$, $d_{\mathrm{i}} \leftarrow \infty$
  $t_1 \leftarrow 1$, $\boldsymbol{Z}_1 \leftarrow \widehat{\boldsymbol{L}}$, $\boldsymbol{L}_0 \leftarrow \widehat{\boldsymbol{L}}$
  while $d_{\mathrm{i}} > \epsilon_{\mathrm{i}}$ **and** $j < J$ **do**
    $j \leftarrow j + 1$
    $\boldsymbol{L}_j \leftarrow \mathcal{T}_{\mu\lambda}^{(\gamma)}\left(\boldsymbol{Z}_j - \mu\mathcal{A}^{\mathrm{H}}\left(\mathcal{A}\left(\boldsymbol{Z}_j\right) - \boldsymbol{y}\right)\right)$
    $t_{j+1} \leftarrow (1 + \sqrt{1 + 4t_j^2})/2$
    $\boldsymbol{Z}_{j+1} \leftarrow \boldsymbol{L}_j + \left(t_j - 1\right)\left(\boldsymbol{L}_j - \boldsymbol{L}_{j-1}\right)/t_{j+1}$
    $d_{\mathrm{i}} \leftarrow \left\|\boldsymbol{L}_j - \boldsymbol{L}_{j-1}\right\|_{\mathrm{F}} / \left\|\boldsymbol{L}_{j-1}\right\|_{\mathrm{F}}$
  end while
  $d_{\mathrm{o}} \leftarrow \left\|\boldsymbol{L}_j - \widehat{\boldsymbol{L}}\right\|_{\mathrm{F}} / \left\|\widehat{\boldsymbol{L}}\right\|_{\mathrm{F}}$
  $\widehat{\boldsymbol{L}} \leftarrow \boldsymbol{L}_j$
  $\gamma \leftarrow c\gamma$
end while

Output: $\widehat{\boldsymbol{L}}$

the Appendix A.5.

Simulation results for random and discrete Fourier transform (DFT) sensing operators are shown in Fig. 6.4.1. As can be seen, since TSVT already achieves a high reconstruction performance, the additional gain of CSRA is not as dramatic as in the compressive sensing (CS) counterpart CSCSA. Nevertheless, especially for DFT sensing operators, CSRA helps to boost the reconstruction performance. A bigger impact is achieved for compressed robust principal component analysis (CRPCA) where CSRA significantly boosts the reconstruction performance as shown in Section 6.6. In summary, CSRA in combination with TSVT is very easy to implement, shows a state-of-the-art convergence rate and reconstruction performance, has low computational complexity as there

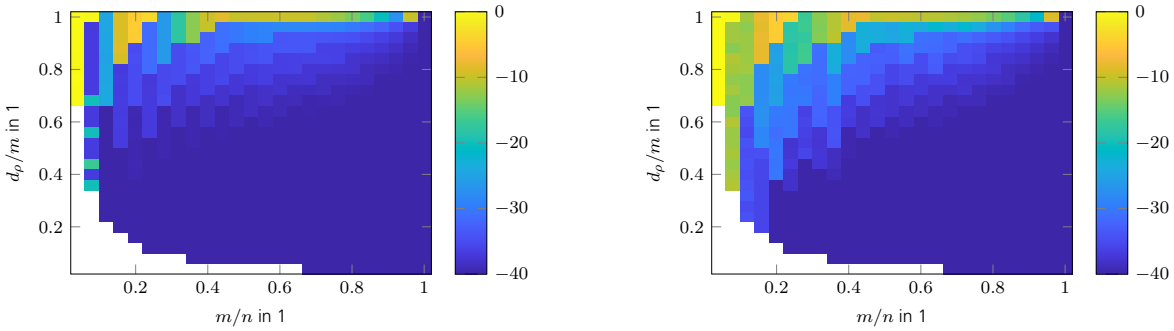

(a) Result for random sensing operator $\mathcal{A} \sim \mathcal{CN}(0,1)$.

(b) Result for random row DFT sensing operator.

Figure 6.4.1.: Phase transition of TSVT + CSRA in squared reconstruction error (SRE) in dB.

are closed form solutions available for all required parameters and subsequent optimization problems, and finally both do not require any unknown parameters in general. Hence, they are well suited for practical applications.

6.5. Bi-Factored Gradient Descent

The bi-factored gradient descent (BFGD) algorithm tries to find a solution to (4.1.2) by solving the equivalent optimization problem

$$\widehat{\boldsymbol{L}} = \arg\min_{\boldsymbol{L}} h \text{ subject to } \operatorname{rank}(\boldsymbol{L}) \leq R, \tag{6.5.1}$$

where R is a chosen constant [43]. Instead of using a hard threshold approach like singular value projection (SVP), the idea in BFGD is to factorize the low-rank matrix as $\boldsymbol{L} = \boldsymbol{U}\boldsymbol{V}^{\mathrm{H}}$ with $\boldsymbol{U} \in \mathbb{C}^{N_1 \times R}$, $\boldsymbol{V} \in \mathbb{C}^{N_2 \times R}$. Program (6.5.1) may then be solved by minimizing

$$F(\boldsymbol{U},\boldsymbol{V}) = h\left(\boldsymbol{U}\boldsymbol{V}^{\mathrm{H}}\right) + \lambda \left\|\boldsymbol{U}^{\mathrm{H}}\boldsymbol{U} - \boldsymbol{V}^{\mathrm{H}}\boldsymbol{V}\right\|_{\mathrm{F}}^{2}. \tag{6.5.2}$$

The second term in (6.5.2) is necessary in order to prevent $\boldsymbol{U}$ and $\boldsymbol{V}$ obtaining large condition numbers which is required by the BFGD algorithm to ensure convergence. Program (6.5.2) can be solved by an alternating minimization scheme as [43]

$$\begin{aligned}\boldsymbol{U}_{i+1} &= \boldsymbol{U}_i - \mu_{\boldsymbol{U}} \nabla_{\boldsymbol{U}} F(\boldsymbol{U}_i, \boldsymbol{V}_i) \\ \boldsymbol{V}_{i+1} &= \boldsymbol{V}_i - \mu_{\boldsymbol{V}} \nabla_{\boldsymbol{V}} F(\boldsymbol{U}_i, \boldsymbol{V}_i),\end{aligned}$$

where $\mu_{\boldsymbol{U}}$ and $\mu_{\boldsymbol{V}}$ denote some step sizes. The BFGD algorithm needs initial solutions $\boldsymbol{U}_0$ and $\boldsymbol{V}_0$ which are sufficiently close to the true solution. One possibility to obtain those is to conduct a few iterations J of the turbo singular value thresholding (TSVT) algorithm. Of particular interest is the question of how to choose the step sizes $\mu_{\boldsymbol{U}}$ and $\mu_{\boldsymbol{V}}$. The existence of an optimal step width was shown in [43, 63, 53, 64], however, no equations based on parameters known in practice are given. Hence, we came up with a new solution for this particular step size determination problem, for which a paper was submitted to EUSIPCO 2020 [44] and is given in the Appendix A.6 by

(A.6.62) and (A.6.63). The phase transition results of BFGD depend on the initial solution delivered and thus on the algorithm creating it as BFGD delivers a refined solution. The benefit over the remaining algorithms is its lower computational burden since singular value decompositions (SVDs) are omitted. Putting all the above steps together, the final BFGD algorithm is listed in Algorithm 6.5. The threshold selections given in Algorithm 6.5 were evaluated numerically and prove to work well in every case.

Algorithm 6.5 The BFGD algorithm.

Input: $\mathcal{A}$, $\boldsymbol{y}$, λ, I, J

Initialization:

$\epsilon \leftarrow \min\left(10^{-4}, 5 \cdot 10^{-3}\lambda\right)$

$\widehat{\boldsymbol{L}}_0 \leftarrow \mathrm{TSVT}\left(\mathcal{A}, \boldsymbol{y}, \lambda, \epsilon, J\right)$

$\boldsymbol{U}'_0, \boldsymbol{\Sigma}'_0, \boldsymbol{V}'_0 \leftarrow \mathrm{SVD}\left(\widehat{\boldsymbol{L}}_0\right)$

$\boldsymbol{U}_0 \leftarrow \boldsymbol{U}'_0\sqrt{\boldsymbol{\Sigma}'_0}$

$\boldsymbol{V}_0 \leftarrow \boldsymbol{V}'_0\sqrt{\boldsymbol{\Sigma}'_0}$

Body:

$i \leftarrow 0$, $d \leftarrow \infty$

while $d > \epsilon$ **and** $t < T$ **do**

  $i \leftarrow t + 1$

  $\mu_{\boldsymbol{U}} \leftarrow$(A.6.62)

  $\mu_{\boldsymbol{V}} \leftarrow$(A.6.63)

  $\boldsymbol{U}_i \leftarrow \boldsymbol{U}_i - \mu_{\boldsymbol{U}}\nabla_{\boldsymbol{U}}F\left(\boldsymbol{U}_i, \boldsymbol{V}_i\right)$

  $\boldsymbol{V}_i \leftarrow \boldsymbol{V}_i - \mu_{\boldsymbol{V}}\nabla_{\boldsymbol{V}}F\left(\boldsymbol{U}_i, \boldsymbol{V}_i\right)$

  $d \leftarrow \left\|\boldsymbol{U}_i\boldsymbol{V}_i^{\mathrm{H}} - \widehat{\boldsymbol{L}}\right\|_{\mathrm{F}} / \left\|\widehat{\boldsymbol{L}}\right\|_{\mathrm{F}}$

  $\widehat{\boldsymbol{L}} \leftarrow \boldsymbol{U}_i\boldsymbol{V}_i^{\mathrm{H}}$

end while

Output: $\widehat{\boldsymbol{L}}$

6.6. Turbo Compressed Robust Principle Component Analysis

The turbo compressed robust principal component analysis (TCRPCA) algorithm is inspired by the turbo algorithm presented in [56]. For TCRPCA, all of the aforementioned reconstruction algorithms for compressive sensing (CS) and affine rank minimization (ARM) problems are combined together. To the contrary of the turbo algorithms presented in [56], we henceforth only apply soft thresholding (ST) operators and additionally improve the reconstruction results by applying complex successive concave sparsity approximation (CSCSA) and complex smoothed rank approximation (CSRA) refinements.

Following the graduated non-convexity (GNC) approach described in Section 6.2, the compressed robust principal component analysis (CRPCA) problem given by (5.1.2)

$$\min_{\boldsymbol{S},\boldsymbol{L}} \lambda_s \left\|\boldsymbol{S}\right\|_0 + \mathrm{rank}\left(\boldsymbol{L}\right) \ \text{subject to}\ h(\boldsymbol{S}, \boldsymbol{L}) \leq \epsilon^2$$

with

$$h(\boldsymbol{S}, \boldsymbol{L}) = \left\|\mathcal{A}\left(\boldsymbol{S} + \boldsymbol{L}\right) - \boldsymbol{y}\right\|_2^2$$

is in a first step relaxed to a convex problem as

$$\widehat{\boldsymbol{S}}_0, \widehat{\boldsymbol{L}}_0 = \underset{\boldsymbol{S},\boldsymbol{L}}{\arg\min}\, \lambda_s \|\boldsymbol{S}\|_1 + \lambda_l \|\boldsymbol{L}\|_* + h(\boldsymbol{S}, \boldsymbol{L}), \tag{6.6.1}$$

which is solved via a combination of turbo shrinkage-thresholding (TST) and turbo singular value thresholding (TSVT) by iteratively updating

$$\begin{aligned}
\boldsymbol{R}_{s,i} &= \boldsymbol{S}_{i-1} - \mu_s \nabla_{\boldsymbol{S}} h\left(\boldsymbol{S}_{i-1}, \boldsymbol{L}_{i-1}\right) \\
\boldsymbol{Z}_{s,i} &= \mathcal{S}_{s,\mu_s\lambda_s}\left(\boldsymbol{R}_{s,i}\right) \\
\boldsymbol{S}_i &= \mathcal{Q}_{\kappa_s}\left(c_{s,i}\left(\boldsymbol{Z}_{s,i} - \alpha_{s,i}\boldsymbol{R}_{s,i}\right)\right)
\end{aligned}$$

$$\begin{aligned}
\boldsymbol{R}_{l,i} &= \boldsymbol{L}_{i-1} - \mu_l \nabla_{\boldsymbol{L}} h\left(\boldsymbol{S}_{i-1}, \boldsymbol{L}_{i-1}\right) \\
\boldsymbol{Z}_{l,i} &= \mathcal{S}_{l,\mu_l\lambda_l}\left(\boldsymbol{R}_{l,i}\right) \\
\boldsymbol{L}_i &= \mathcal{P}_{\varphi_l}\left(c_{l,i}\left(\boldsymbol{Z}_{l,i} - \alpha_{l,i}\boldsymbol{R}_{l,i}\right)\right),
\end{aligned}$$

where the required parameters μ_s, λ_s, $c_{s,i}$, and $\alpha_{s,i}$ are determined as for the TST algorithm explained in Section 6.1 and μ_l, λ_l, $c_{l,i}$, and $\alpha_{l,i}$ as for the TSVT algorithm explained in Section 6.3. The projection parameters $\kappa_s \in (0, 1)$ and φ_l are explained in Chapter 5, where for κ_s a reasonable guess is required and φ_l might be chosen as in (5.2.10). According to numerical simulations, $\kappa_s = 1/4$ worked well, however, this establishes an upper bound on the permitted maximum number of sparse entries! Finally it shall be mentioned, that the projections $\mathcal{Q}_{\kappa_s}$ and $\mathcal{P}_{\varphi_l}$ may be applied only on the first few, e. g. 10, iterations. The intermediate results $\boldsymbol{S}_i$ and $\boldsymbol{L}_i$ then lie in a surrounding of a diffuse sparse and low rank solution and subsequent iterations won't need any further "guidance" by the projection operators. This also circumvents the problem of not knowing the optimal parameters κ_s and φ_l. Once a suitable convex solution was obtained, a refinement is conducted by solving

$$\widehat{\boldsymbol{S}}, \widehat{\boldsymbol{L}} = \underset{\boldsymbol{S},\boldsymbol{L}}{\arg\min}\, \lambda_s F_{0,\gamma_s}\left(\boldsymbol{S}\right) + \lambda_l F_{\mathrm{r},\gamma_l}\left(\boldsymbol{L}\right) + h(\boldsymbol{S}, \boldsymbol{L}), \tag{6.6.2}$$

where $F_{0,\gamma_s}(\cdot)$ is the ℓ_0 approximation function (6.2.4) and $F_{\mathrm{r},\gamma_l}(\cdot)$ is the rank approximation function (6.4.2). Program (6.6.2) is solved via a combination of CSCSA and CSRA by iteratively updating

$$\begin{aligned}
\boldsymbol{S}_i &= \mathcal{T}^{(\gamma_s)}_{0,\mu_s\lambda_s,\gamma_s}\left(\boldsymbol{Z}_{s,i} - \mu_s \nabla_{\boldsymbol{S}} h\left(\boldsymbol{Z}_{s,i}, \boldsymbol{Z}_{l,i}\right)\right) \\
\boldsymbol{L}_i &= \mathcal{T}^{(\gamma_l)}_{\mathrm{r},\mu_l\lambda_l}\left(\boldsymbol{Z}_{l,i} - \mu_l \nabla_{\boldsymbol{L}} h\left(\boldsymbol{Z}_{s,i}, \boldsymbol{Z}_{l,i}\right)\right) \\
t_{i+1} &= \frac{1 + \sqrt{1 + 4t_i^2}}{2} \\
\boldsymbol{Z}_{s,i+1} &= \boldsymbol{S}_i + \frac{(t_i - 1)}{t_{i+1}}\left(\boldsymbol{S}_i - \boldsymbol{S}_{i-1}\right) \\
\boldsymbol{Z}_{l,i+1} &= \boldsymbol{L}_i + \frac{(t_i - 1)}{t_{i+1}}\left(\boldsymbol{L}_i - \boldsymbol{L}_{i-1}\right),
\end{aligned}$$

where $\mathcal{T}_{0,b}^{(a)}(\cdot)$ is the thresholding operator as defined in CSCSA in Section 6.2 and $\mathcal{T}_{\mathrm{r},b}^{(a)}(\cdot)$ is the thresholding operator as defined in CSRA in Section 6.4. The required parameters γ_s and γ_l are also the same as defined in CSCSA and CSRA. Putting all the above steps together, the final TCRPCA algorithm is listed in Algorithm 6.6 which delivers a solution to program (6.6.1) and Algorithm 6.7 which solves for program (6.6.2).

Algorithm 6.6 Part 1 of TCRPCA algorithm delivering convex solution.

Input: $\mathcal{A}$, $\boldsymbol{y}$, λ_s, λ_l, κ_s, φ_l, I

Initialization:

$\epsilon_s \leftarrow \min\left(10^{-4}, 5\cdot 10^{-3}\lambda_s\right)$, $\epsilon_l \leftarrow \min\left(10^{-4}, 5\cdot 10^{-3}\lambda_l\right)$

$\boldsymbol{S}_0 \leftarrow \boldsymbol{0}$, $\boldsymbol{L}_0 \leftarrow \boldsymbol{0}$, $\mu_s \leftarrow n/(M\,\|\mathcal{A}\|_2^2)$, $\mu_l \leftarrow n/(M\,\|\mathcal{A}\|_2^2)$

$i \leftarrow 0$, $d_s \leftarrow \infty$, $d_l \leftarrow \infty$

Body:

while $(d_s > \epsilon$ **or** $d_l > \epsilon)$ **and** $i < I$ **do**

$i \leftarrow i+1$

$\boldsymbol{R}_{s,i} \leftarrow \boldsymbol{S}_{i-1} - \mu_s \nabla_{\boldsymbol{S}} h\left(\boldsymbol{S}_{i-1}, \boldsymbol{L}_{i-1}\right)$

$\boldsymbol{Z}_{s,i} \leftarrow \mathcal{S}_{s,\mu_s\lambda_s}\left(\boldsymbol{R}_{s,i}\right)$

$\alpha_{s,i} \leftarrow$(6.1.5)

$c_{s,i} \leftarrow$(6.1.6)

$\boldsymbol{S}_i \leftarrow \mathcal{Q}_{\kappa_s}\left(c_{s,i}\left(\boldsymbol{Z}_{s,i} - \alpha_{s,i}\boldsymbol{R}_{s,i}\right)\right)$

$\boldsymbol{R}_{l,i} \leftarrow \boldsymbol{L}_{i-1} - \mu_l \nabla_{\boldsymbol{L}} h\left(\boldsymbol{S}_{i-1}, \boldsymbol{L}_{i-1}\right)$

$\boldsymbol{Z}_{l,i} \leftarrow \mathcal{S}_{l,\mu_l\lambda_l}\left(\boldsymbol{R}_{l,i}\right)$

$\alpha_{l,i} \leftarrow$(6.3.7)

$c_{l,i} \leftarrow$(6.3.8)

$\boldsymbol{L}_i \leftarrow \mathcal{P}_{\varphi_l}\left(c_{l,i}\left(\boldsymbol{Z}_{l,i} - \alpha_{l,i}\boldsymbol{R}_{l,i}\right)\right)$

$d_s \leftarrow \|\boldsymbol{S}_i - \boldsymbol{S}_{i-1}\|_{\mathrm{F}} \,/\, \|\boldsymbol{S}_{i-1}\|_{\mathrm{F}}$

$d_l \leftarrow \|\boldsymbol{L}_i - \boldsymbol{L}_{i-1}\|_{\mathrm{F}} \,/\, \|\boldsymbol{L}_{i-1}\|_{\mathrm{F}}$

end while

$K \leftarrow \|\boldsymbol{Z}_{s,i}\|_0$

$R \leftarrow \mathrm{rank}\left(\boldsymbol{Z}_{l,i}\right)$

Output: $\widehat{\boldsymbol{S}} \leftarrow \mathcal{H}_{\mathrm{s},K}\left(\boldsymbol{R}_{s,i}\right)$

Output: $\widehat{\boldsymbol{L}} \leftarrow \mathcal{H}_{\mathrm{l},R}\left(\boldsymbol{R}_{l,i}\right)$

In the following, simulation results are shown to illustrate the performance of TCRPCA for a discrete Fourier transform (DFT) sensing operator. A thorough comparison of TCRPCA to alternatives from the literature is beyond the scope of this work. The reader may refer to extensive review papers e. g. [65]. The simulation parameters and metrics are the same as for the aforementioned algorithms. The phase transition plots now emerge to be of 3D nature since sparsity and low rank measures need to be varied. As can be seen from Fig. 6.6.1, the reconstruction performance is improved by applying the refinement (6.6.2). To see how big the successful reconstruction volume is, the phase transition plane running along the 3 dB margin of the SRE was determined and is shown in Fig. 6.6.2. In general the reconstruction success depends mainly on the sparsity ratio. It was found from simulations, that in order to correctly reconstruct the special case of $\widetilde{\boldsymbol{S}} = \boldsymbol{0}$, the allowed sparsity ratio per row and column needs to be limited to $\kappa_s \leq 0.25$. In case of a higher allowed ratio, $\widetilde{\boldsymbol{S}} = \boldsymbol{0}$ was not found any more. Consequently, only reconstruction problems showing a sparsity ratio of $\kappa/M \leq 0.25$ can be reconstructed successfully. Nevertheless, part 1 of the TCRPCA algorithm achieves this border. Part 2 of TCRPCA does not apply the spar-

Algorithm 6.7 Part 2 of TCRPCA algorithm delivering refined solution.

Input: $\mathcal{A}$, $\boldsymbol{y}$, λ_s, λ_l, $\widehat{\boldsymbol{S}}_0$, $\widehat{\boldsymbol{L}}_0$, I, J

Initialization:

$c \leftarrow (0, 0.5)$, $\mu_s \leftarrow 0.99/\left\|\mathcal{A}\right\|_2^2$, $\mu_l \leftarrow 0.99/\left\|\mathcal{A}\right\|_2^2$

$\epsilon_{s\mathrm{i}} \leftarrow \min\left(10^{-3}, 5\cdot 10^{-3}\lambda_s\right)$, $\epsilon_{s\mathrm{o}} \leftarrow \min\left(10^{-4}, 5\cdot 10^{-3}\lambda_s\right)$

$\epsilon_{l\mathrm{i}} \leftarrow \min\left(10^{-3}, 5\cdot 10^{-3}\lambda_l\right)$, $\epsilon_{l\mathrm{o}} \leftarrow \min\left(10^{-4}, 5\cdot 10^{-3}\lambda_l\right)$

$\gamma_s \leftarrow \max(|\widehat{\boldsymbol{S}}|)$, $\gamma_l \leftarrow \left\|\widehat{\boldsymbol{L}}\right\|_2$

Body:

$i \leftarrow 0$, $d_{\mathrm{so}} \leftarrow \infty$, $d_{\mathrm{lo}} \leftarrow \infty$

while $(d_{\mathrm{so}} > \epsilon_{\mathrm{o}}$ **or** $d_{\mathrm{lo}} > \epsilon_{\mathrm{o}})$ **and** $i < I$ **do**

  $i \leftarrow i+1$, $j \leftarrow 0$, $d_{s\mathrm{i}} \leftarrow \infty$, $d_{l\mathrm{i}} \leftarrow \infty$

  $t_1 \leftarrow 1$, $\boldsymbol{Z}_{s,1} \leftarrow \widehat{\boldsymbol{S}}$, $\boldsymbol{Z}_{l,1} \leftarrow \widehat{\boldsymbol{L}}$, $\boldsymbol{S}_0 \leftarrow \widehat{\boldsymbol{S}}$, $\boldsymbol{L}_0 \leftarrow \widehat{\boldsymbol{L}}$

  while $(d_{s\mathrm{i}} > \epsilon_{\mathrm{i}}$ **or** $d_{l\mathrm{i}} > \epsilon_{\mathrm{i}})$ **and** $j < J$ **do**

    $j \leftarrow j+1$

    $\boldsymbol{S}_j \leftarrow \mathcal{T}^{(\gamma_s)}_{0,\mu_s\lambda_s,\gamma_s}\left(\boldsymbol{Z}_{s,j} - \mu_s\nabla_{\boldsymbol{S}}h\left(\boldsymbol{Z}_{s,j}, \boldsymbol{Z}_{l,j}\right)\right)$

    $\boldsymbol{L}_j \leftarrow \mathcal{T}^{(\gamma_l)}_{\mathrm{r},\mu_l\lambda_l}\left(\boldsymbol{Z}_{l,j} - \mu_l\nabla_{\boldsymbol{L}}h\left(\boldsymbol{Z}_{s,j}, \boldsymbol{Z}_{l,j}\right)\right)$

    $t_{j+1} \leftarrow (1+\sqrt{1+4t_j^2})/2$

    $\boldsymbol{Z}_{s,j+1} \leftarrow \boldsymbol{S}_j + (t_j-1)\left(\boldsymbol{S}_j - \boldsymbol{S}_{j-1}\right)/t_{j+1}$

    $\boldsymbol{Z}_{l,j+1} \leftarrow \boldsymbol{L}_j + (t_j-1)\left(\boldsymbol{L}_j - \boldsymbol{L}_{j-1}\right)/t_{j+1}$

    $d_{s\mathrm{i}} \leftarrow \left\|\boldsymbol{S}_j - \boldsymbol{S}_{j-1}\right\|_{\mathrm{F}} / \left\|\boldsymbol{S}_{j-1}\right\|_{\mathrm{F}}$

    $d_{l\mathrm{i}} \leftarrow \left\|\boldsymbol{L}_j - \boldsymbol{L}_{j-1}\right\|_{\mathrm{F}} / \left\|\boldsymbol{L}_{j-1}\right\|_{\mathrm{F}}$

  end while

  $d_{\mathrm{so}} \leftarrow \left\|\boldsymbol{S}_j - \widehat{\boldsymbol{S}}\right\|_{\mathrm{F}} / \left\|\widehat{\boldsymbol{S}}\right\|_{\mathrm{F}}$

  $d_{\mathrm{lo}} \leftarrow \left\|\boldsymbol{L}_j - \widehat{\boldsymbol{L}}\right\|_{\mathrm{F}} / \left\|\widehat{\boldsymbol{L}}\right\|_{\mathrm{F}}$

  $\widehat{\boldsymbol{S}} \leftarrow \boldsymbol{S}_j$, $\widehat{\boldsymbol{L}} \leftarrow \boldsymbol{L}_j$

  $\gamma_s \leftarrow c\gamma_s$, $\gamma_l \leftarrow c\gamma_l$

end while

Output: $\widehat{\boldsymbol{S}}$,$\widehat{\boldsymbol{L}}$

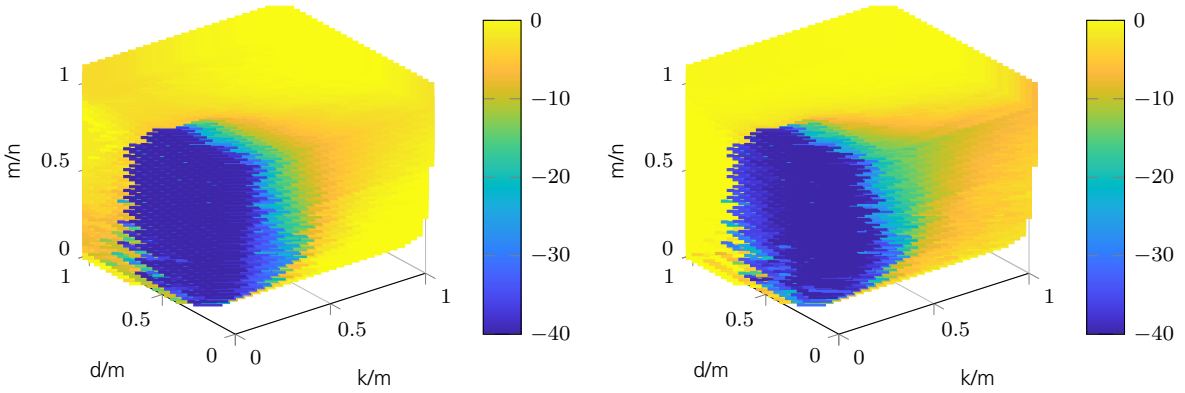

(a) Phase transition plot of $\widehat{\boldsymbol{S}}_0$.

(b) Phase transition plot of $\widehat{\boldsymbol{L}}_0$.

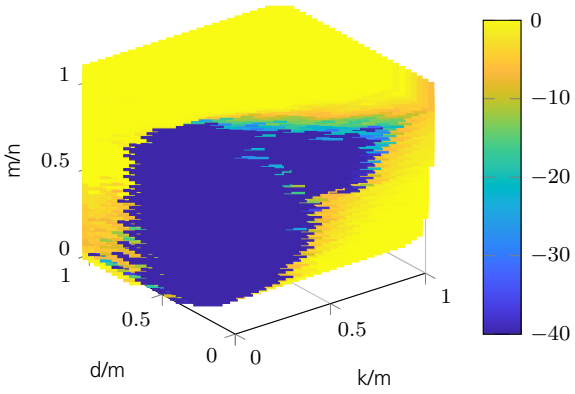

(c) Final phase transition plot of $\widehat{\boldsymbol{S}}$.

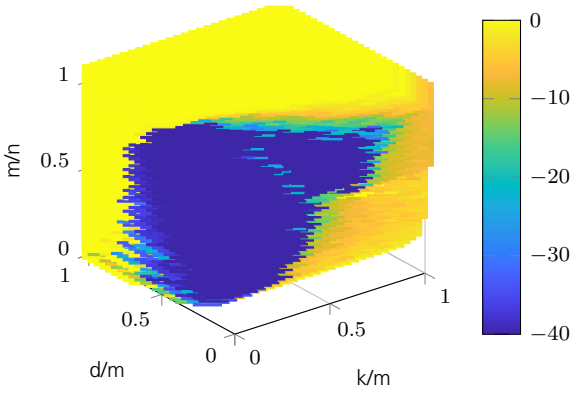

(d) Final phase transition plot of $\widehat{\boldsymbol{L}}$.

Figure 6.6.1.: Phase transition plots of TCRPCA in SRE in dB.

sity ratio operator and is able to extend the region of successful reconstructions for sparsity ratios $\kappa/M > 0.25$. The fact that only problems of low sparsity ratio can be reconstructed successfully is also known from other CRPCA algorithms [53]. In the same manner as for the sparsity ratio κ_s, also the infinity norm thresholding operator (5.2.9) was needed to be limited to $c_\varphi \leq 0.5$ in order to successfully recover the special case of $\widetilde{\boldsymbol{L}} = \boldsymbol{0}$. This incurs likewise restrictions regarding the possible reconstruction performance of the TCRPCA algorithm. If the special cases $\widetilde{\boldsymbol{S}} = \boldsymbol{0}$ and/or $\widetilde{\boldsymbol{L}} = \boldsymbol{0}$ can be excluded, the region of successful reconstructions can be extended by some extend by relaxing κ_s and c_φ, respectively. How to treat the special cases of either $\widetilde{\boldsymbol{S}} = \boldsymbol{0}$ or $\widetilde{\boldsymbol{L}} = \boldsymbol{0}$ in a satisfactory manner, i. e. to relax κ_s and c_φ, is still an open question. The obvious approach of conducting a CS, an ARM, and an CRPCA reconstruction separately and comparing the resulting residual errors to determine if either $\widetilde{\boldsymbol{S}} = \boldsymbol{0}$ or $\widetilde{\boldsymbol{L}} = \boldsymbol{0}$ does not work. Especially in case of low n/M the CRPCA approach always yields the lowest residual error regardless if the scene is strictly sparse or low rank due to its larger degree of freedom. In summary, TCRPCA combines the advantages of all aforementioned CS and ARM algorithms. In general only problems of low sparsity ratio can be reconstructed due to the required rank-sparsity incoherence condition. Nevertheless, TCRPCA achieves a high value of $\kappa/M \leq 0.25$ compared to other CRPCA algorithms e. g. [53].

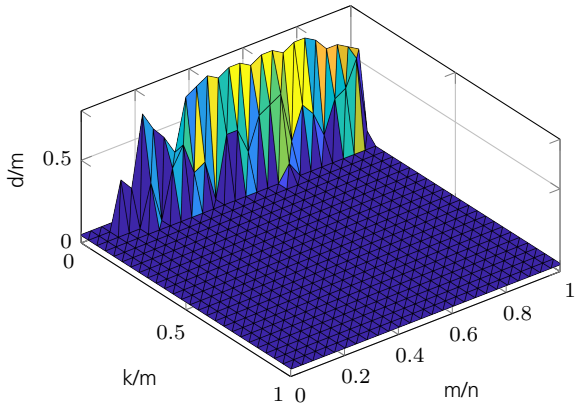

(a) Phase transition plane of $\widehat{\boldsymbol{S}}_0$.

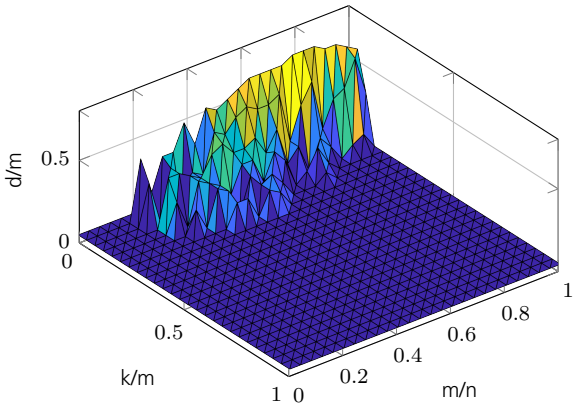

(b) Phase transition plane of $\widehat{\boldsymbol{L}}_0$.

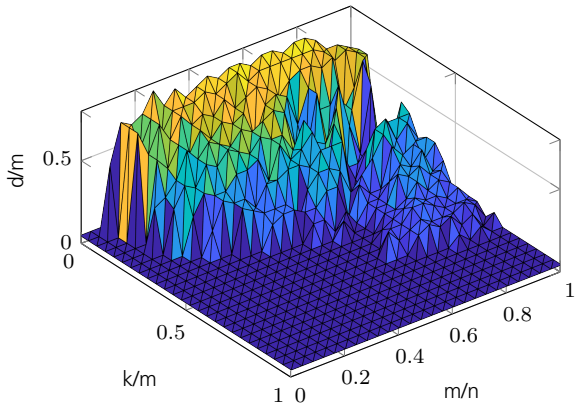

(c) Phase transition plane of $\widehat{\boldsymbol{S}}$.

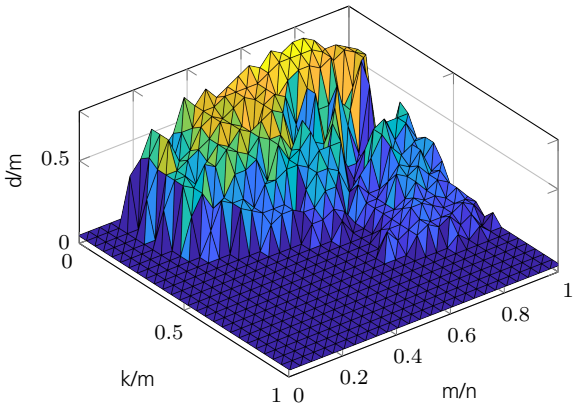

(d) Phase transition plane of $\widehat{\boldsymbol{L}}$.

Figure 6.6.2.: 3 dB margin phase transition planes of TCRPCA.

7. Application of CS and ARM Algorithms to GMTI

In this chapter we illustrate the application of compressive sensing (CS) and affine rank minimization (ARM) algorithms to the ground moving target indication (GMTI) problem. At first, we show where the low-rank property of GMTI signals comes from and illustrate how to exploit it which leads to an auto-clutter focus (ACF) algorithm. Once the low-rank was established, we show the separation of moving from non-moving targets via turbo compressed robust principal component analysis (TCRPCA).

7.1. On the Low-Rank Nature of GMTI Measurements

In this section a different approach compared to the classical space-time adaptive processing (STAP) idea is presented. The fundamental idea is the observation, that in case of a multi channel array, every channel observes the very same clutter scenario. It is therefore possible to form a low-rank matrix from such clutter measurements. This low-rank property can be exploited to estimate certain measurement parameters as discussed in Section 7.2, e. g. the clutter ridge slope β, the velocity misalignment angle φ_{m}, etc., or to separate the low-rank clutter measurements from moving targets which is discussed in Section 7.3. In this section, the two low-rank property natures of clutter measurements are revealed and practical implications regarding limited observation times etc. are discussed[1]. Finally, the low-rank properties of various clutter scenarios are demonstrated by use of simulated examples.

7.1.1. The Primary Low-Rank Form

In Section 2.2, it was shown that measurements from a static clutter scene are of the form

$$\boldsymbol{Y}_{\mathrm{c}}\left(\beta,\varphi_{\mathrm{m}}\right)=\int_{-\bar{d}}^{\bar{d}} x_{\mathrm{c}}\left(\bar{u}\right)\boldsymbol{G}\left(\bar{u},\bar{f}_{\mathrm{Dc}}\left(\bar{u};\beta,\varphi_{\mathrm{m}}\right)\right)\mathrm{d}\bar{u}, \tag{7.1.1}$$

where $x_{\mathrm{c}}\left(\bar{u}\right)$ denotes a clutter amplitude in normalized directional cosine direction $\bar{u}$ and $\boldsymbol{G}\left(\bar{u},\bar{f}_{\mathrm{Dc}}\left(\bar{u};\beta,\varphi_{\mathrm{m}}\right)\right)$ the space time signal matrix defined in (2.1.101) corresponding to the emerging clutter Doppler frequency $\bar{f}_{\mathrm{Dc}}\left(\bar{u};\beta,\varphi_{\mathrm{m}}\right)$. This measurement process is a linear map from the radar scene spanned by $\bar{u}$ and $\bar{f}_{\mathrm{D}}$ into the measurement scene spanned by the spatial

[1] In general there are multiple approaches possible to formulate or introduce a low rank matrix in the signal model. A popular one is the lifting technique which models the scene by use of dyadic products. This approach was studied, however, it was found to not be optimal for the subsequent separation of moving from non-moving targets by use of compressed robust principal component analysis (CRPCA).

and temporal measurement dimensions $d' = n_{\mathrm{rx}}\bar{d}$ and $t' = n_{\mathrm{p}}t_{\mathrm{p}}$. Some more insights can be found by looking at the scalar, non normalized, and continuous version of (7.1.1)

$$\begin{aligned} y_{\mathrm{c}}(d', t'; \beta, \varphi_{\mathrm{m}}) &= \int_{-1}^{1} x_{\mathrm{c}}(u)\, \mathrm{e}^{\mathrm{j}2\pi f_{\mathrm{Dc}}(u;\beta,\varphi_{\mathrm{m}})t'} \mathrm{e}^{\mathrm{j}2\pi u d'} \mathrm{d}u \\ &= \mathcal{F}_u^{-1}\left\{ x_{\mathrm{c}}(u)\, \mathrm{e}^{\mathrm{j}2\pi f_{\mathrm{Dc}}(u;\beta,\varphi_{\mathrm{m}})t'} \right\}, \end{aligned} \tag{7.1.2}$$

which is an inverse Fourier transform (IFT) with respect to u denoted by $\mathcal{F}_u^{-1}$. This form can be further recast by applying a Fourier transform (FT) followed by an IFT with respect to the emerging Doppler frequency f_{D} to

$$\begin{aligned} y_{\mathrm{c}}(d', t'; \beta, \varphi_{\mathrm{m}}) &= \int_{-\infty}^{\infty}\int_{-\infty}^{\infty}\int_{-1}^{1} x_{\mathrm{c}}(u)\, \mathrm{e}^{\mathrm{j}2\pi f_{\mathrm{Dc}}(u;\beta,\varphi_{\mathrm{m}})t'} \mathrm{e}^{\mathrm{j}2\pi u d'} \mathrm{e}^{-\mathrm{j}2\pi f_{\mathrm{D}} t'} \mathrm{e}^{\mathrm{j}2\pi f_{\mathrm{D}} t'} \mathrm{d}u \mathrm{d}t' \mathrm{d}f_{\mathrm{D}} \\ &= \int_{-\infty}^{\infty}\int_{-1}^{1} x_{\mathrm{c}}(u)\, \delta\left(f_{\mathrm{D}} - f_{\mathrm{Dc}}(u;\beta,\varphi_{\mathrm{m}})\right) \mathrm{e}^{\mathrm{j}2\pi u d'} \mathrm{e}^{\mathrm{j}2\pi f_{\mathrm{D}} t'} \mathrm{d}u \mathrm{d}f_{\mathrm{D}} \\ &= \underbrace{\mathcal{F}_{f_{\mathrm{D}}}^{-1} \circ \mathcal{F}_u^{-1}}_{\text{map to meas. dom.}} \left\{ \underbrace{x_{\mathrm{c}}(u)}_{\text{static clutter}} \underbrace{\delta\left(f_{\mathrm{D}} - f_{\mathrm{Dc}}(u;\beta,\varphi_{\mathrm{m}})\right)}_{\text{influence of moving radar}} \right\}, \end{aligned} \tag{7.1.3}$$

which now is of the form of a two dimensional IFT with respect to u and f_{D}, where $\circ$ denotes the composition of functions as $g \circ h(x) = g(h(x))$. Another key observation is, that the measurements are of correlated nature as can be seen from the auto correlation function of $y_{\mathrm{c}}(d', t'; \beta, \varphi_{\mathrm{m}})$. The auto correlation function was introduced in Section 2.2 and in the continuous case is

$$R_{\mathrm{c}}\left(\triangle d', \triangle t'; \beta, \varphi_{\mathrm{m}}\right) = \int_{-1}^{1} P_{\mathrm{c}}(u)\, \mathrm{e}^{\mathrm{j}2\pi u \triangle d' + \mathrm{j}2\pi f_{\mathrm{Dc}}(u;\beta,\varphi_{\mathrm{m}})\triangle t'} \mathrm{d}u, \tag{7.1.4}$$

where (2.2.18) was used. As can be seen, measurements displaced by $\triangle d'$ and $\triangle t'$ for which $u\triangle d' + f_{\mathrm{Dc}}(u;\beta,\varphi_{\mathrm{m}})\triangle t' = 0$ holds are maximally correlated. In summary, the aforementioned observations permit the following useful conclusions which are illustrated in Fig. 7.1.1:

- The static clutter scene $x_{\mathrm{c}}(u)$ is subject to an angle dependent Doppler shift caused by the moving radar. This creates the clutter scene observed by the radar

$$x_{\mathrm{c}}^{\mathrm{sh}}(u, f_{\mathrm{D}}) = x_{\mathrm{c}}(u)\, \delta\left(f_{\mathrm{D}} - f_{\mathrm{Dc}}(u;\beta,\varphi_{\mathrm{m}})\right), \tag{7.1.5}$$

  which contains the famous clutter ridge known from all STAP textbooks e. g. [4, 1, 17] etc.

- The shifted clutter scene is mapped to the measurement domain via a two dimensional IFT

$$y_{\mathrm{c}}(d', t'; \beta, \varphi_{\mathrm{m}}) = \mathcal{F}_{f_{\mathrm{D}}}^{-1} \circ \mathcal{F}_u^{-1}\left\{ x_{\mathrm{c}}^{\mathrm{sh}}(u, f_{\mathrm{D}}) \right\}$$

- The measurements y_{c} are highly correlated along displacements for which $u\triangle d' + f_{\mathrm{Dc}}(u;\beta,\varphi_{\mathrm{m}})\triangle t' = 0$ holds.

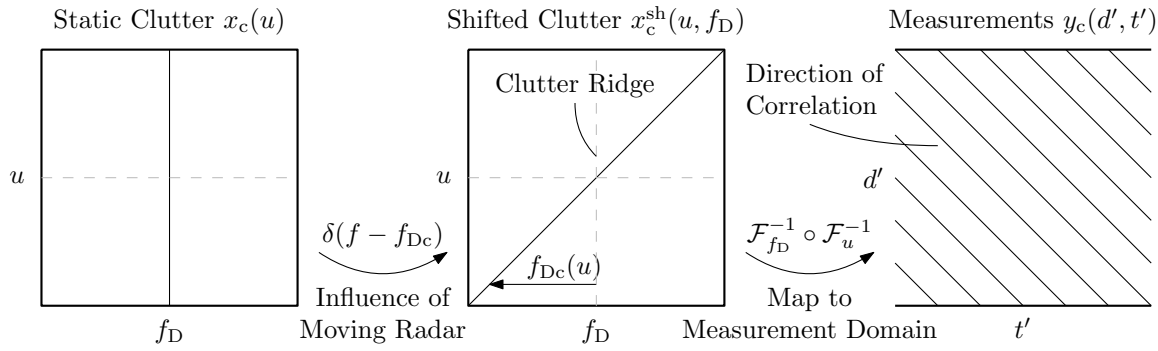

Figure 7.1.1.: Illustration of the measurement process.

The two dimensional IFT in (7.1.3) naturally coincides with the general measurement signal formulation of a multi-channel radar system presented in Section 2.1.4. Hence, the formulation given by (2.1.114) can be directly used to obtain the discretized measurement or sensing model from (7.1.3), which yields

$$\boldsymbol{Y}_c\left(\beta, \varphi_m\right) = \boldsymbol{A}\boldsymbol{X}_c^{sh}\boldsymbol{B}^T \in \mathbb{C}^{N_{rx} \times N_p} \tag{7.1.6}$$

where

$$\boldsymbol{X}_c^{sh} = \left[x_c^{sh}\left(n_u/N_u, n_D/N_D\right)\right]_{n_u \in \Omega_{N_u}, n_D \in \Omega_{N_D}} \in \mathbb{C}^{N_u \times N_D}$$

denotes the discretized shifted clutter scene with the bin indices n_u and n_D defined in (2.1.111) and (2.1.112) and $\boldsymbol{A} \in \mathbb{C}^{N_{rx} \times N_u}$ and $\boldsymbol{B} \in \mathbb{C}^{N_p \times N_D}$ the spatial and temporal steering matrices given by (2.1.115) and (2.1.116). In case of a uniform linear array (ULA) antenna and equidistant pulses, $\boldsymbol{A}$ and $\boldsymbol{B}$ are inverse discrete Fourier transform (IDFT) matrices. For convenient illustration purposes presented in the following, the transformation from the radar scene into the measurement domain is shortly denoted by the measurement operator $\mathcal{B} : \mathbb{C}^{N_u \times N_D} \to \mathbb{C}^{N_{rx} \times N_p}$ as

$$\boldsymbol{Y}_c\left(\beta, \varphi_m\right) = \mathcal{B}\left(\boldsymbol{X}_c^{sh}\right). \tag{7.1.7}$$

The shifted clutter scene is modeled as

$$\boldsymbol{X}_c^{sh} = \mathcal{D}_f(\boldsymbol{X}_c; \beta, \varphi_m), \tag{7.1.8}$$

where $\mathcal{D}_f : \mathbb{C}^{N_u \times N_D} \to \mathbb{C}^{N_u \times N_D}$ is a sub sample shift operator realizing the shift $f_D - f_{Dc}\left(u; \beta, \varphi_m\right)$ from (7.1.3) and $\boldsymbol{X}_c$ denotes the so-called primal, i. e. Doppler focused, low rank form of the clutter. The shift operator is modeled using the modified Fourier shift identity[2]

$$\mathcal{D}_f(\boldsymbol{X}; \beta, \varphi_m) = \left(\boldsymbol{F}_\triangle(\beta, \varphi_m) \odot \left(\boldsymbol{X}\left(\boldsymbol{F}_f^{-1}\right)^T\right)\right)\boldsymbol{F}_f^T \tag{7.1.9}$$

[2]This allows for optimizations later on.

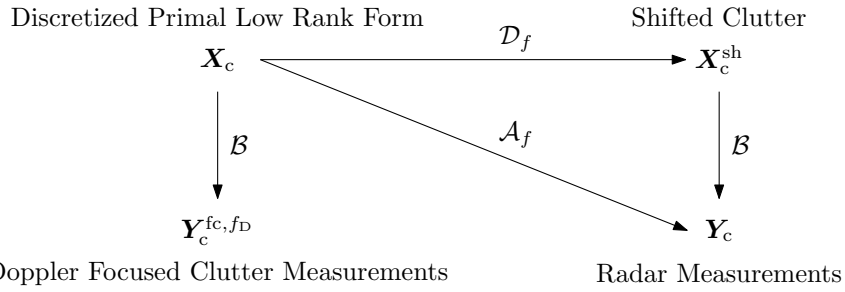

Figure 7.1.2.: Illustration of the discretized primal low rank form sensing model.

with $\boldsymbol{F}_f \in \mathbb{C}^{N_\mathrm{D}\times N_\mathrm{D}}$ denoting a discrete Fourier transform (DFT) matrix resulting in a FT of the $\bar{f}_\mathrm{D}$ dimension, $\odot$ the Hadamard product, and

$$\boldsymbol{F}_\triangle(\beta,\varphi_\mathrm{m}) = \exp\left(-\mathrm{j}2\pi \boldsymbol{n}_{\bar{f}_\mathrm{D}} \bar{\boldsymbol{f}}_\triangle^\mathrm{T}(\beta,\varphi_\mathrm{m})\right) \tag{7.1.10}$$

the Fourier shift matrix with

$$\begin{aligned} \boldsymbol{n}_{\bar{f}_\mathrm{D}} &= [0,1,\ldots,N_\mathrm{D}-1]^\mathrm{T} \\ \bar{\boldsymbol{f}}_\triangle(\beta,\varphi_\mathrm{m}) &= \left[\bar{f}_\mathrm{Dc}\left(i/N_\mathrm{u};\beta,\varphi_\mathrm{m}\right)\right]_{i=-N_\mathrm{u}/2}^{N_\mathrm{u}/2-1}. \end{aligned} \tag{7.1.11}$$

The corresponding Doppler shifts $\bar{f}_\mathrm{Dc}\left(\bar{u};\beta,\varphi_\mathrm{m}\right)$ are given by (2.2.7). In summary, the following sensing model can be formulated by combining (7.1.6) and (7.1.8) to

$$\begin{aligned} \boldsymbol{Y}_\mathrm{c}\left(\beta,\varphi_\mathrm{m}\right) &= \mathcal{B}\circ\mathcal{D}_f(\boldsymbol{X}_\mathrm{c};\beta,\varphi_\mathrm{m}) \\ &= \mathcal{A}_f(\boldsymbol{X}_\mathrm{c};\beta,\varphi_\mathrm{m}). \end{aligned} \tag{7.1.12}$$

Figure 7.1.2 shows an overview of the introduced model, where the "Doppler focused" clutter measurements $\boldsymbol{Y}_\mathrm{c}^{\mathrm{fc},f_\mathrm{D}}$, which correspond to measurements taken from $\boldsymbol{X}_\mathrm{c}$ directly, allow for valuable insights explained further below. As can be readily seen from Fig. 7.1.1, the original discretized clutter scene $\boldsymbol{X}_\mathrm{c}$ is supposed to be a low rank matrix formed by a single column or in other words all clutter contributions are supposed to be located at zero Doppler. Within the scope of this work, this is termed as the primary low-rank form of clutter measurements as it is the physically inspired form. The rank of the clutter scene observed by the radar is increased due to the motion induced Doppler shift. Nevertheless, this process is reversible in case the required parameters β and φ_m are available. These, in general, may be unknown or partially known from inertial measurement unit (IMU) measurements. As a matter of fact, however, it is possible to estimate these parameters from $\boldsymbol{Y}_\mathrm{c}$ directly, exploiting the aforementioned effect of the Doppler shift on the rank of $\boldsymbol{X}_\mathrm{c}^\mathrm{sh}$. This is discussed in more detail in the following Section 7.2.

The sensing model (7.1.12) reveals one important practical limitation which is not considered in the continuous model $y_\mathrm{c}(d',t';\beta,\varphi_\mathrm{m})$: it offers only a limited spatial aperture and sampling time. This gives rise to the following implications:

- Leakage of the clutter signal due to limited angular and Doppler resolution
- Incomplete measurements

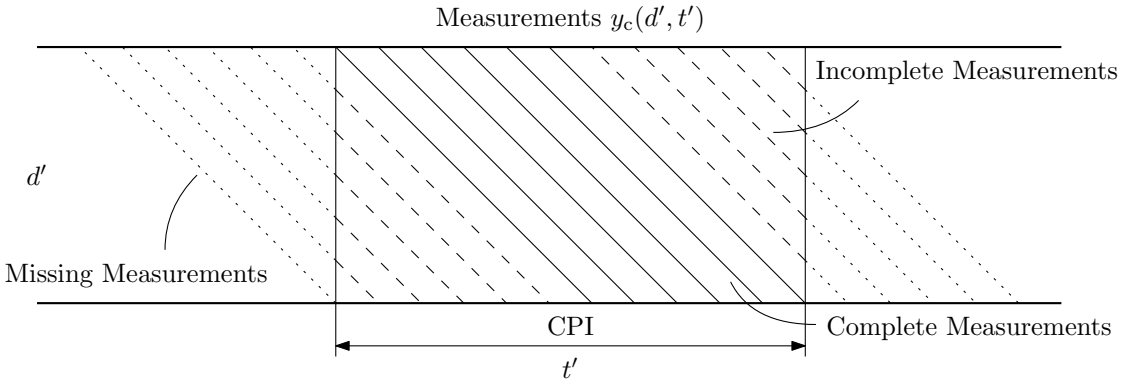

Figure 7.1.3.: Illustration of incomplete measurements due to limited CPI interval.

The limited angular and Doppler resolution causes side lobes in the angular and Doppler dimensions and as such the emerging clutter leakage potentially covers weak moving targets. This effect is circumvented by applying the techniques presented in Section 7.3. The effect of incomplete measurements is more severe but can be handled efficiently as will be discussed in the following sections. Incomplete measurements are all measurements which are cut off at the beginning and at the end of a coherent processing interval (CPI). This is illustrated in Fig. 7.1.3. Since a Fourier transformation assumes periodic signals, the temporal windowing due to the time limited CPI gives rise to a more densely populated spectrum[3] which corresponds to additional clutter leakage. Furthermore, the incomplete measurements also increase the minimum achievable rank of $\boldsymbol{X}_\mathrm{c}$ which can be found from $\boldsymbol{Y}_\mathrm{c}$. This is disadvantageous for the estimation of the parameters β and φ_m, as well as the separation of the low rank clutter from moving targets. To further investigate on this effect, consider how the clutter of the primal low rank form looks in the measurement domain as

$$\boldsymbol{Y}_\mathrm{c}^{\mathrm{fc},f_\mathrm{D}} = \mathcal{B}\left(\boldsymbol{X}_\mathrm{c}\right),$$

with the primal low rank form found from the observed clutter measurements as

$$\boldsymbol{X}_\mathrm{c} = \mathcal{A}_f^{-1}(\boldsymbol{Y}_\mathrm{c}; \beta, \varphi_\mathrm{m}).$$

The result of this inverse sensing operation, $\boldsymbol{Y}_\mathrm{c}^{\mathrm{fc},f_\mathrm{D}}$, is termed "Doppler focused" clutter measurements as the clutter ridge energy is focused onto $\bar{f}_\mathrm{D} = 0$. An illustration of the focused measurements is shown in Fig. 7.1.4[4]. At first note, that the measurement operator $\mathcal{B}$ consists of DFT matrices and as such is a unitary operator. The singular values of a matrix, and its rank respectively, are invariant with respect to unitary operations, hence, the rank of $\boldsymbol{W}$ and $\mathcal{B}\left(\boldsymbol{W}\right)$ are identical. We therefore can make statements regarding the low rank properties in both domains, the measurement as well as the radar scene domain. At this point, looking at the measurement domain is beneficial as will be seen shortly. Furthermore, note that a shift in the Doppler dimension in the radar scene domain corresponds to a shift in the spatial dimension in

[3] This corresponds to the FT of a step function.

[4] Strictly speaking, the illustrations in Fig. 7.1.4 are matrices to the contrary of the illustrations in Fig. 7.1.1 and Fig. 7.1.3, which correspond to the continuous measurement model. For sake of clarity, however, the column and row lines are omitted.

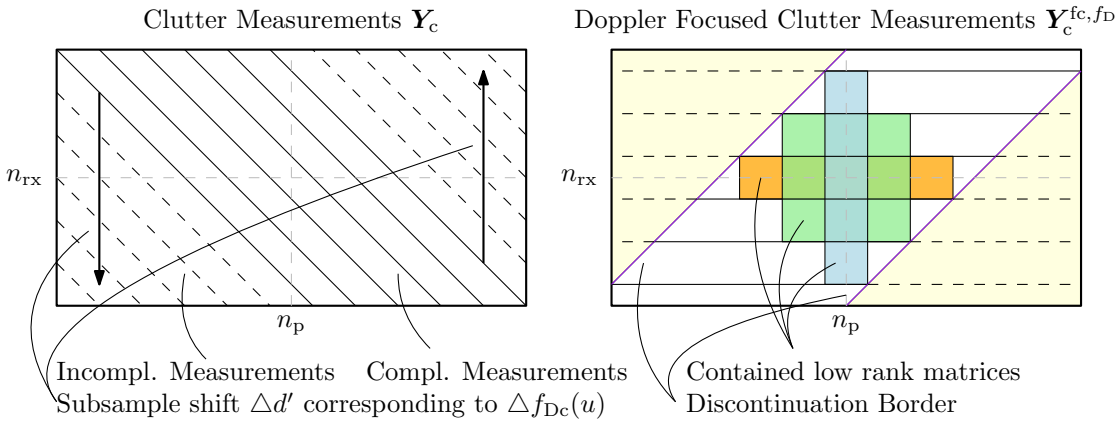

Figure 7.1.4.: Doppler focused clutter measurements $\boldsymbol{Y}_{\mathrm{c}}^{\mathrm{fc},f_{\mathrm{D}}}$ found from observed clutter measurements $\boldsymbol{Y}_{\mathrm{c}}$.

the measurement domain[5], which is indicated by the arrows in the left picture of Fig. 7.1.4. The result after a perfect shift back is illustrated on the right side of Fig. 7.1.4, which consists of three parts, two triangular areas containing the incomplete measurements and a central area holding all correlated complete measurements. The triangular forms emerge due to the cyclic nature of the Fourier shift operator $\mathcal{D}_f$. As can be seen, the Doppler focused measurement matrix $\boldsymbol{Y}_{\mathrm{c}}^{\mathrm{fc},f_{\mathrm{D}}}$ is not a low rank matrix due to the discontinuation border. Low rank matrices are available in the center part only and unfortunately only a small portion of the total measurements $N_{\mathrm{rx}}N_{\mathrm{p}}$ is usable to form those. The only possibility to increase the size of the available low rank matrix is to increase the number of channels N_{rx}, which in case of a radar system is inconvenient. A more advantages form offers the dual low-rank form of clutter measurements, which is presented in the following section.

7.1.2. The Dual Low-Rank Form

The primal low-rank form discussed in the previous section emerges from the physical interpretation of a non moving radar, which corresponds to all clutter components located at zero Doppler. Nevertheless, it is also possible to form a low-rank matrix from the shifted clutter scene $\boldsymbol{X}_{\mathrm{c}}^{\mathrm{sh}}$ by relocating all clutter components at zero angle i. e. $\bar{u}=0$ which may now be denoted as $\boldsymbol{X}_{\mathrm{c}}^{u}$ to distinguish it from the primary form $\boldsymbol{X}_{\mathrm{c}}$. This is illustrated in Fig. 7.1.5, where the shift amount in $\bar{u}$ for given β and φ_{m} is

$$\bar{u}_{\mathrm{c}}(\bar{f}_{\mathrm{D}};\beta,\varphi_{\mathrm{m}}) = -\frac{\bar{f}_{\mathrm{D}}}{\beta}\cos(\varphi_{\mathrm{m}}) + \sqrt{\bar{d}^2\sin^2(\vartheta) - \bar{f}_{\mathrm{D}}{}^2/\beta^2}\sin(\varphi_{\mathrm{m}}) \quad \text{for} \quad \left|\bar{f}_{\mathrm{D}}\right| \leq \bar{d}\sin(\vartheta)\,\beta, \tag{7.1.13}$$

for which (2.2.7) was used. Within (7.1.13), ϑ denotes the polar angle to the current range gate under test as shown in Fig. 2.1.2. In case of a flat earth condition, which is assumed in this work, ϑ renders to be a constant. For all simulations to follow, ϑ is assumed to be known and set to $\vartheta = \pi/2\,\mathrm{rad}$ which is a choice also used in [1]. The area $\bar{f}_{\mathrm{D}} > \bar{d}\sin(\vartheta)\,\beta$ is free of clutter,

[5] Recall, that a shift in Doppler in the radar scene relocates all Doppler components to zero, which in turn corresponds to a non moving radar. For a non moving radar and a static clutter scene, all antenna channels obtain constant measurements from pulse to pulse. Hence, the measurements align along the channel indices.

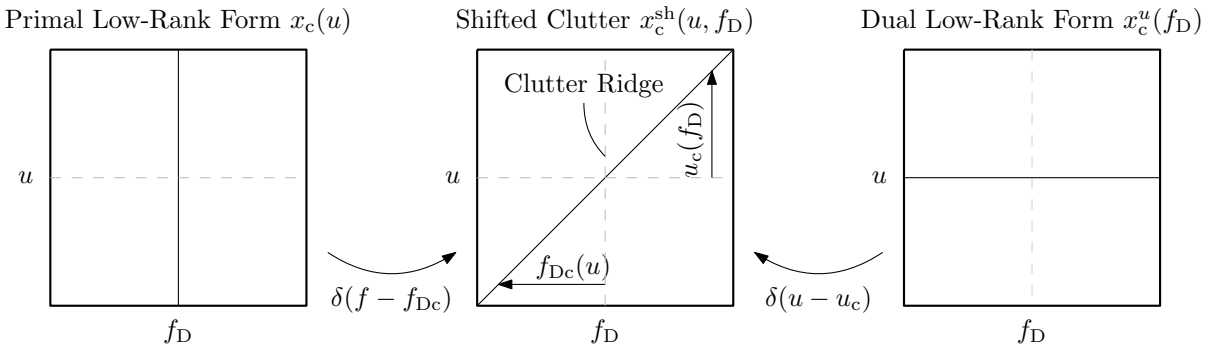

Figure 7.1.5.: Primal and dual low-rank clutter illustration.

however, this case does rarely occur in practice. In order to extend (7.1.13) to be defined for $\bar{f}_{\mathrm{D}} \in [-1/2, 1/2)$, it is modified to

$$\bar{u}_{\mathrm{c}}(\bar{f}_{\mathrm{D}}; \beta, \varphi_{\mathrm{m}}) = -\frac{\bar{f}_{\mathrm{D}}}{\beta} \cos(\varphi_{\mathrm{m}}) + \sqrt{\left|\bar{d}^2 \sin^2(\vartheta) - \bar{f}_{\mathrm{D}}{}^2/\beta^2\right|} \sin(\varphi_{\mathrm{m}}) \,. \tag{7.1.14}$$

This form is advantageous for gradient descent algorithms compared to (7.1.13). The shifted clutter scene is obtained from the discretized dual low rank form as

$$\boldsymbol{X}_{\mathrm{c}}^{\mathrm{sh}} = \mathcal{D}_u(\boldsymbol{X}_{\mathrm{c}}^{u}; \beta, \varphi_{\mathrm{m}}), \tag{7.1.15}$$

where $\mathcal{D}_u : \mathbb{C}^{N_{\mathrm{u}} \times N_{\mathrm{D}}} \to \mathbb{C}^{N_{\mathrm{u}} \times N_{\mathrm{D}}}$ is a sub sample shift operator realizing the shift $u - u_{\mathrm{c}}(f_{\mathrm{D}}; \beta, \varphi_{\mathrm{m}})$. It is modeled using the modified Fourier shift identity[6]

$$\mathcal{D}_u(\boldsymbol{X}; \beta, \varphi_{\mathrm{m}}) = \boldsymbol{F}_u \left(\boldsymbol{U}_{\triangle}(\beta, \varphi_{\mathrm{m}}) \odot \left(\boldsymbol{F}_u^{-1} \boldsymbol{X} \right) \right) \tag{7.1.16}$$

with $\boldsymbol{F}_u$ denoting a DFT matrix resulting in a FT of the $\bar{u}$ dimension and

$$\boldsymbol{U}_{\triangle}(\beta, \varphi_{\mathrm{m}}) = \exp\left(-\mathrm{j} 2\pi \boldsymbol{n}_{\bar{u}} \bar{\boldsymbol{u}}_{\triangle}^{\mathrm{T}}(\beta, \varphi_{\mathrm{m}}) \right) \tag{7.1.17}$$

the Fourier shift matrix with

$$\begin{aligned} \boldsymbol{n}_{\bar{u}} &= [0, 1, \ldots, N_{\mathrm{u}} - 1]^{\mathrm{T}} \\ \bar{\boldsymbol{u}}_{\triangle}(\beta, \varphi_{\mathrm{m}}) &= \left[\bar{u}_{\mathrm{c}}(i/N_{\mathrm{D}}; \beta, \varphi_{\mathrm{m}}) \right]_{i=-N_{\mathrm{D}}/2}^{N_{\mathrm{D}}/2-1} . \end{aligned} \tag{7.1.18}$$

The dual form sensing operator yielding the clutter measurement samples is

$$\begin{aligned} \boldsymbol{Y}_{\mathrm{c}}(\beta, \varphi_{\mathrm{m}}) &= \mathcal{B} \circ \mathcal{D}_u(\boldsymbol{X}_{\mathrm{c}}^{u}; \beta, \varphi_{\mathrm{m}}) \\ &= \mathcal{A}_u(\boldsymbol{X}_{\mathrm{c}}^{u}; \beta, \varphi_{\mathrm{m}}), \end{aligned} \tag{7.1.19}$$

where (7.1.7) and (7.1.15) was used. Figure 7.1.6 shows an overview of the dual low rank form model. Again the "angle focused" clutter measurements

$$\boldsymbol{Y}_{\mathrm{c}}^{\mathrm{fc},u} = \mathcal{B}(\boldsymbol{X}_{\mathrm{c}}^{u}) \tag{7.1.20}$$

[6] This allows for optimizations later on.

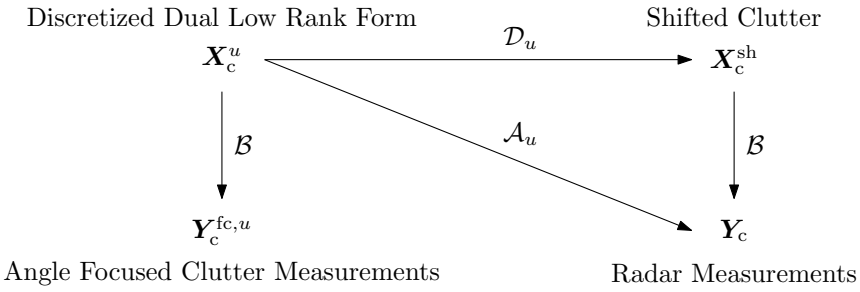

Figure 7.1.6.: Illustration of the discretized primal low rank form sensing model.

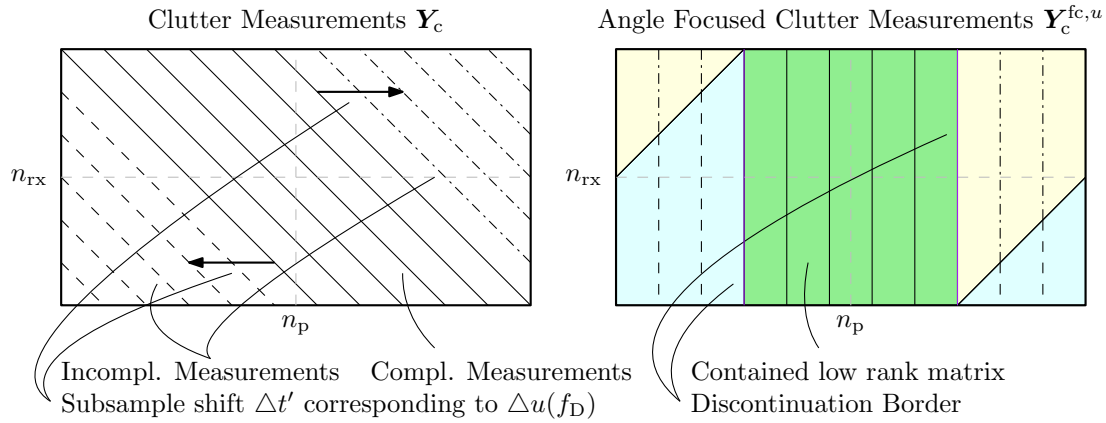

Figure 7.1.7.: Angle focused clutter measurements $\boldsymbol{Y}_{\mathrm{c}}^{\mathrm{fc},u}$ found from observed clutter measurements $\boldsymbol{Y}_{\mathrm{c}}$.

with the dual low rank form found from the observed clutter measurements as

$$\boldsymbol{X}_{\mathrm{c}}^{u} = \mathcal{A}_u^{-1}(\boldsymbol{Y}_{\mathrm{c}}; \beta, \varphi_{\mathrm{m}})$$

yield valuable insight regarding the effect of incomplete measurements. This is illustrated in Fig. 7.1.7. A shift in the angular dimension in the radar scene domain corresponds to a shift in the temporal dimension in the measurement domain. As a consequence, the size of the low-rank matrix contained in $\boldsymbol{Y}_{\mathrm{c}}^{\mathrm{fc},u}$ can be increased by increasing the number of pulses N_{p}[7], which is convenient for pulsed radar systems. Thus, the dual low-rank form is beneficial in terms of sample efficiency and is therefore used in this work. The primary low-rank form is beneficial in case of many available antennas e. g. in sonar applications. The total length of the incomplete measurements in the angle focused measurements $\boldsymbol{Y}_{\mathrm{c}}^{\mathrm{fc},u}$ given in number of pulses n_{tr} equals one aperture length

$$N_{\mathrm{rx}} d = v_{\mathrm{p}} \frac{n_{\mathrm{tr}}}{f_{\mathrm{p}}}$$

and as such the length is approximately

$$n_{\mathrm{tr}}(\beta) \simeq 2 \left\lfloor \frac{N_{\mathrm{rx}}}{\beta} \right\rfloor, \tag{7.1.21}$$

[7] Increasing the number of pulses increases the number of complete measurements.

where (2.2.5) was used. By use of this length, a cutting operator $\mathcal{C} : \mathbb{C}^{N_{\mathrm{rx}} \times N_{\mathrm{p}}} \rightarrow \mathbb{C}^{N_{\mathrm{rx}} \times N_{\mathrm{p}}}$ can be defined as

$$\mathcal{C}(\boldsymbol{Y}, \beta) = \boldsymbol{Z}(\beta) \odot \boldsymbol{Y}, \tag{7.1.22}$$

where

$$\boldsymbol{Z}(\beta) = \left[\mathbf{0}_{N_{\mathrm{rx}} \times n_{\mathrm{tr}}(\beta)/2} \mathbf{1}_{N_{\mathrm{rx}} \times (N_{\mathrm{p}} - n_{\mathrm{tr}})} \mathbf{0}_{N_{\mathrm{rx}} \times n_{\mathrm{tr}}(\beta)/2}\right]$$

is a matrix of zero and one block matrices. Applying the cutting operator onto the back shifted measurement as

$$\boldsymbol{Y}_{\mathrm{c}}^{\mathrm{fcct},u} = \mathcal{C}\left(\boldsymbol{Y}_{\mathrm{c}}^{\mathrm{fc},u}, \beta\right) \tag{7.1.23}$$

sets all non complete measurements within $\boldsymbol{Y}_{\mathrm{c}}^{\mathrm{fc},u}$ to zero, yielding $\boldsymbol{Y}_{\mathrm{c}}^{\mathrm{fcct},u}$ to be a matrix with the same singular values (and thus rank) as of the contained low rank matrix illustrated in Fig. 7.1.7.

Until this point, the low-rank forms of the static clutter measurements were presented from a theoretical point of view. The following section illustrates the dual low-rank form for various simulated clutter scenarios in order to validate the sensing operator formulation (7.1.19).

7.1.3. Evaluation of the Dual Low-Rank Form by Use of Simulations

The theoretic introduction in the previous section may suggest, at a first glance, that the dual low-rank form after excluding incomplete measurements is always a rank one matrix. Unfortunately, this is not the case due to the discretization in the measurement domain. For this to be true, fully correlated measurements are necessary as will be shown in the following. The continuous auto correlation function (7.1.4) reveals perfectly correlated measurements to exist if

$$u \triangle d' + f_{\mathrm{Dc}}\left(u; \beta, \varphi_{\mathrm{m}}\right) \triangle t' = 0$$

holds, which for continuous spatial and temporal displacements $\triangle d'$ and $\triangle t'$ is always possible. In the discretized (and here normalized) version, this condition becomes

$$\bar{u}\tilde{n}_{\mathrm{rx}} + \bar{f}_{\mathrm{Dc}}\left(\bar{u}; \beta, \varphi_{\mathrm{m}}\right) \tilde{n}_{\mathrm{p}} = 0, \tag{7.1.24}$$

where $\tilde{n}_{\mathrm{rx}} \in \mathbb{N}$ and $\tilde{n}_{\mathrm{p}} \in \mathbb{N}$ denote the channel and pulse differences. Condition (7.1.24) is a Diophantine equation which, depending on the parameters β and φ_{m}, may not allow for any non-trivial solution else than $\tilde{n}_{\mathrm{rx}} = \tilde{n}_{\mathrm{p}} = 0$. Hence the clutter measurements may not be fully, but nevertheless strongly correlated. The correlation between the measurement samples is given by (2.2.18) as

$$R_{\mathrm{c}}\left(\tilde{n}_{\mathrm{rx}}, \tilde{n}_{\mathrm{p}}; \beta, \varphi_{\mathrm{m}}\right) = \int_{-\bar{d}}^{\bar{d}} P_{\mathrm{c}}\left(\bar{u}\right) \mathrm{e}^{\mathrm{j}2\pi\bar{u}\tilde{n}_{\mathrm{rx}} + \mathrm{j}2\pi\bar{f}_{\mathrm{Dc}}(\bar{u};\beta,\varphi_{\mathrm{m}})\tilde{n}_{\mathrm{p}}} \mathrm{d}\bar{u},$$

where the clutter distribution was assumed to be independent, i. e. the clutter power is $P_{\mathrm{c}}\left(\bar{u}\right) = \mathrm{E}\left\{\left|x_{\mathrm{c}}\left(\bar{u}\right)\right|^2\right\}$. As an example, in case of no velocity misalignment and homogeneous clutter distribution, the correlation has the closed form solution (2.2.22), which was

$$R_{\mathrm{c}}\left(\tilde{n}_{\mathrm{rx}}, \tilde{n}_{\mathrm{p}}; \beta\right) = 2\bar{d}P_{\mathrm{c}} \operatorname{sinc}\left(2\bar{d}\left(\tilde{n}_{\mathrm{rx}} + \beta\tilde{n}_{\mathrm{p}}\right)\right). \tag{7.1.25}$$

Level	β	φ_{m}	Back-Attenuation	ICM	Remarks
1	$\mathbb{N}$	-	-	-	DPCA condition, measurements fully correlated
2	$\mathbb{R}$	-	-	-	measurements partially correlated
3	$\mathbb{R}$	$\neq 0$	-	-	velocity misalignment present
4	$\mathbb{R}$	$\neq 0$	$\neq 0$	-	reflections from the rear side of the radar present
5	$\mathbb{R}$	$\neq 0$	$\neq 0$	$\neq 0$	ICM further reduces measurement correlation

Table 7.1.1.: Levels of difficulties considered for GMTI simulations.

From this special case it is obvious to see that for different combinations of channels and pulses a high correlation can be present e. g. in case[8]

$$2\bar{d}\left(\tilde{n}_{\mathrm{rx}}+\beta\tilde{n}_{\mathrm{p}}\right)\lesssim\frac{1}{2}.$$

For not fully correlated samples it is not possible to find a mathematically strict low-rank matrix. For strongly correlated samples, however, it is possible to find an accurate approximation or effective low-rank matrix. Consider the noisy sensing operation derived from (7.1.19)

$$\boldsymbol{Y}_{\mathrm{c}}\left(\beta,\varphi_{\mathrm{m}}\right)=\mathcal{A}_u(\boldsymbol{X}_{\mathrm{c}}^u;\beta,\varphi_{\mathrm{m}})+\boldsymbol{N}, \tag{7.1.26}$$

with the entries of $\boldsymbol{N}\sim\mathcal{CN}(0,P_{\mathrm{n}})$ i. i. d., where P_{n} denotes the noise power. The effective rank of $\boldsymbol{X}_{\mathrm{c}}^u$ may now be defined similar to (2.3.9) as the number of singular values $\sigma\left(\boldsymbol{X}_{\mathrm{c}}^u\right)$ which are bigger than the maximum noise singular value $\sigma_{\max}(\boldsymbol{N})=\|\boldsymbol{N}\|_2$

$$\rho_{\mathrm{eff}}=\sum_{i=1}^{\max(N_{\mathrm{u}},N_{\mathrm{D}})}\mathbb{I}\left(\sigma_i\left(\boldsymbol{X}_{\mathrm{c}}^u\right)>\sigma_{\max}(\boldsymbol{N})\right),$$

where $\mathbb{I}(\cdot)$ denotes the indicator function. In the following, this effective rank will be illustrated for various clutter scenarios.

Within the realm of ground moving target indication (GMTI) various decorrelation effects are known which in turn increase the minimum achievable effective rank[9] of $\boldsymbol{X}_{\mathrm{c}}^u$ from $\boldsymbol{Y}_{\mathrm{c}}$. Examples of these decorrelation effects considered within this work are a non present displaced phase center antenna (DPCA) condition i. e. $\beta\in\mathbb{R}$, present velocity misalignment angle i. e. $\varphi_{\mathrm{m}}\neq 0$, reflections from the rear side of the radar denoted as back attenuation[10], and internal clutter motion (ICM). These effects individually and in combination complicate the successful detection of moving targets. For their evaluation, certain "levels of difficulty", as defined in Tab. 7.1.1, are introduced in this work, combining the aforementioned effects in ascending order of severeness. The considered effects are by no means exhaustive. Additional effects, subject to further investigations, are e. g. impacts of non perfectly calibrated antennas, broad band decorrelation effects, range walk decorrelation, etc. More information regarding these effects can be found in [1].

[8] In this case, the correlation would be $\mathrm{sinc}\left(1/2\right)\gtrsim 0.63$.

[9] In the classical STAP theory, these decorrelation effects increase the rank of the covariance matrix, resulting in an increased number of required training samples for its estimation.

[10] This effect may be negligible for side mounted arrays, for bottom mounted circular arrays, however, it is not.

The following simulations show scenarios for the various levels of difficulty as defined in Tab. 7.1.1 for a radar corresponding to the parameters shown in Tab. 1.0.1. Furthermore, a broadside oriented ULA antenna with $d = \lambda_\mathrm{c}/2$ element spacing was assumed. As such the normalized Doppler frequency is $\bar{f}_\mathrm{D} \in [-1/2, 1/2)$ and the normalized direction cosine is $\bar{u} \in [-1/2, 1/2)$. Also, the clutter was assumed to be Rayleigh distributed. The low rank properties of the dual low rank form are evaluated by the following procedure:

- For given parameters β and φ_m, clutter measurements $\boldsymbol{Y}_\mathrm{c}$ are simulated by use of (7.1.1)
- For a comparison with noise singular values a noise matrix $\boldsymbol{N} \sim \mathcal{CN}(0,1)$ is simulated (but not added to $\boldsymbol{Y}_\mathrm{c}$)
- The properties of the low rank forms are evaluated by comparing the respective singular values to the noise singular values in the order described in the former sections:
  - the shifted clutter measurements observed from the radar $\boldsymbol{X}_\mathrm{c}^\mathrm{sh} = \mathcal{B}^{-1}\left(\boldsymbol{Y}_\mathrm{c}\right)$
  - the dual low rank form in the radar scene domain $\boldsymbol{X}_\mathrm{c}^u = \mathcal{D}_u^{-1}(\boldsymbol{X}_\mathrm{c}^\mathrm{sh}; \beta, \varphi_\mathrm{m})$
  - the corresponding angle focused measurement $\boldsymbol{Y}_\mathrm{c}^{\mathrm{fc},u} = \mathcal{B}\left(\boldsymbol{X}_\mathrm{c}^u\right)$
  - the cut angle-focused measurements $\boldsymbol{Y}_\mathrm{c}^{\mathrm{fcct},u} = \mathcal{C}\left(\boldsymbol{Y}_\mathrm{c}^{\mathrm{fc},u}, \beta\right)$ and
  - the respective appearance in the radar scene domain $\boldsymbol{X}_\mathrm{c}^{\mathrm{ct},u} = \mathcal{B}^{-1}\left(\boldsymbol{Y}_\mathrm{c}^{\mathrm{fcct},u}\right)$.

Recall from Section 7.1.1, that $\mathcal{B}$ is a unitary operator and hence $\boldsymbol{Y}_\mathrm{c}^{\mathrm{fc},u}$ and $\boldsymbol{X}_\mathrm{c}^u$, as well as $\boldsymbol{Y}_\mathrm{c}^{\mathrm{fcct},u}$ and $\boldsymbol{X}_\mathrm{c}^{\mathrm{ct},u}$, have the same singular values. Their respective appearances in the measurement and radar scene domain are shown for illustrative purposes only. For the angle focus operations $\mathcal{D}_u^{-1}(\boldsymbol{X}_\mathrm{c}^\mathrm{sh}; \beta, \varphi_\mathrm{m})$, the parameters β and φ_m are assumed to be known. Later on, we attempt to estimate these parameters during the clutter focus procedure, which is presented in Section 7.2.

Dual Low Rank Form for DPCA Condition The following example illustrates the dual low rank form in case of a fulfilled DPCA condition for the specifically chosen parameters $\beta = 1$, and $\varphi_\mathrm{m} = 0$. Within this work, this is termed a level one difficulty as listed in Tab. 7.1.1. The DPCA condition is depicted in Fig. 2.2.3, where preceding antenna phase centers are located at the position of leading phase centers for subsequent pulses. In this case, the entries in $\boldsymbol{Y}_\mathrm{c}$ simplify to

$$y_{\mathrm{c},n_\mathrm{rx}n_\mathrm{p}} = \int_{-\bar{d}}^{\bar{d}} x\left(\bar{u}\right) \mathrm{e}^{\mathrm{j}2\pi\bar{u}(n_\mathrm{rx}+n_\mathrm{p})} \mathrm{d}\bar{u},$$

which obviously gives identical samples for $n_\mathrm{rx} + n_\mathrm{p} = \mathrm{const.}$ in case of static clutter[11]. Furthermore, the correlation of the samples is given by the closed form solution (7.1.25). In this case, the Diophantine equation (7.1.24) allows for non-trivial solutions, hence, there exist channel and pulse differences $\tilde{n}_\mathrm{rx}$ and $\tilde{n}_\mathrm{p}$ such that the correlation (7.1.25) yields a maximum. An illustration of such fully correlated measurements is shown in Fig. 7.1.8. The achievable dual low rank form for such a setting is depicted in Fig. 7.1.9. At first, notice the non low rank nature of the shifted

[11] Which means if the clutter does not change from pulse to pulse.

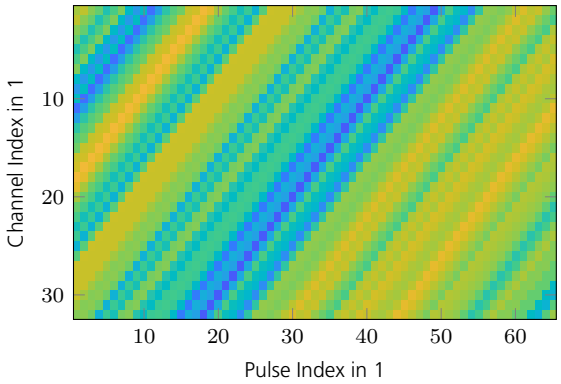

Figure 7.1.8.: Measurement matrix $\boldsymbol{Y}_{\mathrm{c}}$ in case of DPCA condition.

clutter scene $\boldsymbol{X}_{\mathrm{c}}^{\mathrm{sh}}$ from Fig. 7.1.9a and the corresponding singular values in Fig. 7.1.9b. Due to limited angular and Doppler resolution and the incomplete measurement phenomena described in Section 7.1.1, strong clutter leakage is present. The singular values do not drop below the noise singular values, hence, $\boldsymbol{X}_{\mathrm{c}}^{\mathrm{sh}}$ is of full effective rank. The dual low rank form $\boldsymbol{X}_{\mathrm{c}}^{u}$ and the corresponding singular values are shown in Fig. 7.1.9c and 7.1.9d. The clutter ridge is now focused at $\bar{u} = 0$, however, the clutter leakage now shows a diagonal course caused by the circular shift operation $\mathcal{D}_{u}^{-1}$. As a consequence, the clutter singular values in Fig. 7.1.9d show a more concentrated energy at the first singular vectors but due to the diagonal leakage course, the clutter singular values do not drop below the noise singular values. The dual low rank form $\boldsymbol{X}_{\mathrm{c}}^{u}$ therefore also has full effective rank. Nevertheless, $\boldsymbol{X}_{\mathrm{c}}^{u}$ is more similar to a low rank matrix compared to the shifted clutter scene $\boldsymbol{X}_{\mathrm{c}}^{\mathrm{sh}}$. Figure 7.1.9e shows the dual low rank form $\boldsymbol{X}_{\mathrm{c}}^{u}$ in the measurement domain i. e. the angle focused clutter measurements $\boldsymbol{Y}_{\mathrm{c}}^{\mathrm{fc},u}$. At first, notice the three areas: two triangular areas containing the incomplete measurements and a central area holding all fully correlated complete measurements. This arrangement is similar to the sketched version in Fig. 7.1.7. Due to the fulfilled DPCA condition, the complete measurements form constant columns which give a perfect rank one matrix. This matrix is revealed by applying the cutting operator which sets all triangular areas of incomplete measurements to zero. The result $\boldsymbol{Y}_{\mathrm{c}}^{\mathrm{fcct},u}$, the corresponding appearance in the radar scene domain $\boldsymbol{X}_{\mathrm{c}}^{\mathrm{ct},u}$, and the respective singular values are shown in Fig. 7.1.9f, 7.1.9g, and 7.1.9h. As can be seen, the result of the cutting operation reveals a perfect rank one matrix. All clutter leakage effects caused by the incomplete clutter measurements are suppressed, therefore only the clutter ridge focused at $\bar{u} = 0$ remains[12]. The singular values accordingly show a sharp drop off. Such a clean result is possible only due to the fulfilled DPCA condition. The following example illustrates the achievable dual low rank form for non DPCA conditioned measurements.

[12]While the contained low rank matrix is a true rank one matrix, the clutter is unfortunately spiky i. e. the support of the clutter in $\boldsymbol{X}_{\mathrm{c}}^{\mathrm{ct},u}$ is not spread out. As explained in Section 5, this results in an identification issue between sparse and low rank matrices. Hence, without any modifications to turbo compressed robust principal component analysis (TCRPCA) we can not expect to be able to conduct a successful separation of clutter and moving targets. More on this topic will be discussed later.

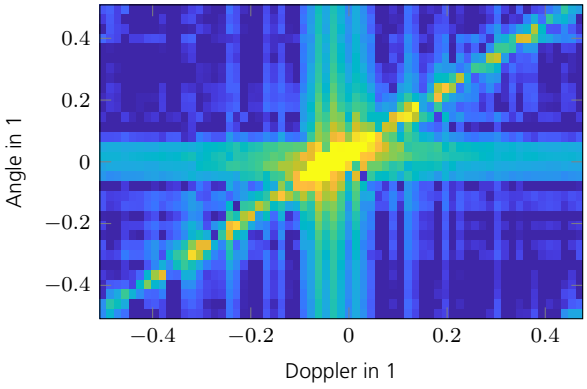

(a) Shifted clutter in scene domain $\boldsymbol{X}_{\mathrm{c}}^{\mathrm{sh}} = \mathcal{B}^{-1}\left(\boldsymbol{Y}_{\mathrm{c}}\right)$.

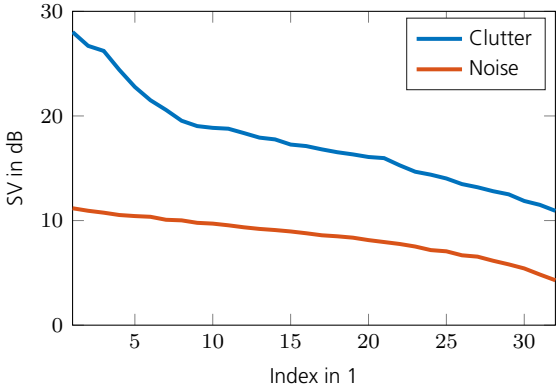

(b) singular value decomposition (SVD) of $\boldsymbol{Y}_{\mathrm{c}}$ and $\boldsymbol{X}_{\mathrm{c}}^{\mathrm{sh}}$.

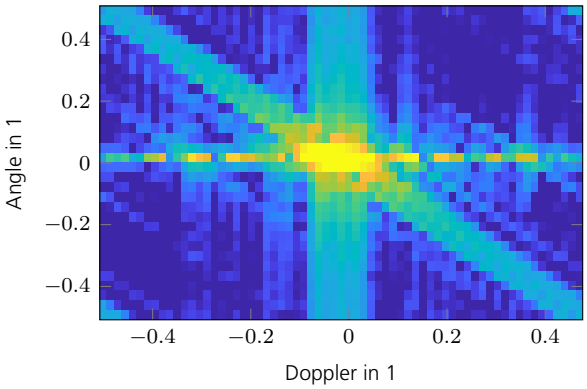

(c) The dual low rank form $\boldsymbol{X}_{\mathrm{c}}^{u} = \mathcal{D}_{u}^{-1}(\boldsymbol{X}_{\mathrm{c}}^{\mathrm{sh}}; \beta, \varphi_{\mathrm{m}})$.

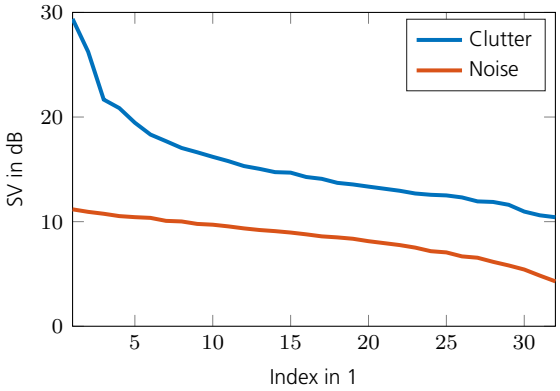

(d) SVD of $\boldsymbol{Y}_{\mathrm{c}}^{\mathrm{fc},u}$ and $\boldsymbol{X}_{\mathrm{c}}^{u}$.

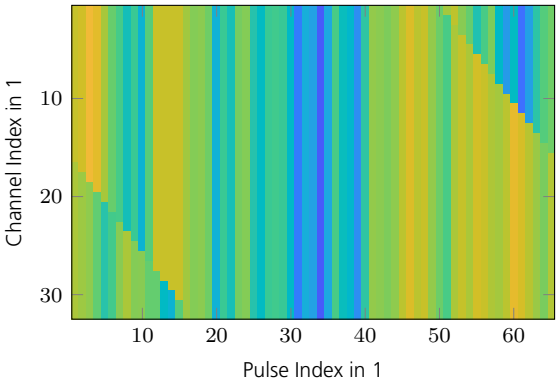

(e) Angle-focused clutter measurements $\boldsymbol{Y}_{\mathrm{c}}^{\mathrm{fc},u} = \mathcal{B}\left(\boldsymbol{X}_{\mathrm{c}}^{u}\right)$.

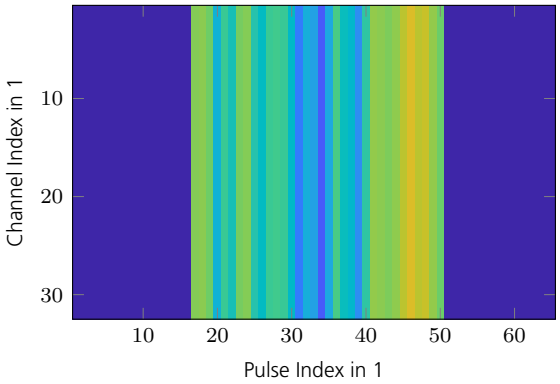

(f) Cut angle-focused measurements $\boldsymbol{Y}_{\mathrm{c}}^{\mathrm{fcct},u} = \mathcal{C}\left(\boldsymbol{Y}_{\mathrm{c}}^{\mathrm{fc},u}, \beta\right)$.

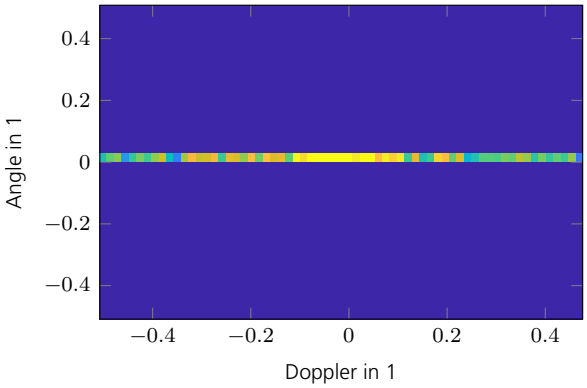

(g) Result of cut in scene domain $\boldsymbol{X}_{\mathrm{c}}^{\mathrm{ct},u} = \mathcal{B}^{-1}\left(\boldsymbol{Y}_{\mathrm{c}}^{\mathrm{fcct},u}\right)$.

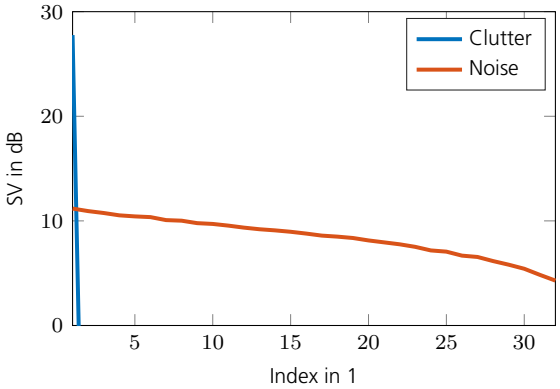

(h) SVD of $\boldsymbol{Y}_{\mathrm{c}}^{\mathrm{fcct},u}$ and $\boldsymbol{X}_{\mathrm{c}}^{\mathrm{ct},u}$.

Figure 7.1.9.: The dual low rank form for a level one setting with $\beta = 1$.

Dual Low Rank Form for Non-DPCA Condition The following example illustrates the dual low rank form in case of a non fulfilled DPCA condition for the specifically chosen parameters $\beta = 2.5$, and $\varphi_{\mathrm{m}} = 0$. Within this work, this is termed a level two difficulty as listed in Tab. 7.1.1. In this case, the Diophantine equation (7.1.24) does allow only for a few non-trivial solutions, hence, the majority of the measurement samples in $\boldsymbol{Y}_{\mathrm{c}}$ are not fully correlated[13]. This increases the minimum achievable rank of the dual low rank form. Furthermore, in case of $\beta > 1$ Doppler ambiguities occur, which in turn also increases the minimum achievable rank[14]. The corresponding measurement matrix $\boldsymbol{Y}_{\mathrm{c}}$ and the dual low rank form are depicted in Fig. 7.1.10 and 7.1.11. The Doppler ambiguities can be seen from the clutter ridge in Fig. 7.1.11a, which after focusing, appear as additional rows in the dual low rank form $\boldsymbol{X}_{\mathrm{c}}^{u}$ as shown in Fig. 7.1.11c. To the contrary of the former level one example where $\beta = 1$, the dual low rank form for $\beta = 2.5$ already is an effective low rank matrix as can be seen from its singular values plotted in Fig. 7.1.11d. This is because the size of incomplete measurements in pulses decreases as β increases according to (7.1.21). Therefore, the ratio of incomplete to complete sample in this example is proportionally less as can be seen in the angle focused clutter measurements $\boldsymbol{Y}_{\mathrm{c}}^{\mathrm{fc},u}$. This is the reason why the singular values of the dual low rank form plotted in Fig. 7.1.11d show a sharper drop off as the incomplete measurements are less influencing. The final contained low rank matrix shown in Fig. 7.1.11g is not a rank one matrix any more due to the non fully correlated samples in $\boldsymbol{Y}_{\mathrm{c}}$ and the occurring Doppler ambiguities. From this example it is foreseeable that any decorrelating effect increases the minimum achievable rank. The next example illustrates that for present velocity misalignment.

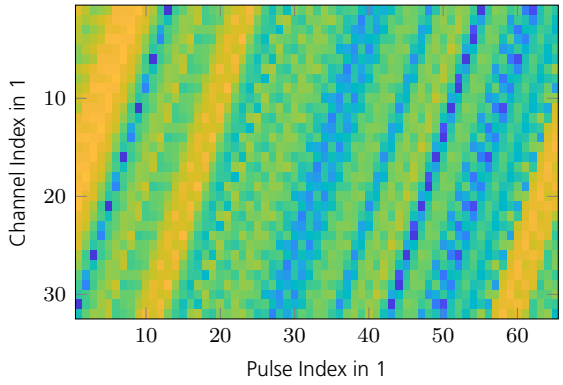

Figure 7.1.10.: Measurement matrix $\boldsymbol{Y}_{\mathrm{c}}$ for a level two setting with $\beta = 2.5$.

Dual Low Rank Form for Additional Velocity Misalignment The following example illustrates the dual low rank form in case of a non fulfilled DPCA condition and additional velocity misalignment for the specifically chosen parameters $\beta = 2.5$, and $\varphi_{\mathrm{m}} = 0.35\,\mathrm{rad}$. Within this work, this is termed a level three difficulty as listed in Tab. 7.1.1. In this case, the Diophantine equation (7.1.24) does allow even less non-trivial solutions, hence, the measurement samples in $\boldsymbol{Y}_{\mathrm{c}}$ are less correlated which in turn further increases the minimum achievable rank of the dual low

[13] For the specific choice of $\beta = 2.5$, the Diophantine equation (7.1.24) becomes $\tilde{n}_{\mathrm{rx}} + 2.5\tilde{n}_{\mathrm{p}} = 0$, i. e. every fifth measurement is fully correlated.

[14] Recall that β is the slope of the clutter ridge, hence, for $\beta > 1$, the clutter ridge "wraps" as soon as the emerging clutter Doppler frequency becomes bigger than the pulse repetition frequency (PRF) as $\left|\bar{f}_{\mathrm{Dc}}\left(\bar{u}\right)\right| > {}^{f_{\mathrm{P}}}/_{2}$.

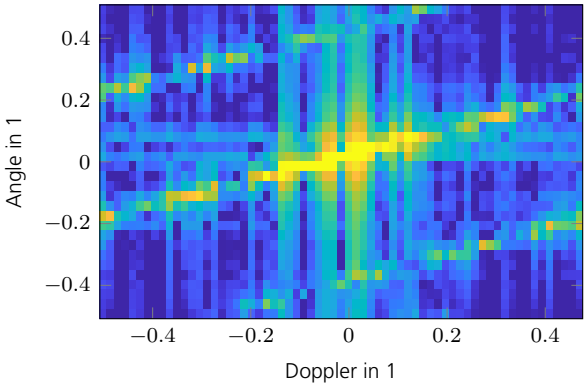

(a) Shifted clutter in scene domain $\boldsymbol{X}_{\mathrm{c}}^{\mathrm{sh}} = \mathcal{B}^{-1}\left(\boldsymbol{Y}_{\mathrm{c}}\right)$.

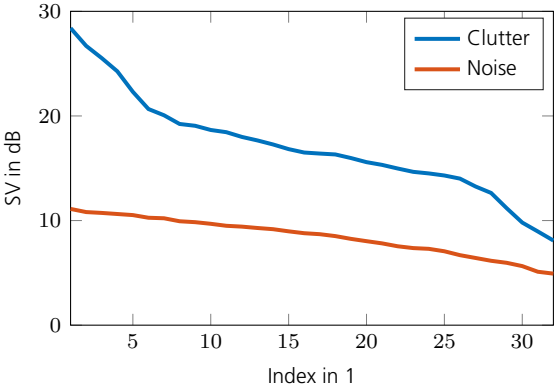

(b) SVD of $\boldsymbol{Y}_{\mathrm{c}}$ and $\boldsymbol{X}_{\mathrm{c}}^{\mathrm{sh}}$.

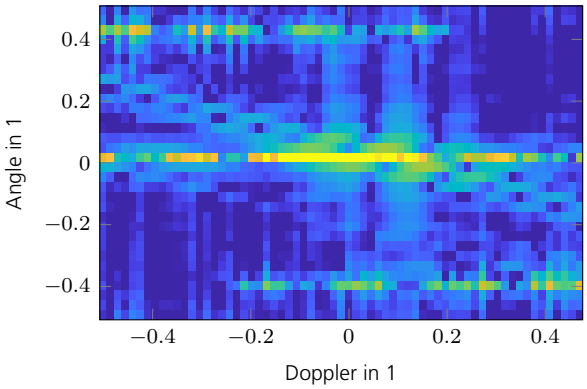

(c) The dual low rank form $\boldsymbol{X}_{\mathrm{c}}^{u} = \mathcal{D}_{u}^{-1}(\boldsymbol{X}_{\mathrm{c}}^{\mathrm{sh}}; \beta, \varphi_{\mathrm{m}})$.

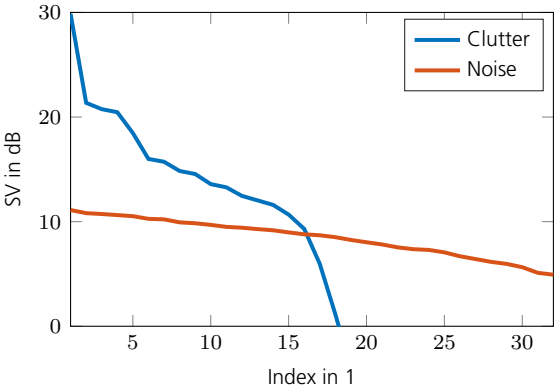

(d) SVD of $\boldsymbol{Y}_{\mathrm{c}}^{\mathrm{fc},u}$ and $\boldsymbol{X}_{\mathrm{c}}^{u}$.

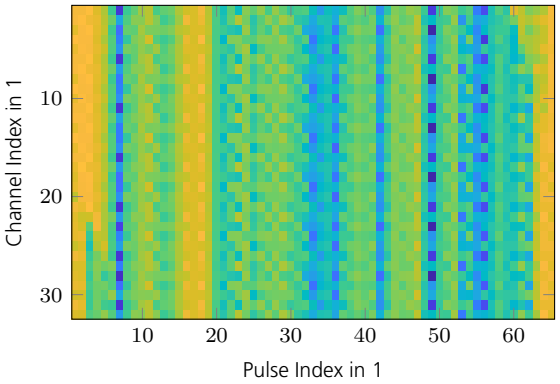

(e) Angle-focused clutter measurements $\boldsymbol{Y}_{\mathrm{c}}^{\mathrm{fc},u} = \mathcal{B}\left(\boldsymbol{X}_{\mathrm{c}}^{u}\right)$.

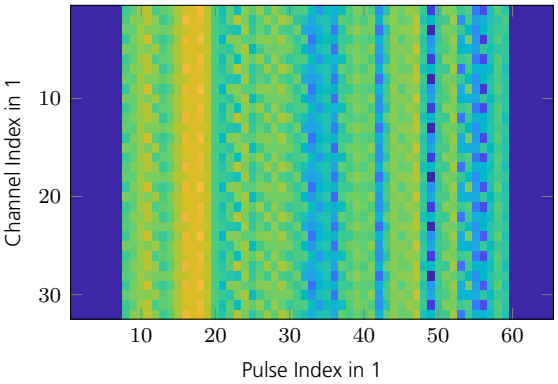

(f) Cut angle-focused measurements $\boldsymbol{Y}_{\mathrm{c}}^{\mathrm{fcct},u} = \mathcal{C}\left(\boldsymbol{Y}_{\mathrm{c}}^{\mathrm{fc},u}, \beta\right)$.

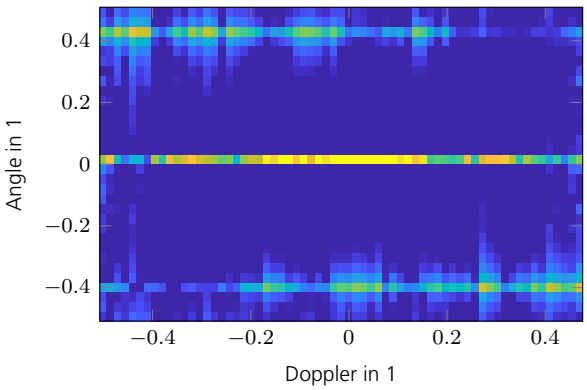

(g) Result of cut in scene domain $\boldsymbol{X}_{\mathrm{c}}^{\mathrm{ct},u} = \mathcal{B}^{-1}\left(\boldsymbol{Y}_{\mathrm{c}}^{\mathrm{fcct},u}\right)$.

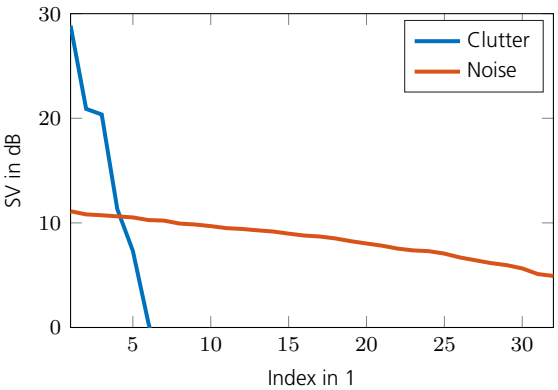

(h) SVD of $\boldsymbol{Y}_{\mathrm{c}}^{\mathrm{fcct},u}$ and $\boldsymbol{X}_{\mathrm{c}}^{\mathrm{ct},u}$.

Figure 7.1.11.: Dual low rank form for level two setting with $\beta = 2.5$.

rank form. The results are shown in Fig. 7.1.12 and Fig. 7.1.13. The effect of velocity misalignment can be seen from the clutter ridge in Fig. 7.1.13a. To the contrary of the former presented examples, where the clutter ridge formed a straight line, the clutter ridge with present velocity misalignment describes a curve [1]. For this reason and in case of $\beta > 1$, the shift operator $\mathcal{D}_u^{-1}$ can not focus the clutter ridge onto single rows any more as can be seen in Fig. 7.1.13c. This is due to the fact that the Doppler ambiguities would require a different shifting amount than the aliased main clutter. Hence, the achievable clutter rank is again increased as can be seen in Fig. 7.1.13h. A velocity misalignment of $0.35\,\mathrm{rad} \simeq 20°$ is of course not a realistic setting but this value was chosen to test the robustness of the dual low rank form. Despite the aforementioned shortcoming of the shifting operator, it is still possible to form a solid dual low rank form from $\boldsymbol{Y}_\mathrm{c}$. The next example illustrates the effects of limited back attenuation i. e. present reflections from the rear side of the radar.

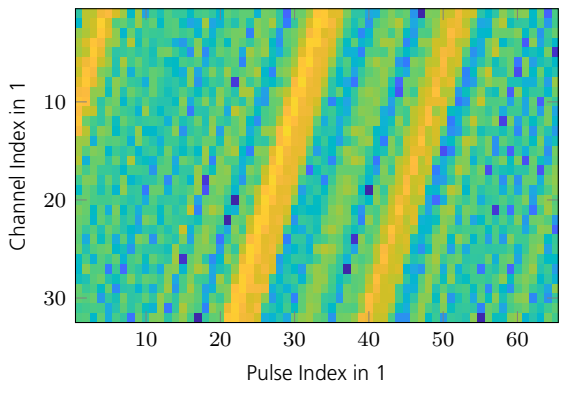

Figure 7.1.12.: Measurement matrix $\boldsymbol{Y}_\mathrm{c}$ for a level three setting with $\beta = 2.5$ and $\varphi_\mathrm{m} = 0.35\,\mathrm{rad}$.

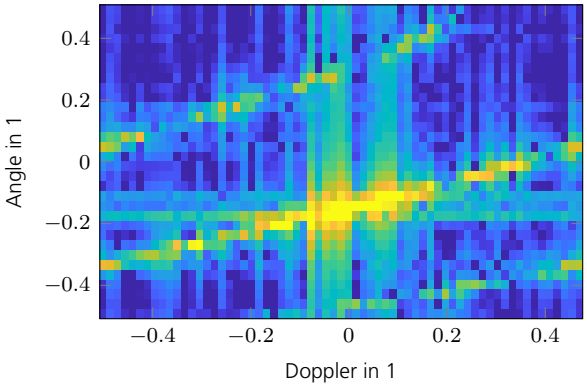

(a) Shifted clutter in scene domain $\boldsymbol{X}_{\mathrm{c}}^{\mathrm{sh}} = \mathcal{B}^{-1}\left(\boldsymbol{Y}_{\mathrm{c}}\right)$.

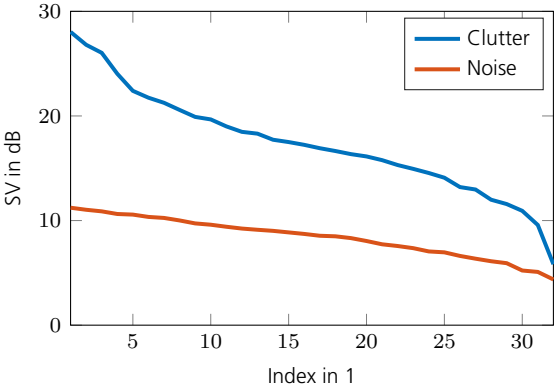

(b) SVD of $\boldsymbol{Y}_{\mathrm{c}}$ and $\boldsymbol{X}_{\mathrm{c}}^{\mathrm{sh}}$.

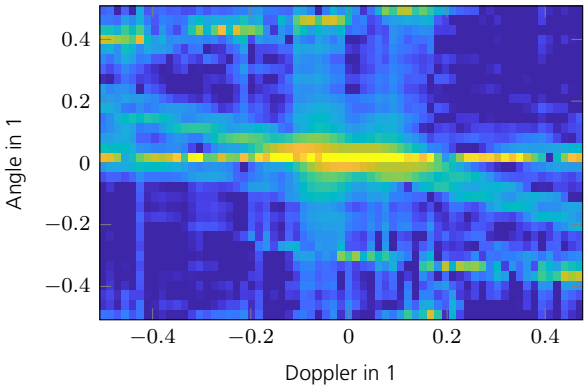

(c) The dual low rank form $\boldsymbol{X}_{\mathrm{c}}^{u} = \mathcal{D}_{u}^{-1}(\boldsymbol{X}_{\mathrm{c}}^{\mathrm{sh}}; \beta, \varphi_{\mathrm{m}})$.

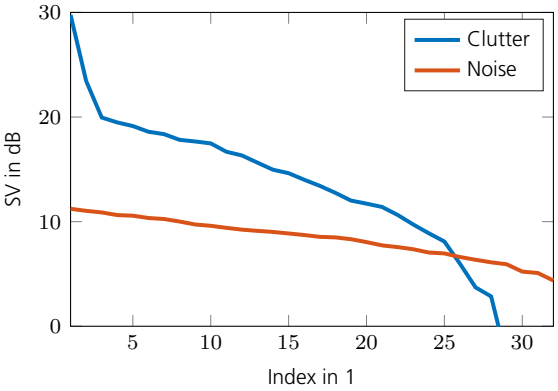

(d) SVD of $\boldsymbol{Y}_{\mathrm{c}}^{\mathrm{fc},u}$ and $\boldsymbol{X}_{\mathrm{c}}^{u}$.

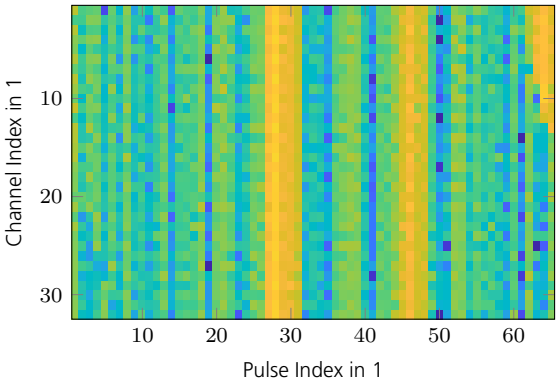

(e) Angle-focused clutter measurements $\boldsymbol{Y}_{\mathrm{c}}^{\mathrm{fc},u} = \mathcal{B}\left(\boldsymbol{X}_{\mathrm{c}}^{u}\right)$.

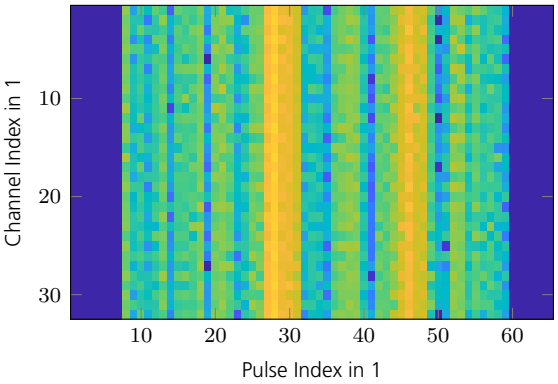

(f) Cut angle-focused measurements $\boldsymbol{Y}_{\mathrm{c}}^{\mathrm{fcct},u} = \mathcal{C}\left(\boldsymbol{Y}_{\mathrm{c}}^{\mathrm{fc},u}, \beta\right)$.

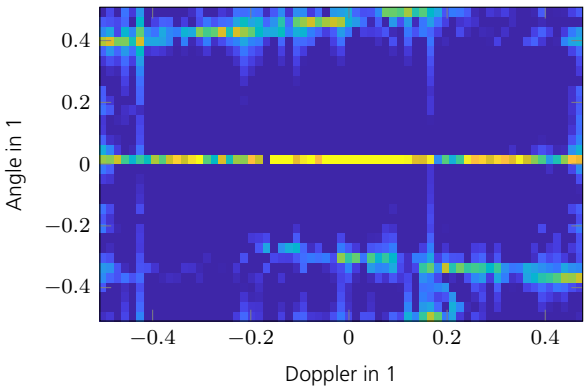

(g) Result of cut in scene domain $\boldsymbol{X}_{\mathrm{c}}^{\mathrm{ct},u} = \mathcal{B}^{-1}\left(\boldsymbol{Y}_{\mathrm{c}}^{\mathrm{fcct},u}\right)$.

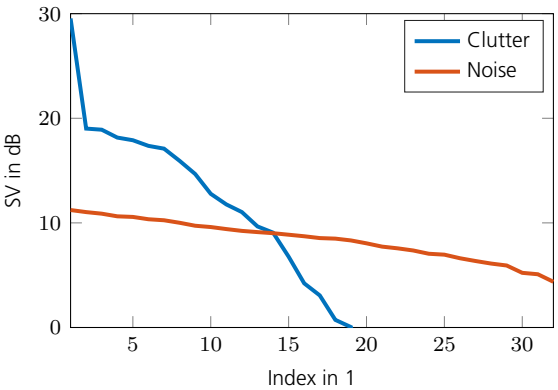

(h) SVD of $\boldsymbol{Y}_{\mathrm{c}}^{\mathrm{fcct},u}$ and $\boldsymbol{X}_{\mathrm{c}}^{\mathrm{ct},u}$.

Figure 7.1.13.: Dual low rank form for a level three setting with $\beta = 2.5$ and $\varphi_{\mathrm{m}} = 0.35\,\mathrm{rad}$.

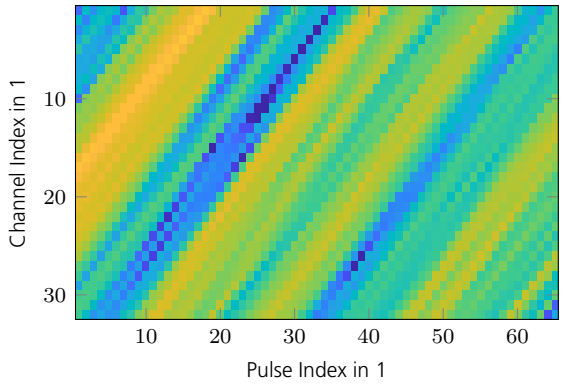

Figure 7.1.14.: Measurement matrix $\boldsymbol{Y}_\mathrm{c}$ of clutter focus illustration for a level four setting with $\beta = 1$, $\varphi_\mathrm{m} = 0.35\,\mathrm{rad}$, and back attenuation of -10 dB.

Dual Low Rank Form for Additional Limited Antenna Back Attenuation The following example illustrates the dual low rank form in case of a non fulfilled DPCA condition, present velocity misalignment, and in addition reflections from the rear side of the radar due to a limited antenna back attenuation of -10 dB for the specifically chosen parameters $\beta = 1$ and $\varphi_\mathrm{m} = 0.35\,\mathrm{rad}$. Within this work, this is termed a level four difficulty as listed in Tab. 7.1.1. The effect of limited back attenuation on the clutter ridge in the shifted clutter scene $\boldsymbol{X}_\mathrm{c}^\mathrm{sh}$ is the clutter ridge to become an ellipse instead of a curve. The size and orientation of the axis of the emerging ellipse depend on the velocity misalignment angle, where for $\varphi_\mathrm{m} = 0\,\mathrm{rad}$ the ellipse collapses to a straight line and for $\varphi_\mathrm{m} = \pi/2\,\mathrm{rad}$ it becomes a circle [1]. The reflections from the rear side potentially increase the minimum achievable rank of the dual low rank form. However, it was found from the simulations shown in Fig. 7.1.14 and Fig. 7.1.15, that limited back attenuation has a minor effect on the achievable rank. A potentially high impact has ICM, which is shown in the next example.

Dual Low Rank Form for Additional Present Internal Clutter Motion The following couple of examples are given to illustrate the impact of present ICM on the minimum achievable rank of the dual low rank form. This phenomena naturally decreases the correlation of the measurement samples in $\boldsymbol{Y}_\mathrm{c}$ as ICM causes the clutter scene to slightly change from pulse to pulse. As a model for ICM, the Billingsley model is used [1]. Within this work, present ICM is termed a level five difficulty as listed in Tab. 7.1.1. To begin with, the first example shows a scenario with fulfilled DPCA condition with the specifically chosen parameters $\beta = 1$, $\varphi_\mathrm{m} = 0°$, infinite back attenuation, and ICM with $\sigma_\mathrm{vel} = 20\,\mathrm{m/s}$. Certainly, a value of $\sigma_\mathrm{vel} = 20\,\mathrm{m/s}$ is unrealistic, yet serves as illustrative example. All other effects are not considered to purely illustrate the effect of ICM on the minimum achievable rank. The simulated clutter measurements $\boldsymbol{Y}_\mathrm{c}$ and the corresponding temporal auto correlation function, the variation of the magnitude, and the variation of the phase of a single clutter patch over pulses due to the ICM effect are shown in Fig. 7.1.16. The impact on the minimum achievable rank is shown in Fig. 7.1.17. As can be seen in Fig. 7.1.17a, the clutter ridge broadens and as a result, the clutter ridge can not be focused onto a single row anymore. Clutter contributions off $\bar{u} = 0$ remain after cutting incomplete measurements as shown in Fig. 7.1.17g. Nevertheless, the measurement samples in $\boldsymbol{Y}_\mathrm{c}$ are still

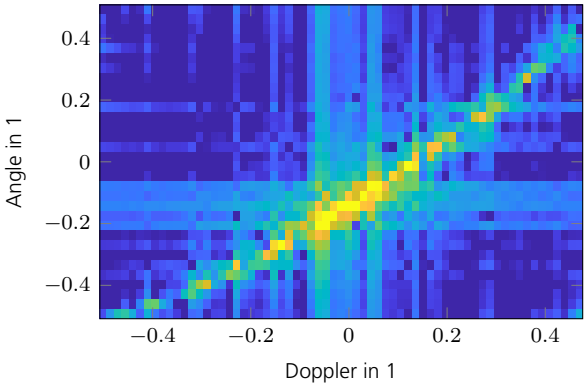

(a) Shifted clutter in scene domain $\boldsymbol{X}_{\mathrm{c}}^{\mathrm{sh}} = \mathcal{B}^{-1}\left(\boldsymbol{Y}_{\mathrm{c}}\right)$.

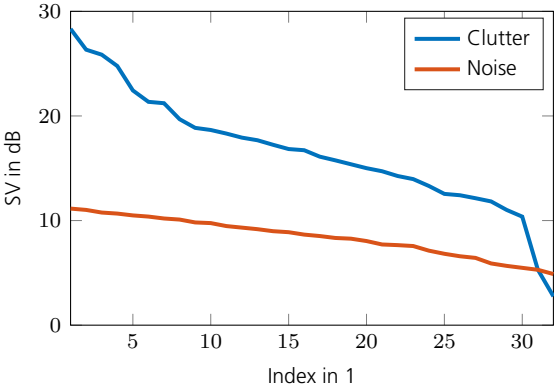

(b) SVD of $\boldsymbol{Y}_{\mathrm{c}}$ and $\boldsymbol{X}_{\mathrm{c}}^{\mathrm{sh}}$.

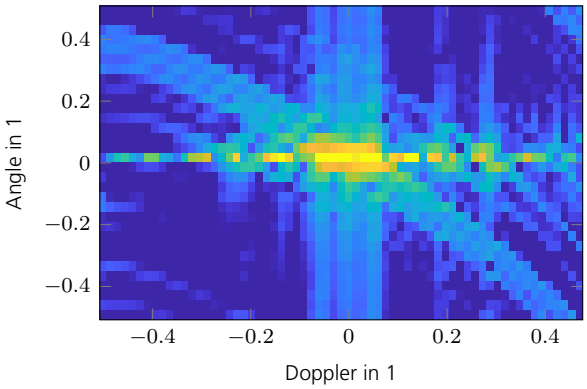

(c) The dual low rank form $\boldsymbol{X}_{\mathrm{c}}^{u} = \mathcal{D}_{u}^{-1}(\boldsymbol{X}_{\mathrm{c}}^{\mathrm{sh}}; \beta, \varphi_{\mathrm{m}})$.

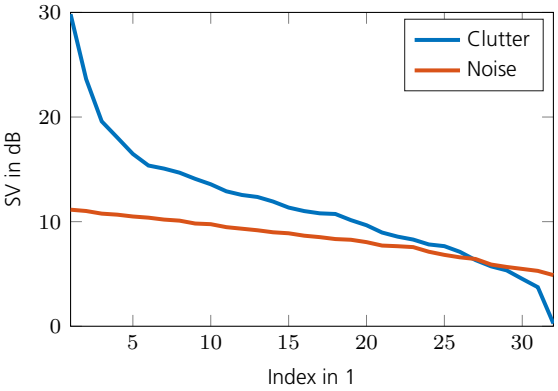

(d) SVD of $\boldsymbol{Y}_{\mathrm{c}}^{\mathrm{fc},u}$ and $\boldsymbol{X}_{\mathrm{c}}^{u}$.

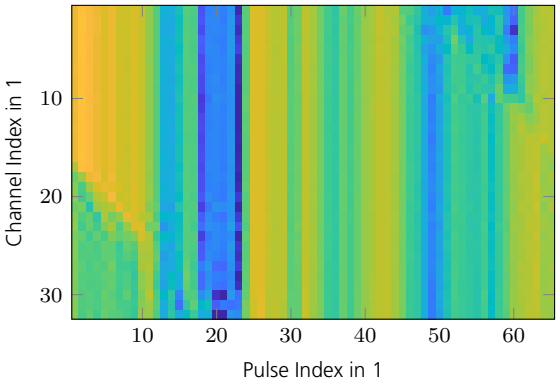

(e) Angle-focused clutter measurements $\boldsymbol{Y}_{\mathrm{c}}^{\mathrm{fc},u} = \mathcal{B}\left(\boldsymbol{X}_{\mathrm{c}}^{u}\right)$.

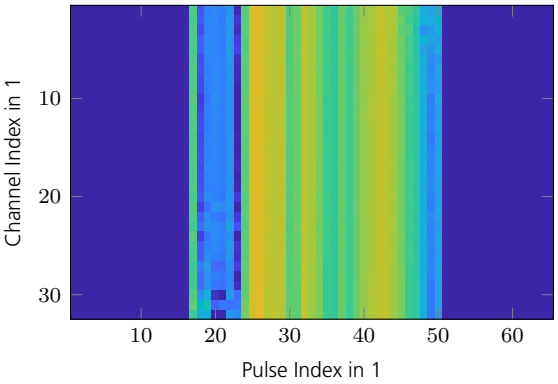

(f) Cut angle-focused measurements $\boldsymbol{Y}_{\mathrm{c}}^{\mathrm{fcct},u} = \mathcal{C}\left(\boldsymbol{Y}_{\mathrm{c}}^{\mathrm{fc},u}, \beta\right)$.

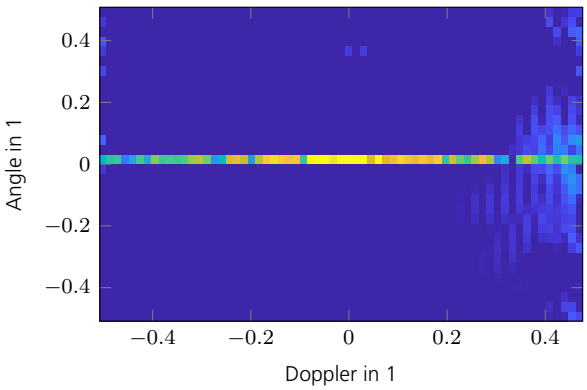

(g) Result of cut in scene domain $\boldsymbol{X}_{\mathrm{c}}^{\mathrm{ct},u} = \mathcal{B}^{-1}\left(\boldsymbol{Y}_{\mathrm{c}}^{\mathrm{fcct},u}\right)$.

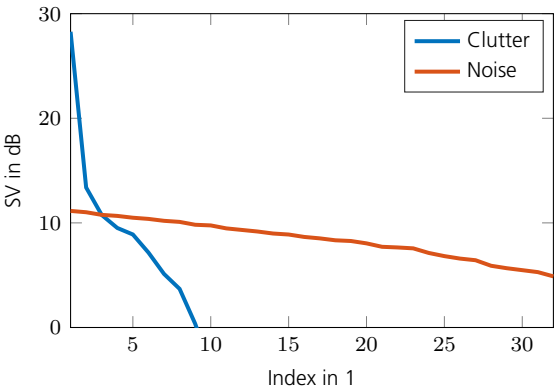

(h) SVD of $\boldsymbol{Y}_{\mathrm{c}}^{\mathrm{fcct},u}$ and $\boldsymbol{X}_{\mathrm{c}}^{\mathrm{ct},u}$.

Figure 7.1.15.: Dual low rank form for a level four setting with $\beta = 1$, $\varphi_{\mathrm{m}} = 0.35\,\mathrm{rad}$, and back attenuation of -10 dB.

partially correlated. Hence, the dual low rank form still contains a convenient low rank matrix as shown by the singular values plotted in Fig. 7.1.17h.

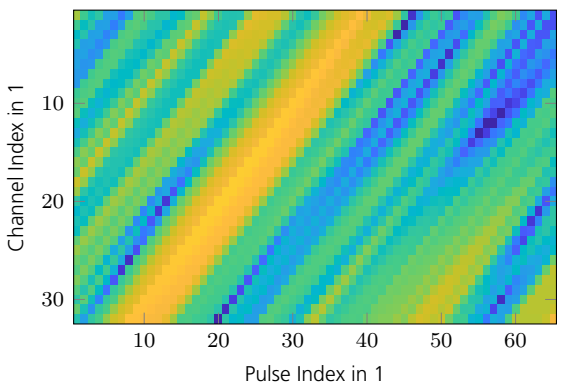

(a) Measurement matrix $\boldsymbol{Y}_{\mathrm{c}}$.

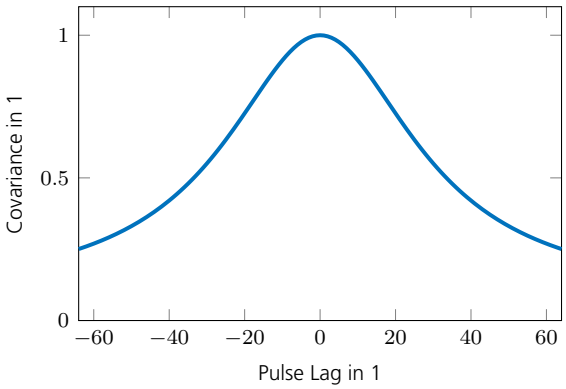

(b) Auto correlation of single clutter patch.

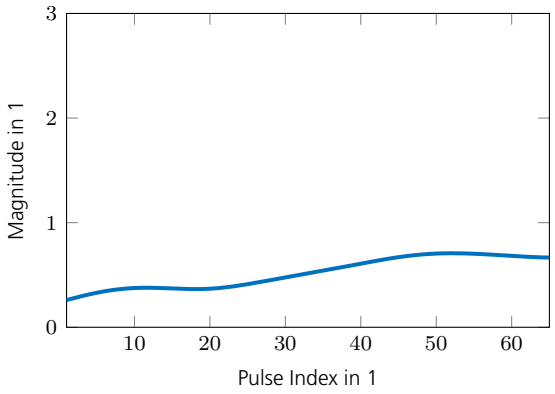

(c) Magnitude variation of a single clutter patch over pulses.

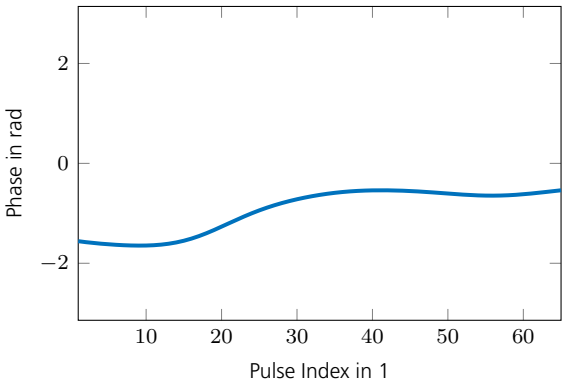

(d) Phase variation of a single clutter patch over pulses.

Figure 7.1.16.: Dual low rank form for a level five setting with $\beta = 1$, $\varphi_{\mathrm{m}} = 0°$, infinite back attenuation, and ICM with $\sigma_{\mathrm{vel}} = 20\,\mathrm{m/s}$.

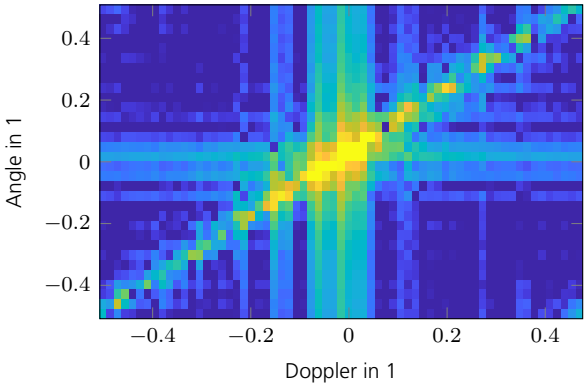

(a) Shifted clutter in scene domain $\boldsymbol{X}_{\mathrm{c}}^{\mathrm{sh}} = \mathcal{B}^{-1}\left(\boldsymbol{Y}_{\mathrm{c}}\right)$.

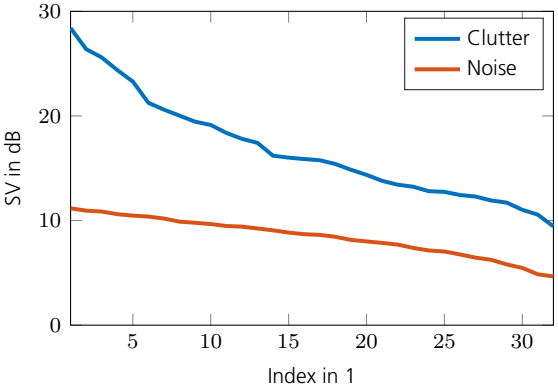

(b) SVD of $\boldsymbol{Y}_{\mathrm{c}}$ and $\boldsymbol{X}_{\mathrm{c}}^{\mathrm{sh}}$.

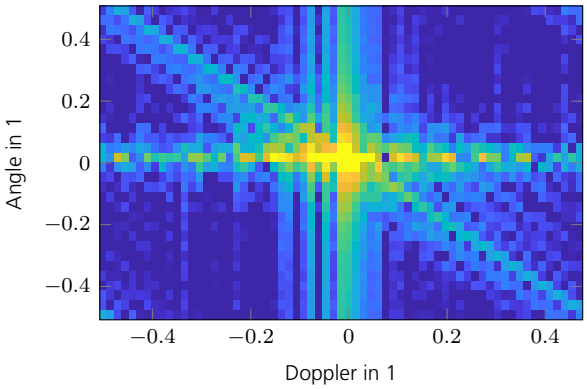

(c) The dual low rank form $\boldsymbol{X}_{\mathrm{c}}^{u} = \mathcal{D}_{u}^{-1}(\boldsymbol{X}_{\mathrm{c}}^{\mathrm{sh}}; \beta, \varphi_{\mathrm{m}})$.

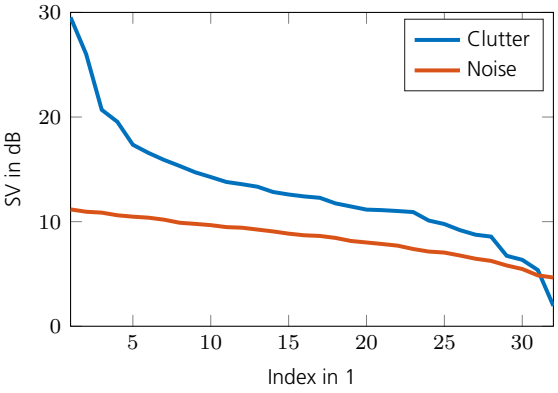

(d) SVD of $\boldsymbol{Y}_{\mathrm{c}}^{\mathrm{fc},u}$ and $\boldsymbol{X}_{\mathrm{c}}^{u}$.

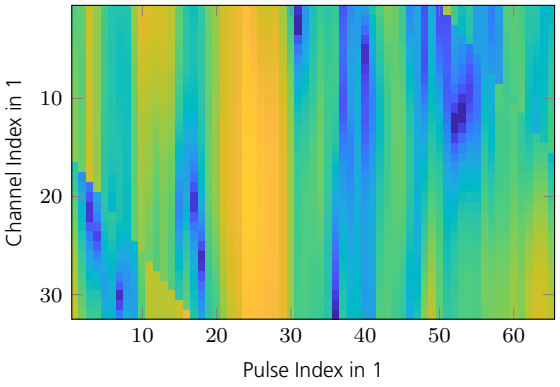

(e) Angle-focused clutter measurements $\boldsymbol{Y}_{\mathrm{c}}^{\mathrm{fc},u} = \mathcal{B}\left(\boldsymbol{X}_{\mathrm{c}}^{u}\right)$.

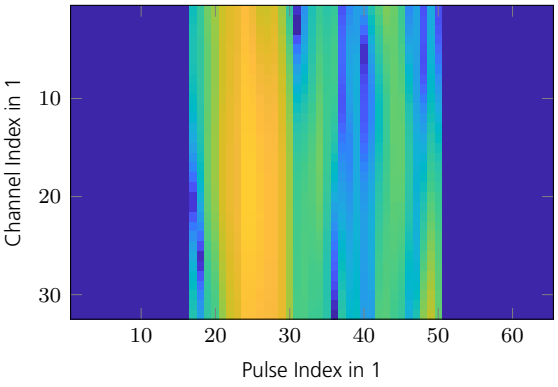

(f) Cut angle-focused measurements $\boldsymbol{Y}_{\mathrm{c}}^{\mathrm{fcct},u} = \mathcal{C}\left(\boldsymbol{Y}_{\mathrm{c}}^{\mathrm{fc},u}, \beta\right)$.

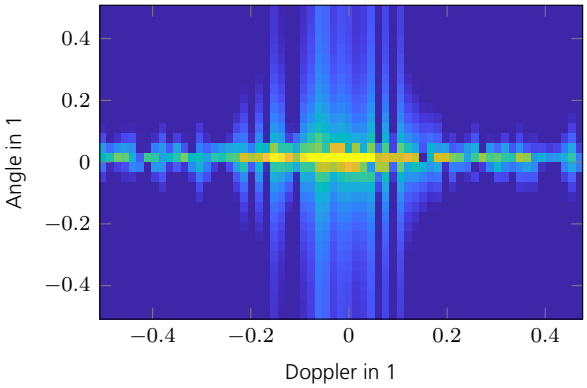

(g) Result of cut in scene domain $\boldsymbol{X}_{\mathrm{c}}^{\mathrm{ct},u} = \mathcal{B}^{-1}\left(\boldsymbol{Y}_{\mathrm{c}}^{\mathrm{fcct},u}\right)$.

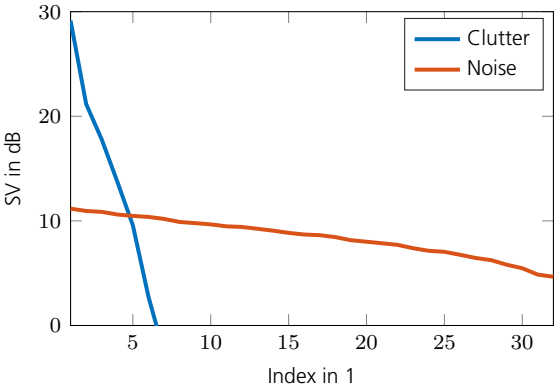

(h) SVD of $\boldsymbol{Y}_{\mathrm{c}}^{\mathrm{fcct},u}$ and $\boldsymbol{X}_{\mathrm{c}}^{\mathrm{ct},u}$.

Figure 7.1.17.: Dual low rank form for a level five setting with $\beta = 1$, $\varphi_{\mathrm{m}} = 0°$, infinite back attenuation, and ICM with $\sigma_{\mathrm{vel}} = 20\,\mathrm{m/s}$.

The next example shown in Fig. 7.1.18 and Fig. 7.1.19 illustrates the effects for $\beta = 2.5$, $\varphi_{\mathrm{m}} = 0.35\,\mathrm{rad}$, back attenuation of -30 dB, and ICM with $\sigma_{\mathrm{vel}} = 20\,\mathrm{m/s}$. This example comprises all aforementioned effects together to form a worst case example. Despite of all present decorrelation effects, the dual low rank form still contains a convenient low rank matrix.

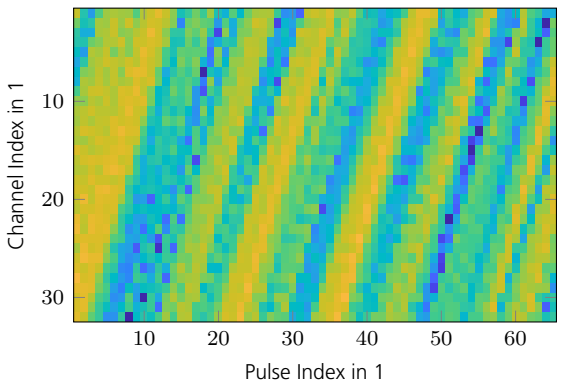

(a) Measurement matrix $\boldsymbol{Y}_{\mathrm{c}}$.

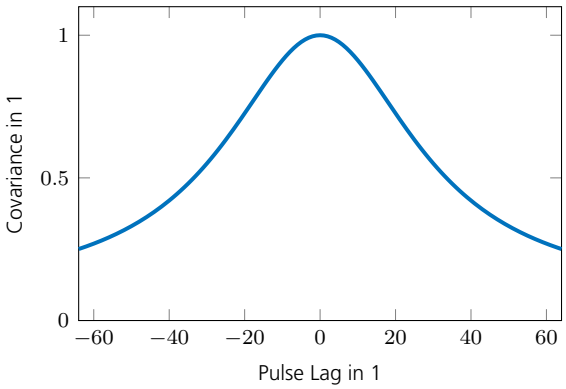

(b) Auto correlation of single clutter patch.

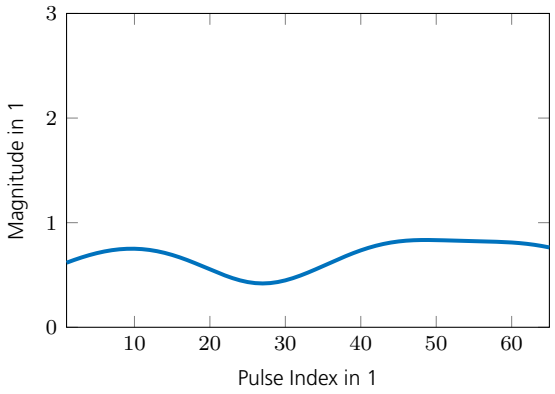

(c) Magnitude variation of a single clutter patch over pulses.

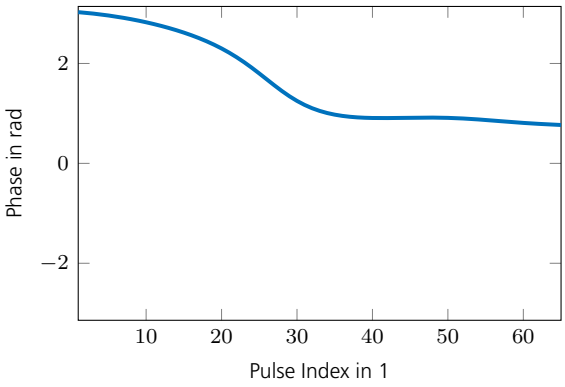

(d) Phase variation of a single clutter patch over pulses.

Figure 7.1.18.: Dual low rank form for a level five setting with $\beta = 2.5$, $\varphi_{\mathrm{m}} = 0.35\,\mathrm{rad}$, back attenuation of -30 dB, and ICM with $\sigma_{\mathrm{vel}} = 20\,\mathrm{m/s}$.

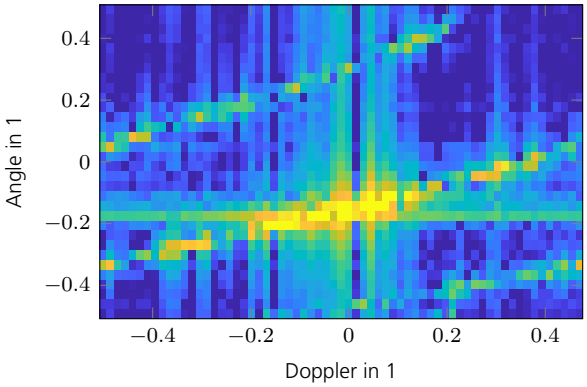

(a) Shifted clutter in scene domain $\boldsymbol{X}_{\mathrm{c}}^{\mathrm{sh}} = \mathcal{B}^{-1}\left(\boldsymbol{Y}_{\mathrm{c}}\right)$.

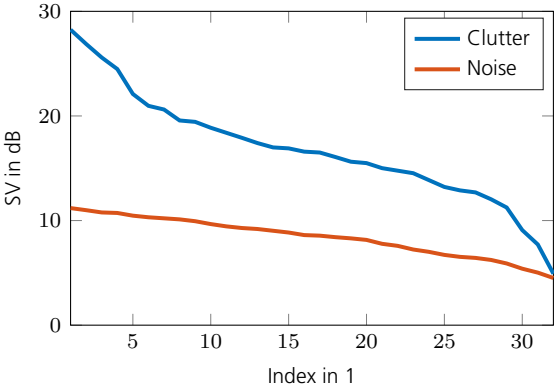

(b) SVD of $\boldsymbol{Y}_{\mathrm{c}}$ and $\boldsymbol{X}_{\mathrm{c}}^{\mathrm{sh}}$.

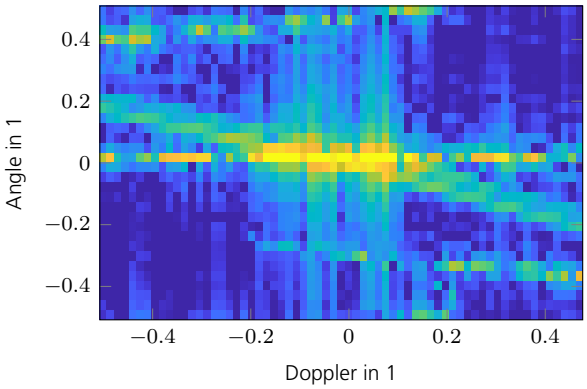

(c) The dual low rank form $\boldsymbol{X}_{\mathrm{c}}^{u} = \mathcal{D}_{u}^{-1}(\boldsymbol{X}_{\mathrm{c}}^{\mathrm{sh}}; \beta, \varphi_{\mathrm{m}})$.

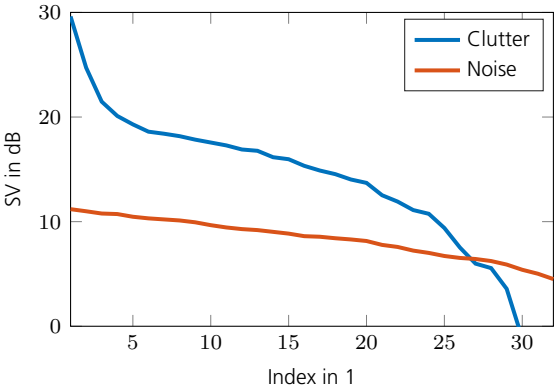

(d) SVD of $\boldsymbol{Y}_{\mathrm{c}}^{\mathrm{fc},u}$ and $\boldsymbol{X}_{\mathrm{c}}^{u}$.

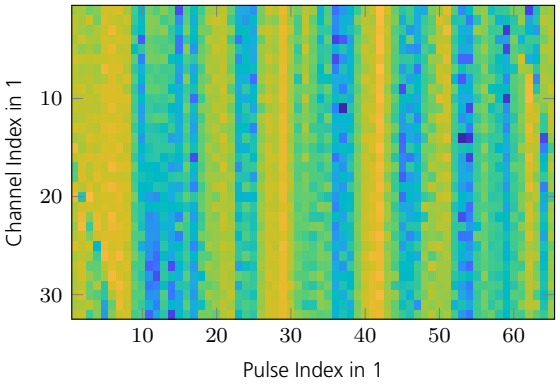

(e) Angle-focused clutter measurements $\boldsymbol{Y}_{\mathrm{c}}^{\mathrm{fc},u} = \mathcal{B}\left(\boldsymbol{X}_{\mathrm{c}}^{u}\right)$.

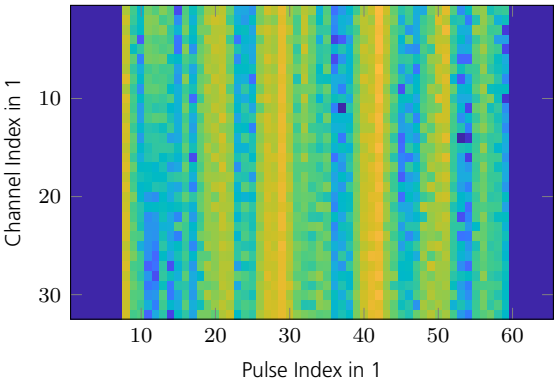

(f) Cut angle-focused measurements $\boldsymbol{Y}_{\mathrm{c}}^{\mathrm{fcct},u} = \mathcal{C}\left(\boldsymbol{Y}_{\mathrm{c}}^{\mathrm{fc},u}, \beta\right)$.

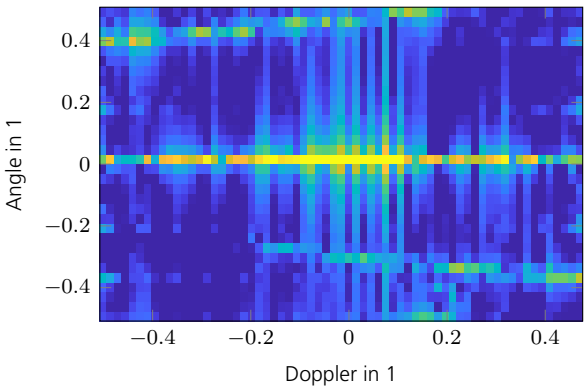

(g) Result of cut in scene domain $\boldsymbol{X}_{\mathrm{c}}^{\mathrm{ct},u} = \mathcal{B}^{-1}\left(\boldsymbol{Y}_{\mathrm{c}}^{\mathrm{fcct},u}\right)$.

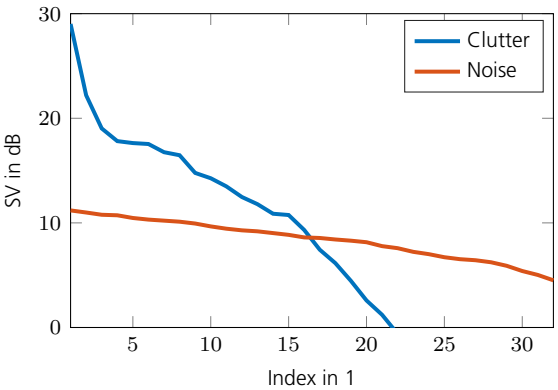

(h) SVD of $\boldsymbol{Y}_{\mathrm{c}}^{\mathrm{fcct},u}$ and $\boldsymbol{X}_{\mathrm{c}}^{\mathrm{ct},u}$.

Figure 7.1.19.: Dual low rank form for a level five setting with $\beta = 2.5$, $\varphi_{\mathrm{m}} = 0.35\,\mathrm{rad}$, back attenuation of -30 dB, and ICM with $\sigma_{\mathrm{vel}} = 20\,\mathrm{m/s}$.

Dual Low Rank Form for Present Targets The following example illustrates the impact of present targets in the radar scene. In Fig. 7.1.20 and Fig. 7.1.21, the result for a setting of $\beta = 2.5$, $\varphi_{\mathrm{m}} = 0.35\,\mathrm{rad}$, back attenuation of -30 dB, ICM with $\sigma_{\mathrm{vel}} = 20\,\mathrm{m/s}$, and additionally $N_{\mathrm{t}} = 4$ targets is shown. As can be seen, the impact is of minor nature. Every present target increases the minimum achievable rank by approximately one. Since we assume moving targets to be sparse and as such the number of present targets is low, this is of no concern. Depending on the signal to noise ratio (SNR) of the target compared to the clutter to noise ratio (CNR), moving targets have limited effect on the low rank form, since the shifting operator $\mathcal{D}_u^{-1}$ keeps point like targets to stay point like. Only strong side lobes of moving targets effect the low rank form as will be shown later.

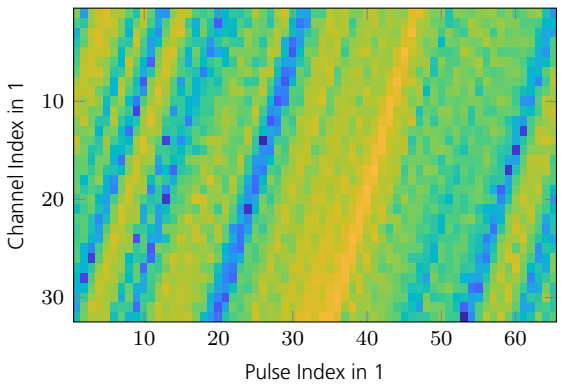

(a) Measurement matrix $\boldsymbol{Y}$.

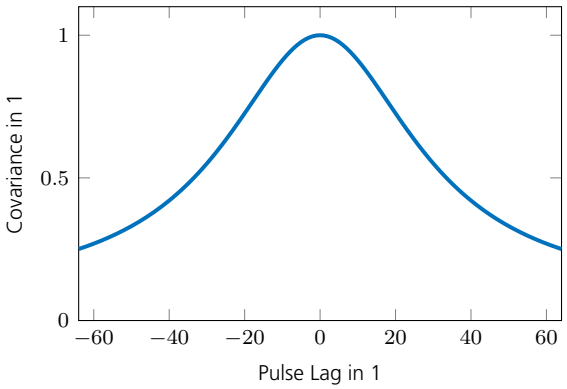

(b) Auto correlation of single clutter patch.

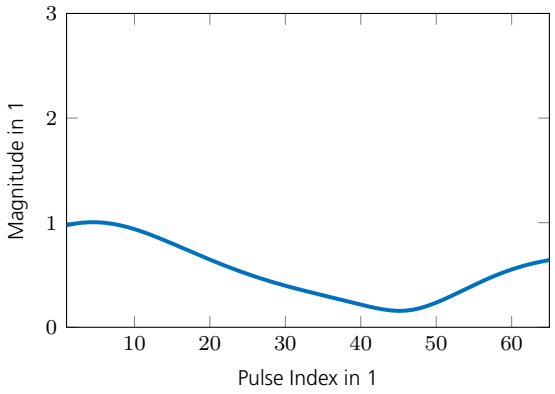

(c) Magnitude variation of a single clutter patch over pulses.

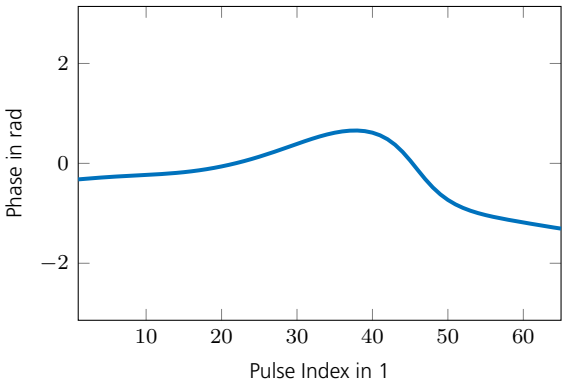

(d) Phase variation of a single clutter patch over pulses.

Figure 7.1.20.: Dual low rank form for a level five setting with $\beta = 2.5$, $\varphi_{\mathrm{m}} = 0.35\,\mathrm{rad}$, back attenuation of -30 dB, ICM with $\sigma_{\mathrm{vel}} = 20\,\mathrm{m/s}$, and $N_{\mathrm{t}} = 4$ present targets.

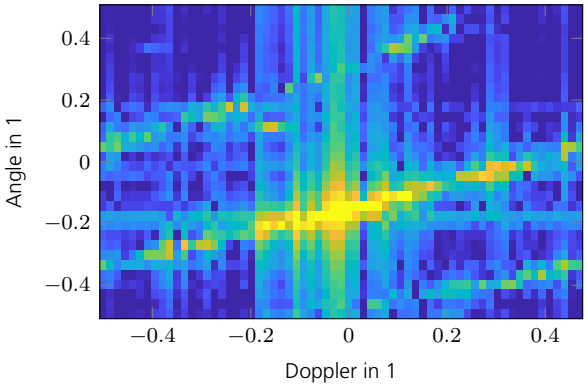

(a) Shifted clutter in scene domain $\boldsymbol{X}_{\mathrm{c}}^{\mathrm{sh}} = \mathcal{B}^{-1}\left(\boldsymbol{Y}_{\mathrm{c}}\right)$.

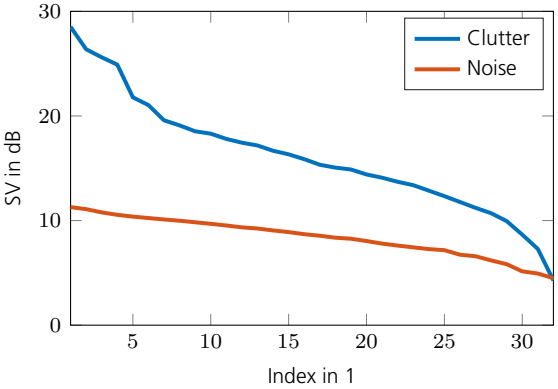

(b) SVD of $\boldsymbol{Y}_{\mathrm{c}}$ and $\boldsymbol{X}_{\mathrm{c}}^{\mathrm{sh}}$.

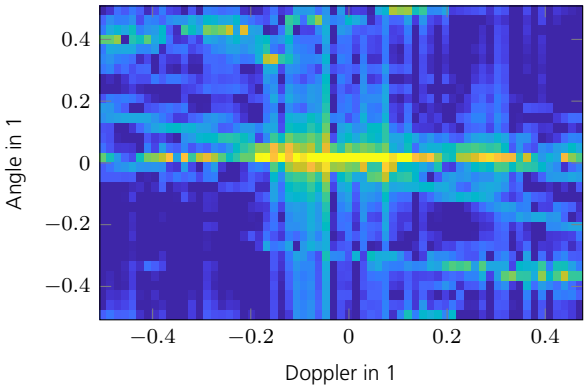

(c) The dual low rank form $\boldsymbol{X}_{\mathrm{c}}^{u} = \mathcal{D}_{u}^{-1}(\boldsymbol{X}_{\mathrm{c}}^{\mathrm{sh}}; \beta, \varphi_{\mathrm{m}})$.

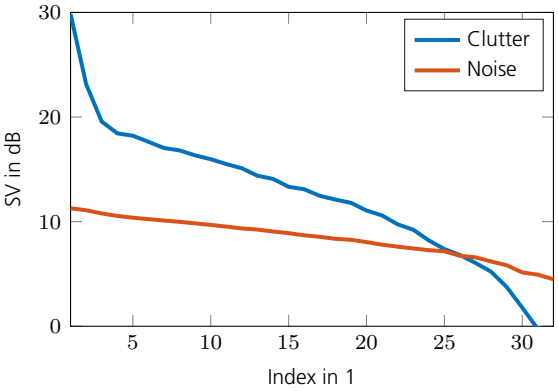

(d) SVD of $\boldsymbol{Y}_{\mathrm{c}}^{\mathrm{fc},u}$ and $\boldsymbol{X}_{\mathrm{c}}^{u}$.

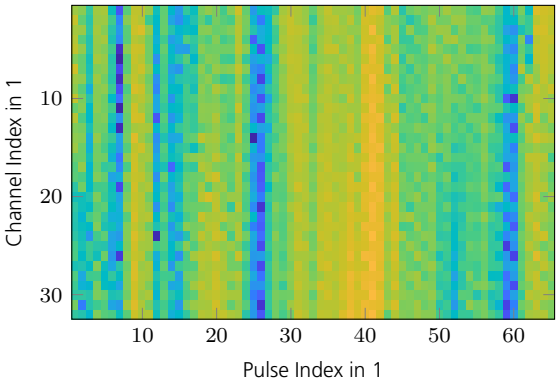

(e) Angle-focused clutter measurements $\boldsymbol{Y}_{\mathrm{c}}^{\mathrm{fc},u} = \mathcal{B}\left(\boldsymbol{X}_{\mathrm{c}}^{u}\right)$.

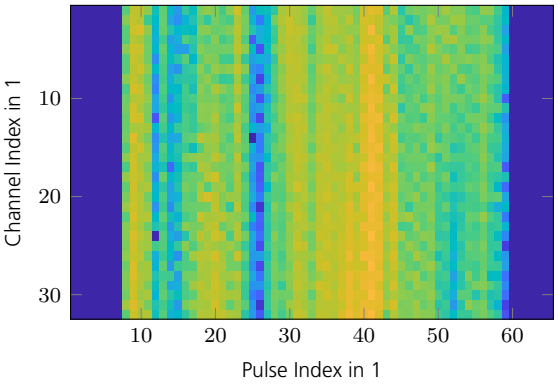

(f) Cut angle-focused measurements $\boldsymbol{Y}_{\mathrm{c}}^{\mathrm{fcct},u} = \mathcal{C}\left(\boldsymbol{Y}_{\mathrm{c}}^{\mathrm{fc},u}, \beta\right)$.

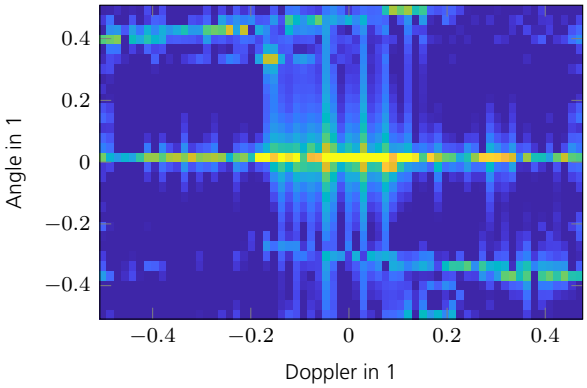

(g) Result of cut in scene domain $\boldsymbol{X}_{\mathrm{c}}^{\mathrm{ct},u} = \mathcal{B}^{-1}\left(\boldsymbol{Y}_{\mathrm{c}}^{\mathrm{fcct},u}\right)$.

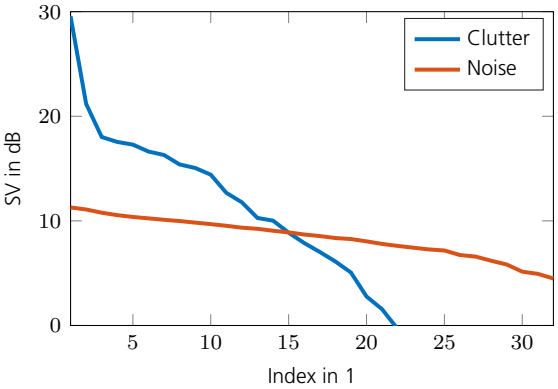

(h) SVD of $\boldsymbol{Y}_{\mathrm{c}}^{\mathrm{fcct},u}$ and $\boldsymbol{X}_{\mathrm{c}}^{\mathrm{ct},u}$.

Figure 7.1.21.: Dual low rank form for a level five setting with $\beta = 2.5$, $\varphi_{\mathrm{m}} = 0.35\,\mathrm{rad}$, back attenuation of -30 dB, ICM with $\sigma_{\mathrm{vel}} = 20\,\mathrm{m/s}$, and $N_{\mathrm{t}} = 4$ present targets.

The examples presented in this section illustrate the impact of decorrelation effects on the minimum achievable rank of the dual low rank form. Although not exhaustive, it was shown that even for severe effects like ICM a convenient dual low rank form exists. This property can be exploited to estimate unknown parameters e. g. β, φ_{m}, etc. To be able to do so, a suitable objective function is required. In the next section, the nuclear norm is shown to be a convenient choice therefore.

7.1.4. The Nuclear Norm as Objective Function for Parameter Estimation

This section examines the nuclear norm in terms of its usability and robustness as objective function to estimate the clutter ridge slope β and the velocity misalignment angle φ_{m}. This idea builds upon the low rank properties of clutter measurements which was shown in the former sections. Next to the general emerging shapes of the objective functions, also their robustness against present targets is elaborated on. It shows, that the nuclear norm is a suitable measure for parameter estimation. This forms the foundation of the auto-clutter focus (ACF) algorithm presented in Section 7.2, which conducts the actual estimation.

One key observation from the examples presented in the former section is to recognize, that the nuclear norm of the dual low rank form $\|\boldsymbol{X}_{\mathrm{c}}^{u}\|_{*}$ is the minimum achievable nuclear norm. If, for instance, the clutter ridge was not focused onto $\bar{u} = 0$ by the shift operator $\mathcal{D}_{u}^{-1}$, the resulting nuclear norm would be bigger compared to the nuclear norm of the perfectly focused clutter ridge $\|\boldsymbol{X}_{\mathrm{c}}^{u}\|_{*}$ because the ridge would run on a diagonal course which in turn would increase the rank. Since the shift amount in $\bar{u}$ depends on the parameters β and φ_{m} as given by (7.1.14), it is possible to use the nuclear norm within an objective function to estimate them as

$$\widehat{\beta}, \widehat{\varphi_{\mathrm{m}}} = \underset{\beta, \varphi_{\mathrm{m}}}{\arg\min}\, f_{*}(\beta, \varphi_{\mathrm{m}}), \tag{7.1.27}$$

where the objective function is defined similar to (7.1.19) as

$$f_{*}(\beta, \varphi_{\mathrm{m}}) = \left\| \mathcal{A}_{u}^{-1}(\boldsymbol{Y}_{\mathrm{c}}; \beta, \varphi_{\mathrm{m}}) \right\|_{*} \tag{7.1.28}$$

$$= \left\| \mathcal{D}_{u}^{-1}(\boldsymbol{X}_{\mathrm{c}}^{\mathrm{sh}}; \beta, \varphi_{\mathrm{m}}) \right\|_{*} \tag{7.1.29}$$

$$= \left\| \widehat{\boldsymbol{X}}_{\mathrm{c}}^{u} \right\|_{*}. \tag{7.1.30}$$

The objective function can be interpreted as a shift in $\bar{u}$ conducted by $\mathcal{D}_{u}^{-1}$, which focuses the clutter ridge energy in $\boldsymbol{X}_{\mathrm{c}}^{\mathrm{sh}}$ along $\bar{u} = 0$. The result of the shift operation $\widehat{\boldsymbol{X}}_{\mathrm{c}}^{u}$ can be interpreted as an estimate of the dual low rank form. The nuclear norm measures how well the clutter ridge was focused and offers the advantage over classical correlation methods to be robust against present targets. Furthermore, it is naturally applicable in case of missing samples by use of affine rank minimization (ARM) approaches as will be shown in Section 7.2. The price to pay, however, is that sufficient channels must be available. As a further refinement, the nuclear norm of the contained low rank matrix within the dual low rank form as sketched in Fig. 7.1.7 can be used for estimation. As shown later, this improves the estimation performance as disturbing incomplete measurements are excluded from the estimation process. The refined objective function can be

defined similar to (7.1.23) as

$$\widehat{\beta}, \widehat{\varphi_{\mathrm{m}}} = \underset{\beta,\varphi_{\mathrm{m}}}{\arg\min}\, f_*^{\mathrm{ct}}(\beta, \varphi_{\mathrm{m}}; \beta_0)$$

with the refined objective function

$$f_*^{\mathrm{ct}}(\beta, \varphi_{\mathrm{m}}; \beta_0) = \left\| \mathcal{C}(\beta_0) \circ \mathcal{B} \circ \widehat{\boldsymbol{X}}_{\mathrm{c}}^{u} \right\|_*, \tag{7.1.31}$$

where $\beta_0 \in \mathbb{R}$ is some parameter chosen to determine the number of pulses to cut according to (7.1.14). Within $f_*^{\mathrm{ct}}(\beta, \varphi_{\mathrm{m}}; \beta_0)$, the Fourier operator $\mathcal{B}$ maps the focused clutter ridge into the measurement domain in which the incomplete measurements are set to zero by the cut operator $\mathcal{C}(\beta_0)$.

The shift operator $\mathcal{D}_u^{-1}$ used in the defined objective functions is a non linear function in terms of the unknown parameters β and φ_{m}. As a consequence, $f_*(\beta, \varphi_{\mathrm{m}})$ and $f_*^{\mathrm{ct}}(\beta, \varphi_{\mathrm{m}}; \beta_0)$ are not convex, hence, no unique minimum exists. Due to the cyclic shift nature of $\mathcal{D}_u^{-1}$, multiple minima emerge for $\beta \to 0$ as in this case $\bar{u}_{\mathrm{c}} \to \infty$ according to (7.1.14). Likewise, the velocity misalignment angle is unique only for $\varphi_{\mathrm{m}} \in [-\pi, \pi)$ as can be seen from (7.1.14). Nevertheless, the objective functions offer suitable shapes for a successful estimation of the parameters as will be shown by the following examples.

As a first illustrative example, Fig. 7.1.22a shows a sweep of β vs. $f_*(\beta, \varphi_{\mathrm{m}})$ for various true parameter choices $\widetilde{\beta}$, where $\widetilde{\varphi_{\mathrm{m}}} = \varphi_{\mathrm{m}} = 0$. Furthermore, Fig. 7.1.22b shows a sweep of β vs. $f_*^{\mathrm{ct}}(\beta, \varphi_{\mathrm{m}}; \beta)$ i. e. with cutting. As a first attempt, the unknown parameter β_0 from which the number of pulses to cut is determined is set as $\beta_0 = \beta$. This means, the number of pulses cut continuously changes. As can be seen, convenient minima mark the true parameter locations for both objective functions. While the refined objective functions $f_*^{\mathrm{ct}}(\beta, \varphi_{\mathrm{m}})$ in Fig. 7.1.22b show steeper minima compared to the uncut versions in Fig. 7.1.22a, they are subject to discontinuities originating from the discrete number of pulses which are cut. Also as $\beta \to 0$, the number of pulses to be cut according to (7.1.14) tends to infinity resulting in all samples to be set to zero. Finding the minimum for the specific choice $\beta_0 = \beta$ is very challenging. However, the steeper minima allow for an improved estimation performance as will shown further below. How to choose β_0 conveniently is presented in the following section. For the remainder of this section, however, β_0 is set to the true parameter as $\beta = \widetilde{\beta}$ in order to evaluate the best achievable objective functions.

In the following examinations, the objective functions $f_*(\beta, \varphi_{\mathrm{m}})$ and $f_*^{\mathrm{ct}}(\beta, \varphi_{\mathrm{m}}; \widetilde{\beta})$ are evaluated for $\beta \in [0.5, 4]$ and $\varphi_{\mathrm{m}} \in [-\pi, \pi)$ for various difficulty scenarios as listed in Tab. 7.1.1. The objective functions are averaged over a 100 Monte Carlo runs and in the following plots, green crosses mark the true parameter locations $\widetilde{\beta}$ and $\widetilde{\varphi_{\mathrm{m}}}$, while red crosses indicates the minimum of the averaged objective functions, and the red dots the minimum in every Monte Carlo realization. Figure. 7.1.23 shows the results of the objective function $f_*(\beta, \varphi_{\mathrm{m}})$ for a level one difficulty setting with $\widetilde{\beta} = 1$. For better illustration also a surface plot is given. As can be seen in Fig. 7.1.23b, the majority of the individual minima marked by the red dots are located closely to the true parameter values. Unfortunately, a few Monte Carlo realizations reveal a low value of $f_*(\beta, \varphi_{\mathrm{m}})$ for a wrongly focused clutter ridge. A more detailed investigation revealed, that these phenomena

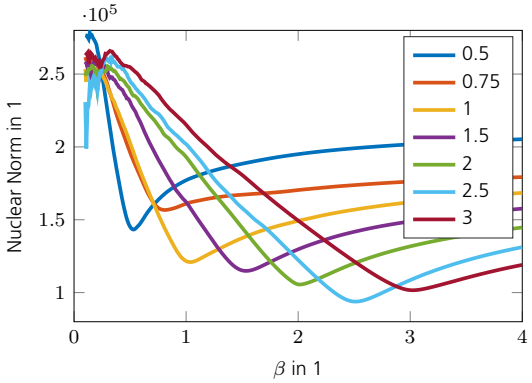

(a) β vs. $f_*(\beta, 0)$ for various $\widetilde{\beta}$.

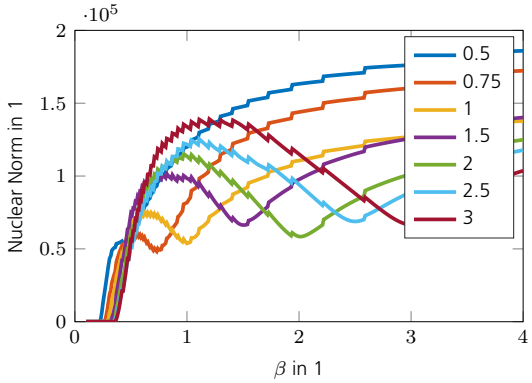

(b) β vs. $f_*^{\mathrm{ct}}(\beta, 0)$ for various $\widetilde{\beta}$.

Figure 7.1.22.: Emerging minima of objective functions for sweeping β.

are caused by the shifted clutter leakage i. e. incomplete measurements. This effect gets even more severe for the remaining scenarios shown in Fig. 7.1.24.

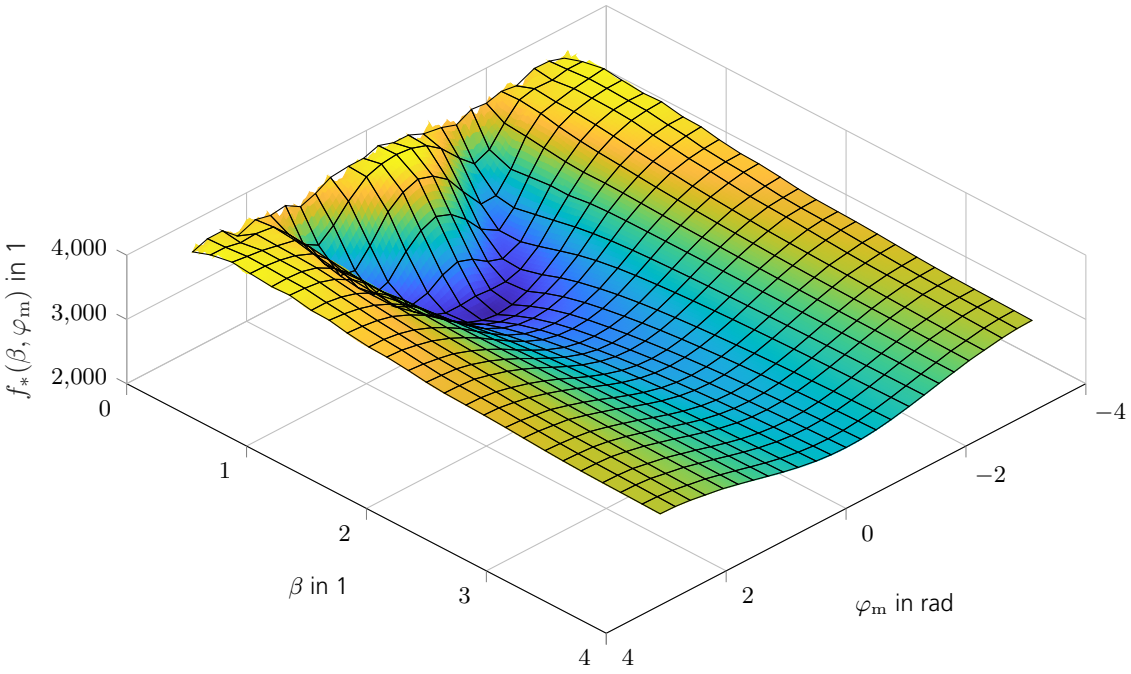

(a) A valley shaped minima marks the true parameter positions.

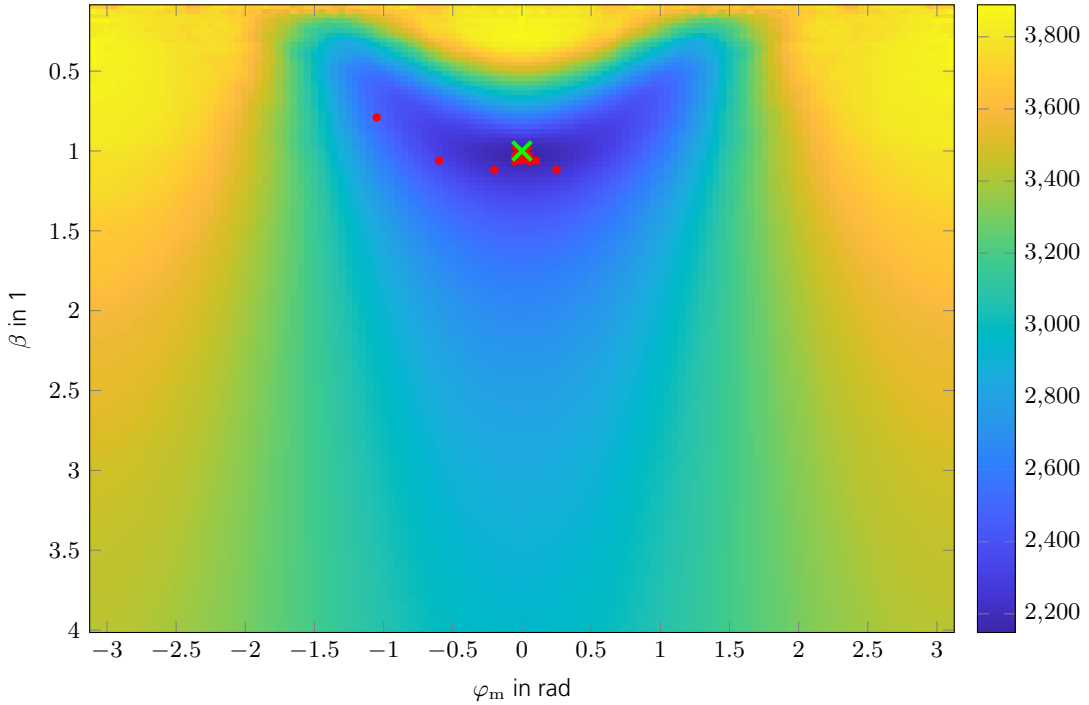

(b) Top view where the green cross marks the true parameter values and the red dots the minima in every Monte Carlo realization.

Figure 7.1.23.: Objective function $f_*(\beta, \varphi_\mathrm{m})$ for a level one setting of $\widetilde{\beta} = 1$ with parameters swept over $\beta \in [0.5, 4]$ and $\varphi_\mathrm{m} \in [-\pi, \pi)$.

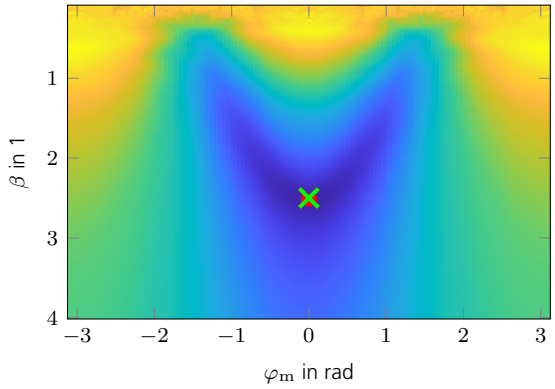

(a) Level two setting with $\widetilde{\beta} = 2.5$.

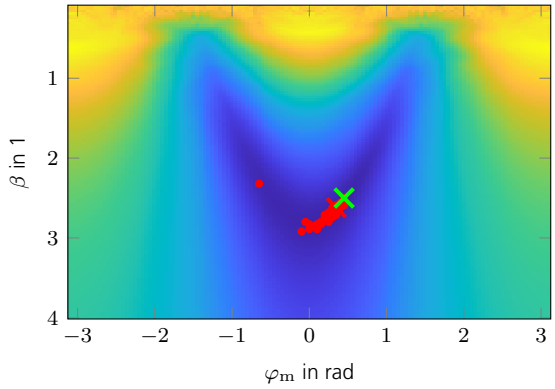

(b) Level three setting with $\widetilde{\beta} = 2.5$ and $\widetilde{\varphi_\mathrm{m}} = 0.35\,\mathrm{rad}$.

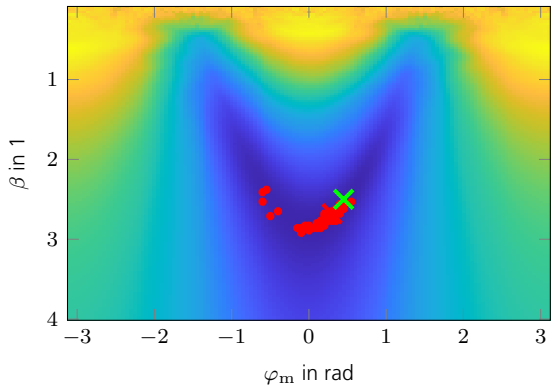

(c) Level five setting with $\widetilde{\beta} = 2.5$, $\widetilde{\varphi_\mathrm{m}} = 0.35\,\mathrm{rad}$, back attenuation of -30 dB, and ICM with $\sigma_\mathrm{vel} = 20\,\mathrm{m/s}$.

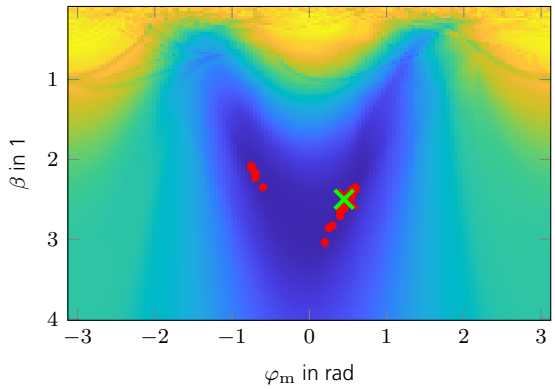

(d) Level five setting with $\widetilde{\beta} = 2.5$, $\widetilde{\varphi_\mathrm{m}} = 0.35\,\mathrm{rad}$, back attenuation of -30 dB, ICM with $\sigma_\mathrm{vel} = 20\,\mathrm{m/s}$, and $N_\mathrm{t} = 4$ present targets.

Figure 7.1.24.: Objective function $f_*(\beta, \varphi_\mathrm{m})$ for a level two to five setting with parameters swept over $\beta \in [0.5, 4]$ and $\varphi_\mathrm{m} \in [-\pi, \pi)$.

The results for the refined objective functions $f_*^\mathrm{ct}(\beta, \varphi_\mathrm{m}; \widetilde{\beta})$ are shown in Fig. 7.1.25. As can be seen, the minima become steeper allowing for a better estimation of $\widetilde{\beta}$ and $\widetilde{\varphi_\mathrm{m}}$. This fact will be seen again in the evaluation of the ACF algorithm in Section 7.2. Furthermore, the minima in the individual Monte Carlo realizations are consistently located close to the true value. This is a major advantage compared to the results shown in Fig. 7.1.23 and Fig. 7.1.24. In summary, well shaped minima occur for β and φ_m. Remarkably, the nuclear norm is robust against present targets as shown in Fig. 7.1.24d and 7.1.25e. This, however, depends on the SNR of the targets compared to the CNR. The influence of very strong targets onto the nuclear norm is discussed further below. Furthermore, taking a closer look onto the emerging nuclear norms reveals a rather flat valley for φ_m. In Fig. 7.1.26, an additional simulation for a zoomed view is shown for the case of $\widetilde{\beta} = 2.5$ and $\widetilde{\varphi_\mathrm{m}} = 0°$. As can be seen, the minima of φ_m are spread out due to the flat valley shape. As a consequence, the velocity misalignment angle φ_m cannot be estimated well enough by use of the nuclear norm. An alternative objective function which allows for a better estimation of φ_m is presented in the following Section 7.2.

The nuclear norm used in the objective functions $f_*(\beta, \varphi_\mathrm{m})$ and $f_*^\mathrm{ct}(\beta, \varphi_\mathrm{m}; \beta_0)$ is robust to some extent for present, very strong, moving targets. Depending on how much leakage in Doppler occurs, the minima marking the true parameter values $\widetilde{\beta}$ and $\widetilde{\varphi_\mathrm{m}}$ may be preserved or

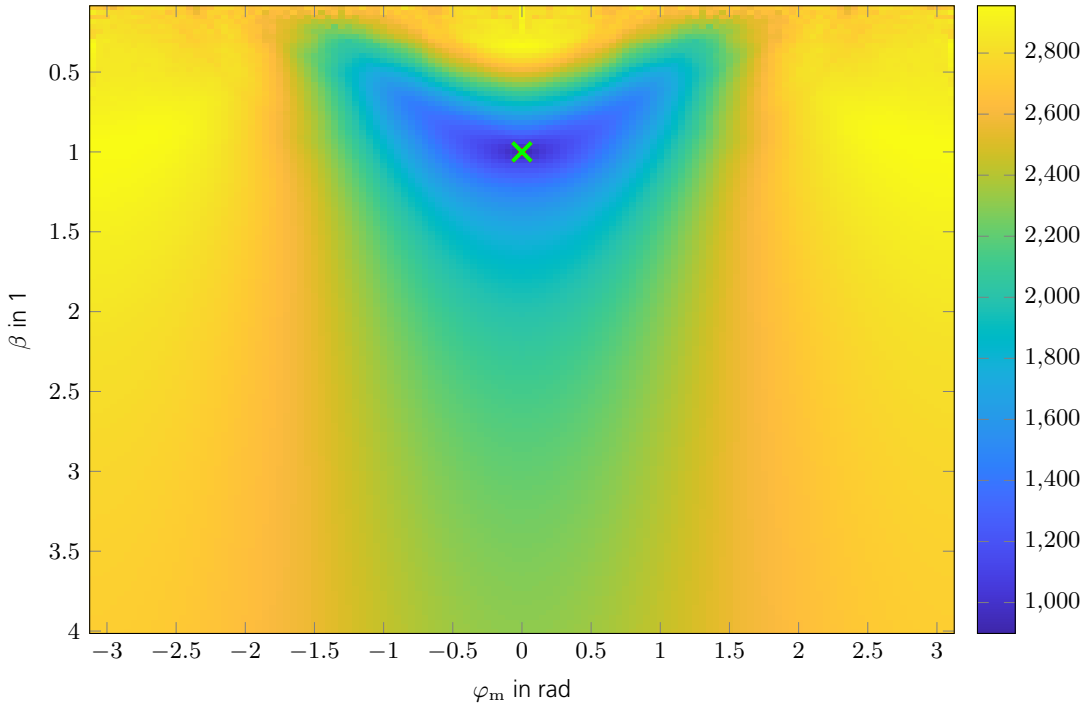

(a) Level one setting with $\widetilde{\beta} = 1$.

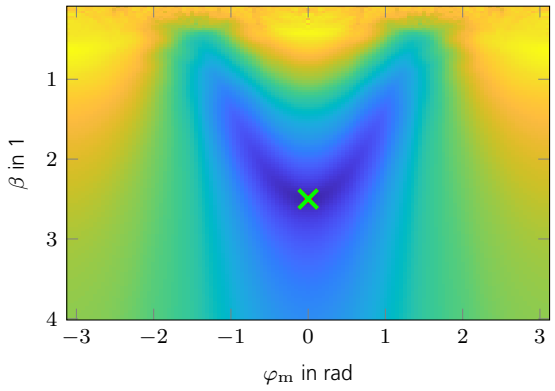

(b) Level two setting with $\widetilde{\beta} = 2.5$.

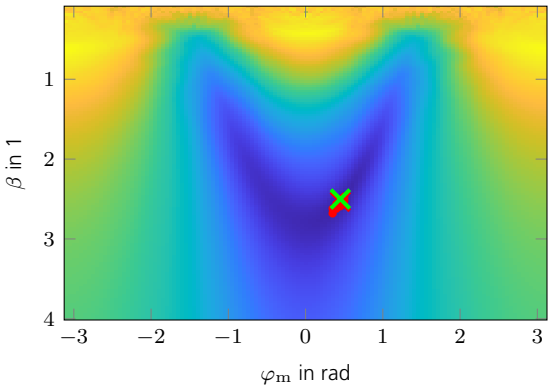

(c) Level three setting with $\widetilde{\beta} = 2.5$ and $\widetilde{\varphi_{\mathrm{m}}} = 0.35\,\mathrm{rad}$.

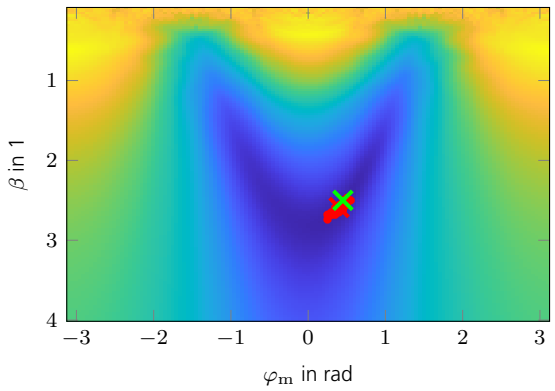

(d) Level five setting with $\widetilde{\beta} = 2.5$, $\widetilde{\varphi_{\mathrm{m}}} = 0.35\,\mathrm{rad}$, back attenuation of -30 dB, and ICM with $\sigma_{\mathrm{vel}} = 20\,\mathrm{m/s}$.

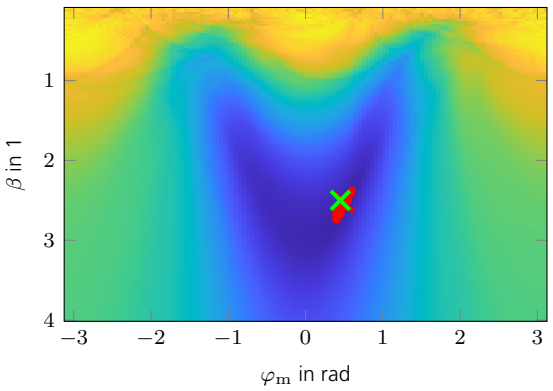

(e) Level five setting with $\widetilde{\beta} = 2.5$, $\widetilde{\varphi_{\mathrm{m}}} = 0.35\,\mathrm{rad}$, back attenuation of -30 dB, ICM with $\sigma_{\mathrm{vel}} = 20\,\mathrm{m/s}$, and $N_{\mathrm{t}} = 4$ present targets.

Figure 7.1.25.: Refined objective function $f_*^{\mathrm{ct}}(\beta, \varphi_{\mathrm{m}}; \widetilde{\beta})$ with parameters swept over $\beta \in [0.5, 4]$ and $\varphi_{\mathrm{m}} \in [-\pi, \pi)$.

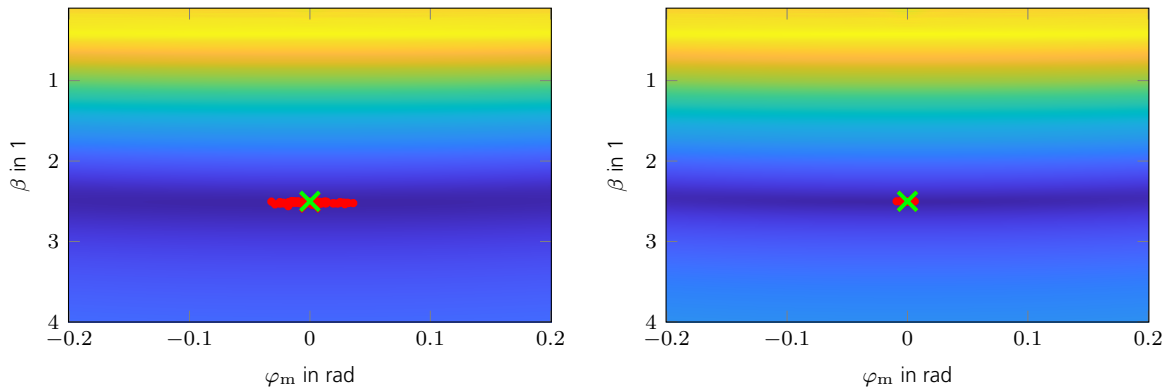

(a) Objective function $f_*(\beta, \varphi_\mathrm{m})$.

(b) Refined objective function $f_*^{\mathrm{ct}}(\beta, \varphi_\mathrm{m}; \widetilde{\beta})$.

Figure 7.1.26.: Zoomed view of objective functions with $\beta \in [0.5, 4]$ and $\varphi_\mathrm{m} \in [-0.2, 0.2]$ for $\widetilde{\beta} = 2.5$ and $\widetilde{\varphi_\mathrm{m}} = 0\,\mathrm{rad}$.

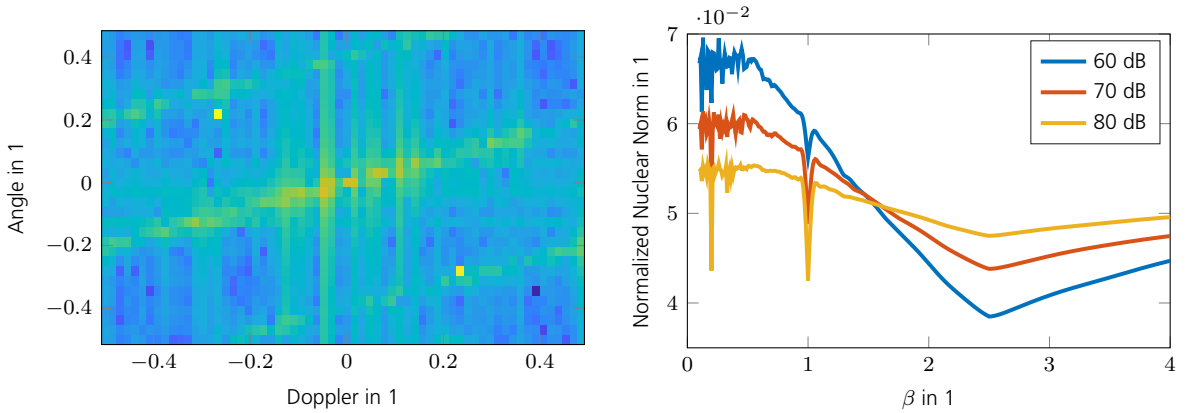

(a) Angle-Doppler scene with very strong targets present.

(b) Resulting nuclear norms, for sake of comparison normalized to unit energy.

Figure 7.1.27.: Impact of strong targets onto objective function $f_*(\beta, \varphi_\mathrm{m})$ - no leakage occurring.

not. An example without Doppler leakage is shown in Fig. 7.1.27, where two very strong targets are present. The objective functions $f_*(\beta, \varphi_\mathrm{m})$ are shown for the case of $\mathrm{CNR} = 60\,\mathrm{dB}$ and SNRs from $60\,\mathrm{dB}$ to $80\,\mathrm{dB}$. For the case of $\beta = 1$ the two point targets become aligned within the same row, causing a very steep minima of the objective function. In the scenario shown, this steep local minima can be evaded without problems. Nevertheless, it is possible to construct a case for which very strong point targets are arranged such that a very steep minima emerges close to the true minima and hence prevent a successful focusing of the clutter ridge. These scenarios, however, are of less practical importance and might be detected by considering additional range gates. A more practical problem occurs for the case of Doppler leakage. This is shown in Fig. 7.1.28, where the point targets are now located half between the grid points such that severe leakage occurs. While the leakage in u has no impact on the nuclear norm used in the objective functions, the leakage in Doppler results in very profound rows which directly compete with the aim of aligning the clutter ridge. As a consequence, the minima marking the true parameter values $\widetilde{\beta}$ and $\widetilde{\varphi_\mathrm{m}}$ vanish in case of very high SNR. One possibility to mitigate this effect is to reduce the Doppler leakage by increasing the number of pulses used per CPI. This, however, might be undesirable

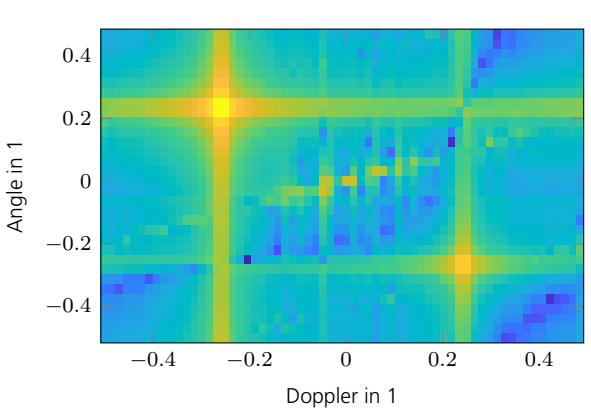

(a) Angle-Doppler scene with very strong targets present.

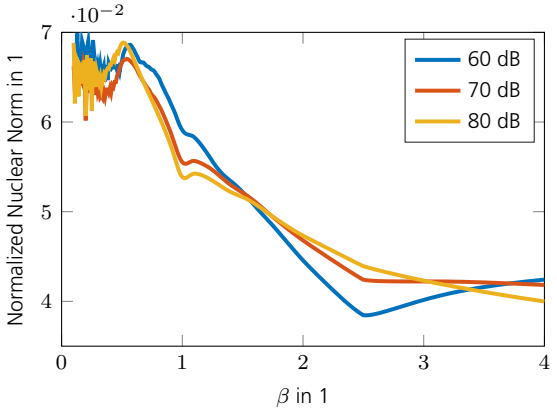

(b) Resulting nuclear norms, for sake of comparison normalized to unit energy.

Figure 7.1.28.: Impact of strong targets onto objective function $f_*(\beta, \varphi_\mathrm{m})$ - sever leakage present.

e. g. in case the CPI or the PRF is limited to a given upper bound.[15]

In summary it is possible to exploit the correlated nature of the clutter samples in the measurement matrix $\boldsymbol{Y}_\mathrm{c}$ to find a matrix of minimum nuclear norm. The main contributions which complicate this attempt are the incomplete measurements in $\boldsymbol{Y}_\mathrm{c}$ which stem from the inherently limited number of pulses available and mainly from velocity misalignment in case of Doppler ambiguities. Furthermore, ICM increases the minimal achievable nuclear norm, broadens the emerging minima in the objective functions and thus decrease the estimation performance. Nevertheless, useful minima are still available since ICM samples are after all correlated. Finally, targets present in the scene are not of concern as long as their SNR is not higher than the CNR. In case of very strong targets, the nuclear norm cannot be used any more to estimate β and φ_m if the targets show strong Doppler leakage effects resulting in very profound rows. In the following section, the ACF algorithm is presented which uses the low rank property of the correlated clutter measurements to estimate the potentially unknown parameters β and φ_m.

7.2. Auto-Clutter Focus

In this section, an auto-clutter focus (ACF) algorithm is presented which exploits the low-rank properties presented in Section 7.1 to determine the parameters β and φ_m, which are the clutter ridge slope and the velocity misalignment angle. Once these parameters are known, they can be used to separate the clutter from moving targets by either using turbo compressed robust principal component analysis (TCRPCA) or by use of a modeled projection filter or a combination of both. These approaches are presented in more detail in Section 7.3.

The ACF problem is as follows, given the single measurement vector of one range-gate under

[15] Windowing techniques to mitigate the leakage effect, unfortunately, do not help in this case since they have a negative effect on the clutter ridge which in turn renders them useless.

test from (2.2.26)

$$\boldsymbol{y} = \sum_{n_\mathrm{t}=0}^{N_\mathrm{t}-1} \boldsymbol{y}_\mathrm{t}\left(x_{n_\mathrm{t}}, \bar{u}_{n_\mathrm{t}}, \bar{f}_{\mathrm{D},n_\mathrm{t}}\right) + \boldsymbol{y}_\mathrm{c}(\widetilde{\beta},\widetilde{\varphi_\mathrm{m}}) + \boldsymbol{n}, \tag{7.2.1}$$

find the parameters β and φ_m. To do so, the correlated nature of the clutter shall be exploited. Furthermore, it is assumed that there are only few moving targets per range gate i. e. targets are sparsely present in (7.2.1). It is further presumed that sufficient channels and pulses are available such that a low-rank matrix of suitable size can be formed from $\boldsymbol{y}$.

In order to estimate the desired parameters from $\boldsymbol{y}$, the following low-rank measurement model is used

$$\boldsymbol{y} = \mathcal{A}\left(\widetilde{\boldsymbol{L}}; \widetilde{\beta}, \widetilde{\varphi_\mathrm{m}}\right) + \boldsymbol{n}, \tag{7.2.2}$$

where $\widetilde{\boldsymbol{L}} \in \mathbb{C}^{N_\mathrm{u}\times N_\mathrm{D}}$ is a low-rank matrix holding the angle-focused clutter contributions as explained in Section 7.1, $\mathcal{A} : \mathbb{C}^{N_\mathrm{u}\times N_\mathrm{D}} \to \mathbb{C}^{M}$ is the clutter focus operator defined further below, $\boldsymbol{y} \in \mathbb{C}^{M}$ is the measurement vector from (7.2.1), and $\boldsymbol{n} \in \mathbb{C}^{M} \sim \mathcal{CN}\left(0, P_\mathrm{n}\right)$ is complex normal i. i. d. noise. For the clutter focus algorithm, $\widetilde{\boldsymbol{L}}$ shall also contain the moving targets present in (7.2.1)[16]. The clutter focus operator $\mathcal{A}$ is defined analogously to the dual low rank form presented in Section 7.1.2 by use of (7.1.19) as

$$\mathcal{A}\left(\boldsymbol{L}; \beta, \varphi_\mathrm{m}\right) = \mathrm{vec}\left(\boldsymbol{A}\mathcal{D}_u(\boldsymbol{L}; \beta, \varphi_\mathrm{m})\boldsymbol{B}^\mathrm{T}\right), \tag{7.2.4}$$

where $\boldsymbol{A} \in \mathbb{C}^{N_\mathrm{rx}\times N_\mathrm{u}}$ and $\boldsymbol{B} \in \mathbb{C}^{N_\mathrm{p}\times N_\mathrm{D}}$ are the spatial and temporal steering matrices given by (2.1.115) and (2.1.116), $\mathcal{D}_u$ is a Fourier shift operator defined in (7.1.16), and $\mathrm{vec}\left(\cdot\right)$ is the vectorization operator which reshapes a matrix into a vector by stacking all columns on top of each other. The measurement model (7.2.2) therefore presumes an angle-focused dual low rank form in the angle-Doppler dimensions of the radar scene denoted by $\boldsymbol{L}$, whose clutter energy is concentrated at $\bar{u} = 0$. It gets shifted in the angular dimension by $\mathcal{D}_u$ according to the parameters β and φ_m to form a diagonal clutter ridge. This form is observed by the moving radar. The shifted radar scene is then mapped to the measurement domain by the spatial and temporal steering matrices $\boldsymbol{A}$ and $\boldsymbol{B}$ and finally vectorized to form the measured space-time measurement vector. This low-rank model of (7.2.1) was justified in Section 7.1. In general, the number of measurements $M = N_\mathrm{rx}N_\mathrm{p}$ might be less than the number of unknowns $n = N_\mathrm{D}N_\mathrm{u}$. Hence, (7.2.2) may be an under-determined system. As explained in Section 7.1.4, a suitable objective function to estimate β is to use the nuclear norm of the estimated low-rank matrix $\widehat{\boldsymbol{L}}$ for which nice minima occur as shown in Fig. 7.1.22a. Unfortunately, $\left\|\widehat{\boldsymbol{L}}\right\|_*$ is not well suited to estimate

[16] It is tempting to already incorporate moving targets into (7.2.2) by extending it to

$$\boldsymbol{y} = \mathcal{A}\left(\widetilde{\boldsymbol{S}} + \widetilde{\boldsymbol{L}}; \widetilde{\beta}, \widetilde{\varphi_\mathrm{m}}\right) + \boldsymbol{n}, \tag{7.2.3}$$

where $\widetilde{\boldsymbol{S}}$ is a sparse matrix intended to hold the moving target contributions. Unfortunately, (7.2.3) is ill-posed in the sense that it is not possible to estimate all unknowns $\widetilde{\boldsymbol{S}}$, $\widetilde{\boldsymbol{L}}$, $\widetilde{\beta}$, and $\widetilde{\varphi_\mathrm{m}}$ simultaneously! Attempting to solve (7.2.3) in an robust principal component analysis (RPCA) like fashion destroys the unique low-rank probability of $\boldsymbol{L}$ for correctly estimated β and φ_m! Quiet frankly, instead of reducing the rank of $\boldsymbol{L}$ by adapting β and φ_m, the rank of $\boldsymbol{L}$ may also be reduced by assigning all non low-rank like entries to $\boldsymbol{S}$. In the extreme case, this results in $\boldsymbol{S}$ containing the whole non-focused clutter ridge.

φ_{m}. As shown in Fig. 7.1.26, $\left\|\widehat{\boldsymbol{L}}\right\|_*$ does not form a narrow minima but remains rather flat. It is therefore necessary to create an additional objective function which allows for a better estimation of φ_{m}. Nevertheless, $\left\|\widehat{\boldsymbol{L}}\right\|_*$ can still be used to estimate β alone. Inspection of Fig. 7.1.26 reveals, that $\left\|\widehat{\boldsymbol{L}}\right\|_*$ is, to some extend, insensitive to wrong intermediate values of φ_{m}. Thus β and φ_{m} can be estimated independently.

7.2.1. Alternative Objective Function for Estimation of Velocity Misalignment Angle

Within this work, a combination of the clutter ridge energy e_{cr} and a clutter ridge antenna pattern correlation coefficient r_{acr} is used as an objective function to estimate $\widetilde{\varphi_{\mathrm{m}}}$ as

$$h_{\varphi_{\mathrm{m}}}(\boldsymbol{L};\beta,\varphi_{\mathrm{m}}) = \frac{1}{\left(e_{\mathrm{cr}} r_{\mathrm{acr}}\right)^2}. \tag{7.2.5}$$

The clutter ridge energy is defined as

$$e_{\mathrm{cr}} = \boldsymbol{l}_{\mathrm{cr}}^{\mathrm{T}} \boldsymbol{l}_{\mathrm{cr}}, \tag{7.2.6}$$

where

$$\boldsymbol{l}_{\mathrm{cr}}^{\mathrm{T}} = \left|\left[\boldsymbol{L}'\right]_{i_{\mathrm{cr}}:}\right| \in \mathbb{R}^{1\times N_{\mathrm{D}}}$$

denotes the element-wise magnitudes of the clutter ridge row in the matrix $\boldsymbol{L}'$ with i_{cr} being the row index corresponding to $\bar{u}=0$. As will be explained in Section 7.2.2 in more detail, the matrix $\boldsymbol{L}'$ is taken to be the result of a gradient update step[17]

$$\boldsymbol{L}' = \boldsymbol{L} - \mu \nabla_{\boldsymbol{L}} h\left(\boldsymbol{L};\beta,\varphi_{\mathrm{m}}\right),$$

with $h\left(\boldsymbol{L};\beta,\varphi_{\mathrm{m}}\right)$ denoting a residual error term defined in (7.2.13). If no targets are present in the range gate-under-test, e_{cr} is maximized for a perfectly focused clutter ridge. This is shown in Fig. 7.2.1. As can be seen, the global maximum marks $\widetilde{\varphi_{\mathrm{m}}}$ well, however, multiple maxima are present. Therefore, either a grid search or a gradient descent algorithm with a well known initial start value is required to find the global maximum. Furthermore, if very strong targets like large ships are present in the scene, the energy in the i_{cr}-th row may also be maximized by setting φ_{m} such that the strong point target is located at $\bar{u}=0$. This is illustrated in Fig. 7.2.2. While in case of a total $\mathrm{SNR}=60\,\mathrm{dB}$ the main clutter just barley creates the global maximum, clearly for a total $\mathrm{SNR}=100\,\mathrm{dB}$ the clutter contribution is not even visible any more. To robustify $h_{\varphi_{\mathrm{m}}}$, a correlation coefficient r_{acr} is introduced to exclude non clutter like entries within $\boldsymbol{l}_{\mathrm{cr}}$ to minimize $h_{\varphi_{\mathrm{m}}}$. It is known from space-time adaptive processing (STAP), that the energy distribution of the clutter ridge follows the product of the antenna patterns and the clutter reflectivity $G_{\mathrm{tx}}\left(\bar{u}\right) G_{\mathrm{rx}}\left(\bar{u}\right) x_{\mathrm{c}}\left(\bar{u}\right)$ for $\bar{u}\in[-1,1)$ [4]. While $x_{\mathrm{c}}\left(\bar{u}\right)$ is of random nature, the antenna patterns are known to some extend and the energy distribution of the clutter ridge can be roughly approximated by

$$G_{\mathrm{trx}}\left(\bar{u}\right) = G_{\mathrm{tx}}\left(\bar{u}\right) G_{\mathrm{rx}}\left(\bar{u}\right).$$

[17] Briefly said, since $\boldsymbol{L}(\beta,\varphi_{\mathrm{m}}) = \mathcal{A}^{-1}\left(\boldsymbol{y};\beta,\varphi_{\mathrm{m}}\right)$ is not available as $\mathcal{A}^{-1}$ does not exist in case of missing samples, the gradient update step coming from the singular value thresholding (SVT) approach is used as an approximation $\boldsymbol{L}(\beta,\varphi_{\mathrm{m}}) \approx \boldsymbol{L}' = \boldsymbol{L} - \mu\nabla_{\boldsymbol{L}} h\left(\boldsymbol{L};\beta,\varphi_{\mathrm{m}}\right)$.

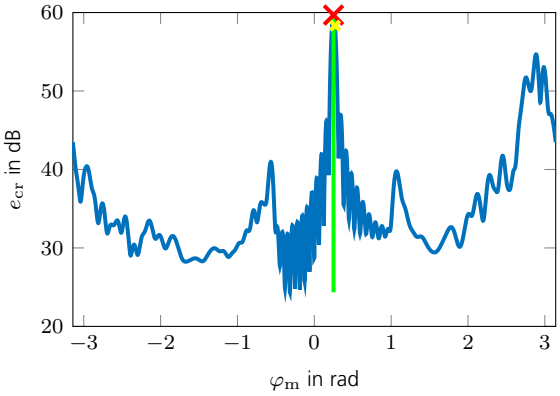

(a) e_{cr} vs. $\varphi_{\mathrm{m}} \in [-\pi, \pi)$.

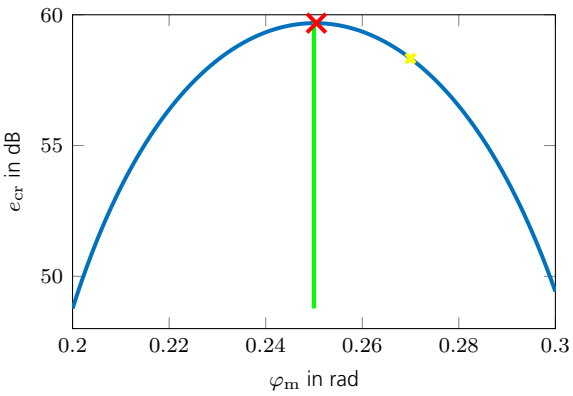

(b) Zoomed view of Fig. 7.2.1a.

Figure 7.2.1.: Clutter-row energy e_{cr} without present targets. The green line indicates the true value $\widetilde{\varphi_{\mathrm{m}}}$, the red cross the global maximum, and the yellow cross the intermediate value φ_{m} from which $\boldsymbol{L}$ was determined.

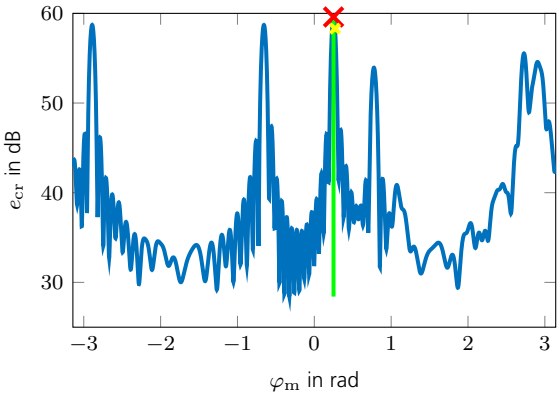

(a) Two targets present with total $\mathrm{SNR} = 60\,\mathrm{dB}$.

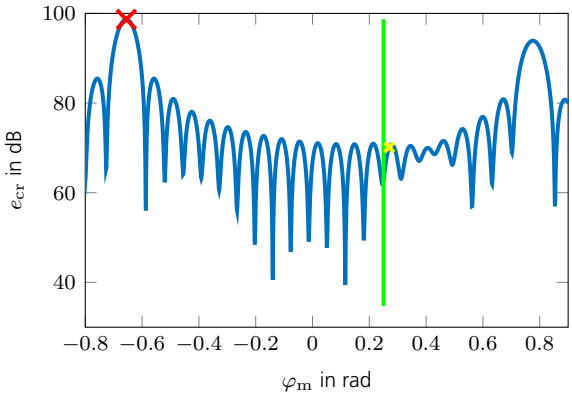

(b) Two targets present with total $\mathrm{SNR} = 100\,\mathrm{dB}$.

Figure 7.2.2.: Clutter-row energy e_{cr} with strong targets present.

Assuming further, that the shifted or focused clutter follows the same distribution, which of course is a very coarse approximation, a correlation coefficient can be setup as

$$r_{\mathrm{acr}} = \frac{\bar{\boldsymbol{l}}_{\mathrm{cr}}^{\mathrm{T}} \boldsymbol{g}_{\mathrm{ap}}}{\left\| \bar{\boldsymbol{l}}_{\mathrm{cr}} \right\|_2} \tag{7.2.7}$$

to compare the clutter ridge row $\boldsymbol{l}_{\mathrm{cr}}$ to the expected one. Within (7.2.7), $\bar{\boldsymbol{l}}_{\mathrm{cr}} \in \mathbb{R}^{N_{\mathrm{D}}}$ denotes the mean free clutter ridge row vector defined as

$$\bar{\boldsymbol{l}}_{\mathrm{cr}} = \boldsymbol{l}_{\mathrm{cr}} - \mu_{\boldsymbol{l}_{\mathrm{cr}}} \mathbf{1}, \tag{7.2.8}$$

with

$$\mu_{\boldsymbol{l}_{\mathrm{cr}}} = \frac{1}{N_{\mathrm{D}}} \sum_{i=1}^{N_{\mathrm{D}}} l_{\mathrm{cr},i} \tag{7.2.9}$$

being the mean value of $\boldsymbol{l}_{\mathrm{cr}}$ and $\mathbf{1} \in \mathbb{N}^{N_{\mathrm{D}}}$ a vector of ones. Furthermore, $\boldsymbol{g}_{\mathrm{ap}} \in \mathbb{R}^{N_{\mathrm{D}}}$ is the normalized mean free antenna pattern vector defined as

$$\boldsymbol{g}_{\mathrm{ap}} = \frac{\boldsymbol{g}_{\mathrm{trx}} - \mu_{\boldsymbol{g}_{\mathrm{trx}}} \mathbf{1}}{\left\| \boldsymbol{g}_{\mathrm{trx}} - \mu_{\boldsymbol{g}_{\mathrm{trx}}} \mathbf{1} \right\|_2},$$

where

$$\boldsymbol{g}_{\mathrm{trx}} = \left[G_{\mathrm{trx}} \left(2\bar{d} \frac{n_{\mathrm{D}}}{N_{\mathrm{D}}} \right) \right]_{n_{\mathrm{D}} = -N_{\mathrm{D}}/2}^{N_{\mathrm{D}}/2-1} \in \mathbb{R}^{N_{\mathrm{D}}}$$

is the antenna pattern product sampled across the visible range and $\mu_{\boldsymbol{g}_{\mathrm{trx}}}$ denotes the mean value of $\boldsymbol{g}_{\mathrm{trx}}$ similar to (7.2.9). By construction, the correlation coefficient r_{acr} takes values between $-1 \leq r_{\mathrm{acr}} \leq 1$. An illustration of r_{acr} for the above examples is shown in Fig. 7.2.3. The case of $\mathrm{SNR} = 60\,\mathrm{dB}$ is shown in Fig. 7.2.3d. Comparing it to Fig. 7.2.2a reveals an increased robustness against point targets present in the scene. In case of extremely strong targets as shown in Fig. 7.2.3f, the product $e_{\mathrm{cr}} r_{\mathrm{acr}}$ alone is not capable of suppressing the target contributions sufficiently. Nevertheless, if all products $e_{\mathrm{cr}} r_{\mathrm{acr}}$ for $r_{\mathrm{acr}} \leq 0.1$ are ignored, e. g. by setting those to a very small value, the clutter ridge maximum can be found also in case of extremely strong present targets. It is worthwhile to note, that e_{cr} alone would not be enough in this case, rather the product $e_{\mathrm{cr}} r_{\mathrm{acr}}$ creates a maximum at the correct value $\widetilde{\varphi_{\mathrm{m}}}$. As illustrated in Fig. 7.2.4, e_{cr} does not show any maximum at the true value $\widetilde{\varphi_{\mathrm{m}}}$, while the product does. Hence, r_{acr} serves the purpose of excluding extremely dissimilar clutter ridges compared the to be expected antenna pattern product. This helps in acquiring some immunity against strong point targets in the range gate-under-test. Yet, if extremely strong targets are closely located at the clutter ridge, this approach might also fail.[18] By combining (7.2.6) and (7.2.7), the objective function (7.2.5) can

[18] One possibility to overcome this issue would be the following: in a first step, the angle-Doppler scene is reconstructed solely by use of a compressive sensing (CS) approach. In a second step, all entries within the scene stronger than the clutter to noise ratio (CNR) are set to zero. In a final step, the corresponding measurement values to the purged scene are fed to the ACF. The use of a CS approach avoids the problem of overwhelming target side lobes. Thus, target energy can be removed from the scene without disturbing clutter contributions too much. As the ACF algorithm is somewhat robust against present target energy, residual target energy after the CS purge should not be of concern.

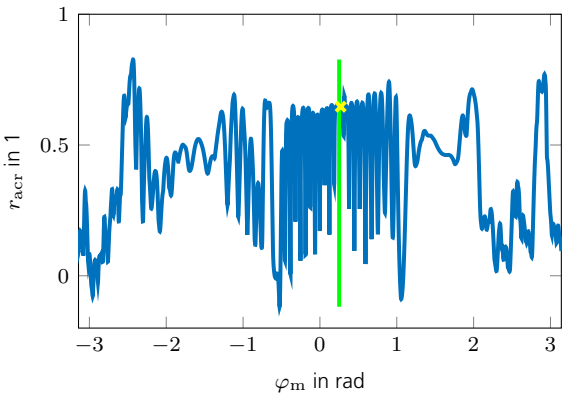

(a) Antenna pattern correlation coefficient r_{acr} in case of no targets present.

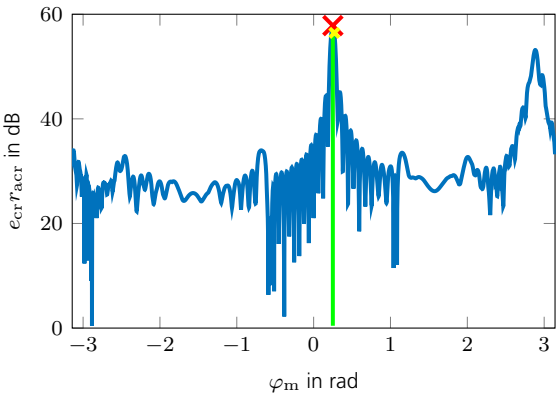

(b) Product $e_{\mathrm{cr}} r_{\mathrm{acr}}$ in case of no targets present.

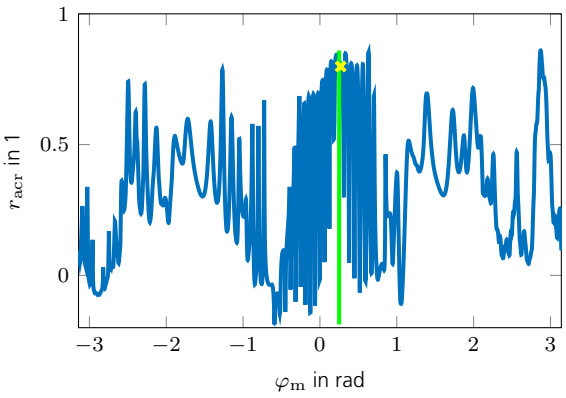

(c) Antenna pattern correlation coefficient r_{acr} in case of two targets present with total $\mathrm{SNR} = 60\,\mathrm{dB}$.

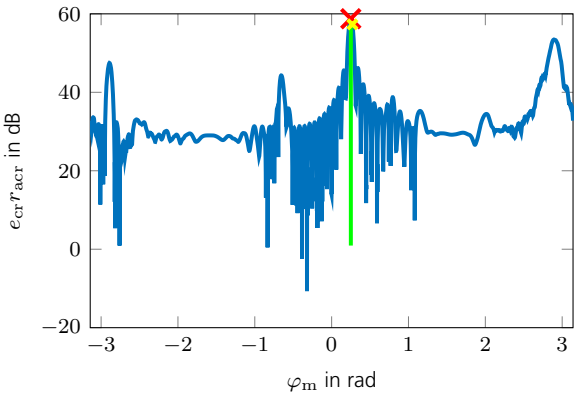

(d) Product $e_{\mathrm{cr}} r_{\mathrm{acr}}$ in case of two targets present with total $\mathrm{SNR} = 60\,\mathrm{dB}$.

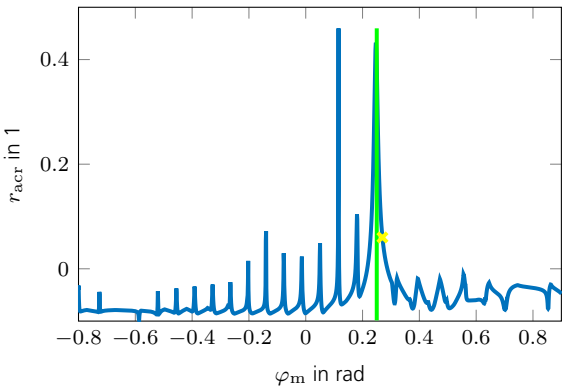

(e) Antenna pattern correlation coefficient r_{acr} in case of two targets present with total $\mathrm{SNR} = 100\,\mathrm{dB}$.

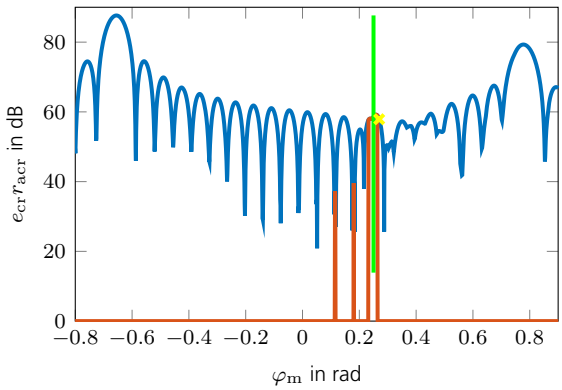

(f) Product $e_{\mathrm{cr}} r_{\mathrm{acr}}$ in case of two targets present with total $\mathrm{SNR} = 100\,\mathrm{dB}$. The orange line indicates $e_{\mathrm{cr}} r_{\mathrm{acr}}$ for $r_{\mathrm{acr}} > 0.1$.

Figure 7.2.3.: Robustification against strong present targets by incorporating the antenna pattern correlation coefficient r_{acr}.

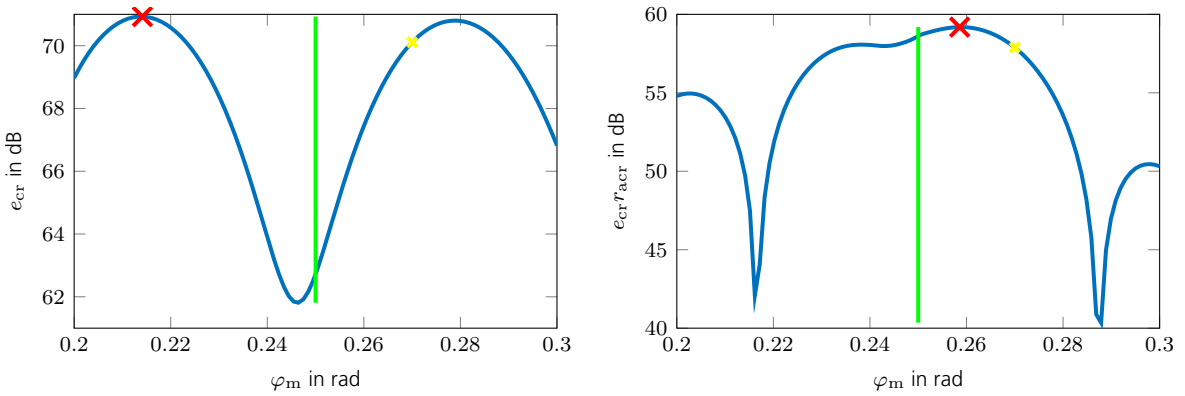

(a) Clutter ridge energy e_{cr} alone. Due to the contributions of extremely strong targets, no maximum is present at $\widetilde{\varphi_{\mathrm{m}}}$.

(b) Product $e_{\mathrm{cr}} r_{\mathrm{acr}}$, where maximum at $\widetilde{\varphi_{\mathrm{m}}}$ again is present.

Figure 7.2.4.: Comparison of e_{cr} to $e_{\mathrm{cr}} r_{\mathrm{acr}}$ for the case of extremely strong present targets.

be reformulated to

$$h_{\varphi_{\mathrm{m}}}(\boldsymbol{L}; \beta, \varphi_{\mathrm{m}}) = \frac{\left\| \bar{\boldsymbol{l}}_{\mathrm{cr}} \right\|_2^2}{\left| \bar{\boldsymbol{l}}_{\mathrm{cr}}^{\mathrm{T}} \boldsymbol{g}_{\mathrm{ap}} \boldsymbol{l}_{\mathrm{cr}}^{\mathrm{T}} \boldsymbol{l}_{\mathrm{cr}} \right|^2}. \tag{7.2.10}$$

This quadratic form can be reformulated as

$$h_{\varphi_{\mathrm{m}}}(\boldsymbol{L}; \beta, \varphi_{\mathrm{m}}) = f_{\varphi_{\mathrm{m}}}(\boldsymbol{L}; \beta, \varphi_{\mathrm{m}})^2$$

with

$$f_{\varphi_{\mathrm{m}}}(\boldsymbol{L}; \beta, \varphi_{\mathrm{m}}) = \frac{\left\| \bar{\boldsymbol{l}}_{\mathrm{cr}} \right\|_2}{\bar{\boldsymbol{l}}_{\mathrm{cr}}^{\mathrm{T}} \boldsymbol{g}_{\mathrm{ap}} \boldsymbol{l}_{\mathrm{cr}}^{\mathrm{T}} \boldsymbol{l}_{\mathrm{cr}}}, \tag{7.2.11}$$

which will be of use in the following. An example of $h_{\varphi_{\mathrm{m}}}$ is shown in Fig. 7.2.5. As can be seen, the true value $\widetilde{\varphi_{\mathrm{m}}}$ can be found at the minimum of $h_{\varphi_{\mathrm{m}}}(\boldsymbol{L})$. Only in the case of extremely strong targets, the minimum does not coincide with the true value. Note that no attempt to cut non redundant samples in order to obtain the embedded low-rank matrix is done here so far. Doing so would result in a non smooth objective function of β and φ_{m}, as shown in Fig. 7.1.22b, which would be extremely difficult to minimize.

7.2.2. The Auto-Clutter Focus Algorithm

To obtain a solution for (7.2.2) the minimization problem

$$\widehat{\boldsymbol{L}}, \widehat{\beta}, \widehat{\varphi_{\mathrm{m}}} = \underset{\boldsymbol{L}, \beta, \varphi_{\mathrm{m}}}{\arg\min} \lambda \left\| \boldsymbol{L} \right\|_* + h(\boldsymbol{L}; \beta, \varphi_{\mathrm{m}}) + h_{\varphi_{\mathrm{m}}}(\boldsymbol{L}; \beta, \varphi_{\mathrm{m}}) \tag{7.2.12}$$

is solved, where

$$h(\boldsymbol{L}; \beta, \varphi_{\mathrm{m}}) = \left\| \boldsymbol{y} - \mathcal{A}\left(\boldsymbol{L}; \beta, \varphi_{\mathrm{m}}\right) \right\|_2^2 \tag{7.2.13}$$

denotes the residual term and $h_{\varphi_{\mathrm{m}}}(\boldsymbol{L}; \beta, \varphi_{\mathrm{m}})$ is defined in (7.2.5). The objective function in (7.2.12) is convex in $\boldsymbol{L}$ but not in β and φ_{m}. For fixed β and φ_{m}, (7.2.12) is a standard affine rank minimization (ARM) problem and can be solved via corresponding approaches like SVT and

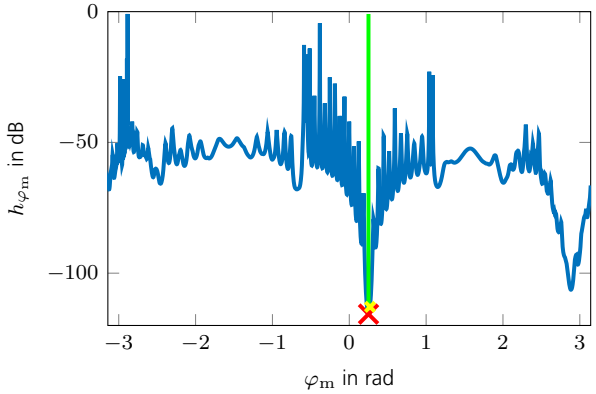

(a) No targets present.

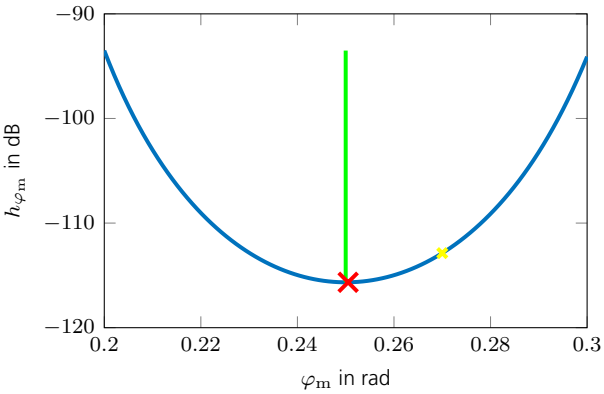

(b) No targets present; zoomed view.

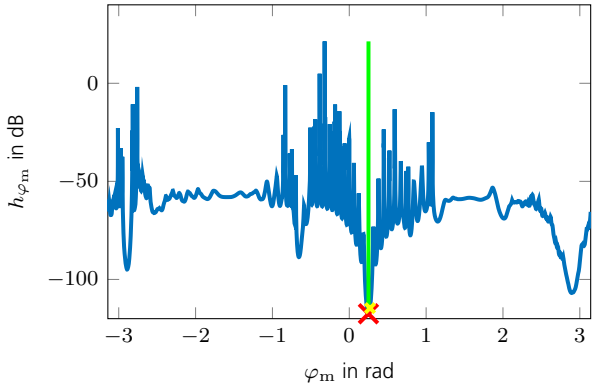

(c) Two targets present with total $\mathrm{SNR} = 60\,\mathrm{dB}$.

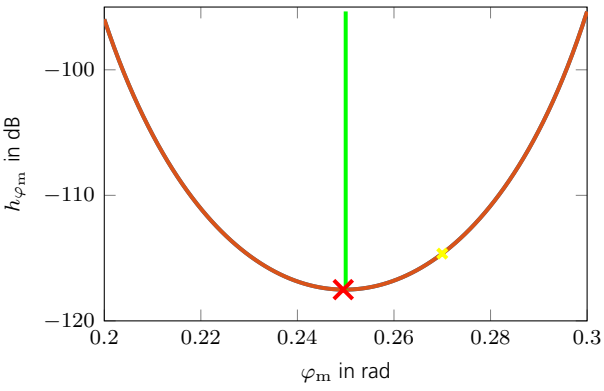

(d) Two targets present with total $\mathrm{SNR} = 60\,\mathrm{dB}$.

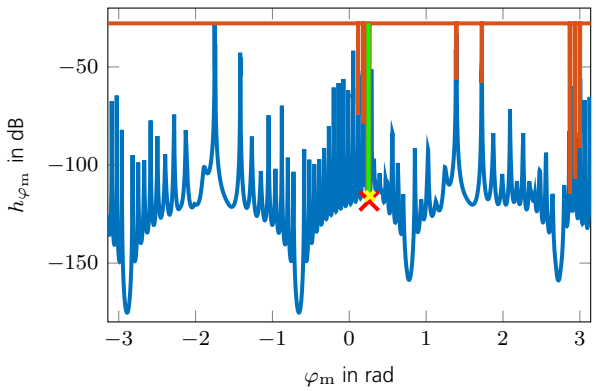

(e) Two targets present with total $\mathrm{SNR} = 100\,\mathrm{dB}$.

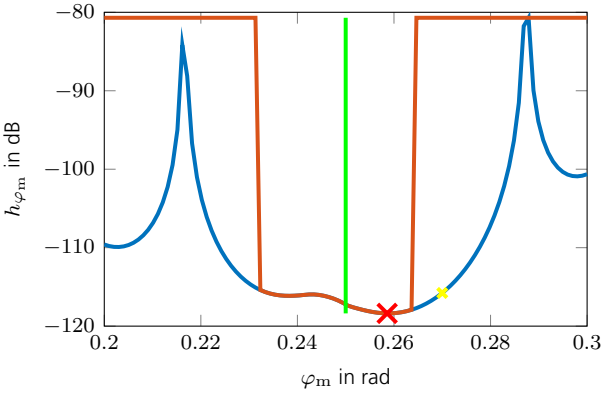

(f) Two targets present with total $\mathrm{SNR} = 100\,\mathrm{dB}$.

Figure 7.2.5.: Objective function h_{φ_m} vs. φ_m. The green line indicates the true value $\widetilde{\varphi_\mathrm{m}}$, the red cross the global minimum, and the yellow cross the intermediate value φ_m from which $\boldsymbol{L}$ was determined.

turbo singular value thresholding (TSVT) presented in Chapter 4 and 6.3. Finding a solution for β and φ_{m}, however, is not trivial. A direct gradient descent approach to estimate β is not possible since the required gradient $\nabla_\beta \|\boldsymbol{L}\|_*$ is not available. At first, the nuclear norm is non differentiable.[19] At second, $\boldsymbol{L}$ is not available in form of a closed form solution like in Section 7.1, where the clutter focus operator $\mathcal{A}_u(\boldsymbol{L};\beta,\varphi_{\mathrm{m}})$ was taken to be invertible, which allowed for the explicit form $\boldsymbol{L} = \mathcal{A}_u^{-1}(\boldsymbol{Y};\beta,\varphi_{\mathrm{m}})$ to exist. Nevertheless, it is possible to use the residual term $h(\boldsymbol{L};\beta,\varphi_{\mathrm{m}})$ as a guidance function to estimate β. Hence, instead of the unavailable gradient function $\nabla_\beta \|\boldsymbol{L}\|_*$, $\nabla_\beta h(\boldsymbol{L};\beta,\varphi_{\mathrm{m}})$ will be used. Finding the velocity misalignment angle φ_{m} is also demanding, since the substitute function $h_{\varphi_{\mathrm{m}}}$ has multiple minima. For the derivation to follow, it is assumed, that an initial value $\varphi_{\mathrm{m},0}$ close enough to the true solution $\widetilde{\varphi_{\mathrm{m}}}$ is known such that $\widetilde{\varphi_{\mathrm{m}}}$ can be found by use of a gradient descent approach. In case such an initial value is not available, a grid search strategy to find the global minimum can be used. In summary, the solution to (7.2.12) can be found by the iterative procedure

$$\begin{aligned}\boldsymbol{L}_i &= \mathrm{TSVT}(\boldsymbol{L}_{i-1})\\ \beta_i &= \beta_{i-1} - \mu_{\beta,i}\nabla_\beta h(\boldsymbol{L}_i;\beta_{i-1},\varphi_{\mathrm{m},i-1})\\ \varphi_{\mathrm{m},i} &= \varphi_{\mathrm{m},i-1} - \mu_{\varphi_{\mathrm{m}},i}\nabla_{\varphi_{\mathrm{m}}} h_{\varphi_{\mathrm{m}}}(\boldsymbol{L}_i;\beta_i,\varphi_{\mathrm{m},i-1}),\end{aligned} \tag{7.2.14}$$

where $\mathrm{TSVT}(\boldsymbol{L})$ denotes one TSVT step given by (6.3.2). The gradients $\nabla_\beta h$ and $\nabla_{\varphi_{\mathrm{m}}} h_{\varphi_{\mathrm{m}}}$ are derived in closed form in Appendix A.7.2 and A.7.3. The step sizes μ_β and $\mu_{\varphi_{\mathrm{m}}}$ are determined by use of a Levenberg-Marquardt (LM) approach, which is a method to solve non-linear least square problems [67]. In the framework of the LM algorithm, let

$$\boldsymbol{r}_i = \boldsymbol{y} - \mathcal{A}(\boldsymbol{L}_i;\beta_{i-1},\varphi_{\mathrm{m},i-1})$$

denote the error vector whose ℓ_2 norm equals the residual term to be minimized, namely

$$\|\boldsymbol{r}_i\|_2^2 = h(\boldsymbol{L}_i;\beta_{i-1},\varphi_{\mathrm{m},i-1}).$$

Furthermore, let

$$\begin{aligned}\boldsymbol{J}_{r,i} &= \left[\frac{\partial \boldsymbol{r}_i}{\partial\beta}, \frac{\partial \boldsymbol{r}_i}{\partial\varphi_{\mathrm{m}}}\right] \in \mathbb{C}^{M\times 2}\\ &= -\left[\frac{\partial\mathcal{A}(\boldsymbol{L}_i;\beta_{i-1},\varphi_{\mathrm{m},i-1})}{\partial\beta}, \frac{\partial\mathcal{A}(\boldsymbol{L}_i;\beta_{i-1},\varphi_{\mathrm{m},i-1})}{\partial\varphi_{\mathrm{m}}}\right]\end{aligned}$$

denote the corresponding Jacobi matrix, where the required derivatives are given in the Appendix A.7 by (A.7.9) and (A.7.21), respectively. Finally, let $\lambda_{\mathrm{lm}} \in \mathbb{R}^+$ be a damping factor and $c_{\mathrm{lm,up}} \in \mathbb{R}^+$ and $c_{\mathrm{lm,dn}} \in \mathbb{R}^+$ two adjustment coefficients. Then, a suitable step size $\mu_{\beta,i}$ can

[19] Although a subgradient exists which might be used for a gradient descent approach [66]!

be found by the iterative procedure

$$\begin{aligned}\mu_{\beta,i} &= \left[\left(\boldsymbol{J}_{r,i}^{\mathrm{H}}\boldsymbol{J}_{r,i} + \lambda_{\mathrm{lm}}\boldsymbol{I}\right)^{-1}\right]_{1,1}\\ \beta_i &= \beta_{i-1} - \mu_{\beta,i}\nabla_{\beta}h\left(\boldsymbol{L}_i;\beta_{i-1},\varphi_{\mathrm{m},i-1}\right)\\ \lambda_{\mathrm{lm}} &= \begin{cases}\lambda_{\mathrm{lm}}/c_{\mathrm{lm,dn}} & \text{if } h\left(\boldsymbol{L}_i;\beta_i,\varphi_{\mathrm{m},i-1}\right) < h\left(\boldsymbol{L}_i;\beta_{i-1},\varphi_{\mathrm{m},i-1}\right)\\ \lambda_{\mathrm{lm}}c_{\mathrm{lm,up}} & \text{else}\end{cases}\end{aligned}$$

until $h\left(\boldsymbol{L}_i;\beta_i,\varphi_{\mathrm{m},i-1}\right) < h\left(\boldsymbol{L}_i;\beta_{i-1},\varphi_{\mathrm{m},i-1}\right)$[20]. A similar approach works for $\mu_{\varphi_{\mathrm{m}}}$, for which the error vector is $f_{\varphi_{\mathrm{m}}}(\boldsymbol{L}_i;\beta_i,\varphi_{\mathrm{m},i-1})$ defined in (7.2.11). The required Jacobi matrix, or scalar in this case, is

$$J_{f_{\varphi_{\mathrm{m}}},i} = \frac{\partial f_{\varphi_{\mathrm{m}}}(\boldsymbol{L}_i;\beta_i,\varphi_{\mathrm{m},i-1})}{\partial\varphi_{\mathrm{m}}},$$

which is given in the Appendix A.7.3 by (A.7.22). Putting all the above steps together, the ACF algorithm is listed in Algorithm 7.1. The input parameter λ is determined as in the TSVT algorithm given by (6.3.3). The maximum number of LM step size adaption iterations is denoted by J, which is necessary to avoid a dead lock in case a local minimum was found from which no improvement in $h\left(\boldsymbol{L}_i;\beta,\varphi_{\mathrm{m}}\right)$ is possible.

The key idea of the minimization approach given in (7.2.14) is in a first step to find a matrix of lower nuclear norm. This matrix "looks" more similar to a focused one since homogeneous rows[21] are more emphasized. The second step follows this "guidance" and adjusts β to reflect the newly found homogeneity. In doing so, it follows the descending direction of $\|\boldsymbol{L}\|_*$, which ultimately leads to the true value $\widetilde{\beta}$. The third step attempts to focus the main energy onto the $\bar{u} = 0$ row by adjusting φ_{m}. The sequence of the first two steps in (7.2.14) is therefore crucial and cannot be interchanged. Some examples illustrating this minimization procedure are shown in Fig. 7.2.6.

Once a minimum and some reasonable estimate of β and φ_{m} is found, a refined estimation of these parameters can be conducted by repeating the ACF algorithm a second time but with a preceding preparation of the measurement samples $\boldsymbol{y}$. As was shown in Section 7.1, setting incomplete measurement samples in the measurement matrix $\boldsymbol{Y}$ to zero suppresses clutter leakage and narrows the minimum in the objective function marking the true value in $\|\boldsymbol{L}\|_*$ as shown in Fig. (7.1.25). This knowledge can be exploited by forming a cut measurement matrix $\boldsymbol{Y}_{\mathrm{cut}}$ similar to (7.1.23). This can be done by at first creating an up-sampled measurement matrix $\boldsymbol{Y}_{\mathrm{up}} \in \mathbb{C}^{N_{\mathrm{u}}\times N_{\mathrm{D}}}$ defined as

$$\left[\boldsymbol{Y}_{\mathrm{up}}\right]_{ij} = \begin{cases} y_k & \text{if } k = i + jN_{\mathrm{u}} \in \Omega_y\\ 0 & \text{else}\end{cases}, \tag{7.2.15}$$

where $i = 0,1,\ldots,N_{\mathrm{u}}-1$, $j = 0,1,\ldots,N_{\mathrm{D}}-1$, and Ω_y denotes the sample index set. Obviously, in case of no missing samples, $\boldsymbol{Y}_{\mathrm{up}} = \boldsymbol{Y}$. In the next step, this up-sampled measurement matrix is angle-focused, followed by setting all incomplete samples to zero and shift back to the original

[20] Note, that $\mu_{\beta,i} \in \mathbb{R}$ in any case since the inverse of a hermitian matrix is also hermitian.
[21] Or columns, which, however, in this case is not wanted.

Algorithm 7.1 The ACF algorithm.

Input: $\mathcal{A}$, $\boldsymbol{y}$, λ, I, β_0, $\varphi_{\mathrm{m},0}$, J, $\lambda_{\mathrm{lm},\beta}$, $c_{\mathrm{lm,dn},\beta}$, $c_{\mathrm{lm,up},\beta}$, $\lambda_{\mathrm{lm},\varphi_\mathrm{m}}$, $c_{\mathrm{lm,dn},\varphi_\mathrm{m}}$, $c_{\mathrm{lm,up},\varphi_\mathrm{m}}$

Initialization:

$\epsilon \leftarrow \min\left(10^{-4}, 5\cdot 10^{-3}\lambda\right)$

$i \leftarrow 0$, $j \leftarrow 0$, $d \leftarrow \infty$, $\boldsymbol{L}_0 \leftarrow \boldsymbol{0}$, $\mu \leftarrow n/(M\left\|\mathcal{A}\right\|_2^2)$

Body:

while $d > \epsilon$ **and** $i < I$ **do**

$i \leftarrow i+1$

$\boldsymbol{R}_i \leftarrow \boldsymbol{L}_{i-1} - \mu\nabla_{\boldsymbol{L}} h\left(\boldsymbol{L}_{i-1};\beta_{i-1},\varphi_{\mathrm{m},i-1}\right)$

$\boldsymbol{Z}_i \leftarrow \mathcal{S}_{\mathrm{l},\mu\lambda}\left(\boldsymbol{R}_i\right)$

$\alpha_i \leftarrow \begin{cases} \frac{1}{n}\mathrm{div}\left(\mathcal{S}_{l,\mu\lambda}\left(\boldsymbol{R}_i\right)\right) & \text{if } \boldsymbol{R}\in\mathbb{R}^{N_1\times N_2} \\ \frac{1}{2n}\mathrm{div}\left(\mathcal{S}_{l,\mu\lambda}\left(\boldsymbol{R}_i\right)\right) & \text{if } \boldsymbol{R}\in\mathbb{C}^{N_1\times N_2} \end{cases}$

$c_i \leftarrow \left\langle \boldsymbol{Z}_i - \alpha_i\boldsymbol{R}_i, \boldsymbol{R}_i\right\rangle_{\mathrm{F}} / \left\|\boldsymbol{Z}_i - \alpha_i\boldsymbol{R}_i\right\|_{\mathrm{F}}^2$

$\boldsymbol{L}_i \leftarrow c_i\left(\boldsymbol{Z}_i - \alpha_i\boldsymbol{R}_i\right)$

$\boldsymbol{J}_{r,i} \leftarrow -\left[\frac{\partial\mathcal{A}(\boldsymbol{L}_i;\beta_{i-1},\varphi_{\mathrm{m},i-1})}{\partial\beta}, \frac{\partial\mathcal{A}(\boldsymbol{L}_i;\beta_{i-1},\varphi_{\mathrm{m},i-1})}{\partial\varphi_\mathrm{m}}\right]$

$\mu_{\beta,i} \leftarrow \left[\left(\boldsymbol{J}_{r,i}^{\mathrm{H}}\boldsymbol{J}_{r,i} + \lambda_{\mathrm{lm},\beta}\boldsymbol{I}\right)^{-1}\right]_{1,1}$

$\beta_i \leftarrow \beta_{i-1} - \mu_{\beta,i}\nabla_\beta h\left(\boldsymbol{L}_i;\beta_{i-1},\varphi_{\mathrm{m},i-1}\right)$

$\lambda_{\mathrm{lm},\beta} \leftarrow \begin{cases} \lambda_{\mathrm{lm},\beta}/c_{\mathrm{lm,dn},\beta} & \text{if } h\left(\boldsymbol{L}_i;\beta_i,\varphi_{\mathrm{m},i-1}\right) < h\left(\boldsymbol{L}_i;\beta_{i-1},\varphi_{\mathrm{m},i-1}\right) \\ \lambda_{\mathrm{lm},\beta}c_{\mathrm{lm,up},\beta} & \text{else} \end{cases}$

while $h\left(\boldsymbol{L}_i;\beta_i,\varphi_{\mathrm{m},i-1}\right) > h\left(\boldsymbol{L}_i;\beta_{i-1},\varphi_{\mathrm{m},i-1}\right)$ **and** $j < J$ **do**

$\mu_{\beta,i} \leftarrow \left[\left(\boldsymbol{J}_{r,i}^{\mathrm{H}}\boldsymbol{J}_{r,i} + \lambda_{\mathrm{lm},\beta}\boldsymbol{I}\right)^{-1}\right]_{1,1}$

$\beta_i \leftarrow \beta_{i-1} - \mu_{\beta,i}\nabla_\beta h\left(\boldsymbol{L}_i;\beta_{i-1},\varphi_{\mathrm{m},i-1}\right)$

$\lambda_{\mathrm{lm},\beta} \leftarrow \begin{cases} \lambda_{\mathrm{lm},\beta}/c_{\mathrm{lm,dn},\beta} & \text{if } h\left(\boldsymbol{L}_i;\beta_i,\varphi_{\mathrm{m},i-1}\right) < h\left(\boldsymbol{L}_i;\beta_{i-1},\varphi_{\mathrm{m},i-1}\right) \\ \lambda_{\mathrm{lm},\beta}c_{\mathrm{lm,up},\beta} & \text{else} \end{cases}$

$j \leftarrow j+1$

end while

$j \leftarrow 0$

$J_{f_{\varphi_\mathrm{m}},i} \leftarrow \frac{\partial f_{\varphi_\mathrm{m}}(\boldsymbol{L}_i;\beta_i,\varphi_{\mathrm{m},i-1})}{\partial\varphi_\mathrm{m}}$

$\mu_{\varphi_\mathrm{m},i} \leftarrow \left(J_{f_{\varphi_\mathrm{m}},i}^2 + \lambda_{\mathrm{lm},\varphi_\mathrm{m}}\right)^{-1}$

$\varphi_{\mathrm{m},i} \leftarrow \varphi_{\mathrm{m},i-1} - \mu_{\varphi_\mathrm{m},i}\nabla_{\varphi_\mathrm{m}} h_{\varphi_\mathrm{m}}\left(\boldsymbol{L}_i;\beta_i,\varphi_{\mathrm{m},i-1}\right),$

$\lambda_{\mathrm{lm},\varphi_\mathrm{m}} \leftarrow \begin{cases} \lambda_{\mathrm{lm},\varphi_\mathrm{m}}/c_{\mathrm{lm,dn},\varphi_\mathrm{m}} & \text{if } h_{\varphi_\mathrm{m}}\left(\boldsymbol{L}_i;\beta_i,\varphi_{\mathrm{m},i-1}\right) < h_{\varphi_\mathrm{m}}\left(\boldsymbol{L}_i;\beta_{i-1},\varphi_{\mathrm{m},i-1}\right) \\ \lambda_{\mathrm{lm},\varphi_\mathrm{m}}c_{\mathrm{lm,up},\varphi_\mathrm{m}} & \text{else} \end{cases}$

while $h_{\varphi_\mathrm{m}}\left(\boldsymbol{L}_i;\beta_i,\varphi_{\mathrm{m},i-1}\right) > h_{\varphi_\mathrm{m}}\left(\boldsymbol{L}_i;\beta_{i-1},\varphi_{\mathrm{m},i-1}\right)$ **and** $j < J$ **do**

$\mu_{\varphi_\mathrm{m},i} \leftarrow \left(J_{f_{\varphi_\mathrm{m}},i}^2 + \lambda_{\mathrm{lm},\varphi_\mathrm{m}}\right)^{-1}$

$\varphi_{\mathrm{m},i} \leftarrow \varphi_{\mathrm{m},i-1} - \mu_{\varphi_\mathrm{m},i}\nabla_{\varphi_\mathrm{m}} h_{\varphi_\mathrm{m}}\left(\boldsymbol{L}_i;\beta_i,\varphi_{\mathrm{m},i-1}\right),$

$\lambda_{\mathrm{lm},\varphi_\mathrm{m}} \leftarrow \begin{cases} \lambda_{\mathrm{lm},\varphi_\mathrm{m}}/c_{\mathrm{lm,dn},\varphi_\mathrm{m}} & \text{if } h_{\varphi_\mathrm{m}}\left(\boldsymbol{L}_i;\beta_i,\varphi_{\mathrm{m},i-1}\right) < h_{\varphi_\mathrm{m}}\left(\boldsymbol{L}_i;\beta_{i-1},\varphi_{\mathrm{m},i-1}\right) \\ \lambda_{\mathrm{lm},\varphi_\mathrm{m}}c_{\mathrm{lm,up},\varphi_\mathrm{m}} & \text{else} \end{cases}$

$j \leftarrow j+1$

end while

$j \leftarrow 0$

$d \leftarrow \left\|\boldsymbol{L}_i - \boldsymbol{L}_{i-1}\right\|_{\mathrm{F}} / \left\|\boldsymbol{L}_{i-1}\right\|_{\mathrm{F}}$

end while

Output: $\widehat{\beta} \leftarrow \beta_i$, $\widehat{\varphi_\mathrm{m}} \leftarrow \varphi_{\mathrm{m},i}$

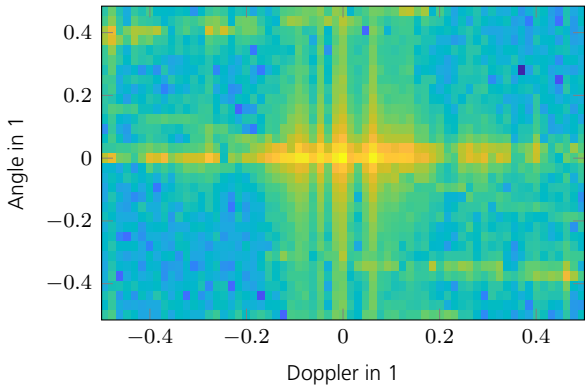

(a) Initial $\boldsymbol{L}_{i-1}$ before TSVT step.

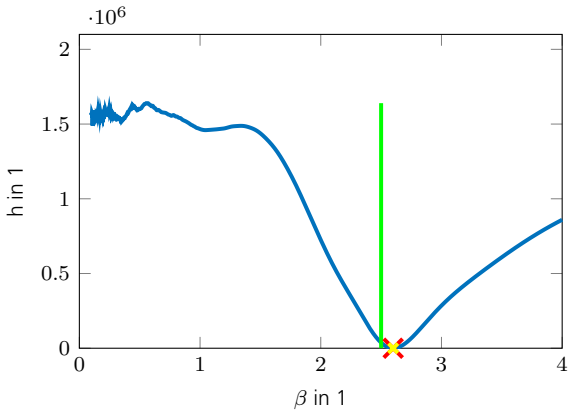

(b) Residual term $h\left(\boldsymbol{L}_{i-1};\beta_{i-1},\varphi_{\mathrm{m},i-1}\right)$. Minimum is at current position β_{i-1}.

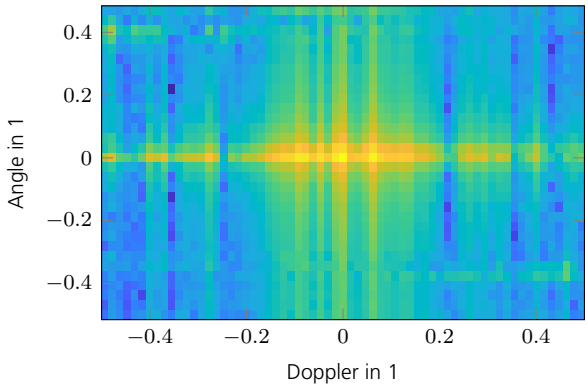

(c) Result of TSVT step $\boldsymbol{L}_i$.

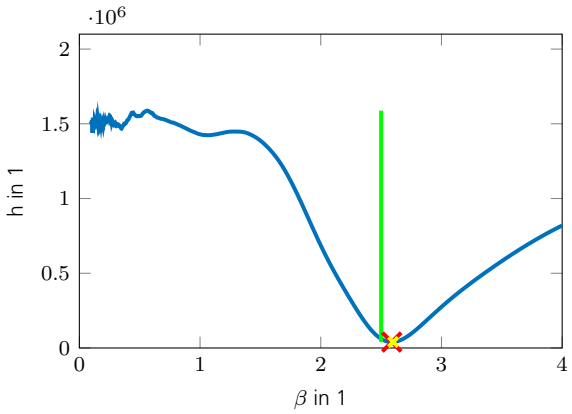

(d) Residual term $h\left(\boldsymbol{L}_{i};\beta_{i-1},\varphi_{\mathrm{m},i-1}\right)$. The minimum is slightly shifted toward true value $\widetilde{\beta}$. A zoomed view is shown in Fig. 7.2.6e.

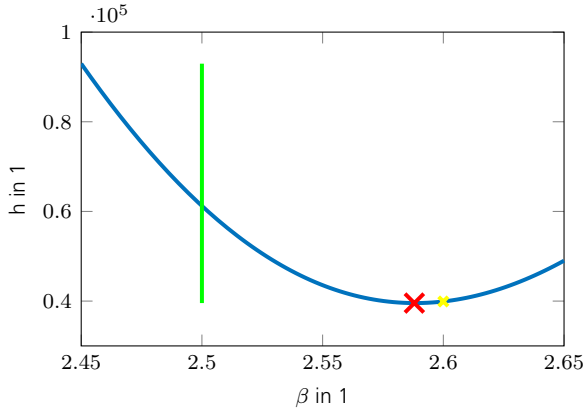

(e) Zoom of $h\left(\boldsymbol{L}_{i};\beta_{i-1},\varphi_{\mathrm{m},i-1}\right)$.

Figure 7.2.6.: Illustration of the ACF algorithm. The green line indicates the true value $\widetilde{\beta}$, the red cross the global minimum, and the yellow cross the intermediate value β_{i-1}.

form[22]. This is done by applying the concatenation of a sub-sample shift operator $\mathcal{D}'(\beta, \varphi_\mathrm{m})$ and the cut operator $\mathcal{C}(\beta)$ from (7.1.22) onto $\boldsymbol{Y}_\mathrm{up}$ as

$$\boldsymbol{Y}_\mathrm{cut} = \mathcal{D}'^{-1}(\widehat{\beta}, \widehat{\varphi_\mathrm{m}}) \circ \mathcal{C}(\widehat{\beta}) \circ \mathcal{D}'(\widehat{\beta}, \widehat{\varphi_\mathrm{m}}) \circ \boldsymbol{Y}_\mathrm{up}, \tag{7.2.16}$$

where $\circ$ denotes the concatenation of functions[23]. The shift operator

$$\mathcal{D}'(\beta, \varphi_\mathrm{m}) \circ \boldsymbol{Y}_\mathrm{up} = \left(\boldsymbol{U}_\triangle(\beta, \varphi_\mathrm{m}) \odot (\boldsymbol{Y}_\mathrm{up}\boldsymbol{F}_t)\right) \boldsymbol{F}_t^{-1}$$

is defined similar to $\mathcal{D}_u$ as in (7.1.16) but operates in the measurement domain, where the shift matrix $\boldsymbol{U}_\triangle$ is defined in (7.1.17) and $\boldsymbol{F}_t$ denotes a discrete Fourier transform (DFT) matrix resulting in a Fourier transform (FT) of the slow time dimension. The "pre-cut" measurement sample vector then finally is

$$\boldsymbol{y}_\mathrm{cut} = \boldsymbol{Y}_{\mathrm{cut},\Omega_y}. \tag{7.2.17}$$

This procedure is illustrated in Fig. 7.2.7, where the arrows indicate the shift direction of the operators $\mathcal{D}'$. This procedure of cutting incomplete samples in order to refine the estimation can be repeated until convergence as illustrated in Fig. 7.2.8.

In the following, some ACF reconstructions are shown for various scenarios. For all of them, the true values were defined to be $\widetilde{\beta} = 1$ and $\widetilde{\varphi}_\mathrm{m} = 0$, and initial start values were chosen to be $\beta_0 = 2$ and $\varphi_{\mathrm{m},0} = 0.04$ unless otherwise stated. The number of samples available shall be defined by use of the sub sampling factor - symbol: SSFs (SSFs)

$$\mathrm{SSF_c} = \frac{N_\mathrm{c}}{N_\mathrm{u}}$$

and

$$\mathrm{SSF_p} = \frac{N_\mathrm{p}}{N_\mathrm{D}}.$$

In the first example shown in Fig. 7.2.9, all measurement samples are available and no targets are present. The family of residual error terms shown in Fig. 7.2.9e illustrate the "guidance" process which leads the estimation of β to the minimum marked by the nuclear norm shown in Fig. 7.2.9f. The results of the refinement estimation using pre-cut samples $\boldsymbol{y}_\mathrm{cut}$ are shown in Fig. 7.2.9g and 7.2.9h, where the estimation was improved within only a few additional iterations. The corresponding error terms are shown in Fig. 7.2.10. Note, that since the residual term h changes from iteration to iteration, it does not necessarily decrease monotonically. In the next example shown in Fig. 7.2.11, two targets are present with a total $\mathrm{SNR} = 60\,\mathrm{dB}$. The most notably difference compared to the former example is the increased number of iterations required to find the true value of β. For stronger targets this behavior is even more severe. Nevertheless, the high number of required iterations in this example stems from the very poor initial value of β_0 which was chosen for the sake of illustration. In a practical setup, the initial value should be far better determinable. The next example in Fig. 7.2.12 illustrates the reconstruction in case of missing channels, where only half the number of channels is available. The position of the

[22] The angle-focus operation creates a matrix as sketched in Fig. 7.1.7.

[23] The concatenation symbol allows for a simpler notation in case of multiple operators applied onto some variable e. g. $(g \circ f)(x) = g(f(x))$.

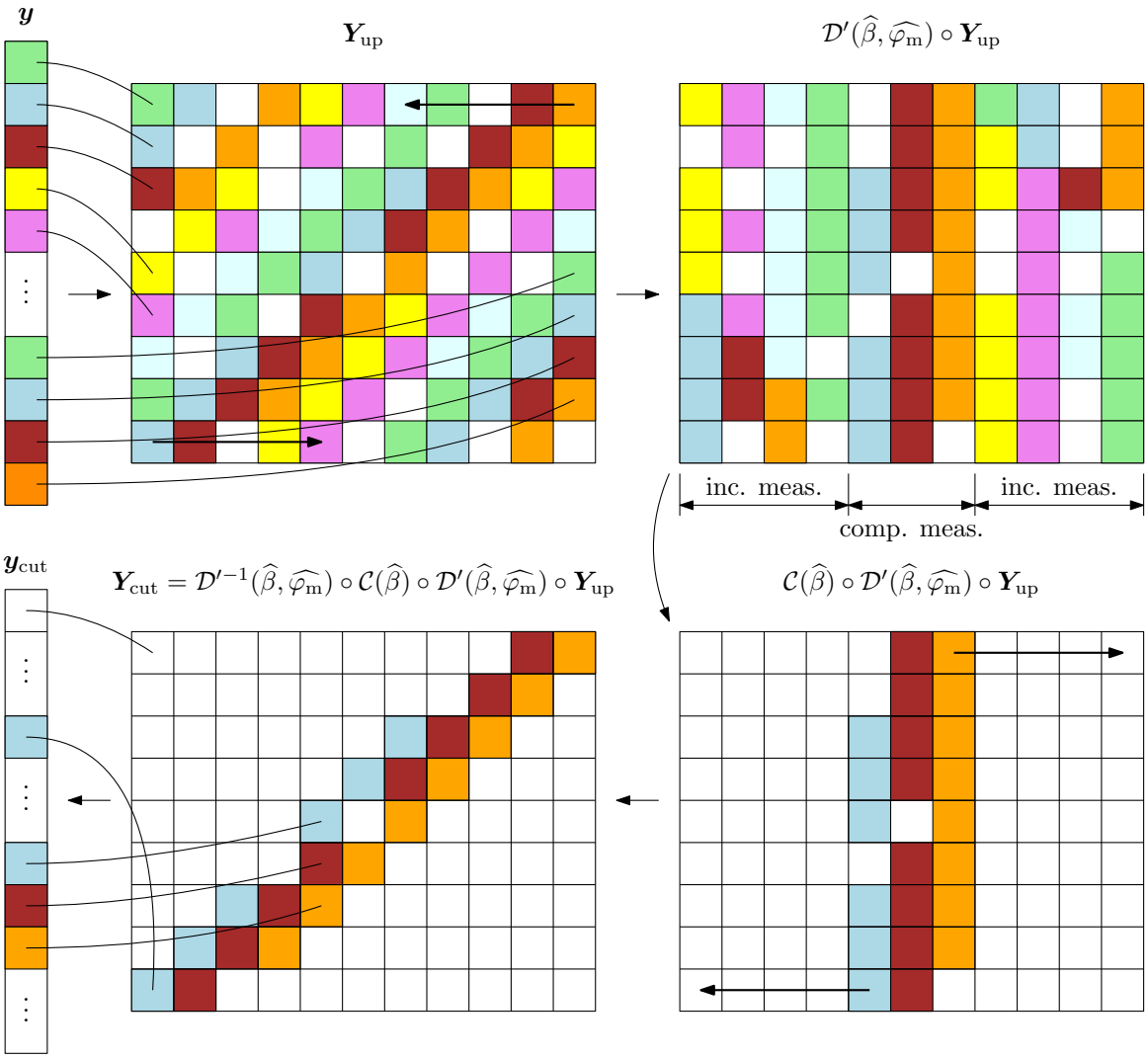

Figure 7.2.7.: Measurement data preparation by setting all incomplete measurement samples to zero.

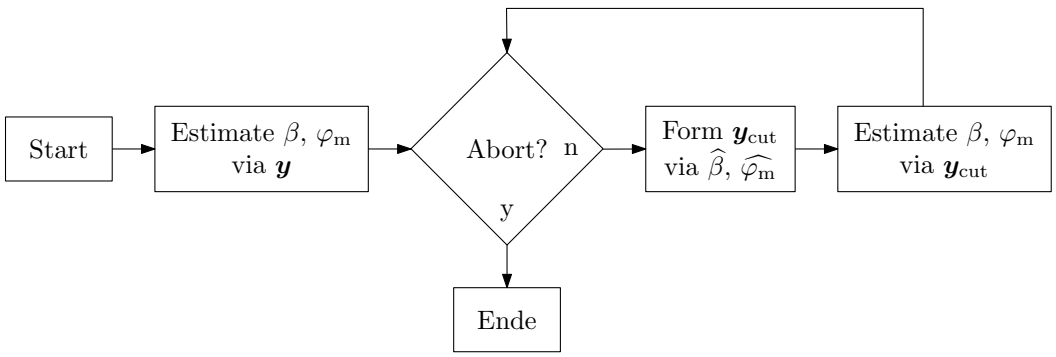

Figure 7.2.8.: Cyclic refinement of estimation of β and φ_{m} until convergence.

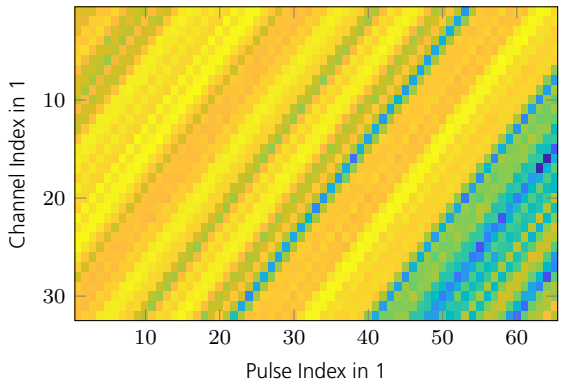

(a) Measurement sample matrix $\boldsymbol{Y}$.

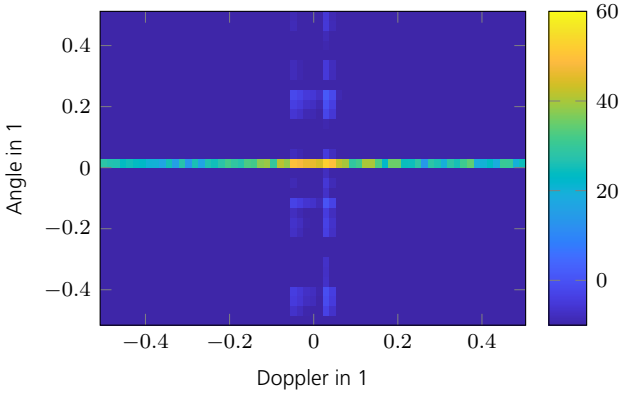

(b) Final estimated focused clutter scene $\widehat{\boldsymbol{L}}$.

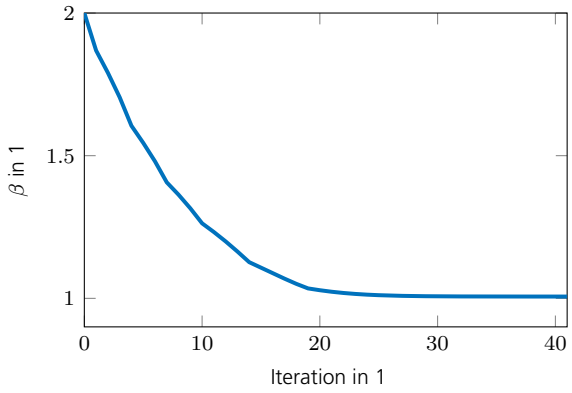

(c) Progress of β vs. iteration index.

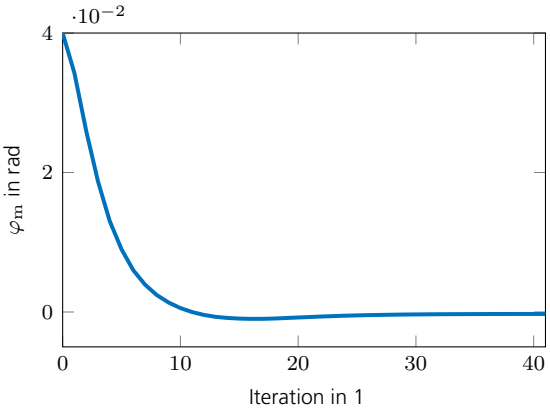

(d) Progress of φ_{m} vs. iteration index.

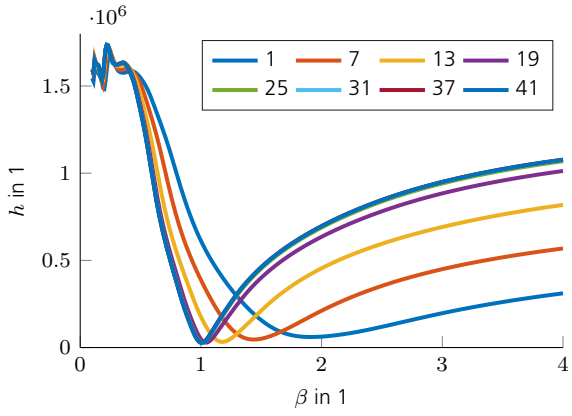

(e) h vs. β at various iteration indices of ACF procedure.

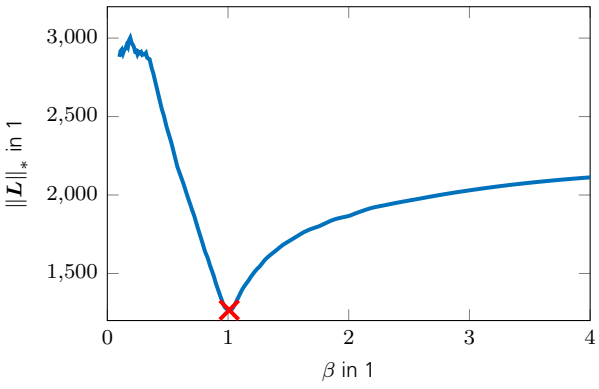

(f) Nuclear norm vs. β marking $\widetilde{\beta}$.

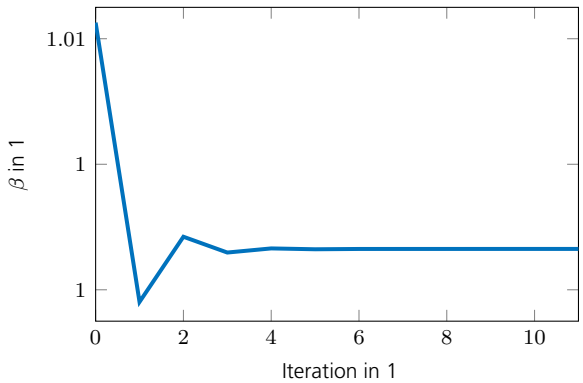

(g) Refined estimation of β using $\boldsymbol{y}_{\mathrm{cut}}$.

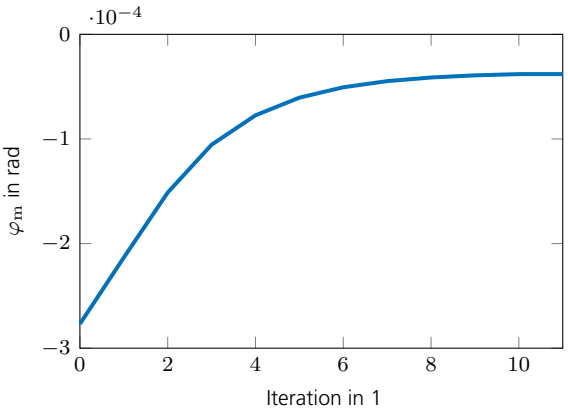

(h) Refined estimation of φ_{m} using $\boldsymbol{y}_{\mathrm{cut}}$.

Figure 7.2.9.: Illustration of ACF reconstruction, where $\mathrm{SSF_c} = \mathrm{SSF_p} = 1$ and $N_{\mathrm{t}} = 0$.

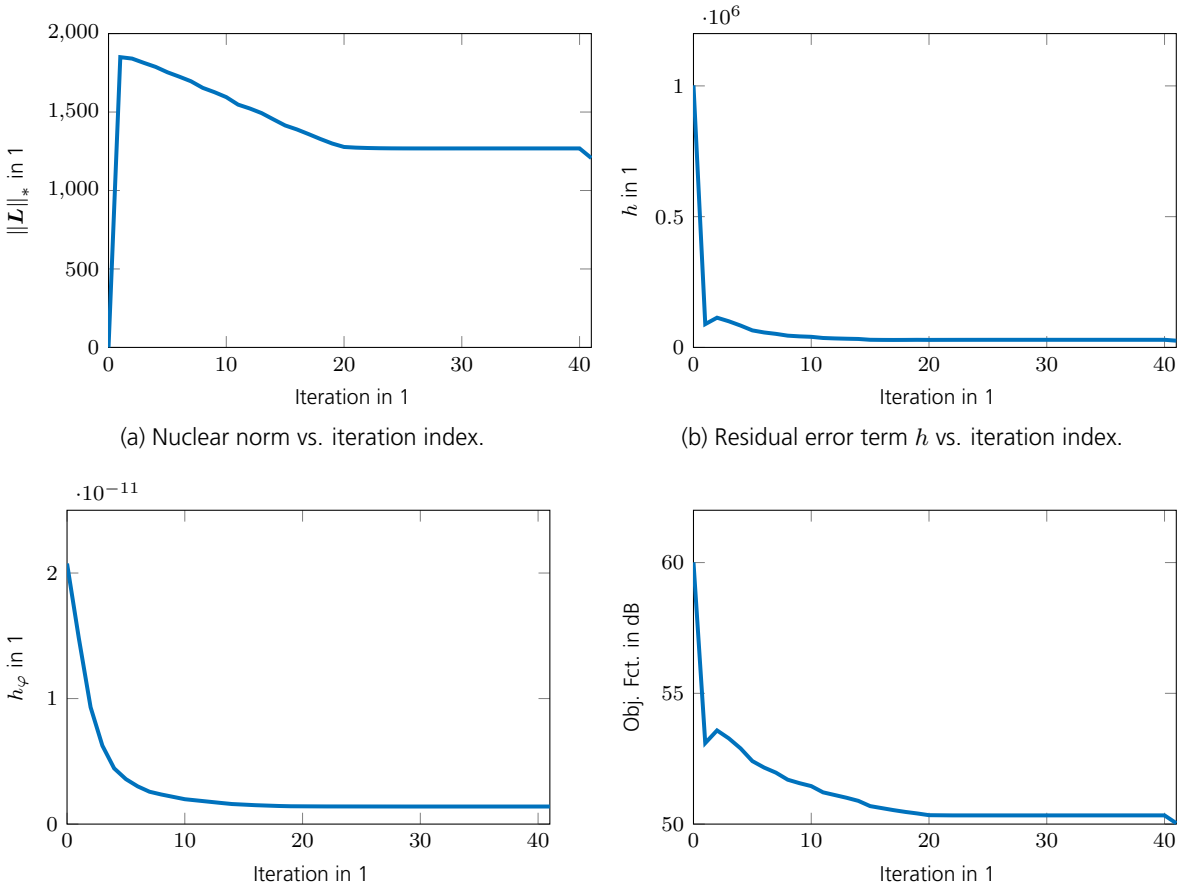

(a) Nuclear norm vs. iteration index.

(b) Residual error term h vs. iteration index.

(c) Velocity misalignment term h_{φ_m} vs. iteration index.

(d) Total objective function (7.2.12).

Figure 7.2.10.: Objective function terms corresponding to example depicted in Fig. 7.2.9.

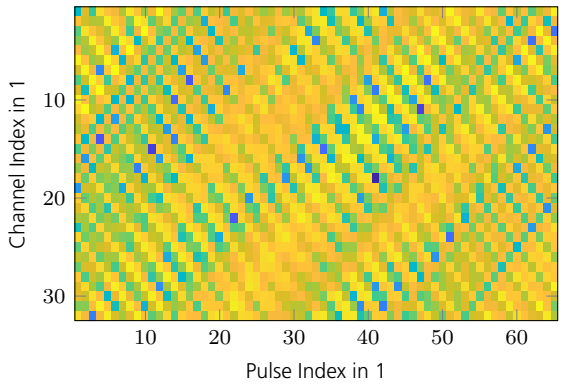

(a) Measurement sample matrix $\boldsymbol{Y}$.

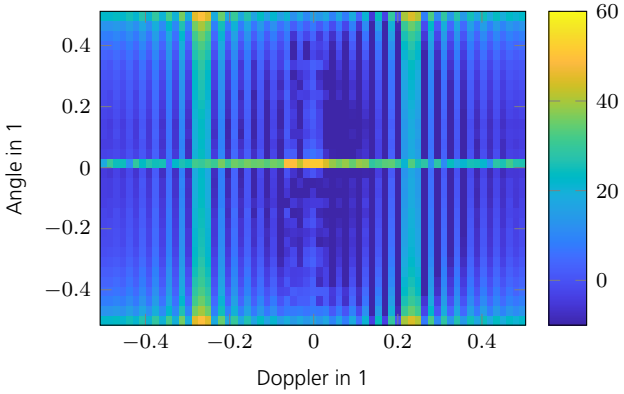

(b) Final estimated focused clutter scene $\widehat{\boldsymbol{L}}$.

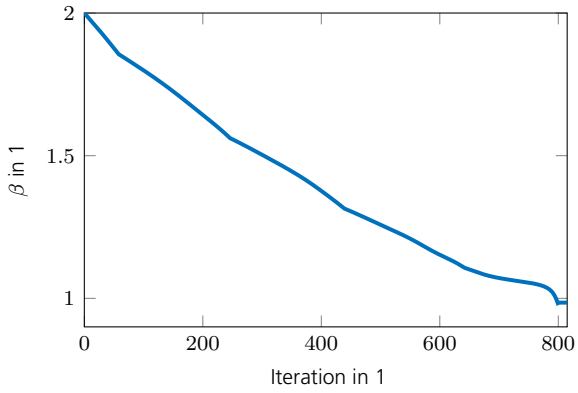

(c) Progress of β vs. iteration index.

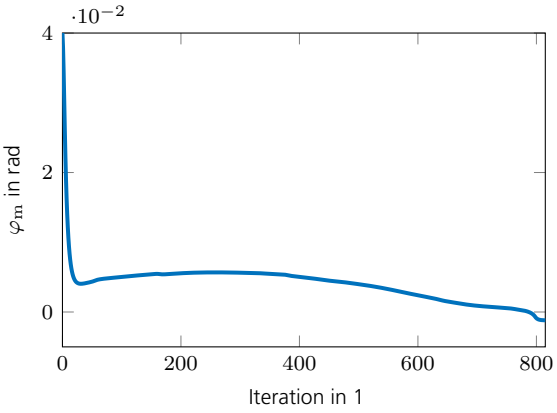

(d) Progress of φ_{m} vs. iteration index.

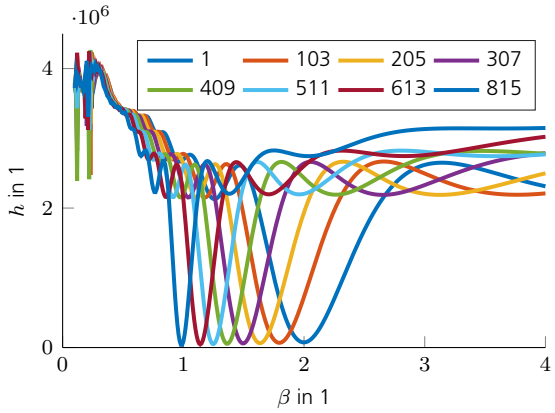

(e) h vs. β at various iteration indices of ACF procedure.

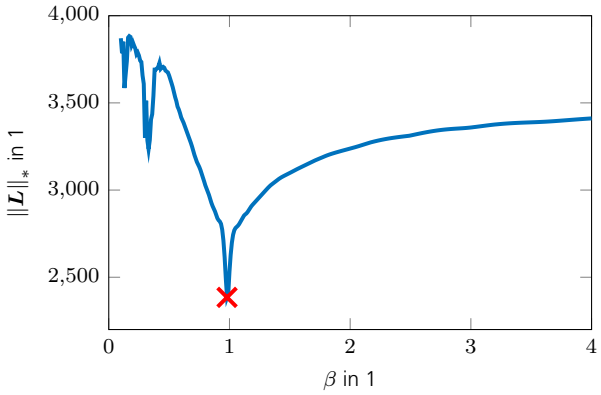

(f) Nuclear norm vs. β marking $\widetilde{\beta}$.

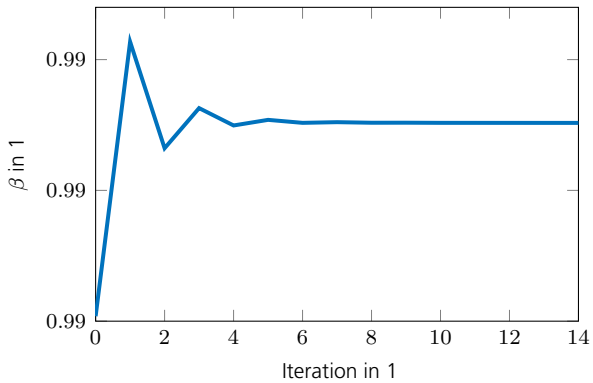

(g) Refined estimation of β using $\boldsymbol{y}_{\mathrm{cut}}$.

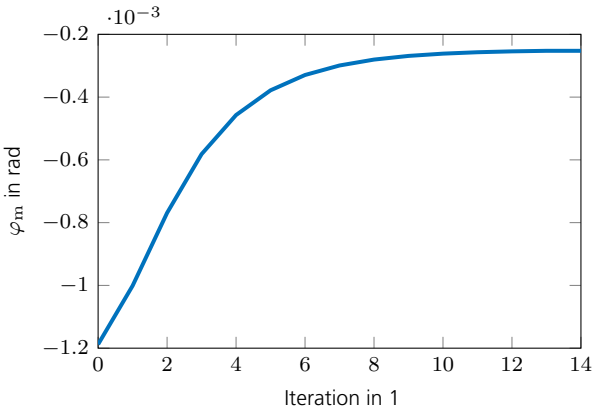

(h) Refined estimation of φ_{m} using $\boldsymbol{y}_{\mathrm{cut}}$.

Figure 7.2.11.: Illustration of ACF reconstruction, where $\mathrm{SSF_c} = \mathrm{SSF_p} = 1$ and $N_{\mathrm{t}} = 2$.

available channels was chosen randomly. The ACF approach has no problems estimating the desired parameters for this case. The example shown in Fig. 7.2.13 illustrates the reconstruction in case of missing pulses, where only half the number of pulses is used. The position of the available pulses was again chosen randomly. Compared to the case of missing channels, the ACF approach is more susceptible for missing pulses. As can be seen from Fig. 7.2.13f, the nuclear norm reveals more local minima. For a successful reconstruction, an initial value β_0 close enough to the true minimum is necessary. For the results shown in Fig. 7.2.13, an initial value of $\beta_0 = 1.1$ was used. Also of interest is the fact that the pre-cut of the measurement samples allows for significant improvement of the estimated parameters. The final example shown in Fig. 7.2.14 depicts the case for missing channels and pulses at the same time. The chosen setting is an extreme case where only half of the channels and half of the pulses are available which are only $25\,\%$ of the total number of possible samples. Even worse, the position of the samples are severely structured which can not be avoided since only full rows or columns can be removed from the full sample measurement due to the radar setup. As a consequence, the nuclear norm shows multiple minima, where the global one marks the true value of β in this case.[24] The reconstruction approached the true value only because the start value $\beta_0 = 1.1$ was close enough to the local minimum. A second consequence of the structured sub-sampling is the reduced restricted rank isometry property (RRIP) of the sensing operator. Hence, the estimated parameters $\widehat{\beta}$ and $\widehat{\varphi_{\mathrm{m}}}$ are not as well estimated as in the previous examples.

To the best of the authors knowledge, there is no non NP-hard optimization algorithm available which finds for given sub-sample factors the channel and pulse indices such that the RRIP constant $\delta_R(\mathcal{A})$ explained in Chapter 4 is minimized. This renders to be a discrete optimization problem, one of the most difficult types. Another measure which is more practical than the RRIP constant $\delta_R(\mathcal{A})$ is the mutual coherence of the sensing operator. A low coherence results also in a low RRIP. For the sensing operator in this work, the mutual coherence may be defined as[25]

$$\mu_{\mathcal{A}} = \left\| \mathrm{vec}\left(\tilde{\boldsymbol{A}}^{\mathrm{H}} \tilde{\boldsymbol{A}} \right) \right\|_1 , \tag{7.2.18}$$

where

$$\tilde{\boldsymbol{A}} = \boldsymbol{B} \otimes \boldsymbol{A} \in \mathbb{C}^{N_{\mathrm{c}} N_{\mathrm{p}} \times N_{\mathrm{u}} N_{\mathrm{D}}} \tag{7.2.19}$$

with $\boldsymbol{A}$ and $\boldsymbol{B}$ being the space and time steering matrices given in (2.1.115) and (2.1.116).[26] For a uniform linear array (ULA), the spatial steering matrix can be formulated as

$$\boldsymbol{A} = \boldsymbol{S}_{\mathrm{c}} \boldsymbol{F}_1^{-1}, \tag{7.2.20}$$

where $\boldsymbol{F}_1^{-1} \in \mathbb{C}^{N_{\mathrm{u}} \times N_{\mathrm{u}}}$ is a inverse discrete Fourier transform (IDFT) matrix and $\boldsymbol{S}_{\mathrm{c}} \in \{0,1\}^{N_{\mathrm{c}} \times N_{\mathrm{u}}}$

[24] However, it is not always the case that the global minimum marks the true value of β.

[25] From numerical experiments, the ℓ_1 norm resulted in best reconstruction performance compared to a traditional Frobenius norm or the infinity norm.

[26] The mutual coherence formulation works because the columns of $\tilde{\boldsymbol{A}}$ all have the same norm and thus no further normalization is required.

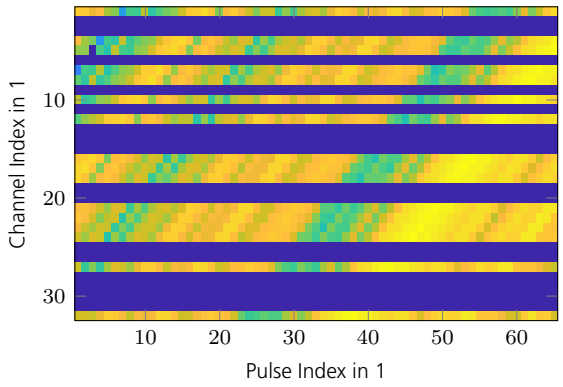

(a) Up-sampled measurement matrix $\boldsymbol{Y}_{\mathrm{up}}$.

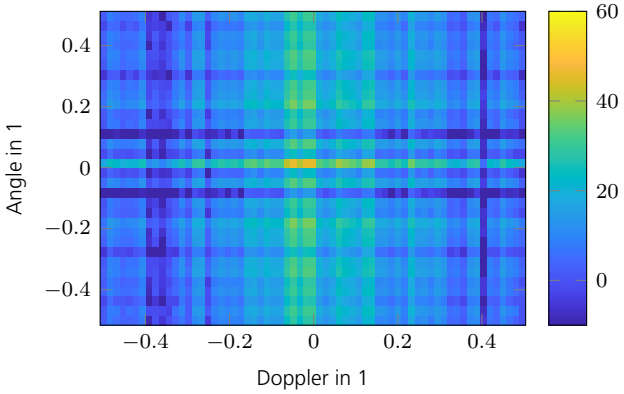

(b) Final estimated focused clutter scene $\widehat{\boldsymbol{L}}$.

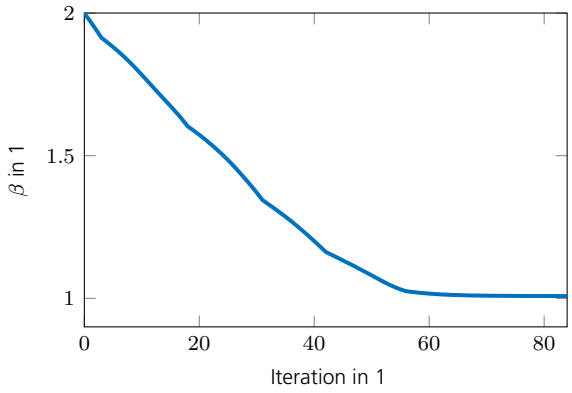

(c) Progress of β vs. iteration index.

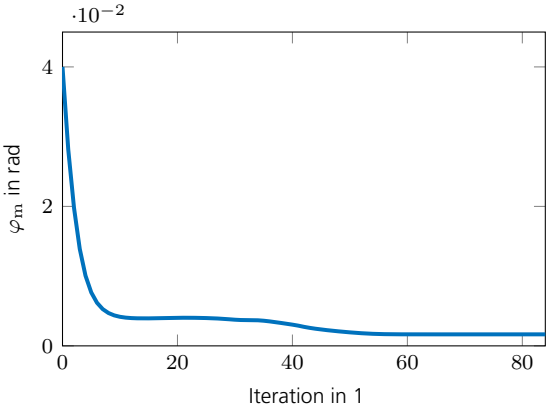

(d) Progress of φ_{m} vs. iteration index.

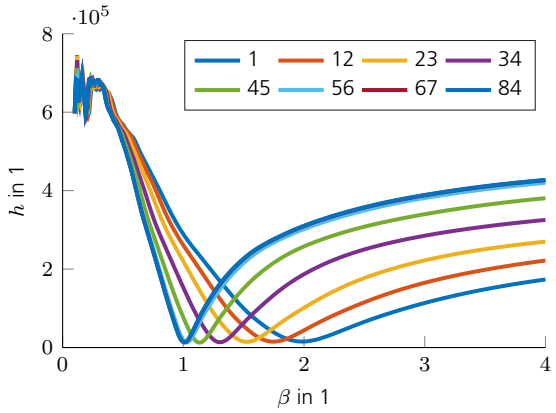

(e) h vs. β at various iteration indices of ACF procedure.

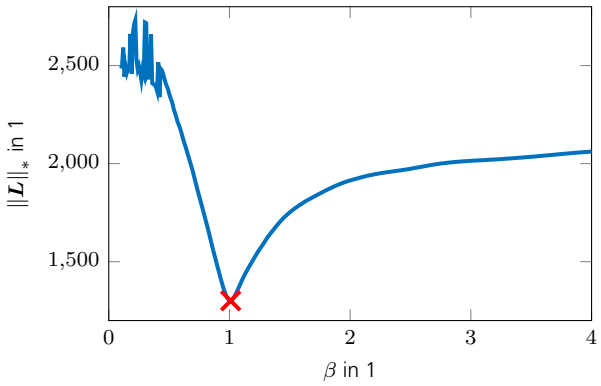

(f) Nuclear norm vs. β marking $\widetilde{\beta}$.

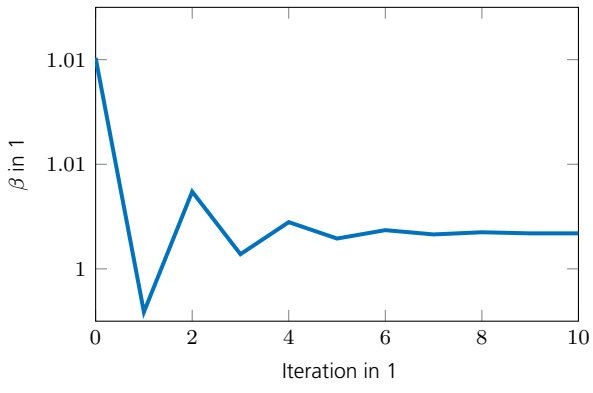

(g) Refined estimation of β using $\boldsymbol{y}_{\mathrm{cut}}$.

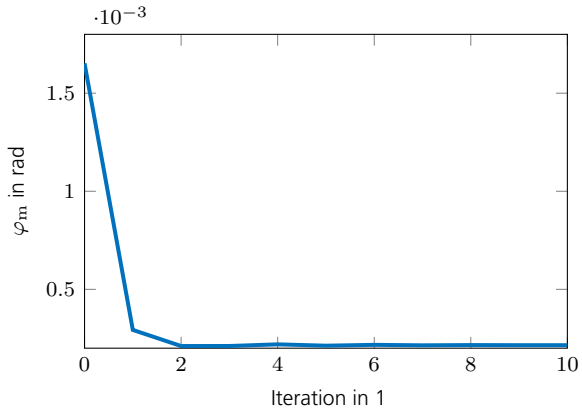

(h) Refined estimation of φ_{m} using $\boldsymbol{y}_{\mathrm{cut}}$.

Figure 7.2.12.: Illustration of ACF reconstruction, where $\mathrm{SSF_c} = 0.5$, $\mathrm{SSF_p} = 1$, and $N_{\mathrm{t}} = 0$.

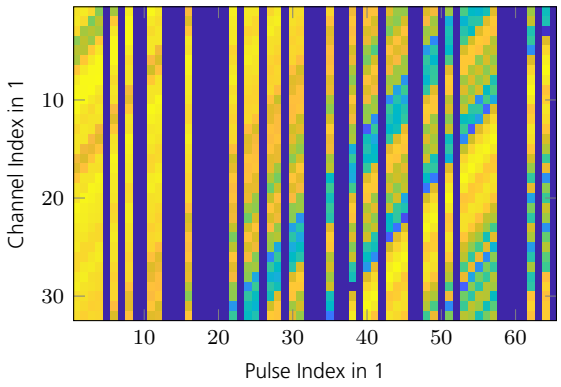

(a) Up-sampled measurement matrix $\boldsymbol{Y}_{\mathrm{up}}$.

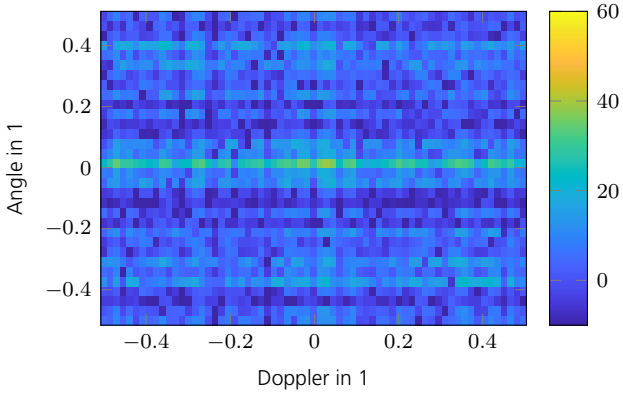

(b) Final estimated focused clutter scene $\widehat{\boldsymbol{L}}$.

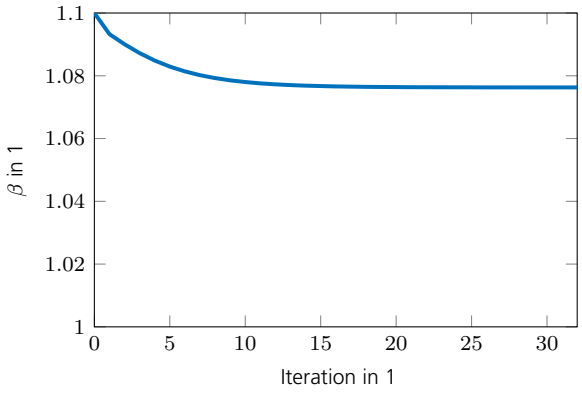

(c) Progress of β vs. iteration index.

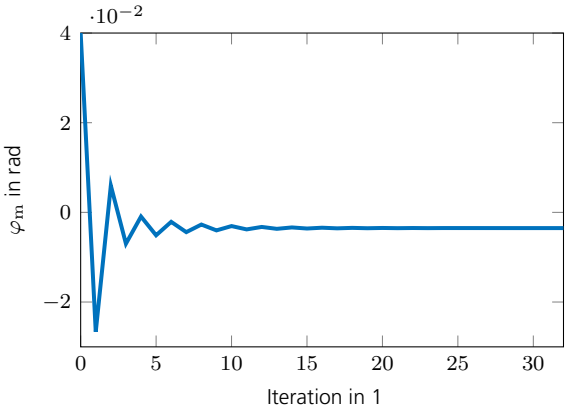

(d) Progress of φ_{m} vs. iteration index.

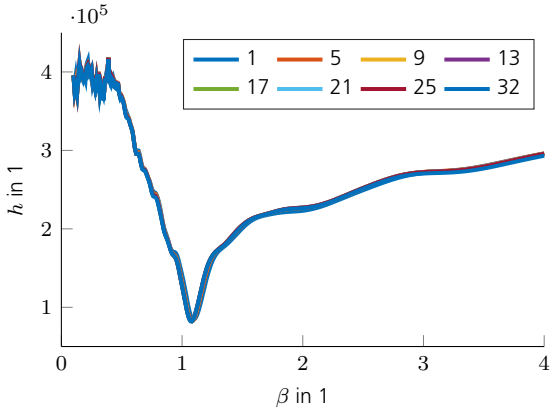

(e) h vs. β at various iteration indices of ACF procedure.

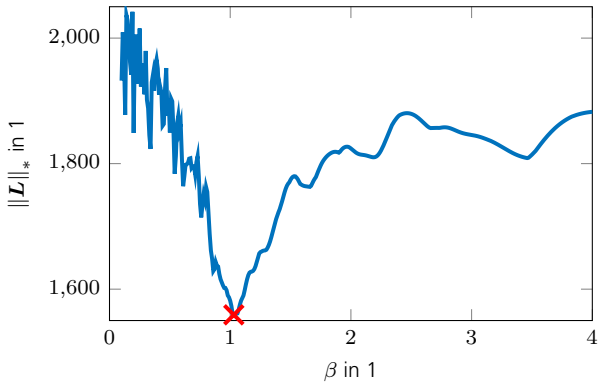

(f) Nuclear norm vs. β marking $\widetilde{\beta}$.

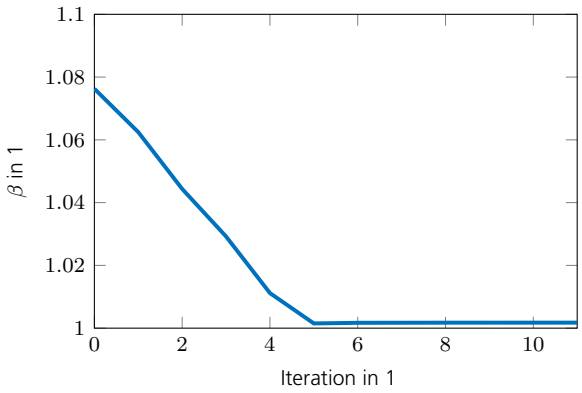

(g) Refined estimation of β using $\boldsymbol{y}_{\mathrm{cut}}$.

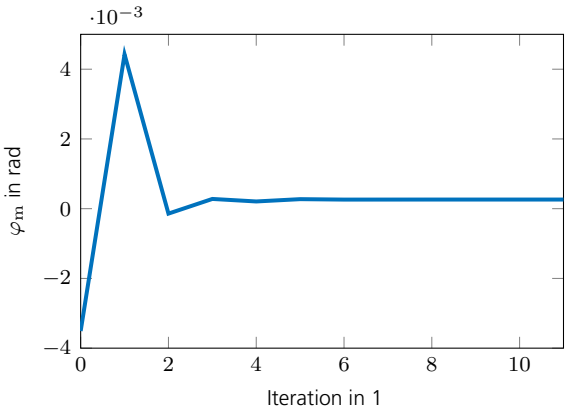

(h) Refined estimation of φ_{m} using $\boldsymbol{y}_{\mathrm{cut}}$.

Figure 7.2.13.: Illustration of ACF reconstruction, where $\mathrm{SSF_c} = 1$, $\mathrm{SSF_p} = 0.5$, and $N_{\mathrm{t}} = 0$.

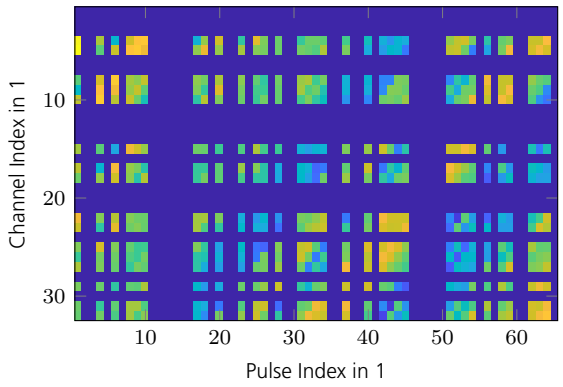

(a) Up-sampled measurement matrix $\boldsymbol{Y}_{\mathrm{up}}$.

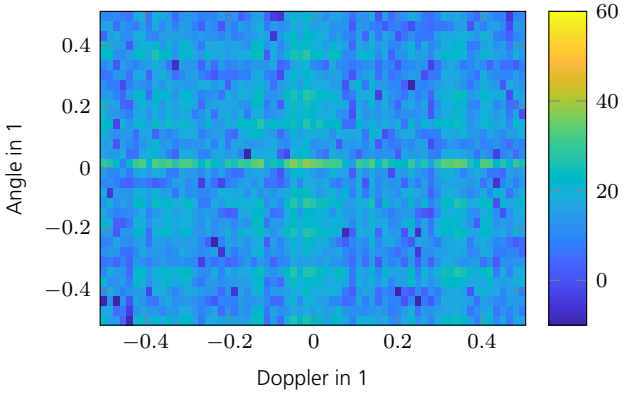

(b) Final estimated focused clutter scene $\widehat{\boldsymbol{L}}$.

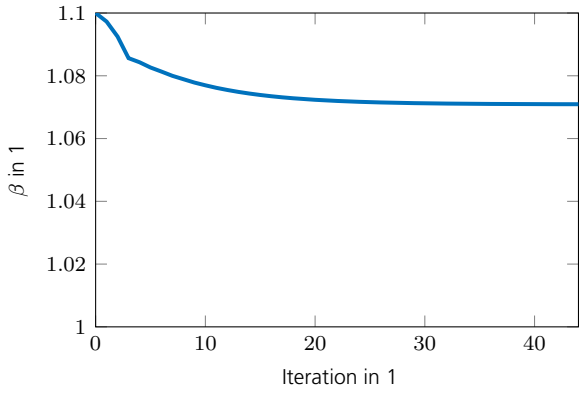

(c) Progress of β vs. iteration index.

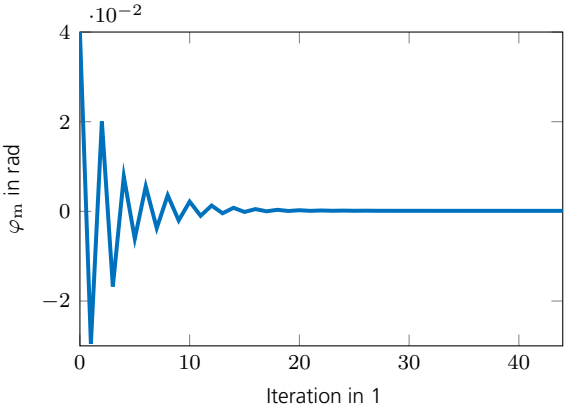

(d) Progress of φ_{m} vs. iteration index.

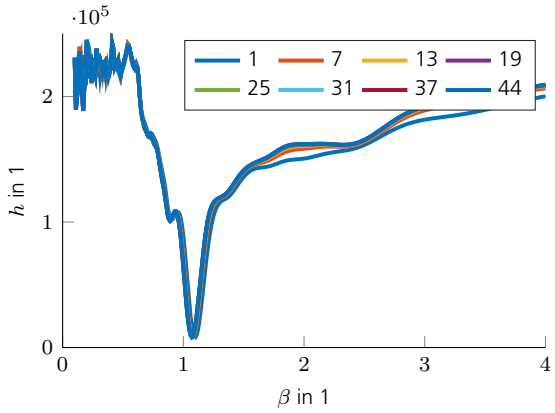

(e) h vs. β at various iteration indices of ACF procedure.

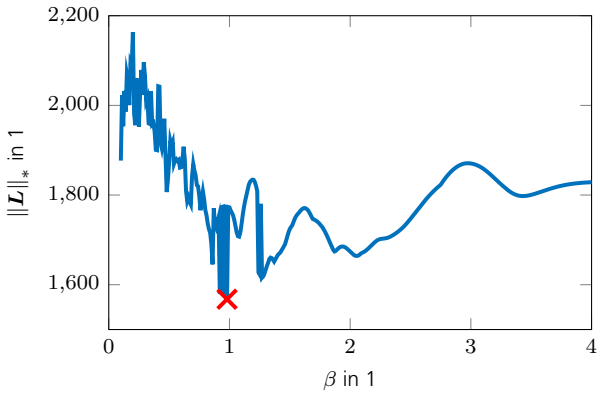

(f) Nuclear norm vs. β marking $\widetilde{\beta}$.

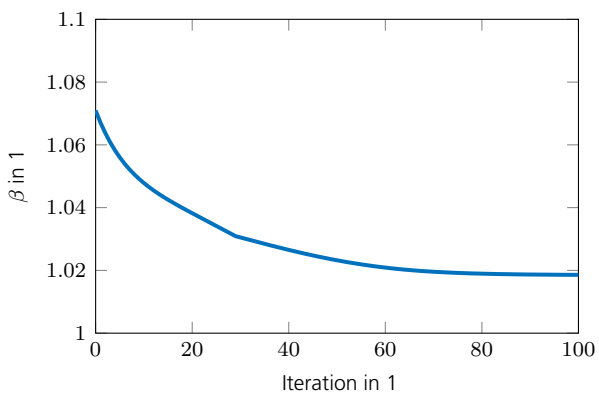

(g) Refined estimation of β using $\boldsymbol{y}_{\mathrm{cut}}$.

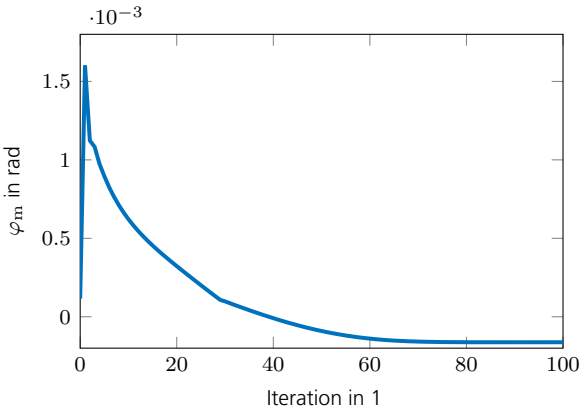

(h) Refined estimation of φ_{m} using $\boldsymbol{y}_{\mathrm{cut}}$.

Figure 7.2.14.: Illustration of ACF reconstruction, where $\mathrm{SSF_c} = 0.5$, $\mathrm{SSF_p} = 0.5$, and $N_{\mathrm{t}} = 0$.

is a row selection matrix whose entries are

$$[\boldsymbol{S}_{\mathrm{c}}]_{ij} = \begin{cases} 1 & \text{if } \Omega_{\mathrm{c}}(i) = j \\ 0 & \text{else} \end{cases}$$

with Ω_{c} being an ordered channel index set. The same can be done for the selected pulses as

$$\boldsymbol{B} = \boldsymbol{S}_{\mathrm{p}} \boldsymbol{F}_2^{-1}, \tag{7.2.21}$$

where $\boldsymbol{F}_2^{-1} \in \mathbb{C}^{N_{\mathrm{D}} \times N_{\mathrm{D}}}$ again is a IDFT matrix and $\boldsymbol{S}_{\mathrm{p}} \in \{0,1\}^{N_{\mathrm{p}} \times N_{\mathrm{D}}}$ is a pulse selection matrix defined as

$$[\boldsymbol{S}_{\mathrm{p}}]_{ij} = \begin{cases} 1 & \text{if } \Omega_{\mathrm{p}}(i) = j \\ 0 & \text{else} \end{cases}$$

with Ω_{p} being an ordered pulse index set. To optimize the sensing operator $\mathcal{A}$ for given channel and pulse SSFs, the following optimization problem

$$\widehat{\Omega}_{\mathrm{c}}, \widehat{\Omega}_{\mathrm{p}} = \underset{\Omega_{\mathrm{c}}, \Omega_{\mathrm{p}}}{\arg\min}\, \mu_{\mathcal{A}} \tag{7.2.22}$$

may be solved. An efficient algorithm to find a solution to (7.2.22) is beyond the scope of this work as the problem renders to be NP-hard. Nevertheless, in order to avoid obviously inconvenient index sets $\boldsymbol{S}_{\mathrm{c}}$ and $\boldsymbol{S}_{\mathrm{p}}$ for the simulations to follow, 600 random index sets are generated for which the ones minimizing $\mu_{\mathcal{A}}$ are used to setup the sensing operator $\mathcal{A}$. While this approach avoids obviously bad choices of index sets, it is not guaranteed that "good" choices are found. The total number of combinations to check is

$$N_{\mathrm{comb}} = \begin{pmatrix} N_{\mathrm{c}} \\ \mathrm{SSF}_{\mathrm{c}} N_{\mathrm{c}} \end{pmatrix} \begin{pmatrix} N_{\mathrm{p}} \\ \mathrm{SSF}_{\mathrm{p}} N_{\mathrm{p}} \end{pmatrix}$$

which for $\mathrm{SSF}_{\mathrm{c}} = \mathrm{SSF}_{\mathrm{p}} = 0.5$, $N_{\mathrm{c}} = 32$, and $N_{\mathrm{p}} = 64$ results in approximately $N_{\mathrm{comb}} = 1.1 \cdot 10^{27}$ combinations. The chance of finding a "good" index set is clearly small. Nevertheless, the higher the SSFs are chosen, the less combinations are possible and thus the higher are the chances of finding better index sets. This effect can be observed in the statistical evaluations presented in the following section.

The RRIP may also be improved by adapting the radar transmit signal. This approach, however, is beyond the scope of this work. The interested reader may refer to [68].

7.2.3. Statistical Evaluation

A statistical evaluation of the ACF algorithm is shown in the following for which $N_{\mathrm{mc}} = 100$ Monte Carlo runs were conducted. For all simulations $\mathrm{CNR} = \mathrm{SNR} = 60\,\mathrm{dB}$ was used. To allow for a convenient overview, a success threshold is used. All estimations for which $\left|\widehat{\beta} - \widetilde{\beta}\right| < 0.1$ and $|\widehat{\varphi_{\mathrm{m}}} - \widetilde{\varphi_{\mathrm{m}}}| < 0.01$ rad are considered successful. This is a pure arbitrary choice to define a success, nevertheless, its purpose is solely to allow for a clear presentation of the estimation results. The

success rate presented in the following is defined to be the ratio $n_{\mathrm{succ}}/N_{\mathrm{mc}}$, where n_{succ} is the number of successful estimations. It depends on the initial values β_0 and $\varphi_{\mathrm{m},0}$, especially if only a few channels or pulses are available. For all simulation to follow, an initialization error of $\triangle\beta_0 = \beta_0 - \widetilde{\beta} = 0.1$ and $\triangle\varphi_{\mathrm{m},0} = \varphi_{\mathrm{m},0} - \widetilde{\varphi_{\mathrm{m}}} = 0.01$ rad was chosen which are the same values used in the success definitions. As the ACF algorithm either converges or diverges, the success rate corresponds to the ACFs convergence rate.

As mentioned in the previous section, cutting improves the estimation performance. The estimation was therefore conducted in two steps which are hereafter referred to as primal and refinement estimations. In the primal estimation step, the ACF algorithm was executed using the original measurement data $\boldsymbol{y}$. In the second refinement estimation step, the ACF algorithm was executed using pre-cut measurement data $\boldsymbol{y}_{\mathrm{cut}}$. The cutting was conducted according to (7.1.21) and (7.1.22) using the estimated parameter $\widehat{\beta}$ from the primal step. At this point it shall be mentioned, that while cutting allows for a refined estimation, it also reduces the CNR which in turn may degrade the estimation performance. The smaller β is, the more pulses need to be cut according to (7.1.21). Hence, this effect is bigger for small β. For the simulation results presented in the following, the number of pulses was kept constant, rendering the CNR to vary for different $\widetilde{\beta}$. The effect of this can be seen in Fig. 7.2.15, where the reconstruction success for the primal and the refined estimation is shown. The primal estimation shown in Fig. 7.2.15a reveals high success rates also for certain scenarios of low SSFs. The uneven distribution of success is explained by the non optimal RRIP constant of the sensing operator $\mathcal{A}$ as explained in the previous section. The refined estimation shown in Fig. 7.2.15c reveals an improved success rate for scenarios using many pulses. However, the success rate for scenarios using a low number of pulses deteriorate due to the aforementioned loss of CNR. This effect is almost non observable any more for simulation settings using $\widetilde{\beta} = 2.5$, where the number of pulses to cut is lower. In the following, only the refined success rates are shown for sweeps with respect to the SSFs. The results for level one to five settings are shown in Fig 7.2.16 until Fig. 7.2.20. Next to the success rate with respect to the SSFs, also some histograms for the case of $\mathrm{SSF_c} = \mathrm{SSF_p} = 1$, and mean and standard deviations are shown. The effect of the refinement step is clearly visible as can be seen from all presented scenarios. The offset error as well as the standard deviation are significantly improved. Furthermore, as was illustrated in Fig. 7.2.13 in the previous section, the ACF shows a susceptibility with respect to missing pulses. This can be explained by the fact that missing pulses cause disturbances in the Doppler dimension which results in densely populated rows of the unfocused clutter scene. This causes the same effects as leakage of strong targets in the Doppler domain, which was discussed in Section 7.1. Such strong rows compete with the unfocused clutter ridge and as such result in multiple minima of the nuclear norm. A successful reconstruction therefore depends on the initial value β_0 which needs to be close enough to the true value $\widetilde{\beta}$. For the setup simulated here, the reconstruction success for β is high for as long as $\mathrm{SSF_p} \geq 0.8$, except where severe internal clutter motion (ICM) is present. The ACF algorithm is robust regarding missing channels. This can be explained by the fact that missing channels introduce disturbances in the angle domain. To the contrary of disturbances in the Doppler domain, disturbances in the angle domain do not harm the clutter focus operations. Recall, that the focus operation is conducted by shifts in the angle domain i. e. columns in this work. Such shifts do

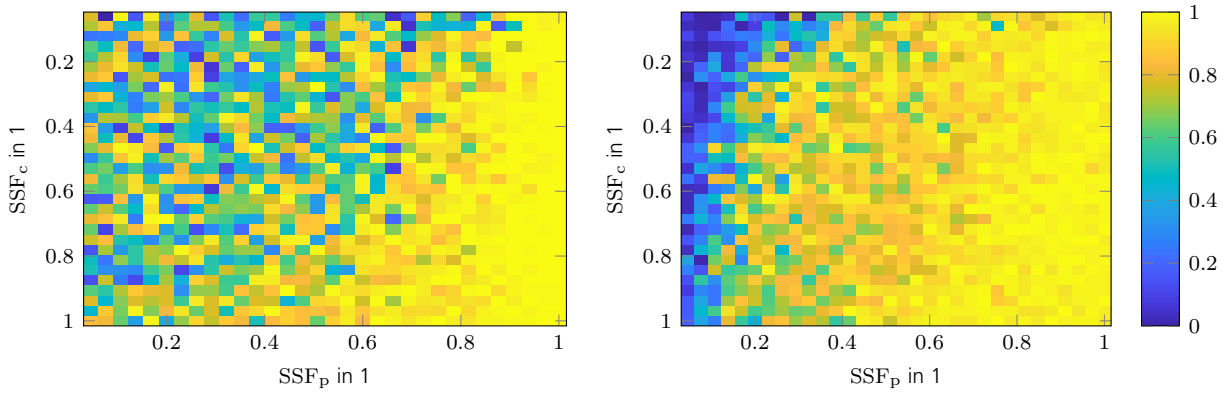

(a) Primal reconstruction success of β.

(b) Primal reconstruction success of φ_m.

(c) Refined reconstruction success of β.

(d) Refined reconstruction success of φ_m.

Figure 7.2.15.: Comparison of primal and refined reconstruction success of ACF algorithm for a level one setting with $\widetilde{\beta} = 1$ and $\widetilde{\varphi_m} = 0$ rad.

not form diagonal entries in this case, hence no competing minima in the nuclear norm emerge. Comparing the reconstruction success for $\widetilde{\beta} = 1$ in Fig. 7.2.16 to $\widetilde{\beta} = 2.5$ in the following figures reveals a reduced success rate for a lower number of pulses. A reason for the higher success rate in case of $\widetilde{\beta} = 1$ might be the unrealistic displaced phase center antenna (DPCA) condition, which allows for the maximum possible correlation of space-time samples. The reduced correlation for $\widetilde{\beta} = 2.5$ causes the lower success rate. Quite interestingly, the estimation performance of φ_{m} is better for the $\widetilde{\beta} = 2.5$ case even for uncut measurement data. The reason therefore is subject to further investigation. Comparing Fig. 7.2.17 to Fig. 7.2.18 shows that present velocity misalignment has merely no impact on the reconstruction success. The impact of ICM becomes evident by comparing Fig. 7.2.18 to Fig. 7.2.19. Due to the induced reduction of the space-time sample correlation, the standard deviation increases for both parameters. Especially the estimation of the velocity misalignment angle is effected due to the broadening of the clutter ridge in the Doppler dimension. The presence of strong targets further diminishes the reconstruction success as shown in Fig. 7.2.20.

7.2.4. Comparison with Alternative Methods

The ACF algorithm presented in this chapter attempts to estimate the clutter ridge slope β and the velocity misalignment angle φ_{m}. Recall from (2.2.5) that β depends on the platform velocity, hence by estimating β, the velocity of the platform relative to the earth can be determined. These are only two of many parameters, which are of interest for vehicle platforms e. g. airplanes, satellites, drones, cars, robots etc. The ACF algorithm is not limited to estimate only the aforementioned parameters, rather it can be extended to a full calibration procedure to also capture e. g. precise knowledge of the position of the phase centers, channel alignment, antenna coupling etc.[27] The ACF algorithm therefore belongs to the broader regime of calibration procedures.

A variety of calibration methods exist. These differ in terms of the parameters to be determined and the measurement data available. In general, they can be divided into direct an indirect approaches. A direct method uses one or more known targets (mostly point scatterers) and adjusts the required parameters in a direct minimization procedure e. g. [69]. This allows an absolute calibration of the radar system, which is required e. g. for satellite remote sensing applications. If no known targets are available, measurements of unknown scenarios have to be used. This is the application area of the ACF algorithm. Many alternative estimation procedures exists e. g. [70, 71, 72, 73]. These approaches are extremely diverse, ranging from iterative procedures to fast approximations, leveraging along track interference phases for baseline estimation, clutter Doppler centroid determination for platform yaw, pitch, and roll angles, antenna attitude angle offsets, channel phase corrections, platform velocity estimation via direction of arrival measurements etc. Compared to the ACF approach presented in this work, they have two major requirements: suitable homogeneously distributed clutter and no targets present in the training data. The ACF does not have these prerequisites and thus can be applied in heterogeneous and busy radar scenes. The price to pay, however, is the required increased number of channels.

[27] This is subject to future works.

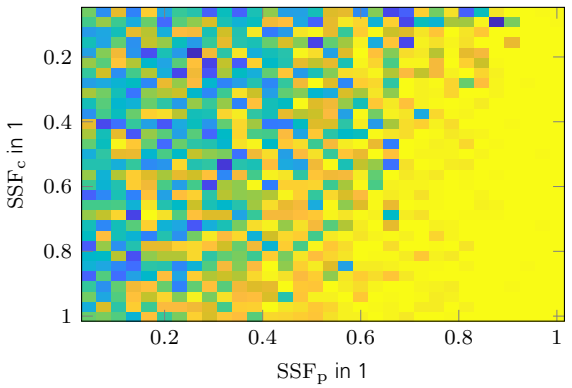

(a) Reconstruction success of β.

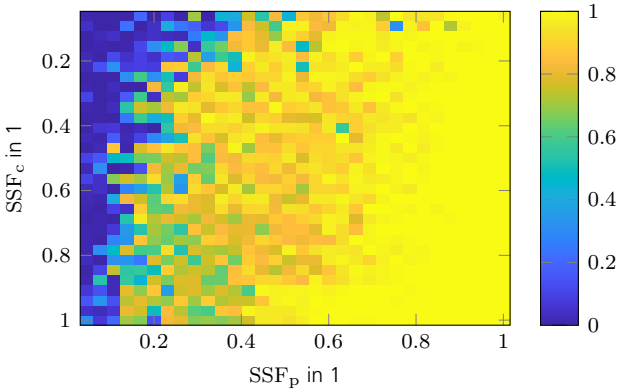

(b) Reconstruction success of φ_m.

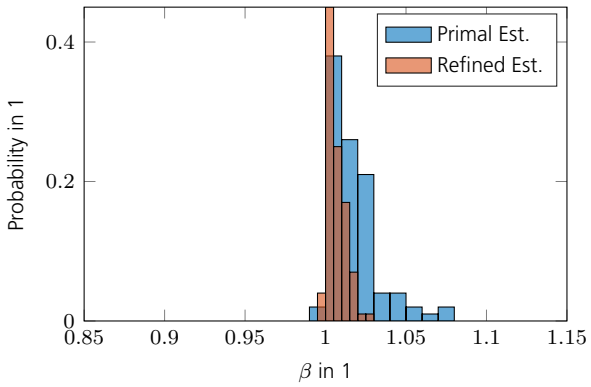

(c) Histogram of β for $\mathrm{SSF_c} = \mathrm{SSF_p} = 1$.

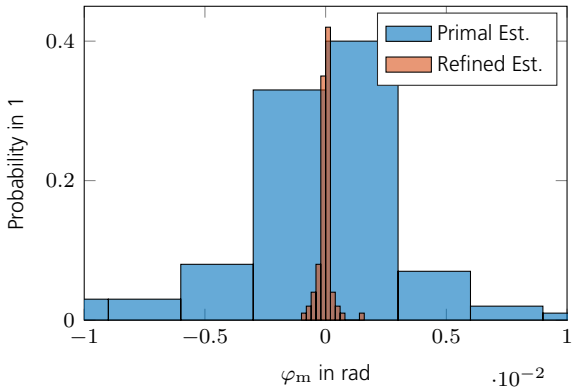

(d) Histogram of φ_m for $\mathrm{SSF_c} = \mathrm{SSF_p} = 1$.

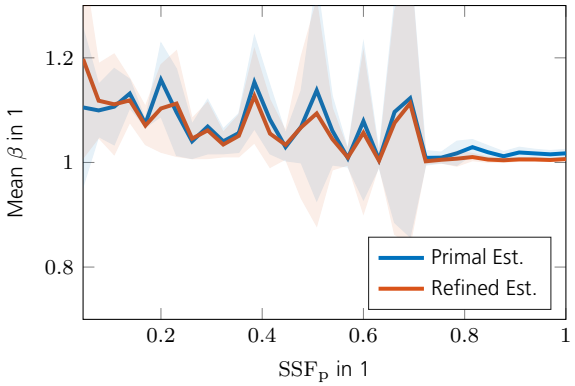

(e) Mean and standard deviation of β for $\mathrm{SSF_c} = 1$.

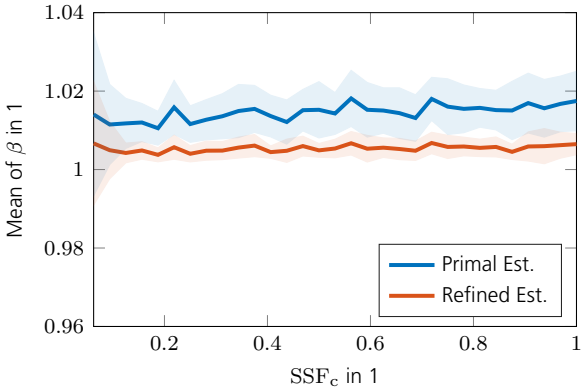

(f) Mean and standard deviation of β for $\mathrm{SSF_p} = 1$.

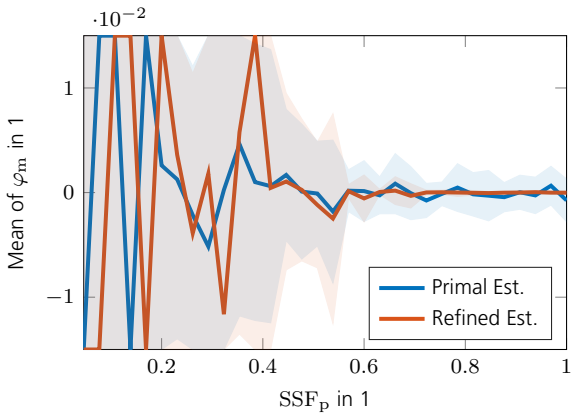

(g) Mean and standard deviation of φ_m for $\mathrm{SSF_p} = 1$.

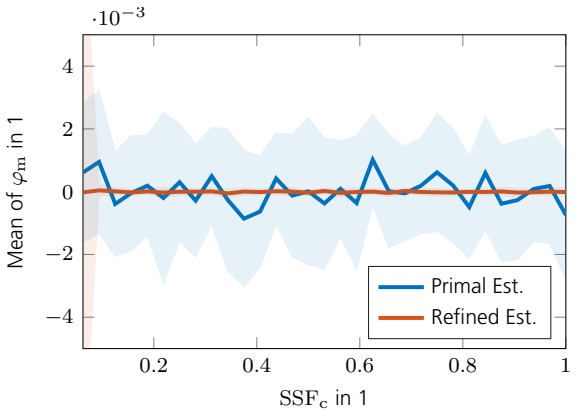

(h) Mean and standard deviation of φ_m for $\mathrm{SSF_c} = 1$.

Figure 7.2.16.: Reconstruction success of ACF algorithm for a level one setting with $\widetilde{\beta} = 1$.

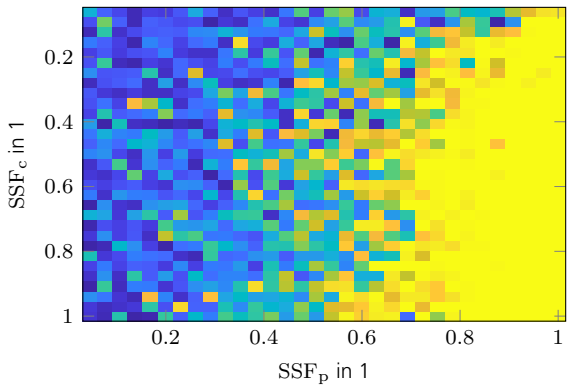

(a) Reconstruction success of β.

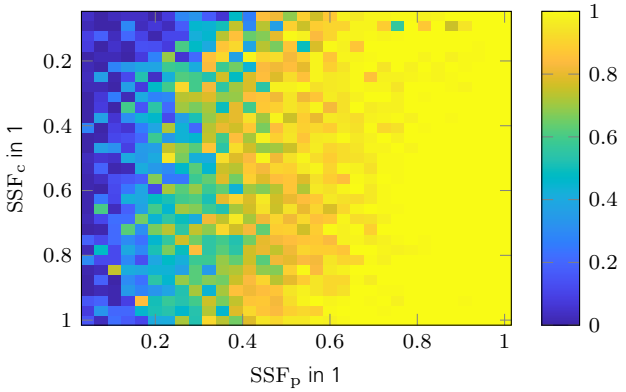

(b) Reconstruction success of φ_m.

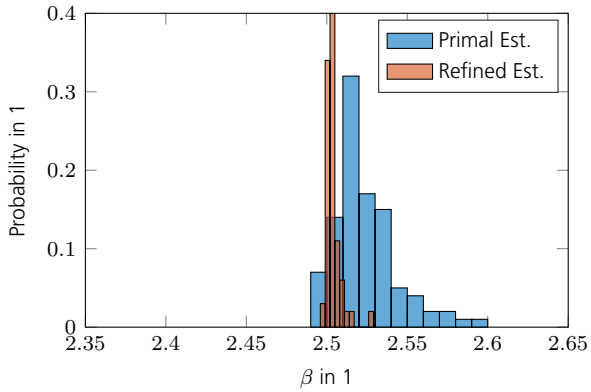

(c) Histogram of β for $\mathrm{SSF_c} = \mathrm{SSF_p} = 1$.

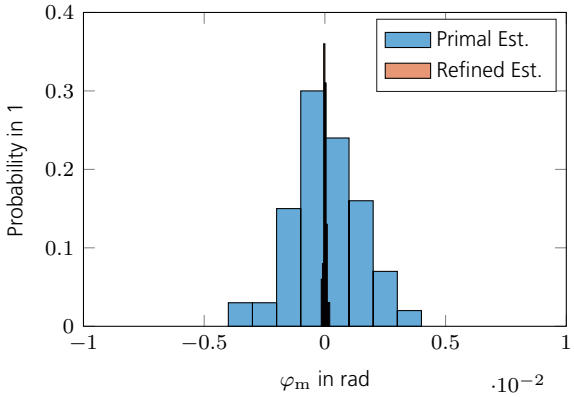

(d) Histogram of φ_m for $\mathrm{SSF_c} = \mathrm{SSF_p} = 1$.

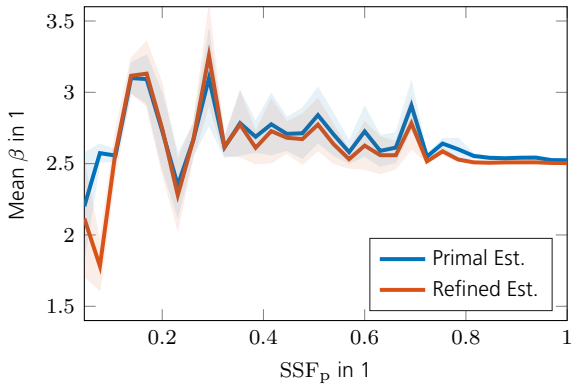

(e) Mean and standard deviation of β for $\mathrm{SSF_c} = 1$.

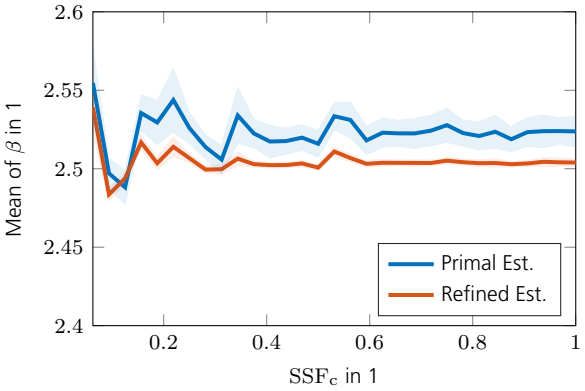

(f) Mean and standard deviation of β for $\mathrm{SSF_p} = 1$.

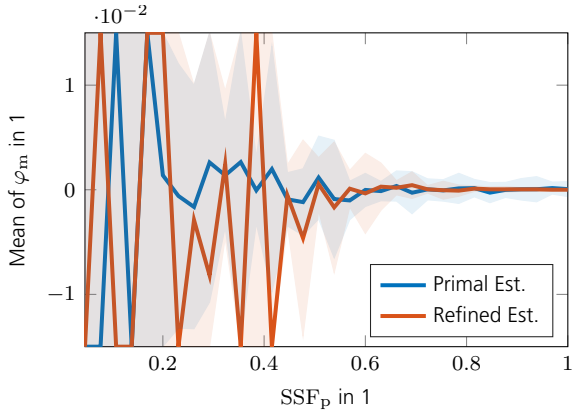

(g) Mean and standard deviation of φ_m for $\mathrm{SSF_p} = 1$.

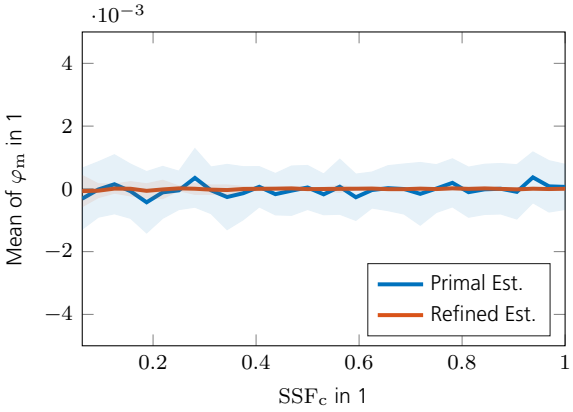

(h) Mean and standard deviation of φ_m for $\mathrm{SSF_c} = 1$.

Figure 7.2.17.: Reconstruction success of ACF algorithm for a level two setting with $\widetilde{\beta} = 2.5$.

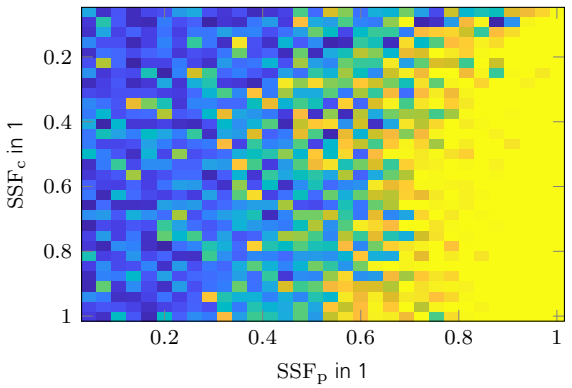

(a) Reconstruction success of β.

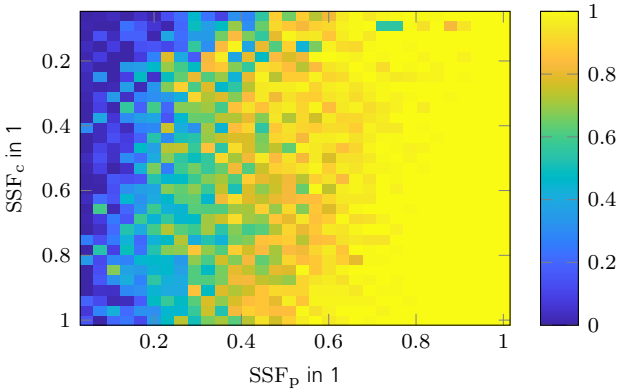

(b) Reconstruction success of φ_m.

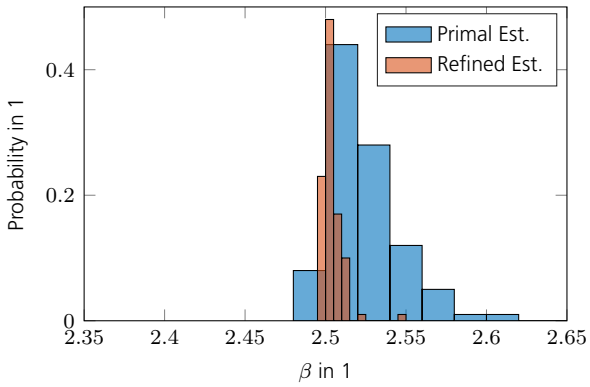

(c) Histogram of β for $\mathrm{SSF_c} = \mathrm{SSF_p} = 1$.

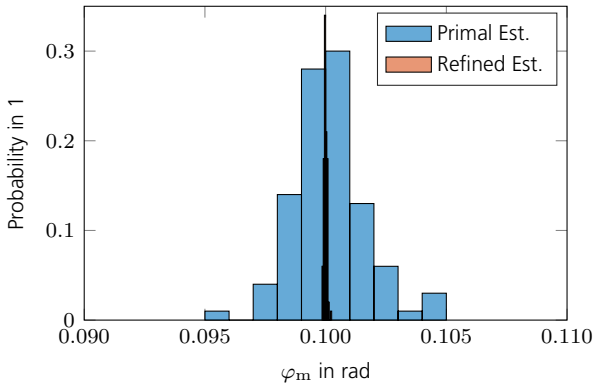

(d) Histogram of φ_m for $\mathrm{SSF_c} = \mathrm{SSF_p} = 1$.

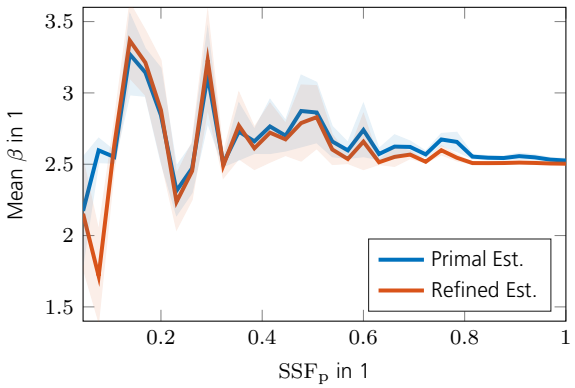

(e) Mean and standard deviation of β for $\mathrm{SSF_c} = 1$.

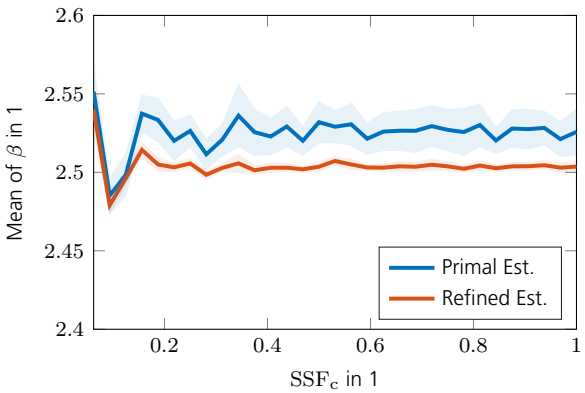

(f) Mean and standard deviation of β for $\mathrm{SSF_p} = 1$.

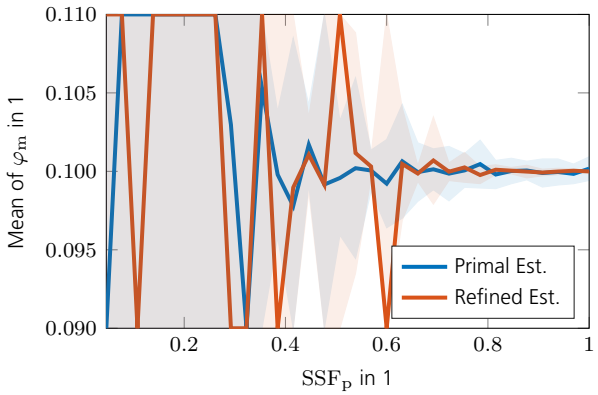

(g) Mean and standard deviation of φ_m for $\mathrm{SSF_p} = 1$.

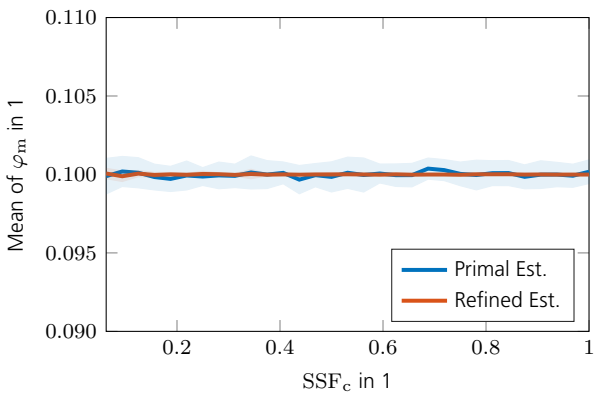

(h) Mean and standard deviation of φ_m for $\mathrm{SSF_c} = 1$.

Figure 7.2.18.: Reconstruction success of ACF algorithm for $\widetilde{\beta} = 2.5$ and $\widetilde{\varphi_m} = 0.35\,\mathrm{rad}$.

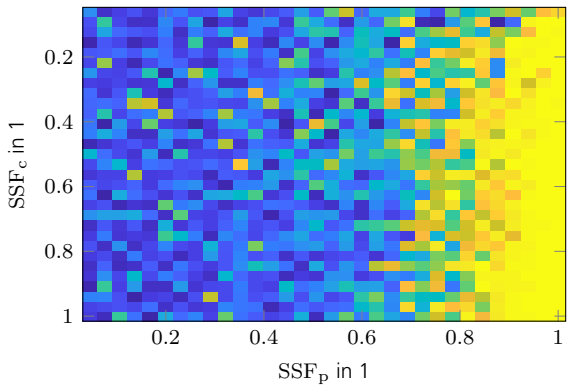

(a) Reconstruction success of β.

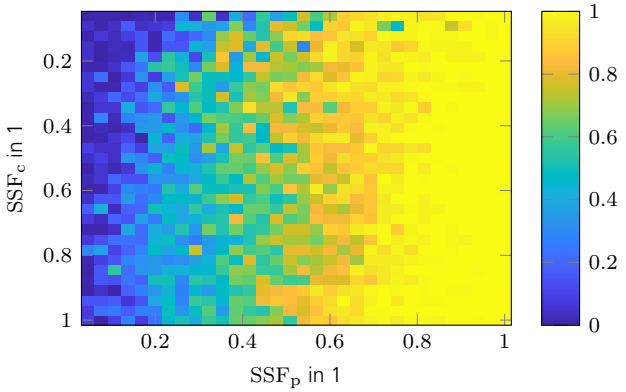

(b) Reconstruction success of φ_m.

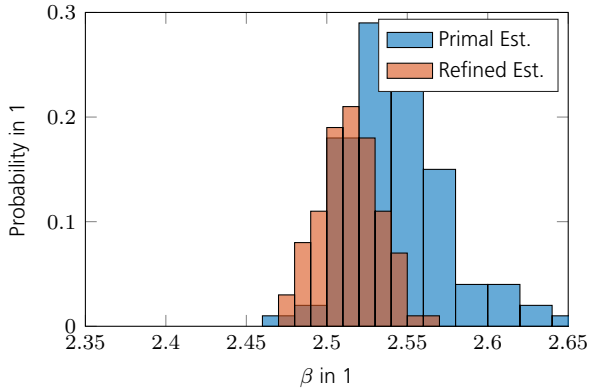

(c) Histogram of β for $\mathrm{SSF_c} = \mathrm{SSF_p} = 1$.

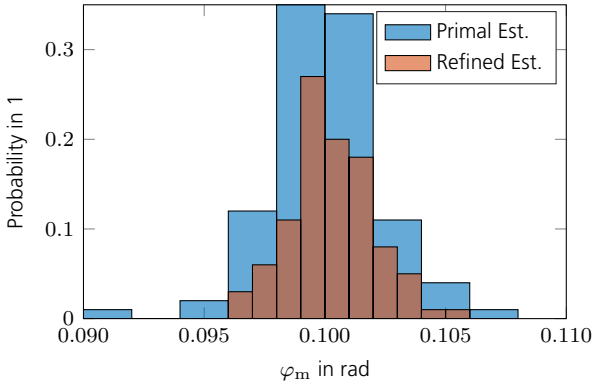

(d) Histogram of φ_m for $\mathrm{SSF_c} = \mathrm{SSF_p} = 1$.

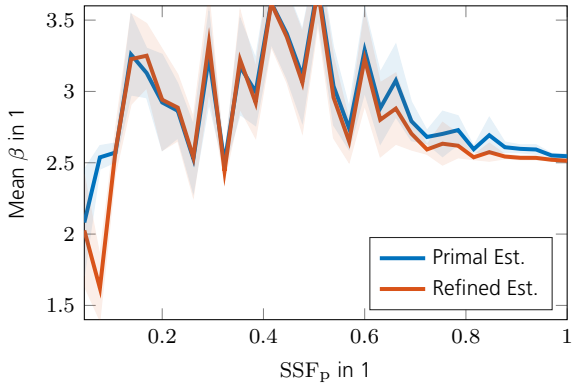

(e) Mean and standard deviation of β for $\mathrm{SSF_c} = 1$.

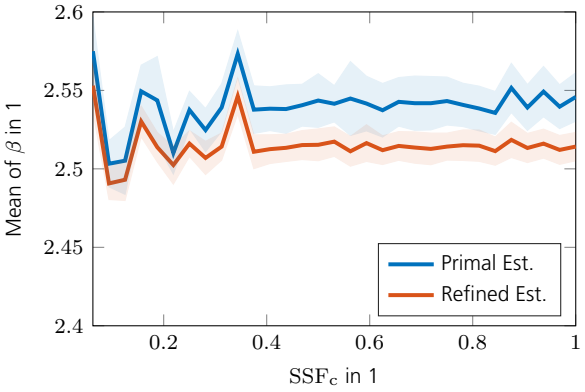

(f) Mean and standard deviation of β for $\mathrm{SSF_p} = 1$.

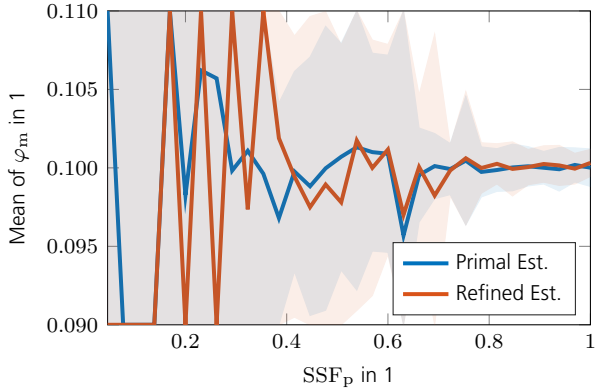

(g) Mean and standard deviation of φ_m for $\mathrm{SSF_p} = 1$.

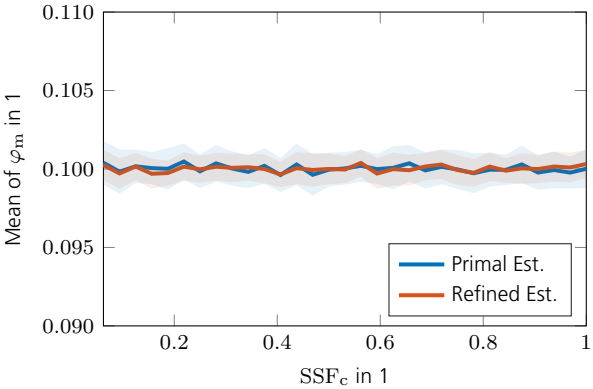

(h) Mean and standard deviation of φ_m for $\mathrm{SSF_c} = 1$.

Figure 7.2.19.: Reconstruction success of ACF algorithm for a level five setting with $\widetilde{\beta} = 2.5$, $\widetilde{\varphi_m} = 0.35\,\mathrm{rad}$, back attenuation of -30 dB, and ICM with $\sigma_{vel} = 20\,\mathrm{m/s}$.

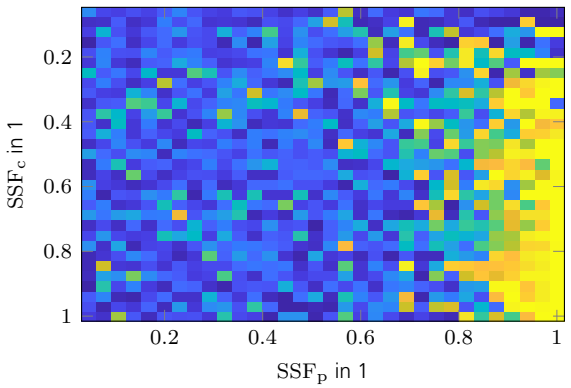

(a) Reconstruction success of β.

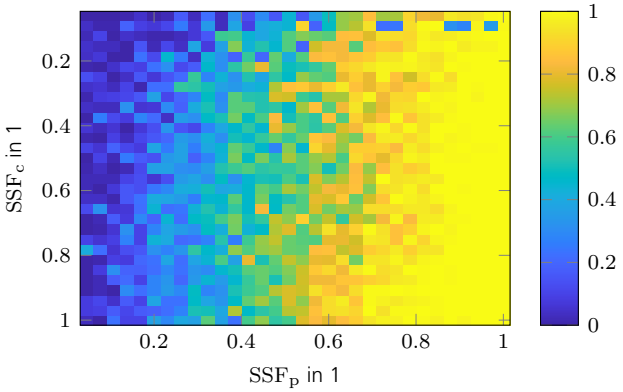

(b) Reconstruction success of φ_m.

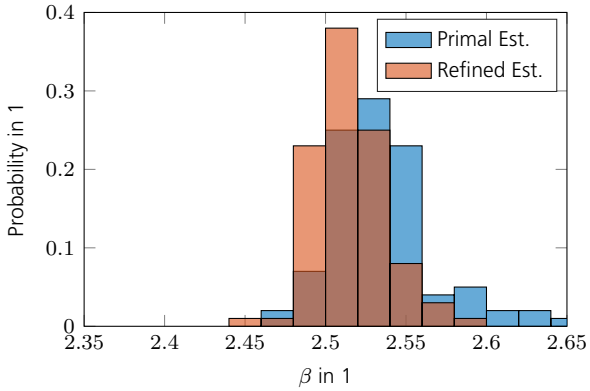

(c) Histogram of β for $\mathrm{SSF_c} = \mathrm{SSF_p} = 1$.

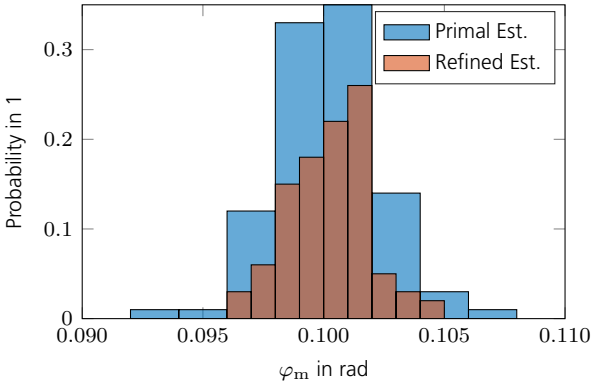

(d) Histogram of φ_m for $\mathrm{SSF_c} = \mathrm{SSF_p} = 1$.

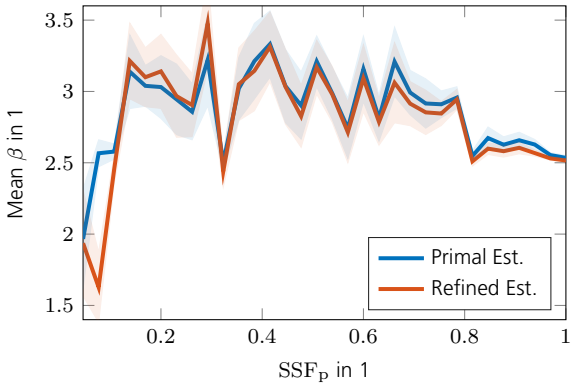

(e) Mean and standard deviation of β for $\mathrm{SSF_c} = 1$.

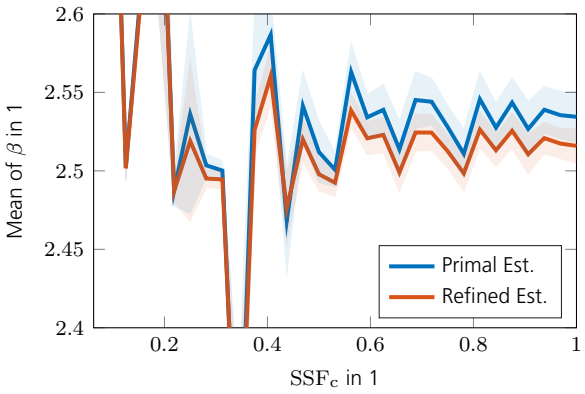

(f) Mean and standard deviation of β for $\mathrm{SSF_p} = 1$.

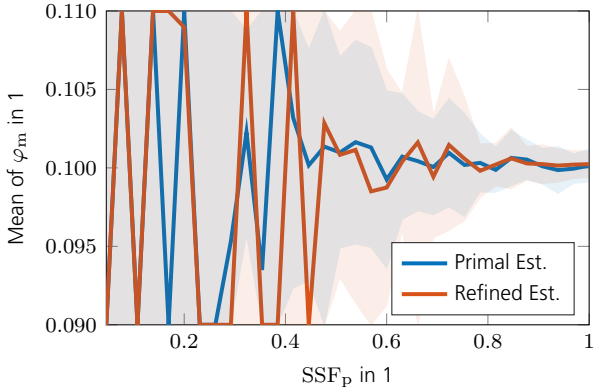

(g) Mean and standard deviation of φ_m for $\mathrm{SSF_p} = 1$.

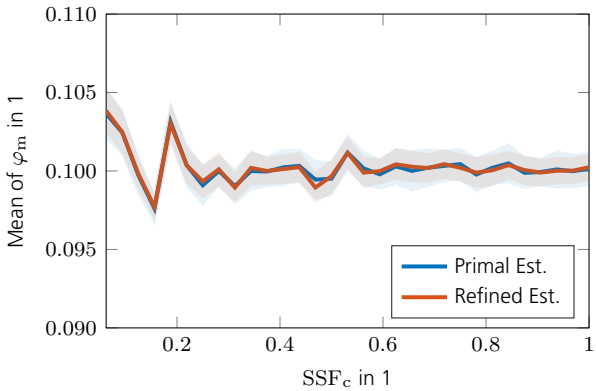

(h) Mean and standard deviation of φ_m for $\mathrm{SSF_c} = 1$.

Figure 7.2.20.: Reconstruction success of ACF algorithm for $\widetilde{\beta} = 2.5$, $\widetilde{\varphi_m} = 0.35\,\mathrm{rad}$, back attenuation of -30 dB, ICM with $\sigma_{vel} = 20\,\mathrm{m/s}$, and $N_t = 4$ targets.

7.2.5. Summary

In this section, an ACF algorithm was presented which estimates the two parameters β and φ_{m}, which are the clutter ridge slope and the velocity misalignment angle. The estimation of β is done by exploiting the low rank property of the focused clutter ridge scene. It was shown that well usable minima occur, provided the sensing operator $\mathcal{A}$ offers a sufficiently low RRIP property. Unfortunately, the low rank property develops a rather wide-shaped or flat minimum with respect to the velocity misalignment angle φ_{m}. As a consequence, φ_{m} can not be estimated accurately enough. To circumvent this problem, an alternative objective function which measures the energy and shape of the focused clutter ridge was introduced. However, this objective function posses multiple minima which requires either a good initial start value or a global minimization scheme to estimate φ_{m} correctly. Both objective functions, the low rank property and the clutter ridge energy approach, are robust against targets present in the range gate under test provided the $\mathrm{SNR} \simeq \mathrm{CNR}$ for a worst case scenario (i. e. in case of severe target leakage). As a future extension, the ACF may be robustified against extremely strong targets by a preceding pure CS reconstruction which removes or thresholds target contributions stronger than the expected clutter power. The performance of the ACF algorithm was shown for missing channels and/or pulses. The algorithm is rather robust against missing channels yet somewhat susceptible against missing pulses. The estimation of the parameters can be improved by cutting non redundant samples within the measurement matrix $\boldsymbol{Y}$. This causes the minimum of the nuclear norm objective function to become more narrow which in turn allows for a better estimation. Finally, a statistical evaluation by use of Monte Carlo simulations was presented. For the parameter chosen in this simulation, the reconstruction success was high as long as $\mathrm{SSF_p} > 0.8$. This boundary depends on the initial value β_0 . In summary, the overall estimation performance depends heavily on the RRIP property of the sensing operator $\mathcal{A}$. Removing channels and pulses tend to be a very structured way of removing samples which resulting in a higher RRIP. A possible future improvement might be to enhanced the sensing operator to incorporate more "randomness". This might be done by adjusting the signal waveform as in e. g. [68]. Once the parameters β and φ_{m} are known, they can be used to focus the radar scene and separate the clutter from moving targets in a subsequent step by use of RPCA. This is shown in the following section.

7.3. Separation of Moving Targets from Stationary Clutter

In this section, the separation of a focused clutter scene from moving targets is discussed. In the first section, the separation model is presented. In the following Section 7.3.2, some preconditioning of the measurement vector $\boldsymbol{y}$ with the aim of suppressing spiky clutter contributions are discussed. Finally, a statistical evaluation of the presented approaches is shown in Section 7.3.4. Unless otherwise stated, the simulation setting for examples shown in the following is a level three setting as defined in Tab. 7.1.1 with $\widetilde{\beta} = 2.5$, $\widetilde{\varphi_{\mathrm{m}}} = 0.35\,\mathrm{rad}$, $\mathrm{CNR_{tot}} = 60\,\mathrm{dB}$, antenna back attenuation of $-30\,\mathrm{dBm}$, a single target $N_{\mathrm{t}} = 1$ with $\mathrm{SNR} = 15\,\mathrm{dB}$, and $\mathrm{SSF_p} = \mathrm{SSF_c} = 1$. The position of the target is marked with a red circle[28].

[28] The separation procedure is capable of detecting multiple moving targets, however, for the sake of illustration only one is considered here.

7.3.1. The Separation Model

In order to separate stationary clutter from moving targets, the following measurement model is used

$$\boldsymbol{y}_{\mathrm{in}} = \mathcal{A}\left(\widetilde{\boldsymbol{S}} + \widetilde{\boldsymbol{L}}; \widehat{\beta}, \widehat{\varphi_{\mathrm{m}}}\right) + \boldsymbol{n}, \tag{7.3.1}$$

where $\widetilde{\boldsymbol{L}} \in \mathbb{C}^{N_{\mathrm{u}} \times N_{\mathrm{D}}}$ is a low rank matrix intended to hold the clutter contributions, $\widetilde{\boldsymbol{S}} \in \mathbb{C}^{N_{\mathrm{u}} \times N_{\mathrm{D}}}$ is a sparse matrix holding the moving targets, $\mathcal{A} : \mathbb{C}^{N_{\mathrm{u}} \times N_{\mathrm{D}}} \rightarrow \mathbb{C}^{M}$ is the radar sensing operator, $\boldsymbol{y}_{\mathrm{in}} \in \mathbb{C}^{M}$ is some preconditioned measurement vector, $\widehat{\beta}$ and $\widehat{\varphi_{\mathrm{m}}}$ are the previously estimated parameters, and $\boldsymbol{n} \in \mathbb{C}^{M} \sim \mathcal{CN}\left(0, P_{\mathrm{n}}\right)$ is complex normal i. i. d. noise. The need for a preconditioned measurement vector $\boldsymbol{y}_{\mathrm{in}}$ is discussed further below. At this point note, that $\boldsymbol{y}_{\mathrm{in}} = \boldsymbol{y}$ is not suitable because in this case $\widehat{\boldsymbol{S}}$ would contain diagonal running clutter leakage entries as explained in detail in Section 7.1. The clutter sensing operator is the same as defined in (7.2.4). To obtain a solution for (7.3.1) the minimization problem

$$\begin{aligned} \widehat{\boldsymbol{L}}, \widehat{\boldsymbol{S}} = \underset{\boldsymbol{L},\boldsymbol{S}}{\arg\min}\, \lambda_l \left\|\boldsymbol{L}\right\|_* + \lambda_s \left\|\boldsymbol{S}\right\|_1 \\ \text{s.t. } \left\|\boldsymbol{y} - \mathcal{A}\left(\boldsymbol{S} + \boldsymbol{L}; \widehat{\beta}, \widehat{\varphi_{\mathrm{m}}}\right)\right\|_2^2 < \varepsilon^2, \end{aligned} \tag{7.3.2}$$

is solved, for which the turbo compressed robust principal component analysis (TCRPCA) algorithm presented in Section 6.6 is used. As was explained in detail in Section 5, a unique separation within (7.3.2) would require the rank-sparsity incoherence condition to be fulfilled. This means that sparse entries within $\widetilde{\boldsymbol{S}}$ must be uniformly distributed (and hence must not form clusters) and entries within $\widetilde{\boldsymbol{L}}$ must be evenly distributed in magnitude, dense, and not spiky. Unfortunately, the latter condition is not fulfilled given the concentrated clutter ridge. To guide the separation into a favorable direction, the sparsity ratio operator $\mathcal{Q}_{\kappa_{\mathrm{s}}}\left(\boldsymbol{S}\right)$ defined in (5.2.8) and the infinity norm thresholding operator $\mathcal{P}_{\varphi}\left(\boldsymbol{L}\right)$ defined in (5.2.9) are used. These operators prevent clustering of sparse entries and spiky low rank entries. The infinity thresholding operator $\mathcal{P}_{\varphi}\left(\boldsymbol{L}\right)$ is applied only at the first few iterations, since it finally needs to contain the spiky clutter ridge contradicting the thresholding of such. The purpose of $\mathcal{P}_{\varphi}\left(\boldsymbol{L}\right)$ in the first few iteration is to prevent the low rank solution $\boldsymbol{L}$ to acquire strong sparse entries, which should be reconstructed within $\boldsymbol{S}$. Furthermore, no sparse entries are allowed to be placed at the focused clutter ridge at $\bar{u} = 0$ including aliased Doppler frequencies as at this position only non-moving clutter patches are located. For all examples shown, these forbidden areas are marked as shaded areas. In addition, all reconstructions within $\boldsymbol{S}$ showing an $\mathrm{SNR} < 10\,\mathrm{dB}$ are also set to zero. This is motivated from the fact that a reliable detection needs at least $\mathrm{SNR} \geq 10\,\mathrm{dB}$ according to standard detection theory [4]. The final goal is $\widehat{\boldsymbol{S}}$ to contain only sparse moving targets and $\widehat{\boldsymbol{L}}$ to contain the clutter ridge including all clutter leakage contributions. This, however, renders to be a challenging task as spiky clutter residuals tend to remain within $\widehat{\boldsymbol{S}}$. In order to prevent such, the measurement vector $\boldsymbol{y}$ can be preconditioned with the aim of decreasing spiky clutter contributions. This is discussed in the following section.

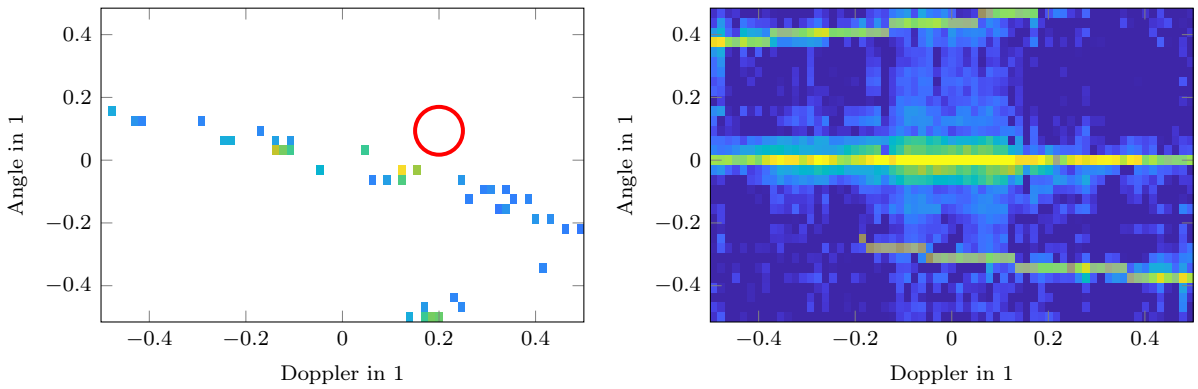

(a) Reconstructed sparse matrix $\widehat{\boldsymbol{S}}$.

(b) Reconstructed low-rank matrix $\widehat{\boldsymbol{L}}$.

Figure 7.3.1.: Separation result for the case of $\boldsymbol{y}_{\mathrm{in}} = \boldsymbol{y}$.

7.3.2. On the Preconditioning of the Measurement Samples

The need of a preconditioned $\boldsymbol{y}_{\mathrm{in}}$ becomes immediately apparent in case one tries to conduct the separation for the choice $\boldsymbol{y}_{\mathrm{in}} = \boldsymbol{y}$. The separation result is shown in Fig. 7.3.1, where $\widehat{\boldsymbol{S}}$ contains diagonal running (Doppler) clutter leakage entries stemming from incomplete clutter samples. A detailed explanation of this phenomena was given in Section 7.1. Since such diagonal running entries are not low rank alike at all, it is not possible to enforce their reconstruction within $\widehat{\boldsymbol{L}}$. Within Fig. 7.3.1a, the red circle marks the position where the target is supposed to be. Evidently, it is not reconstructed as the moving target has to compete with the clutter leakage. For the given case of $\mathrm{SNR} = 15\,\mathrm{dB}$ and $\mathrm{CNR} = 60\,\mathrm{dB}$, the target is too weak compared to the clutter leakage energy. In Fig. 7.3.1b, the shaded pixels mark areas which are blocked to be reconstructed in $\widehat{\boldsymbol{S}}$. It renders to be necessary to remove diagonal clutter leakage components in a first step. One obvious way to do so to choose $\boldsymbol{y}_{\mathrm{in}} = \boldsymbol{y}_{\mathrm{cut}}$ as defined in (7.2.17). The separation result for this choice is shown in Fig. 7.3.2. Evidently, the moving target is successfully reconstructed within $\widehat{\boldsymbol{S}}$. Unfortunately, also quiet much unwanted clutter leakage energy, i. e. false alarms, is found within $\widehat{\boldsymbol{S}}$, especially at locations from aliased Doppler frequencies. The reason therefore is, that in case of Doppler aliasing and present velocity misalignment, the clutter ridge can no longer be focused onto a single row as was explained in Section 7.1. Non focused clutter samples are neither low rank alike and therefore are likely to be placed within $\widehat{\boldsymbol{S}}$. One possibility to treat this problem is to consider only that part in $\bar{u}$ which does not contain clutter ambiguities e. g. ignore all outside of $\bar{u} \in [-0.2, 0.2]$. If case this is not possible, further approaches are necessary. In the following, two ideas are presented.

An alternative approach to suppress unwanted clutter contributions is to use the estimated parameters $\widehat{\beta}$ and $\widehat{\varphi_{\mathrm{m}}}$ to setup a projection filter. As explained in detail in Section 2.2, the clutter subspace does not span the total signal space, hence by projecting the measurements onto the complementary clutter subspace, the clutter signals can be suppressed. The clutter subspace is spanned by the space-time clutter manifold vector $\boldsymbol{g}_{\mathrm{c}}\left(\bar{u}; \beta, \varphi_{\mathrm{m}}\right)$ defined in (2.2.9) for $\bar{u} \in [-\bar{d}, \bar{d})$. For discretized $\bar{u}$, this clutter vector can be stacked into a matrix as defined in (2.2.12) as

$$\boldsymbol{G}_{\mathrm{c}}\left(\beta, \varphi_{\mathrm{m}}\right) = \left[\boldsymbol{g}_{\mathrm{c}}\left(\bar{u}_{n_{\mathrm{c}}}; \beta, \varphi_{\mathrm{m}}\right)\right]_{n_{\mathrm{c}}=-N_{\mathrm{c}}/2}^{N_{\mathrm{c}}/2-1} \in \mathbb{C}^{N_{\mathrm{rx}} N_{\mathrm{p}} \times N_{\mathrm{c}}}. \tag{7.3.3}$$

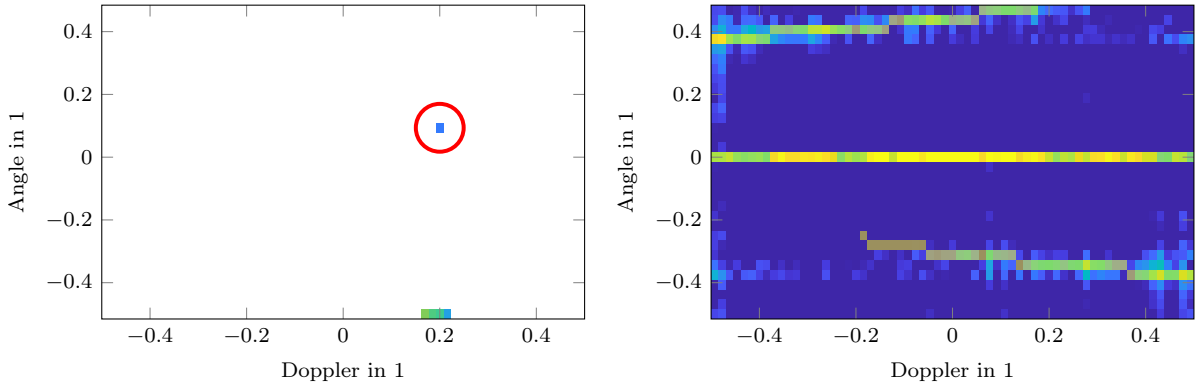

(a) Reconstructed sparse matrix $\widehat{\boldsymbol{S}}$.

(b) Reconstructed low-rank matrix $\widehat{\boldsymbol{L}}$.

Figure 7.3.2.: Separation result for the case of $\boldsymbol{y}_{\mathrm{in}} = \boldsymbol{y}_{\mathrm{cut}}$.

In the limit of $N_{\mathrm{c}} \to \infty$, this matrix spans the same space as the manifold vector $\boldsymbol{g}_{\mathrm{c}}(\bar{u}; \beta, \varphi_{\mathrm{m}})$. A basis $\boldsymbol{U}_{\mathrm{c}}$ for the column subspace spanned by $\boldsymbol{G}_{\mathrm{c}}(\beta, \varphi_{\mathrm{m}})$ can be found in the least minimum square error sense by use of an singular value decomposition (SVD) as

$$\boldsymbol{G}_{\mathrm{c}}(\beta, \varphi_{\mathrm{m}}) = \boldsymbol{U}_{\mathrm{c}} \boldsymbol{\Sigma}_{\mathrm{c}} \boldsymbol{V}_{\mathrm{c}}^{\mathrm{H}}.$$

From basic properties of the SVD, the column space $\boldsymbol{U}_{\mathrm{c}}$ of $\boldsymbol{G}_{\mathrm{c}}(\beta, \varphi_{\mathrm{m}})$ can be identified with the Eigenvectors of $\boldsymbol{G}_{\mathrm{c}}(\beta, \varphi_{\mathrm{m}}) \boldsymbol{G}_{\mathrm{c}}^{\mathrm{H}}(\beta, \varphi_{\mathrm{m}})$ since

$$\begin{aligned} \boldsymbol{G}_{\mathrm{c}}(\beta, \varphi_{\mathrm{m}}) \boldsymbol{G}_{\mathrm{c}}^{\mathrm{H}}(\beta, \varphi_{\mathrm{m}}) &= \boldsymbol{U}_{\mathrm{c}} \boldsymbol{\Sigma}_{\mathrm{c}} \boldsymbol{V}_{\mathrm{c}}^{\mathrm{H}} \boldsymbol{V}_{\mathrm{c}} \boldsymbol{\Sigma}_{\mathrm{c}} \boldsymbol{U}_{\mathrm{c}}^{\mathrm{H}} \\ &= \boldsymbol{U}_{\mathrm{c}} \boldsymbol{\Lambda}_{\mathrm{c}} \boldsymbol{U}_{\mathrm{c}}^{\mathrm{H}}, \end{aligned}$$

where $\boldsymbol{V}_{\mathrm{c}}^{\mathrm{H}} \boldsymbol{V}_{\mathrm{c}} = \boldsymbol{I}$ was used and $\boldsymbol{\Lambda}_{\mathrm{c}} = \boldsymbol{\Sigma}_{\mathrm{c}} \boldsymbol{\Sigma}_{\mathrm{c}}$ are the corresponding Eigenvalues. In the limit of $N_{\mathrm{c}} \to \infty$, the matrix product $\boldsymbol{G}_{\mathrm{c}}(\beta, \varphi_{\mathrm{m}}) \boldsymbol{G}_{\mathrm{c}}^{\mathrm{H}}(\beta, \varphi_{\mathrm{m}})$ becomes

$$\begin{aligned} \lim_{N_{\mathrm{c}} \to \infty} \boldsymbol{G}_{\mathrm{c}} \boldsymbol{G}_{\mathrm{c}}^{\mathrm{H}} &= \lim_{N_{\mathrm{c}} \to \infty} \sum_{n_{\mathrm{c}} = -N_{\mathrm{c}}/2}^{N_{\mathrm{c}}/2-1} \boldsymbol{g}_{\mathrm{c}}(\bar{u}_{n_{\mathrm{c}}}) \boldsymbol{g}_{\mathrm{c}}^{\mathrm{H}}(\bar{u}_{n_{\mathrm{c}}}) \\ &= \int_{-\bar{d}}^{\bar{d}} \boldsymbol{g}_{\mathrm{c}}(\bar{u}; \beta, \varphi_{\mathrm{m}}) \boldsymbol{g}_{\mathrm{c}}^{\mathrm{H}}(\bar{u}; \beta, \varphi_{\mathrm{m}}) \, \mathrm{d}\bar{u} \end{aligned}$$

As shown in detail in Section 2.2, this integral form coincides with the model for a clutter covariance matrix

$$\boldsymbol{R}_{\mathrm{c}}(\beta, \varphi_{\mathrm{m}}) = \int_{-\bar{d}}^{\bar{d}} \boldsymbol{g}_{\mathrm{c}}(\bar{u}; \beta, \varphi_{\mathrm{m}}) \boldsymbol{g}_{\mathrm{c}}^{\mathrm{H}}(\bar{u}; \beta, \varphi_{\mathrm{m}}) \, \mathrm{d}\bar{u}, \tag{7.3.4}$$

which is similar to (2.2.17), however, with the further assumption that the clutter patch power is constant with $P_{\mathrm{c}}(\bar{u}) = 1$. Following the explanations given in Section 2.3.3, a projection onto the complementary clutter subspace is given by

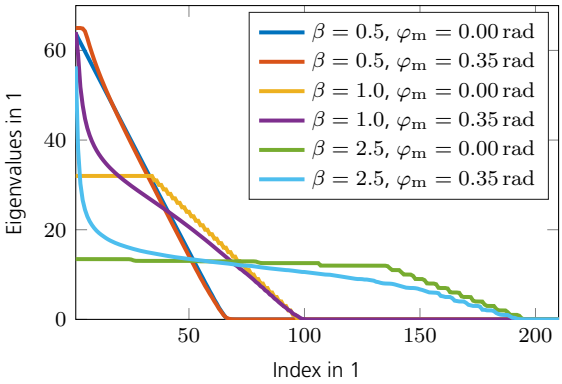

Figure 7.3.3.: Eigenvalues of $\boldsymbol{R}_\mathrm{c}\left(\beta, \varphi_\mathrm{m}\right)$ for $\beta \in \{0.5, 1, 2.5\}$ and $\varphi_\mathrm{m} \in \{0, 0.35\}$.

$$\mathcal{P}_\mathrm{c}^{\perp} = \boldsymbol{I} - \boldsymbol{U}_\mathrm{eff}\boldsymbol{U}_\mathrm{eff}^\mathrm{H},$$

where

$$\boldsymbol{U}_\mathrm{eff} = [\boldsymbol{u}_{\mathrm{c},i}]_{i=1}^{\rho_\mathrm{eff}} \in \mathbb{C}^{N_\mathrm{rx}N_\mathrm{p}\times\rho_\mathrm{eff}}$$

spans the effective clutter subspace. To the contrary as explained in Section 2.3.3, where not $\boldsymbol{R}_\mathrm{c}$ but only $\boldsymbol{R}_\mathrm{cn} = \boldsymbol{R}_\mathrm{c} + \boldsymbol{R}_\mathrm{n}$ was available, the effective rank can be easily determined from $\boldsymbol{\Lambda}_\mathrm{c}$. Due to the absence of noise eigenvalues, a sharp drop of the clutter eigenvalues marking ρ_eff can always be found. An example of emerging eigenvalues for various $\boldsymbol{R}_\mathrm{c}\left(\beta, \varphi_\mathrm{m}\right)$ is shown in Fig. 7.3.3. For all simulations to follow, the effective rank was chosen to be the number of eigenvalues greater than 10^{-12}. All remaining eigenvalues are accounted to be non zero only due to numerical noise. With this projection at hand, a preconditioned measurement vector can be setup as

$$\boldsymbol{y}_\mathrm{in} = \mathcal{P}_\mathrm{c}^{\perp}\boldsymbol{y} = \boldsymbol{y}_\mathrm{pp}. \tag{7.3.5}$$

While projection filters are very effective, they are susceptible to parameter variations i. e. the parameters need to be known very precisely. An example for this preconditioning is shown in Fig. 7.3.4. The parameters were estimated to be $\widehat{\beta} = 2.5038$ and $\widehat{\varphi_\mathrm{m}} = 0.3500175\,\mathrm{rad}$ using the auto-clutter focus (ACF) algorithm. As can be seen, the clutter energy is suppressed completely. Nevertheless, if the parameters are estimated not well enough, clutter residuals will occur. The filter characteristic in terms of signal to interference and noise ratio (SINR) loss as defined in (2.3.11) is shown in Fig. 7.3.4c and Fig. 7.3.4d. Within Fig. 7.3.4c and all following figures, the curves denoted as true and estimated refer to filters setup using the true and estimated parameters β and φ_m. The curves optimal denote the optimal SINR loss as defined in (2.3.4). Next, the projection matrix may further be used to setup a matched subspace detector. Following the explanations given in Section 2.3, the corresponding filter vector becomes

$$\boldsymbol{w}_\mathrm{msd} = \frac{\mathcal{P}_\mathrm{c}^{\perp}\boldsymbol{g}}{\sqrt{\boldsymbol{g}^\mathrm{H}\mathcal{P}_\mathrm{c}^{\perp}\boldsymbol{g}}}, \tag{7.3.6}$$

with

$$\boldsymbol{y}_\mathrm{in} = \boldsymbol{w}_\mathrm{msd}^\mathrm{H}\boldsymbol{y} = \boldsymbol{y}_\mathrm{msd}$$

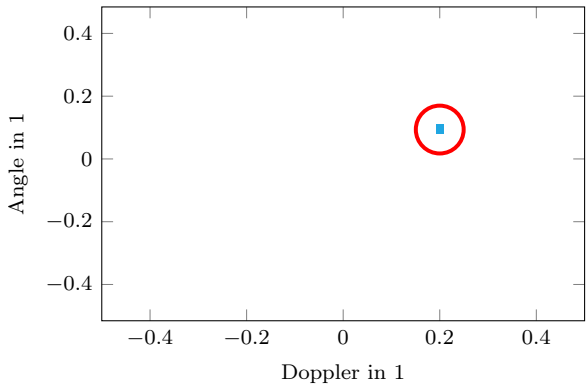

(a) Reconstructed sparse matrix $\widehat{\boldsymbol{S}}$.

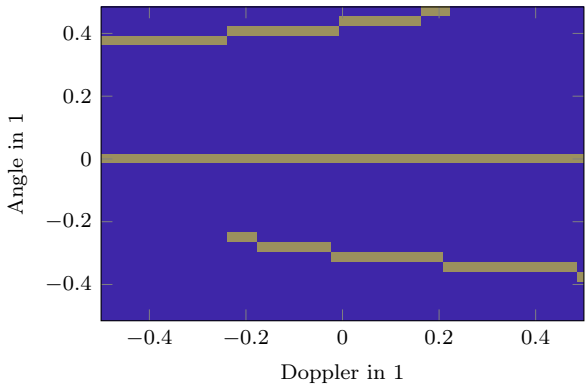

(b) Reconstructed low-rank matrix $\widehat{\boldsymbol{L}}$.

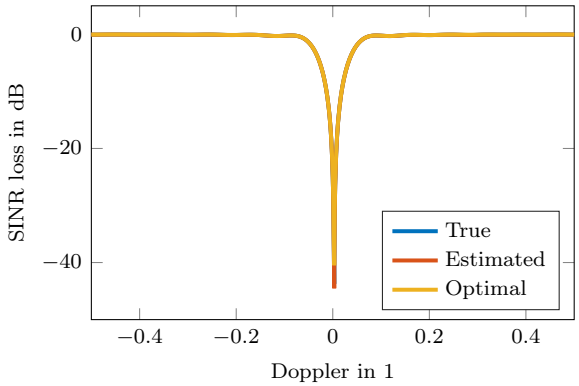

(c) SINR loss of $\mathcal{P}_{\mathrm{c}}^{\perp}$ at $\bar{u} = -0.17$.

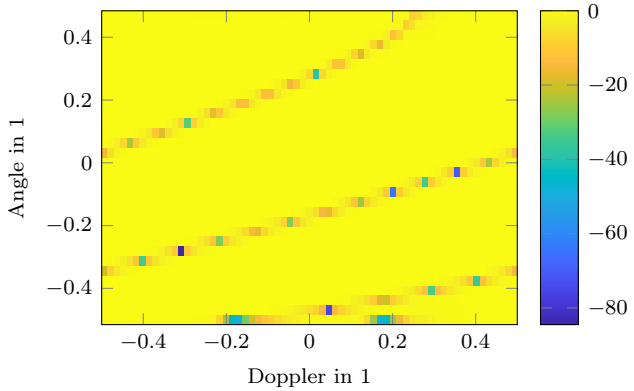

(d) SINR loss of $\mathcal{P}_{\mathrm{c}}^{\perp}$.

Figure 7.3.4.: Separation result for the case of $\boldsymbol{y}_{\mathrm{in}} = \boldsymbol{y}_{\mathrm{pp}}$.

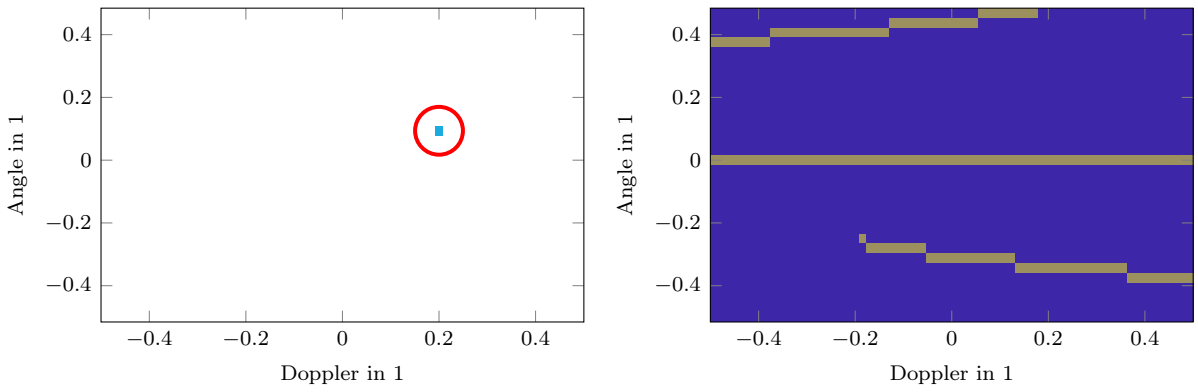

(a) Reconstructed sparse matrix $\widehat{\boldsymbol{S}}$. (b) Reconstructed low-rank matrix $\widehat{\boldsymbol{L}}$.

Figure 7.3.5.: Separation result for the case of $\boldsymbol{y}_{\mathrm{in}} = \boldsymbol{y}_{\mathrm{msd}}$.

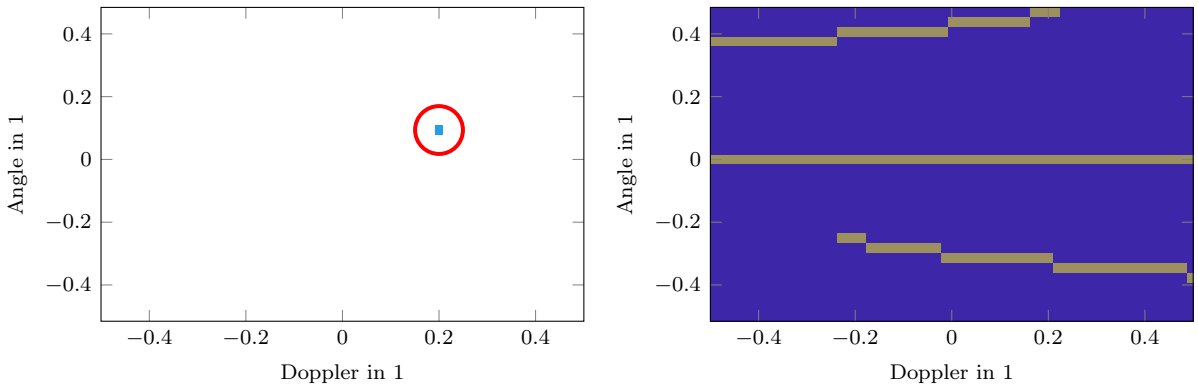

(a) Reconstructed sparse matrix $\widehat{\boldsymbol{S}}$. (b) Reconstructed low-rank matrix $\widehat{\boldsymbol{L}}$.

Figure 7.3.6.: Separation result for the case of $\boldsymbol{y}_{\mathrm{in}} = \boldsymbol{y}_{\mathrm{cut,pp}}$.

The matched subspace detector filter aims to suppress the clutter contributions and simultaneously establishes a flat noise level suitable for thresholding (hence the name detector). An example is shown in Fig. 7.3.5. The filter characteristic in terms of SINR loss is the same as for the projection filter (7.3.5). The results are very similar to the projection filter, however, the separation in $\widehat{\boldsymbol{S}}$ appear somewhat more populated. Finally, it is also possible to combine cutting and filtering, which especially comes in handy in case of badly estimated parameters. This is shown in Fig. 7.3.6. The results for the matched subspace detector filter are very similar and are omitted here. An example for badly estimated parameters is shown in Fig. 7.3.7, where $\widehat{\beta} = \widetilde{\beta} + 0.1$ and $\widehat{\varphi_{\mathrm{m}}} = \widetilde{\varphi_{\mathrm{m}}} + 5 \cdot 10^{-4}$ rad was used. As can be seen, more clutter residuals occur. However, a major part of the clutter contributions was suppressed. The target was successfully found by use of the TCRPCA separation. An advantage of such a pre-filter step is to reduce the spikiness of the clutter mitigating the rank-sparsity incoherence condition requirement. The effect of wrongly estimated parameters on the filtering is shown in Fig. 7.3.7d, where the difference in dB of the SINR losses for the estimated parameters and the optimal filter characteristic is shown. Especially for Doppler frequencies off zero, the filter notches separate leaving clutter contributions remain in the filtered measurement data.

As a final remark it shall be mentioned here, that the methods for clutter separation presented

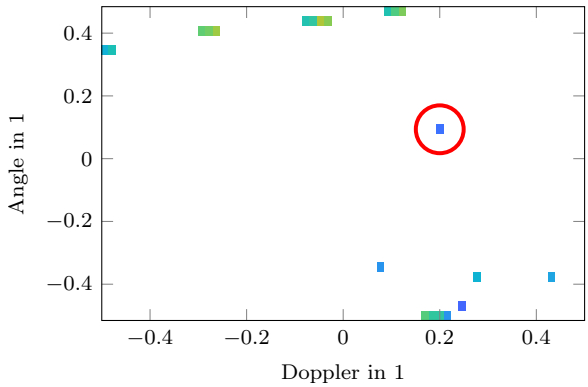

(a) Reconstructed sparse matrix $\widehat{\boldsymbol{S}}$.

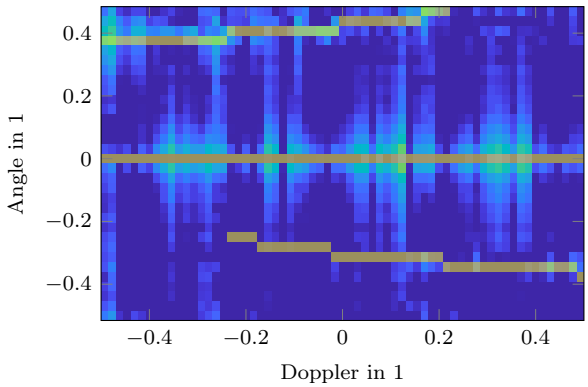

(b) Reconstructed low-rank matrix $\widehat{\boldsymbol{L}}$.

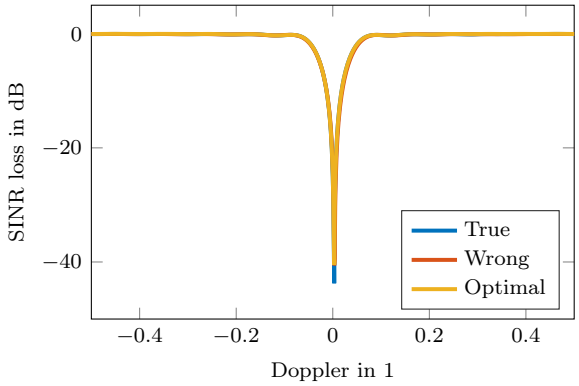

(c) SINR loss of $\mathcal{P}_{\mathrm{c}}^{\perp}$ at $\bar{u} = -0.17$.

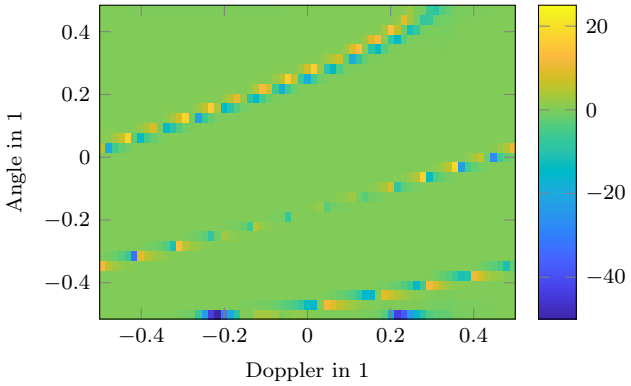

(d) SINR loss difference $\mathrm{SINR}_{\mathrm{pp}} - \mathrm{SINR}_{\mathrm{opt}}$ in dB.

Figure 7.3.7.: Separation result for the case of $\boldsymbol{y}_{\mathrm{in}} = \boldsymbol{y}_{\mathrm{cut,pp}}$ for wrongly estimated parameters $\widehat{\beta} = \widetilde{\beta} + 0.1$ and $\widehat{\varphi_{\mathrm{m}}} = \widetilde{\varphi_{\mathrm{m}}} + 5 \cdot 10^{-4}$ rad.

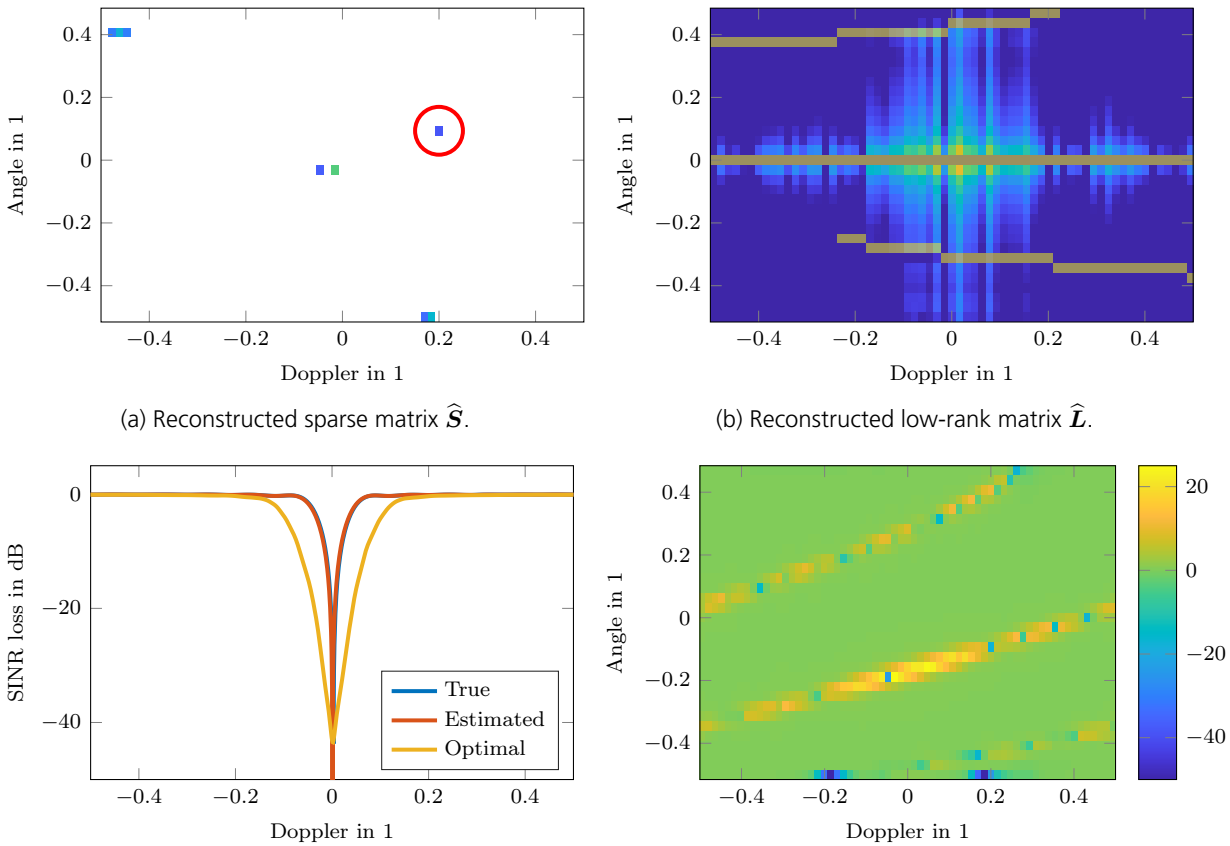

(a) Reconstructed sparse matrix $\widehat{\boldsymbol{S}}$.

(b) Reconstructed low-rank matrix $\widehat{\boldsymbol{L}}$.

(c) SINR loss of $\mathcal{P}_{\mathrm{c}}^{\perp}$ at $\bar{u} = -0.17$.

(d) SINR loss difference $\mathrm{SINR}_{\mathrm{pp}} - \mathrm{SINR}_{\mathrm{opt}}$ in dB.

Figure 7.3.8.: Separation result for the case of $\boldsymbol{y}_{\mathrm{in}} = \boldsymbol{y}_{\mathrm{cut,pp}}$ including ICM with $\sigma_{\mathrm{vel}} = 20\,\mathrm{m/s}$.

so far are not suitable to handle clutter stemming from internal clutter motion (ICM). By its very nature, ICM is a moving clutter source. The compressed robust principal component analysis (CRPCA) approach as well as the filter model are suitable for non moving clutter only. An example including ICM is shown in Fig. 7.3.8 for $\sigma_{\mathrm{vel}} = 20\,\mathrm{m/s}$. As can be seen from the optimal filter characteristic in Fig. 7.3.8c, the clutter ridge broadens due to ICM. Since the covariance model in (7.3.4) does not incorporate ICM, the derived filters result in filter characteristics showing a too narrow filter notch. As a consequence, much clutter residuals remain for the CRPCA algorithm to handle. Depending on the amount of remaining ICM clutter, spiky residuals may remain which are reconstructed within $\widehat{\boldsymbol{S}}$ as shown in Fig. 7.3.8a. One possibility to mitigate this effect is to allow the low-rank solution $\widehat{\boldsymbol{L}}$ to contain ICM clutter by reducing the cost factor λ_l. This, however, bears the risk to miss weak moving targets as those contributions may also be accounted to $\widehat{\boldsymbol{L}}$. Another possibility is to adapt the model filter (7.3.4), introducing additional parameters to estimate. This is subject to further investigation and is not treated within this work.

Except from the subspace projection approach (7.3.5), all methods presented above require all measurements i. e. $\mathrm{SSF_p} = \mathrm{SSF_c} = 1$. Since CRPCA is applicable also in case of missing samples, the preconditioning needs to be extended adequately. This is discussed in the following section.

7.3.3. On the Sub-Sampling Effects on Separation

In the previous section, the separation of static clutter from moving targets was presented for the case of no sub sampling. Since CRPCA is used, it is conceivable to conduct the separation also in case of missing samples, as was done for the parameter estimation in Section 7.2. A practical use case therefore would be to save antenna channels in order to reduce weight and cost of the radar sensor. Another one would be to skip pulses during a coherent processing interval (CPI) and instead use the available time to conduct a different radar task e. g. tracking etc. In order to be able to handle missing samples, the impact of the sub sampling process onto the preconditioning of the measurement sample vector $\boldsymbol{y}$ needs to be accounted for. In the following, the filtering of $\boldsymbol{y}$ is conducted by the use of the complementary clutter space projection $\mathcal{P}_{\mathrm{c}}^{\perp}$ only. Let

$$\boldsymbol{y}_{\mathrm{up}} = \mathrm{vec}\left(\boldsymbol{Y}_{\mathrm{up}}\right) \in \mathbb{C}^{N_{\mathrm{u}}N_{\mathrm{D}}}$$

be the vectorized version of the up sampled measurement matrix $\boldsymbol{Y}_{\mathrm{up}}$ as defined in (7.2.15). With this definition at hand, a preconditioned measurement vector may be set up in a similar manner to (7.3.5) as

$$\boldsymbol{y}_{\mathrm{in}} = \left(\mathcal{P}_{\mathrm{c}}^{\perp}\boldsymbol{y}_{\mathrm{up}}\right)_{\Omega_y} \in \mathbb{C}^{N_{\mathrm{c}}N_{\mathrm{p}}}, \tag{7.3.7}$$

where Ω_y denotes the sample index set and $\boldsymbol{x}_{\Omega_y}$ means selecting all entries within $\boldsymbol{x}$ defined in Ω_y yielding a vector of reduced size. However, the preconditioning defined in (7.3.7) is not feasible. At first, $\mathcal{P}_{\mathrm{c}}^{\perp}\boldsymbol{y}_{\mathrm{up}}$ yields a vector being an element of the complementary clutter space, as desired, yet gives a densely populated vector in general. At second, applying the sub sampling operator is equivalent to setting all entries within the up sampled vector to zero which are not in Ω_y. This yields a vector which in general is not an element of the complementary clutter subspace defined by the range of $\mathcal{P}_{\mathrm{c}}^{\perp}$. Let

$$\mathcal{S}(\Omega_y^{\perp}) = \left\{\boldsymbol{x} \in \mathbb{C}^{N_{\mathrm{u}}N_{\mathrm{D}}} | \boldsymbol{x}_{\Omega_y^{\perp}} = 0\right\}$$

be the set of all vectors which have zero-entries at the complementary sample index set $\Omega_y^{\perp}$. By definition, $\boldsymbol{y}_{\mathrm{up}} \in \mathcal{S}(\Omega_y^{\perp})$. Furthermore, let

$$\mathcal{C}(\mathcal{P}_{\mathrm{c}}^{\perp}) = \left\{\boldsymbol{x} \in \mathbb{C}^{N_{\mathrm{u}}N_{\mathrm{D}}} | \boldsymbol{x} \in \mathrm{range}(\mathcal{P}_{\mathrm{c}}^{\perp})\right\}$$

be the set of all vectors in the range of the complementary clutter subspace. Both sets $\mathcal{S}(\Omega_y^{\perp})$ and $\mathcal{C}(\mathcal{P}_{\mathrm{c}}^{\perp})$ are closed convex subspaces.[29] For a successful clutter suppression, the preconditioned and up sampled measurement vector needs to be an element of the intersection $\mathcal{S}(\Omega_y^{\perp}) \cap \mathcal{C}(\mathcal{P}_{\mathrm{c}}^{\perp})$. One possibility to find a suitable $\boldsymbol{y}_{\mathrm{in}}$ is to use the method of alternating projection as

$$\boldsymbol{x}_i = \mathcal{P}_{\mathcal{S}} \circ \mathcal{P}_{\mathcal{C}} \circ \boldsymbol{x}_{i-1} \tag{7.3.8}$$

until a suitable abortion criteria is met. In this scheme, $\mathcal{P}_{\mathcal{S}}$ and $\mathcal{P}_{\mathcal{C}}$ denote projections onto the corresponding vector spaces $\mathcal{S}(\Omega_y^{\perp})$ and $\mathcal{C}(\mathcal{P}_{\mathrm{c}}^{\perp})$. It is well known, that the method of alternating

[29] This can be seen immediately from the definition of a convex set: Let $\mathcal{S}$ be a subset of $\mathbb{C}^n$. $\mathcal{S}$ is a convex set if it is closed under convex combinations. Thus, for any $k > 0$, for any vectors $\boldsymbol{v}_1, \ldots, \boldsymbol{v}_k \in \mathcal{S}$, and for any scalars $\lambda_1, \ldots, \lambda_k \in \mathbb{R}_+$ satisfying $\sum_{i=1}^{k} \lambda_i = 1$, the convex combination $\sum_{i=1}^{k} \lambda_i \boldsymbol{v}_i$ is also in $\mathcal{S}$. Furthermore, $\mathcal{S}$ is a subspace if it is closed under any linear combination. Thus, any subspace is also a convex set.

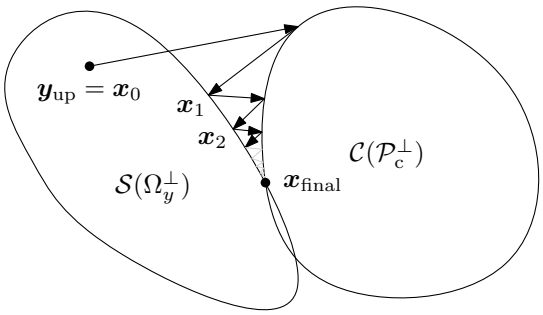

Figure 7.3.9.: The alternating projection scheme for sub sampled filtering.

projections finds a point of the intersection of two closed convex sets given the sets are not disjoint and the angle of interception is sharp i. e. the cosine of the angle between the subspaces is positive [74]. An illustration of this projection scheme is shown in Fig. 7.3.9. It shall be noted, that the matched subspace detection filter $\boldsymbol{w}_{\mathrm{msd}}$ given in (7.3.6) cannot be used instead of the projection filter $\mathcal{P}_{\mathrm{c}}^{\perp}$, since $\boldsymbol{w}_{\mathrm{msd}}$ is not idempotent, a prerequisite for a valid projection operator. The final preconditioned measurement vector is obtained by sub sampling as

$$\boldsymbol{y}_{\mathrm{in}} = \boldsymbol{x}_{\mathrm{final},\Omega_y},$$

where $\boldsymbol{x}_{\mathrm{final}}$ is the final result of the alternating projection scheme. An algorithm conducting (7.3.8) called alternating projection sub sample filtering (APSF) is given in Algorithm 7.2. Instead

Algorithm 7.2 The APSF algorithm.

Input: $\boldsymbol{y}_{\mathrm{up}}$, Ω_y, $\Omega_y^{\perp}$, $\mathcal{P}_{\mathrm{c}}^{\perp}$, I
Initialization:
1: $\boldsymbol{x}_0 \leftarrow \boldsymbol{y}_{\mathrm{up}}$
2: $i \leftarrow 0$, $d \leftarrow \infty$, $\epsilon \leftarrow 10^{-8}$
Body:
1: **while** $d > \epsilon$ **and** $i < I$ **do**
2: $i \leftarrow i + 1$
3: $\boldsymbol{x}_i \leftarrow \mathcal{P}_{\mathrm{c}}^{\perp} \boldsymbol{x}_{i-1}$
4: $\boldsymbol{x}_{i,\Omega_y^{\perp}} \leftarrow 0$
5: $d \leftarrow \|\boldsymbol{x}_i - \boldsymbol{x}_{i-1}\|_2^2 \,/\, \|\boldsymbol{x}_{i-1}\|_2^2$
6: **end while**
Output: $\boldsymbol{y}_{\mathrm{in}} \leftarrow \boldsymbol{x}_{i,\Omega_y}$

of $\boldsymbol{y}_{\mathrm{up}}$, also the pre-cut measurement vector $\boldsymbol{y}_{\mathrm{cut}} = \mathrm{vec}\,(\boldsymbol{Y}_{\mathrm{cut}})$ defined in (7.2.16) can be used for a further clutter suppression. This is done in the following. In Fig. 7.3.10, the first few intermediate and the final result of the filtering scheme is shown in the focused scene domain as $\mathcal{A}^{-1}\left(\boldsymbol{x}_i; \widetilde{\beta}, \widetilde{\varphi_{\mathrm{m}}}\right)$ for the case of $\mathrm{SSF_c} = 0.5$, $\mathrm{SSF_p} = 1$.[30] For a better illustration, the target energy was increased to $\mathrm{SNR} = 45\,\mathrm{dB}$. Due to the sub sampling in the channel domain, distortions in the angle domain emerge, however, due to cutting no diagonal clutter residuals emerge. Iteration by iteration, the distorted clutter energy is reduced by the APSF procedure. In the final result, only the strong target remains as desired. In Fig. 7.3.11, the results for the case of $\mathrm{SSF_c} = 1$,

[30] Note that since $\boldsymbol{x}_i \in \mathbb{C}^{N_{\mathrm{u}} N_{\mathrm{D}}}$ is an up sampled vector, the sensing operator is invertible, hence $\mathcal{A}^{-1}$ exists. The result is the same as applying the hermitian sensing operator $\mathcal{A}^{\mathrm{H}}$ onto the sub sampled measurement vector.

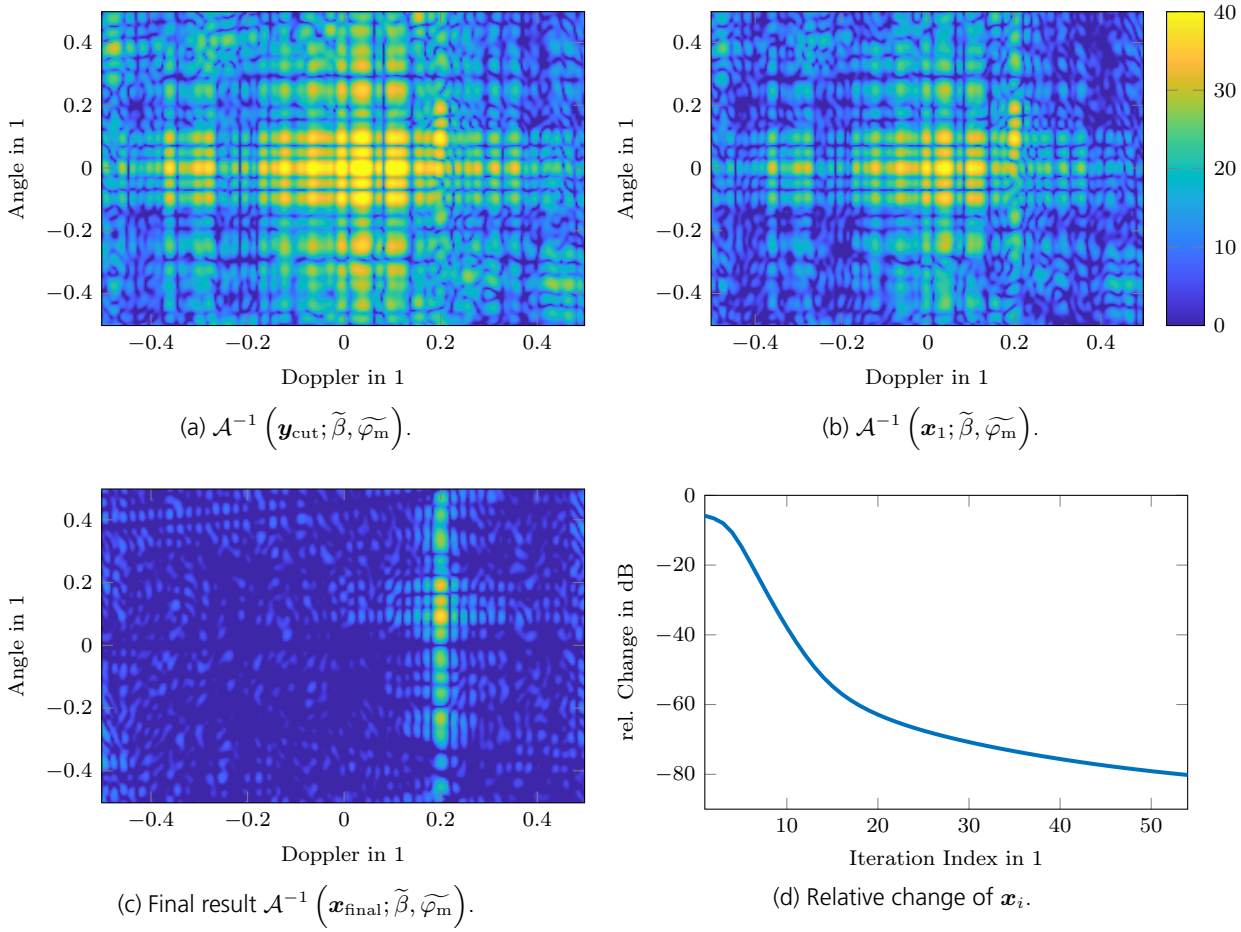

(a) $\mathcal{A}^{-1}\left(\boldsymbol{y}_{\mathrm{cut}}; \widetilde{\beta}, \widetilde{\varphi_{\mathrm{m}}}\right)$.

(b) $\mathcal{A}^{-1}\left(\boldsymbol{x}_1; \widetilde{\beta}, \widetilde{\varphi_{\mathrm{m}}}\right)$.

(c) Final result $\mathcal{A}^{-1}\left(\boldsymbol{x}_{\mathrm{final}}; \widetilde{\beta}, \widetilde{\varphi_{\mathrm{m}}}\right)$.

(d) Relative change of $\boldsymbol{x}_i$.

Figure 7.3.10.: Intermediate and final result of the APSF algorithm in the scene domain for the case of $\boldsymbol{y}_{\mathrm{in}} = \boldsymbol{y}_{\mathrm{cut}}$, $\mathrm{SSF_c} = 0.5$, and $\mathrm{SSF_p} = 1$.

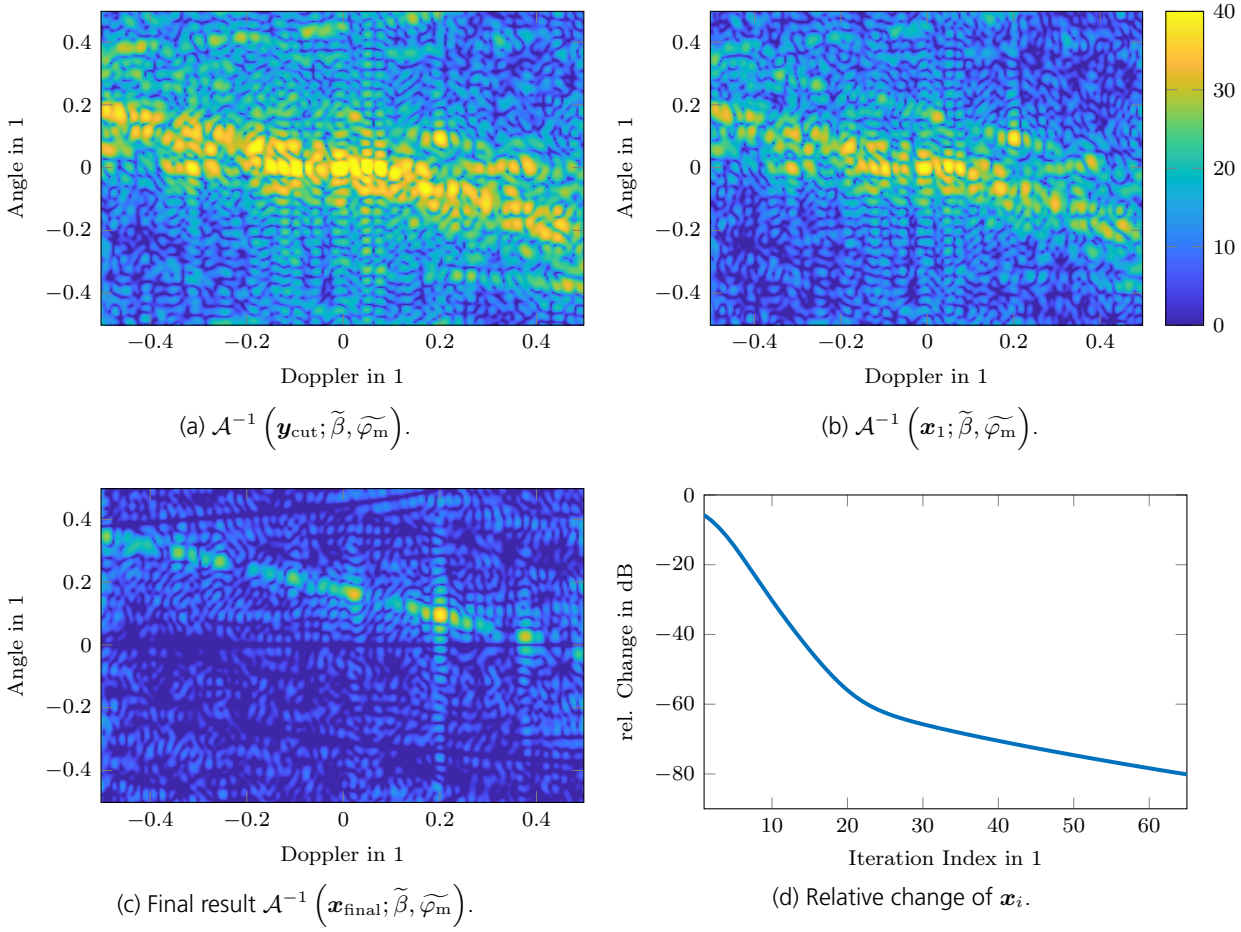

(a) $\mathcal{A}^{-1}\left(\boldsymbol{y}_{\mathrm{cut}};\widetilde{\beta},\widetilde{\varphi_{\mathrm{m}}}\right)$.

(b) $\mathcal{A}^{-1}\left(\boldsymbol{x}_1;\widetilde{\beta},\widetilde{\varphi_{\mathrm{m}}}\right)$.

(c) Final result $\mathcal{A}^{-1}\left(\boldsymbol{x}_{\mathrm{final}};\widetilde{\beta},\widetilde{\varphi_{\mathrm{m}}}\right)$.

(d) Relative change of $\boldsymbol{x}_i$.

Figure 7.3.11.: Intermediate and final result of the APSF algorithm in the scene domain for the case of $\boldsymbol{y}_{\mathrm{in}} = \boldsymbol{y}_{\mathrm{cut}}$, $\mathrm{SSF_c} = 1$, and $\mathrm{SSF_p} = 0.5$.

$\mathrm{SSF_p} = 0.5$ is shown. Note here, that although cutting was conducted, diagonal clutter residuals occur. This is a direct consequence of focusing the clutter ridge in the angle domain. As was explained in Section 7.1, focusing in the angle domain is equivalent to shift space-time samples in the time domain. In case of no missing pulses, non redundant clutter samples occur only at the edges of the measurement map $\boldsymbol{Y}$ and can be cut in the time domain. Cutting in the time domain is advantageous as it is easier and cheaper to obtain a larger number of pulses compared to channels. In case of missing pulses, multiple non redundant samples emerge in the middle of $\boldsymbol{Y}$ and can not be get rid by cutting except a very large amount of pulses is available. To the contrary, skipping channels in combination with a clutter focus in the angle domain does not yield any non redundant sample arrangements. Hence, diagonal entries do not occur as was the case in the latter example. Nevertheless, in case the parameters β and φ_{m} are known very well, the projection filter also cancels the effect of the non redundant samples as shown in Fig. 7.3.11c. It shall be mentioned, that if the clutter ridge is not focused in the angle but in the Doppler domain, the sub sampling effect is exactly the opposite. In this case, skipping pulses would not cause any non redundant arrangements, while missing channels would. A possible combination of both clutter focus approaches is beyond the scope of this work.

As was seen from the figures shown before, cutting alone is not sufficient anymore to handle

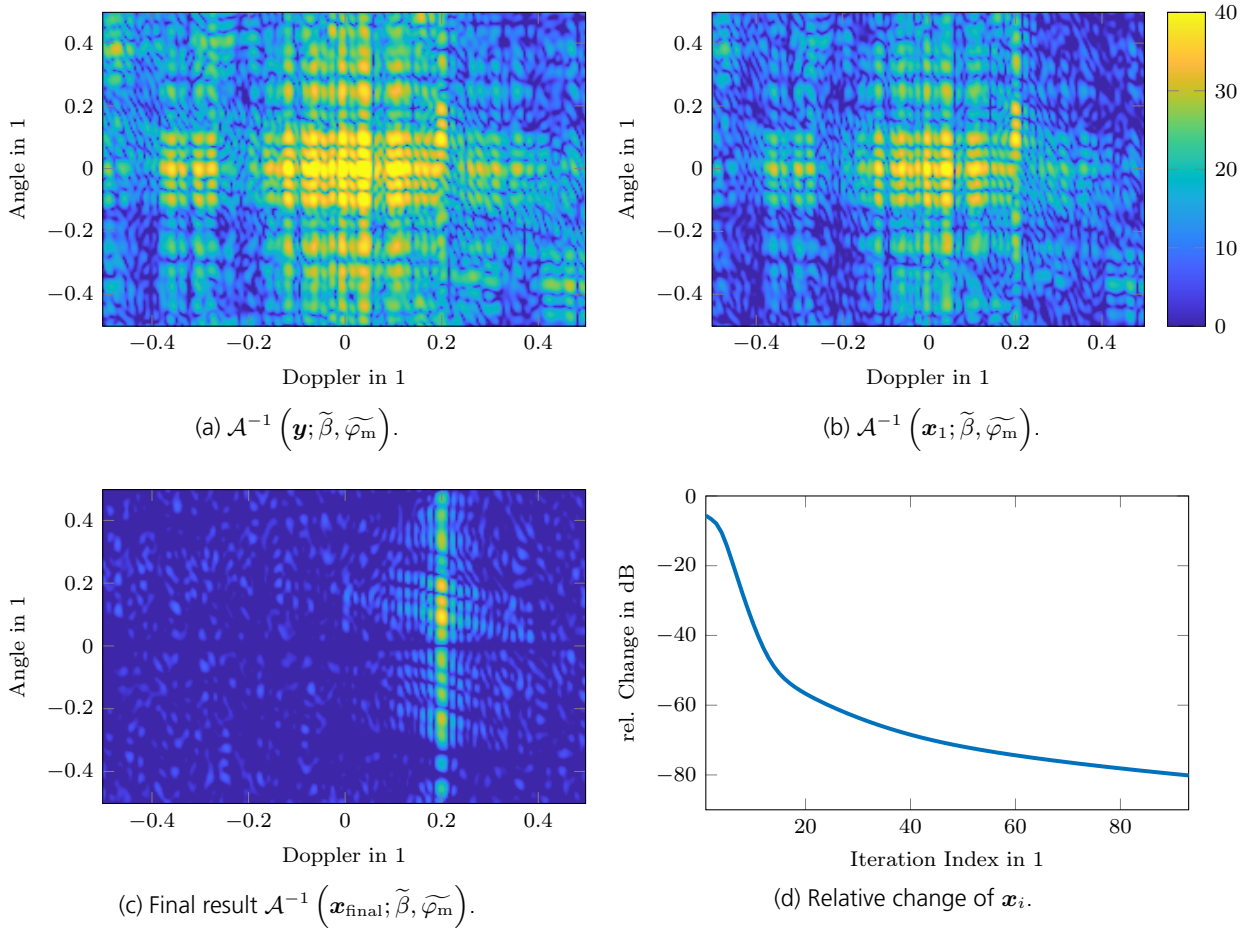

(a) $\mathcal{A}^{-1}\left(\boldsymbol{y};\widetilde{\beta},\widetilde{\varphi_{\mathrm{m}}}\right)$.

(b) $\mathcal{A}^{-1}\left(\boldsymbol{x}_1;\widetilde{\beta},\widetilde{\varphi_{\mathrm{m}}}\right)$.

(c) Final result $\mathcal{A}^{-1}\left(\boldsymbol{x}_{\mathrm{final}};\widetilde{\beta},\widetilde{\varphi_{\mathrm{m}}}\right)$.

(d) Relative change of $\boldsymbol{x}_i$.

Figure 7.3.12.: Intermediate and final result of the APSF algorithm in the scene domain for the case of $\boldsymbol{y}_{\mathrm{in}} = \boldsymbol{y}$, $\mathrm{SSF_c} = 0.5$, and $\mathrm{SSF_p} = 1$.

the impact of non redundant samples in case of missing pulses. Hence, cutting can be neglected as a preconditioning step of $\boldsymbol{y}_{\mathrm{in}}$ at all. The success of the separation therefore depends purely on the quality of the estimated parameters β and φ_{m}. In Fig. 7.3.12 and Fig. 7.3.13, the filter results without cutting are shown. As can be noticed, the signal to noise ratio (SNR) of the target is slightly higher. This is due to two facts, first of all as no pulses were cut, no target energy is lost. Secondly, the target is not smeared in angle dimension, a consequence of cutting. However, this is a leakage effect which in general always might happen. Another beneficial effect compared to the cut versions above is the less structured clutter floor. Especially close at the clutter ridge, structured clutter residuals emerge when cutting was conducted. These residuals might be reconstructed within the sparse matrix $\boldsymbol{S}$, increasing the false alarm rate.

An alternative approach compared to the alternating projection scheme is to incorporate the filtering step into the robust principal component analysis (RPCA) algorithm and use $\boldsymbol{y}_{\mathrm{in}} = \boldsymbol{y}$. Just like the sparsity ratio operator $\mathcal{Q}_{\kappa_{\mathrm{s}}}(\boldsymbol{S})$ defined in (5.2.8), the filter step can be introduced as an additional restriction of the sparse reconstruction $\boldsymbol{S}$. This approach would also allow to apply the matched subspace detector filter $\boldsymbol{w}_{\mathrm{msd}}$ for sub sampled reconstructions. However, this renders the RPCA separation problem to be incomplete in the sense that non redundant clutter samples which would be placed within $\boldsymbol{S}$ are not accounted for. Due to their non-low rank nature, the

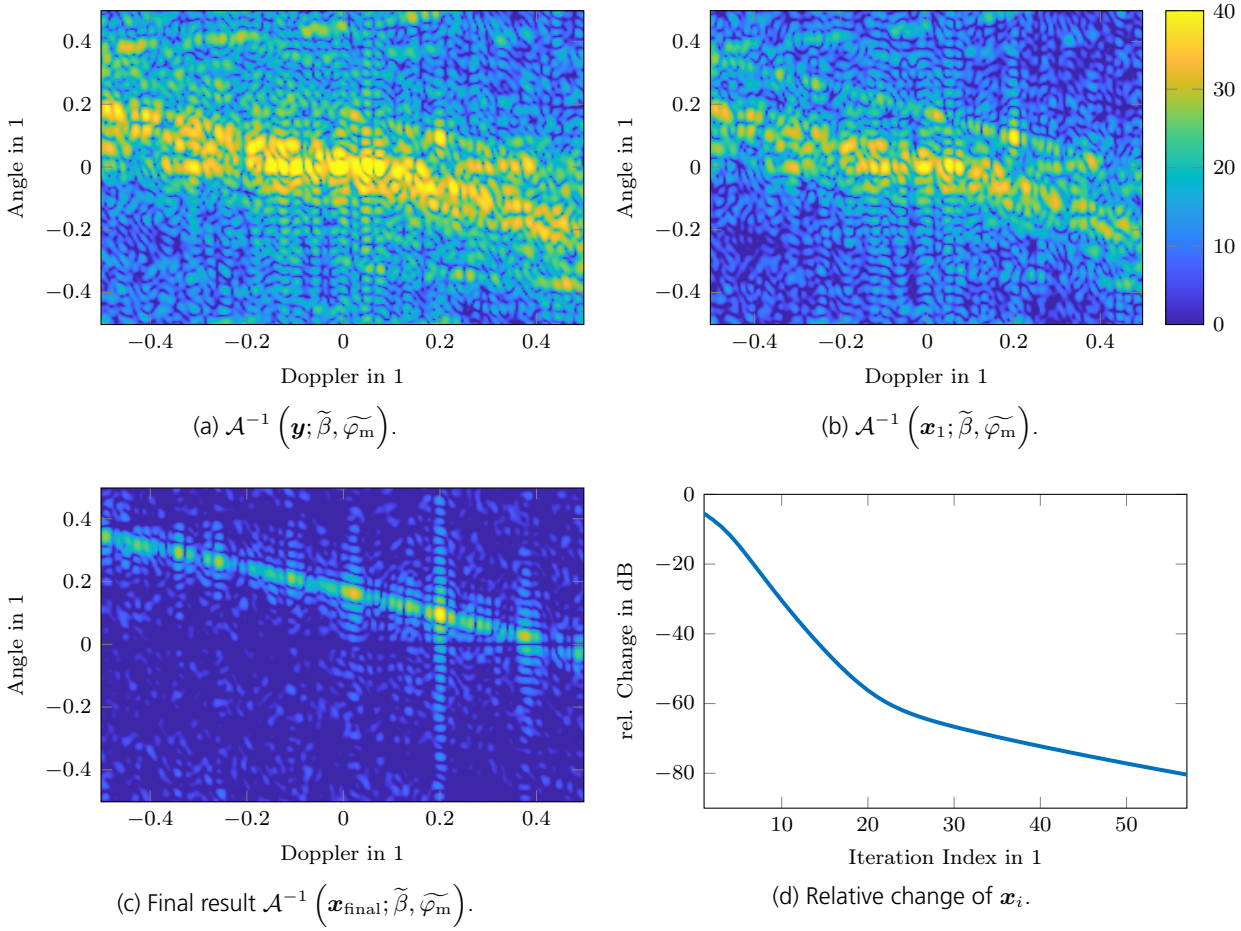

(a) $\mathcal{A}^{-1}\left(\boldsymbol{y};\widetilde{\beta},\widetilde{\varphi_{\mathrm{m}}}\right)$.

(b) $\mathcal{A}^{-1}\left(\boldsymbol{x}_1;\widetilde{\beta},\widetilde{\varphi_{\mathrm{m}}}\right)$.

(c) Final result $\mathcal{A}^{-1}\left(\boldsymbol{x}_{\mathrm{final}};\widetilde{\beta},\widetilde{\varphi_{\mathrm{m}}}\right)$.

(d) Relative change of $\boldsymbol{x}_i$.

Figure 7.3.13.: Intermediate and final result of the APSF algorithm in the scene domain for the case of $\boldsymbol{y}_{\mathrm{in}} = \boldsymbol{y}$, $\mathrm{SSF_c} = 1$, and $\mathrm{SSF_p} = 0.5$.

energy of these samples also will not be placed in the low rank reconstruction $\boldsymbol{L}$. Consequently, the residual error term h holds them. This renders to be a potential bias in the reconstruction scheme since the gradients depend on the residual term. In summary, the measurement and the separation model would not coincide, rendering the separation result questionable. Therefore, all separations shown in the following were conducted using the APSF algorithm to generate a preconditioned measurement vector $\boldsymbol{y}_{\mathrm{in}}$.

7.3.4. Statistical Evaluation

In this section, a statistical evaluation of the separation of moving targets from static clutter is presented. Since ICM is not covered by the approaches presented in this work, no statistical evaluation therefore was conducted therefore. In the following, the detection performance of the RPCA approach was evaluated. To do so, a sweep versus SNR was conducted for $N_{\mathrm{mc}} = 100$ Monte Carlo runs each with a fixed $\mathrm{CNR} = 60\,\mathrm{dB}$. In every run, the parameters $\widehat{\beta}$ and $\widehat{\varphi_{\mathrm{m}}}$ were at first estimated using the ACF algorithm presented in Section 7.2. Thereafter, the target clutter separation was conducted using the RPCA based separation approach presented before. As a preconditioning, the APSF algorithm given in Algorithm 7.2 was used in case of scenarios with missing channels or pulses. In case of $\mathrm{SSF_p} = \mathrm{SSF_c} = 1$, also the matched subspace detector filter was applied. The probability of detection p_{D} was thereafter determined by checking if a target is present within the sparse reconstruction $\widehat{\boldsymbol{S}}$ at the known target position. Dividing the number of detections by N_{mc} yields the estimate $\widehat{p_{\mathrm{D}}}$. To check that the determined $\widehat{p_{\mathrm{D}}}$ curve is not too severely biased from false detections[31], the signal was removed from the Monte Carlo realization and the detection test was repeated. If in this case a detection was still present, this was caused by clutter and noise energy only. This verification curve is termed false detection rate or $\widehat{p_{\mathrm{D}}}$ false in the following. The general false alarm rate p_{FA} was checked by conducting simulations without present targets and counting all detections within $\widehat{\boldsymbol{S}}$. Dividing this number of false detections by N_{mc} and the number of bins i. e. $N_{\mathrm{p}}N_{\mathrm{c}}$ yields the estimate $\widehat{p_{\mathrm{FA}}}$. However, the required amount of Monte Carlo (MC) runs to estimate p_{FA} reliably is extremely high! It is not computationally feasible and thus the results are not representative.[32] They are therefore not shown in this work and merely serve the purpose of checking for possible weaknesses of the preconditioning and the RPCA approach. For the sake of comparison, the preconditioning

[31] Detections caused from noise and clutter energy only, not from signal energy.

[32] The MC estimation procedure of determining p_{FA} is a scaled Bernoulli process i. e. the estimator is

$$\widehat{p_{\mathrm{FA}}} = \frac{\sum_i^{N_{\mathrm{mc}}N_{\mathrm{c}}N_{\mathrm{p}}} X_i}{N_{\mathrm{mc}}N_{\mathrm{c}}N_{\mathrm{p}}},$$

where X_i is a Bernoulli distributed random variable (RV) representing the detection of a target (detected or not detected). The estimator $\widehat{p_{\mathrm{FA}}}$ is therefore binomially distributed with standard deviation

$$\sigma(\widehat{p_{\mathrm{FA}}}) = \sqrt{\frac{\widehat{p_{\mathrm{FA}}}(1-\widehat{p_{\mathrm{FA}}})}{N_{\mathrm{mc}}N_{\mathrm{c}}N_{\mathrm{p}}}}.$$

The typical desired false alarm probability of space-time adaptive processing (STAP) detectors is 10^{-6}. If this level is to be estimated up to 1% accuracy, the required number of MC runs is $N_{\mathrm{mc}} \simeq 4.8 \cdot 10^6$. The corresponding 95% confidence interval is $10^{-6} \pm 1.96 \cdot 10^{-8}$ for which the Wald approximation was used. If every MC run requires $10\,\mathrm{sec}$ this would take $\sim 1\mathrm{1/2}$ years to complete.

The standard deviation of $p_{\mathrm{D}} = 0.9$ for $N_{\mathrm{mc}} = 100$ results to $\sigma(p_{\mathrm{D}})/p_{\mathrm{D}} = 3.\dot{3}\%$ with a 95% confidence interval of 0.9 ± 0.058.

and the separation approach was also conducted using the true parameters $\widetilde{\beta}$ and $\widetilde{\varphi_{\mathrm{m}}}$. This allows to determine the influence of the ACF algorithm on the separation results. The simulation results for p_{D} versus SNR are shown in Fig. 7.3.14, where the solid lines mark the results using the estimated parameter $\widehat{\beta}$ and $\widehat{\varphi_{\mathrm{m}}}$ and the dashed lines the results using the true parameter $\widetilde{\beta}$ and $\widetilde{\varphi_{\mathrm{m}}}$. Figure 7.3.14a illustrates the results in case of channel sub sampling but with all pulses available. As explained in Section 7.2, this setting allows for the parameters $\widehat{\beta}$ and $\widehat{\varphi_{\mathrm{m}}}$ to be well estimable. Consequently, the solid and dashed lines lie close together. The results in case of missing pulses but all channels available are shown in Fig. 7.3.14b. This setup aggravates the estimation of $\widehat{\beta}$ and $\widehat{\varphi_{\mathrm{m}}}$, consequently the detection performance using these is diminished compared to the ideal case using $\widetilde{\beta}$ and $\widetilde{\varphi_{\mathrm{m}}}$. This is also the reason $\mathrm{SSF_p} = 0.5$ is not shown in Fig. 7.3.14b as the estimation of $\widehat{\beta}$ and $\widehat{\varphi_{\mathrm{m}}}$ failed completely. As a benchmark, the p_{D} vs SNR curve corresponding to a matched filter (MF) detector is shown as well.[33] As was explained in Section 2.3.4, the MF detector assumes the true covariance matrix to be known which allows for optimal detection and thus represents the best possible detection performance. Comparing different detectors is usually done for a fixed p_{FA} and comparing their p_{D} versus SNR curves. Since the p_{FA} of the presented approach can not be determined reliably, the MF curve was fitted to the comparable case of $\mathrm{SSF_c} = \mathrm{SSF_p} = 1$. The corresponding threshold value of the MF detector is $12\,\mathrm{dB}$ which is equivalent to a $p_{\mathrm{FA}} \simeq 1.31 \cdot 10^{-7}$ [76]. The estimated probability of false alarm (PFA) of the RPCA approach, yet statistically not reliable, was found to be of the same order of magnitude. Although this statement would need to be verified by further simulations, this indicates that the presented approach achieves the best possible performance in the $\mathrm{SSF_c} = \mathrm{SSF_p} = 1$ case. The false detection rate is shown in Fig. 7.3.14c and Fig. 7.3.14d. As can be seen, false detections are practically nonexistent. The p_{D} curves are therefore merely not biased due to false detections. The result for the matched subspace detector filter is shown in Fig. 7.3.15, where only the case $\mathrm{SSF_p} = \mathrm{SSF_c} = 1$ is applicable. The performance is comparable to the projection filter shown above. Just as the case with the MF, the matched subspace detection filter and the projection filter can not be compared directly here. From the plot it seems, that the matched subspace detection filter shows slightly higher detection performance, however, the unreliably estimated PFA seemed to be a bit higher than that of the projection filter. Nevertheless, their performances are quite equivalent giving the projection filter a slight advantage in less required computation time. The separation performance with respect to the sub sampling factor - symbol: SSFs (SSFs) is shown in Fig. 7.3.16. The performance depends mainly on the quality of the estimated parameters $\widehat{\beta}$ and $\widehat{\varphi_{\mathrm{m}}}$ as can be seen by comparing the corresponding results in Fig. 7.3.16a and Fig. 7.3.16c to those where the true parameters were used in Fig. 7.3.16b and Fig. 7.3.16d. In case of less used pulses, the estimated parameters deviate such that the subspace projection filter used in the preconditioning step can not sufficiently cancel the clutter

[33] generalized likelihood ratio test (GLRT) and adaptive matched filter (AMF) benchmarks are not shown for two reason. At first, the corresponding p_{D} equations contain factorials of the product $N_{\mathrm{p}}N_{\mathrm{c}}$, which in this work was chosen to be 2048 [24, 75]. However, the maximum computable factorial using the commonly available IEEE-754 float double precision format is $170! \simeq 7.3 \cdot 10^{306}$. Therefore, the corresponding p_{D} curves can not be computed without significant effort. Furthermore, the GLRT and AMF detectors suffer an SNR loss due to the required estimation of the unknown covariance matrix and the estimation of a constant false alarm rate (CFAR) threshold. This loss depends on the the number of training data range gates. Commonly, the number of training gates has to be two to five times the number of $N_{\mathrm{p}}N_{\mathrm{c}}$. The minimal required number of training gates for the scenario depicted in this work is far beyond any practical meaning. Hence a comparison to these detectors renders to be of no use.

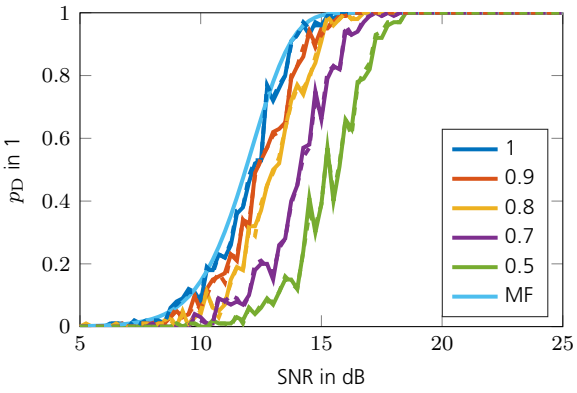

(a) p_D vs. SNR and SSF_c for $SSF_p = 1$.

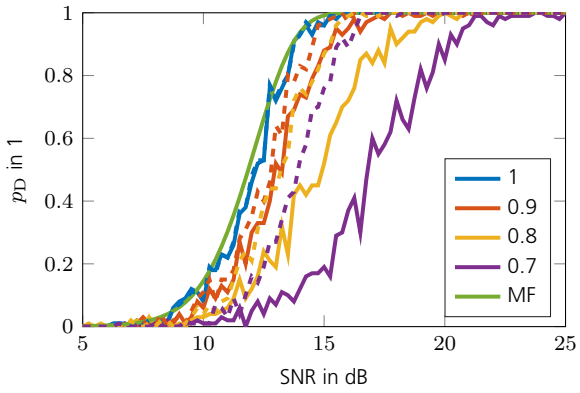

(b) p_D vs. SNR and SSF_p for $SSF_c = 1$.

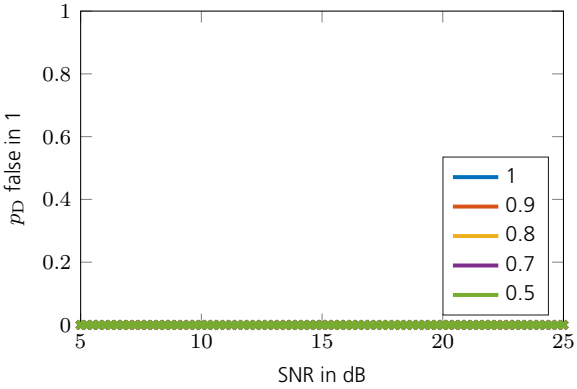

(c) False detection rate vs. SSF_c and SNR for $SSF_p = 1$.

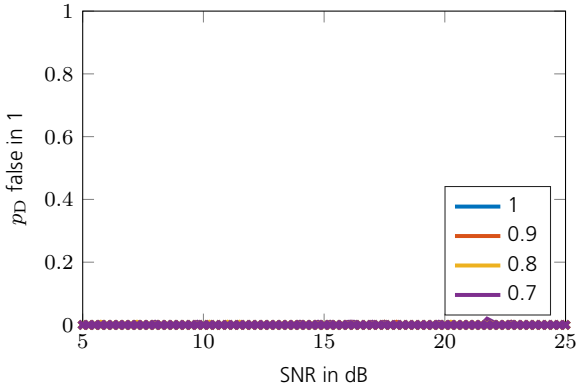

(d) False detection rate vs. SSF_p and SNR for $SSF_c = 1$.

Figure 7.3.14.: Separation results using APSF for preconditioning. Solid lines mark results using the estimated parameters $\widehat{\beta}$ and $\widehat{\varphi_m}$ and dashed lines using true parameters $\widetilde{\beta}$ and $\widetilde{\varphi_m}$.

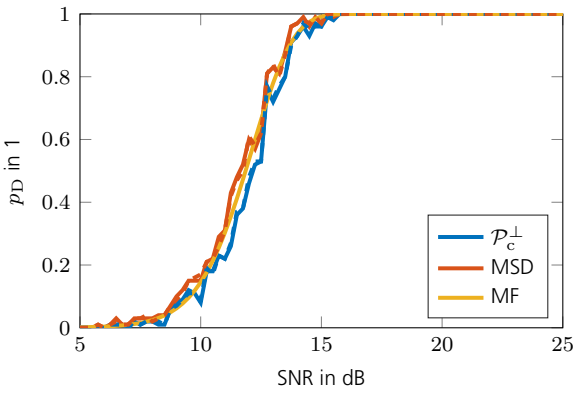

(a) p_D vs. SNR.

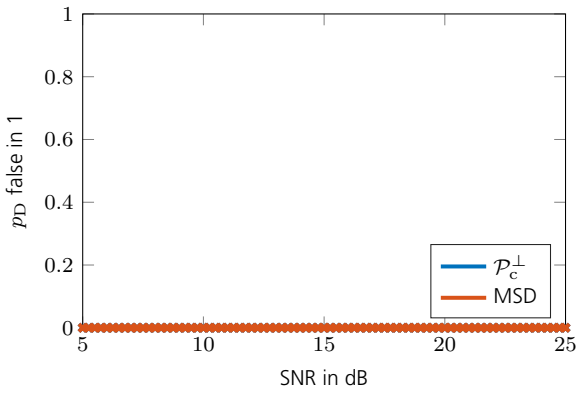

(b) False detection rate vs. SNR.

Figure 7.3.15.: Separation results using the matched subspace detection filter $\boldsymbol{w}_{msd}$ from 7.3.6 for preconditioning. Solid lines mark results using the estimated parameters $\widehat{\beta}$ and $\widehat{\varphi_m}$ and dashed lines using true parameters $\widetilde{\beta}$ and $\widetilde{\varphi_m}$. Sub sampling is not applicable, hence $SSF_c = SSF_p = 1$.

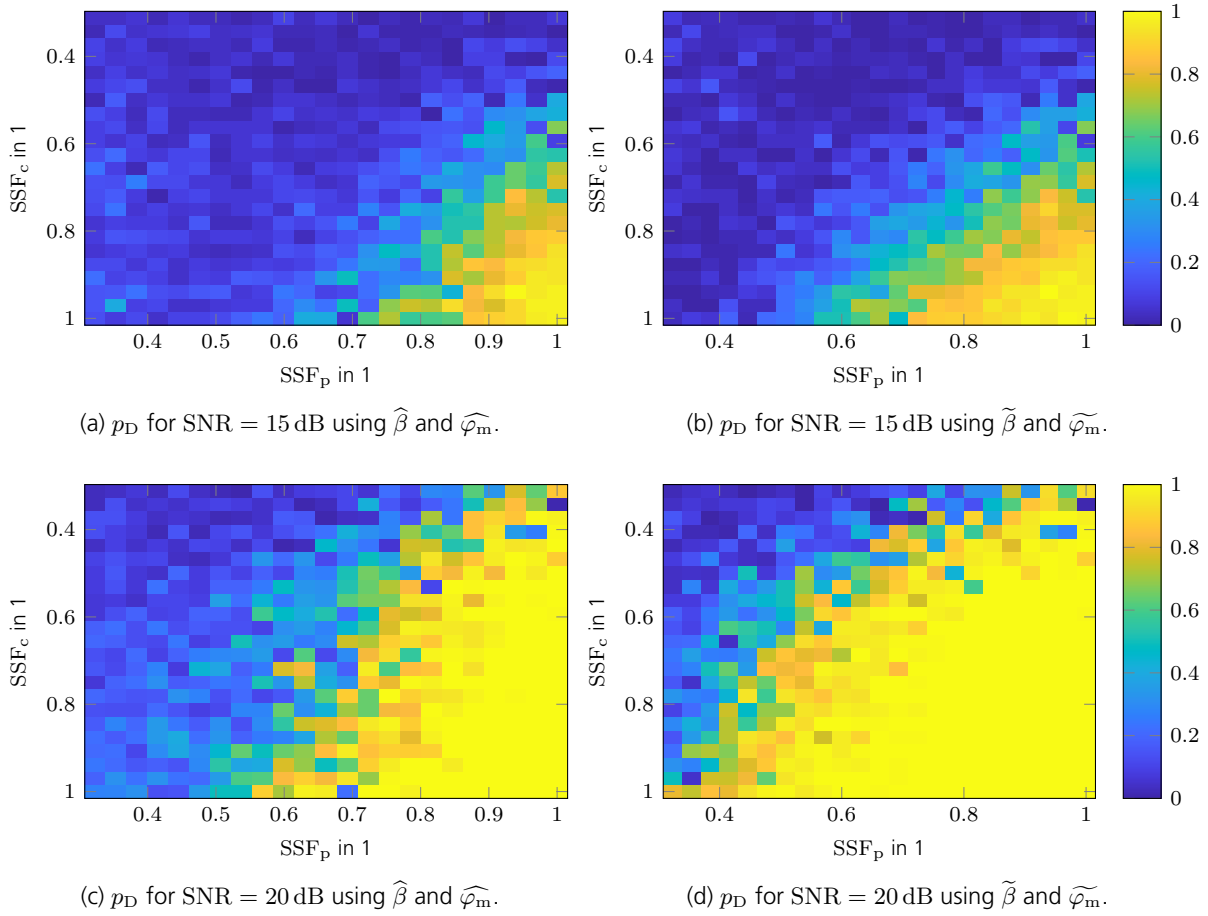

(a) p_D for SNR $= 15\,\mathrm{dB}$ using $\widehat{\beta}$ and $\widehat{\varphi_m}$.

(b) p_D for SNR $= 15\,\mathrm{dB}$ using $\widetilde{\beta}$ and $\widetilde{\varphi_m}$.

(c) p_D for SNR $= 20\,\mathrm{dB}$ using $\widehat{\beta}$ and $\widehat{\varphi_m}$.

(d) p_D for SNR $= 20\,\mathrm{dB}$ using $\widetilde{\beta}$ and $\widetilde{\varphi_m}$.

Figure 7.3.16.: Separation results vs. SSFs using APSF for preconditioning.

or the clutter spikiness. It therefore seems a viable goal to improve the estimation performance in a future work.

7.3.5. Summary

In this section, the separation of moving targets from static clutter using CRPCA was presented. The sensing operator used for separation is the same used for the ACF algorithm which focuses the clutter ridge onto $\bar{u} = 0$. In order to obtain a low rank matrix for static clutter contributions, a preconditioning of the measurement signal is required. If this step would be omitted, diagonal entries within $\widehat{\boldsymbol{S}}$ would emerge from non redundant clutter samples. A detailed explanation of this fact was given in Section 7.1. Various preconditioning approaches were tested, namely the cutting of the measurement matrix $\boldsymbol{Y}$ as was done for the ACF algorithm, a subspace projection filter and a matched subspace detection filter. The approach of cutting non redundant samples alone is sub optimal as it leaves the resulting low rank matrix to be of spiky nature. This contradicts the prerequisites of the CRPCA approach, which requires non-spiky entries within the low rank matrix in order to allow for a diffuse separation. As a consequence, many clutter residual entries may remain in $\widehat{\boldsymbol{S}}$. Nonetheless, cutting may be combined with the latter two approaches for increased robustness of the CRPCA based separation against badly estimated parameters $\widehat{\beta}$ and $\widehat{\varphi_m}$. This, however, is only applicable in case of no sub sampling. The subspace projection filter

and the matched subspace detector filter suppress all clutter contributions completely in case the parameters $\widehat{\beta}$ and $\widehat{\varphi_{\mathrm{m}}}$ were estimated well enough. In this case, the low rank matrix renders to be empty with moving targets located in the sparse matrix only. If the parameters were estimated badly, clutter residuals occur which, however, are of less spiky nature as the filters suppress a big part of the clutter ridge energy. Clutter residuals are therefore more likely reconstructed within the low rank matrix $\widehat{\boldsymbol{L}}$ enhancing the robustness of the CRPCA separation approach. In case of well estimated parameters, the presented filters are also capable of suppressing excessively strong clutter contributions due to the orthogonal projection approach. The common problem in setting up projection filters of choosing the clutter subspace size is circumvented due to the absence of noise in the covariance matrix model (7.3.4). The size of the clutter subspace therefore can be determined by counting all eigenvalues of the clutter covariance matrix $\boldsymbol{R}_{\mathrm{c}}$ greater than a numerical noise threshold. Both filters yield similar detection performance. The preconditioning approaches of cutting and the matched subspace detection filter do not allow for any spatial or temporal sub sampling. The subspace projection filter, however, can be extended to the APSF algorithm which successfully suppresses clutter contributions within a sub sampled measurement vector. The presented filter schemes are applicable for static clutter only as they do not include ICM effects. Extending the model filters to include these is subject to future work.

Finally, the probability of detection p_{D} and the false alarm probability p_{FA} were evaluated for the subspace projection filter and the matched subspace detection filter preconditioning approaches. In general, the detection performance mainly depends on the preconditioning step and less on the CRPCA settings. In case the parameters $\widehat{\beta}$ and $\widehat{\varphi_{\mathrm{m}}}$ can be estimated good enough, the clutter can be well suppressed which naturally yields a high detection performance. The ACF algorithm presented in this work estimates the required parameters well in case of missing channels, yet is susceptible for missing pulses. This is reflected in the detection performance. How to improve the estimation performance further is an interesting research question, however, is beyond the scope of this work. Furthermore, p_{D} decreases the less pulses and channels are used, also in case of a perfect preconditioning. This a quite natural behavior of compressive sensing algorithms. The performance may be enhanced by improving the restricted isometry property (RIP) and restricted rank isometry property (RRIP) properties of the sensing operator $\mathcal{A}$ e. g. by adapting the radar transmit signal. The reader may refer to [68]. The false alarm probability p_{FA} was evaluated briefly and also depends heavily on the quality of the estimated parameters. Although the numerical simulations regarding the PFA are not statistically reliable (due to the extremely high amount of required MC runs), the performance in terms of p_{D} and p_{FA} are comparable to a MF detector and as such achieve near optimal detection performance.

8. Conclusion

Although extensive research was conducted in the recent decades to mitigate the shortcomings of space-time adaptive processing (STAP), no attempt was made so far to evade its fundamental problem: the need for training data. In this work, initial approaches to do so are presented using low-rank and compressed sensing methods.

Within the realm of ground moving target indication (GMTI), space-time adaptive processing is the state-of-the-art algorithm to detect moving targets. A basic part of STAP is its adaptive nature i. e. an optimal filter to suppress clutter contributions is formed by using measured training data taken from the very same radar scene. In order for this to work, several prerequisites are necessary:

- sufficient, independently sampled training data is available
- all training data shares the same clutter structure as the cell under test (CUT)
- no training data contains any moving target signals contributions.

If all of the listed points can be met, STAP is an ideal method to use. It does not require any knowledge of the measurement process e. g. the radar velocity and orientation, array configuration, pulse repetition frequency (PRF), antenna beam pattern etc. In its very essence, STAP composes a filter which cancels every signal contribution present in the training data. If the first two prerequisites are not met, clutter residuals will occur as the composed filter does not fit to the clutter structure of the CUT. A moving target present in the training data results in target masking as the composed filter is trained to also cancel such signal contributions. Extensive research was conducted to mitigate the prerequisites of STAP, however, training data remains to be still needed. Therefore, all aforementioned shortcomings are still present.

In this work, attempts to evade the need for training data and as such the shortcomings of STAP are presented. Rather than using training data, the measurement data of the CUT alone is used to obtain sufficient information in order to separate clutter from moving targets. This is accomplished by exploiting the correlated nature of the measurement process. As this is the first attempt to do so, an idealized measurement process and radar scene are assumed:

- perfectly calibrated uniform linear array (ULA) antenna array
- sufficient radar channels (32 channels used in this work)
- flat earth condition
- rough knowledge of radar velocity and orientation (e. g. through inertial measurement unit (IMU))

- no polar velocity misalignment i. e. $\vartheta_{\mathrm{m}} = \pi/2\,\mathrm{rad}$
- moving targets are of type Swerling 0 and only sparsely present

The methods presented in this work are based on low-rank and compressed sensing methods. Most standard methods from the literature, however, do not consider the practical needs of radar signal processing e. g. they suffer from restrictions to real numbers, slow convergence rate, low reconstruction performance, or knowledge of unknown parameters like the precise number of sparse entries or the exact rank of a low-rank matrix. The first contributions of this work to radar signal processing was to combine and extend compressive sensing (CS) and affine rank minimization (ARM) algorithms to comprise a set of high performance CS, ARM, and compressed robust principal component analysis (CRPCA) algorithms as there are:

- turbo shrinkage-thresholding (TST)
- complex successive concave sparsity approximation (CSCSA)
- turbo singular value thresholding (TSVT)
- complex smoothed rank approximation (CSRA)
- turbo compressed robust principal component analysis (TCRPCA).

These algorithms avoid the aforementioned shortcomings and show state-of-the-art reconstruction performance as was shown by use of phase transition plots. They furthermore offer very high convergence rates next to low computational complexity due to the use of closed form solutions of subsequent optimization problems. The only parameter required to know is the noise power P_{n}, which is commonly known in radar applications. In case of very big low rank matrices to reconstruct, the required singular value decomposition (SVD) computation step might be a bottleneck in terms of computational complexity. To circumvent this problem, an alternative algorithm called bi-factored gradient descent (BFGD) may be used. It avoids the usage of SVDs, however, requires an initial solution somewhat close to the final solution. A contribution to the BFGD algorithm presented in this work is the derivation of an optimal step size formula which improves the convergence speed.

The partitioning of the radar signals into stationary and moving targets is done in three steps:

1. focusing of the clutter ridge and estimation of the parameters β and φ_{m} i. e. the clutter ridge slope and the velocity misalignment angle
2. preconditioning of the measurement signal $\boldsymbol{y}$ using β and φ_{m}
3. separation of preconditioned and focused radar scene into stationary and moving targets.

Therefore, the following contributions to radar signal processing were developed:

- auto-clutter focus (ACF) algorithm
- a model based projection filter
- alternating projection sub sample filtering (APSF) algorithm

- an CRPCA based separation model.

The key idea to separate moving targets from stationary clutter from CUT measurement data only is to exploit the correlated nature of the clutter signals to form a low rank matrix. In the radar scene, i. e. in the angle-Doppler domain, this is accomplished by focusing the clutter ridge onto $\bar{u} = 0$ or $\bar{f}_{\mathrm{D}} = 0$, where in this work the focusing on $\bar{u} = 0$ is used. For the focusing operation cyclic sub sample shifts in the $\bar{u}$ dimension of the radar scene are used. The shift amount $\triangle\bar{u}$ depends on the parameters β and φ_{m}. The ACF algorithm now estimates these parameters using a low rank and an energy objective function i. e. for correctly chosen parameters, the focused clutter scene has minimal rank with the clutter ridge being focused onto $\bar{u} = 0$ (except for aliased clutter signals). This approach is to some extend robust against targets present in the CUT. As long as $\mathrm{SNR} \lesssim \mathrm{CNR}$, the ACF algorithm is successful. In case of low Doppler leakage also stronger targets are not of concern. Moving targets which appear as sparse entries in the radar scene remain sparse by the clutter focus operation. Hence, the radar scene after focusing is the sum of a low rank and a sparse matrix $\boldsymbol{L} + \boldsymbol{S}$. This superposition is separated into $\boldsymbol{S}$ and $\boldsymbol{L}$ by use of an CRPCA approach. However, before being able to do so a preconditioning step is necessary. For a successful separation using the CRPCA approach the so called rank-sparsity incoherence condition must be fulfilled. Among other things this means that the low rank matrix $\boldsymbol{L}$ must not contain spiky entries unlike the clutter ridge itself. While it is easily possible to exclude the clutter ridge at $\bar{u} = 0$ from being reconstructed within $\boldsymbol{S}$, this is not possible for aliased clutter signals or strong clutter leakage. Therefore, the previously estimated parameters β and φ_{m} are used to setup a model based projection filter to suppress clutter contributions. In case of missing pulses or channels, the preconditioning is accomplished by the APSF algorithm. In the best case i. e. if the parameters β and φ_{m} were estimated good enough, the projection filter cancels all clutter contributions within the preconditioning step, rendering the final low rank matrix to be empty. In case the parameters are erroneous, clutter residuals occur. Nevertheless, the preconditioning step reduces the spikiness of the clutter residuals allowing the CRPCA approach to reconstruct these residuals within the low rank matrix $\boldsymbol{L}$ as desired. The approach and techniques presented in this work a capable of handling static clutter only. As such, effects like internal clutter motion (ICM) are not covered and are subject to future research. The presented approach was extensively evaluated in terms of parameter estimation performance and probability of detection p_{D} by use of Monte Carlo simulations for various sub sampling factor - symbol: SSFs (SSFs). Due to the excessive amount of Monte Carlo runs needed to adequately estimated the false alarm probability, p_{FA} was not evaluated. The overall success in case of missing pulses or channels heavily depends on the sensing operator $\mathcal{A}$. Especially the position of the missing pulses or channels determine the separation quality. Unfortunately, selecting optimal pulse and channel positions is an NP-hard problem. Within this work, 300 combinations of various pulse and channel locations were evaluated for every SSF in order to avoid obvious sub optimal arrangements. Other common approaches like adjusting the transmit signal to improve the sensing operator $\mathcal{A}$ are not considered in this work. The separation approach presented in this work works well in case of missing channels, yet is susceptible for missing pulses. This is a consequence of the choice to focus the clutter ridge onto $\bar{u} = 0$ and might be improved by additionally focusing the clutter ridge onto $\bar{f}_{\mathrm{D}} = 0$ followed by a subsequent fusion of the results. The probability of detection was deter-

mined for a detection threshold of $10\,\mathrm{dB}$ and compared to the standard adaptive matched filter (AMF) detector. In case of no missing pulses or channels, the detection performances coincide. In case of missing samples, the detection performance diminishes slightly. Successful detections are currently possible for $\mathrm{SSF_p} \geq 0.5$ and $\mathrm{SSF_p} \geq 0.7$ in case of $\mathrm{SNR} = 20\,\mathrm{dB}$. It mainly depends on the parameter estimation quality. An interesting future research topic would be how to further improve the parameter estimation. The false alarm probability was not fully evaluated, however, heuristically comparable with the false alarm rate of a corresponding matched filter. A subsequent validation of the detections e. g. by use of trackers seems mandatory.

In summary, the presented approach is capable of separating static from moving targets by use of CUT measurements only. As this is a complete new approach of solving the GMTI problem, there are many further interesting research questions e. g.:

- extension of ACF algorithm to incorporate polar velocity misalignment errors ϑ_m and non-flat earth condition
- further robustification of ACF algorithm against very strong targets present in the CUT
- setup a refined parameter estimation algorithm[1]
- extension of the projection filter to incorporate ICM
- effects of sub optimal antenna calibration
- experimental validation

Undoubtedly, the experimental validation of the presented approaches is of utmost interest. So far, this could not be realized due to the lack of GMTI systems having the required amount of channels available. One could obviously claim, that the high number of required channels is a severe practical drawback of the presented approach. Quite the contrary, the approaches presented in this work answer the question of what can be done better given so many channels are available. At the time writing this work, fully digital front ends become more and more common. The question is therefore not whether so many channels will ever be available but how best to use them when they are. The plain STAP approach does not benefit from an increased number of channels, rather it becomes more and more demanding in terms of required amount of training data. The presented approaches give a sophisticated answer of what can be done better. Nevertheless, much further research is required before practical use can be considered.

[1] A quit interesting approach would be to use the model projection filter $\mathcal{P}_\mathrm{c}^{\perp}(\beta, \varphi_\mathrm{m})$ to further estimate the parameters. The key idea would be to use the filtered signal energy $\left\|\mathcal{P}_\mathrm{c}^{\perp}(\beta, \varphi_\mathrm{m})\boldsymbol{y}\right\|_2^2$ as objective function i. e. for correctly selected parameters all of the clutter energy would be suppressed creating a suitable minima. However, there are two obvious challenges. At first, this approach is not invariant with respect to present targets. For wrongly chosen parameters, the projection filter may suppress a target. Strong present targets therefore create wrong local minima for the proposed objective function. This might be circumvented by using the ACF algorithm, which is invariant regarding present targets, to obtain a first estimate of β and φ_m. This initial estimate is then further refined using the projection filter. This approach evades wrong local minima given strong moving targets are not positioned too close to the clutter ridge. The second challenge is that a gradient descent approach is very demanding. The projection filter requires an eigenvalue decomposition of the model covariance matrix $\boldsymbol{R}_\mathrm{c}(\beta, \varphi_\mathrm{m}) = \boldsymbol{U}_\mathrm{c}\boldsymbol{\Lambda}_\mathrm{c}\boldsymbol{U}_\mathrm{c}^\mathrm{H}$, hence this results in the need to derive the eigenvectors with respect to the parameters. It is well known, that the derivative of eigenvectors is a tedious task as it is computable in a single iteration only if the corresponding eigenvalues are simple i. e. unique. This may not be fulfilled, e. g. in the simple case of $\beta = 1$ and $\varphi_\mathrm{m} = 0$ where only repetitive eigenvalues occur. Finally, the eigenvalue decomposition of the possibly big covariance matrix $\boldsymbol{R}_\mathrm{c}$ has a high computational complexity.

A. Mathematical Derivations

A.1. Wirtinger Derivatives

In this work, gradient descent approaches are used for minimizing real valued objective functions of complex arguments. A convenient way to calculate the required gradients are the Wirtinger derivatives

$$\begin{aligned}\frac{\partial}{\partial u} &= \frac{1}{2}\left(\frac{\partial}{\partial u_{\mathrm{re}}} - \mathrm{j}\frac{\partial}{\partial u_{\mathrm{im}}}\right)\\ \frac{\partial}{\partial u^*} &= \frac{1}{2}\left(\frac{\partial}{\partial u_{\mathrm{re}}} + \mathrm{j}\frac{\partial}{\partial u_{\mathrm{im}}}\right),\end{aligned}$$

where $u_{\mathrm{re}} = \mathrm{Re}\{u\}$ and $u_{\mathrm{im}} = \mathrm{Im}\{u\}$. Some useful properties are

$$\begin{aligned}\frac{\partial u}{\partial u^*} &= 0\\ \frac{\partial u^*}{\partial u} &= 0\\ \frac{\partial f^*}{\partial u^*} &= \left(\frac{\partial f}{\partial u}\right)^*\\ \frac{\partial f^*}{\partial u} &= \left(\frac{\partial f}{\partial u^*}\right)^*.\end{aligned}$$

Furthermore, the complex product and chain rules are required, which are

$$\begin{aligned}\frac{\partial fg}{\partial u} &= \frac{\partial f}{\partial u}g + f\frac{\partial g}{\partial u}\\ \frac{\partial fg}{\partial u^*} &= \frac{\partial f}{\partial u^*}g + f\frac{\partial g}{\partial u^*}\\ \frac{\partial h(g)}{\partial u} &= \frac{\partial h}{\partial g}\frac{\partial g}{\partial u} + \frac{\partial h}{\partial g^*}\frac{\partial g^*}{\partial u}.\\ \frac{\partial h(g)}{\partial u^*} &= \frac{\partial h}{\partial g}\frac{\partial g}{\partial u^*} + \frac{\partial h}{\partial g^*}\frac{\partial g^*}{\partial u^*}.\end{aligned}$$

A gradient indicating a descendant direction in the real and imaginary domain can be found as [77][1]

$$\nabla_{\boldsymbol{X}} f(\boldsymbol{X}) = \left(\frac{\partial f(\boldsymbol{X})}{\partial \boldsymbol{X}^*}\right)^{\mathrm{T}}.$$

[1] It is also possible to choose $\nabla_{\boldsymbol{X}} h(\boldsymbol{X}) = 2\left(\frac{\partial h(\boldsymbol{X})}{\partial \boldsymbol{X}}\right)^{\mathrm{T}}$ as a gradient, however, this is not the common form usually chosen in the literature.

Within this work, the derivative of a scalar function w. r. t. a vector $\boldsymbol{x} = [x_1, x_2, \ldots, x_N]^{\mathrm{T}} \in \mathbb{C}^N$ is defined as

$$\frac{\partial f(\boldsymbol{x})}{\partial \boldsymbol{x}} = \begin{bmatrix} \frac{\partial f(\boldsymbol{x})}{\partial x_1} & \frac{\partial f(\boldsymbol{x})}{\partial x_2} & \cdots & \frac{\partial f(\boldsymbol{x})}{\partial x_N} \end{bmatrix} \in \mathbb{C}^{1\times N}$$

and w. r. t. a matrix

$$\boldsymbol{X} = \begin{bmatrix} x_{11} & x_{12} & \cdots & x_{1M} \\ x_{21} & x_{22} & & \\ \vdots & & \ddots & \\ x_{N1} & & & x_{NM} \end{bmatrix} \in \mathbb{C}^{N\times M}$$

as

$$\frac{\partial f(\boldsymbol{X})}{\partial \boldsymbol{X}} = \begin{bmatrix} \frac{\partial f(\boldsymbol{x})}{\partial x_{11}} & \frac{\partial f(\boldsymbol{x})}{\partial x_{21}} & \cdots & \frac{\partial f(\boldsymbol{x})}{\partial x_{N1}} \\ \frac{\partial f(\boldsymbol{x})}{\partial x_{12}} & \frac{\partial f(\boldsymbol{x})}{\partial x_{22}} & & \\ \vdots & & \ddots & \\ \frac{\partial f(\boldsymbol{x})}{\partial x_{1M}} & & & \frac{\partial f(\boldsymbol{x})}{\partial x_{MN}} \end{bmatrix} \in \mathbb{C}^{M\times N}.$$

The derivative of a vector $\boldsymbol{y} = [y_1, y_2, \ldots, y_P]^{\mathrm{T}} \in \mathbb{C}^P$ w. r. t. to a vector $\boldsymbol{x} \in \mathbb{C}^N$ is defined as

$$\frac{\partial \boldsymbol{y}}{\partial \boldsymbol{x}} = \begin{bmatrix} \frac{\partial y_1}{\partial x_1} & \frac{\partial y_1}{\partial x_2} & \cdots & \frac{\partial y_1}{\partial x_N} \\ \frac{\partial y_2}{\partial x_1} & \frac{\partial y_2}{\partial x_2} & & \\ \vdots & & \ddots & \\ \frac{\partial y_P}{\partial x_1} & & & \frac{\partial y_P}{\partial x_N} \end{bmatrix} \in \mathbb{C}^{P\times N}.$$

The gradient of a scalar function w. r. t. a vector $\boldsymbol{x} \in \mathbb{C}^N$ is defined as[2]

$$\nabla_{\boldsymbol{x}} f(\boldsymbol{x}) = \left(\frac{\partial f(\boldsymbol{x})}{\partial \boldsymbol{x}^*}\right)^{\mathrm{T}} = \begin{bmatrix} \frac{\partial f(\boldsymbol{x})}{\partial x_1^*} \\ \frac{\partial f(\boldsymbol{x})}{\partial x_2^*} \\ \vdots \\ \frac{\partial f(\boldsymbol{x})}{\partial x_N^*} \end{bmatrix} \in \mathbb{C}^N$$

[2] As an example, the gradient of $\|\boldsymbol{x}\|_2^2$ therefore is

$$\nabla_{\boldsymbol{x}} \|\boldsymbol{x}\|_2^2 = \left(\frac{\partial \|\boldsymbol{x}\|_2^2}{\partial \boldsymbol{x}^*}\right)^{\mathrm{T}} = \left(\begin{bmatrix} \frac{\partial \|\boldsymbol{x}\|_2^2}{\partial x_1^*} & \frac{\partial \|\boldsymbol{x}\|_2^2}{\partial x_2^*} & \cdots & \frac{\partial \|\boldsymbol{x}\|_2^2}{\partial x_N^*} \end{bmatrix}\right)^{\mathrm{T}}$$
$$= \begin{bmatrix} \frac{\partial \sum_{i=1}^N x_i^* x_i}{\partial x_1^*} \\ \frac{\partial \sum_{i=1}^N x_i^* x_i}{\partial x_2^*} \\ \vdots \\ \frac{\partial \sum_{i=1}^N x_i^* x_i}{\partial x_N^*} \end{bmatrix} = \begin{bmatrix} x_1 \\ x_2 \\ \vdots \\ x_N \end{bmatrix} = \boldsymbol{x}.$$

and w. r. t. a matrix $\boldsymbol{X} \in \mathbb{C}^{N \times M}$ as

$$\nabla_{\boldsymbol{X}} f(\boldsymbol{X}) = \left(\frac{\partial f(\boldsymbol{X})}{\partial \boldsymbol{X}^*} \right)^{\mathrm{T}} = \begin{bmatrix} \frac{\partial f(\boldsymbol{x})}{\partial x_{11}^*} & \frac{\partial f(\boldsymbol{x})}{\partial x_{12}^*} & \cdots & \frac{\partial f(\boldsymbol{x})}{\partial x_{1M}^*} \\ \frac{\partial f(\boldsymbol{x})}{\partial x_{21}^*} & \frac{\partial f(\boldsymbol{x})}{\partial x_{22}^*} & & \\ \vdots & & \ddots & \\ \frac{\partial f(\boldsymbol{x})}{\partial x_{N1}^*} & & & \frac{\partial f(\boldsymbol{x})}{\partial x_{NM}^*} \end{bmatrix} \in \mathbb{C}^{N \times M}.$$

A.2. Fundamentals

In this section more fundamental derivatives are shown in more detail.

A.2.1. Antenna Gain and Reflection Coefficients

In this section the antenna gain coefficients $g_{\mathrm{tx}}(\vec{u}_x, \omega)$ and $g_{\mathrm{rx}}(\vec{u}_x, \omega)$ introduced in Section 2.1.1 are derived. Starting with the transmit (TX) case, the spherical wave emitted by a TX is

$$\vec{e}_{\mathrm{tx}}(\vec{x}, t, \omega) = \vec{i}_{\mathrm{tx}} \frac{a(\omega)\, g_{\mathrm{tx}}(\vec{u}_x, \omega)}{\|\vec{x}\|} \mathrm{e}^{\mathrm{j}(\omega t - k\|\vec{x}\|)}, \tag{A.2.1}$$

where $a(\omega) \in \mathbb{C}$ denotes the complex magnitude of the harmonic input signal of the TX antenna and $g_{\mathrm{tx}}(\vec{u}_x, \omega)$ an antenna gain coefficient translating the input harmonic signal into an electromagnetic (EM) field quantity. The antenna gain $G_{\mathrm{tx}}(\vec{u}_x, \omega)$ is defined as [5]

$$G_{\mathrm{tx}}(\vec{u}_x, \omega) = \varepsilon_{\mathrm{r}}(\omega)\, D(\vec{u}_x, \omega), \tag{A.2.2}$$

where $0 \leq \varepsilon_{\mathrm{r}}(\omega) \leq 1$ is the antenna efficiency parameter and

$$D(\vec{u}_x, \omega) = \frac{U(\vec{u}_x, \omega)}{U_{\mathrm{ave}}} = 4\pi \frac{U(\vec{u}_x, \omega)}{P_{\mathrm{w}}} \tag{A.2.3}$$

is the antenna directivity with P_{w} denoting the power of the emitted wave. Within (A.2.3)

$$U(\vec{u}_x, \omega) = \left\| \vec{S}(\vec{x}, \omega) \right\| \|\vec{x}\|^2 \tag{A.2.4}$$

denotes the radian intensity (which is independent of the total distance $\|\vec{x}\|$) with

$$\left\| \vec{S}(\vec{x}, \omega) \right\| = \frac{1}{2\eta_{\mathrm{w}}} \|\vec{e}_{\mathrm{tx}}(\vec{x}, t, \omega)\|^2 \tag{A.2.5}$$

denoting the magnitude of the pointing vector or the power density at point $\vec{x}$. Within (A.2.5), $\eta_{\mathrm{w}} = \sqrt{\mu_0/\varepsilon_0} \simeq 120\pi\,\Omega$ is the free space impedance which accounts for a transformation from the signal into an EM field quantity. Combining (A.2.1), (A.2.2), (A.2.3), (A.2.4), and (A.2.5) yields for the antenna gain

$$G_{\mathrm{tx}}(\vec{u}_x, \omega) = \frac{4\pi}{2\eta_{\mathrm{w}}} |g_{\mathrm{tx}}(\vec{u}_x, \omega)|^2, \tag{A.2.6}$$

where $P_{\mathrm{w}} = |a(\omega)|^2 \varepsilon_{\mathrm{r}}(\omega)$ was used.

The receive antenna gain coefficient $g_{\mathrm{rx}}\left(\vec{u}_x,\omega\right)$ translates an incoming EM wave into a signal quantity. It therefore can be derived in an analogous manner as $g_{\mathrm{tx}}\left(\vec{u}_x,\omega\right)$, however, it needs to be extended by an antenna cross section factor $\lambda^2/4\pi$. This can readily be found from the radar equation

$$P_{\mathrm{r}}\left(\omega\right)=\frac{P_{\mathrm{t}}\left(\omega\right)G_{\mathrm{tx}}\left(\vec{u}_{\mathrm{tx}},\omega\right)G_{\mathrm{rx}}\left(\vec{u}_{\mathrm{rx}},\omega\right)\sigma_{\mathrm{r}}}{\left(4\pi\right)^3 r_{\mathrm{tx}}^2 r_{\mathrm{rx}}^2}$$

from which

$$G_{\mathrm{rx}}\left(\vec{u}_x,\omega\right)=\frac{\left(4\pi\right)^2 2\eta_{\mathrm{w}}}{\lambda^2}\left|g_{\mathrm{rx}}\left(\vec{u}_x,\omega\right)\right|^2 \tag{A.2.7}$$

and

$$\sigma_{\mathrm{r}}=\left|\alpha_{\mathrm{r}}\right|^2$$

follows. Notice in (A.2.7) the factor $2\eta_{\mathrm{w}}$ which accounts for the transformation from an EM field into a signal quantity.

A.2.2. Target Induced Phase Modulation for Constant Velocity

A moving target induces a phase modulation of the transmit signal $s'_{\mathrm{tx}}\left(t'\right)$ namely

$$s_{\mathrm{t}}\left(t'\right)=\int_{-\infty}^{\infty}S'_{\mathrm{tx}}\left(\omega\right)\mathrm{e}^{-\mathrm{j}\omega\tau_{\mathrm{tx}}\left(t'\right)}\mathrm{e}^{-\mathrm{j}\omega t'}\mathrm{d}\omega, \tag{A.2.8}$$

where t' denotes the point in time where the center of the pulse hits the target, $S'_{\mathrm{tx}}\left(\omega\right)$ the Fourier transform of $s'_{\mathrm{tx}}\left(t'\right)$, and

$$\tau_{\mathrm{tx}}\left(t'\right)=\frac{r_{\mathrm{tx}}\left(t'\right)}{c_0} \tag{A.2.9}$$

is the travel time from the TX antenna to the point target. Due to the time dependence of the delay $\tau_{\mathrm{tx}}\left(t'\right)$, (A.2.8) can not be solved in a close form. One idea to achieve a closed form solution is to assume that (A.2.9) is somewhat constant during the time the pulse hits the target i. e.

$$\tau_{\mathrm{tx}}\left(t_{\mathrm{il}}\right)\simeq\tau_{\mathrm{txc}}$$

with the choice

$$\tau_{\mathrm{txc}}=\left.\frac{r_{\mathrm{tx}}\left(x\right)}{c_0}\right|_{x=t'}.$$

In this case (A.2.8) becomes

$$s_{\mathrm{t}}\left(t'\right)\simeq s'_{\mathrm{tx}}\left(t'-\tau_{\mathrm{txc}}\right). \tag{A.2.10}$$

The implications of this approximation can be measured by e. g. a cross correlation loss (CL) between (A.2.8) and (A.2.10) which seems reasonable as this corresponds to a subsequently applied pulse compression. A closed form solution can be obtained by assuming the point target moves at constant radial velocity v_{rt} during the illumination period T_{il}. In this case (A.2.9) can be written as

$$\tau_{\mathrm{tx}}\left(t_{\mathrm{il}}\right)=\tau_{\mathrm{txc}}+\left(t_{\mathrm{il}}-t'\right)\frac{v_{\mathrm{rt}}}{c_0}=\tau_{\mathrm{txc}}+\frac{\triangle t v_{\mathrm{rt}}}{c_0}$$

with $\triangle t \in \left[-\frac{T_{\mathrm{il}}}{2}, \frac{T_{\mathrm{il}}}{2}\right]$. The illumination time is given by 2.1.46 as

$$T_{\mathrm{il}} = T_{\mathrm{p}} \sqrt{\frac{c_0 + v_{\mathrm{rtx,max}}}{c_0 - v_{\mathrm{rtx,max}}}}$$

Using the correlation Fourier pair

$$\mathcal{F}\left\{\mathrm{corr}\left\{f_1, f_2\right\}(L)\right\} = \mathcal{F}\left\{f_1\right\}^* \mathcal{F}\left\{f_2\right\}$$

with $\mathcal{F}\left\{f_1\right\} = S'_{\mathrm{tx}}(\omega)\, \mathrm{e}^{-\mathrm{j}\omega\tau_{\mathrm{tx}}(t_{\mathrm{il}})}$, $\mathcal{F}\left\{f_2\right\} = S'_{\mathrm{tx}}(\omega)\, \mathrm{e}^{-\mathrm{j}\omega\tau_{\mathrm{txc}}}$, and L denoting the lag, the correlation is

$$\begin{aligned}\mathrm{corr}\left\{s_{\mathrm{t}}(t_{\mathrm{il}}), s'_{\mathrm{tx}}\left(t' - \tau_{\mathrm{txc}}\right)\right\}(L) &= \mathcal{F}^{-1}\left\{\left|S'_{\mathrm{tx}}(\omega)\right|^2 \mathrm{e}^{-\mathrm{j}\omega\frac{\triangle t v_{\mathrm{rt}}}{c_0}}\right\} \\ &= R_{s'_{\mathrm{tx}}s'_{\mathrm{tx}}}\left(L - \frac{\triangle t v_{\mathrm{rt}}}{c_0}\right), \end{aligned} \tag{A.2.11}$$

where $R_{s'_{\mathrm{tx}}s'_{\mathrm{tx}}}(x)$ denotes the auto correlation of s'_{tx}. The CL of (A.2.8) and (A.2.10) is determined at $L = 0$ and $\triangle t = \frac{T_{\mathrm{il}}}{2}$, hence

$$\mathrm{CL} = R_{s'_{\mathrm{tx}}s'_{\mathrm{tx}}}\left(\frac{T_{\mathrm{il}} v_{\mathrm{rt}}}{2c_0}\right). \tag{A.2.12}$$

In case of a chirp wave form, (A.2.12) becomes [78]

$$\mathrm{CL}_{\mathrm{chirp}} = \Lambda\left(\frac{v_{\mathrm{rt}}}{2c_0}\right) \mathrm{sinc}\left(\frac{b_{\mathrm{r}} T_{\mathrm{il}} v_{\mathrm{rt}}}{2c_0} \Lambda\left(\frac{v_{\mathrm{rt}}}{2c_0}\right)\right) \tag{A.2.13}$$

with

$$\Lambda(x) = \max\left(1 - |x|, 0\right).$$

A.2.3. Range Walk for Airborne Radar

The range walk in case of an airborne radar can be divided in two limiting scenarios. In the first case, the range walk is limited by the amount the radar is moving $\triangle r_{\mathrm{p}}$. This scenario is sketched in Fig. A.2.1 where $r(t)$ denotes the current slant range, $r(t_{\mathrm{cen}}) = r_{\mathrm{c}}$ the slant range at the point in time where the center of the antenna beam hits the target, and $r(t_{\mathrm{cls}}) = r_0$ is the closest slant range to the target. Furthermore, θ_{s} is the antenna squint angle. The range walk is defined as

$$\triangle r_{\mathrm{walk},1} = r(t) - r_{\mathrm{c}}, \tag{A.2.14}$$

where

$$r^2(t) = r_{\mathrm{c}}^2 + \triangle r_{\mathrm{p}}^2 - 2 r_{\mathrm{c}} \triangle r_{\mathrm{p}} \sin(\theta_{\mathrm{s}}) \tag{A.2.15}$$

with

$$\triangle r_{\mathrm{p}} = v_{\mathrm{p}}(t - t_{\mathrm{cen}}) = v_{\mathrm{p}} \triangle t \tag{A.2.16}$$

and

$$r_{\mathrm{c}} = \frac{r_0}{\cos(\theta_{\mathrm{s}})}. \tag{A.2.17}$$

Commonly of interest is the time span of a half coherent processing interval (CPI)

$$\triangle t = \frac{N_\mathrm{p} t_\mathrm{p}}{2}$$

to determine if targets can be considered non moving, or the maximal travel time

$$\triangle t = \frac{r_\mathrm{max}}{c_0}$$

to verify the stop-and-go approximation described in Section 2.1.3. Combining (A.2.14), (A.2.15), and (A.2.16) yields

$$\triangle r_{\mathrm{walk},1} = \sqrt{\frac{r_0^2}{\cos^2(\theta_\mathrm{s})} + v_\mathrm{p}^2 \triangle t^2 - 2 r_0 v_\mathrm{p} \triangle t \tan(\theta_\mathrm{s})} - \frac{r_0}{\cos(\theta_\mathrm{s})} \tag{A.2.18}$$

or in case no squint is applied

$$\triangle r_{\mathrm{walk},1} = \sqrt{r_0^2 + v_\mathrm{p}^2 \triangle t^2} - r_0.$$

In the second scenario, the range walk is limited by the visible area determined by the antenna beam width (ABW)

$$\triangle r_\mathrm{ABW} = r_0 \left(\tan\left(\theta_\mathrm{s} + \frac{\mathrm{ABW}}{2}\right) - \tan\left(\theta_\mathrm{s} - \frac{\mathrm{ABW}}{2}\right)\right).$$

This scenario is sketched in Fig. A.2.2, where

$$r_1 = \frac{r_0}{\cos\left(\theta_\mathrm{s} + \frac{\mathrm{ABW}}{2}\right)}$$
$$r_2 = \frac{r_0}{\cos\left(\theta_\mathrm{s} - \frac{\mathrm{ABW}}{2}\right)}$$

denote the leading and trailing edge of the visible area. The range walk, depending on the squint angle, therefore is

$$\triangle r_{\mathrm{walk},2} = \begin{cases} |r_1 - r_2| & \theta_\mathrm{s} \geq \frac{\mathrm{ABW}}{2} \\ \max(r_1, r_2) - r_0 & \text{else} \end{cases}. \tag{A.2.19}$$

Depending on whether the radar movement $\triangle r_\mathrm{p}$ or the visible area is smaller, the effective range walk is

$$\triangle r_\mathrm{walk} = \begin{cases} r_{\mathrm{walk},1} & \triangle r_\mathrm{p} < \triangle r_\mathrm{ABW} \\ r_{\mathrm{walk},2} & \text{else} \end{cases}. \tag{A.2.20}$$

A.2.4. Maximum Observable Radial Velocity in GMTI Scenario

The maximal radial velocity observable by the radar in the ground moving target indication (GMTI) case is of interest for validating common radar signal approximations as given in Section 2.1.3 or for the selection of a suitable pulse repetition frequency (PRF). It depends on the platform

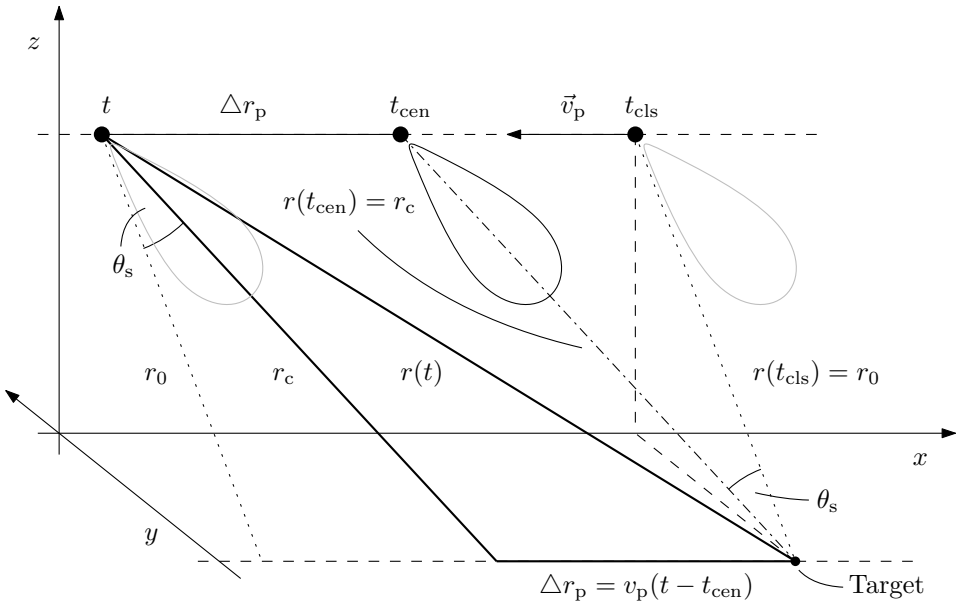

Figure A.2.1.: Range walk for non moving target in case of constant platform velocity v_p.

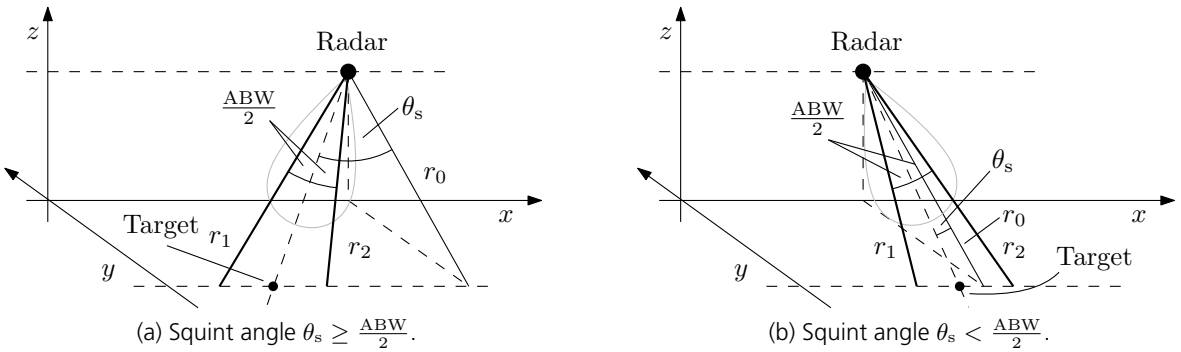

(a) Squint angle $\theta_\mathrm{s} \geq \frac{\mathrm{ABW}}{2}$.

(b) Squint angle $\theta_\mathrm{s} < \frac{\mathrm{ABW}}{2}$.

Figure A.2.2.: Range walk deduced from the ABW depending visible area.

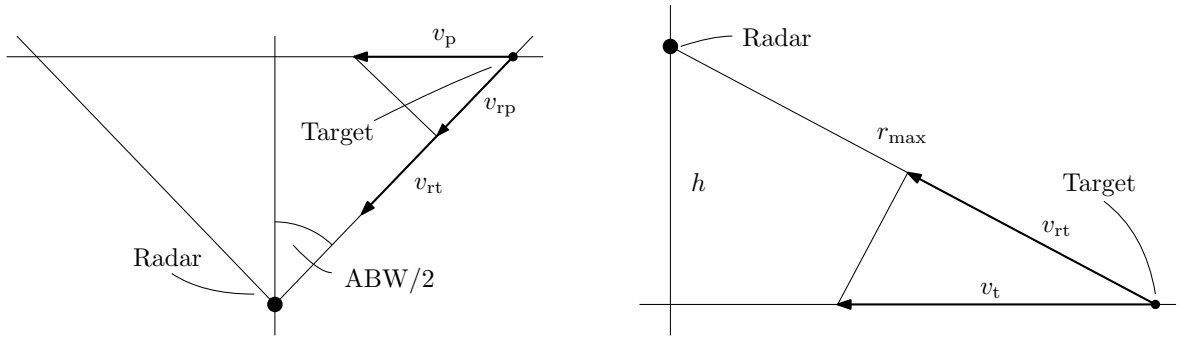

(a) Velocities in the plane spanned by the radar and $\vec{v}_\mathrm{p}$.

(b) Velocities in the plane spanned by the radar and $\vec{v}_\mathrm{p}$.

Figure A.2.3.: Worst case of observable radial velocity for broad side oriented antenna.

and target velocities v_p and v_t and is restricted by the antenna beam width, which limits the area the target is visible. In general is $v_\mathrm{r,max} = \langle \vec{u}_\mathrm{sl}, \vec{v}_\mathrm{t} - \vec{v}_\mathrm{p} \rangle$, where $\vec{u}_\mathrm{sl}$ points into the direction of the n-th considerable side lobe of the antenna pattern and $\vec{v}_\mathrm{t}$ and $\vec{v}_\mathrm{p}$ are to be taken to achieve the maximum possible $v_\mathrm{r,max}$ according to the measurement scenario. The worst case for a broadside directed antenna is depicted in Fig. A.2.3 with the target moving in radial direction, where Fig. A.2.3a depicts the superposition of radial velocity components from v_p and v_t and Fig. A.2.3b the observable radial velocity of a point target v_rt. The total radial velocity in this case is

$$\begin{aligned} v_\mathrm{r,tot} &= v_\mathrm{rt} + v_\mathrm{rp} \\ &= \sqrt{1 - \left(\frac{h_\mathrm{p}}{r_\mathrm{max}}\right)^2}\, v_\mathrm{t} + \sin\left(\frac{\mathrm{ABW}}{2}\right) v_\mathrm{p} \\ &\simeq v_\mathrm{t} + \frac{\mathrm{ABW} v_\mathrm{p}}{2}, \end{aligned} \tag{A.2.21}$$

where $\frac{\mathrm{ABW}}{2}$ was considered as visible angle and in the last line the assumption $h_\mathrm{p} \ll r_\mathrm{max}$ and $\sin\left(\frac{\mathrm{ABW}}{2}\right) \simeq \frac{\mathrm{ABW}}{2}$ were assumed.

A.3. Derivation of the Divergence of the Complex Thresholding Operator

In this section, the divergence of the complex thresholding operator is derived in closed form. The required Wirtinger derivatives are listed in Appendix A.1. The complex soft thresholding operator is defined as [79]

$$\mathcal{S}_\mathrm{S}^{(a)}(z) = \mathrm{sgn}(z) \max(0, |z| - a), \tag{A.3.1}$$

where $z \in \mathbb{C}$, $a \in \mathbb{R}_+$, and

$$\mathrm{sgn}(z) = \begin{cases} 0 & \text{if } z = 0 \\ \frac{z}{|z|} & \text{else} \end{cases}$$

is the complex sign function. A useful alternative formulation of the second term in (A.3.1) is

$$\max(0, |z| - a) = \begin{cases} 0 & \text{if } |z| \leq a \\ |z| - a & \text{if } |z| > a \end{cases}. \tag{A.3.2}$$

Furthermore, for some matrix $\boldsymbol{Z} \in \mathbb{C}^{N_1 \times N_2}$, the complex soft thresholding operator is defined as an element-wise operation as

$$\left[\mathcal{S}_{\mathrm{S}}^{(a)}(\boldsymbol{Z})\right]_{ij} = \mathcal{S}_{\mathrm{S}}^{(a)}(z_{ij}) \tag{A.3.3}$$

with $i = 1, 2, \ldots, N_1$ and $j = 1, 2, \ldots, N_2$. Finally, the definition of the divergence for a scalar complex function $f : \mathbb{C} \to \mathbb{C}$ is

$$\operatorname{div} f = 2 \operatorname{Re}\left(\frac{\partial f(z)}{\partial z}\right)$$

and for a multidimensional function $\boldsymbol{F} : \mathbb{C}^N \to \mathbb{C}^N$ [80]

$$\operatorname{div} \boldsymbol{F} = \sum_{i=1}^{N} 2 \operatorname{Re}\left(\frac{\partial F_i(\boldsymbol{Z})}{\partial z_i}\right). \tag{A.3.4}$$

Combining (A.3.3) and (A.3.4) yields the desired divergence

$$\operatorname{div}\left(\mathcal{S}_{\mathrm{S}}^{(a)}(\boldsymbol{Z})\right) = \sum_{i,j=1}^{N_1,N_2} 2 \operatorname{Re}\left(\frac{\partial\left[\mathcal{S}_{\mathrm{S}}^{(a)}(\boldsymbol{Z})\right]_{ij}}{\partial z_{ij}}\right). \tag{A.3.5}$$

Using (A.3.2), the required derivative is

$$\frac{\partial\left[\mathcal{S}_{\mathrm{S}}^{(a)}(\boldsymbol{Z})\right]_{ij}}{\partial z_{ij}} = \frac{\partial \mathcal{S}_{\mathrm{S}}^{(a)}(z_{ij})}{\partial z_{ij}} = \underbrace{\frac{\partial \operatorname{sgn}(z_{ij})}{\partial z_{ij}} \max(0, |z_{ij}| - a)}_{T_1} + \underbrace{\operatorname{sgn}(z) \frac{\partial \max(0, |z_{ij}| - a)}{\partial z_{ij}}}_{T_2}$$

with the derivative in T_1 being

$$\begin{aligned} \frac{\partial \operatorname{sgn}(z_{ij})}{\partial z_{ij}} &= \begin{cases} 0 & \text{if } z_{ij} = 0 \\ \frac{\partial \frac{z_{ij}}{|z_{ij}|}}{\partial z_{ij}} & \text{else} \end{cases} \\ &= \begin{cases} 0 & \text{if } z_{ij} = 0 \\ \frac{1}{2|z_{ij}|} & \text{else} \end{cases}, \end{aligned} \tag{A.3.6}$$

where

$$\begin{aligned}\frac{\partial \frac{z_{ij}}{|z_{ij}|}}{\partial z_{ij}} &= \frac{\frac{\partial z_{ij}}{\partial z_{ij}} |z_{ij}| - z_{ij} \frac{\partial |z_{ij}|}{\partial z_{ij}}}{|z_{ij}|^2} \\ &= \frac{|z_{ij}| - z_{ij} \frac{z_{ij}^*}{2|z_{ij}|}}{|z_{ij}|^2} \\ &= \frac{1}{2|z_{ij}|}\end{aligned}$$

and

$$\frac{\partial |z_{ij}|}{\partial z_{ij}} = \frac{\partial \left(z_{ij}^* z_{ij}\right)^{\frac{1}{2}}}{\partial z_{ij}} = \frac{z_{ij}^*}{2|z_{ij}|} \tag{A.3.7}$$

was used. Note, that the discontinuity at $z_{ij} = 0$ can be discarded since $\mathcal{S}_{\mathrm{S}}^{(a)}(z) = 0$ for $|z| < a$. Combining (A.3.2) and (A.3.6) yields

$$T_1 = \begin{cases} 0 & \text{if } |z_{ij}| \leq a \\ \frac{|z_{ij}| - a}{2|z_{ij}|} & \text{if } |z_{ij}| > a \end{cases}. \tag{A.3.8}$$

The required derivative in term T_2 is

$$\begin{aligned}\frac{\partial \max(0, |z_{ij}| - a)}{\partial z_{ij}} &= \begin{cases} 0 & \text{if } |z_{ij}| < a \\ \text{not differentiable} & \text{if } |z_{ij}| = a \\ \frac{z_{ij}^*}{2|z_{ij}|} & \text{if } |z_{ij}| > a. \end{cases} \\ &= \begin{cases} 0 & \text{if } |z| \leq a \\ \frac{z_{ij}^*}{2|z_{ij}|} & \text{if } |z| > a \end{cases},\end{aligned}$$

where the set $\{z : |z| = a\}$ has Lebesgue measure zero and can be discarded due to weak differentiability. As such

$$T_2 = \begin{cases} 0 & \text{if } |z_{ij}| \leq a \\ \frac{1}{2} & \text{if } |z_{ij}| > a \end{cases}, \tag{A.3.9}$$

where (A.3.7) was used again. Combining (A.3.5), (A.3.8), and (A.3.9) yields for the divergence

$$\operatorname{div}\left(\mathcal{S}_{\mathrm{S}}^{(a)}(\boldsymbol{Z})\right) = \sum_{i,j=1}^{N_1,N_2} \left(2 - \frac{a}{|z_{ij}|}\right) \mathbb{I}(|z_{ij}| > a),$$

where $\mathbb{I}(\cdot)$ denotes the indicator function.

A.4. Complex Successive Concave Sparsity Approximation

In this chapter, based on the successive concave sparsity approximation (SCSA) algorithm [58], we derive a new algorithm called complex successive concave sparsity approximation (CSCSA) for the

recovery of complex sparse vectors in the field of compressive sensing (CS). The following section covers the derivation of the CSCSA algorithm. In section A.4.2, we show some simulation results.

A.4.1. Derivative of the CSCSA Algorithm

The primary objective is to recover an unknown sparse vector $\boldsymbol{s} \in \mathbb{C}^{N_{\mathrm{sc}}}$, where the number of sparse entries $\kappa \ll N_{\mathrm{sc}}$, from a limited number of noisy observations of the form

$$\boldsymbol{y} = \boldsymbol{A}\boldsymbol{s} + \boldsymbol{n}, \tag{A.4.1}$$

where $\boldsymbol{A} \in \mathbb{C}^{M \times N_{\mathrm{sc}}}$ ($M < N_{\mathrm{sc}}$) is a known affine transformation, $\boldsymbol{y} \in \mathbb{C}^{M}$ is a measurement vector, and $\boldsymbol{n} \in \mathbb{C}^{M}$ is additive noise. To find a solution to this under-determined linear system, we seek the closest sparse solution which is consistent with the measurements via

$$\min_{\boldsymbol{s}} \|\boldsymbol{s}\|_0 \ \text{subject to}\ h(\boldsymbol{s}) \leq \epsilon^2, \tag{A.4.2}$$

where $\|\cdot\|_x$ denotes the ℓ_x norm,

$$h(\boldsymbol{s}) = \|\boldsymbol{A}\boldsymbol{s} - \boldsymbol{y}\|_2^2$$

is the residual error, and $\epsilon^2 \geq \|\boldsymbol{n}\|_2^2$ is some constant noise energy. Unfortunately problem (A.4.2) is NP-hard to solve. In order to make the recovery tractable we may approximate the quasi ℓ_0 norm by a suitable function. A very well known relaxation of A.4.2 is the basis pursuit denoise (BPDN) approach which is [39]

$$\min_{\boldsymbol{s}} \|\boldsymbol{s}\|_1 \ \text{subject to}\ h(\boldsymbol{s}) \leq \epsilon^2. \tag{A.4.3}$$

The ℓ_1 norm is known to be the tightest convex relaxation of the original CS problem (A.4.2). However, despite the convexity of the BPDN approach, there is a large gap between the sufficient conditions for the robust recovery of sparse vectors using (A.4.2) and (A.4.3)[3]. In order to narrow this gap while making the recovery tractable we may approximate the ℓ_0 norm by a smooth function.

The ℓ_0 norm of $\boldsymbol{s} = \begin{bmatrix} s_1 & \cdots & s_{N_{\mathrm{sc}}} \end{bmatrix}^{\mathrm{T}}$ is defined as the number of non zero elements in $\boldsymbol{s}$. Let

$$\delta(x) = \begin{cases} 1 & \text{if } x = 0 \\ 0 & \text{else} \end{cases} \tag{A.4.4}$$

be the Kronecker delta function, then we can define the ℓ_0 norm of $\boldsymbol{s}$ as

$$\|\boldsymbol{s}\|_0 = \sum_{i=1}^{N_{\mathrm{sc}}} \left[1 - \delta\left(|s_i|\right)\right], \tag{A.4.5}$$

[3] This means the problem at hand must be less difficult in terms measurement ratio M/N_{sc}, sparsity ratio κ/N_{sc}, restricted isometry property (RIP) condition etc. if solved by use of an ℓ_1 approach compared to an ℓ_0 approach. Hence, the reconstruction performance may be improved if an ℓ_0 solution is approximated.

where $|s_i|$ denotes the magnitude of s_i. To make (A.4.5) smooth we may approximation it by

$$1 - \delta(|s|) \approx 1 - \exp\left(-\frac{|s|}{\gamma}\right) = f_\gamma\left(|s|\right).$$

The function $f_\gamma\left(|s|\right)$ converges point wise to $1 - \delta\left(|s|\right)$ as

$$\lim_{\gamma \to 0^+} f_\gamma\left(|s|\right) = \begin{cases} 1 & \text{if } |s| = 0 \\ 0 & \text{else} \end{cases}.$$

Thus we can define

$$\|\boldsymbol{s}\|_0 \approx \sum_{i=1}^{N_{\text{sc}}} f_\gamma\left(|s_i|\right) = F_\gamma\left(|\boldsymbol{s}|\right), \tag{A.4.6}$$

where $|\boldsymbol{s}|$ denotes a vector which holds the magnitudes of the elements of $\boldsymbol{s}$. The optimization problem (A.4.2) may now be relaxed to

$$\min_{\boldsymbol{s}} F_\gamma\left(|\boldsymbol{s}|\right) \text{ subject to } h\left(\boldsymbol{s}\right) \leq \epsilon^2. \tag{A.4.7}$$

The constrained optimization problem (A.4.7) can be converted to an unconstrained one by use of regularization. This yields

$$\min_{\boldsymbol{s}} \lambda_\gamma F_\gamma\left(|\boldsymbol{s}|\right) + h\left(\boldsymbol{s}\right), \tag{A.4.8}$$

where λ_γ is a regularization parameter which may depend on γ. Program (A.4.7) is of the form

$$\min_{\boldsymbol{s}} \lambda \rho\left(\boldsymbol{s}\right) + h\left(\boldsymbol{s}\right), \tag{A.4.9}$$

where $h\left(\boldsymbol{s}\right)$ is convex and differentiable with Lipschitz continuous gradient and $\lambda > 0$ is some regularization parameter. In case of a least absolute shrinkage and selection operator (LASSO) or ℓ_1 approach $\rho\left(\boldsymbol{s}\right)$ is convex and non smooth. For the approach considered in (A.4.8) $\rho\left(\boldsymbol{s}\right)$ is concave, smooth but not differentiable at $\boldsymbol{s} = \boldsymbol{0}$. In both cases the iterative thresholding (IT) method can be utilized to conduct the desired minimization. For a fixed γ, a solution to program (A.4.8) can be obtained by iteratively solving

$$\boldsymbol{s}_{l+1} = \arg\min_{\boldsymbol{s}} \left\{ \left(\boldsymbol{s} - \boldsymbol{s}_l\right)^{\text{H}} \nabla h\left(\boldsymbol{s}_l\right) + \frac{1}{2\mu} \|\boldsymbol{s} - \boldsymbol{s}_l\|_2^2 + \lambda_\gamma F_\gamma\left(|\boldsymbol{s}|\right) \right\} \tag{A.4.10}$$

until convergence, where $\mu > 0$ is some step size. This program can be viewed as a proximal regularization of the linearized function $h\left(\boldsymbol{s}\right)$ [41].

Solution to Unconstrained Minimization Problem for a Fixed γ

Program (A.4.10) can be simplified to

$$\boldsymbol{s}_{l+1} = \arg\min_{\boldsymbol{s}} \left\{ \frac{1}{2\mu} \|\boldsymbol{s} - \left(\boldsymbol{s}_l - \mu \nabla h\left(\boldsymbol{s}_l\right)\right)\|_2^2 + \lambda_\gamma F_\gamma\left(|\boldsymbol{s}|\right) \right\} \tag{A.4.11}$$

ignoring constant terms unimportant regarding the minimization. For the special case of choosing $F_\gamma\left(|\boldsymbol{s}|\right)$ as done in (A.4.6), it is possible to derive a close form solution of (A.4.11). For a given $\boldsymbol{s}_l$

we can further simplify (A.4.11) to

$$\boldsymbol{s}_{l+1} = \arg\min_{\boldsymbol{s}} \left\{ \frac{1}{2\mu} \left\| \boldsymbol{s} - \boldsymbol{s}_{l0} \right\|_2^2 + \lambda_\gamma F_\gamma \left(|\boldsymbol{s}| \right) \right\}. \tag{A.4.12}$$

Noticing that $F_\gamma \left(|\boldsymbol{s}| \right)$ is a separable function the minimization in (A.4.12) can be conducted element wise and as such we only need to solve

$$s_{l+1,i} = \arg\min_{s} \underbrace{\left\{ \frac{1}{2\mu} \left| s - s_{l0,i} \right|^2 + \lambda_\gamma f_\gamma \left(|s| \right) \right\}}_{L\left(s, s_{l0,i}\right)}. \tag{A.4.13}$$

The scalar function $L(s, s_{l0,i})$ in (A.4.13) as such is not holomorphic[4], however, since we are only interested in minimizing $L(s, s_{l0,i})$ we utilize the Wirtinger derivatives listed in Appendix A.1 to calculate the root of the gradient

$$\nabla_s L \left(s, s_{l0,i} \right) = \frac{\partial L(s, s_{l0,i})}{\partial s^*}, \tag{A.4.14}$$

where $\cdot^*$ denotes complex conjugation. The derivative needed in (A.4.14) is

$$\frac{\partial L \left(s, s_{l0,i} \right)}{\partial s^*} = \frac{1}{2\mu} \underbrace{\frac{\partial \left| s - s_{l0,i} \right|^2}{\partial s^*}}_{T_1} + \lambda_\gamma \underbrace{\frac{\partial f_\gamma \left(|s| \right)}{\partial s^*}}_{T_2}, \tag{A.4.15}$$

where the term T_1 in (A.4.15) results to

$$\begin{aligned} T_1 = \frac{\partial \left| s - s_{l0,i} \right|^2}{\partial s^*} &= \frac{\partial \left(s - s_{l0,i} \right)^* \left(s - s_{l0,i} \right)}{\partial s^*} \\ &= \frac{\partial \left(s - s_{l0,i} \right)^*}{\partial s^*} \left(s - s_{l0,i} \right) + \left(s - s_{l0,i} \right)^* \frac{\partial \left(s - s_{l0,i} \right)}{\partial s^*} \\ &= s - s_{l0,i} \end{aligned} \tag{A.4.16}$$

[4] A holomorphic function is a complex-valued function which posses a unique derivative. For this to hold, the Cauchy-Riemann equations need to hold or equivalently, the Wirtinger derivative requires to be $\partial L(s, s_{l0,i}) / \partial s^* = 0$. This does not hold as shown in (A.4.14) until (A.4.18).

and term T_2 to

$$\begin{aligned} T_2 &= \frac{\partial f_\gamma(|s|)}{\partial s^*} = \frac{\partial\left(1-\exp\left(-\frac{|s|}{\gamma}\right)\right)}{\partial s^*} = -\frac{\partial \exp\left(-\frac{|s|}{\gamma}\right)}{\partial s^*} \\ &= -\left(\frac{\partial \exp(a)}{\partial a}\right)\left(-\frac{\partial \frac{|s|}{\gamma}}{\partial s^*}\right) - \underbrace{\left(\frac{\partial \exp(a)}{\partial a^*}\right)}_{a\in\mathbb{R}}\left(-\frac{\partial\left(\frac{|s|}{\gamma}\right)^*}{\partial s^*}\right) \\ &= -2\left(\frac{\partial \exp(a)}{\partial a}\right)\left(-\frac{1}{\gamma}\frac{\partial |s|}{\partial s^*}\right) \\ &= \frac{2}{\gamma}\exp\left(-\frac{|s|}{\gamma}\right)\left(\frac{\partial (s^*s)^{\frac{1}{2}}}{\partial s^*}\right) = \frac{2}{\gamma}\exp\left(-\frac{|s|}{\gamma}\right)\left(\frac{1}{2|s|}\frac{\partial s^* s}{\partial s^*}\right) \\ &= \frac{s}{\gamma|s|}\exp\left(-\frac{|s|}{\gamma}\right). \end{aligned} \tag{A.4.17}$$

Combining (A.4.14), (A.4.15), (A.4.16), and (A.4.17) yields

$$\nabla_s L(s, s_{l0,i}) = \frac{1}{2\mu}(s - s_{l0,i}) + \lambda_\gamma \frac{s}{\gamma|s|}\exp\left(-\frac{|s|}{\gamma}\right). \tag{A.4.18}$$

Setting (A.4.18) to zero yields

$$\frac{s - s_{l0,i}}{2\mu} = -\frac{\lambda_\gamma}{\gamma}\frac{s}{|s|}\exp\left(-\frac{|s|}{\gamma}\right). \tag{A.4.19}$$

Since $s \in \mathbb{C}$ we have to enforce equality of real and imaginary parts of (A.4.19) or its arguments and magnitudes. Considering the arguments in (A.4.19) we observe

$$\arg(s - s_{l0,i}) = \pm\pi + \arg(s) \tag{A.4.20}$$

or equivalently

$$\arg(s_{l0,i} - s) = \arg(s). \tag{A.4.21}$$

The structure of (A.4.19) given the insight from (A.4.20) and (A.4.21) is illustrated in Fig. A.4.1. From (A.4.20) we know that s and $s_{l0,i}$ must lie on a straight line passing through the origin. Furthermore, from (A.4.21) we know that $|s_{l0,i}| \leq |s|$. In summary we can observe that for an arbitrary $s_{l0,i}$,

$$s \in A = \{x \in \mathbb{C} | x = \beta s_{l0,i}, 0 \leq \beta \leq 1\}, \tag{A.4.22}$$

where $\beta \in \mathbb{R}$. From this we can conclude

$$\arg(s) = \arg(s_{l0,i}). \tag{A.4.23}$$

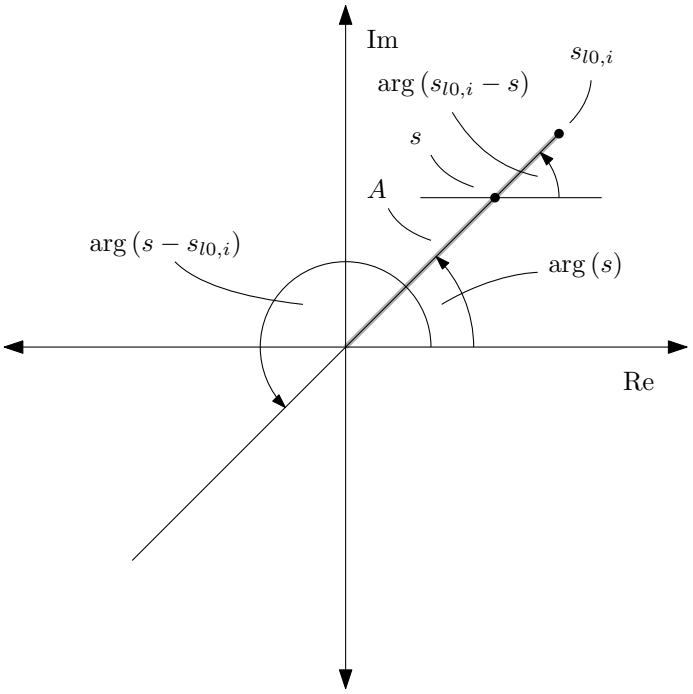

Figure A.4.1.: Structure of equation (A.4.19).

Using (A.4.23) we can simplify (A.4.19) to

$$\begin{aligned}\frac{|s|\,\mathrm{e}^{\mathrm{j}\arg(s_{l0,i})}-|s_{l0,i}|\,\mathrm{e}^{\mathrm{j}\arg(s_{l0,i})}}{2\mu} &= -\frac{\lambda_\gamma}{\gamma}\frac{|s|\,\mathrm{e}^{\mathrm{j}\arg(s_{l0,i})}}{|s|}\exp\left(-\frac{|s|}{\gamma}\right)\\ \Rightarrow \frac{|s|-|s_{l0,i}|}{2\mu} &= -\frac{\lambda_\gamma}{\gamma}\exp\left(-\frac{|s|}{\gamma}\right)\end{aligned} \tag{A.4.24}$$

In order to solve (A.4.24) we may use the multi-valued Lambert *W* function or product logarithm which is defined implicitly by

$$W(z)\mathrm{e}^{W(z)} = z, \tag{A.4.25}$$

where in general $z \in \mathbb{C}$ is possible, however, in this work it is sufficient to restrict $z \in \mathbb{R}$. In this real valued case, the Lambert *W* function is single valued for $z \geq 0$, double valued for $z \in [-1/\mathrm{e}, 0)$ and undefined for $z < -1/\mathrm{e}$. The two branches for $z \in [-1/\mathrm{e}, 0)$ are usually distinguished and denoted as

$$W_0(z) \geq -1 \tag{A.4.26}$$

$$W_{-1}(z) \leq -1. \tag{A.4.27}$$

To apply the Lambert *W* function we modify (A.4.24) by extending both sides with $2\mu/\gamma \exp(-|s_{l0,i}|/\gamma)$ to

$$\underbrace{\frac{|s|-|s_{l0,i}|}{\gamma}}_{W(z)}\exp\underbrace{\left(\frac{|s|-|s_{l0,i}|}{\gamma}\right)}_{W(z)} = \underbrace{-\frac{2\lambda_\gamma\mu}{\gamma^2}\exp\left(-\frac{|s_{l0,i}|}{\gamma}\right)}_{z}. \tag{A.4.28}$$

The Lambert *W* function as defined in (A.4.25) can readily be identified within (A.4.28) and as such the two solutions

$$|s_1| = \gamma W_0(z) + |s_{l0,i}| \tag{A.4.29}$$

$$|s_2| = \gamma W_{-1}(z) + |s_{l0,i}|, \tag{A.4.30}$$

can be found, where

$$z = -\frac{2\lambda_\gamma \mu}{\gamma^2} \exp\left(-\frac{|s_{l0,i}|}{\gamma}\right) \tag{A.4.31}$$

and $W_0(\cdot)$ denotes the upper branch and $W_{-1}(\cdot)$ the lower branch of the multi-valued Lambert *W* function. Combining (A.4.23), (A.4.29), and (A.4.30) yields the final solutions

$$s_1 = \gamma W_0(z)\, \mathrm{e}^{\mathrm{j}\arg\left(s_{l0,i}\right)} + s_{l0,i} \tag{A.4.32}$$

$$s_2 = \gamma W_{-1}(z)\, \mathrm{e}^{\mathrm{j}\arg\left(s_{l0,i}\right)} + s_{l0,i}. \tag{A.4.33}$$

Since we require only one solution we check whether (A.4.32) or (A.4.33) results in a lower $L(s, s_{l0,i})$ (if possible). Inserting (A.4.32) into $L(s, s_{l0,i})$ yields

$$\begin{aligned}
L(s_1, s_{l0,i}) &= \frac{1}{2\mu}|s_1 - s_{l0,i}|^2 + \lambda_\gamma f_\gamma(|s_1|) \\
&= \frac{1}{2\mu}\left|(\gamma W_0(z) + |s_{l0,i}|)\, \mathrm{e}^{\mathrm{j}\arg\left(s_{l0,i}\right)} - s_{l0,i}\right|^2 + \lambda_\gamma \left(1 - \mathrm{e}^{-\frac{\gamma W_0(z) + \left|s_{l0,i}\right|}{\gamma}}\right) \\
&= \frac{1}{2\mu}|\gamma W_0(z)|^2 + \lambda_\gamma - \lambda_\gamma \mathrm{e}^{-\frac{\gamma W_0(z) + \left|s_{l0,i}\right|}{\gamma}} \\
&= \lambda_\gamma + \frac{\gamma^2}{\mu}\left(\frac{1}{2}W_0^2(z) \underbrace{-\frac{\lambda_\gamma \mu}{\gamma^2}\mathrm{e}^{-\frac{\left|s_{l0,i}\right|}{\gamma}}}_{z/2} \mathrm{e}^{-W_0(z)}\right) \\
&= \lambda_\gamma + \frac{\gamma^2}{2\mu}\left(W_0^2(z) + W_0(z)\right),
\end{aligned} \tag{A.4.34}$$

where we used identity (A.4.25) in the last step. Similar steps yield

$$L(s_2, s_{l0,i}) = \lambda_\gamma + \frac{\gamma^2}{2\mu}\left(W_{-1}^2(z) + W_{-1}(z)\right). \tag{A.4.35}$$

Lemma A.1. *For any* $z \in [-1/\mathrm{e}, 0)$, $W_0^2(z) + W_0(z) \leq W_{-1}^2(z) + W_{-1}(z)$.

Proof. Beginning with $W_0(z)$, using $-1 \leq W_0(z) \leq 0$ from (A.4.26) yields

$$W_0^2(z) + W_0(z) = \underbrace{(W_0(z) + 1)}_{\geq 0}\underbrace{W_0(z)}_{\leq 0} \leq 0.$$

Similar steps for $W_{-1}(z)$ using $W_{-1}(z) \leq -1$ from (A.4.27) yield

$$W_{-1}^2(z) + W_{-1}(z) = \underbrace{(W_{-1}(z) + 1)}_{\leq 0}\underbrace{W_{-1}(z)}_{<0} \geq 0.$$

Combining both results completes the proof. Lemma A.1 tells us that s_2 from (A.4.33) can not be the minimizer of $L(s, s_{l0,i})$ from (A.4.13). □

Since for $z < -\frac{1}{\mathrm{e}}$, $W(z)$ is not defined, we should have

$$z \geq -\frac{1}{\mathrm{e}}$$
$$-\frac{2\lambda_\gamma \mu}{\gamma^2} \exp\left(-\frac{|s_{l0,i}|}{\gamma}\right) \geq -\frac{1}{\mathrm{e}}$$

or

$$|s_{l0,i}| \geq \gamma \left(1 + \ln\left(\frac{2\lambda_\gamma \mu}{\gamma^2}\right)\right). \tag{A.4.36}$$

If (A.4.36) is contradicted, no solution to (A.4.19) exists. In this case we can tell that $L\left(s, s_{l0,i}\right)$ from (A.4.13) is a strict monotonically increasing function in s and as such the minimizer of $L\left(s, s_{l0,i}\right)$ lies at $s = 0$ since from (A.4.22) we know $s = \beta s_{l0,i}$ for $\beta \in [0, 1]$.

As a remaining point we need to check for $L\left(s, s_{l0,i}\right)$ to be convex in order to ensure s_1 from (A.4.29) is a global minimum. To do so, we first use $\arg(s) = \arg\left(s_{l0,i}\right)$ from (A.4.23) and insert it into $L'\left(|s|, |s_{l0,i}|\right)$ which yields

$$\begin{aligned} L'\left(|s|, |s_{l0,i}|\right) &= \frac{1}{2\mu} \left| |s| \, \mathrm{e}^{\mathrm{j}\arg\left(s_{l0,i}\right)} - |s_{l0,i}| \, \mathrm{e}^{\mathrm{j}\arg\left(s_{l0,i}\right)} \right|^2 + \lambda_\gamma f_\gamma\left(|s|\right) \\ &= \frac{1}{2\mu} \left(|s| - |s_{l0,i}|\right)^2 + \lambda_\gamma f_\gamma\left(|s|\right). \end{aligned} \tag{A.4.37}$$

Now $L'\left(|s|, |s_{l0,i}|\right) : \mathbb{R} \to \mathbb{R}$ and thus it is easy to check its convexity by use of its second derivative

$$\frac{\partial^2 L'\left(|s|, |s_{l0,i}|\right)}{\partial |s|^2} = \frac{1}{\mu} - \frac{\lambda_\gamma}{\gamma^2} \mathrm{e}^{-\frac{|s|}{\gamma}} \geq 0. \tag{A.4.38}$$

From (A.4.38) we can conclude that if

$$\gamma^2 \geq \lambda_\gamma \mu, \tag{A.4.39}$$

$L'\left(|s|, |s_{l0,i}|\right)$ and thus $L\left(s, s_{l0,i}\right)$ is convex for any $s = \beta s_{l0,i}$, where $\beta \in [0, 1]$. If condition (A.4.39) is contradicted, s_1 from (A.4.32) is not necessarily the minimizer of $L'\left(|s|, |s_{l0,i}|\right)$. In this case the minimizer may also be at $s = 0$ which becomes clear if we sketch the curve of $L'\left(|s|, |s_{l0,i}|\right)$. Since $\nabla_s L\left(s, s_{l0,i}\right)$ from (A.4.18) posses two roots at s_1 and s_2 and further since

$$\lim_{s \to \infty} L'\left(|s|, |s_{l0,i}|\right) = \infty$$

we know that $L'\left(|s|, |s_{l0,i}|\right)$ has three or four extreme values. This is illustrated in Fig. A.4.2a. As can be seen, $|s_1|$is the minimum, whereas $|s_2|$ may be a maximum or a saddle point. All together we see that the minimizer of $L'\left(|s|, |s_{l0,i}|\right)$ is either at $s = s_1$ or $s = 0$. The possible additional case of s_1 and s_2 being saddle points is sketched in Fig. A.4.2b. In this case the minimizer is $s = 0$. It is hard to determine analytically if $s = s_1$ or $s = 0$ is the minimizer of $L\left(s, s_{l0,i}\right)$, however, it is easy to compare the cost function for both values to find it. In summary, the minimizer of $L\left(s, s_{l0,i}\right)$ and thus the solution to (A.4.13) can be defined as the one dimensional shrinkage

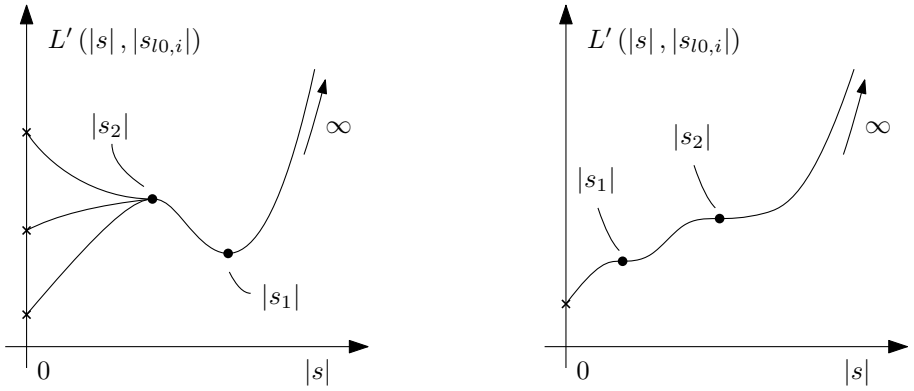

(a) Minimum at $|s_1|$and maximum or saddle point at $|s_2|$.

(b) Saddle point at $|s_1|$ and $|s_2|$.

Figure A.4.2.: Curve sketching of $L'(|s|, |s_{l0,i}|)$.

operator

$$\mathcal{T}_{\mu\lambda_\gamma}^{(\gamma)}(s_{l0,i}) = \begin{cases} 0 & |s_{l0,i}| < \gamma\left(1 + \ln\left(\frac{2\lambda_\gamma\mu}{\gamma^2}\right)\right) \\ 0 & L'(0, |s_{l0,i}|) < L'(|s_1|, |s_{l0,i}|), \\ s_1 & \text{otherwise} \end{cases} \tag{A.4.40}$$

where s_1 is defined as in (A.4.32) and $L'(\cdot, |s_{l0,i}|)$ is as defined in (A.4.37). Using this threshold operator, the solution to (A.4.8) can be acquired by iteratively updating

$$\boldsymbol{s}_{l+1} = \mathcal{T}_{\mu\lambda_\gamma}^{(\gamma)}(\boldsymbol{s}_l - \mu\nabla h(\boldsymbol{s}_l)). \tag{A.4.41}$$

Step Width and Convergence

In [58], the proof of convergence of (A.4.41) builds upon the Lipschitz continuity of $h(\boldsymbol{s})$ and some upper bound for $F_\gamma(|\boldsymbol{s}|)$. Here, we derive the required smallest Lipschitz constant M_L of $h(\boldsymbol{s})$ and the upper bound for $F_\gamma(|\boldsymbol{s}|)$ for the complex case and leave the rest of the proof to [58]. Since $h(\boldsymbol{s})$ is convex and of class C^2, we can determine the Lipschitz constant of $\nabla h(\boldsymbol{s})$ as

$$\nabla_{\boldsymbol{s}}^2 h(\boldsymbol{s}) \preceq M_\mathrm{L}\boldsymbol{I} \Leftrightarrow \left\|\nabla^2 h(\boldsymbol{s})\right\|_2 \leq M_\mathrm{L}, \tag{A.4.42}$$

where $\|\boldsymbol{Z}\|_2$ denotes the spectral norm of $\boldsymbol{Z}$ i.e. the largest singular value of $\boldsymbol{Z}$. The complex Hessian is defined as [81]

$$\nabla_{\boldsymbol{s}}^2 h(\boldsymbol{s}) = \frac{\partial^2 h(\boldsymbol{s})}{\partial \boldsymbol{s}^* \partial \boldsymbol{s}^\mathrm{T}} \tag{A.4.43}$$

and the required derivative for

$$h(\boldsymbol{s}) = \|\boldsymbol{A}\boldsymbol{s} - \boldsymbol{y}\|_2^2$$

results to

$$\begin{aligned}\frac{\partial h(\boldsymbol{s})}{\partial \boldsymbol{s}^*} &= \frac{\partial \|\boldsymbol{A}\boldsymbol{s}-\boldsymbol{y}\|_2^2}{\partial \boldsymbol{s}^*} = \frac{(\boldsymbol{A}\boldsymbol{s}-\boldsymbol{y})^{\mathrm{H}}(\boldsymbol{A}\boldsymbol{s}-\boldsymbol{y})}{\partial \boldsymbol{s}^*} \\ &= \frac{(\boldsymbol{s}^*)^{\mathrm{T}}\boldsymbol{A}^{\mathrm{H}}(\boldsymbol{A}\boldsymbol{s}-\boldsymbol{y})}{\partial \boldsymbol{s}^*} = \frac{\left(\boldsymbol{A}^{\mathrm{H}}(\boldsymbol{A}\boldsymbol{s}-\boldsymbol{y})\right)^{\mathrm{T}}\boldsymbol{s}^*}{\partial \boldsymbol{s}^*} \\ &= \left(\boldsymbol{A}^{\mathrm{H}}(\boldsymbol{A}\boldsymbol{s}-\boldsymbol{y})\right)^{\mathrm{T}} \\ \frac{\partial h(\boldsymbol{s})}{\partial \boldsymbol{s}^*\partial \boldsymbol{s}^{\mathrm{T}}} &= \frac{\partial \left(\boldsymbol{A}^{\mathrm{H}}(\boldsymbol{A}\boldsymbol{s}-\boldsymbol{y})\right)^{\mathrm{T}}}{\partial \boldsymbol{s}^{\mathrm{T}}} = \frac{\partial \boldsymbol{A}^{\mathrm{H}}(\boldsymbol{A}\boldsymbol{s}-\boldsymbol{y})}{\partial \boldsymbol{s}} \\ &= \boldsymbol{A}^{\mathrm{H}}\boldsymbol{A}. \end{aligned} \tag{A.4.44}$$

Combining (A.4.42), (A.4.43), and (A.4.44) yields for the smallest Lipschitz constant

$$M_{\mathrm{L}} = \left\|\boldsymbol{A}^{\mathrm{H}}\boldsymbol{A}\right\|_2. \tag{A.4.45}$$

For the required upper bound of $F_\gamma(|\boldsymbol{s}|)$ we need to find the smallest number M'_{L} such that

$$\lambda_\gamma \nabla^2_{\boldsymbol{s}} F_\gamma(|\boldsymbol{s}|) \succeq -M'_{\mathrm{L}}\boldsymbol{I}. \tag{A.4.46}$$

The required derivatives for complex Hessian $\nabla^2_{\boldsymbol{s}} F_\gamma(|\boldsymbol{s}|)$ results to

$$\begin{aligned}\frac{\partial F_\gamma(|\boldsymbol{s}|)}{\partial \boldsymbol{s}^*} &= \left[\frac{\partial F_\gamma(|\boldsymbol{s}|)}{\partial s_t^*}\right]\Big|_{t=1,\dots,N_{\mathrm{sc}}} = \left[\frac{\partial \sum_{i=1}^{N_{\mathrm{sc}}} 1-\exp\left(-\frac{|s_i|}{\gamma}\right)}{\partial s_t^*}\right]\Big|_{t=1,\dots,N_{\mathrm{sc}}} \\ &= \left[\frac{s_t}{\gamma|s_t|}\exp\left(-\frac{|s_t|}{\gamma}\right)\right]\Big|_{t=1,\dots,N_{\mathrm{sc}}},\end{aligned}$$

which we know from (A.4.17) and

$$\frac{F_\gamma(|\boldsymbol{s}|)}{\partial \boldsymbol{s}^*\partial \boldsymbol{s}^{\mathrm{T}}} = \frac{1}{\gamma}\operatorname{diag}\left(\left[\frac{\partial \frac{s_t}{|s_t|}\exp\left(-\frac{|s_t|}{\gamma}\right)}{\partial s_t}\right]\Big|_{t=1,\dots,N_{\mathrm{sc}}}\right). \tag{A.4.47}$$

The required derivative in (A.4.47) is

$$\frac{\partial \frac{s_t}{|s_t|}\exp\left(-\frac{|s_t|}{\gamma}\right)}{\partial s_t} = \underbrace{\frac{\partial \frac{s_t}{|s_t|}}{\partial s_t}\exp\left(-\frac{|s_t|}{\gamma}\right)}_{T_3} + \underbrace{\frac{s_t}{|s_t|}\frac{\partial \exp\left(-\frac{|s_t|}{\gamma}\right)}{\partial s_t}}_{T_4}. \tag{A.4.48}$$

From (A.4.22) and as depicted in Fig. A.4.1 we know that we can restrict the domain of $F_\gamma(\cdot)$ to the set $A = \{x \in \mathbb{C} | x = \beta s_t, 0 \le \beta \le 1\}$ or in other words we vary s_t only as such that the argument of s_t is constant. Therefore, term T_3 in (A.4.48) results to zero

$$T_3 = \frac{\partial \frac{s_t}{|s_t|}}{\partial s_t}\exp\left(-\frac{|s_t|}{\gamma}\right) = 0.$$

Term T_4 in (A.4.48) gives

$$\begin{aligned} T_4 &= \frac{s_t}{|s_t|} \frac{\partial \exp\left(-\frac{|s_t|}{\gamma}\right)}{\partial s_t} \\ &= -\frac{s_t}{|s_t|} \frac{s_t^*}{\gamma\,|s_t|} \exp\left(-\frac{|s_t|}{\gamma}\right) \\ &= -\frac{1}{\gamma} \exp\left(-\frac{|s_t|}{\gamma}\right), \end{aligned} \tag{A.4.49}$$

where we used (A.4.17) to get the required derivative. Combining (A.4.47), (A.4.48), and (A.4.49) yields

$$\begin{aligned} \nabla_{\boldsymbol{s}}^2 F_\gamma\left(|\boldsymbol{s}|\right) &= -\frac{1}{\gamma^2} \operatorname{diag}\left(\left[\exp\left(-\tfrac{|s_t|}{\gamma}\right)\right]\Big|_{t=1,\ldots,N_{\mathrm{sc}}}\right) \\ &= -\frac{1}{\gamma^2} \operatorname{diag}\left(\left[\exp\left(-\tfrac{|\boldsymbol{s}_t|}{\gamma}\right)\right]\right) \end{aligned} \tag{A.4.50}$$

Inserting (A.4.50) into (A.4.46) gives

$$-\frac{\lambda_\gamma}{\gamma^2} \operatorname{diag}\left(\left[\exp\left(-\tfrac{|\boldsymbol{s}_t|}{\gamma}\right)\right]\right) \succeq -M_{\mathrm{L}}' \boldsymbol{I} \Leftrightarrow -\frac{\lambda_\gamma}{\gamma^2} \exp\left(-\frac{|s_t|}{\gamma}\right) \geq -M_{\mathrm{L}}'$$

and results for the smallest value of M_{L}' to

$$M_{\mathrm{L}}' = \frac{\lambda_\gamma}{\gamma^2}. \tag{A.4.51}$$

For any step width

$$\mu \in \left(0, \frac{1}{M_{\mathrm{L}} + M_{\mathrm{L}}'}\right)$$

the sequence $\{\boldsymbol{s}_l\}$ generated by (A.4.10) converges to a stationary point of (A.4.8), where M_{L} is from (A.4.45) and M_{L}' is from (A.4.51).

The Regularization Parameter λ_γ

As derived in [58] we set

$$\lambda_\gamma = \lambda\gamma.$$

Initialization

As pointed out in the graduated non-convexity (GNC) procedure, we initially solve (A.4.8) for $\gamma \to \infty$. Following the same argumentation as stated above, let $\widehat{\boldsymbol{s}}$ be the unique solution to

$$\min_{\boldsymbol{s}} \|\boldsymbol{s}\|_1 \ \text{subject to}\ \boldsymbol{A}\boldsymbol{s} = \boldsymbol{y},$$

which is the equivalent noiseless optimization problem to A.4.3. In [58] it was shown that, for $\gamma \to \infty$, the following statement holds

$$\lim_{\gamma\to\infty} \arg\min_{\boldsymbol{s}} \left\{ F_\gamma\left(|\boldsymbol{s}|\right) \middle|\, \boldsymbol{A}\boldsymbol{s} = \boldsymbol{y} \right\} = \arg\min_{\boldsymbol{s}} \left\{ \|\boldsymbol{s}\|_1 \middle|\, \boldsymbol{A}\boldsymbol{s} = \boldsymbol{y} \right\} = \widehat{\boldsymbol{s}},$$

provided that the ℓ_1 minimization has a unique solution (which is not strictly convex). We therefore conclude, that (A.4.7), for $\gamma \to \infty$, can be optimized by solving the BPDN problem A.4.3. To do so, the fast iterative shrinkage-thresholding algorithm (FISTA) algorithm or the highly improved version turbo shrinkage-thresholding (TST) presented in Section 6.1 may be used. Furthermore, γ_0 is set to $\gamma_0 = \max(|\boldsymbol{s}_0|)$, where $\boldsymbol{s}_0$ is the solution of A.4.3. This is different as done in [58], where γ_0 was set to $\gamma_0 = 8\max(|\boldsymbol{s}_0|)$ which is equivalent to the solution obtained by the BPDN approach. This iteration is not necessary and we start with an already decreased γ_0.

The final algorithm is listed in Algorithm 6.2.

Remarks

In the following some remarks on the CSCSA algorithm are stated.

Remark A.1. The CSCSA algorithm acts for big γ like the FISTA algorithm i.e. an ℓ_1 minimizer. It therefore is sensitive to non-normalized columns of the sensing operator $\boldsymbol{A}$. In case one of the columns of $\boldsymbol{A}$ has a significant higher ℓ_2 norm than the remaining columns, an ℓ_1 minimization algorithm tends to overrate its corresponding sparse entry in $\boldsymbol{s}$ and thus does not tend to minimize the desired ℓ_0 norm any more. The reconstruction of the desired $\boldsymbol{s}$ may fail therefore!

Remark A.2. For the required initial solution $\boldsymbol{s}_0$ any ℓ_1 minimizing algorithm may be used e.g. FISTA, spectral projected gradient for ℓ_1 (SPGL1), etc.

Remark A.3. The CSCSA algorithm will attain a relative residual error $\|\boldsymbol{A}\boldsymbol{s}_i - \boldsymbol{y}\|_2 / \|\boldsymbol{y}\|_2^2 \simeq 1/\mathrm{SNR}$ equal to the signal to noise ratio (SNR) of the signal. In case the initial solution $\boldsymbol{s}_0$ has a relative residual error smaller than the given SNR the CSCSA algorithm will increase it again until it attains the signals SNR. In return for this deterioration the squared reconstruction error (SRE) is improved.

A.4.2. Additional Simulation Results

In the following, additional phase transition diagrams are shown. Also, an additional error metric is introduced, namely the mean support recovery rate (SRR) $\frac{1}{N_{\mathrm{mc}}} \sum_{i=1}^{N_{\mathrm{mc}}} \mathrm{card}\,(\hat{\tau} \cap \tau^*) / \mathrm{card}\,(\tau^*)$, where $\hat{\tau}$ denotes the support set of $\hat{\boldsymbol{s}}$, τ^* the support set of the true solution $\boldsymbol{s}^*$, and $\mathrm{card}\,(\cdot)$ the cardinality operator. This error metric tells us how well the algorithm finds the correct position of the sparse entries. The simulation parameters are the same as introduced in Chapter 3. The sensing operators used to test the algorithm are:

1. Random matrix whose entries are drawn independently from a zero-mean, unit-variance complex Gaussian distribution $\mathcal{CN}(0, 1)$ with normalized columns.

2. Randomly selected rows of a discrete Fourier transform (DFT) matrix with normalized columns.

3. Rows from a DFT matrix selected in a structured manner, meaning the rows were chosen as equally spaced as possible.

4. Rows from a DFT matrix selected for sub sampling factors $\mathrm{SSF} = 1 - 10$. For this setup, with $n_{\mathrm{b}} = 1024$, $N_{\mathrm{sc}} = n_{\mathrm{b}} + n_{\triangle}$ was chosen such that $M = N_{\mathrm{sc}}/\mathrm{SSF} \in \mathbb{N}$, where $n_{\triangle}$ was selected as small as possible.

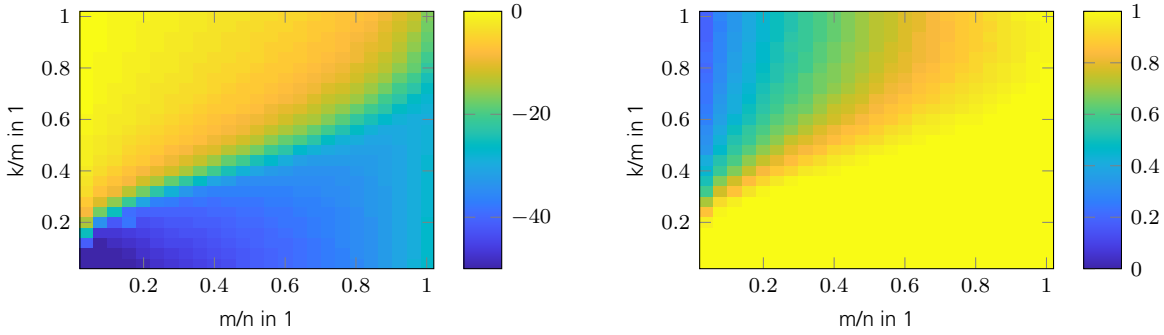

(a) Mean SRE in dB.

(b) Mean SRR in 1.

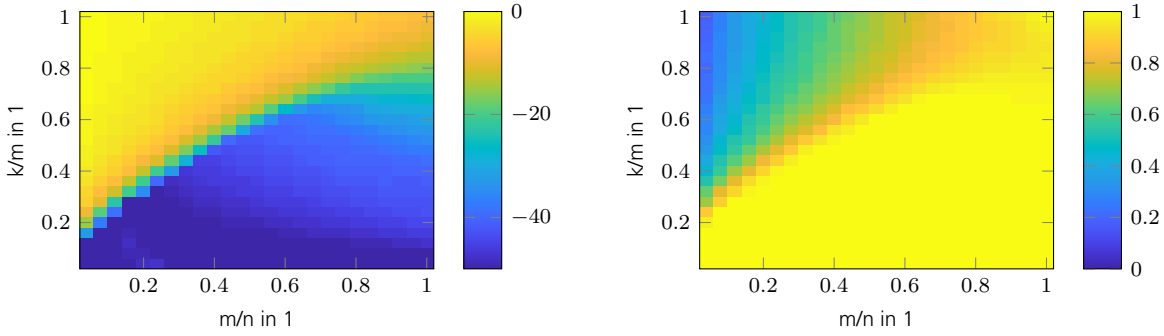

(c) Mean SRE in dB.

(d) Mean SRR in 1.

Figure A.4.3.: Results of random sensing operator. Top row: results for SPGL1 algorithm and bottom row: SPGL1-CSCSA combination.

5. DFT matrix with correlated columns. This occurs often in case of beamforming algorithms, for which a higher angular resolution is desired. In this case, the number of angular bins is increased which corresponds to zero padding, hence correlated columns in the DFT matrix. Correlated columns reduce the RIP constant of the sensing operator and therefore the reconstruction performance. As an illustrative example, reconstructions for a uniform linear array (ULA) antenna with four antennas but 41 angular directions are shown.

As an additional reference, the SPGL1 algorithm[5] was also included. The resulting phase transition diagrams for a complex random sensing matrix with normalized columns are shown in Fig. A.4.3. As can be seen, the CSCSA algorithm improves the results of the SPGL1 algorithm for a sparsity ratio of $\kappa/M \leq 0.7$. Above this value, the reconstruction performance deteriorates. Further evaluations have shown, that the complex random sensing matrix is responsible therefore, yet the precise reasons are subject to further investigation. This aforementioned deterioration does not occur in the DFT sensing case which is shown in the following Fig. A.4.4 As can be seen, for the DFT sensing operator with randomly chosen rows, the CSCSA algorithm uniformly improves upon the SPGL1 results. Its success heavily depends on the random nature of the selected rows. In case of a structured selection strategy, the reconstruction performance deteriorates significantly. This is shown in in Fig. A.4.5, where the rows were equidistantly chosen selected. As can be seen, the CSCSA algorithm can not improve upon the SPGL1 results.

An even more severe case is regular sub sampling where e. g. only $1/2$, $1/3$, etc. samples are

[5] Available at https://github.com/mpf/spgl1

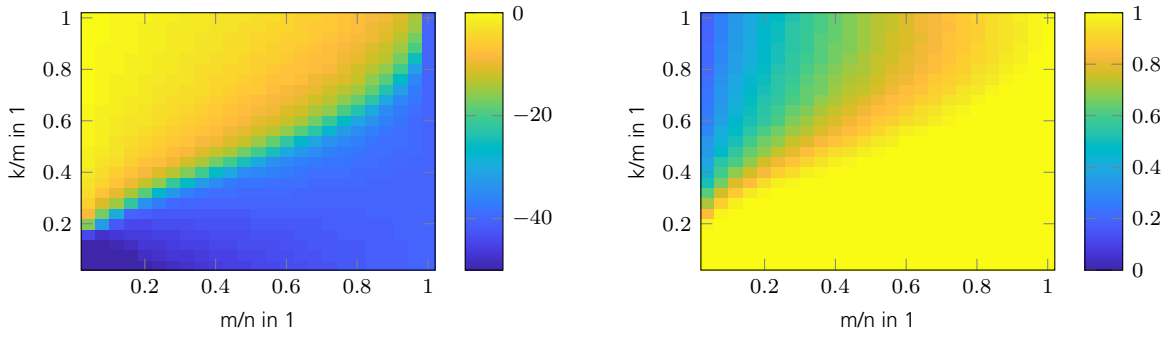

(a) Mean SRE in dB.

(b) Mean SRR in 1.

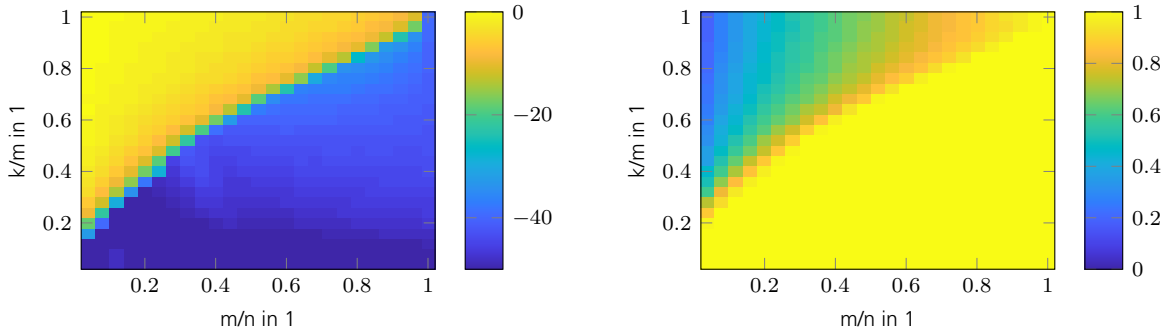

(c) Mean SRE in dB.

(d) Mean SRR in 1.

Figure A.4.4.: Results of random row DFT sensing operator. Top row: Results for SPGL1 algorithm and bottom row: SPGL1-CSCSA combination.

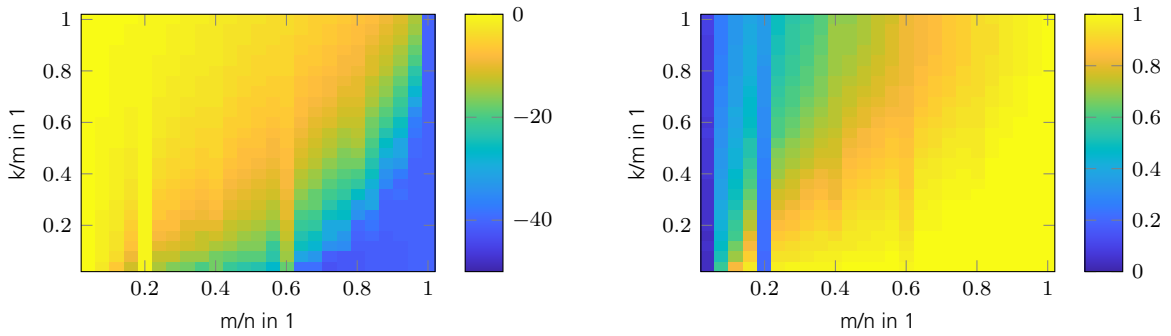

(a) Mean SRE in dB.

(b) Mean SRR in 1.

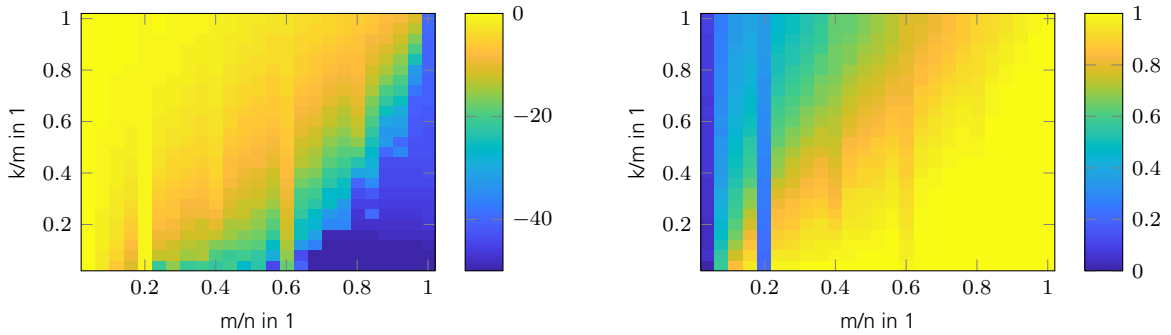

(c) Mean SRE in dB.

(d) Mean SRR in 1.

Figure A.4.5.: Results for structured DFT sensing operator. Top row: results of SPGL1 algorithm and bottom row: SPGL1-CSCSA combination.

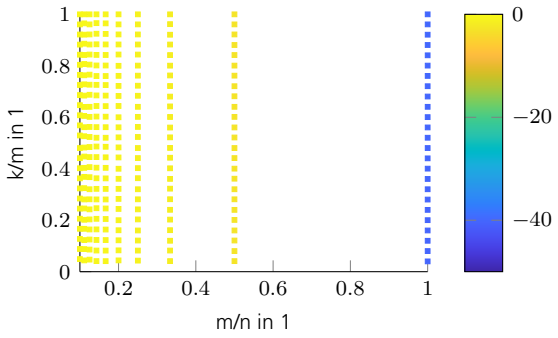

(a) Mean SRE in dB.

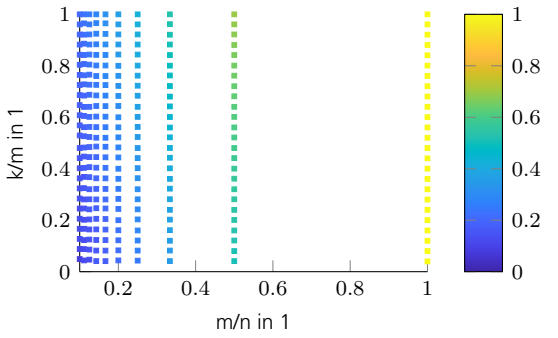

(b) Mean SRR in 1.

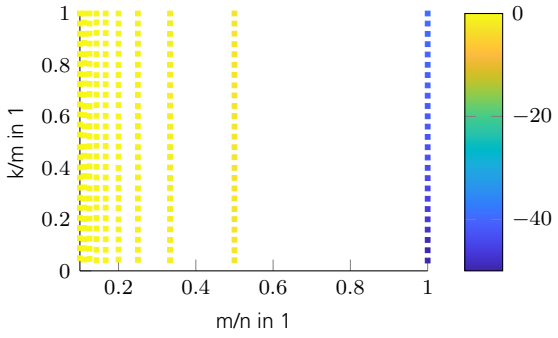

(c) Mean SRE in dB.

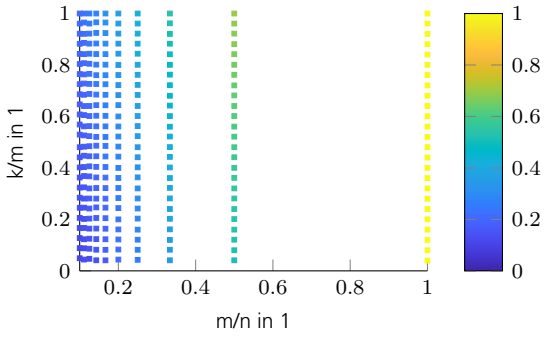

(d) Mean SRR in 1.

Figure A.4.6.: Results for $\mathrm{SSF} = 1 - 10$ of DFT sensing operator. Top two: results of SPGL1 algorithm and bottom row: SPGL1-CSCSA algorithm.

used. The reconstruction performance is shown in Fig. A.4.6. As can be seen, not even $\mathrm{SSF} = 1/2$ can be reconstructed successfully. The last example shows reconstruction results for a beamformer for a ULA with four antenna elements but 41 angular directions. This corresponds to a DFT sensing operator with highly correlated columns. In this case, only very sparse scenes can be successfully reconstructed, hence a phase transition diagram is not of use. Hence, a different simulation was set up, where the sparsity was fixed to $\kappa = 2$ and the position of one sparse entry was swept trough all possible indices. This illustrates the resolution performance of the CS beamformer approach. This simulation is shown in Fig. A.4.7 and Fig. A.4.8. Figure A.4.7a shows the true location of the two targets, where target two is shifted through all angular positions. The auto-correlation matrix of the DFT sensing matrix is shown in Fig. A.4.7b. Evidently, consecutive columns are highly correlated. Figure A.4.7c to Fig. A.4.7j show the reconstructed scenes for different reconstruction algorithms and phase differences between the two targets. As can be seen, the reconstructed positions of the SPGL1 algorithm appears blurred, yet the CSCSA algorithm significantly cleans the scenes up. As a reference, Fig. A.4.8 shows the results in case of a classical ℓ_2 reconstruction a. k. a pseudo inverse. Evidently, the CS approach including the CSCSA algorithm show superior performance. The simulation was repeated with even higher correlated columns for which the results are shown in Fig. A.4.8 and Fig. A.4.8. The improvements of CSCSA upon SPGL1 with respect to resolution performance are evident.

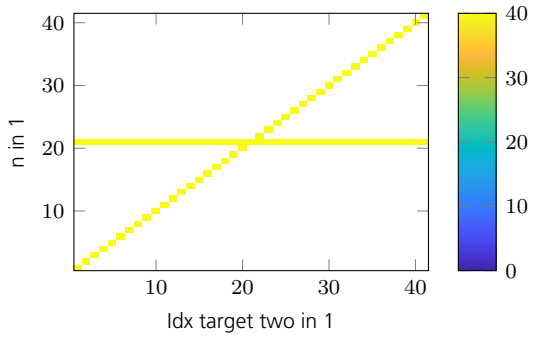

(a) True scene input data in dB.

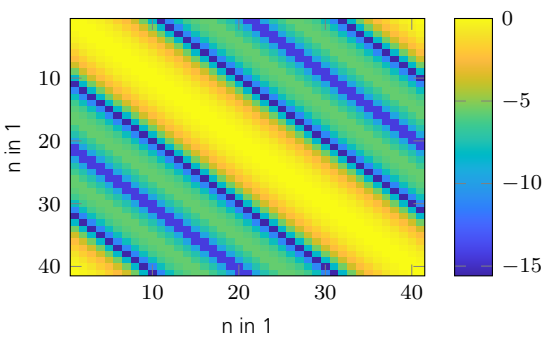

(b) Auto correlation $\boldsymbol{A}^{\mathrm{H}}\boldsymbol{A}$ of DFT sensing operator in dB.

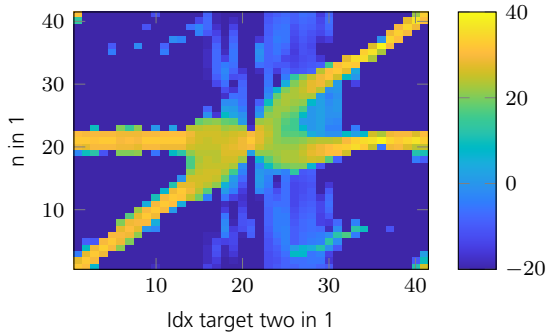

(c) Reconstruction of SPGL1 algorithm in dB for a phase difference of $2.11\,\mathrm{rad}$.

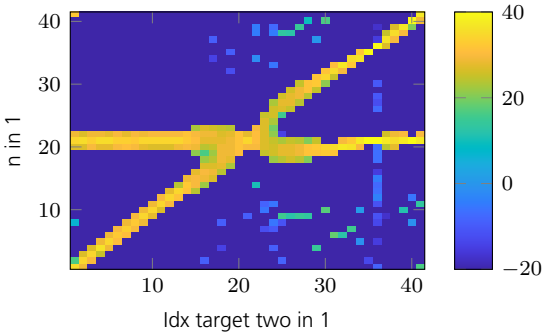

(d) Reconstruction of SPGL1-CSCSA algorithm in dB for a phase difference of $2.11\,\mathrm{rad}$.

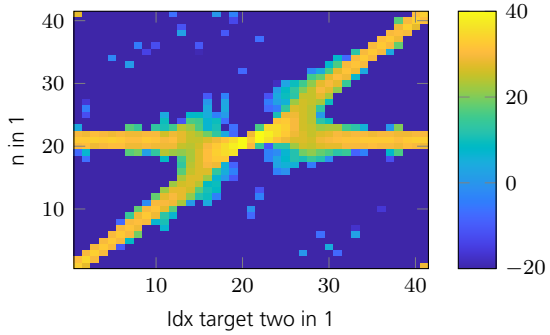

(e) Reconstruction of SPGL1 algorithm in dB for zero phase difference.

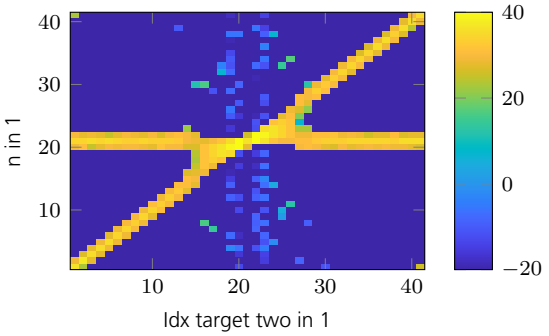

(f) Reconstruction of SPGL1-CSCSA algorithm in dB for zero phase difference.

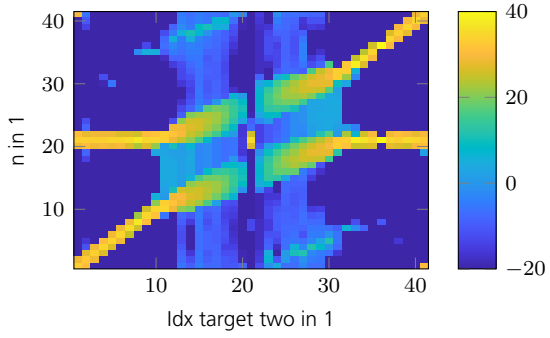

(g) Reconstruction of SPGL1 algorithm in dB for a phase offset of $\pi\,\mathrm{rad}$.

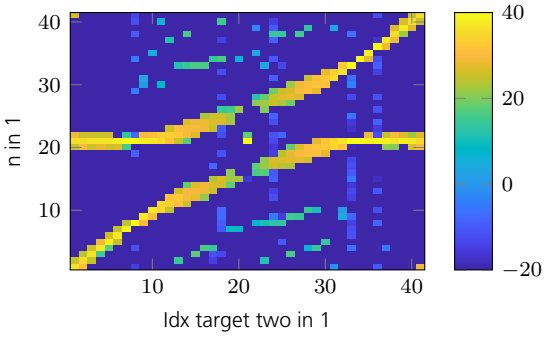

(h) Reconstruction of SPGL1-CSCSA algorithm in dB for a phase offset of $\pi\,\mathrm{rad}$.

Figure A.4.7.: Results for correlated columns DFT sensing operator for $\kappa = 2$ sparse entries swept along $N_{\mathrm{sc}} = 41$ with $M = 4$ measurements.

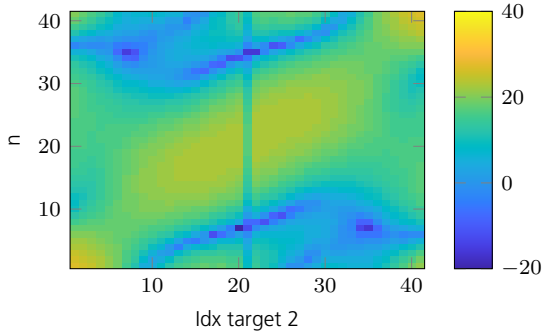

(i) Reconstruction by use of classical pseudo inverse algorithm in dB for zero phase difference.

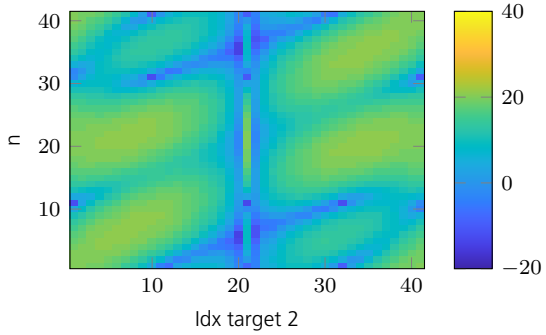

(j) Reconstruction by use of classical pseudo inverse algorithm in dB for a phase difference of π rad.

Figure A.4.7.: Results for correlated columns DFT sensing operator for $\kappa = 2$ sparse entries swept along $N_{\mathrm{sc}} = 41$ with $M = 4$ measurements.

A.5. Complex smoothed rank approximation

In this chapter, based on the smoothed rank function (SRF) algorithm [61] and the smoothed rank approximation (SRA) approach in [62], we derive a new algorithm called complex smoothed rank approximation (CSRA) for the recovery of complex low-rank matrices in the field of affine rank minimization (ARM). The following section covers the derivation of the CSRA algorithm.

A.5.1. Derivative of the CSRA algorithm

The primary objective is to recover an unknown low-rank matrix $\widetilde{\boldsymbol{L}} \in \mathbb{C}^{N_1 \times N_2}$, where the rank $\operatorname{rank}\left(\widetilde{\boldsymbol{L}}\right) = r \ll n_{\min} = \min\left(N_1, N_2\right)$, from a limited number of noisy observations of the form

$$\boldsymbol{y} = \mathcal{A}\left(\widetilde{\boldsymbol{L}}\right) + \boldsymbol{n}, \tag{A.5.1}$$

where $\mathcal{A} \in \mathbb{C}^{M \times N_1 \times N_2}$ $(M < N_1 N_2)$ is a known affine transformation, $\boldsymbol{y} \in \mathbb{C}^M$ is a measurement vector, and $\boldsymbol{n} \in \mathbb{C}^M$ is additive noise with zero mean and variance P_{n}. To find a solution to this under-determined linear system, we seek the closest low-rank solution which is consistent with the measurements via

$$\min_{\boldsymbol{L}} \operatorname{rank}\left(\boldsymbol{L}\right) \ \text{subject to} \ \left\|\mathcal{A}\left(\boldsymbol{L}\right) - \boldsymbol{y}\right\|_2^2 \leq \epsilon^2, \tag{A.5.2}$$

where $\|\cdot\|_x$ denotes the ℓ_x norm and $\epsilon^2 = \|\boldsymbol{n}\|_2^2$ is some constant error energy. Unfortunately problem (A.5.2) is NP-hard to solve. In order to make the recovery tractable we may approximate the rank by a suitable function. A very well known relaxation of (A.5.2) is the nuclear norm minimization (NNM) approach which is

$$\min_{\boldsymbol{L}} \|\boldsymbol{L}\|_* \ \text{subject to} \ \left\|\mathcal{A}\left(\boldsymbol{L}\right) - \boldsymbol{y}\right\|_2^2 \leq \epsilon^2, \tag{A.5.3}$$

where $\|\boldsymbol{L}\|_*$ is the nuclear norm of $\boldsymbol{L}$ which is the sum of the singular values of $\boldsymbol{L}$ [45]. The nuclear norm is known to be the tightest convex relaxation of the original rank minimization

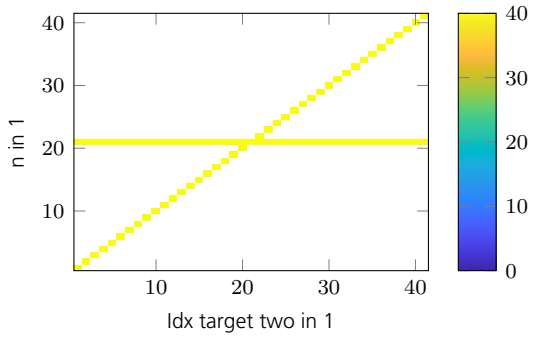

(a) True scene input data in dB.

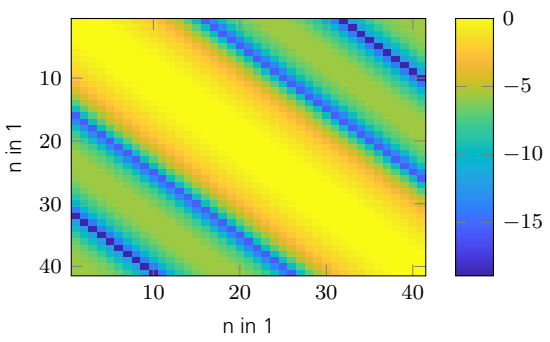

(b) Auto correlation $\boldsymbol{A}^{\mathrm{H}}\boldsymbol{A}$ of DFT sensing operator in dB.

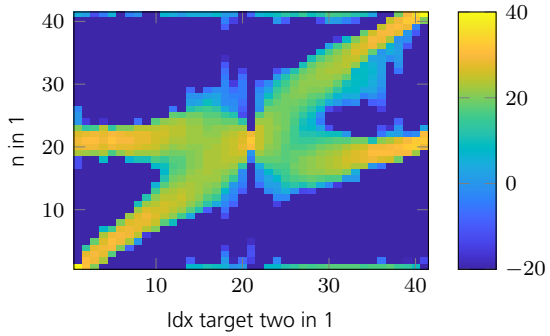

(c) Reconstruction of SPGL1 algorithm in dB for a phase difference of 2.11 rad.

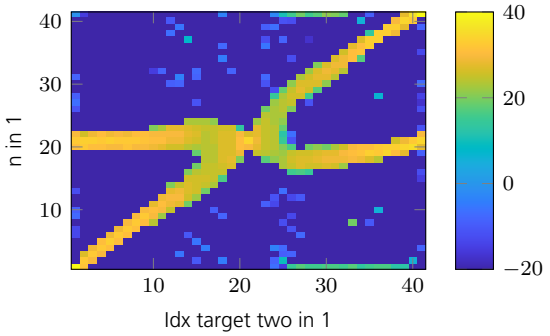

(d) Reconstruction of SPGL1-CSCSA algorithm in dB for a phase difference of 2.11 rad.

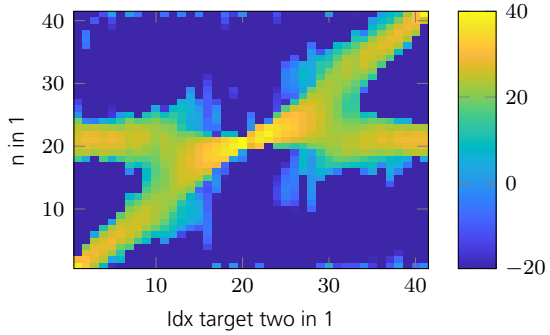

(e) Reconstruction of SPGL1 algorithm in dB for zero phase.

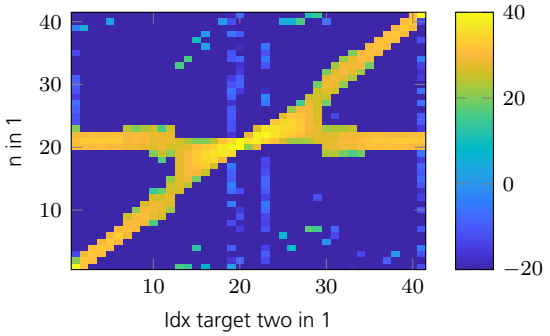

(f) Reconstruction of SPGL1-CSCSA algorithm in dB for zero phase difference.

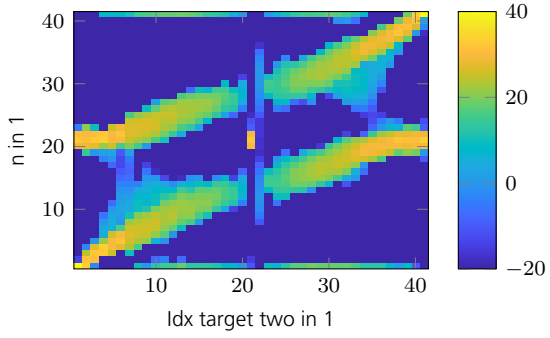

(g) Reconstruction of SPGL1 algorithm in dB zero for a phase offset of π rad.

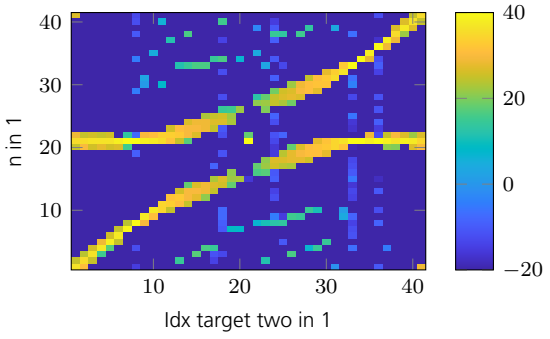

(h) Reconstruction of SPGL1-CSCSA algorithm in dB for a phase offset of π rad.

Figure A.4.8.: Results for different correlated columns DFT sensing operator for $\kappa = 2$ sparse entries swept along $N_{\mathrm{sc}} = 41$ with $M = 4$ measurements.

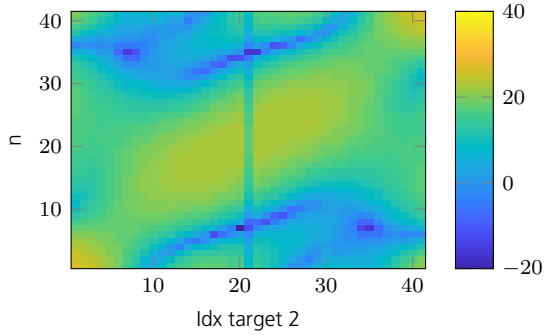

(i) Reconstruction by use of classical pseudo inverse algorithm in dB for zero phase difference.

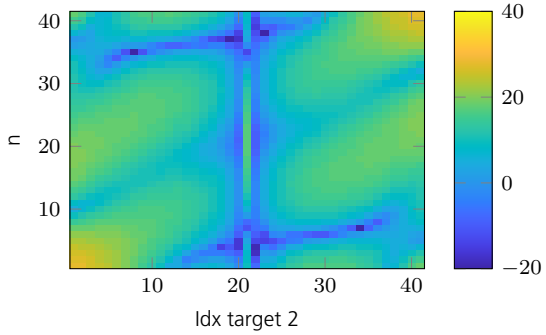

(j) Reconstruction by use of classical pseudo inverse algorithm in dB for phase difference of π rad.

Figure A.4.8.: Results for correlated columns DFT sensing operator for $\kappa = 2$ sparse entries swept along $N_{\mathrm{sc}} = 41$ with $M = 4$ measurements.

problem (A.5.2). However, despite the convexity of the NNM approach, there is a large gap between the sufficient conditions for the robust recovery of low-rank matrices using (A.5.2) and (A.5.3) [82].

In order to narrow this gap a different replacement for the rank function is proposed. The rank of $\boldsymbol{L} = \boldsymbol{U}\boldsymbol{\Sigma}\boldsymbol{V}^{\mathrm{H}}$, where $\boldsymbol{\Sigma} = \operatorname{diag}(\boldsymbol{\sigma})$, is defined as the number of non zero elements in $\boldsymbol{\sigma}$, where the vector $\boldsymbol{\sigma} = \begin{bmatrix} \sigma_1 & \cdots & \sigma_{n_{\min}} \end{bmatrix}^{\mathrm{T}}$ holds the singular values of $\boldsymbol{L}$. We thus can define the rank of $\boldsymbol{L}$ as

$$\operatorname{rank}(\boldsymbol{L}) = \|\boldsymbol{\sigma}\|_0 = \sum_{i=1}^{n_{\min}} \left[1 - \delta\left(\sigma_i(\boldsymbol{L})\right)\right], \tag{A.5.4}$$

where $\|\cdot\|_0$ is the number of non-zero elements[6] a. k. a. pseudo-zero-norm, $\sigma_i(\boldsymbol{L})$ is the i^{th} largest singular value of $\boldsymbol{L}$, and $\delta(x)$ is the Kronecker delta function defined in (A.4.4). To make (A.5.4) smooth we may apply the same idea as used in A.4

$$f_\gamma(x) = 1 - \delta(x) \approx 1 - \exp\left(-\frac{|x|}{\gamma}\right).$$

Thus we can define

$$\operatorname{rank}(\boldsymbol{L}) \approx \sum_{i=1}^{n_{\min}} f_\gamma\left(\sigma_i(\boldsymbol{L})\right) = F'_\gamma\left(\boldsymbol{\sigma}(\boldsymbol{L})\right) = F_\gamma(\boldsymbol{L}), \tag{A.5.5}$$

where $\boldsymbol{\sigma}(\boldsymbol{X})$ yields the singular values of $\boldsymbol{X}$ arranged as a vector. The rank approximation function $F'_\gamma(\boldsymbol{x})$ defined in (A.5.5) is absolutely symmetric, which means $F'_\gamma(\boldsymbol{x})$ is invariant under arbitrary permutations and sign changes of the elements of $\boldsymbol{x}$. Based on this property, the following theorem from [83] can be applied.

Theorem A.1. *The function $F(\boldsymbol{Z})$ is unitarily invariant if $F(\boldsymbol{Z}) = F'(\boldsymbol{\sigma}(\boldsymbol{Z})) = F' \circ \boldsymbol{\sigma}(\boldsymbol{Z})$ provided $F'(\boldsymbol{z})$ is absolutely symmetric [83].*

This property is useful when we try to minimize the rank approximation function (A.5.5). The

[6] Well known from compressive sensing (CS), see Chapter 3.

optimization problem (A.5.2) may now be relaxed to

$$\min_{\boldsymbol{L}} F_\gamma(\boldsymbol{L}) \text{ subject to } \|\mathcal{A}(\boldsymbol{L}) - \boldsymbol{y}\|_2^2 \leq \epsilon^2. \tag{A.5.6}$$

The constrained optimization problem (A.5.6) can be converted to an unconstrained one by use of regularization. This yields

$$\min_{\boldsymbol{L}} \lambda F_\gamma(\boldsymbol{L}) + \|\mathcal{A}(\boldsymbol{L}) - \boldsymbol{y}\|_2^2, \tag{A.5.7}$$

where λ is a regularization parameter. Program (A.5.7) is of the form

$$\min_{\boldsymbol{L}} \lambda\rho(\boldsymbol{L}) + h(\boldsymbol{L}), \tag{A.5.8}$$

where $h(\boldsymbol{L})$ is convex and differentiable with Lipschitz continuous gradient. In case of the NNM approach (A.5.3), $\rho(\boldsymbol{L})$ is convex and non smooth. For the approach considered in (A.5.7), $\rho(\boldsymbol{L})$ is not concave nor convex (since $f_\gamma(x)$ is defined also for negative numbers) and not smooth i. e. not differentiable at the origin. Nevertheless, the iterative thresholding (IT) method can be utilized to conduct the desired minimization. For a fixed γ, a solution to program (A.5.7) can be obtained by iteratively solving

$$\boldsymbol{L}_{j+1} = \arg\min_{\boldsymbol{L}} \left\{ \langle \boldsymbol{L} - \boldsymbol{L}_j, \nabla h(\boldsymbol{L}_j)\rangle_{\mathrm{F}} + \frac{1}{2\mu}\|\boldsymbol{L} - \boldsymbol{L}_j\|_{\mathrm{F}}^2 + \lambda F_\gamma(\boldsymbol{L}) \right\} \tag{A.5.9}$$

until convergence, where $\mu > 0$ is some step size.

Solution to unconstrained minimization problem for a fixed γ

Program (A.5.9) can be simplified to

$$\boldsymbol{L}_{j+1} = \arg\min_{\boldsymbol{L}} \left\{ \frac{1}{2\mu}\|\boldsymbol{L} - (\boldsymbol{L}_j - \mu\nabla h(\boldsymbol{L}_j))\|_{\mathrm{F}}^2 + \lambda F_\gamma(\boldsymbol{L}) \right\} \tag{A.5.10}$$

ignoring constant terms unimportant regarding the minimization. For a given $\boldsymbol{L}_j$ we can further simplify (A.5.10) to

$$\boldsymbol{L}_{j+1} = \arg\min_{\boldsymbol{L}} \left\{ \frac{1}{2\mu}\|\boldsymbol{L} - \boldsymbol{L}_{0j}\|_{\mathrm{F}}^2 + \lambda F_\gamma(\boldsymbol{L}) \right\}, \tag{A.5.11}$$

where

$$\boldsymbol{L}_{0j} = \boldsymbol{L}_j - \mu\nabla h(\boldsymbol{L}_j) \tag{A.5.12}$$

is the result of the gradient update step. In order to minimize (A.5.11) we can use Theorem 2 of [83].

Theorem A.2. *For unitarily invariant functions $F(\boldsymbol{Z}) = F' \circ \boldsymbol{\sigma}(\boldsymbol{Z})$ the optimal solution to the problem*

$$\min_{\boldsymbol{Z}} F(\boldsymbol{Z}) + c\|\boldsymbol{Z} - \boldsymbol{A}\|_{\mathrm{F}}^2$$

is

$$\widehat{\boldsymbol{Z}} = \boldsymbol{U}\widehat{\boldsymbol{\Sigma}}_{\boldsymbol{Z}}\boldsymbol{V}^{\mathrm{H}},$$

where $\boldsymbol{A} = \boldsymbol{U}\boldsymbol{\Sigma}_{\boldsymbol{A}}\boldsymbol{V}^{\mathrm{H}}$ is the singular value decomposition (SVD) decomposition of $\boldsymbol{A}$ and $\widehat{\boldsymbol{\Sigma}}_{\boldsymbol{Z}} =$

$\operatorname{diag}(\widehat{\boldsymbol{\sigma}})$ *is obtained by solving the separable minimization problem*

$$\widehat{\boldsymbol{\sigma}} = \arg\min \left\{ \lambda F'(\boldsymbol{\sigma}) + c \left\| \boldsymbol{\sigma} - \boldsymbol{\sigma}_{\boldsymbol{A}} \right\|_2^2 \right\},$$

where $\boldsymbol{\sigma}_{\boldsymbol{A}} = \boldsymbol{\sigma}(\boldsymbol{A})$ *[83].*

It shall be noted, that theorem A.2 also works if $F(\boldsymbol{Z})$ would not be a unitarily invariant function, provided $F(\boldsymbol{Z}) = F(\boldsymbol{\Sigma}_{\boldsymbol{Z}})$, where $\boldsymbol{\Sigma}_{\boldsymbol{Z}} = \operatorname{diag}(\boldsymbol{\sigma}(\boldsymbol{Z}))$, which is inherently fulfilled since $\boldsymbol{\Sigma}_{\boldsymbol{Z}}$ is a real positive diagonal matrix. We therefore can use theorem A.2 to obtain

$$\boldsymbol{L}_{j+1} = \boldsymbol{U}_{0j} \widehat{\boldsymbol{\Sigma}}_{\boldsymbol{L}} \boldsymbol{V}_{0j}^{\mathrm{H}}, \tag{A.5.13}$$

where

$$\boldsymbol{L}_{0j} = \boldsymbol{U}_{0j} \boldsymbol{\Sigma}_{0j} \boldsymbol{V}_{0j}^{\mathrm{H}} \tag{A.5.14}$$

is the SVD of $\boldsymbol{L}_{0j}$, $\widehat{\boldsymbol{\Sigma}}_{\boldsymbol{L}} = \operatorname{diag}(\widehat{\boldsymbol{\sigma}})$, and

$$\widehat{\boldsymbol{\sigma}} = \underset{\boldsymbol{\sigma} \geq \boldsymbol{0}}{\arg\min} \left\{ \lambda F'_{\gamma}(\boldsymbol{\sigma}) + \frac{1}{2\mu} \left\| \boldsymbol{\sigma} - \boldsymbol{\sigma}_{0j} \right\|_2^2 \right\}, \tag{A.5.15}$$

where $\boldsymbol{\sigma}_{0j} = \boldsymbol{\sigma}(\boldsymbol{L}_{0j})$. In (A.5.15) we additionally demand $\boldsymbol{\sigma} \geq \boldsymbol{0}$ since singular values are always positive. The objective function (A.5.15) is the sum of a concave and convex function (since $\boldsymbol{\sigma} \geq \boldsymbol{0}$). To the contrary of [62], we do not solve (A.5.15) by applying a differenct of convex (D.C.) optimization strategy. A better approach, first shown in [58], is to utilize the Lambert *W* function

$$W(z) \mathrm{e}^{W(z)} = z, \tag{A.5.16}$$

which allows for a closed form solution of (A.5.15). We start by noticing that the minimization in (A.5.15) is separable and as such can be conducted element wise as

$$\widehat{\sigma}_i = \underset{\sigma \geq 0}{\arg\min} \left\{ \lambda f_{\gamma}(\sigma) + \frac{1}{2\mu} (\sigma - \sigma_{0j,i})^2 \right\}. \tag{A.5.17}$$

Defining the argument of (A.5.17) as

$$L(\sigma, \sigma_{0j,i}) = \lambda f_{\gamma}(\sigma) + \frac{1}{2\mu} (\sigma - \sigma_{0j,i})^2, \tag{A.5.18}$$

taking its derivative with respect to σ and setting it to zero yields after short manipulation

$$\frac{\sigma - \sigma_{0j,i}}{\mu} = -\frac{\lambda}{\gamma} \frac{\sigma}{|\sigma|} \exp\left(-\frac{\sigma}{\gamma}\right) = -\frac{\lambda}{\gamma} \exp\left(-\frac{\sigma}{\gamma}\right), \tag{A.5.19}$$

where we used the fact that $\sigma \geq 0$. To apply the Lambert *W* function we modify (A.5.19) to

$$\frac{\sigma - \sigma_{0j,i}}{\gamma} \exp\left(\frac{\sigma - \sigma_{0j,i}}{\gamma}\right) = -\frac{\lambda \mu}{\gamma^2} \exp\left(-\frac{\sigma_{0j,i}}{\gamma}\right). \tag{A.5.20}$$

Applying the Lambert *W* function on both sides of (A.5.20) gives two solutions

$$\sigma_1 = \gamma W_0(z) + \sigma_{0j,i} \tag{A.5.21}$$

$$\sigma_2 = \gamma W_{-1}(z) + \sigma_{0j,i}, \tag{A.5.22}$$

where

$$z = -\frac{\lambda\mu}{\gamma^2}\exp\left(-\frac{\sigma_{0j,i}}{\gamma}\right) \tag{A.5.23}$$

and $W_0(\cdot)$ denotes the upper branch and $W_{-1}(\cdot)$ the lower branch of the multi-valued Lambert *W* function. The rest of the derivation is left to look up in [58]. The solution to (A.5.17) is the shrinkage operator

$$\mathcal{T}_{\mu\lambda}^{(\gamma)}(x) = \begin{cases} 0 & x < \gamma\left(1 + \ln\left(\frac{\mu\lambda}{\gamma^2}\right)\right) \\ 0 & L(0,x) < L(\sigma_1, x) \\ \sigma_1 & \text{otherwise} \end{cases}, \tag{A.5.24}$$

where σ_1 is (A.5.21) and $L(\cdot,\cdot)$ is (A.5.18). The solution to (A.5.11) is therefore

$$\boldsymbol{L}_{j+1} = \boldsymbol{U}_{0j}\,\mathrm{diag}\left(\mathcal{T}_{\mu\lambda}^{(\gamma)}(\boldsymbol{\sigma}_{0j})\right)\boldsymbol{V}_{0j}^{\mathrm{H}},$$

where $\mathcal{T}_{\mu\lambda}^{(\gamma)}(\boldsymbol{\sigma}_{0j}) = \left[\mathcal{T}_{\mu\lambda}^{(\gamma)}(\sigma_{0j,1}) \quad \cdots \quad \mathcal{T}_{\mu\lambda}^{(\gamma)}(\sigma_{0j,n_{\min}})\right]^{\mathrm{T}}$ is the vector operator version of (A.5.24), $\boldsymbol{\sigma}_{0j} = \boldsymbol{\sigma}(\boldsymbol{L}_{0j})$, $\boldsymbol{L}_{0j}$ is (A.5.12), and $\boldsymbol{U}_{0j}$ and $\boldsymbol{V}_{0j}^{\mathrm{H}}$ are defined in (A.5.14).

The regularization parameter λ

A short remark at the beginning: The approach in [58] to choose $\lambda \hat{=} \lambda_\gamma = \lambda\gamma$ did not work well in our case. Simulations showed better results by simply taking $\lambda_\gamma = \lambda$. If the first choice $\lambda_\gamma = \lambda\gamma$ was used, the singular value vector was made non sparse. This did not happen by using $\lambda_\gamma = \lambda$.

For the CSRA algorithm the regularization parameter λ may be determined by

$$\lambda = 2c_{\mathrm{r}}\sqrt{P_{\mathrm{n}}}\Phi^{-1}\left(1 - \frac{\alpha_{\mathrm{r}}}{2n}\right)\sqrt{\max(N_1, N_2)}, \tag{A.5.25}$$

as introduced in Section 6.3.

The step size μ

For this particular approach there is no easy way to find a valid step size. Since the function $F_\gamma(\boldsymbol{L})$ defined in (A.5.5) is not convex or concave a Lipschitz approach does not work in general. A step size found to be working well is $\mu \in \left(0, \frac{1}{M_{\mathrm{L}}}\right)$, where $M_{\mathrm{L}} = \|\mathcal{A}\|_2^2$, which is a guaranteed stable step size for the singular value thresholding (SVT) algorithm [45]. This seems reasonable considering the similarities of SVT and the algorithm presented here since both follow the IT approach. It would be also possible to apply a line search strategy as presented e. g. in [84]. However, simulations showed that it is sufficient to use a step size of $\mu = {}^{0.99}/_{\|\mathcal{A}\|_2^2}$. This is guaranteed stable step size and the convergence speed does not suffer considerably.

Unique solution

In general, it is very difficult to prove a unique solution to problem (A.5.2) can be acquired by solving (A.5.6) consecutively as we let $\gamma \to 0^+$. However, we use the same approach as in [58], where for an equivalent sparse problem such a convergence was proven not for a noisy but for an equivalent noiseless optimization problem. In [58] it was shown by simulations, that this convergence property also holds in the noisy case. In this work here, we therefore also only show the desired convergence property to a unique solution for an equivalent noiseless optimization problem.

Let $\widetilde{\boldsymbol{L}}$ be the unique solution to

$$\min_{\boldsymbol{L}} \operatorname{rank}(\boldsymbol{L}) \ \text{subject to} \ \mathcal{A}(\boldsymbol{L}) = \boldsymbol{y}, \tag{A.5.26}$$

which is the noiseless equivalent to (A.5.2) and let $\boldsymbol{L}_\gamma$ denote, for a specific γ, a solution to

$$\min_{\boldsymbol{L}} F_\gamma(\boldsymbol{L}) \ \text{subject to} \ \mathcal{A}(\boldsymbol{L}) = \boldsymbol{y}, \tag{A.5.27}$$

which is the noiseless equivalent to (A.5.6). Since (A.5.26) and (A.5.27) are the same optimization problems as discussed in [82], we can directly follow their conclusion concerning a unique solution which states

$$\lim_{\gamma \to 0^+} \boldsymbol{L}_\gamma = \widetilde{\boldsymbol{L}}.$$

This result shows that the solutions $\boldsymbol{L}_\gamma$ of (A.5.27) tend towards the minimum rank solution of (A.5.26) for $\gamma \to 0^+$. We therefore conclude that consecutive solutions of (A.5.6) approximate the solution to (A.5.2).

Convergence

A convergence analysis can be found in [62] which is directly applicable to the approach presented in this chapter. Remark: In [62], the unitarily invariant function property is also stated for functions whose domain is only the positive orthant $\mathbb{R}^+$. This relaxation allows for $F'(\boldsymbol{\sigma})$ to be concave and more important to be differentiable at the origin. This is used in the convergence analysis. If this would be wrong, we could not use the convergence analysis any more. Nevertheless, since Lemma A.2 is also valid for non unitarily invariant functions, the minimization approach used here is still valid. Remark 2: The convergence analysis uses a decreasing step size of $\rho \leftarrow c\rho$ for a $c < 1$. Since we use a static step size, the convergence proof does not hold for us any longer.

Initialization

As pointed out in the graduated non-convexity (GNC) procedure, we initially solve (A.5.6) for $\gamma \to \infty$. Following the same argumentation as stated above, let $\widehat{\boldsymbol{L}}$ be the unique solution to

$$\min_{\boldsymbol{L}} \|\boldsymbol{L}\|_* \ \text{subject to} \ \mathcal{A}(\boldsymbol{L}) = \boldsymbol{y},$$

which is the equivalent NNM noiseless optimization problem to (A.5.3). In [82] it was shown that, for $\gamma \to \infty$, the following statement holds

$$\lim_{\gamma \to \infty} \arg\min_{\boldsymbol{L}} \{ F_\gamma(\boldsymbol{L}) | \, \mathcal{A}(\boldsymbol{L}) = \boldsymbol{y} \} = \arg\min_{\boldsymbol{L}} \{ \|\boldsymbol{L}\|_* | \, \mathcal{A}(\boldsymbol{L}) = \boldsymbol{y} \} = \widehat{\boldsymbol{L}},$$

provided that NNM has a unique solution. We therefore conclude, that (A.5.6), for $\gamma \to \infty$, can be optimized by solving (A.5.3). For solving (A.5.3) we may use the SVT algorithm or the highly improved version turbo singular value thresholding (TSVT) presented in Section 6.1. Furthermore, γ_0 is set to $\sigma_1(\boldsymbol{L}_0) = \|\boldsymbol{L}_0\|_2$, where $\boldsymbol{L}_0$ is the solution of (A.5.3). This is different as done in [82], where γ_0 was set to $8\sigma_1(\boldsymbol{L}_0)$. Since, as explained in [82], $8\sigma_1(\boldsymbol{L}_0)$ is equivalent to the solution obtained by the SVT algorithm, this iteration is not necessary and we start with an already decreased γ_0. The final algorithm is listed in Algorithm 6.4.

A.6. Optimal Step Size Determination for Finding Low-Rank Solutions via Non-Convex Bi-Factored Matrix Factorization

Low-rank matrices appear frequently in signal processing applications e.g. in the field of remote sensing, machine learning, etc. The fundamental problem is to recover an unknown low-rank matrix $\boldsymbol{L} \in \mathbb{C}^{N_1 \times N_2}$ from a limited number of noisy observations of the form

$$\boldsymbol{y} = \mathcal{A}(\boldsymbol{L}) + \boldsymbol{n},$$

where $\mathcal{A} : \mathbb{C}^{N_1 \times N_2} \to \mathbb{C}^M$ is a known affine transformation, $\boldsymbol{y} \in \mathbb{C}^M$ is a measurement vector, and $\boldsymbol{n} \in \mathbb{C}^M$ is additive noise. This problem can be cast as affine rank minimization (ARM) problem:

$$\begin{aligned} \min_{\boldsymbol{L}} & f(\boldsymbol{L}) \coloneqq \frac{1}{2}\|\boldsymbol{y} - \mathcal{A}(\boldsymbol{L})\|_2^2 \\ \text{s.t. } & \operatorname{rank}(\boldsymbol{L}) \leq r, \end{aligned} \tag{A.6.1}$$

where $\|\cdot\|_2$ denotes the ℓ_2 norm [85]. One method to solve (A.6.1) is an iterative procedure called the bi-factored gradient descent (BFGD) algorithm [43]. The algorithm is of the form

$$\boldsymbol{U}_{t+1} = \boldsymbol{U}_t - \mu_{\boldsymbol{U}} \nabla_{\boldsymbol{U}} F(\boldsymbol{U}_t, \boldsymbol{V}_t) \tag{A.6.2}$$

$$\boldsymbol{V}_{t+1} = \boldsymbol{V}_t - \mu_{\boldsymbol{V}} \nabla_{\boldsymbol{V}} F(\boldsymbol{U}_t, \boldsymbol{V}_t), \tag{A.6.3}$$

where the matrix $\boldsymbol{L}$ was factorized as $\boldsymbol{L} = \boldsymbol{U}\boldsymbol{V}^{\mathrm{H}}$ with $\boldsymbol{U} \in \mathbb{C}^{N_1 \times r}$, $\boldsymbol{V} \in \mathbb{C}^{N_2 \times r}$, $\mu_{\boldsymbol{U}}$ and $\mu_{\boldsymbol{V}}$ denote the step sizes, t indicates the iteration step, and $\nabla_{\boldsymbol{Z}}$ denotes the gradient with respect to $\boldsymbol{Z}$. For the specific case of the original objective function $f(\cdot)$ in (A.6.1) being both (restricted) strongly convex and smooth, an additional convex regularizer $g : \mathbb{C}^{r \times r} \to \mathbb{C}$ is required as

$$F(\boldsymbol{U}, \boldsymbol{V}) = f\left(\boldsymbol{U}\boldsymbol{V}^{\mathrm{H}}\right) + \lambda g\left(\boldsymbol{U}^{\mathrm{H}}\boldsymbol{U} - \boldsymbol{V}^{\mathrm{H}}\boldsymbol{V}\right), \tag{A.6.4}$$

where $\lambda \in \mathbb{R}^+$ determines the weighting of the regularization term. The additional regularizer is necessary in order to prevent $\boldsymbol{U}_t$ and $\boldsymbol{V}_t$ obtaining large condition numbers in any iteration step which is required by the BFGD algorithm to ensure convergence. It is required that:

1. g is convex and minimized at zero point i.e. $\nabla g(0) = 0$.
2. The gradient, $\nabla g\left(\boldsymbol{U}^{\mathrm{H}}\boldsymbol{U} - \boldsymbol{V}^{\mathrm{H}}\boldsymbol{V}\right) \in \mathbb{C}^{r \times r}$, is symmetric for any such pair.
3. g is μ_g-strongly convex and L_g-smooth [43].

Of particular interest is the question of how to choose the step sizes $\mu_{\boldsymbol{U}}$ and $\mu_{\boldsymbol{V}}$. The existence of an optimal step width was shown in [43, 63, 53, 64], however, no equations based on parameters known in practice are given. For the special case of $g(\cdot)$ being the quadratic Frobenius norm

$$g(\cdot) = \|\cdot\|_{\mathrm{F}}^2$$

we develop an optimal step size calculation here. The step sizes $\mu_{\boldsymbol{U}}$ and $\mu_{\boldsymbol{V}}$ are chosen such that the objective function (A.6.4) is minimized in every step subject to given gradients

$$\boldsymbol{G}_{\boldsymbol{U}} = \nabla_{\boldsymbol{U}} F(\boldsymbol{U}, \boldsymbol{V}) \tag{A.6.5}$$

$$\boldsymbol{G}_{\boldsymbol{V}} = \nabla_{\boldsymbol{V}} F(\boldsymbol{U}, \boldsymbol{V}) \tag{A.6.6}$$

as such

$$\mu_{\boldsymbol{U}} = \arg\min_{\mu} F(\boldsymbol{U} - \mu \boldsymbol{G}_{\boldsymbol{U}}, \boldsymbol{V}) \tag{A.6.7}$$

$$\mu_{\boldsymbol{V}} = \arg\min_{\mu} F(\boldsymbol{U}, \boldsymbol{V} - \mu \boldsymbol{G}_{\boldsymbol{V}}). \tag{A.6.8}$$

We conduct the minimization by setting the derivatives to zero

$$\frac{\partial F(\boldsymbol{U} - \mu \boldsymbol{G}_{\boldsymbol{U}}, \boldsymbol{V})}{\partial \mu} = 0 \tag{A.6.9}$$

$$\frac{\partial F(\boldsymbol{U}, \boldsymbol{V} - \mu \boldsymbol{G}_{\boldsymbol{V}})}{\partial \mu} = 0. \tag{A.6.10}$$

The derivatives in (A.6.9) and (A.6.10) are third order polynomials in μ and as such have in general three arbitrary roots which may be real positive, real negative, or complex. However, for valid step sizes, a single positive real root is needed. In the following we first illustrate the derivation of (A.6.9) and (A.6.10) regarding $\mu_{\boldsymbol{U}}$ and $\mu_{\boldsymbol{V}}$. Thereafter prove only one unique real positive root exists in the framework of the BFGD algorithm.

Derivative regarding $\mu_{\boldsymbol{U}}$

The regularized objective function (A.6.4) using the Frobenius norm for $g(\cdot)$ is in extended form

$$F(\boldsymbol{U} - \mu \boldsymbol{G}_{\boldsymbol{U}}, \boldsymbol{V}) = \underbrace{\frac{1}{2} \left\| \boldsymbol{y} - \mathcal{A}\left((\boldsymbol{U} - \mu \boldsymbol{G}_{\boldsymbol{U}}) \boldsymbol{V}^{\mathrm{H}} \right) \right\|_2^2}_{D_{\boldsymbol{U}}} + \underbrace{\lambda \left\| (\boldsymbol{U} - \mu \boldsymbol{G}_{\boldsymbol{U}})^{\mathrm{H}} (\boldsymbol{U} - \mu \boldsymbol{G}_{\boldsymbol{U}}) - \boldsymbol{V}^{\mathrm{H}} \boldsymbol{V} \right\|_{\mathrm{F}}^2}_{S_{\boldsymbol{U}}} \tag{A.6.11}$$

and its gradient is

$$\boldsymbol{G}_{\boldsymbol{U}} = -\mathcal{A}^*(\tilde{\boldsymbol{y}}) \boldsymbol{V} + 4\lambda \boldsymbol{U} \boldsymbol{X} \tag{A.6.12}$$

$$\tilde{\boldsymbol{y}} = \boldsymbol{y} - \mathcal{A}\left(\boldsymbol{U} \boldsymbol{V}^{\mathrm{H}} \right) \tag{A.6.13}$$

$$\boldsymbol{X} = \boldsymbol{U}^{\mathrm{H}} \boldsymbol{U} - \boldsymbol{V}^{\mathrm{H}} \boldsymbol{V}, \tag{A.6.14}$$

where $\mathcal{A}^{\mathrm{H}}(\cdot)$ is the Hermitian adjoint operator of $\mathcal{A}$. We first treat the data fidelity term $D_{\boldsymbol{U}}$ of (A.6.11), which we simplify by use of (A.6.13) to

$$\begin{aligned} D_{\boldsymbol{U}} &= \frac{1}{2}\left\|\boldsymbol{y} - \mathcal{A}\left(\left(\boldsymbol{U} - \mu\boldsymbol{G}_{\boldsymbol{U}}\right)\boldsymbol{V}^{\mathrm{H}}\right)\right\|_2^2 = \frac{1}{2}\left\|\boldsymbol{y} - \mathcal{A}\left(\boldsymbol{U}\boldsymbol{V}^{\mathrm{H}}\right) + \mu\mathcal{A}\left(\boldsymbol{G}_{\boldsymbol{U}}\boldsymbol{V}^{\mathrm{H}}\right)\right\|_2^2 \\ &= \frac{1}{2}\left\|\tilde{\boldsymbol{y}} + \mu\mathcal{A}\left(\boldsymbol{G}_{\boldsymbol{U}}\boldsymbol{V}^{\mathrm{H}}\right)\right\|_2^2 \end{aligned} \tag{A.6.15}$$

Its derivative is

$$\begin{aligned} \frac{\partial D_{\boldsymbol{U}}}{\partial\mu} &= \frac{\partial}{\partial\mu}\frac{1}{2}\left(\tilde{\boldsymbol{y}}^{\mathrm{H}}\tilde{\boldsymbol{y}} + 2\mu\,\mathrm{Re}\left\{\tilde{\boldsymbol{y}}^{\mathrm{H}}\mathcal{A}\left(\boldsymbol{G}_{\boldsymbol{U}}\boldsymbol{V}^{\mathrm{H}}\right)\right\} + \mu^2\left\|\mathcal{A}\left(\boldsymbol{G}_{\boldsymbol{U}}\boldsymbol{V}^{\mathrm{H}}\right)\right\|_2^2\right) \\ &= \mathrm{Re}\underbrace{\left\{\tilde{\boldsymbol{y}}^{\mathrm{H}}\mathcal{A}\left(\boldsymbol{G}_{\boldsymbol{U}}\boldsymbol{V}^{\mathrm{H}}\right)\right\}}_{T_0} + \mu\left\|\mathcal{A}\left(\boldsymbol{G}_{\boldsymbol{U}}\boldsymbol{V}^{\mathrm{H}}\right)\right\|_2^2, \end{aligned} \tag{A.6.16}$$

where we may simplify the term T_0 further by utilizing the sum notation as

$$T_0 = \tilde{\boldsymbol{y}}^{\mathrm{H}}\mathcal{A}\left(\boldsymbol{G}_{\boldsymbol{U}}\boldsymbol{V}^{\mathrm{H}}\right) \Leftrightarrow \tilde{y}_i^* a_{ijb}^* v_{br}^* g_{\boldsymbol{U}jr} \tag{A.6.17}$$

and noticing that (A.6.12) in sum notation can be expressed as

$$\begin{aligned} \left(\boldsymbol{G}_{\boldsymbol{U}}\right)_{jr} &= -\left(\mathcal{A}^*\left(\tilde{\boldsymbol{y}}\right)\boldsymbol{V}\right)_{jr} + 4\lambda\left(\boldsymbol{U}\boldsymbol{X}\right)_{jr} \\ &\triangleq g_{\boldsymbol{U}jr} = -a_{ijp}\tilde{y}_i v_{pr} + 4\lambda u_{jm}x_{mr}, \end{aligned} \tag{A.6.18}$$

where $g_{\boldsymbol{U}jr} = \left(\boldsymbol{G}_{\boldsymbol{U}}\right)_{jr}$ is the entry of $\boldsymbol{G}_{\boldsymbol{U}}$ at index (j,r). From (A.6.18) we can isolate the term

$$\tilde{y}_i a_{ijp} v_{pr} = -g_{\boldsymbol{U}jr} + 4\lambda u_{jm}x_{mr}$$

and insert it into (A.6.17) as

$$\begin{aligned} T_0 &= \left(-g_{\boldsymbol{U}jr}^* + 4\lambda u_{jm}^* x_{mr}^*\right) g_{\boldsymbol{U}jr} \\ &= -g_{\boldsymbol{U}jr}^* g_{\boldsymbol{U}jr} + 4\lambda u_{jm}^* x_{mr}^* g_{\boldsymbol{U}jr} \\ &\triangleq -\left\|\boldsymbol{G}_{\boldsymbol{U}}\right\|_{\mathrm{F}}^2 + 4\lambda\left\langle\boldsymbol{U}\boldsymbol{X}, \boldsymbol{G}_{\boldsymbol{U}}\right\rangle_{\mathrm{F}} \\ &= -\left\|\boldsymbol{G}_{\boldsymbol{U}}\right\|_{\mathrm{F}}^2 + 4\lambda\left\langle\boldsymbol{X}, \boldsymbol{U}^{\mathrm{H}}\boldsymbol{G}_{\boldsymbol{U}}\right\rangle_{\mathrm{F}}, \end{aligned} \tag{A.6.19}$$

where $\langle\cdot,\cdot\rangle_{\mathrm{F}}$ denotes the Frobenius product. Inserting (A.6.19) into (A.6.16) yields

$$\frac{\partial D_{\boldsymbol{U}}}{\partial\mu} = -\left\|\boldsymbol{G}_{\boldsymbol{U}}\right\|_{\mathrm{F}}^2 + 4\lambda\,\mathrm{Re}\left\{\left\langle\boldsymbol{X}, \boldsymbol{U}^{\mathrm{H}}\boldsymbol{G}_{\boldsymbol{U}}\right\rangle_{\mathrm{F}}\right\} + \mu\left\|\mathcal{A}\left(\boldsymbol{G}_{\boldsymbol{U}}\boldsymbol{V}^{\mathrm{H}}\right)\right\|_2^2. \tag{A.6.20}$$

Next we treat the scale difference term $S_{\boldsymbol{U}}$ of (A.6.11), which we simplify as

$$\begin{aligned} S_{\boldsymbol{U}} &= \left\|\left(\boldsymbol{U} - \mu\boldsymbol{G}_{\boldsymbol{U}}\right)^{\mathrm{H}}\left(\boldsymbol{U} - \mu\boldsymbol{G}_{\boldsymbol{U}}\right) - \boldsymbol{V}^{\mathrm{H}}\boldsymbol{V}\right\|_{\mathrm{F}}^2 = \left\|\boldsymbol{U}'^{\mathrm{H}}\boldsymbol{U}' - \boldsymbol{V}^{\mathrm{H}}\boldsymbol{V}\right\|_{\mathrm{F}}^2 \\ &= \left\|\boldsymbol{X}'\right\|_{\mathrm{F}}^2, \end{aligned} \tag{A.6.21}$$

where

$$\boldsymbol{U}' = \boldsymbol{U} - \mu \boldsymbol{G}_{\boldsymbol{U}}.$$

From (A.6.21) and (A.6.14) we also find

$$\boldsymbol{X}' = \boldsymbol{X} - \mu \left(\boldsymbol{U}^{\mathrm{H}} \boldsymbol{G}_{\boldsymbol{U}} + \boldsymbol{G}_{\boldsymbol{U}}^{\mathrm{H}} \boldsymbol{U} \right) + \mu^2 \boldsymbol{G}_{\boldsymbol{U}}^{\mathrm{H}} \boldsymbol{G}_{\boldsymbol{U}}. \tag{A.6.22}$$

At this point we introduce some abbreviations to further simplify (A.6.22) as

$$\boldsymbol{A} = \boldsymbol{G}_{\boldsymbol{U}}^{\mathrm{H}} \boldsymbol{U} + \boldsymbol{U}^{\mathrm{H}} \boldsymbol{G}_{\boldsymbol{U}} \tag{A.6.23}$$

$$\boldsymbol{B} = \boldsymbol{G}_{\boldsymbol{U}}^{\mathrm{H}} \boldsymbol{G}_{\boldsymbol{U}}, \tag{A.6.24}$$

so

$$\boldsymbol{X}' = \boldsymbol{X} - \mu \boldsymbol{A} + \mu^2 \boldsymbol{B} \tag{A.6.25}$$

Due to a better handling of the Frobenius norm we we again utilize the sum notation

$$\left(\boldsymbol{X}' \right)_{ij} = x'_{ij} = u'^{*}_{si} u'_{sj} - v^{*}_{ti} v_{tj}$$

to find the derivative as

$$\begin{aligned} \frac{\partial S_{\boldsymbol{U}}}{\partial \mu} &= \lambda \frac{\partial}{\partial \mu} \left\| \boldsymbol{X}' \right\|_{\mathrm{F}}^2 = \lambda \frac{\partial x'^{*}_{ij} x'_{ij}}{\partial \mu} \\ &= \lambda \left(\frac{\partial x'^{*}_{ij}}{\partial \mu} x'_{ij} + \frac{\partial x'_{ij}}{\partial \mu} x'^{*}_{ij} \right) \\ &= 2\lambda \operatorname{Re} \left\{ \frac{\partial x'_{ij}}{\partial \mu} x'^{*}_{ij} \right\} \end{aligned} \tag{A.6.26}$$

since

$$\frac{\partial x'^{*}_{ij}}{\partial \mu} = \left(\frac{\partial x'_{ij}}{\partial \mu} \right)^{*}$$

because $\mu \in \mathbb{R}$. The required derivative is

$$\begin{aligned} \frac{\partial x'_{ij}}{\partial \mu} &= \frac{\partial u'^{*}_{si} u'_{sj}}{\partial \mu} = \frac{\partial \left(\boldsymbol{U}^{*} - \mu \boldsymbol{G}_{\boldsymbol{U}}^{*} \right)_{si} \left(\boldsymbol{U} - \mu \boldsymbol{G}_{\boldsymbol{U}} \right)_{sj}}{\partial \mu} \\ &= \frac{\partial \left(\boldsymbol{U}^{*} - \mu \boldsymbol{G}_{\boldsymbol{U}}^{*} \right)_{si}}{\partial \mu} \left(\boldsymbol{U} - \mu \boldsymbol{G}_{\boldsymbol{U}} \right)_{sj} + \left(\boldsymbol{U}^{*} - \mu \boldsymbol{G}_{\boldsymbol{U}}^{*} \right)_{si} \frac{\partial \left(\boldsymbol{U} - \mu \boldsymbol{G}_{\boldsymbol{U}} \right)_{sj}}{\partial \mu} \\ &= - \left(\boldsymbol{G}_{\boldsymbol{U}}^{*} \right)_{si} \left(\boldsymbol{U} - \mu \boldsymbol{G}_{\boldsymbol{U}} \right)_{sj} - \left(\boldsymbol{U}^{*} - \mu \boldsymbol{G}_{\boldsymbol{U}}^{*} \right)_{si} \left(\boldsymbol{G}_{\boldsymbol{U}}^{*} \right)_{sj} \\ &= - \left(\boldsymbol{G}_{\boldsymbol{U}}^{\mathrm{H}} \left(\boldsymbol{U} - \mu \boldsymbol{G}_{\boldsymbol{U}} \right) \right)_{ij} - \left(\left(\boldsymbol{U} - \mu \boldsymbol{G}_{\boldsymbol{U}} \right)^{\mathrm{H}} \boldsymbol{G}_{\boldsymbol{U}} \right)_{ij} \\ &= \left(-\boldsymbol{G}_{\boldsymbol{U}}^{\mathrm{H}} \left(\boldsymbol{U} - \mu \boldsymbol{G}_{\boldsymbol{U}} \right) - \left(\boldsymbol{U} - \mu \boldsymbol{G}_{\boldsymbol{U}} \right)^{\mathrm{H}} \boldsymbol{G}_{\boldsymbol{U}} \right)_{ij} \\ &= \left(2\mu \boldsymbol{G}_{\boldsymbol{U}}^{\mathrm{H}} \boldsymbol{G}_{\boldsymbol{U}} - \boldsymbol{G}_{\boldsymbol{U}}^{\mathrm{H}} \boldsymbol{U} - \boldsymbol{U}^{\mathrm{H}} \boldsymbol{G}_{\boldsymbol{U}} \right)_{ij} \\ &= \left(2\mu \boldsymbol{B} - \boldsymbol{A} \right)_{ij}, \end{aligned} \tag{A.6.27}$$

where at the last step we inserted the abbreviations (A.6.23) and (A.6.24). Inserting (A.6.27) into (A.6.26) yields

$$\begin{aligned}\frac{\partial S}{\partial \mu} &= 2\lambda \operatorname{Re}\left\{x_{ij}'^{*}\left(2\mu\boldsymbol{B}-\boldsymbol{A}\right)_{ij}\right\} \\ &= 2\lambda \operatorname{Re}\left\{\left\langle \boldsymbol{X}', 2\mu\boldsymbol{B}-\boldsymbol{A}\right\rangle_{\mathrm{F}}\right\}. \end{aligned} \tag{A.6.28}$$

By combining (A.6.20) and (A.6.28) we have in total

$$\begin{aligned}\frac{\partial F\left(\boldsymbol{U}-\mu\boldsymbol{G}_{\boldsymbol{U}},\boldsymbol{V}\right)}{\partial \mu} = \frac{\partial D_{\boldsymbol{U}}}{\partial \mu}+\frac{\partial S_{\boldsymbol{U}}}{\partial \mu} &= -\left\|\boldsymbol{G}_{\boldsymbol{U}}\right\|_{\mathrm{F}}^{2}+\mu\left\|\mathcal{A}\left(\boldsymbol{G}_{\boldsymbol{U}}\boldsymbol{V}^{\mathrm{H}}\right)\right\|_{2}^{2} \\ &\quad+\underbrace{4\lambda \operatorname{Re}\left\{\left\langle \boldsymbol{X}, \boldsymbol{U}^{\mathrm{H}}\boldsymbol{G}_{\boldsymbol{U}}\right\rangle_{\mathrm{F}}\right\}+2\lambda \operatorname{Re}\left\{\left\langle \boldsymbol{X}', 2\mu\boldsymbol{B}-\boldsymbol{A}\right\rangle_{\mathrm{F}}\right\}}_{T_1}. \end{aligned} \tag{A.6.29}$$

We may further simplify the term T_1 as

$$\begin{aligned}T_1 &= 4\lambda \operatorname{Re}\left\{\left\langle \boldsymbol{X}, \boldsymbol{U}^{\mathrm{H}}\boldsymbol{G}_{\boldsymbol{U}}\right\rangle_{\mathrm{F}}\right\}+2\lambda \operatorname{Re}\left\{\left\langle \boldsymbol{X}', 2\mu\boldsymbol{B}-\boldsymbol{A}\right\rangle_{\mathrm{F}}\right\} \\ &= 2\lambda \operatorname{Re}\left\{2\left\langle \boldsymbol{X}, \boldsymbol{U}^{\mathrm{H}}\boldsymbol{G}_{\boldsymbol{U}}\right\rangle_{\mathrm{F}}+\left\langle \boldsymbol{X}', 2\mu\boldsymbol{B}-\boldsymbol{A}\right\rangle_{\mathrm{F}}\right\} \end{aligned}$$

and insert (A.6.22) as

$$\begin{aligned}T_1 &= 2\lambda \operatorname{Re}\left\{2\left\langle \boldsymbol{X}, \boldsymbol{U}^{\mathrm{H}}\boldsymbol{G}_{\boldsymbol{U}}\right\rangle_{\mathrm{F}}+\left\langle \boldsymbol{X}', 2\mu\boldsymbol{B}-\boldsymbol{A}\right\rangle_{\mathrm{F}}\right\} \\ &= 2\lambda \operatorname{Re}\big\{2\left\langle \boldsymbol{X}, \boldsymbol{U}^{\mathrm{H}}\boldsymbol{G}_{\boldsymbol{U}}\right\rangle_{\mathrm{F}}+\underbrace{\left\langle \boldsymbol{X}-\mu\boldsymbol{A}+\mu^{2}\boldsymbol{B}, 2\mu\boldsymbol{B}-\boldsymbol{A}\right\rangle_{\mathrm{F}}}_{T_2}\big\}. \end{aligned} \tag{A.6.30}$$

Next we expand term T_2 and further simplify it which yields

$$\begin{aligned}T_2 &= \left\langle \boldsymbol{X}-\mu\boldsymbol{A}+\mu^{2}\boldsymbol{B}, 2\mu\boldsymbol{B}-\boldsymbol{A}\right\rangle_{\mathrm{F}} \\ &= 2\mu^{3}\left\|\boldsymbol{B}\right\|_{\mathrm{F}}^{2}-\mu^{2}\underbrace{\left(2\left\langle \boldsymbol{A}, \boldsymbol{B}\right\rangle_{\mathrm{F}}+\left\langle \boldsymbol{B}, \boldsymbol{A}\right\rangle_{\mathrm{F}}\right)}_{T_3}+\mu\left(2\left\langle \boldsymbol{X}, \boldsymbol{B}\right\rangle_{\mathrm{F}}+\left\|\boldsymbol{A}\right\|_{\mathrm{F}}^{2}\right)-\left\langle \boldsymbol{X}, \boldsymbol{A}\right\rangle_{\mathrm{F}}. \end{aligned} \tag{A.6.31}$$

The term T_3 can be combined as

$$\begin{aligned}T_3 &= 2\left\langle \boldsymbol{A}, \boldsymbol{B}\right\rangle_{\mathrm{F}}+\left\langle \boldsymbol{B}, \boldsymbol{A}\right\rangle_{\mathrm{F}} \\ &= 3\operatorname{Re}\left\{\left\langle \boldsymbol{A}, \boldsymbol{B}\right\rangle_{\mathrm{F}}\right\}+\mathrm{j}\operatorname{Im}\left\{\left\langle \boldsymbol{A}, \boldsymbol{B}\right\rangle_{\mathrm{F}}\right\}, \end{aligned} \tag{A.6.32}$$

where the imaginary part can be skipped since only the real part is taken in (A.6.30). Inserting (A.6.31) and (A.6.32) into (A.6.30) yields

$$T_1 = 2\lambda \operatorname{Re}\big\{2\mu^{3}\left\|\boldsymbol{B}\right\|_{\mathrm{F}}^{2}-\mu^{2}3\left\langle \boldsymbol{A}, \boldsymbol{B}\right\rangle_{\mathrm{F}}+\mu\left(2\left\langle \boldsymbol{X}, \boldsymbol{B}\right\rangle_{\mathrm{F}}+\left\|\boldsymbol{A}\right\|_{\mathrm{F}}^{2}\right)+\underbrace{2\left\langle \boldsymbol{X}, \boldsymbol{U}^{\mathrm{H}}\boldsymbol{G}_{\boldsymbol{U}}\right\rangle_{\mathrm{F}}-\left\langle \boldsymbol{X}, \boldsymbol{A}\right\rangle_{\mathrm{F}}}_{T_4}\big\}. \tag{A.6.33}$$

Finally we can combine term T_4 as

$$\begin{aligned} T_4 &= 2\left\langle \boldsymbol{X}, \boldsymbol{U}^{\mathrm{H}}\boldsymbol{G}_{\boldsymbol{U}}\right\rangle_{\mathrm{F}} - \langle \boldsymbol{X}, \boldsymbol{A}\rangle_{\mathrm{F}} \\ &= 2\left\langle \boldsymbol{X}, \boldsymbol{U}^{\mathrm{H}}\boldsymbol{G}_{\boldsymbol{U}}\right\rangle_{\mathrm{F}} - \left\langle \boldsymbol{X}, \boldsymbol{G}_{\boldsymbol{U}}^{\mathrm{H}}\boldsymbol{U} + \boldsymbol{U}^{\mathrm{H}}\boldsymbol{G}_{\boldsymbol{U}}\right\rangle_{\mathrm{F}} \\ &= \left\langle \boldsymbol{X}, \boldsymbol{U}^{\mathrm{H}}\boldsymbol{G}_{\boldsymbol{U}} - \boldsymbol{G}_{\boldsymbol{U}}^{\mathrm{H}}\boldsymbol{U}\right\rangle_{\mathrm{F}} \\ &= \langle \boldsymbol{X}, \boldsymbol{C}\rangle_{\mathrm{F}}\,, \end{aligned} \tag{A.6.34}$$

where in addition to (A.6.23) and (A.6.23) the abbreviation

$$\boldsymbol{C} = \boldsymbol{U}^{\mathrm{H}}\boldsymbol{G}_{\boldsymbol{U}} - \boldsymbol{G}_{\boldsymbol{U}}^{\mathrm{H}}\boldsymbol{U} \tag{A.6.35}$$

was introduced. Combining (A.6.34), (A.6.33), and (A.6.29) yields the final form

$$\begin{aligned} \frac{\partial F\left(\boldsymbol{U} - \mu\boldsymbol{G}_{\boldsymbol{U}}, \boldsymbol{V}\right)}{\partial \mu} = &- \left\|\boldsymbol{G}_{\boldsymbol{U}}\right\|_{\mathrm{F}}^2 + 2\lambda\,\mathrm{Re}\Big\{2\mu^3\left\|\boldsymbol{B}\right\|_{\mathrm{F}}^2 - 3\mu^2\left\langle \boldsymbol{A}, \boldsymbol{B}\right\rangle_{\mathrm{F}} \\ &+ \mu\left(2\left\langle \boldsymbol{X}, \boldsymbol{B}\right\rangle_{\mathrm{F}} + \left\|\boldsymbol{A}\right\|_{\mathrm{F}}^2 + \frac{1}{2\lambda}\left\|\mathcal{A}\left(\boldsymbol{G}_{\boldsymbol{U}}\boldsymbol{V}^{\mathrm{H}}\right)\right\|_2^2\right) + \left\langle \boldsymbol{X}, \boldsymbol{C}\right\rangle_{\mathrm{F}}\Big\}. \end{aligned} \tag{A.6.36}$$

Derivative regarding $\mu_{\boldsymbol{V}}$

The derivative regarding $\mu_{\boldsymbol{V}}$ from (A.6.10) is computed in an analogous manner to that of $\mu_{\boldsymbol{U}}$ from (A.6.9), however, some minor differences exist. Therefore the derivation is again shown step by step. The regularized objective function (A.6.4) using the Frobenius norm for $g\left(\cdot\right)$ is in extended form

$$F\left(\boldsymbol{U}, \boldsymbol{V} - \mu\boldsymbol{G}_{\boldsymbol{V}}\right) = \underbrace{\frac{1}{2}\left\|\boldsymbol{y} - \mathcal{A}\left(\boldsymbol{U}\left(\boldsymbol{V} - \mu\boldsymbol{G}_{\boldsymbol{V}}\right)^{\mathrm{H}}\right)\right\|_2^2}_{D_{\boldsymbol{V}}} + \underbrace{\lambda\left\|\boldsymbol{U}^{\mathrm{H}}\boldsymbol{U} - \left(\boldsymbol{V} - \mu\boldsymbol{G}_{\boldsymbol{V}}\right)^{\mathrm{H}}\left(\boldsymbol{V} - \mu\boldsymbol{G}_{\boldsymbol{V}}\right)\right\|_{\mathrm{F}}^2}_{S_{\boldsymbol{V}}} \tag{A.6.37}$$

and its gradient is

$$\boldsymbol{G}_{\boldsymbol{V}} = -\left(\mathcal{A}^*\left(\tilde{\boldsymbol{y}}\right)\right)^{\mathrm{H}}\boldsymbol{U} - 4\lambda\boldsymbol{V}\boldsymbol{X}. \tag{A.6.38}$$

We first treat the data fidelity term $D_{\boldsymbol{V}}$ of (A.6.37), which we simplify by use of (A.6.38) as

$$\begin{aligned} D_{\boldsymbol{V}} &= \frac{1}{2}\left\|\boldsymbol{y} - \mathcal{A}\left(\boldsymbol{U}\left(\boldsymbol{V} - \mu\boldsymbol{G}_{\boldsymbol{V}}\right)^{\mathrm{H}}\right)\right\|_2^2 = \frac{1}{2}\left\|\boldsymbol{y} - \mathcal{A}\left(\boldsymbol{U}\boldsymbol{V}^{\mathrm{H}}\right) + \mu\mathcal{A}\left(\boldsymbol{U}\boldsymbol{G}_{\boldsymbol{V}}^{\mathrm{H}}\right)\right\|_2^2 \\ &= \frac{1}{2}\left\|\tilde{\boldsymbol{y}} + \mu\mathcal{A}\left(\boldsymbol{U}\boldsymbol{G}_{\boldsymbol{V}}^{\mathrm{H}}\right)\right\|_2^2 \end{aligned}$$

Its derivative is

$$\begin{aligned} \frac{\partial D_{\boldsymbol{V}}}{\partial \mu} &= \frac{\partial}{\partial \mu}\frac{1}{2}\left(\tilde{\boldsymbol{y}}^{\mathrm{H}}\tilde{\boldsymbol{y}} + 2\mu\,\mathrm{Re}\left\{\tilde{\boldsymbol{y}}^{\mathrm{H}}\mathcal{A}\left(\boldsymbol{U}\boldsymbol{G}_{\boldsymbol{V}}^{\mathrm{H}}\right)\right\} + \mu^2\left\|\mathcal{A}\left(\boldsymbol{U}\boldsymbol{G}_{\boldsymbol{V}}^{\mathrm{H}}\right)\right\|_2^2\right) \\ &= \underbrace{\mathrm{Re}\left\{\tilde{\boldsymbol{y}}^{\mathrm{H}}\mathcal{A}\left(\boldsymbol{U}\boldsymbol{G}_{\boldsymbol{V}}^{\mathrm{H}}\right)\right\}}_{T_5} + \mu\left\|\mathcal{A}\left(\boldsymbol{U}\boldsymbol{G}_{\boldsymbol{V}}^{\mathrm{H}}\right)\right\|_2^2. \end{aligned} \tag{A.6.39}$$

We may simplify the term T_5 in (A.6.39) further as

$$T_5 = \tilde{\boldsymbol{y}}^{\mathrm{H}} \mathcal{A}\left(\boldsymbol{U}\boldsymbol{G}_{\boldsymbol{V}}^{\mathrm{H}}\right) \Leftrightarrow \tilde{y}_i^* a_{iok}^* u_{or} g_{\boldsymbol{V}kr}^* \tag{A.6.40}$$

and noticing that (A.6.38) in sum notation can be expressed as

$$\begin{aligned}(\boldsymbol{G}_{\boldsymbol{V}})_{kr} &= -\left(\left(\mathcal{A}^*\left(\tilde{\boldsymbol{y}}\right)\right)^{\mathrm{H}} \boldsymbol{U}\right)_{kr} - 4\lambda \left(\boldsymbol{V}\boldsymbol{X}\right)_{kr} \\ &\triangleq g_{\boldsymbol{V}kr} = -a_{iok}^* \tilde{y}_i^* u_{or} - 4\lambda v_{km} x_{mr}.\end{aligned} \tag{A.6.41}$$

From (A.6.41) we can isolate the term

$$\tilde{y^*}_i a_{iok}^* u_{or} = -g_{\boldsymbol{V}kr} - 4\lambda v_{km} x_{mr}$$

and insert it into (A.6.40) as

$$\begin{aligned}T_5 &= \left(-g_{\boldsymbol{V}kr} - 4\lambda v_{km} x_{mr}\right) g_{\boldsymbol{V}kr}^* \\ &= -g_{\boldsymbol{V}kr}^* g_{\boldsymbol{V}kr} - 4\lambda g_{\boldsymbol{V}kr}^* v_{km} x_{mr} \\ &\triangleq -\left\|\boldsymbol{G}_{\boldsymbol{V}}\right\|_{\mathrm{F}}^2 - 4\lambda \left\langle \boldsymbol{G}_{\boldsymbol{V}}, \boldsymbol{V}\boldsymbol{X}\right\rangle_{\mathrm{F}} \\ &= -\left\|\boldsymbol{G}_{\boldsymbol{V}}\right\|_{\mathrm{F}}^2 - 4\lambda \left\langle \boldsymbol{V}^{\mathrm{H}}\boldsymbol{G}_{\boldsymbol{V}}, \boldsymbol{X}\right\rangle_{\mathrm{F}}.\end{aligned} \tag{A.6.42}$$

Inserting (A.6.42) into (A.6.39) yields

$$\frac{\partial D_{\boldsymbol{V}}}{\partial \mu} = -\left\|\boldsymbol{G}_{\boldsymbol{V}}\right\|_{\mathrm{F}}^2 - 4\lambda \operatorname{Re}\left\{\left\langle \boldsymbol{V}^{\mathrm{H}}\boldsymbol{G}_{\boldsymbol{V}}, \boldsymbol{X}\right\rangle_{\mathrm{F}}\right\} + \mu \left\|\mathcal{A}\left(\boldsymbol{U}\boldsymbol{G}_{\boldsymbol{V}}^{\mathrm{H}}\right)\right\|_2^2. \tag{A.6.43}$$

Next we treat the scale difference term $S_{\boldsymbol{V}}$ of (A.6.37), which we simplify as

$$\begin{aligned}S_{\boldsymbol{V}} &= \left\|\boldsymbol{U}^{\mathrm{H}}\boldsymbol{U} - \left(\boldsymbol{V} - \mu\boldsymbol{G}_{\boldsymbol{V}}\right)^{\mathrm{H}}\left(\boldsymbol{V} - \mu\boldsymbol{G}_{\boldsymbol{V}}\right)\right\|_{\mathrm{F}}^2 = \left\|\boldsymbol{U}^{\mathrm{H}}\boldsymbol{U} - \boldsymbol{V}'^{\mathrm{H}}\boldsymbol{V}'\right\|_{\mathrm{F}}^2 \\ &= \left\|\boldsymbol{X}''\right\|_{\mathrm{F}}^2,\end{aligned} \tag{A.6.44}$$

where

$$\boldsymbol{V}' = \boldsymbol{V} - \mu\boldsymbol{G}_{\boldsymbol{V}}.$$

From (A.6.44) and (A.6.14) we also find

$$\boldsymbol{X}'' = \boldsymbol{X} + \mu\left(\boldsymbol{G}_{\boldsymbol{V}}^{\mathrm{H}}\boldsymbol{V} + \boldsymbol{V}^{\mathrm{H}}\boldsymbol{G}_{\boldsymbol{V}}\right) - \mu^2 \boldsymbol{G}_{\boldsymbol{V}}^{\mathrm{H}}\boldsymbol{G}_{\boldsymbol{V}}. \tag{A.6.45}$$

At this point we introduce some abbreviations to further simplify (A.6.45) as

$$\boldsymbol{D} = \boldsymbol{G}_{\boldsymbol{V}}^{\mathrm{H}}\boldsymbol{V} + \boldsymbol{V}^{\mathrm{H}}\boldsymbol{G}_{\boldsymbol{V}} \tag{A.6.46}$$

$$\boldsymbol{E} = \boldsymbol{G}_{\boldsymbol{V}}^{\mathrm{H}}\boldsymbol{G}_{\boldsymbol{V}}, \tag{A.6.47}$$

so

$$\boldsymbol{X}'' = \boldsymbol{X} + \mu\boldsymbol{D} - \mu^2\boldsymbol{E}. \tag{A.6.48}$$

Due to a better handling of the Frobenius norm we use the sum notation

$$\left(\boldsymbol{X}''\right)_{ij} = x''_{ij} = u^*_{si} u_{sj} - v'^*_{ti} v'_{tj},$$

where

$$v'_{xy} = \left(\boldsymbol{V}'\right)_{xy},$$

to find the derivative as

$$\begin{aligned}
\frac{\partial S_{\boldsymbol{V}}}{\partial \mu} &= \lambda \frac{\partial}{\partial \mu} \left\| \boldsymbol{X}'' \right\|_{\mathrm{F}}^2 = \lambda \frac{\partial x''^*_{ij} x''_{ij}}{\partial \mu} \\
&= \lambda \left(\frac{\partial x''^*_{ij}}{\partial \mu} x''_{ij} + \frac{\partial x''_{ij}}{\partial \mu} x''^*_{ij} \right) \\
&= 2\lambda \operatorname{Re} \left\{ \frac{\partial x''_{ij}}{\partial \mu} x''^*_{ij} \right\}
\end{aligned} \tag{A.6.49}$$

since

$$\frac{\partial x''^*_{ij}}{\partial \mu} = \left(\frac{\partial x''_{ij}}{\partial \mu} \right)^*$$

because $\mu \in \mathbb{R}$. The required derivative is

$$\begin{aligned}
\frac{\partial x''_{ij}}{\partial \mu} &= -\frac{\partial v'^*_{ti} v'_{tj}}{\partial \mu} = -\frac{\partial \left(\boldsymbol{V}^* - \mu \boldsymbol{G}^*_{\boldsymbol{V}}\right)_{ti} \left(\boldsymbol{V} - \mu \boldsymbol{G}_{\boldsymbol{V}}\right)_{tj}}{\partial \mu} \\
&= -\frac{\partial \left(\boldsymbol{V}^* - \mu \boldsymbol{G}^*_{\boldsymbol{V}}\right)_{ti}}{\partial \mu} \left(\boldsymbol{V} - \mu \boldsymbol{G}_{\boldsymbol{V}}\right)_{tj} - \left(\boldsymbol{V}^* - \mu \boldsymbol{G}^*_{\boldsymbol{V}}\right)_{ti} \frac{\partial \left(\boldsymbol{V} - \mu \boldsymbol{G}_{\boldsymbol{V}}\right)_{tj}}{\partial \mu} \\
&= \left(\boldsymbol{G}^*_{\boldsymbol{V}}\right)_{ti} \left(\boldsymbol{V} - \mu \boldsymbol{G}_{\boldsymbol{V}}\right)_{tj} + \left(\boldsymbol{V}^* - \mu \boldsymbol{G}^*_{\boldsymbol{V}}\right)_{ti} \left(\boldsymbol{G}^*_{\boldsymbol{V}}\right)_{tj} \\
&= \left(\boldsymbol{G}^{\mathrm{H}}_{\boldsymbol{V}} \left(\boldsymbol{V} - \mu \boldsymbol{G}_{\boldsymbol{V}}\right)\right)_{ij} + \left(\left(\boldsymbol{V} - \mu \boldsymbol{G}_{\boldsymbol{V}}\right)^{\mathrm{H}} \boldsymbol{G}_{\boldsymbol{V}} \right)_{ij} \\
&= \left(\boldsymbol{G}^{\mathrm{H}}_{\boldsymbol{V}} \left(\boldsymbol{V} - \mu \boldsymbol{G}_{\boldsymbol{V}}\right) + \left(\boldsymbol{V} - \mu \boldsymbol{G}_{\boldsymbol{V}}\right)^{\mathrm{H}} \boldsymbol{G}_{\boldsymbol{V}} \right)_{ij} \\
&= \left(-2\mu \boldsymbol{G}^{\mathrm{H}}_{\boldsymbol{V}} \boldsymbol{G}_{\boldsymbol{V}} + \boldsymbol{G}^{\mathrm{H}}_{\boldsymbol{V}} \boldsymbol{V} + \boldsymbol{V}^{\mathrm{H}} \boldsymbol{G}_{\boldsymbol{V}} \right)_{ij} \\
&= \left(-2\mu \boldsymbol{E} + \boldsymbol{D}\right)_{ij},
\end{aligned} \tag{A.6.50}$$

where at the last step we inserted the abbreviations (A.6.46) and (A.6.47). Inserting (A.6.50) into (A.6.49) yields

$$\begin{aligned}
\frac{\partial S_{\boldsymbol{V}}}{\partial \mu} &= 2\lambda \operatorname{Re} \left\{ x''^*_{ij} \left(-2\mu \boldsymbol{E} + \boldsymbol{D}\right)_{ij} \right\} \\
&= 2\lambda \operatorname{Re} \left\{ \left\langle \boldsymbol{X}'', -2\mu \boldsymbol{E} + \boldsymbol{D} \right\rangle_{\mathrm{F}} \right\}.
\end{aligned} \tag{A.6.51}$$

By combining (A.6.43) and (A.6.51) we have in total

$$\begin{aligned}
\frac{\partial F\left(\boldsymbol{U}, \boldsymbol{V} - \mu \boldsymbol{G}_{\boldsymbol{V}}\right)}{\partial \mu} = \frac{\partial D_{\boldsymbol{V}}}{\partial \mu} + \frac{\partial S_{\boldsymbol{V}}}{\partial \mu} &= -\left\| \boldsymbol{G}_{\boldsymbol{V}} \right\|_{\mathrm{F}}^2 + \mu \left\| \mathcal{A}\left(\boldsymbol{U} \boldsymbol{G}^{\mathrm{H}}_{\boldsymbol{V}}\right) \right\|_2^2 \\
&\underbrace{-4\lambda \operatorname{Re} \left\{ \left\langle \boldsymbol{V}^{\mathrm{H}} \boldsymbol{G}_{\boldsymbol{V}}, \boldsymbol{X} \right\rangle_{\mathrm{F}} \right\} + 2\lambda \operatorname{Re} \left\{ \left\langle \boldsymbol{X}'', -2\mu \boldsymbol{E} + \boldsymbol{D} \right\rangle_{\mathrm{F}} \right\}}_{T_6}.
\end{aligned} \tag{A.6.52}$$

We may further simplify the last two terms of the latter as

$$\begin{aligned} T_6 &= -4\lambda \operatorname{Re}\left\{\left\langle \boldsymbol{V}^{\mathrm{H}}\boldsymbol{G}_{\boldsymbol{V}}, \boldsymbol{X}\right\rangle_{\mathrm{F}}\right\} + 2\lambda \operatorname{Re}\left\{\left\langle \boldsymbol{X}'', -2\mu\boldsymbol{E} + \boldsymbol{D}\right\rangle_{\mathrm{F}}\right\} \\ &= 2\lambda \operatorname{Re}\left\{-2\left\langle \boldsymbol{V}^{\mathrm{H}}\boldsymbol{G}_{\boldsymbol{V}}, \boldsymbol{X}\right\rangle_{\mathrm{F}} + \left\langle \boldsymbol{X}'', -2\mu\boldsymbol{E} + \boldsymbol{D}\right\rangle_{\mathrm{F}}\right\} \end{aligned}$$

and insert (A.6.45) as

$$\begin{aligned} T_6 &= 2\lambda \operatorname{Re}\left\{-2\left\langle \boldsymbol{V}^{\mathrm{H}}\boldsymbol{G}_{\boldsymbol{V}}, \boldsymbol{X}\right\rangle_{\mathrm{F}} + \left\langle \boldsymbol{X}'', -2\mu\boldsymbol{E} + \boldsymbol{D}\right\rangle_{\mathrm{F}}\right\} \\ &= 2\lambda \operatorname{Re}\Big\{-2\left\langle \boldsymbol{V}^{\mathrm{H}}\boldsymbol{G}_{\boldsymbol{V}}, \boldsymbol{X}\right\rangle_{\mathrm{F}} + \underbrace{\left\langle \boldsymbol{X} + \mu\boldsymbol{D} - \mu^2\boldsymbol{E}, -2\mu\boldsymbol{E} + \boldsymbol{D}\right\rangle_{\mathrm{F}}}_{T_7}\Big\}. \end{aligned} \tag{A.6.53}$$

Next we expand term T_7 and further simplify which yields

$$\begin{aligned} T_7 &= \left\langle \boldsymbol{X} + \mu\boldsymbol{D} - \mu^2\boldsymbol{E}, -2\mu\boldsymbol{E} + \boldsymbol{D}\right\rangle_{\mathrm{F}} \\ &= 2\mu^3 \left\|\boldsymbol{E}\right\|_{\mathrm{F}}^2 - \mu^2\underbrace{\left(2\left\langle \boldsymbol{D}, \boldsymbol{E}\right\rangle_{\mathrm{F}} + \left\langle \boldsymbol{E}, \boldsymbol{D}\right\rangle_{\mathrm{F}}\right)}_{T_8} + \mu\left(-2\left\langle \boldsymbol{X}, \boldsymbol{E}\right\rangle_{\mathrm{F}} + \left\|\boldsymbol{D}\right\|_{\mathrm{F}}^2\right) + \left\langle \boldsymbol{X}, \boldsymbol{D}\right\rangle_{\mathrm{F}}. \end{aligned} \tag{A.6.54}$$

The term T_8 can be combined as

$$\begin{aligned} T_8 &= 2\left\langle \boldsymbol{D}, \boldsymbol{E}\right\rangle_{\mathrm{F}} + \left\langle \boldsymbol{E}, \boldsymbol{D}\right\rangle_{\mathrm{F}} \\ &= 3\operatorname{Re}\left\{\left\langle \boldsymbol{D}, \boldsymbol{E}\right\rangle_{\mathrm{F}}\right\} + \mathrm{j}\operatorname{Im}\left\{\left\langle \boldsymbol{D}, \boldsymbol{E}\right\rangle_{\mathrm{F}}\right\}, \end{aligned} \tag{A.6.55}$$

where the imaginary part can be skipped since only the real part is taken in (A.6.53). Inserting (A.6.54) and (A.6.55) into (A.6.53) yields

$$T_6 = 2\lambda \operatorname{Re}\Big\{2\mu^3 \left\|\boldsymbol{E}\right\|_{\mathrm{F}}^2 - 3\mu^2\left\langle \boldsymbol{D}, \boldsymbol{E}\right\rangle_{\mathrm{F}} + \mu\left(-2\left\langle \boldsymbol{X}, \boldsymbol{E}\right\rangle_{\mathrm{F}} + \left\|\boldsymbol{D}\right\|_{\mathrm{F}}^2\right)\underbrace{-2\left\langle \boldsymbol{V}^{\mathrm{H}}\boldsymbol{G}_{\boldsymbol{V}}, \boldsymbol{X}\right\rangle_{\mathrm{F}} + \left\langle \boldsymbol{X}, \boldsymbol{D}\right\rangle_{\mathrm{F}}}_{T_9}\Big\}. \tag{A.6.56}$$

Finally we can combine term T_9 as

$$\begin{aligned} T_9 &= \operatorname{Re}\left\{-2\left\langle \boldsymbol{V}^{\mathrm{H}}\boldsymbol{G}_{\boldsymbol{V}}, \boldsymbol{X}\right\rangle_{\mathrm{F}} + \left\langle \boldsymbol{X}, \boldsymbol{D}\right\rangle_{\mathrm{F}}\right\} \\ &= \operatorname{Re}\left\{-2\left\langle \boldsymbol{X}, \boldsymbol{V}^{\mathrm{H}}\boldsymbol{G}_{\boldsymbol{V}}\right\rangle_{\mathrm{F}} + \left\langle \boldsymbol{X}, \boldsymbol{G}_{\boldsymbol{V}}^{\mathrm{H}}\boldsymbol{V} + \boldsymbol{V}^{\mathrm{H}}\boldsymbol{G}_{\boldsymbol{V}}\right\rangle_{\mathrm{F}}\right\} \\ &= \operatorname{Re}\left\{\left\langle \boldsymbol{X}, \boldsymbol{G}_{\boldsymbol{V}}^{\mathrm{H}}\boldsymbol{V} - \boldsymbol{V}^{\mathrm{H}}\boldsymbol{G}_{\boldsymbol{V}}\right\rangle_{\mathrm{F}}\right\} \\ &= \operatorname{Re}\left\{\left\langle \boldsymbol{X}, \boldsymbol{F}\right\rangle_{\mathrm{F}}\right\}, \end{aligned} \tag{A.6.57}$$

where we introduced an additional abbreviation

$$\boldsymbol{F} = \boldsymbol{G}_{\boldsymbol{V}}^{\mathrm{H}}\boldsymbol{V} - \boldsymbol{V}^{\mathrm{H}}\boldsymbol{G}_{\boldsymbol{V}}. \tag{A.6.58}$$

Please note that switching the entries in the Frobenius product as done above is only possible since we are only interested in the real part. Combining (A.6.57), (A.6.56), and (A.6.52) yields

the final form

$$\frac{\partial F\left(\boldsymbol{U}, \boldsymbol{V}-\mu \boldsymbol{G}_{\boldsymbol{V}}\right)}{\partial \mu} = -\left\|\boldsymbol{G}_{\boldsymbol{V}}\right\|_{\mathrm{F}}^{2} + 2\lambda \operatorname{Re}\Big\{ 2\mu^{3}\left\|\boldsymbol{E}\right\|_{\mathrm{F}}^{2} - 3\mu^{2}\left\langle \boldsymbol{D}, \boldsymbol{E}\right\rangle_{\mathrm{F}} + \mu\left(-2\left\langle \boldsymbol{X}, \boldsymbol{E}\right\rangle_{\mathrm{F}} + \left\|\boldsymbol{D}\right\|_{\mathrm{F}}^{2} + \frac{1}{2\lambda}\left\|\mathcal{A}\left(\boldsymbol{U}\boldsymbol{G}_{\boldsymbol{V}}^{\mathrm{H}}\right)\right\|_{2}^{2}\right) + \left\langle \boldsymbol{X}, \boldsymbol{F}\right\rangle_{\mathrm{F}}\Big\} \tag{A.6.59}$$

Unique solutions for $\mu_{\boldsymbol{U}}$ and $\mu_{\boldsymbol{V}}$

As can be seen from (A.6.36) and (A.6.59), the derivatives are third order polynomials in μ and as such have in general three arbitrary roots. However, for valid step sizes, we need a single positive real root. We prove that this is always the case in the framework of the BFGD algorithm by first showing that only one real root exists and second that this real root is positive.

Single real root Since the regularized objective function (A.6.4) is the sum of two functions $f\left(\cdot\right)$ and $g\left(\cdot\right)$ which are convex in $\boldsymbol{U}$ and $\boldsymbol{V}$, (A.6.4) is convex in $\boldsymbol{U}$ and $\boldsymbol{V}$ too. Therefore it has only one global minimum and thus only one real point where its derivative is zero. The same holds for the restricted functions in (A.6.7) and (A.6.8). The derivatives (A.6.36) and (A.6.59) thus can only have one real and two complex roots.

Positive real root To prove this single real root is positive, we take a closer look at the polynomial´s coefficients. The polynomial has the general form

$$a\mu^{3} + b\mu^{2} + c\mu + d = 0.$$

By use of Descartes' rule of signs we can determine the sign of the roots, for which we only need to know the signs of the coefficients [86]. Those are shown in Tab. A.6.1. The coefficient a is positive. The sign of coefficient b is unknown because $\boldsymbol{A}$ and $\boldsymbol{D}$ are indefinite matrices. The matrices $\boldsymbol{B}$ and $\boldsymbol{E}$ are positive semidefinite, however, this is not of use here. Coefficient c is almost surely positive since $\boldsymbol{X} = \boldsymbol{U}^{\mathrm{H}}\boldsymbol{U} - \boldsymbol{V}^{\mathrm{H}}\boldsymbol{V}$ is the difference of almost identical covariance matrices. Since $\boldsymbol{U}$ and $\boldsymbol{V}$ stem from a singular value decomposition (SVD) as $\boldsymbol{L} = \bar{\boldsymbol{U}}\boldsymbol{\Sigma}\bar{\boldsymbol{V}}^{\mathrm{H}}$ and $\boldsymbol{U} = \bar{\boldsymbol{U}}\boldsymbol{\Sigma}^{1/2}$ and $\boldsymbol{V} = \bar{\boldsymbol{V}}\boldsymbol{\Sigma}^{1/2}$, $\boldsymbol{X}$ has only entries close to zero. We thus may neglect $\left\langle \boldsymbol{X}, \boldsymbol{B}\right\rangle_{\mathrm{F}}$ and $\left\langle \boldsymbol{X}, \boldsymbol{E}\right\rangle_{\mathrm{F}}$ compared to the remaining terms in (A.6.36) and (A.6.59). The same argument holds for coefficient d where we may neglect $\left\langle \boldsymbol{X}, \boldsymbol{C}\right\rangle_{\mathrm{F}}$ and $\left\langle \boldsymbol{X}, \boldsymbol{F}\right\rangle_{\mathrm{F}}$. In summary we have

$$+\left|a\right|\mu^{3} \pm \left|b\right|\mu^{2} \pm \left|c\right|\mu - \left|d\right| = 0$$

which yields either one or three change of signs. According to Descartes' rule we have for

1 change of signs: 1 positive real root and 2 negative or complex roots

3 changes of signs: 1 or 3 positive real roots, 2 or 0 complex roots, and 0 negative roots

In either case we are guaranteed to have at least one positive real root Q.E.D. In case of three changes of signs we are guaranteed to only have one positive real root due to the convex objective function. By taking care that $d < 0$, we ensure to have a positive real root. The sings of b and c do not matter.

Since we can neglect the impact of $\boldsymbol{X}$ due to the reasons stated above, we may simplify (A.6.36) and (A.6.59) as

$$\begin{aligned}\frac{\partial F\left(\boldsymbol{U}-\mu\boldsymbol{G}_{\boldsymbol{U}},\boldsymbol{V}\right)}{\partial\mu} &\simeq 4\lambda\mu^3\left\|\boldsymbol{B}\right\|_{\mathrm{F}}^2-6\lambda\mu^2\operatorname{Re}\left\{\left\langle\boldsymbol{A},\boldsymbol{B}\right\rangle_{\mathrm{F}}\right\}\\ &\quad+\mu\left(2\lambda\left\|\boldsymbol{A}\right\|_{\mathrm{F}}^2+\left\|\mathcal{A}\left(\boldsymbol{G}_{\boldsymbol{U}}\boldsymbol{V}^{\mathrm{H}}\right)\right\|_2^2\right)-\left\|\boldsymbol{G}_{\boldsymbol{U}}\right\|_{\mathrm{F}}^2=p_{\boldsymbol{U}} \qquad \text{(A.6.60)}\\ \frac{\partial F\left(\boldsymbol{U},\boldsymbol{V}-\mu\boldsymbol{G}_{\boldsymbol{V}}\right)}{\partial\mu} &\simeq 4\lambda\mu^3\left\|\boldsymbol{E}\right\|_{\mathrm{F}}^2-6\lambda\mu^2\operatorname{Re}\left\{\left\langle\boldsymbol{D},\boldsymbol{E}\right\rangle_{\mathrm{F}}\right\}\\ &\quad+\mu\left(2\lambda\left\|\boldsymbol{D}\right\|_{\mathrm{F}}^2+\left\|\mathcal{A}\left(\boldsymbol{U}\boldsymbol{G}_{\boldsymbol{V}}^{\mathrm{H}}\right)\right\|_2^2\right)-\left\|\boldsymbol{G}_{\boldsymbol{V}}\right\|_{\mathrm{F}}^2=p_{\boldsymbol{V}}. \qquad \text{(A.6.61)}\end{aligned}$$

The optimal step sizes (A.6.7) and (A.6.8) are thus

$$\mu_{\boldsymbol{U}}=\text{real root of}\left(p_{\boldsymbol{U}}\right) \qquad \text{(A.6.62)}$$

$$\mu_{\boldsymbol{V}}=\text{real root of}\left(p_{\boldsymbol{V}}\right), \qquad \text{(A.6.63)}$$

where $\text{real root of}\left(\cdot\right)$ denotes an operator which yields only the pure real root of the three possible roots of (A.6.60) and (A.6.61).

Coefficient	(A.6.36) or (A.6.59)	Sign
a	$4\lambda\left\|\boldsymbol{B}\right\|_{\mathrm{F}}^2$ or $4\lambda\left\|\boldsymbol{E}\right\|_{\mathrm{F}}^2$	≥ 0
b	$-6\lambda\operatorname{Re}\left\{\left\langle\boldsymbol{A},\boldsymbol{B}\right\rangle_{\mathrm{F}}\right\}$ or $-6\lambda\operatorname{Re}\left\{\left\langle\boldsymbol{D},\boldsymbol{E}\right\rangle_{\mathrm{F}}\right\}$	$\gtrless 0$
c	$2\lambda\operatorname{Re}\left\{2\left\langle\boldsymbol{X},\boldsymbol{B}\right\rangle_{\mathrm{F}}+\left\|\boldsymbol{A}\right\|_{\mathrm{F}}^2\right\}+\left\|\mathcal{A}\left(\boldsymbol{G}_{\boldsymbol{U}}\boldsymbol{V}^{\mathrm{H}}\right)\right\|_2^2$ or $2\lambda\operatorname{Re}\left\{-2\left\langle\boldsymbol{X},\boldsymbol{E}\right\rangle_{\mathrm{F}}+\left\|\boldsymbol{D}\right\|_{\mathrm{F}}^2\right\}+\left\|\mathcal{A}\left(\boldsymbol{U}\boldsymbol{G}_{\boldsymbol{V}}^{\mathrm{H}}\right)\right\|_2^2$	$\gtrsim 0$
d	$-\left\|\boldsymbol{G}_{\boldsymbol{U}}\right\|_{\mathrm{F}}^2+2\lambda\operatorname{Re}\left\{\left\langle\boldsymbol{X},\boldsymbol{C}\right\rangle_{\mathrm{F}}\right\}$ or $-\left\|\boldsymbol{G}_{\boldsymbol{V}}\right\|_{\mathrm{F}}^2+2\lambda\operatorname{Re}\left\{\left\langle\boldsymbol{X},\boldsymbol{F}\right\rangle_{\mathrm{F}}\right\}$	$\lesssim 0$

Table A.6.1.: Signs of coefficients of (A.6.36) and (A.6.59).

Simulation Results

A Matlab program was designed to test the proposed step size calculation. The BFGD algorithm was used to solve (A.6.1), where the step sizes were calculated in every iteration step using (A.6.62) and (A.6.63). The dimension size was set exemplarily to $N_1=N_2=70$, the rank to $r=14$, the number of measurements to $M=N_1N_2/2=2450$, $\lambda={}^1\!/_8$, and the entries of the affine transformation $\mathcal{A}$, $\boldsymbol{U}_{\text{true}}$, and $\boldsymbol{V}_{\text{true}}$ were drawn from complex standard normal distributed random samples. The columns of the matrices $\boldsymbol{U}_{\text{true}}$ and $\boldsymbol{V}_{\text{true}}$ were further orthogonalized and their respective ℓ_2 norms were equalized such as if $\boldsymbol{U}_{\text{true}}$ and $\boldsymbol{V}_{\text{true}}$ would stem from an SVD. The initial solutions $\boldsymbol{U}_0$ and $\boldsymbol{V}_0$ were obtained by perturbing $\boldsymbol{U}_{\text{true}}$ and $\boldsymbol{V}_{\text{true}}$ by adding substantial complex standard normal distributed noise followed by the orthogonalization and equalization procedure described before. The results are shown on the left of Fig. A.6.1 where the relative square data fidelity error $\left\|\tilde{\boldsymbol{y}}\right\|_2^2/\left\|\boldsymbol{y}\right\|_2^2$ for a fixed step size of $\mu_{\boldsymbol{U}}=\mu_{\boldsymbol{V}}=0.001$ and for the proposed step size determination are shown. It can be seen that the error drops at a faster rate

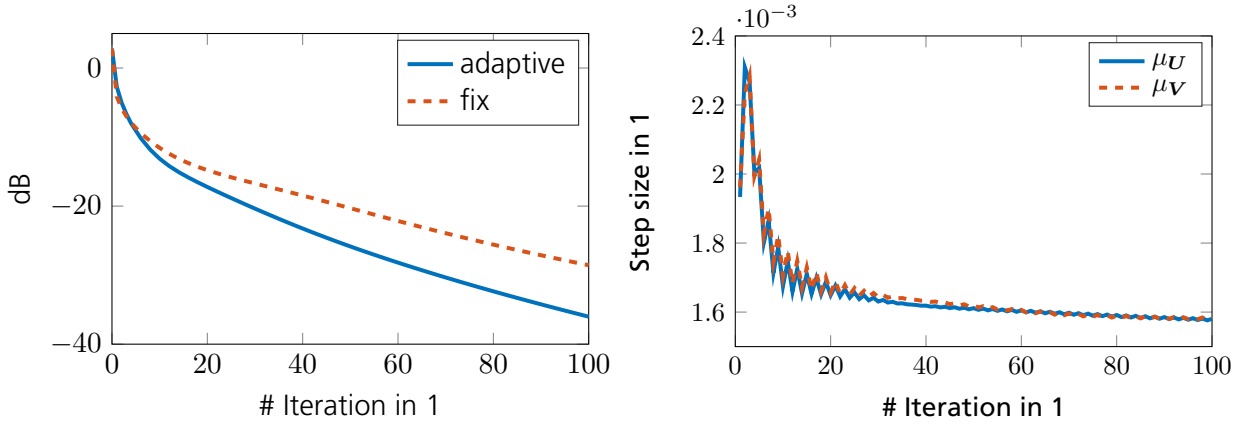

Figure A.6.1.: Left: Relative square data fidelity error. Right: Step sizes.

using the proposed step size determination. The determined step sizes in every iteration step are shown on the right of Fig. A.6.1. One may deduce from the similarity of the two graphs that it is possible to reduce the computational burden of the step size determination by using the same step size for both $\mu_{\boldsymbol{U}}$ and $\mu_{\boldsymbol{V}}$ accepting a slightly worse convergence rate. Furthermore, one may determine an optimal fixed step size from a reasonably converged step size sequence as apparent in Fig. A.6.1 (right).

A.7. Derivation of Some Useful Gradients

In this section some useful gradients are derived required for compressive sensing (CS), affine rank minimization (ARM), and the auto-clutter focus algorithm.

A.7.1. The Gradient $\nabla_s h$ and $\nabla_L h$

These gradients are required for CS and ARM algorithms. Since their mathematical structure is the same, the gradient is derived for $\nabla_{\boldsymbol{X}} h$. As the arguments are complex elements, the Wirtinger derivatives listed in Appendix A.1 are used to determine the required gradients. At first notice, that $h(\boldsymbol{X}) : \mathbb{C}^{n_1 \times n_2} \to \mathbb{R}$ is not a holomorphic function which can be seen by noticing that

$$\frac{\partial |f(\boldsymbol{X})|^2}{\partial f(\boldsymbol{X})^*} = \frac{\partial f(\boldsymbol{X}) f(\boldsymbol{X})^*}{\partial f(\boldsymbol{X})^*} = f(\boldsymbol{X}) \neq 0,$$

which is the required condition. Nevertheless, a gradient indicating a descendant direction in the real and imaginary domain can be found as[7]

$$\nabla_{\boldsymbol{X}} f(\boldsymbol{X}) = \left(\frac{\partial f(\boldsymbol{X})}{\partial \boldsymbol{X}^*} \right)^{\mathrm{T}}.$$

[7] It is also possible to choose $\nabla_{\boldsymbol{X}} h(\boldsymbol{X}) = 2 \left(\frac{\partial h(\boldsymbol{X})}{\partial \boldsymbol{X}} \right)^{\mathrm{T}}$ as a gradient, however, this is not the common form usually chosen in the literature.

As such, the desired derivative of the residual error term is

$$\begin{aligned}\nabla_{\boldsymbol{X}} h(\boldsymbol{X}) &= \left(\frac{\partial \left\|\boldsymbol{y}-\mathcal{A}\left(\boldsymbol{X}\right)\right\|_2^2}{\partial \boldsymbol{X}^*}\right)^{\mathrm{T}} \\ &= \frac{\partial \left\|\boldsymbol{y}-\mathcal{A}\left(x_{kl}\right)\right\|_2^2}{\partial x_{ij}^*},\end{aligned} \tag{A.7.1}$$

where $\boldsymbol{X} \in \mathbb{C}^{n_1 \times n_2}$, $\mathcal{A}: \mathbb{C}^m \to \mathbb{C}^{n_1 \times n_2}$ is an affine linear transformation, and $\boldsymbol{y} \in \mathbb{C}^m$. Using the chain rule, (A.7.1) can be expanded by

$$\frac{\partial \left\|\boldsymbol{y}-\mathcal{A}\left(x_{kl}\right)\right\|_2^2}{\partial x_{ij}^*} = \underbrace{\frac{\partial a^2}{\partial a}\frac{\partial \left\|\boldsymbol{b}\right\|_2}{\partial \boldsymbol{b}}\frac{-\partial \mathcal{A}\left(x_{kl}\right)}{\partial x_{ij}}\frac{\partial x_{ij}}{\partial x_{ij}^*}}_{T_1} + \underbrace{\frac{\partial a^2}{\partial a^*}\frac{\partial \left(\left\|\boldsymbol{b}\right\|_2\right)^*}{\partial \boldsymbol{b}^*}\frac{-\partial \left(\mathcal{A}\left(x_{kl}\right)\right)^*}{\partial x_{ij}^*}\frac{\partial x_{ij}^*}{\partial x_{ij}^*}}_{T_2},$$

with the intermediate variables

$$\begin{aligned}a &= \left\|\boldsymbol{y}-\mathcal{A}\left(x_{kl}\right)\right\|_2 \\ \boldsymbol{b} &= \boldsymbol{y}-\mathcal{A}\left(x_{kl}\right).\end{aligned}$$

The first term T_1 is zero since

$$\frac{\partial x_{ij}}{\partial x_{ij}^*} = 0.$$

Within the second term T_2, the following results emerge

$$\begin{aligned}\frac{\partial a^2}{\partial a^*} &= \frac{\partial a^2}{\partial a} = 2a \\ \frac{\partial \left(\left\|\boldsymbol{b}\right\|_2\right)^*}{\partial \boldsymbol{b}^*} &= \left(\frac{\partial \left\|\boldsymbol{b}\right\|_2}{\partial \boldsymbol{b}}\right)^* = \left(\frac{\partial \left(\boldsymbol{b}^{\mathrm{H}}\boldsymbol{b}\right)^{1/2}}{\partial \boldsymbol{b}}\right)^* = \left(\frac{1}{2\left\|\boldsymbol{b}\right\|_2}\frac{\partial \boldsymbol{b}^{\mathrm{H}}\boldsymbol{b}}{\partial \boldsymbol{b}}\right)^* = \left(\frac{\boldsymbol{b}^{\mathrm{H}}}{2\left\|\boldsymbol{b}\right\|_2}\right)^* = \frac{\boldsymbol{b}^{\mathrm{T}}}{2\left\|\boldsymbol{b}\right\|_2} \\ \frac{-\partial \left(\mathcal{A}\left(x_{kl}\right)\right)^*}{\partial x_{ij}^*} &= -\frac{\partial \mathcal{A}^*\left(x_{kl}^*\right)}{\partial x_{ij}^*} = \frac{\partial \sum_{k,l}\mathcal{A}_{hkl}^* x_{kl}^*}{\partial x_{ij}^*} = \mathcal{A}_{hij}^*.\end{aligned}$$

Combining them together yields

$$\begin{aligned}\frac{\partial \left\|\boldsymbol{y}-\mathcal{A}\left(x_{kl}\right)\right\|_2^2}{\partial x_{ij}^*} &= \sum_h \left[\left(\boldsymbol{y}-\mathcal{A}\left(x_{kl}\right)\right)^{\mathrm{T}}\right]_h \mathcal{A}_{hij}^* \\ &= \mathcal{A}^{\mathrm{H}}\left(\boldsymbol{y}-\mathcal{A}\left(\boldsymbol{X}\right)\right).\end{aligned}$$

As such, in case of CS the desired gradient is

$$\nabla_{\boldsymbol{s}} h = \frac{\partial \left\|\boldsymbol{y}-\mathcal{A}\left(\boldsymbol{s}\right)\right\|_2^2}{\partial \boldsymbol{s}^*} = \mathcal{A}^{\mathrm{H}}\left(\boldsymbol{y}-\mathcal{A}\left(\boldsymbol{s}\right)\right)$$

and like wise for the ARM case

$$\nabla_{\boldsymbol{L}} h = \frac{\partial \left\|\boldsymbol{y}-\mathcal{A}\left(\boldsymbol{L}\right)\right\|_2^2}{\partial \boldsymbol{L}^*} = \mathcal{A}^{\mathrm{H}}\left(\boldsymbol{y}-\mathcal{A}\left(\boldsymbol{L}\right)\right). \tag{A.7.2}$$

A.7.2. The Gradient $\nabla_\beta h$

The residual error term is given by (7.2.13) as

$$h(\boldsymbol{L};\beta,\varphi_\mathrm{m}) = \|\boldsymbol{y} - \mathcal{A}\left(\boldsymbol{L};\beta,\varphi_\mathrm{m}\right)\|_2^2 .$$

Since $\beta \in \mathbb{R}$, the required gradient is

$$\nabla_\beta h\left(\boldsymbol{L};\beta,\varphi\right) = 2\,\mathrm{Re}\left\{\left(\mathcal{A}\left(\boldsymbol{L};\beta,\varphi_\mathrm{m}\right) - \boldsymbol{y}\right)^\mathrm{H} \frac{\partial \mathcal{A}\left(\boldsymbol{L};\beta,\varphi_\mathrm{m}\right)}{\partial\beta}\right\}. \tag{A.7.3}$$

The sensing operator is given by (7.2.4) as

$$\mathcal{A}\left(\boldsymbol{L};\beta,\varphi_\mathrm{m}\right) = \mathrm{vec}\left(\boldsymbol{A}\mathcal{D}^{-1}(\boldsymbol{L};\beta,\varphi_\mathrm{m})\boldsymbol{B}^\mathrm{T}\right),$$

hence

$$\begin{aligned}\frac{\partial \mathcal{A}\left(\boldsymbol{L};\beta,\varphi_\mathrm{m}\right)}{\partial\beta} &= \frac{\partial\,\mathrm{vec}\left(\boldsymbol{A}\mathcal{D}^{-1}(\boldsymbol{L};\beta,\varphi_\mathrm{m})\boldsymbol{B}^\mathrm{T}\right)}{\partial\beta}\\ &= \mathrm{vec}\left(\frac{\partial \boldsymbol{A}\mathcal{D}^{-1}(\boldsymbol{L};\beta,\varphi_\mathrm{m})\boldsymbol{B}^\mathrm{T}}{\partial\beta}\right)\\ &= \mathrm{vec}\left(\boldsymbol{A}\frac{\partial \mathcal{D}^{-1}(\boldsymbol{L};\beta,\varphi_\mathrm{m})}{\partial\beta}\boldsymbol{B}^\mathrm{T}\right).\end{aligned}$$

Next, the shifting operator $\mathcal{D}^{-1}$ is

$$\mathcal{D}^{-1}(\boldsymbol{L};\beta,\varphi_\mathrm{m}) = \boldsymbol{F}_1\left(\boldsymbol{U}_\triangle^*(\beta,\varphi_\mathrm{m}) \odot \left(\boldsymbol{F}_1^{-1}\boldsymbol{L}\right)\right)$$

with the shift matrix $\boldsymbol{U}_\triangle(\beta,\varphi_\mathrm{m})$ being

$$\boldsymbol{U}_\triangle(\beta,\varphi_\mathrm{m}) = \exp\left(\mathrm{j}2\pi\boldsymbol{n}_{\bar{u}}\bar{\boldsymbol{u}}_\triangle^\mathrm{T}(\beta,\varphi_\mathrm{m})\right).$$

The required run and shift vectors are

$$\begin{aligned}\boldsymbol{n}_{\bar{u}} &= [0,1,\ldots,N_\mathrm{u}-1]^\mathrm{T}\\ \bar{\boldsymbol{u}}_\triangle(\beta,\varphi_\mathrm{m}) &= \left[\triangle\bar{u}\left(i/N_\mathrm{D};\beta,\varphi_\mathrm{m}\right)\right]_{i=-N_\mathrm{D}/2}^{N_\mathrm{D}/2-1}\end{aligned} \tag{A.7.4}$$

and the shift amount $\triangle\bar{u}$ is given by (7.1.14) as

$$\triangle\bar{u}(\bar{f}_\mathrm{D};\beta,\varphi_\mathrm{m}) = -\frac{\bar{f}_\mathrm{D}}{\beta}\cos(\varphi_\mathrm{m}) + \sqrt{\left|\bar{d}^2\sin^2\left(\vartheta\right) - \bar{f}_\mathrm{D}{}^2/\beta^2\right|}\sin\left(\varphi_\mathrm{m}\right). \tag{A.7.5}$$

As such, the required derivation of the shifting operator is

$$\begin{aligned}\frac{\partial \mathcal{D}^{-1}(\boldsymbol{L};\beta,\varphi_\mathrm{m})}{\partial\beta} &= \frac{\partial \boldsymbol{F}_1\left(\boldsymbol{U}_\triangle^*(\beta,\varphi_\mathrm{m}) \odot \left(\boldsymbol{F}_1^{-1}\boldsymbol{L}\right)\right)}{\partial\beta}\\ &= \boldsymbol{F}_1\left(\frac{\partial \boldsymbol{U}_\triangle^*(\beta,\varphi_\mathrm{m})}{\partial\beta} \odot \left(\boldsymbol{F}_1^{-1}\boldsymbol{L}\right)\right).\end{aligned}$$

The derivation of the shift matrix is

$$\frac{\partial \boldsymbol{U}_{\triangle}^{*}(\beta,\varphi_{\mathrm{m}})}{\partial\beta} = -\mathrm{j}2\pi\left(\boldsymbol{n}_{\bar{u}}\frac{\partial \bar{\boldsymbol{u}}_{\triangle}^{\mathrm{T}}(\beta,\varphi_{\mathrm{m}})}{\partial\beta}\right)\odot \boldsymbol{U}_{\triangle}^{*}(\beta,\varphi_{\mathrm{m}})$$

and the required derivation of the shift vector

$$\frac{\partial \bar{\boldsymbol{u}}_{\triangle}(\beta,\varphi_{\mathrm{m}})}{\partial\beta} = \left[\frac{\partial \triangle\bar{u}\left(i/N_{\mathrm{D}};\beta,\varphi_{\mathrm{m}}\right)}{\partial\beta}\right]_{i=-N_{\mathrm{D}}/2}^{N_{\mathrm{D}}/2-1}. \tag{A.7.6}$$

Finally, the derivation of the shift amount is

$$\frac{\partial \triangle\bar{u}\left(\bar{f}_{\mathrm{D}};\beta,\varphi_{\mathrm{m}}\right)}{\partial\beta} = \frac{\bar{f}_{\mathrm{D}}}{\beta^2}\cos(\varphi_{\mathrm{m}}) + \frac{\bar{f}_{\mathrm{D}}{}^2\sin\left(\varphi_{\mathrm{m}}\right)\left(\bar{d}^2\sin^2\left(\vartheta\right)-\bar{f}_{\mathrm{D}}{}^2/\beta^2\right)}{\beta^3\left(\bar{d}^2\sin^2\left(\vartheta\right)-\bar{f}_{\mathrm{D}}{}^2/\beta^2\right)^{3/2}}. \tag{A.7.7}$$

For the special case of

$$\bar{d}\sin\left(\varphi\right) = \bar{f}_{\mathrm{D}}/\beta, \tag{A.7.8}$$

which may occur only if $\beta < 1$, the derivation (A.7.7) does not exist. In this case, the derivation is simply defined to be zero as

$$\frac{\partial \triangle\bar{u}\left(\bar{f}_{\mathrm{D}};\beta,\varphi_{\mathrm{m}}\right)}{\partial\beta} = \begin{cases} \frac{\bar{f}_{\mathrm{D}}}{\beta^2}\cos(\varphi_{\mathrm{m}}) + \frac{\bar{f}_{\mathrm{D}}{}^2\sin(\varphi_{\mathrm{m}})\left(\bar{d}^2\sin^2(\vartheta)-\bar{f}_{\mathrm{D}}{}^2/\beta^2\right)}{\beta^3\left(\bar{d}^2\sin^2(\vartheta)-\bar{f}_{\mathrm{D}}{}^2/\beta^2\right)^{3/2}} & \text{if } \bar{d}\sin\left(\varphi\right)\neq\bar{f}_{\mathrm{D}}/\beta \\ 0 & \text{else} \end{cases}.$$

This is not of concern as long as $N_{\mathrm{D}} \gg 2$. If the special case (A.7.8) occurs, exactly two zeros emerge in the vector (A.7.6). If $N_{\mathrm{D}} \gg 2$, the artificially introduced zeros do not disturb the gradient result (A.7.3) as sufficient other Doppler bins where the derivation exists are available. This was verified by numerical simulations. In summary, the derivation of the sensing operator is

$$\frac{\partial \mathcal{A}\left(\boldsymbol{L};\beta,\varphi_{\mathrm{m}}\right)}{\partial\beta} = \mathrm{vec}\left(-\mathrm{j}2\pi\boldsymbol{A}\boldsymbol{F}_1\left(\left(\boldsymbol{n}_{\bar{u}}\frac{\partial \bar{\boldsymbol{u}}_{\triangle}^{\mathrm{T}}(\beta,\varphi_{\mathrm{m}})}{\partial\beta}\right)\odot \boldsymbol{U}_{\triangle}^{*}(\beta,\varphi_{\mathrm{m}})\odot\left(\boldsymbol{F}_1^{-1}\boldsymbol{L}\right)\right)\boldsymbol{B}^{\mathrm{T}}\right). \tag{A.7.9}$$

A.7.3. The Gradient $\nabla_{\varphi_{\mathrm{m}}} h_{\varphi_{\mathrm{m}}}$

The objective function used to estimate φ_{m} is given by (7.2.10) and can be formulated as

$$h_{\varphi_{\mathrm{m}}}(\boldsymbol{L};\beta,\varphi_{\mathrm{m}}) = f(\boldsymbol{L};\beta,\varphi_{\mathrm{m}})^2$$

with

$$f(\boldsymbol{L};\beta,\varphi_{\mathrm{m}}) = \frac{\left\|\bar{\boldsymbol{l}}_{\mathrm{cr}}\right\|_2}{\bar{\boldsymbol{l}}_{\mathrm{cr}}^{\mathrm{T}}\boldsymbol{g}_{\mathrm{ap}}\boldsymbol{l}_{\mathrm{cr}}^{\mathrm{T}}\boldsymbol{l}_{\mathrm{cr}}}.$$

The mean free clutter ridge row given by (7.2.8) can also be reformulated to

$$\begin{aligned}\bar{\boldsymbol{l}}_{\mathrm{cr}} &= \boldsymbol{l}_{\mathrm{cr}} - \mu_{\boldsymbol{l}_{\mathrm{cr}}}\mathbf{1} \\ &= \boldsymbol{l}_{\mathrm{cr}} - \mathbf{1} \otimes \frac{\mathbf{1}^{\mathrm{T}}\boldsymbol{l}_{\mathrm{cr}}}{N_{\mathrm{D}}},\end{aligned}$$

where

$$\boldsymbol{l}_{\mathrm{cr}} = \left|\left[\boldsymbol{L}'\right]_{i_{\mathrm{cr}}:}\right|^{\mathrm{T}}$$

with

$$\boldsymbol{L}' = \boldsymbol{L} - \mu\nabla_{\boldsymbol{L}} h\left(\boldsymbol{L};\beta,\varphi_{\mathrm{m}}\right). \tag{A.7.10}$$

The required gradient therefore is

$$\nabla_{\varphi_{\mathrm{m}}} h_{\varphi_{\mathrm{m}}}(\boldsymbol{L};\beta,\varphi_{\mathrm{m}}) = \underbrace{\frac{\partial h_{\varphi_{\mathrm{m}}}(\boldsymbol{L};\beta,\varphi_{\mathrm{m}})}{\partial \boldsymbol{l}_{\mathrm{cr}}}}_{T_1} \mathrm{Re}\left\{\underbrace{\frac{\partial \boldsymbol{l}_{\mathrm{cr}}}{\partial\left(\left[\boldsymbol{L}'\right]_{i_{\mathrm{cr}}:}\right)^{\mathrm{T}}}}_{T_2}\underbrace{\frac{\partial\left(\left[\boldsymbol{L}'\right]_{i_{\mathrm{cr}}:}\right)^{\mathrm{T}}}{\partial\varphi_{\mathrm{m}}}}_{T_3}\right\}. \tag{A.7.11}$$

The term T_1 results to

$$\frac{\partial h_{\varphi_{\mathrm{m}}}(\boldsymbol{L};\beta,\varphi_{\mathrm{m}})}{\partial \boldsymbol{l}_{\mathrm{cr}}} = 2f(\boldsymbol{L};\beta,\varphi_{\mathrm{m}})\underbrace{\frac{\partial f(\boldsymbol{L};\beta,\varphi_{\mathrm{m}})}{\partial \boldsymbol{l}_{\mathrm{cr}}}}_{T_4}. \tag{A.7.12}$$

Using the quotient rule, the required derivative T_4 is

$$\frac{\partial f(\boldsymbol{L};\beta,\varphi_{\mathrm{m}})}{\partial \boldsymbol{l}_{\mathrm{cr}}} = \frac{\frac{\partial\left\|\bar{\boldsymbol{l}}_{\mathrm{cr}}\right\|_2}{\partial \boldsymbol{l}_{\mathrm{cr}}}\bar{\boldsymbol{l}}_{\mathrm{cr}}^{\mathrm{T}}\boldsymbol{g}_{\mathrm{ap}}\boldsymbol{l}_{\mathrm{cr}}^{\mathrm{T}}\boldsymbol{l}_{\mathrm{cr}} - \left\|\bar{\boldsymbol{l}}_{\mathrm{cr}}\right\|_2 \frac{\partial \bar{\boldsymbol{l}}_{\mathrm{cr}}^{\mathrm{T}}\boldsymbol{g}_{\mathrm{ap}}\boldsymbol{l}_{\mathrm{cr}}^{\mathrm{T}}\boldsymbol{l}_{\mathrm{cr}}}{\partial \boldsymbol{l}_{\mathrm{cr}}}}{\left(\bar{\boldsymbol{l}}_{\mathrm{cr}}^{\mathrm{T}}\boldsymbol{g}_{\mathrm{ap}}\boldsymbol{l}_{\mathrm{cr}}^{\mathrm{T}}\boldsymbol{l}_{\mathrm{cr}}\right)^2}. \tag{A.7.13}$$

The first derivative in T_4 is

$$\begin{aligned}\frac{\partial\left\|\bar{\boldsymbol{l}}_{\mathrm{cr}}\right\|_2}{\partial \boldsymbol{l}_{\mathrm{cr}}} &= \frac{1}{2\left\|\bar{\boldsymbol{l}}_{\mathrm{cr}}\right\|_2}\frac{\partial \bar{\boldsymbol{l}}_{\mathrm{cr}}^{\mathrm{T}}\bar{\boldsymbol{l}}_{\mathrm{cr}}}{\partial \boldsymbol{l}_{\mathrm{cr}}} \\ &= \frac{\bar{\boldsymbol{l}}_{\mathrm{cr}}^{\mathrm{T}}}{\left\|\bar{\boldsymbol{l}}_{\mathrm{cr}}\right\|_2}\tilde{\boldsymbol{N}},\end{aligned} \tag{A.7.14}$$

where

$$\begin{aligned}\frac{\partial \bar{\boldsymbol{l}}_{\mathrm{cr}}^{\mathrm{T}}\bar{\boldsymbol{l}}_{\mathrm{cr}}}{\partial \boldsymbol{l}_{\mathrm{cr}}} &= 2\bar{\boldsymbol{l}}_{\mathrm{cr}}^{\mathrm{T}}\frac{\partial \bar{\boldsymbol{l}}_{\mathrm{cr}}}{\partial \boldsymbol{l}_{\mathrm{cr}}} = 2\bar{\boldsymbol{l}}_{\mathrm{cr}}^{\mathrm{T}}\tilde{\boldsymbol{N}} \\ \tilde{\boldsymbol{N}} = \frac{\partial \bar{\boldsymbol{l}}_{\mathrm{cr}}}{\partial \boldsymbol{l}_{\mathrm{cr}}} &= \frac{\partial\left(\boldsymbol{l}_{\mathrm{cr}} - \mathbf{1}\otimes\frac{\mathbf{1}^{\mathrm{T}}\boldsymbol{l}_{\mathrm{cr}}}{N_{\mathrm{D}}}\right)}{\partial \boldsymbol{l}_{\mathrm{cr}}} = \boldsymbol{I} - \frac{\partial \mathbf{1}\otimes\frac{\mathbf{1}^{\mathrm{T}}\boldsymbol{l}_{\mathrm{cr}}}{N_{\mathrm{D}}}}{\partial \boldsymbol{l}_{\mathrm{cr}}} = \boldsymbol{I} - \frac{1}{N_{\mathrm{D}}}\odot\mathbf{1}_{N_{\mathrm{D}}\times N_{\mathrm{D}}} \\ \frac{\partial \mathbf{1}\otimes\frac{\mathbf{1}^{\mathrm{T}}\boldsymbol{l}_{\mathrm{cr}}}{N_{\mathrm{D}}}}{\partial \boldsymbol{l}_{\mathrm{cr}}} &= \left[\frac{\partial\frac{\mathbf{1}^{\mathrm{T}}\boldsymbol{l}_{\mathrm{cr}}}{N_{\mathrm{D}}}}{\partial l_{\mathrm{cr},j}}\right]_{j=1}^{N_{\mathrm{D}}} = \mathbf{1}\otimes\frac{\partial\frac{\mathbf{1}^{\mathrm{T}}\boldsymbol{l}_{\mathrm{cr}}}{N_{\mathrm{D}}}}{\partial \boldsymbol{l}_{\mathrm{cr}}} = \mathbf{1}\otimes\left(\mathbf{1}^{\mathrm{T}}\otimes\frac{1}{N_{\mathrm{D}}}\right) = \frac{1}{N_{\mathrm{D}}}\odot\mathbf{1}_{N_{\mathrm{D}}\times N_{\mathrm{D}}}\end{aligned}$$

was used. The second derivative in T_4 is

$$\begin{aligned}\frac{\partial \bar{\boldsymbol{l}}_{\mathrm{cr}}^{\mathrm{T}} \boldsymbol{g}_{\mathrm{ap}} \boldsymbol{l}_{\mathrm{cr}}^{\mathrm{T}} \boldsymbol{l}_{\mathrm{cr}}}{\partial \boldsymbol{l}_{\mathrm{cr}}} &= \boldsymbol{l}_{\mathrm{cr}}^{\mathrm{T}} \boldsymbol{l}_{\mathrm{cr}} \frac{\partial \bar{\boldsymbol{l}}_{\mathrm{cr}}^{\mathrm{T}} \boldsymbol{g}_{\mathrm{ap}}}{\partial \boldsymbol{l}_{\mathrm{cr}}} + \bar{\boldsymbol{l}}_{\mathrm{cr}}^{\mathrm{T}} \boldsymbol{g}_{\mathrm{ap}} \frac{\partial \boldsymbol{l}_{\mathrm{cr}}^{\mathrm{T}} \boldsymbol{l}_{\mathrm{cr}}}{\partial \boldsymbol{l}_{\mathrm{cr}}} \\ &= \boldsymbol{l}_{\mathrm{cr}}^{\mathrm{T}} \boldsymbol{l}_{\mathrm{cr}} \boldsymbol{g}_{\mathrm{ap}}^{\mathrm{T}} \tilde{\boldsymbol{N}} + 2 \bar{\boldsymbol{l}}_{\mathrm{cr}}^{\mathrm{T}} \boldsymbol{g}_{\mathrm{ap}} \boldsymbol{l}_{\mathrm{cr}}^{\mathrm{T}},\end{aligned} \tag{A.7.15}$$

where

$$\frac{\partial \bar{\boldsymbol{l}}_{\mathrm{cr}}^{\mathrm{T}} \boldsymbol{g}_{\mathrm{ap}}}{\partial \boldsymbol{l}_{\mathrm{cr}}} = \frac{\partial \boldsymbol{g}_{\mathrm{ap}}^{\mathrm{T}} \bar{\boldsymbol{l}}_{\mathrm{cr}}}{\partial \boldsymbol{l}_{\mathrm{cr}}} = \boldsymbol{g}_{\mathrm{ap}}^{\mathrm{T}} \frac{\partial \bar{\boldsymbol{l}}_{\mathrm{cr}}}{\partial \boldsymbol{l}_{\mathrm{cr}}} = \boldsymbol{g}_{\mathrm{ap}}^{\mathrm{T}} \tilde{\boldsymbol{N}}$$

and

$$\frac{\partial \boldsymbol{l}_{\mathrm{cr}}^{\mathrm{T}} \boldsymbol{l}_{\mathrm{cr}}}{\partial \boldsymbol{l}_{\mathrm{cr}}} = 2 \boldsymbol{l}_{\mathrm{cr}}^{\mathrm{T}}$$

was used. Inserting (A.7.13), (A.7.14), and (A.7.15) into (A.7.12) yields for the first term T_1 after some manipulations

$$\frac{\partial h_{\varphi_{\mathrm{m}}}(\boldsymbol{L}; \beta, \varphi_{\mathrm{m}})}{\partial \boldsymbol{l}_{\mathrm{cr}}} = \frac{2}{\left(\bar{\boldsymbol{l}}_{\mathrm{cr}}^{\mathrm{T}} \boldsymbol{g}_{\mathrm{ap}} \boldsymbol{l}_{\mathrm{cr}}^{\mathrm{T}} \boldsymbol{l}_{\mathrm{cr}}\right)^2} \left(\bar{\boldsymbol{l}}_{\mathrm{cr}}^{\mathrm{T}} \tilde{\boldsymbol{N}} - \frac{\bar{\boldsymbol{l}}_{\mathrm{cr}}^{\mathrm{T}} \bar{\boldsymbol{l}}_{\mathrm{cr}} \left(\boldsymbol{l}_{\mathrm{cr}}^{\mathrm{T}} \boldsymbol{l}_{\mathrm{cr}} \boldsymbol{g}_{\mathrm{ap}}^{\mathrm{T}} \tilde{\boldsymbol{N}} + 2 \bar{\boldsymbol{l}}_{\mathrm{cr}}^{\mathrm{T}} \boldsymbol{g}_{\mathrm{ap}} \boldsymbol{l}_{\mathrm{cr}}^{\mathrm{T}} \right)}{\bar{\boldsymbol{l}}_{\mathrm{cr}}^{\mathrm{T}} \boldsymbol{g}_{\mathrm{ap}} \boldsymbol{l}_{\mathrm{cr}}^{\mathrm{T}} \boldsymbol{l}_{\mathrm{cr}}} \right). \tag{A.7.16}$$

The second term T_2 in (A.7.11) is

$$\begin{aligned}\frac{\partial \boldsymbol{l}_{\mathrm{cr}}}{\partial \left([\boldsymbol{L}']_{i_{\mathrm{cr}}:} \right)^{\mathrm{T}}} &= \left(\frac{\partial \left| [\boldsymbol{L}']_{i_{\mathrm{cr}}:} \right|}{\partial [\boldsymbol{L}']_{i_{\mathrm{cr}}:}} \right)^{\mathrm{T}} \\ &= \left[\frac{\partial |l'_i|}{\partial l'_j} \right]^{\mathrm{T}}\end{aligned} \tag{A.7.17}$$

where

$$\left[\boldsymbol{L}' \right]_{i_{\mathrm{cr}}:}^{\mathrm{T}} = \left[l'_k \right]_{k \in \Omega_{\mathrm{cr}}}$$

was used with $i, j, k \in \Omega_{\mathrm{cr}}$ denoting the clutter ridge index set. The required derivative is

$$\begin{aligned}\frac{\partial |l'_i|}{\partial l'_j} &= \frac{\partial \left(l'^*_i l'_i \right)^{1/2}}{\partial l'_j} \\ &= \frac{\partial \left(l'^*_i l'_i \right)^{1/2}}{\partial l'^*_i l'_i} \frac{\partial l'^*_i l'_i}{\partial l'_j} + \frac{\partial \left(l'^*_i l'_i \right)^{1/2}}{\partial \left(l'^*_i l'_i \right)^*} \frac{\partial l'^*_i l'_i}{\partial l'^*_i} \\ &= 2 \frac{\partial \left(l'^*_i l'_i \right)^{1/2}}{\partial l'^*_i l'_i} \frac{\partial l'^*_i l'_i}{\partial l'_j} \\ &= \frac{1}{|l'_i|} \delta_{ij} l'^*_i \\ &= \operatorname{diag} \left(\left[\frac{l'^*_i}{|l'_i|} \right]_{i=1}^{N_{\mathrm{D}}} \right) \in \mathbb{C}^{N_{\mathrm{D}} \times N_{\mathrm{D}}}.\end{aligned} \tag{A.7.18}$$

where the Wirtinger derivatives need to be used since $l'_i \in \mathbb{C}$. Substituting (A.7.18) into (A.7.17) yields for the term T_2

$$\frac{\partial \boldsymbol{l}_{\mathrm{cr}}}{\partial \left([\boldsymbol{L}']_{i_{\mathrm{cr}}:} \right)^{\mathrm{T}}} = \operatorname{diag} \left(\left[\frac{l'^*_i}{|l'_i|} \right]_{i=1}^{N_{\mathrm{D}}} \right). \tag{A.7.19}$$

The last term T_3 is

$$\frac{\partial \left([\boldsymbol{L}']_{i_{\mathrm{cr}}:}\right)^{\mathrm{T}}}{\partial \varphi_{\mathrm{m}}} = \left(\left[\frac{\partial \boldsymbol{L}'}{\partial \varphi_{\mathrm{m}}} \right]_{i_{\mathrm{cr}}:} \right)^{\mathrm{T}}. \tag{A.7.20}$$

The required derivative is

$$\begin{aligned} \frac{\partial \boldsymbol{L}'}{\partial \varphi_{\mathrm{m}}} &= \frac{\partial \left(\boldsymbol{L} - \mu \nabla_{\boldsymbol{L}} h\left(\boldsymbol{L}; \beta, \varphi_{\mathrm{m}}\right)\right)}{\partial \varphi_{\mathrm{m}}} \\ &= -\mu \frac{\partial \mathcal{A}^{\mathrm{H}}\left(\mathcal{A}\left(\boldsymbol{L}; \beta, \varphi_{\mathrm{m}}\right) - \boldsymbol{y}\right)}{\partial \varphi_{\mathrm{m}}} \\ &= \mu \mathcal{A}^{\mathrm{H}} \left(\frac{\partial \mathcal{A}\left(\boldsymbol{L}; \beta, \varphi_{\mathrm{m}}\right)}{\partial \varphi_{\mathrm{m}}} \right) \end{aligned}$$

where (A.7.10) and (A.7.2) was used. The derivative of the sensing operator is similar to (A.7.9), however, with a different inner derivative as

$$\frac{\partial \mathcal{A}\left(\boldsymbol{L}; \beta, \varphi_{\mathrm{m}}\right)}{\partial \varphi_{\mathrm{m}}} = \mathrm{vec}\left(-\mathrm{j}2\pi \boldsymbol{A} \boldsymbol{F}_1 \left(\left(\boldsymbol{n}_{\bar{u}} \frac{\partial \bar{\boldsymbol{u}}_{\triangle}^{\mathrm{T}}(\beta, \varphi_{\mathrm{m}})}{\partial \varphi_{\mathrm{m}}} \right) \odot \boldsymbol{U}_{\triangle}^{*}(\beta, \varphi_{\mathrm{m}}) \odot \left(\boldsymbol{F}_1^{-1} \boldsymbol{L} \right) \right) \boldsymbol{B}^{\mathrm{T}} \right) \tag{A.7.21}$$

with

$$\frac{\partial \bar{\boldsymbol{u}}_{\triangle}(\beta, \varphi_{\mathrm{m}})}{\partial \varphi_{\mathrm{m}}} = \left[\frac{\partial \triangle \bar{u}\left(i/N_{\mathrm{D}}; \beta, \varphi_{\mathrm{m}}\right)}{\partial \varphi_{\mathrm{m}}} \right]_{i=-N_{\mathrm{D}}/2}^{N_{\mathrm{D}}/2-1}$$

and

$$\frac{\partial \triangle \bar{u}\left(\bar{f}_{\mathrm{D}}; \beta, \varphi_{\mathrm{m}}\right)}{\partial \varphi_{\mathrm{m}}} = \frac{\bar{f}_{\mathrm{D}}}{\beta} \sin(\varphi_{\mathrm{m}}) + \cos\left(\varphi_{\mathrm{m}}\right) \sqrt{\left| \bar{d}^2 \sin^2\left(\vartheta\right) - \bar{f}_{\mathrm{D}}{}^2/\beta^2 \right|},$$

where (A.7.4) and (A.7.5) was used. Recapturing (A.7.11), the wanted derivative is

$$\nabla_{\varphi_{\mathrm{m}}} h_{\varphi_{\mathrm{m}}}(\boldsymbol{L}; \beta, \varphi_{\mathrm{m}}) = \underbrace{\frac{\partial h_{\varphi_{\mathrm{m}}}(\boldsymbol{L}; \beta, \varphi_{\mathrm{m}})}{\partial \boldsymbol{l}_{\mathrm{cr}}}}_{T_1} \mathrm{Re}\left\{ \underbrace{\frac{\partial \boldsymbol{l}_{\mathrm{cr}}}{\partial \left([\boldsymbol{L}']_{i_{\mathrm{cr}}:}\right)^{\mathrm{T}}}}_{T_2} \underbrace{\frac{\partial \left([\boldsymbol{L}']_{i_{\mathrm{cr}}:}\right)^{\mathrm{T}}}{\partial \varphi_{\mathrm{m}}}}_{T_3} \right\}$$

with T_1 given by (A.7.16), T_2 by (A.7.19), and T_3 by (A.7.20).

The Jacobi derivative required for the Levenberg-Marquardt (LM) step size determination in Chapter 7.2.2 is

$$\frac{\partial f(\boldsymbol{L}; \beta, \varphi_{\mathrm{m}})}{\partial \varphi_{\mathrm{m}}} = \underbrace{\frac{\partial f(\boldsymbol{L}; \beta, \varphi_{\mathrm{m}})}{\partial \boldsymbol{l}_{\mathrm{cr}}}}_{T_4} \mathrm{Re}\left\{ \underbrace{\frac{\partial \boldsymbol{l}_{\mathrm{cr}}}{\partial \left([\boldsymbol{L}']_{i_{\mathrm{cr}}:}\right)^{\mathrm{T}}}}_{T_2} \underbrace{\frac{\partial \left([\boldsymbol{L}']_{i_{\mathrm{cr}}:}\right)^{\mathrm{T}}}{\partial \varphi_{\mathrm{m}}}}_{T_3} \right\} \tag{A.7.22}$$

with T_2 given by (A.7.19), T_3 by (A.7.20), and T_4 by (A.7.13).

Publications

Some ideas and figures have appeared previously in the following publications:

- Reinhard Panhuber and Ludger Prünte. "Step Size Determination for Finding Low-Rank Solutions Via Non-Convex Bi-Factored Matrix Factorization." In: 2020 28th European Signal Processing Conference (EUSIPCO). 2021, pp. 2100–2104.
- Reinhard Panhuber and Ludger Prünte. "Complex Successive Concave Sparsity Approximation." In: 2020 21st International Radar Symposium (IRS). 2020, pp. 67–72.
- Auto-Clutter Focus Algorithm was filed for patent

Acronyms

ABW	antenna beam width - symbol: ABW
ACE	adaptive coherence estimator
ACF	auto-clutter focus
AF	ambiguity function - symbol: A
AMF	adaptive matched filter
APSF	alternating projection sub sample filtering
ARM	affine rank minimization
BFGD	bi-factored gradient descent
BPDN	basis pursuit denoise
CDF	cumulative density function
CFAR	constant false alarm rate
CL	correlation loss - symbol: CL
CNR	clutter to noise ratio - symbol: CNR
CPI	coherent processing interval
CRPCA	compressed robust principal component analysis
CS	compressive sensing
CSCSA	complex successive concave sparsity approximation
CSRA	complex smoothed rank approximation
CUT	cell under test
CW	continuous wave
D.C.	differenct of convex
DFT	discrete Fourier transform
DL	diagonal loading
DPCA	displaced phase center antenna
DSB	delay and sum beamforming

EM	electromagnetic
FFT	fast Fourier transform
FIR	finite impulse response
FISTA	fast iterative shrinkage-thresholding algorithm
FT	Fourier transform
GLRT	generalized likelihood ratio test
GMTI	ground moving target indication
GNC	graduated non-convexity
GPS	global positioning system
HT	hard thresholding
ICM	internal clutter motion
IDFT	inverse discrete Fourier transform
IFT	inverse Fourier transform
IMU	inertial measurement unit
IT	iterative thresholding
KA STAP	knowledge-aided STAP
LASSO	least absolute shrinkage and selection operator
LFM	linear frequency modulation
LIDAR	light detection and ranging
LM	Levenberg-Marquardt
LO	local oscillator
LOS	line of sight
MC	Monte Carlo
MDV	minimum detectable velocity
MF	matched filter
MS	matched subspace

MVDR minimum variance distortionless response

NIHT normalized iterative hard thresholding
NMF normalized matched filter
NN neural network
NNM nuclear norm minimization

PCP principal component pursuit
PFA probability of false alarm - symbol: p_{FA}
PRF pulse repetition frequency - symbol: f_{p}
PRI pulse repetition interval - symbol: t_{p}

RCS radar cross section - symbol: σ_{r}
ReLU rectified linear unit
RF radio frequency
RIP restricted isometry property
RMB Reed, Mallot, and Brennan
ROIL right-orthogonally invariant linear
RPCA robust principal component analysis
RRIP restricted rank isometry property
RTDT round trip delay time - symbol: τ
RV random variable
RX receive

SAR synthetic aperture radar
SCM sample covariance matrix
SCSA successive concave sparsity approximation
SINR signal to interference and noise ratio - symbol: SINR
SIRV spherically invariant random vector
SNR signal to noise ratio - symbol: SNR
SPGL1 spectral projected gradient for ℓ_1
SRA smoothed rank approximation
SRE squared reconstruction error - symbol: SRE
SRF smoothed rank function

SRR	support recovery rate
SSF	sub sampling factor - symbol: SSF
ST	soft thresholding
STAP	space-time adaptive processing
STAR	space-time autoregressive
SVD	singular value decomposition
SVP	singular value projection
SVT	singular value thresholding
SVT-Turbo-CS	singular value thresholding-turbo-compressive sensing
TARM	turbo affine rank minimization
TCRPCA	turbo compressed robust principal component analysis
TEM	transverse electromagnetic
TST	turbo shrinkage-thresholding
TSVT	turbo singular value thresholding
TX	transmit
ULA	uniform linear array
WSS	wide-sense stationary

Notations

$\mathbf{1}_A$	Indicator function $\mathbf{1}_A : X \to \{0,1\}$ as $\mathbf{1}_A(x) = \begin{cases} 1 & \text{if } x \in A \\ 0 & \text{else} \end{cases}$ with A being a subset of X
x	Scalar variable
$\boldsymbol{x}$	Column vector in $\mathbb{C}^N$ comprised from scalar entries $\boldsymbol{x} = [x_1, \cdots, x_N]^{\mathrm{T}}$
$\vec{x}$	Geometrical 3D vector
$\boldsymbol{X}$	Matrix in $\mathbb{C}^{N_1 \times N_2}$ comprised from column vectors $\boldsymbol{X} = [\boldsymbol{x}_1, \cdots, \boldsymbol{x}_{N_2}]$
$\mathcal{X}$	Tensor, operator, or set
$x_i = [\boldsymbol{x}]_i$	The i-th entry of vector $\boldsymbol{x}$
$\boldsymbol{x}_i = [\boldsymbol{X}]_{:i}$	The i-th column of matrix $\boldsymbol{X}$
$\boldsymbol{y}_i = [\boldsymbol{X}]_{i:}$	The i-th row of matrix $\boldsymbol{X} \in \mathbb{C}^{N_1 \times N_2}$ where $\boldsymbol{y}_i \in \mathbb{C}^{N_2 \times 1}$ is a column vector. Instead of $\boldsymbol{y}_i$ any other lower case letter but that of the matrix may be used as it is especially reserved for its column vector
$x_{ij} = [\boldsymbol{X}]_{ij}$	The (i,j)-th entry of matrix $\boldsymbol{X}$
$x_{ij\cdots k} = [\mathcal{X}]_{ij\cdots k}$	The $(i,j,\cdots,k)$-th entry of tensor $\mathcal{X}$
$\mathrm{card}\,\{\mathcal{S}\}$	Cardinality of set $\mathcal{S}$
$\mathcal{CN}(\mu, \sigma^2)$	Complex normal distributed e. g. x is a complex normal distributed RV with mean μ and variance σ^2 as $x \sim \mathcal{CN}\left(\mu, \sigma^2\right)$
x^*	Complex conjugate
$(f_1 * f_2)(t)$	Convolution of $f_1(x)$ and $f_2(x)$ as $\int_{-\infty}^{\infty} f_1(\tau)\, f_2(x-\tau)\, \mathrm{d}\tau$
$\mathrm{corr}\,\{f_1, f_2\}(\tau)$	Correlation of $f_1(x)$ and $f_2(x)$ as $\int_{-\infty}^{\infty} f_1^*(x)\, f_2(x+\tau)\, \mathrm{d}x$
$\mathrm{diag}\,\{\boldsymbol{x}\}$	Matrix with diagonal entries from $\boldsymbol{x}$ and zero elsewhere

$\operatorname{diag}\{\boldsymbol{X}\}$	Vector from the diagonal entries of $\boldsymbol{X}$
$\mathrm{E}\{x\}$	Expectation value of random variable x
$\mathcal{X}^{\mathrm{H}}$	Hermitian adjoint - if applied onto a matrix $\boldsymbol{X}$ or vector $\boldsymbol{x}$ this coincides with Hermitian transpose or conjugate transpose
$\operatorname{Im}\{x\}$	Imaginary part of number
δ_{ij}	Kronecker delta function $\delta_{ij} = 1$ if $i = j$
$\|\vec{x}\|$	ℓ_2 norm of geometric vector
$\|\boldsymbol{X}\|_{\mathrm{F}}$	Frobenius norm
$\|\boldsymbol{X}\|_{\infty}$	Infinity norm denoting the biggest entry in magnitude from $\boldsymbol{X}$
$\|x\|$	Magnitude of scalar value
$\|\boldsymbol{X}\|_{*}$	Nuclear norm
$\|\boldsymbol{X}\|$	Spectral norm a. k. a. operator norm
$\|\boldsymbol{x}\|_{p}$	ℓ_p norm
$\|\boldsymbol{x}\|_{0}$	ℓ_0 quasinorm i. e. number of non zero entries in $\boldsymbol{x}$
$\langle \boldsymbol{X}, \boldsymbol{Y} \rangle_{\mathrm{F}}$	Frobenius product
$\boldsymbol{X} \odot \boldsymbol{Y}$	Hadamard product
$\langle \vec{x}, \vec{y} \rangle$	Inner vector product
$\boldsymbol{X} \otimes \boldsymbol{Y}$	Kronecker product
$\operatorname{rank}\{\boldsymbol{X}\}$	Rank of matrix $\boldsymbol{X}$ i. e. number of linear independent rows or columns. Equivalent to the number of non zero singular values of $\boldsymbol{X}$
$\operatorname{Re}\{x\}$	Real part of number
$\lfloor x \rfloor$	Round off to next integer value
$\lfloor x \rceil$	Round to closest integer value
$\lceil x \rceil$	Round up to next integer value
$\operatorname{sgn}(z)$	Complex sign function $\operatorname{sgn} : \mathbb{C} \to \mathbb{C}$ defined as $\operatorname{sgn}(z) = \begin{cases} 0 & \text{if } z = 0 \\ \frac{z}{\lvert z \rvert} & \text{else} \end{cases}$
$\widehat{x}$	Estimated value of variable x
$\widetilde{x}$	True value of to be estimated variable x
$\operatorname{supp}(\boldsymbol{X})$	Support of matrix $\boldsymbol{X}$ i. e. a list of indices of the non zero entries of $\boldsymbol{X}$

$\boldsymbol{X}^{\mathrm{T}}$	Matrix transpose
$\mathrm{vec}\{\boldsymbol{X}\}$	Vectorization of matrix $\boldsymbol{X} \in \mathbb{C}^{n_1 \times n_2}$ by stacking all columns on top of each other i. e. $\mathrm{vec}\{\boldsymbol{X}\} = \left[\boldsymbol{x}_1^{\mathrm{T}}, \cdots, \boldsymbol{x}_{n_2}^{\mathrm{T}}\right]^{\mathrm{T}}$

Symbols

Symbol	Description	Unit
A	Ambiguity function (AF)	
ABW	Antenna beam width (ABW)	deg
α_r	Reflectivity coefficient	
$\boldsymbol{A}$	Space matrix formed by space steering vectors as $\boldsymbol{A} = [\boldsymbol{a}\left(n_\mathrm{u}/N_\mathrm{u}\right)]_{n_\mathrm{u}=0}^{N_\mathrm{u}-1} \in \mathbb{C}^{N_\mathrm{rx}\times N_\mathrm{u}}$	
$\mathcal{A}$	Linear map $\mathcal{A} : \mathbb{C}^{N_1\times N_2} \to \mathbb{C}^{M}$ from scene into measurement domain	
$\boldsymbol{a}$	Space vector a. k. a. angular steering vector corresponding to a point target	
β	Slope of clutter ridge in case of no missalignment i. e. $\beta = \bar{f}_\mathrm{D}/\bar{u} = 2v_\mathrm{p}/f_\mathrm{p}/d$	
$\boldsymbol{B}$	Time matrix formed by time steering vectors as $\boldsymbol{B} = [\boldsymbol{b}\left(n_\mathrm{D}/N_\mathrm{D}\right)]_{n_\mathrm{D}=0}^{N_\mathrm{D}-1} \in \mathbb{C}^{N_\mathrm{p}\times N_\mathrm{D}}$	
b_r	Range/fast time bandwidth	Hz
$\boldsymbol{b}$	Time vector a. k. a. temporal steering vector corresponding to a point target	
c_0	speed of light	m/s
C_dn	Complex down conversion coefficient with respect to given base band frequency f_b	
CL	Correlation loss (CL)	
CNR	Clutter to noise ratio (CNR) after pulse compression and integration over pulses and channels	
C_up	Complex up conversion coefficient with respect to given base band frequency f_b	
d	Distance between consecutive channels for a ULA antenna	m
δr	Range resolution as $\delta r = \frac{c_0}{2b_\mathrm{r}}$	m
δu	Angular array resolution which for a ULA phased array is $\delta u = N_\mathrm{rx}/\bar{d}$	
d_F	Fraunhofer distance $d_\mathrm{F} = 2D^2/\lambda_\mathrm{r}$ with $D > 2.5\lambda_\mathrm{r}$ denoting biggest antenna apperture size	m
$\bar{d}$	Normalized distance between consecutive channels for a ULA antenna i. e. $\bar{d} = d/\lambda_\mathrm{c}$	

Symbol	Description	Unit
$\vec{e}_{\mathrm{sc}}$	EM wave scattered by a target	
$\vec{e}_{\mathrm{tx}}$	EM wave transmitted by a TX antenna	
ε_0	Vacuum permittivity $\varepsilon_0 = 8.8541878128(13) \cdot 10^{-10}$	F/m
η_{w}	Impedance of free space $\eta_{\mathrm{w}} = 376.730313668(57) \approx 120\pi$	Ω
f_{b}	Instantaneous base band frequency of the radar signal	Hz
f_{c}	Center frequency of radar signal	Hz
f_{D}	Doppler frequency	Hz
f_{Dc}	Clutter Doppler frequency	Hz
$\bar{f}_{\mathrm{Dc}}$	Normalized clutter Doppler frequency $\bar{f}_{\mathrm{Dc}} = f_{\mathrm{Dc}}/f_{\mathrm{p}}$	
$\bar{f}_{\mathrm{D}}$	Normalized Doppler frequency $\bar{f}_{\mathrm{D}} = f_{\mathrm{D}}/f_{\mathrm{p}}$	
f_{Dt}	Target Doppler frequency	Hz
$\bar{f}_{\mathrm{Dt}}$	Normalized target Doppler frequency $\bar{f}_{\mathrm{Dt}} = f_{\mathrm{Dt}}/f_{\mathrm{p}}$	
f_{p}	Pulse repetition frequency (PRF)	Hz
f_{r}	Instantaneous frequency of radar signal $f_{\mathrm{r}} = f_{\mathrm{c}} + f_{\mathrm{b}}$	Hz
g	Space-time sample denoting the deterministic signal part of the radar signal model	
$\boldsymbol{G}$	Space-time matrix corresponding to a point target i. e. $\boldsymbol{G} = \boldsymbol{a}\boldsymbol{b}^{\mathrm{T}}$	
G_{rx}	RX antenna gain	1
G_{tx}	TX antenna gain	1
$\boldsymbol{g}$	Space-time vector corresponding to a point target i. e. $\boldsymbol{g} = \boldsymbol{b} \otimes \boldsymbol{a}$	
$\boldsymbol{g}_{\mathrm{c}}$	Space-time vector corresponding to a single clutter patch x_{c}	
$H_{\mathrm{b,rx}}$	Base band transfere function of an RX path	
$H_{\mathrm{b,tx}}$	Base band transfere function of a TX path	
h_{p}	Flight altitute above ground	m
$H_{\mathrm{r,rx}}$	RF band transfere function of an RX path excluding antenna	
$H_{\mathrm{r,tx}}$	RF band transfere function of a TX path excluding antenna	
κ	Number of sparse or non-zero entries	
k_{b}	Wave number corresponding to instantaneous base band frequency of radar signal i. e. $k_{\mathrm{b}} = 2\pi/\lambda_{\mathrm{b}}$	rad/m
k_{c}	Wave number corresponding to center frequency of radar signal i. e. $k_{\mathrm{c}} = 2\pi/\lambda_{\mathrm{c}}$	rad/m
k_{r}	Wave number corresponding to instantaneous frequency of radar signal i. e. $k_{\mathrm{r}} = 2\pi/\lambda_{\mathrm{r}}$	rad/m

Symbol	Description	Unit
$\boldsymbol{L}$	Low rank matrix	
Λ	Triangular or tent function $\Lambda(x) = \max(1 - \lvert x\rvert, 0)$	
λ_b	Wave length corresponding to instantaneous base band frequency of radar signal $\lambda_\mathrm{b} = c_0/f_\mathrm{b}$	m
λ_c	Wave length corresponding to center frequency of radar signal $\lambda_\mathrm{c} = c_0/f_\mathrm{c}$	m
λ_r	Wave length corresponding to instantaneous frequency of radar signal $\lambda_\mathrm{r} = c_0/f_\mathrm{r}$	m
M	Number of measurements	
μ_0	Magnetic permeability of free space $\mu_0 = 1.25663706212(19) \cdot 10^{-6} \approx 4\pi \times 10^{-7}$	N
$\boldsymbol{n}$	Noise vector	
N_c	Number of clutter patches	
N_D	Number of Doppler bins	
N_mc	Number of Monte Carlo runs	
N_p	Number of pulses	
N_rx	Number of RX channels	
N_t	Number of targets in radar scene	
N_tx	Number of TX channels	
N_u	Number of cone angle or looking direction bins	
ω_b	Instantaneous base band angular frequency of the radar signal i. e. $\omega_\mathrm{b} = 2\pi f_\mathrm{b}$	s^{-1}
ω_c	Center angular frequency of radar signal i. e. $\omega_\mathrm{c} = 2\pi f_\mathrm{c}$	s^{-1}
ω_D	Angular Doppler frequencey i. e. $\omega_\mathrm{D} = 2\pi f_\mathrm{D}$	s^{-1}
ω_r	Instantaneous radio angular frequency of the radar signal i. e. $\omega_\mathrm{r} = 2\pi f_\mathrm{r}$	s^{-1}
$\vec{p}$	Vector pointing to phase center of RX channel	m
P_c	Clutter power defined as $P_\mathrm{c} = E\left\{\lvert x_\mathrm{c}\rvert^2\right\}$	W
p_D	Probability of detection	
p_FA	Probability of false alarm (PFA)	
ϕ_c	Phase offset corresponding to f_c	rad
ϕ_dn	Phase offset occuring during down-mixing from radio frequency (RF) band into base band	rad
φ_m	Missalignment angle between platform velocity vector and antenna x axis $\varphi_\mathrm{m} = \angle(\vec{v}_\mathrm{p}, \vec{x}_\mathrm{ant})$	rad
ϕ_up	Phase offset occuring during up-mixing from base band into RF band	rad

Symbol	Description	Unit
φ	Azimuthal angle - part of spherical target coordinates	rad
P_n	Noise power	W
ψ	Cone angle between the LOS vector and antenna y axis $\psi = \angle(\vec{u}, \vec{y}_\mathrm{ant})$	rad
P_t	Target power defined as $P_\mathrm{t} = E\left\{\lvert x_\mathrm{t}\rvert^2\right\}$	W
P_tx	Transmit signal power	W
$\vec{q}$	Vector pointing to phase center of TX channel	m
$\boldsymbol{R}$	Covariance matrix	
r	Range	m
$\boldsymbol{R}_\mathrm{c}$	Clutter covariance matrix	
ρ	Rank of matrix	
$\boldsymbol{S}$	Sparse matrix	
s	Deterministic signal	
σ_r	Radar cross section (RCS)	m^2
SINR	Signal to interference and noise ratio (SINR)	
SNR	Signal to noise ratio (SNR) after pulse compression and integration over pulses and channels	
SRE	Squared reconstruction error (SRE)	
SSF	Sub sampling factor (SSF)	
τ	Round trip delay time (RTDT)	s
θ	Cone angle between the LOS vector and antenna x axis $\theta = \angle(\vec{u}, \vec{x}_\mathrm{ant})$	rad
ϑ_m	Polar angle between platform velocity vector $\vec{v}_\mathrm{p}$ and antenna z axis in antenna reference frame a. k. a. polar misalignment angle with respect to a ULA oriented along the x axis	rad
ϑ	Polar angle - part of spherical target coordinates	rad
T_p	pulse length	s
t_p	Pulse repetition interval (PRI)	s
u	Directional cosine i. e. cosine of cone angle $u = \cos(\theta)$	
$\bar{u}$	Normalized directional cosine $\bar{u} = u\bar{d}$	
$\vec{u}$	LOS unit vector pointing from the antenna center to scatterer	
$\vec{u}_\mathrm{t}$	LOS unit vector pointing from the antenna center to target	
v	y axis component of LOS vector $\vec{u}$ and likewise $v = \cos(\psi)$	
v_p	Platform velocity relative to the earth surface fixed reference frame	m/s
$\vec{v}_\mathrm{p}$	Platform velocity vector relative to earth surface fixed reference frame	m/s

Symbol	Description	Unit
v_r	From the radar observed radial velocity i. e. relative to antenna reference frame	m/s
v_rt	From the radar observed radial velocity of a target i. e. relative to antenna reference frame	m/s
v_t	Target velocity relative to the earth surface fixed reference frame	m/s
$\vec{v}_\mathrm{t}$	Target velocity vector relative to the earth surface fixed reference frame	m/s
w	z axis component of LOS vector $\vec{u}$ and likewise $v = \cos(\vartheta)$	
$\boldsymbol{w}$	Filter vector	
$\boldsymbol{X}$	Radar scene a. k. a. reflectivity or scatter map in angle-Doppler domain $\boldsymbol{X} \in \mathbb{C}^{N_\mathrm{u} \times N_\mathrm{D}}$	
x_c	Amplitude of a single clutter patch	
$\boldsymbol{x}_\mathrm{c}$	Vector of clutter amplitudes $x_\mathrm{c}(u)$ corresponding to N_c clutter patches equally distributed on the interval $[-1, 1)$	
$\boldsymbol{X}_\mathrm{t}$	Radar scene comprised from target contributions only	
x_t	Amplitude of a single target in angle-Doppler domain	
$\boldsymbol{Y}$	Measurement matrix in channel-pulse domain $\boldsymbol{Y} \in \mathbb{C}^{N_\mathrm{rx} \times N_\mathrm{p}}$	
$\boldsymbol{y}$	Measurement vector $\boldsymbol{y} \in \mathbb{C}^{M}$	
$\boldsymbol{Y}_\mathrm{c}$	Measurement matrix comprised from clutter contributions only	
$\boldsymbol{y}_\mathrm{c}$	Clutter measurement vector	
$\boldsymbol{y}_\mathrm{t}$	Target measurement vector	

Glossary

Affine Rank Minimization (ARM) In affine rank minimization, one observes M measurements as $\boldsymbol{y} = \mathcal{A}(\boldsymbol{L}) + \boldsymbol{n}$, where $\mathcal{A} : \mathbb{C}^{n_1 \times n_2} \to \mathbb{C}^M$ is a known linear map, $\boldsymbol{L} \in \mathbb{C}^{n_1 \times n_2}$ is an unknown low rank matrix, and $\boldsymbol{n} \in \mathbb{C}^M$ is an error vector. The goal of affine rank minimization (ARM) is to reconstruct $\boldsymbol{L}$ from the observed M measurements, where the dimension $n_1 \times n_2$ is usually much larger than the number of measurements.

Antenna Beam Width (ABW) The horizontal half power or 3 dB width of the antenna main beam - symbol: ABW.

Compressed Robust Principal Component Analysis (CRPCA) Compressed robust principal component analysis is a signal processing technique that allows for the reconstruction of a low-rank matrix $\boldsymbol{L}$ and a sparse matrix $\boldsymbol{S}$ from noisy measurements as $\boldsymbol{y} = \mathcal{A}(\boldsymbol{S} + \boldsymbol{L}) + \boldsymbol{z}$. This is possible, if the so called rank-sparsity incoherence is fulfilled.

Compressive Sensing (CS) Compressive sensing is a signal processing technique that allows for signals to be reconstructed with lower sampling rate than with Nyquist´s Law. This is possible if the signal is sparse under some transformation and thus allows for finding solutions to underdetermined linear systems through optimization techniques .

Ground Moving Target Indication (GMTI) The aim of GMTI is to detect targets moving relative to the earth surface and to estimate their positions, velocities, and moving directions. The fundamental difficulty of GMTI is the successful suppression of clutter i. e. reflections from the earth's surface. This is especially challenging in heterogeneous terrain e. g. if land-water transitions, strong single scatterers such as poles and buildings, etc. occur in the radar scene .

Internal Clutter Motion (ICM) ICM refers to interfering reflections from slightly moving objects e. g. Trees or fields in the wind, waves in the sea, etc. This additional clutter complicates the detection of moving targets as it increases the MDV .

Rectified Linear Unit (ReLU) In the context of neural networks, ReLU is an activation function defined as $f(x) = \max(0, x)$ [87].

Right-orthogonally Invariant Linear (ROIL) Consider a linear operator $\mathcal{A}$ with matrix form $\boldsymbol{A}$, the SVD of $\boldsymbol{A}$ is $\boldsymbol{A} = \boldsymbol{U}_A \boldsymbol{\Sigma}_A \boldsymbol{V}_A^{\mathrm{H}}$. If $\boldsymbol{V}_A$ is a Haar distributed random matrix independent of $\boldsymbol{\Sigma}_A$, we say that $\mathcal{A}$ is a right-orthogonally invariant linear (ROIL) operator.

Robust Principal Component Analysis (RPCA) Robust principal component analysis is a signal processing technique that allows for the decomposition of a matrix $\boldsymbol{M}$ into a low-rank matrix $\boldsymbol{L}$ and a sparse matrix $\boldsymbol{S}$ as $\boldsymbol{M} = \boldsymbol{S} + \boldsymbol{L}$. This is possible, if the so called rank-sparsity incoherence is fulfilled .

Round Trip Delay Time (RTDT) The time a wave needs to travel to a target and return - symbol: τ.

Bibliography

[1] J.R. Guerci. *Space-Time Adaptive Processing for Radar, Second Edition*. Artech House radar library. Artech House Publishers, 2014. isbn: 9781608078219. url: https://books.google.de/books?id=5efmBgAAQBAJ.

[2] M.A. Richards. *Fundamentals of Radar Signal Processing*. Professional Engineering. Mcgraw-hill, 2005. isbn: 9780071444743. url: https://books.google.co.in/books?id=VOvsJ7G1oDEC.

[3] W. A. Davis. "RF Mixers". In: *Radio Frequency Circuit Design*. 2010, pp. 289–319. doi: 10.1002/9780470768020.ch11.

[4] Joachim H. G. Ender. *Introduction to Radar*. University Lecture.

[5] W.L. Stutzman and G.A. Thiele. *Antenna Theory and Design*. Antenna Theory and Design. Wiley, 2012. isbn: 9780470576649. url: https://books.google.at/books?id=xhZRA1K57wIC.

[6] P.A. Tipler, G. Mosca, and D. Pelte. *Physik für Wissenschaftler und Ingenieure*. Spektrum Akad. Verlag, 2004. isbn: 9783827411648. url: https://books.google.at/books?id=pSThOAAACAAJ.

[7] Z. Idriss, R. G. Raj, and R. M. Narayanan. "Matched Illumination Waveform Optimization for Radar Imaging". In: *2020 IEEE International Radar Conference (RADAR)*. 2020, pp. 952–957. doi: 10.1109/RADAR42522.2020.9114628.

[8] Jose-Maria Munoz-Ferreras and Roberto Gomez-Garcia. "Beyond the Stop-and-Go Assumption in Pulse-Doppler Radar Sensors". In: *Sensors Journal, IEEE* 14 (Sept. 2014), pp. 3046–3051. doi: 10.1109/JSEN.2014.2323422.

[9] Q. Zhang et al. "Echo Model Without Stop-and-Go Approximation for Bistatic SAR With Maneuvers". In: *IEEE Geoscience and Remote Sensing Letters* 16.7 (2019), pp. 1056–1060. doi: 10.1109/LGRS.2019.2891510.

[10] R.J. Mailloux. *Phased Array Antenna Handbook, Third Edition*. Artech House antennas and electromagnetics analysis library. Artech House Publishers, 2017. isbn: 9781630815080. url: http://twanclik.free.fr/electricity/electronic/pdfdone11/Phased.Array.Antenna.Handbook.Artech.House.Publishers.Second.Edition.eBook-kB.pdf.

[11] B. Friedlander. "Array calibration in the presence of linear manifold distortion". In: *2017 51st Asilomar Conference on Signals, Systems, and Computers*. 2017, pp. 1199–1203. doi: 10.1109/ACSSC.2017.8335541.

[12] B. Friedlander. "Local Calibration of Antenna Arrays". In: *2018 52nd Asilomar Conference on Signals, Systems, and Computers*. 2018, pp. 1137–1141. doi: 10.1109/ACSSC.2018.8645517.

[13] B. Friedlander. "Antenna Array Calibration with Model Mismatch". In: *2019 53rd Asilomar Conference on Signals, Systems, and Computers*. 2019, pp. 1284–1288. doi: 10.1109/IEEECONF44664.2019.9048733.

[14] B. Friedlander. "The Extended Manifold for Diversely Polarized Antenna Arrays". In: *2019 53rd Asilomar Conference on Signals, Systems, and Computers*. 2019, pp. 1262–1266. doi: 10.1109/IEEECONF44664.2019.9048956.

[15] B. Friedlander. "The Extended Manifold for Antenna Arrays". In: *IEEE Transactions on Signal Processing* 68 (2020), pp. 493–502. doi: 10.1109/TSP.2020.2964213.

[16] Tao Su and Hao Ling. "On modeling mutual coupling in antenna arrays using the coupling matrix". In: *Microwave and Optical Technology Letters* 28 (Feb. 2001), pp. 231–237. doi: 10.1002/1098-2760(20010220)28:4<231::AID-MOP1004>3.0.CO;2-P.

[17] J. Ward. *Space-Time Adaptive Processing for Airborne Radar*. 1994.

[18] T. Arens et al. *Ergänzungen und Vertiefungen zu Arens et al., Mathematik*. Springer Berlin Heidelberg, 2017. isbn: 9783662535851. url: https://books.google.de/books?id=DtgoDwAAQBAJ.

[19] George A. Campbell and Ronald M. Foster. "Fourier integrals for practical applications". In: 1931.

[20] P. Parker and A. Swindlehurst. "Space-time autoregressive filtering for matched subspace STAP". In: *IEEE Transactions on Aerospace and Electronic Systems* 39.2 (Apr. 2003), pp. 510–520. doi: 10.1109/TAES.2003.1207263.

[21] J. A. Russ, D. W. Casbeer, and A. L. Swindlehurst. "STAP detection using space-time autoregressive filtering". In: *Proceedings of the 2004 IEEE Radar Conference (IEEE Cat. No.04CH37509)*. Apr. 2004, pp. 541–545. doi: 10.1109/NRC.2004.1316483.

[22] Joachim Ender. "Space-time processing for multichannel synthetic aperture radar". In: *Electronics and Communication Engineering Journal* 11 (Mar. 1999), pp. 29–38. doi: 10.1049/ecej:19990106.

[23] Alberto Zanella and Marco Chiani. "The PDF of the lth Largest Eigenvalue of Central Wishart Matrices and its Application to the Performance Analysis of MIMO Systems". In: *IEEE GLOBECOM 2008 - 2008 IEEE Global Telecommunications Conference*. 2008, pp. 1–6. doi: 10.1109/GLOCOM.2008.ECP.210.

[24] E. J. Kelly. "An Adaptive Detection Algorithm". In: *IEEE Transactions on Aerospace and Electronic Systems* AES-22.2 (Mar. 1986), pp. 115–127. issn: 1557-9603. doi: 10.1109/TAES.1986.310745.

[25] F. C. Robey et al. "A CFAR adaptive matched filter detector". In: *IEEE Transactions on Aerospace and Electronic Systems* 28.1 (1992), pp. 208–216. doi: 10.1109/7.135446.

[26] Antonio De Maio. "A new derivation of the adaptive matched filter". In: *IEEE Signal Processing Letters* 11.10 (2004), pp. 792–793. doi: 10.1109/LSP.2004.835464.

[27] E. Conte, M. Lops, and G. Ricci. "Adaptive detection schemes in compound-Gaussian clutter". In: *IEEE Transactions on Aerospace and Electronic Systems* 34.4 (Oct. 1998), pp. 1058–1069. issn: 1557-9603. doi: 10.1109/7.722671.

[28] Ismail Ben Atitallah et al. "Optimal Design of Large Dimensional Adaptive Subspace Detectors". In: *IEEE Transactions on Signal Processing* 64.19 (Oct. 2016), pp. 4922–4935. issn: 1941-0476. doi: 10.1109/TSP.2016.2573750.

[29] L. L. Scharf and B. Friedlander. "Matched subspace detectors". In: *IEEE Transactions on Signal Processing* 42.8 (Aug. 1994), pp. 2146–2157. issn: 1941-0476. doi: 10.1109/78.301849.

[30] S. Kraut, L. L. Scharf, and L. T. McWhorter. "Adaptive subspace detectors". In: *IEEE Transactions on Signal Processing* 49.1 (Jan. 2001), pp. 1–16. issn: 1941-0476. doi: 10.1109/78.890324.

[31] J. S. Bergin et al. "GMTI STAP in target-rich environments: site-specific analysis". In: *Proceedings of the 2002 IEEE Radar Conference (IEEE Cat. No.02CH37322)*. Apr. 2002, pp. 391–396. doi: 10.1109/NRC.2002.999750.

[32] Paul G. Kealey and David M. Carrington. *Robust radar detection of moving ground targets with STAP*. Oct. 2007. doi: 10.1049/cp:20070674.

[33] Huiyong Li et al. "A training samples selection method based on system identification for STAP". In: *Signal Processing* 142 (2018), pp. 119–124. issn: 0165-1684. doi: https://doi.org/10.1016/j.sigpro.2017.07.008. url: https://www.sciencedirect.com/science/article/pii/S0165168417302542.

[34] S. M. Kogon and M. A. Zatman. "STAP adaptive weight training using phase and power selection criteria". In: *Conference Record of Thirty-Fifth Asilomar Conference on Signals, Systems and Computers (Cat.No.01CH37256)*. Vol. 1. Nov. 2001, 98–102 vol.1. doi: 10.1109/ACSSC.2001.986887.

[35] Kristjan H. Greenewald, Edmund G. Zelnio, and Alfred O. Hero. "Kronecker STAP and SAR GMTI". In: *Algorithms for Synthetic Aperture Radar Imagery XXIII* (May 2016). Ed. by Edmund Zelnio and Frederick D.Editors Garber. doi: 10.1117/12.2223896. url: http://dx.doi.org/10.1117/12.2223896.

[36] Y.C. Eldar and G. Kutyniok. *Compressed Sensing: Theory and Applications*. Cambridge University Press, 2012. isbn: 9781107394391. url: https://books.google.de/books?id=9ccLAQAAQBAJ.

[37] A. De Maio, Y.C. Eldar, and A.M. Haimovich. *Compressed Sensing in Radar Signal Processing*. Cambridge University Press, 2019. isbn: 9781108576949. url: https://books.google.de/books?id=Oge5DwAAQBAJ.

[38] David Donoho and Jared Tanner. "Observed universality of phase transitions in high- dimensional geometry, with implications for modern data analysis and signal processing". In: *Philosophical Transactions of the Royal Society A: Mathematical, Physical and Engineering Sciences* 367.1906 (2009), pp. 4273–4293. doi: 10.1098/rsta.2009.0152.

[39] Shaobing Chen and D. Donoho. "Basis pursuit". In: *Proceedings of 1994 28th Asilomar Conference on Signals, Systems and Computers*. Vol. 1. Oct. 1994, 41–44 vol.1. doi: 10.1109/ACSSC.1994.471413.

[40] Peter J. Bickel, Ya'acov Ritov, and Alexandre B. Tsybakov. "Simultaneous analysis of Lasso and Dantzig selector". In: *arXiv e-prints*, arXiv:0801.1095 (Jan. 2008), arXiv:0801.1095. arXiv: 0801.1095 [math.ST].

[41] Amir Beck and Marc Teboulle. "A fast iterative shrinkage-thresholding algorithm for linear inverse problems". In: *SIAM Journal on Imaging Sciences* 2.1 (2009), pp. 183–202. url: https://www.ceremade.dauphine.fr/~carlier/FISTA.

[42] T. Blumensath and M. E. Davies. "Normalized Iterative Hard Thresholding: Guaranteed Stability and Performance". In: *IEEE Journal of Selected Topics in Signal Processing* 4.2 (Apr. 2010), pp. 298–309. doi: 10.1109/JSTSP.2010.2042411.

[43] Dohyung Park et al. *Finding Low-Rank Solutions via Non-Convex Matrix Factorization, Efficiently and Provably*. 2016. doi: 10.48550/ARXIV.1606.03168. url: https://arxiv.org/abs/1606.03168.

[44] Reinhard Panhuber and Ludger Prünte. "Step Size Determination for Finding Low-Rank Solutions Via Non-Convex Bi-Factored Matrix Factorization". In: *2020 28th European Signal Processing Conference (EUSIPCO)*. 2021, pp. 2100–2104. doi: 10.23919/Eusipco47968.2020.9287665.

[45] Jian-Feng Cai, Emmanuel J. Candès, and Zuowei Shen. *A Singular Value Thresholding Algorithm for Matrix Completion*. 2008. arXiv: 0810.3286 [math.OC].

[46] Raja Giryes and Deanna Needell. *Near Oracle Performance and Block Analysis of Signal Space Greedy Methods*. 2014. doi: 10.48550/ARXIV.1402.2601. url: https://arxiv.org/abs/1402.2601.

[47] M. Gavish and D. L. Donoho. "Optimal Shrinkage of Singular Values". In: *IEEE Transactions on Information Theory* 63.4 (Apr. 2017), pp. 2137–2152. doi: 10.1109/TIT.2017.2653801.

[48] Raghu Meka, Prateek Jain, and Inderjit S. Dhillon. *Guaranteed Rank Minimization via Singular Value Projection*. 2009. arXiv: 0909.5457 [cs.LG].

[49] Anastasios Kyrillidis and Volkan Cevher. *Matrix Recipes for Hard Thresholding Methods*. 2012. arXiv: 1203.4481 [cs.NA].

[50] Thierry Bouwmans, Necdet Serhat Aybat, and El-hadi Zahzah. *Handbook of robust low-rank and sparse matrix decomposition: Applications in image and video processing*. CRC Press, 2016.

[51] Venkat Chandrasekaran et al. "Rank-Sparsity Incoherence for Matrix Decomposition". In: *SIAM Journal on Optimization* 21.2 (Apr. 2011), pp. 572–596. issn: 1095-7189. doi: 10.1137/090761793. url: http://dx.doi.org/10.1137/090761793.

[52] Emmanuel J. Candès et al. "Robust Principal Component Analysis?" In: *CoRR* abs/0912.3599 (2009). arXiv: 0912.3599. url: http://arxiv.org/abs/0912.3599.

[53] Xiao Zhang, Lingxiao Wang, and Quanquan Gu. *A Unified Framework for Low-Rank plus Sparse Matrix Recovery*. 2017. doi: 10.48550/ARXIV.1702.06525. url: https://arxiv.org/abs/1702.06525.

[54] Junjie Ma, Xiaojun Yuan, and Li Ping. "Turbo Compressed Sensing with Partial DFT Sensing Matrix". In: *IEEE Signal Processing Letters* 22.2 (Feb. 2015), pp. 158–161. issn: 1558-2361. doi: 10.1109/LSP.2014.2351822.

[55] Zhipeng Xue, Junjie Ma, and Xiaojun Yuan. "Denoising-Based Turbo Compressed Sensing". In: *IEEE Access* 5 (2017), pp. 7193–7204. issn: 2169-3536. doi: 10.1109/ACCESS.2017.2697978.

[56] Xuehai He, Zhipeng Xue, and Xiaojun Yuan. "Learned Turbo Message Passing for Affine Rank Minimization and Compressed Robust Principal Component Analysis". In: *IEEE Access* 7 (2019), pp. 140606–140617. issn: 2169-3536. doi: 10.1109/ACCESS.2019.2942204.

[57] Zhipeng Xue et al. "TARM: A Turbo-Type Algorithm for Affine Rank Minimization". In: *IEEE Transactions on Signal Processing* 67.22 (Nov. 2019), pp. 5730–5745. issn: 1941-0476. doi: 10.1109/TSP.2019.2944740.

[58] Mohammadreza Malek-Mohammadi et al. "Successive Concave Sparsity Approximation for Compressed Sensing". In: *IEEE Transactions on Signal Processing* 64 (Nov. 2016), pp. 1–1. doi: 10.1109/TSP.2016.2585096.

[59] Reinhard Panhuber and Ludger Prünte. "Complex Successive Concave Sparsity Approximation". In: *2020 21st International Radar Symposium (IRS)*. 2020, pp. 67–72. doi: 10.23919/IRS48640.2020.9253770.

[60] E. J. Candès, C. A. Sing-Long, and J. D. Trzasko. "Unbiased Risk Estimates for Singular Value Thresholding and Spectral Estimators". In: *IEEE Transactions on Signal Processing* 61.19 (Oct. 2013), pp. 4643–4657. doi: 10.1109/TSP.2013.2270464.

[61] M. Malek-Mohammadi et al. "Recovery of Low-Rank Matrices Under Affine Constraints via a Smoothed Rank Function". In: *IEEE Transactions on Signal Processing* 62.4 (Feb. 2014), pp. 981–992. doi: 10.1109/TSP.2013.2295557.

[62] H. Ye et al. "A Novel Rank Approximation Method for Mixture Noise Removal of Hyperspectral Images". In: *IEEE Transactions on Geoscience and Remote Sensing* 57.7 (July 2019), pp. 4457–4469. doi: 10.1109/TGRS.2019.2891288.

[63] Stephen Tu et al. *Low-rank Solutions of Linear Matrix Equations via Procrustes Flow*. 2015. doi: 10.48550/ARXIV.1507.03566. url: https://arxiv.org/abs/1507.03566.

[64] Qinqing Zheng and John Lafferty. *Convergence Analysis for Rectangular Matrix Completion Using Burer-Monteiro Factorization and Gradient Descent*. 2016. doi: 10.48550/ARXIV.1605.07051. url: https://arxiv.org/abs/1605.07051.

[65] Thierry Bouwmans et al. "Decomposition into low-rank plus additive matrices for background/foreground separation: A review for a comparative evaluation with a large-scale dataset". In: *Computer Science Review* 23 (Feb. 2017), pp. 1–71. issn: 1574-0137. doi: 10.1016/j.cosrev.2016.11.001. url: http://dx.doi.org/10.1016/j.cosrev.2016.11.001.

[66] G.A. Watson. "Characterization of the subdifferential of some matrix norms". In: *Linear Algebra and its Applications* 170 (1992), pp. 33–45. issn: 0024-3795. doi: https://doi.org/10.1016/0024-3795(92)90407-2. url: https://www.sciencedirect.com/science/article/pii/0024379592904072.

[67] Mark K. Transtrum, Benjamin B. Machta, and James P. Sethna. "Geometry of nonlinear least squares with applications to sloppy models and optimization". In: *Phys. Rev. E* 83 (3 Mar. 2011), p. 036701. doi: 10.1103/PhysRevE.83.036701. url: https://link.aps.org/doi/10.1103/PhysRevE.83.036701.

[68] Laura Anitori and Joachim Ender. "Waveform Design for Sparse Signal Processing in Radar". In: *2021 IEEE Radar Conference*. May 2021, pp. 1–6. doi: 10.1109/RadarConf2147009.2021.9455313.

[69] Marc Jäger, Rolf Scheiber, and Andreas Reigber. "Robust, Model-Based External Calibration of Multi-Channel Airborne SAR Sensors Using Range Compressed Raw Data". In: *Remote Sensing* 11 (Nov. 2019). doi: 10.3390/rs11222674.

[70] Armin Walter Doerry et al. "Estimating Radar Velocity using Direction of Arrival Measurements". In: (Sept. 2014). doi: 10.2172/1323271. url: https://www.osti.gov/biblio/1323271.

[71] Christoph H. Gierull. *Digital channel balancing of along-track interferometric SAR data*. Defence R & D Canada-Ottawa, 2003. url: https://cradpdf.drdc-rddc.gc.ca/PDFS/unc06/p519189.pdf.

[72] Douglas L. Bickel. "A Concept for Platform Velocity Estimation Using a Multiphase Center Radar". In: (Nov. 2019). doi: 10.2172/1592858. url: https://www.osti.gov/biblio/1592858.

[73] André Barros Cardoso da Silva et al. "In-Flight Multichannel Calibration for Along-Track Interferometric Airborne Radar". In: *IEEE Transactions on Geoscience and Remote Sensing* 59.4 (2021), pp. 3104–3121. doi: 10.1109/TGRS.2020.3011287.

[74] Catalin Badea, Sophie Grivaux, and Vladimir Muller. *The rate of convergence in the method of alternating projections*. 2010. arXiv: 1006.2047 [math.FA].

[75] F.C. Robey et al. "A CFAR adaptive matched filter detector". In: *IEEE Transactions on Aerospace and Electronic Systems* 28.1 (Jan. 1992), pp. 208–216. issn: 1557-9603. doi: 10.1109/7.135446.

[76] D.K. Barton. *Radar Equations for Modern Radar*. Artech House radar library. Artech House, 2013. isbn: 9781608075218. url: https://books.google.de/books?id=n4FsPITxhK4C.

[77] R.B. Burckel and R. Remmert. *Theory of Complex Functions*. Graduate Texts in Mathematics / Readings in Mathematics. Springer New York, 1999. isbn: 9780387971957. url: https://books.google.de/books?id=CC0dQxtYb6kC.

[78] A. Hein. *Processing of SAR Data: Fundamentals, Signal Processing, Interferometry*. Signals and Communication Technology. Springer Berlin Heidelberg, 2013. isbn: 9783662094570. url: https://books.google.at/books?id=LCvrCAAAQBAJ.

[79] Simon Foucart and Holger Rauhut. *A Mathematical Introduction to Compressive Sensing*. 2013. isbn: 9780817649487 0817649484. doi: 10.1007/978-0-8176-4948-7.

[80] D.G. Zill and W.S. Wright. *Differential Equations with Boundary-Value Problems*. Cengage Learning, 2012. isbn: 9781111827069. url: https://books.google.de/books?id=0UX8e0xdOr0C.

[81] A. van den Bos. "Complex gradient and Hessian". In: *IEE Proceedings - Vision, Image and Signal Processing* 141.6 (Dec. 1994), pp. 380–383. issn: 1350-245X. doi: 10.1049/ip-vis:19941555.

[82] M. Malek-Mohammadi, M. Babaie-Zadeh, and M. Skoglund. "Iterative Concave Rank Approximation for Recovering Low-Rank Matrices". In: *IEEE Transactions on Signal Processing* 62.20 (Oct. 2014), pp. 5213–5226. doi: 10.1109/TSP.2014.2340820.

[83] Zhao Kang et al. "LogDet Rank Minimization with Application to Subspace Clustering". In: *Computational Intelligence and Neuroscience* 2015 (2015). doi: 10.1155/2015/824289.

[84] L. Wang, J. Hu, and C. Chen. "On Accelerated Singular Value Thresholding Algorithm for Matrix Completion". In: *Applied Mathematics* 5 (2014), pp. 3445–3451. doi: 10.4236/am.2014.521322. url: https://www.scirp.org/journal/paperinformation.aspx?paperid=52232.

[85] M. A. Davenport and J. Romberg. "An Overview of Low-Rank Matrix Recovery From Incomplete Observations". In: *IEEE Journal of Selected Topics in Signal Processing* 10.4 (June 2016), pp. 608–622. issn: 1932-4553. doi: 10.1109/JSTSP.2016.2539100.

[86] R. Descartes. "La géometrie (Discours de la méthode, third part)". In: 1637, p. 373.

[87] Xavier Glorot, Antoine Bordes, and Yoshua Bengio. "Deep Sparse Rectifier Neural Networks". In: *Proceedings of the Fourteenth International Conference on Artificial Intelligence and Statistics*. Ed. by Geoffrey Gordon, David Dunson, and Miroslav Dudík. Vol. 15. Proceedings of Machine Learning Research. Fort Lauderdale, FL, USA: PMLR, Nov. 2011, pp. 315–323. url: https://proceedings.mlr.press/v15/glorot11a.html.